

Proceedings of an International Conference on Transport, Atmosphere and Climate (TAC)

Oxford, United Kingdom, 26th to 29th June 2006



Edited by

Robert Sausen, Anja Blum, David S. Lee and Claus Brüning



DLR



Manchester
Metropolitan
University



Department for
Transport



<http://www.pa.op.dlr.de/tac/proceedings.html>

Edited by

Robert Sausen¹, Anja Blum¹, David S. Lee² and Claus Brüning³

Oberpfaffenhofen, September 2007

¹ Institut für Physik der Atmosphäre, Deutsches Zentrum für Luft- und Raumfahrt e.V., Oberpfaffenhofen, Germany

² Dalton Research Institute, Manchester Metropolitan University, Department of Environmental and Geographical Sciences, United Kingdom

³ European Commission, DG Research, Directorate Environment, Unit 'Climate Change and Environmental Risks', Brussels, Belgium

Foreword

The "International Conference on Transport, Atmosphere and Climate (TAC)" held in Oxford (United Kingdom), 2006, was organised with the objective of updating our knowledge on the atmospheric impacts of transport, three years after the "European Conference on Aviation, Atmosphere and Climate (AAC)" in Friedrichshafen (Lake Constance, Germany).

While the AAC conference concentrated on aviation, the scope was widened to include all modes of transport in order to allow a equitable comparison of the impacts on the atmospheric composition and on climate. In particular, the conference covered the following topics:

- engine emissions (gaseous and particulate),
- emission scenarios and emission data bases,
- near field and plume processes, effective emissions,
- impact on the chemical composition of the atmosphere,
- impact on aerosols,
- contrails, contrail cirrus, ship tracks,
- indirect cloud effects (e.g., aerosol-cloud interaction),
- radiative forcing,
- impact on climate,
- metrics for measuring climate change and damage,
- mitigation of transport impacts by technological means, i.e., environmental impacts of modifications to vehicles and engines (e.g., low NO_x engines, alternative fuels),
- mitigation of impacts by operational means (e.g., air traffic management, environmentally friendly flight and ship routing).

The conference was also a forum for dialogue of the QUANTIFY¹ project participants with the wider scientific community. At the same time, the conference marked the start of the EC funded project ATTICA², which has the objective of providing a "European Assessment of Transport Impacts on Climate Change and Ozone Depletion".

The conference benefited from substantial financial support from the United Kingdom Department for Transport and the European Commission's DG Research, to whom the organizers are extremely grateful.

139 participants attended the TAC conference and there were 60 oral and 33 poster presentations. Extended abstracts of most of the presentations are included in this book of proceedings. After peer review, a subset of the papers will be published in a special issue of the journal *Meteorologische Zeitschrift*.

Robert Sausen
Institut für Physik der Atmosphäre
Deutsches Zentrum für Luft- und Raumfahrt e.V.
Oberpfaffenhofen, Germany

David S. Lee
Dalton Research Institute
Manchester Metropolitan University
Manchester, United Kingdom

¹ QUANTIFY is an EC funded Integrated Project entitled "Quantifying the Climate Impact of Global and European Transport Systems", see also <http://ip.quantify.eu>.

² <http://ssa-attica.eu/>

Program Committee

Prof. Robert Sausen, DLR, Germany (chair)
Roger Gardner, DfT, United Kingdom (co-chair)
Dr. Claus Brüning, EC
Fritz Fleischer, MAN B&W, Germany
Dr. Sandro Fuzzi, ISAC, Italy
Dr. Don Grainger, University of Oxford, United Kingdom
Dr. Karlheinz Haag, Lufthansa, Germany
Dr. Dietrich Knörzer, EC
Prof. David S. Lee, MMU, United Kingdom (chair Local Organising Committee)
Dr. Anette Näs, FOI, Sweden
Olivier Penanhoat, SNECMA, France
Prof. Joyce Penner, University of Michigan, USA
Prof. John Pyle, University of Cambridge, United Kingdom
Dr. Claudia Stubenrauch, LMD, France
Tim Wallington, Ford, USA

Table of Contents

Foreword	2
Program Committee	4
Table of Contents	5
Conference Agenda	9
Poster session 1	13
Poster session 2	14

Engine emissions, emission inventories and scenarios

Light Duty Vehicle Emissions <i>T.J. Wallington, J.L. Sullivan</i>	16
Physico-Chemical Characterization of Soot Emitted by a Commercial Aircraft Engine: Morphology, Size, Structure, and Elemental Composition <i>D. Delhaye, E. Ruiz, D. Ferry, B. Demirdjian, J. Suzanne, O. Penanhoat, J. Gouge</i>	22
Development of an Emissions Database to Inform Comparisons of Various Transportation Modes <i>P.E. Yelvington, R.C. Miake-Lye, S.C. Herndon, E.C. Wood, T.B. Onasch</i>	27
In-Situ Microphysical Measurements In Rocket Plumes With The Cloud And Aerosol Spectrometer (CAS) <i>D. Baumgardner, M. Flores, G. L. Kok, D. Toohey, R. Hermann, M. Ross, T. Thompson, L. Avallone, L. Kalnajs</i>	34
Historical and future development of air transport fuel efficiency <i>P. M. Peeters, J. Middel</i>	42
Contracting UK carbon emissions: implications for UK aviation <i>K. Anderson, A. Bows</i>	48
Estimates of UK CO ₂ Emissions from Aviation Using Air Traffic Data <i>T. Pejovic, R.B. Noland, V. Williams, R. Toumi</i>	55
Global road transport's emission inventory for the year 2000 <i>H. Steller, J. Borken</i>	61
Forecasted Maritime Shipping Emissions for Belgium with an Activity Based Emission Model <i>L. Schrooten, I. De Vlieger, L. Int Panis, R. Torfs</i>	67

Near field and plume processes, effective emissions

Measurement method for emissions from inland navigation <i>A. Kraai, A. Hensen, G.P.A. Kos, H.P.J. de Wilde, J.H. Duyzer, H. Weststrate, J.C.Th. Hollander</i>	72
Particle Emissions from Ship Engines: Emission Properties and Transformation in the Marine Boundary Layer <i>A. Petzold, B. Weinzierl, M. Fiebig, M. Lichtenstern, P. Lauer, C. Gurk, K. Franke, E. Weingartner</i>	78
Aircraft-based Trace Gas Measurements in a Primary European Ship Corridor <i>H. Schlager, R. Baumann, M. Lichtenstern, A. Petzold, F. Arnold, M. Speidel, C. Gurk, H. Fischer</i>	83
Airport Emission Studies of Gaseous and Particulate Emissions <i>S.C. Herndon, E.C. Woods, M.J. Northway, T.B. Onasch, P.E. Yelvington, R.C. Miake-Lye, W. Berk Knighton</i>	89

Near field and plume processes, effective emissions

PM Emissions from Advected Aircraft Plumes at the Oakland International Airport <i>P.D. Whitefield, P. Lobo, D.E. Hagen</i>	95
Water- H ₂ SO ₄ - soot interaction in aircraft plume <i>O.B. Popovicheva, N.M. Persiantseva, A.M Starik, N.K. Shonija</i>	101
Numerical simulation of aircraft plumes using a mesoscale code <i>R. Paugam, R. Paoli, D. Cariolle, B. Cuenot</i>	107
Gas Turbine (Turbo Fan Engine) and IC Engine Emissions <i>H.-J. Bauer, U. Spicher</i>	116
Aerosol Evolution from a busy Road in North-West England <i>B. Davison, D. Whyatt, C Boardman</i>	133
Investigation of road traffic and wood burning emissions in Switzerland using a mobile laboratory <i>S. Weimer, C. Mohr, A.S.H. Prévôt, M. Mohr</i>	137

Impact on atmospheric composition

Results of the SCENIC project: impacts of supersonic aircraft emissions upon the atmosphere <i>Dessens O., H. L. Rogers, J.A. Pyle, C. Marizy, M. Gauss, G. Pitari</i>	141
Response in ozone and methane to small emission changes and dependence on cruise altitude <i>M.O. Köhler, O. Dessens, H.L. Rogers, O. Wild, J.A. Pyle</i>	147
Multi-model Simulations of the Impact of International Shipping on Atmospheric Chemistry and Climate in 2000 and 2030 <i>V. Eyring, A. Lauer, D.S. Stevenson, F.J. Dentener, T. Butler, M.G. Lawrence, W.J. Collins, M. Sanderson, K. Ellingsen, M. Gauss, I.S.A. Isaksen, D.A. Hauglustaine, S. Szopa, A. Richter, J.M. Rodriguez, S.E. Strahan, K. Sudo, O. Wild, T.P.C. van Noije</i>	154
Natural versus man-made trends in cirrus clouds <i>Kostas Eleftheratos, Christos S. Zerefos, Prodromos Zanis, George Tselioudis</i>	160

Impact on clouds

Application of LES and binned microphysics for sensitivity study on contrail evolution <i>W.W. Huebsch*, D.C. Lewellen</i>	167
Global distribution of ship tracks from one year of AATSR-data <i>M. Schreier, H. Bovensmann, H. Mannstein, V. Eyring</i>	173
Assessment of a Global Contrail Modelling Method <i>K. Klima, I. Waitz</i>	178
Probabilistic Forecast of Contrails within Cirrus Coverage <i>D. P. Duda, R. Palikonda, P. Minnis</i>	184

Radiative forcing and impact on climate

Climate sensitivity of radiative impacts from transport systems <i>M. Ponater, V. Grewe, R. Sausen, U. Schumann, S. Pechtl, E. J. Highwood, N. Stuber</i>	190
Results from pulse scenario experiments with the CNRM-CM3 global coupled model <i>D. Olivié, H. Teyssède, D. Salas-Méla, J.-F. Royer, F. Karcher, D. Cariolle</i>	196
Quantifying the effects of aviation on radiative forcing and temperature with a climate response model <i>L. Lim, D.S. Lee, R. Sausen, M. Ponater</i>	202
Radiative forcing and temperature response from shipping <i>D.S. Lee, L. Lim, V. Eyring, R. Sausen, Ø. Endresen, H.-L. Behrens</i>	208
Contrails, contrail cirrus, and ship tracks <i>K. Gierens</i>	214

Mitigation by technical and operational means

Novel engine concept to suppress contrail and cirrus cloud formation <i>F. Noppel, R. Singh, M. Taylor</i>	221
On how to consider the Earth's Atmosphere in Aircraft Design <i>R. Egelhofer, C. Marizy, C. Bickerstaff</i>	228
Operational impacts of trajectory adjustments to avoid ice supersaturated regions <i>V. Williams, R. B. Noland, R. Toumi R.</i>	235

POSTER SESSION 1

Engine emissions, emission inventories and scenarios

The effect of temporal resolution of PAH emission data on transport and deposition patterns simulated with the Community Multiscale Air Quality modelling system (CMAQ) <i>I. Bewersdorff, A. Aulinger, V. Matthias, M. Quante</i>	241
Physical Characterization of PM Emissions from In-Service Commercial Gas Turbine Engines – Projects APEX and JETS APEX2 <i>D.E. Hagen, P. Lobo, P.D. Whitefield</i>	247
Aircraft Emissions Characterization <i>S.C. Herndon, T.B. Onasch, J.T. Jayne, E.C. Wood, P.E. Yelvington, J. Wormhoudt, M.J. Northway, P. Mortimer, D.R. Worsnop, M.S. Zahniser, D.D. Nelson, J.H. Shorter, J.B. McManus and R.C. Miake-Lye, W. Berk Knighton, L.C. Marr, B.E. Anderson, C.-L. Wey, P.D. Whitefield</i>	252
New Aviation Scenarios for 2050 <i>B. Owen, D. S. Lee, L. Lim</i>	256

Near field and plume processes, effective emissions

SPIDER model process studies of aircraft plume dilution using simplified chemistry <i>N. Dotzek, R. Sausen</i>	261
---	-----

POSTER SESSION 2**Impact on clouds**

Aerodynamically induced formation of contrails <i>K. Gierens, B. Kärcher, H. Mannstein, B. Mayer</i>	267
Contrails in a global climate model – effect of reducing systematic errors <i>A. Guldberg</i>	273
Comparison of cirrus cloud coverage calculated from reanalysis meteorological data with satellite data <i>L. Lim, D.S. Lee, R. Ismail, R.G. Grainger, K. Gierens, M. Ponater</i>	279
Simulation of Contrails in the vortex regime – Examination of the microphysical properties <i>S. Unterstrasser, K. Gierens, P. Spichtinger</i>	284

Impact on atmospheric composition

Homogeneous freezing of ice particles, including effects of aerosol size distribution in the University of L'Aquila CCM <i>G. Pitari, D. Iachetti and V. Montanaro</i>	289
---	-----

Radiative forcing and impact on climate

Calculating contrail radiative forcing with the Edwards-Slingo radiative transfer code <i>R. Rodriguez de Leon, D.S. Lee</i>	295
---	-----

Mitigation by technical and operational means

Pedestrian exposure to vehicle emissions: the role of traffic signal timings <i>Muhammad M. Ishaque, R.B. Noland</i>	298
Potential methods to include the full climate impact of aviation emissions into the European Emissions Trading Scheme an their scientific integrity <i>D.S. Lee, R.C.N. Wit</i>	304
List of Participants:	309
Index of Authors	319

Conference Agenda

Sunday, 25 June 2006

- 18:00 Registration
20:00 End of Sunday registration time

Monday, 26 June 2006

- 08:30 Registration

Opening ceremony

Chair: Sausen

- 09:45 The Right Honourable Douglas Alexander MP, Secretary of State for Transport, UK:
Opening Address
- 10:05 Pierre Valette, Acting Director, European Commission, DG RTD I. Environment:
European Climate Research and Policy – the Role of Transport
- 10:20 Prof Frank Kelly, Chief Scientist DfT, UK:
Transport and Climate – the UK Perspective
- 10:35 Prof John Brooks, Vice Chancellor of Manchester Metropolitan University, UK:
Welcome Address
- 10:40 Prof Ulrich Schumann, Deutsches Zentrum für Luft- und Raumfahrt e.V., Germany:
Welcome Address on Behalf of the Board of DLR
- 10:45 Lee,
Introduction to Oxford

Opening ceremony

Chair: Lee

- 10:50 *Coffee*
- 11:20 Sausen, *An introduction to QUANTIFY*

Engine emissions, emission inventories and scenarios

- 12:00 Wallington, *Light Duty Vehicle Emissions*
- 12:20 Delhayé, Ferry, Demirdjian, Ruiz, Penanhoat, Gouge, Suzanne, *Physico-chemical characterization of soot emitted by a commercial aircraft engine: morphology, size, structure, and elemental composition*
- 12:40 Yelvington, Herndon, Wood, Onasch, Miake-Lye, *Development of an emissions database to inform comparisons of various transportation modes*
- 13:00 *Lunch*
- 14:00 North, Noland, Ochieng, Polak, *Modelling of particulate matter mass emissions from a light-duty diesel vehicle*
- 14:20 Wey, Anderson, Howard, Kinsey, Miake-Lye, Whitefield, *An overview of the aircraft particle emissions experiment (APEX) series*
- 14:50 Baumgardner, Kok, Avallone, Kalnajs, Herman, Ross, Thompson, Toohey, *In-Situ Microphysical Measurements In Rocket Plumes With The Cloud And Aerosol Spectrometer (CAS)*
- 15:10 Peeters, Middel, *Historical and future development of air transport fuel efficiency*
- 15:30 Bows, Anderson, *Contracting UK carbon emissions: implications for UK aviation*

Engine emissions, emission inventories and scenarios

- 15:50 *Tea* **Chair: Wallington**
- 16:10 Pejovic, Noland, Williams, Toumi, *Calculating UK CO₂ emissions using real air traffic data*
- 16:30 Steller, Borken, *First validation of a global road transport emission inventory for the year 2000*
- 16:50 Schrooten, De Vlieger, Int Panis, Torfs, *Forecasted maritime shipping emissions for Belgium with an activity based emission model.*

Near field and plume processes, effective emissions

- 17:10 Kraai, Hensen, Duyzer, Hollander, *Measurement method for emissions from inland navigation*
- 17:30 Petzold, Weinzierl, Lichtenstern, Schlager, Gurk, Franke, Weingartner, Baltensperger, *Particle Emissions from Ship Engines: Emission Properties and Transformation in the Marine Boundary Layer*
- 17:50 Schlager, Arnold, Petzold, Rappenglueck, Gurk, *Aircraft measurements in primary European ship corridors*
- 18:10 *End of presentations*
- 18:20 *Ice breaker*

Tuesday, 27 June 2006**Near field and plume processes, effective emissions****Chair: Schlager**

- 09:10 Miake-Lye, Herndon, Knighton, Onasch, Jayne, Northway, Wood, *Airport Emission Studies of Gaseous and Particulate Emissions*
- 09:30 Whitefield, Lobo, Hagen, *PM emissions from advected aircraft plumes at the Oakland International Airport*
- 09:50 Popovicheva, Starik, Persiantseva, Shonija, *Water-H₂SO₄-soot interaction in aircraft plume*
- 10:10 Paugam, Cariolle, Paoli, Cuenot, *Numerical Simulations of aircraft plumes using a meso scale code*
- 10:30 *Coffee* **Chair: Waitz**
- 11:00 Bauer, *Emissions of Gas Turbines and IC Engines*
- 11:40 Davison, Boardman, Whyatt, *Aerosol Evolution from a busy Road in North-West England*
- 12:00 Weimer, Mohr, Prévôt, Bach, Baltensperger, Lohmann, *Investigations of road traffic emissions in Switzerland using a mobile laboratory*

Impact on atmospheric composition

- 12:20 Dessens, Marizy, Simon, Grewe, Ramaroson, Pitari, Rogers, Pyle, *Results of the SCENIC project: impacts of supersonic aircraft emissions upon the atmosphere.*
- 12:40 Köhler, Dessens, Wild, Rogers, Pyle, *Changes in Ozone and Methane due to Aircraft NO_x: Sensitivity to Cruise Altitude*

Impact on atmospheric composition

- 13:00 *Lunch* **Chair: Penner**
- 14:00 Halenka, Huszar, Moldanova, *Ship emissions impact on atmospheric composition - case study*
- 14:20 Eyring, Stevenson, Lauer, Dentener, Butler, Collins, Ellingsen, Gauss, Hauglustaine, Lawrence, Rodriguez, Sanderson, Strahan, Sudo, van Noije, Wild, *Multi-model simulations of the impact of international shipping on atmospheric chemistry and climate in 2030*
- 14:40 Collins, Sanderson, *The impact of increasing ship emissions on air quality and deposition over Europe*
- 15:00 Introduction to posters I
- 15:30 *tea* **Chair: Grainger**
- 16:00 Poster Session I
- 17:00 Niemeier, Granier, *Simulation of future road and ship traffic impact on air pollution*

Impact on clouds

- 17:20 Minnis, Duda, Nguyen, Palikonda, Sun-Mack, *Analysis of missing contrail effects during USA air traffic shutdown*
- 17:40 Eleftheratos, Zerefos, Tselioudis, *Natural versus man-made trends in cirrus clouds*
- 18:00 *End of presentations*
- 18:15 *Walking tour*

Wednesday, 28 June 2006

Impact on clouds

Chair: Eyring

- 09:10 Mannstein, Krebs, *Contrail cirrus coverage and radiative forcing derived from satellite data*
- 09:30 Huebsch, Lewellen, *Sensitivity Study on Contrail Evolution*
- 09:50 Dedesh, Grigoryev, *Development of methods to research atmosphere contaminations, conditions of formation and composition of airplanes' condensation trails*
- 10:10 Fichter, *How to prepare your proceedings contribution*
- 10:30 *Coffee* **Chair: Schumann**
- 11:00 Shine, Metrics
- 11:40 Penner, Chen, *Effects of soot aerosols from aircraft on cirrus clouds*
- 12:00 Devasthale, Grassl, *Detection and quantification of impact of traffic emissions on clouds*
- 12:20 Schreier, Mannstein, Eyring, Bovensmann, *Global Distribution of ship tracks from one year of AATSR data*
- 12:40 Klima, Waitz, Baughcum, *Assessment of a Global Contrail Modeling Method*
- 13:00 *Lunch* **Chair: Fuglestedt**
- 14:00 Duda, Palikonda, Minnis, *Probabilistic Forecast of Contrails within Cirrus Coverage*

Radiative forcing and impact on climate

- 14:20 Stuber, Forster, Rädcl, Shine, *The importance of the diurnal and annual cycle of air traffic for contrail radiative forcing*
- 14:40 Grewe, Stenke, Ponater, Sausen, Pitari, Iachetti, Rogers, Dessens, Pyle, Isaksen, Gulstad, Marizy, Pascuillo, *Climate impact of supersonic air traffic: An approach to optimize a potential future supersonic fleet – Results from the SCENIC EU-project*
- 15:00 Introduction to posters II
- 15:30 *tea* **Chair: Moldanová**
- 16:00 Poster Session II
- 17:00 Fuglestedt, Berntsen, Myhre, Rypdal, Bieltvedt Skeie, *Climate Impacts of Transport Systems: Chemical responses and radiative forcing*
- 17:20 Rädcl, Shine, *Sensitivity of radiative forcing due to aircraft altitude*
- 17:40 Ponater, Pechtl, Grewe, Matthes, Sausen, Schumann, *Climate Sensitivity of Radiative Impacts from Transport Systems*
- 18:00 *End of presentations*
- 19:30 *Banquet*

Thursday, 29 June 2006**Radiative forcing and impact on climate****Chair: Shine**

- 09:10 Olivié, Teyssèdre, Salas-Mélia, Cariolle, Royer, Karcher, *Results from pulse scenario experiments with the CNRM-CM3 global coupled model*
- 09:30 Lim, Lee, Sausen, *A climate response model for calculating aviation effects*
- 09:50 Lukachko, Waitz, Marais, *Valuing the Impact of Aviation on Climate*
- 10:10 Lee, Eyring, Lim, Sausen, *Radiative forcing and temperature response from global shipping emissions*
- 10:30 *Coffee* **Chair: Minnis**
- 11:00 Gierens, Contrails, contrail cirrus and ship tracks

Mitigation by technical and operational means

- 12:00 Noppel, Singh, Taylor, *Clean Exhaust Engine Concept*
- 12:20 Egelhofer, Marizy, Bickerstaff, *On how to consider the Earth's atmosphere in aircraft design*
- 12:40 Edwards, *The reduction of transport emissions in Jamaica through the manipulation of road network condition*
- 13:00 *Lunch* **Chair: Sausen**
- 14:00 Williams, Noland, Toumi, *Operational impacts of trajectory adjustments to avoid ice-supersaturated regions*

Concluding Session

- 14:20 *Summary, conclusions, awards, ...*
- 15:30 *tea*

LIST OF POSTERS

Poster session 1

Engine emissions, emission inventories and scenarios

- Anderson, Bows: *The neglect of international aviation and shipping emissions has led to serious flaws in the UK's climate change targets*
- Anderson, Winstead, Chen, Hudgins, Thornhill: *Concentrations and characteristics of particles within commercial aircraft exhaust plumes*
- Bewersdorff, Aulinger, Matthias: *The effect of temporal resolution of PAH emission data on transport and deposition patterns simulated with the Community Multiscale Air Quality Model (CMAQ)*
- Hagen, Lobo, Whitefield: *Physical Characterization of PM emissions from In-service Commercial Gas Turbine Engines – Projects APEX and JETS APEX2*
- Miake-Lye, Herndon, Knighton, Onasch, Jayne, Northway, Wood, Wormhoudt, Yelvington: *Aircraft Engine Emissions Characterization in APEX-series Measurement Studies*
- Middel, Berghof: *Quantification of Constrained Scenarios on Aviation and Emissions (CONSAVE 2050)*
- Owen, Lee, Lim: *New aviation scenarios for 2050*
- Petron, Miller, Frost, Peters, Bruhwiler, Tans: *Transportation and the Carbon Cycle*

Near field and plume processes, effective emissions

- Dotzek, Sausen: *SPIDER model process studies of aircraft plume dilution using simplified chemistry*
- Franke, Eyring, Sander, Lauer, Hendricks, Sausen, Bovensmann: *Ship emissions in the marine boundary layer: Ozone production and effective emissions*
- Moldanová, Schlager: *Ship plume chemistry – a model study*
- Paoli, Garnier, Mirabel, Cuenot: *Large-eddy simulation of a turbulent jet and wake vortex interaction: particle formation and evolution in the near-field of an aircraft*
- Velchev, Vignati, Hjorth, Dentener, Raes: *Measurements of ozone and Black Carbon along a Mediterranean cruise track during the winter season 2005-2006 ; comparison with TM5 model*

Poster session 2

Impact on clouds

Gierens, Kärcher, Mannstein, Mayer: *Aerodynamically induced condensation trails*

Guldberg: *Contrails in a global climate model – effect of reducing systematic errors*

Lim, Lee, Gierens, Ponater, Ismail, Grainger: *Comparison of cirrus cloud coverage from ECMWF and NCEP data compared with GRAPE data*

Palikonda, Minnis, Duda, Ayers, Garber: *Diurnal and Inter-annual variability of Contrail Coverage derived from AVHRR data over continental United States of America and surrounding areas.*

Samuelson, Davison, MacKenzie: *Seasonal and spatial variation in contrail cover over the UK (2001-2006)*

Unterstrasser, Gierens: *Initial conditions for contrail-to-cirrus transition*

Impact on atmospheric composition

Meijer, Velthoven: *The importance of wet deposition for the different transport modes*

Pitari, Iachetti, Montanaro: *Homogeneous freezing of ice particles, including effects of aerosol size distribution in the University of L'Aquila CCM.*

Radiative forcing and impact on climate

Meyer, Matheys, Van Mierlo, Macharis, Matthews, van Ypersele: *Aviation and the Belgian Climate Policy : Integration Options and Impacts - ABC Impacts*

Rodriguez de Leon, Lee: *Calculating contrail RF with the Edwards-Slingo radiative transfer code*

Teyssèdre, Olivié, Michou, Chéroux, Karcher, Cariolle: *On the coupling of the MOCAGE-Climat CTM with the CNRM climatic system*

Mitigation by technical and operational means

Ishaque, Noland: *Pedestrian exposure to vehicle emissions: The role of traffic signal timings*

Lee, Wit: *Potential methods to include the full climate impact of aviation emissions into the European Emissions Trading Scheme and their scientific integrity*

Mannstein, Spichtinger, Gierens: *How to avoid contrail cirrus*

Ponater, Pechtl, Sausen, Schumann, Hüttig: *Climate Impact Reduction due to Cryoplane Introduction: A state-of-the-art assessment*

Salami, Idowu, Balogun: *West African weather Systems in the development of tropical cyclones*

Extended Abstracts

Light Duty Vehicle Emissions

T.J. Wallington*, J.L. Sullivan

Research and Advanced Engineering, Ford Motor Company, Dearborn, MI 48121-2053, USA

Keywords: Light Duty Vehicles, CO, CO₂ HC, NO_x, PM, HFC-134a, CH₄, N₂O emissions

ABSTRACT: Vehicles emit carbon dioxide (CO₂), carbon monoxide (CO), nitrogen oxides (NO_x), hydrocarbons (HC), particulate matter (PM), hydrofluorocarbon 134a (HFC-134a), methane (CH₄), and nitrous oxide (N₂O). An understanding of these emissions is needed in discussions of climate change and local air pollution issues. To facilitate such discussions an overview of past, present, and likely future emissions from light duty vehicles is presented. Emission control technologies have reduced the emissions of CO, VOCs, PM, HFC-134a, CH₄, and N₂O from modern vehicles to low levels.

1. INTRODUCTION

Recognition of the contribution of vehicle emissions to local air pollution and climate change has led to a considerable research effort focussed on understanding the nature and quantity of vehicle emissions and developing control technologies to reduce these emissions. We present an overview of six important aspects of light duty (< 8,500 lbs) vehicle emissions. First, the life-cycle CO₂ emissions from a typical vehicle. Second, the historical data for emissions of HC, CO, and NO_x. Third, the use of diesel particulate filter technology to mitigate PM emissions. Fourth, the magnitude of R-134a, N₂O, and CH₄ emissions from the global vehicle fleet. Fifth, the projections of CO, VOC, NO_x, and PM emissions from the global vehicle fleet up till 2050. Finally, the options to reduce the vehicle life cycle CO₂ emissions.

2. LIFE CYCLE CO₂ EMISSIONS

The life cycle CO₂ emissions for a typical mid-sized car in the US are given in Table 1. The "in-use" portion (fuel combustion) accounts for approximately 90% of the life cycle CO₂ emissions. Reducing the life cycle CO₂ emissions requires careful attention to the in-use portion.

Table 1: Life cycle CO₂ impact for typical mid-sized car

	Tonnes of CO ₂	% of total
Raw material production (steel, aluminium, plastics, ...)	3.5	5.7%
Ford manufacturing/assembly	2.5	4.0%
Manufacturing logistics	0.1	0.2%
Fuel (120,000 miles at 22.9 miles per US gallon) WTW ¹	55.1	88.9%
Maintenance and repair	0.6	1.0%
End of life/recycling	0.1	0.2%
Total Lifecycle	61.9	100%

¹ well to wheels analysis

3. HC, CO, AND NO_x EMISSIONS

Incomplete combustion leads to the presence of hydrocarbons (HC) and carbon monoxide (CO) in vehicle exhaust. Formation of NO by the Zeldovich mechanism (Zeldovich, 1946) leads to the

* Corresponding author: T. J. Wallington, Research & Advanced Engineering, Ford Motor Company, Dearborn, MI 48121-2053, USA. Email: twalling@ford.com

emission of NO_x. Recognition of the contribution of vehicle exhaust to the formation of photochemical smog in large urban areas such as Los Angeles in the 1950s led to the adoption of regulations controlling vehicle emissions starting in the 1960s in California. The development of vehicle emission control technology over the past 4 decades has led to large decreases in the emissions from new vehicles (per mile driven) as illustrated in Table 2.

Table 2. Historical perspective on vehicle HC, CO, and NO_x emissions

Year	HC (g/mile)	CO (g/mile)	NO _x (g/mile)
1957-1962 US Fleet ¹	8.8	81.6	3.7
1963-1967 US Fleet ¹	9.1	92.8	3.5
1963-1967 US Fleet ¹	4.7	58.7	4.9
1975/1976 US Federal	1.5	15	3.1
1991 US Federal	0.41	3.4	1.0
1994 US Federal	0.41	3.4	0.4
2000 Europe Stage III ^{2,3}	0.32	3.8	0.24
2004 US Federal	0.125	1.7	0.2
2005 Europe Stage IV ^{2,4}	0.16	1.6	0.13
2007 US Federal ^{5,6}	0.075	3.4	0.05

¹ from Table 3 in Fegraus et al., 1973;

² gasoline;

³ 80 K km;

⁴ 100 K km;

⁵ Tier II bin 5 average requirement;

⁶ 50 K mile

Data for the 1957-1967 fleet are averages from several hundred vehicles tested in the laboratory. The more recent data are regulatory standards which new vehicles must meet. As seen from Table 2, there has been major and continuing progress in reducing the emissions of HC, CO, and NO_x from new vehicles. Over the past 40 years the emissions (g/mile) of hydrocarbons and CO has declined by approximately 2 orders of magnitude. NO_x emissions have declined by a factor of forty. It should be noted that because of increases in the vehicle fleet the reductions in the total emissions from the global vehicle fleet do not parallel those given in Table 2. However, as discussed in section 6, in spite of projected increases in the on-road vehicle fleet, the total emissions of "criteria" pollutants (ie, HC, CO, NO_x, and PM) are projected to decline substantially in the coming decades.

4. PARTICULATE MATTER (PM)

Combustion in diesel engines is initiated by spraying liquid diesel fuel into the combustion cylinder. Combustion in gasoline engines is initiated by a spark which ignites a homogeneous mixture of gasoline vapor and air. Diesel exhaust contains more PM (by a factor of approximately 50-100 on a mass basis) than gasoline exhaust. The higher particulate emissions arise from the incomplete combustion of liquid fuel droplets near the fuel injector. Although most of the particulates are burned by the excess O₂ in the cylinder before leaving the engine, some survive and leave in the engine-out exhaust as small particles (10-100 nm diameter). Control of particulate emissions is a significant issue for diesel engines. The recent development of diesel particulate filters (DPFs) that filter solid particles from the exhaust constitutes a significant advance in emissions control. As indicated in Figure 1, DPFs are highly effective at reducing exhaust PM to very low levels. DPFs have been introduced commercially and seem likely to become widely used in areas where PM emissions are a concern. As of July 2005 over 1 million DPF equipped vehicles had been sold by PSA Peugeot Citroën. The Ford Motor Company will equip diesel vehicles with DPFs starting in 2007 in the US and in 2005 in Europe. As discussed in section 6, the increased use of DPFs in the on-road vehicle fleet will contribute to the projected decline in PM emissions in the coming decades.

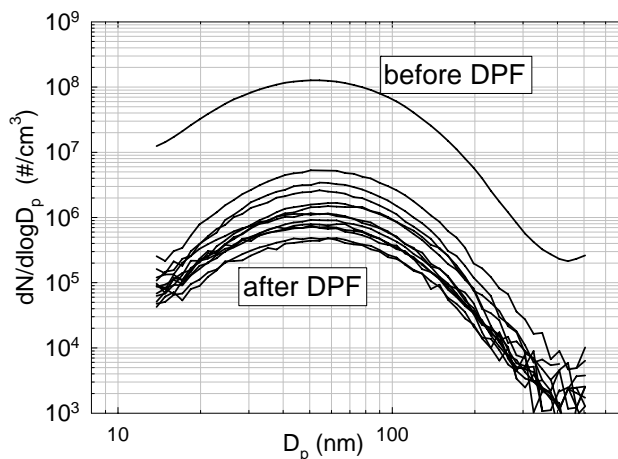


Figure 1: Illustration of Diesel Particulate Filter effectiveness (adapted from Guo et al., 2003).

5. HYDROFLUOROCARBON-134A (CF₃CH₂F), NITROUS OXIDE (N₂O), METHANE (CH₄)

Hydrofluorocarbon-134a (also known as HFC-134a, R-134a, or CF₃CH₂F) is used as the replacement for CFC-12 (also known as R-12 or CF₂Cl₂) in vehicle air conditioning units. There are four emission modes of R-134a from vehicles; regular, irregular, servicing, and disposal. Regular loss refers to the slow leakage from hoses and seals. Irregular losses are caused by failures of the system. As their names suggest, servicing and disposal losses are incurred during servicing and disposal of the vehicle. The results from several studies of R-134a emission have been reported. Schwarz et al. (2001) give a total emission per vehicle of 0.24 ± 0.06 g/day. Siegl et al. (2002) estimate a total emission rate of 0.41 ± 0.27 g/day. Stemmler et al. (2004) determined the sum of regular and irregular loss to be 0.336 g/day. Finally, Vincent et al. (2004) estimate a total emission rate of 0.24 g/day. Within the likely experimental uncertainties, there is reasonable agreement between the results of the studies. Assuming 0.3 ± 0.1 g/day emission, 10000 miles per year travelled, 25 miles per US gallon fuel economy, and a global warming potential for R-134a of 1300 (100 year time horizon) Siegl et al. (2002) estimated that the global warming impact of R-134a leakage from an AC equipped vehicle is approximately 3-5% of that of the CO₂ emitted by the vehicle.

Nitrous oxide (N₂O) is produced as an intermediate during the reduction of NO_x in three way catalyst systems. Some N₂O escapes further reduction to N₂ and exits with the exhaust flow through the tailpipe into the atmosphere. N₂O has a global warming potential of 330 (100 year time horizon) and is an important greenhouse gas. Several studies of the emissions of N₂O from vehicles have been performed over the past 15 years. Berges et al. (1993) reported emission factors (g of N₂O/g of CO₂) of $(6 \pm 3) \times 10^{-5}$ and $(14 \pm 9) \times 10^{-5}$ from tunnel studies in 1992 in Germany and Sweden, respectively. Becker et al. (1999, 2000) reported emission factors of $(6 \pm 2) \times 10^{-5}$ and $(4.1 \pm 1.2) \times 10^{-5}$ from tunnel studies in Germany in 1997. Jimenez et al. (2000) used open path, cross road laser techniques to measure emission factors of $(8.8 \pm 2.8) \times 10^{-5}$ and $(12.8 \pm 0.39) \times 10^{-5}$ from on-road vehicles in California in 1996 and New Hampshire in 1998, respectively. Becker et al. (2000) conducted a laboratory dynamometer study of 26 light duty cars and trucks and measured an average N₂O emission of 12 ± 8 mg/km. Behrentz et al. (2004) conducted a similar test using 37 vehicles and found an emission rate of 20 ± 4 mg/km. Huai et al. (2004) studied 60 vehicles, nearly half of which had N₂O emission rate < 10 mg/mile. Emission rates from the remaining vehicles varied significantly with the highest emissions being observed for older catalyst technologies. The results from all these studies are in broad agreement (within a factor of 2). Becker et al. (1999) have estimated that N₂O emissions from vehicles have a global warming impact which is 1-3% of that of the CO₂ emissions from vehicles.

Methane (CH₄) is produced in small quantities by combustion reactions occurring in internal combustion engines. Nam et al. (2004) analyzed CH₄ emissions from 30 different cars and trucks and recommended use of an emission factor (g of CH₄/g of CO₂) of $(15 \pm 4) \times 10^{-5}$ for the US on-road fleet. Using a global warming potential of 23, Nam et al. (2004) calculated that the global warming impact of CH₄ emissions from vehicles is 0.3-0.4% of that of the CO₂ emissions from ve-

hicles. The environmental impact of CH₄ emissions from vehicles is negligible and likely to remain so for the foreseeable future.

6. PROJECTIONS OF FUTURE HC, CO, NO_x AND PM EMISSIONS

The International Energy Agency (IEA) and World Business Council for Sustainable Development (WBCSD) have developed the Sustainable Mobility Project (SMP) spreadsheet model (<http://www.wbcd.org>) which projects emissions from global transportation over the time period 2000-2050. Many of the world's leading automotive related companies were involved in developing the model (WBCSD, 2004).

Figure 2 shows the projected increase in CO₂ emissions in the SMP Reference Case (WBCSD, 2004). Figure 3 shows the projected decrease in NO_x emissions. The top panels give the emissions from Organization of Economic Cooperation and Development, (OECD) countries, the bottom panels give the projected emissions from non-OECD countries. Emissions reductions for CO, HC, and PM are projected to be comparable to those for NO_x. Large reductions in the emissions of HC, CO, NO_x, and PM are anticipated from the on-road global vehicle fleet over the coming decades. The projected decreases reflect the diffusion of modern emission control technology into the on-road fleet.

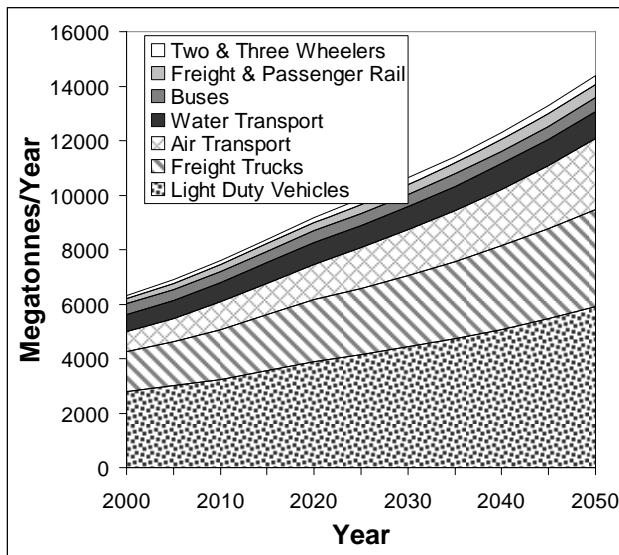


Figure 2: Projected transportation CO₂ emissions in the SMP Reference Case (WBCSD, 2004).

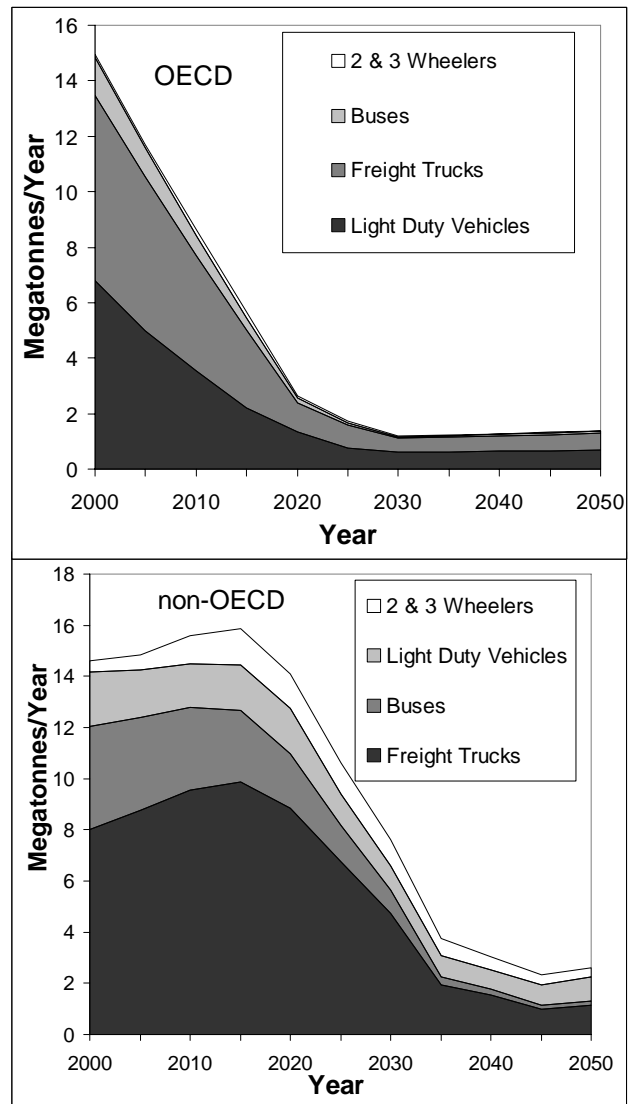


Figure 3: Projected NO_x emissions from OECD (top panel) and non-OECD (bottom panel) countries in SMP Reference Case (WBCSD, 2004).

7. OPTIONS TO REDUCE LIFE CYCLE CO₂ EMISSIONS

Options to reduce vehicle life-cycle CO₂ emissions include: (i) ecodriving, (ii) weight reduction, (iii), power reduction, (iv) dieselization, (v) hybrid technology, (vi) biomass derived fuels, (vii) electric vehicles, (viii) hydrogen internal combustion engine (H₂ICE) vehicles, and (ix) hydrogen fuel cell vehicles.

Ecodriving refers to driving in an ecological and economical fashion (driving at posted speed limits, accelerating smoothly, braking gradually, ensuring for proper tire pressure, replacing air filters as needed, using appropriate engine oils, etc.). Reducing the weight of the vehicle reduces its energy consumption, light weight magnesium and aluminium alloys are finding increased use in automotive applications. The life cycle CO₂ benefit associated with vehicle weight reduction by material substitution depends on the material (aluminum, magnesium, fiber composites, etc.) replacing the base case material (usually steel) and/or iron) and the efficiency of the powertrain efficiency. There is a tradeoff between the extra energy almost always usually required to make an "alternative material" relative to its ferrous counterpart and the operational energy saved in reducing the vehicle inertial weight. As the energy efficiency of the powertrain increases, the life cycle energy and carbon dioxide emissions benefit of weight reduction decreases (Sullivan et al.; 1995, 1998). For today's vehicles, weight reduction via material substitution is generally beneficial. Reducing the power of the engine reduces its energy requirement but also reduces the vehicle's performance which is not desirable. Diesel engines are more efficient than gasoline engines for two main reasons. First, diesels do not suffer from the pumping losses associated with the throttling necessary in gasoline engines. Second, diesel engines operate at a higher compression ratio than gasoline engines. Motivated by a desire to increase the fuel efficiency of their vehicles, automobile manufacturers are exploring new technologies which will make gasoline engines more diesel-like in their operation. Sullivan et al. (2004) have estimated that on a well-to-wheels per vehicle per mile basis, the CO₂ reduction opportunity for replacing a gasoline vehicle with its equivalent diesel counterpart was 24-33% in 2004 and will decrease to 14-27% by 2015.

Hybrid vehicles are propelled down the road by a combination of an electric motor and an internal combustion engine (gasoline for all hybrids currently on the market). All the energy used to propel the vehicle comes from chemical energy in the gasoline in the fuel tank (although the battery alone can propel the vehicle, the energy in the battery comes from combustion of gasoline). Regenerative braking is used to capture energy during braking and charge the battery. When there is little, or no load, on the engine (e.g. stopped at lights, travelling slowly in congested traffic) the gasoline engine shuts down to save fuel. Hybrid vehicles offer substantial fuel savings in city driving but offer more modest savings in highway driving. The 2.3 L Ford Hybrid Escape has city and highway fuel economies of 36 and 31 miles per US gallon. The 2.3 L Ford Escape has city and highway fuel economies of 23 and 26 miles per US gallon.

The use of biomass derived fuel such as ethanol or biodiesel can lead to a significant reduction in the well-to-wheels CO₂ emissions. In principal, if little, or no, fossil fuel is used in the production of the biofuel then the net CO₂ emissions associated with combustion of the fuel in the vehicle will approach zero. As seen from Table 1, fuel combustion accounts for approximately 90% of the vehicle life cycle CO₂ emissions. Hence, in principle, the use of biofuels offers an opportunity to reduce the CO₂ emissions significantly. At the present time it is unclear whether biofuels can be produced with sufficiently low fossil fuel inputs, in sufficient quantities, and at sufficiently low cost to make a major impact. Biofuels are an area of current research interest.

Electric vehicles do not emit CO₂ and, if the electricity used to charge the battery has a low fossil fuel burden, then the use of electric vehicles would lead to a decrease in CO₂ emissions. The mass use of electric vehicles awaits the development of cheap, robust, high energy density, rapidly rechargeable batteries. Hydrogen can be burnt in internal combustion engines (H₂ICE) or used in fuel cells. Hydrogen fuel cell vehicles have received considerable attention due to their potential to be much more efficient than gasoline vehicles on the road today. However, there are formidable technical challenges to be overcome before hydrogen will see mass use as a transportation fuel. These include: the high cost and environmental impacts associated with hydrogen production and distribution; low energy density, which makes storing sufficient hydrogen on a vehicle difficult; fuel cell cost; and fuel cell durability.

8. CONCLUSIONS

Vehicles emit carbon dioxide (CO₂), carbon monoxide (CO), nitrogen oxides (NO_x), hydrocarbons (HC), particulate matter (PM), hydrofluorocarbons-134a (HFC-134a), methane (CH₄), and nitrous oxide (N₂O). There has been substantial progress in reducing the emission of criteria pollutants (CO, NO_x, HC, PM) linked to photochemical air pollution. Emissions of CO, NO_x, HC, PM, HFC-134a, CH₄, and N₂O are small and/or short term issues. CO₂ is a large and long term issue.

ACKNOWLEDGEMENTS

We thank Matti Maricq (Ford Motor Company) for helpful discussions.

REFERENCES

- Becker, K.H., J.C. Lörzer, and R. Kurtenbach, P. Wiesen, T.E. Jensen, and T.J. Wallington, 1999, Nitrous oxide (N₂O) emissions from vehicles, *Environ. Sci. Technol.*, *33*, 4134.
- Becker, K.H., J.C. Lörzer, and R. Kurtenbach, P. Wiesen, T.E. Jensen, and T.J. Wallington, 2000, Contribution of vehicle exhaust to the global N₂O budget, *Chemosphere Global Change Sci.*, *2*, 387.
- Behrentz, E., R. Ling, P. Rieger, and A.M. Winer, 2004, Measurements of nitrous oxide emissions from light-duty motor vehicles: a pilot study, *Atmos. Environ.*, *38*, 4291.
- Fegraus, C.E., C.J. Domke, and J. Marzen, 1973, Contribution of the vehicle population to atmospheric pollution, *Society of Automotive Engineers Paper 730530*.
- Guo, G., N. Xu, P.M. Laing, R.H. Hammerle, and M.M. Maricq, 2003, Performance of a catalyzed diesel particulate filter system during soot accumulation and regeneration, *Society of Automotive Engineers Paper 2003-01-0047*.
- Huai, T., T.D. Durbin, J.W. Miller, and J.M. Norbeck, 2004, Estimates of emission rates from light-duty vehicles using different chassis dynamometer test cycles, *Atmos. Environ.*, *38*, 6621
- Jimenez, J.L., J.B. McManus, J.H. Shorter, D.D. Nelsen, M.S. Zahniser, M. Koplw, G.J. McRae, C.E. Kolb, 2000, *Chemosphere Global Change Sci.*, *2*, 397.
- Nam, E.K., T.E. Jensen, and T.J. Wallington, 2004, Methane emissions from vehicles, *Environ. Sci. Technol.*, *38*, 2005.
- Schwartz, W., 2001, Emission of Refrigerant R-134a from Mobile Air-Conditioning Systems, Öko-Recherche, Frankfurt am Main, Report 360 09 006.
- Schwarz, W., and J. Harnish, 2003, Establishing the leakage rates of mobile air conditioners, Final report B4-3040/2002/337136/MAR/C1, European Commission.
- Stemmler, K., S. O'Doherty, B. Buchmann, and S. Reimann, 2004, Emissions of the refrigerants HFC-134a, HCFC-22, and CFC-12 from road traffic: results from a tunnel study (Gubrist Tunnel, Switzerland), *Environ. Sci. Technol.*, *38*, 1998.
- Sullivan, J.L., R.E. Baker, B.A. Boyer, R.H. Hammerle, T.E. Kenney, L. Muniz, T.J. Wallington, 2004, CO₂ emission benefit of diesel (versus gasoline) powered vehicles, *Environ. Sci. Technol.*, *38*, 3217.
- Sullivan, J.L., and J. Hu, 1995, Life Cycle Energy Analysis for Automobiles, Proceedings of the 1995 Total Life Cycle Conference, *Society of Automotive Engineers Paper 951829*
- Sullivan, J.L., M. Costic, and W. Han, 1998, Automotive life cycle assessment: overview, metrics, and examples, SAE Congress, Spring 1998, *Society of Automotive Engineers Paper 980467*
- Vincent, R., K. Cleary, A. Ayala and R. Corey, 2004, Emissions of HFC-134a from light-duty vehicles in California, *Society of Automotive Engineers Paper 2004-01-2256*.
- World Business Council for Sustainable Development, 2004, Mobility 2030: meeting the challenges to sustainability, ISBN: 2-940240-57-4, Geneva, Switzerland.
- Zeldovich, J., 1946, The oxidation of nitrogen in combustion and explosions, *Acta Physicochimica URSS*, *21*,4.

Physico-Chemical Characterization of Soot Emitted by a Commercial Aircraft Engine : Morphology, Size, Structure, and Elemental Composition

D. Delhaye, E. Ruiz
ONERA, DMPH/EAG, BP-72, F-92322, Châtillon, France

D. Ferry^{*}, B. Demirdjian, J. Suzanne
CRMCN-CNRS (UPR 7251), Campus de Luminy, Case 913, F-13288 cedex 9, Marseille, France

O. Penanhoat, J. Gouge
SNECMA, Villaroche center, Rond point René Ravaud, F-77550, Moissy-Cramayel, France

Keywords: soot morphology, size distribution, structure, electron microscopy

ABSTRACT: We present here experimental studies performed on soot particles collected from a commercial aircraft engine. Electron microscopy techniques are used to determine the morphology, the microstructure, and the size distribution of primary soot particles. Their elemental composition is also determined as well as their vibrational characteristics by the mean of X-ray energy dispersive spectrometry and Fourier transform infrared spectroscopy.

1 INTRODUCTION

Nowadays, understanding the aviation's impact on the radiative forcing, climate change, air quality and human health is a challenging task (J.E. Penner *et al.*, 1999). Although only a few percent of the global fuel is used by air traffic, the major part of aircraft exhausts is emitted into sensitive atmospheric regions, namely the troposphere and lower stratosphere. Carbonaceous particles, such as aircraft engine soot, released in the upper troposphere are a major concern with regards to climate response impacts. Indeed, aviation-produced soot aerosols are suspected to enhance contrails and cirrus formation (Schumann *et al.*, 2002 ; Schumann, 2005), giving rise to a positive radiative forcing (Seinfeld, 1998). Numerous observations have shown that persistent contrails can evolve into extensive artificial cirrus clouds (Seinfeld, 1998 ; Schröder *et al.*, 2000) and the potential modification of natural cirrus caused by aircraft-produced carbonaceous particles via heterogeneous ice nucleation (Lohmann *et al.*, 2004) have been estimated with general circulation models. However, results obtained with these models largely depend on their ability to represent the sources, transport pathways, and sinks of various aerosol types in the atmosphere. Recent climate models with sophisticated aerosol modules have been developed (Stier *et al.*, 2005 ; Lauer *et al.*, 2005) but they need to be complemented by field and laboratory measurements with regard to the physico-chemical properties of atmospheric aerosols as well as their ice nucleation properties. In spite of many efforts undertaken to date by the scientific community, there is still a lack of knowledge about the structure, the morphology, the composition, and the reactivity of aircraft engine soot particles. In order to contribute to this effort, we present here an experimental study of the physico-chemical properties of soot particles emitted by a commercial aircraft engine.

2 EXPERIMENTS

The soot sampling is made on a civil aero-engine bench at SNECMA Villaroche center (France) during Landing/Take-Off (LTO) cycles. Jet A1 fuel containing 0.15 wt% of sulfur is used during the engine runs. Soot particles are collected by direct impaction on polycarbonate membranes (Nu-

^{*} *Corresponding author:* Daniel Ferry, CRMCN-CNRS (UPR 7251), Campus de Luminy, Case 913, F-13288 cedex 9, Marseille, France. Email: ferry@crmcn.univ-mrs.fr

cleopore® Isopore), silicon windows (UQG Ltd, Cambridge), and electron microscope grids (Holey carbon film, Oxford Instruments) that are located in the exhaust flux axis at 27 m behind the commercial aircraft engine. Size and morphology of the particles are determined by using a high resolution scanning electron microscope (SEM) JSM-6320F (Jeol) having a spatial resolution of 1.2×10^{-9} m at 15 kV and a transmission electron microscope (TEM) JEM 2000FX (Jeol) having a spatial resolution of 0.28×10^{-9} m at 200 kV. Both microscopes are equipped with a X-ray energy dispersive spectrometer (EDS, TRACOR series II) that enables to determine the elemental chemical composition of our samples. Chemical elements having atomic number larger than 5 are detectable by this technique at concentrations > 0.1 wt%. Soot particles that impact the TEM grids are imaged by using the phase contrast imaging method and their microstructure is determined by electron diffraction. Polycarbonate membranes, which are not conductive, are coated with an amorphous thin carbon film that makes them conductive prior to SEM investigations. The Image J software package, which is freely available (<http://rsb.info.nih.gov/ij/>), is used for analyzing both SEM and TEM images. Soot samples collected onto silicon windows are studied by Fourier transform infrared spectrometry (FTIR) (Equinox 55, BRUKER) in transmission mode in order to characterize the surface functional groups.

3 RESULTS

3.1 Morphology and size distribution of soot primary particles

A typical SEM micrograph of a soot sample collected on a polycarbonate membrane and coated with an amorphous carbon film is shown in figure 1a. Small aggregates made of a few spherical soot primary particles are sparsely deposited but clearly visible near the black disk that corresponds to a pore of the membrane. The spherical shape of soot primary particles is also observed in figure 1b that shows a chain of primary particles recorded during a TEM experiment.

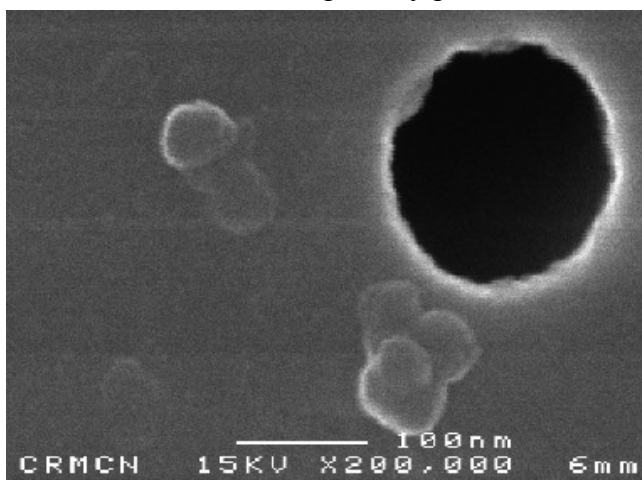


Figure 1a. SEM image recorded at 15 kV and a magnification of 200,000. The black disc corresponds to a pore of the membrane. Small aggregates of aircraft engine soot are located near the pore.

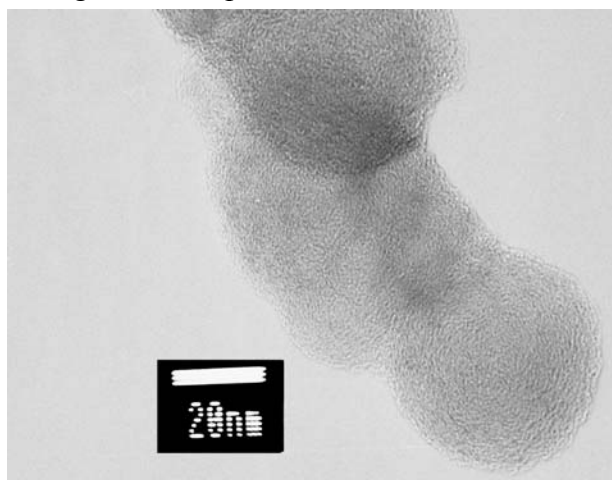


Figure 1b. TEM image of a chain of spherical soot primary particles recorded at 200 kV and a magnification of 300,000.

We rarely observe primary particles as single discrete spherules among our numerous SEM and TEM images. They mainly appear as small asymmetric aggregates or elongated chains with a limited number of particles, like diesel soot particles (Van Poppel, 2005). The size distribution, fractal dimension, and the number of primary particles of these aggregates and chains will be presented in a forthcoming

paper. We present here in figure 2 the primary particles size distributions derived from SEM and TEM analyses. The diameter of over 10,007 and 13,494 primary particles is measured respectively on TEM and SEM images.

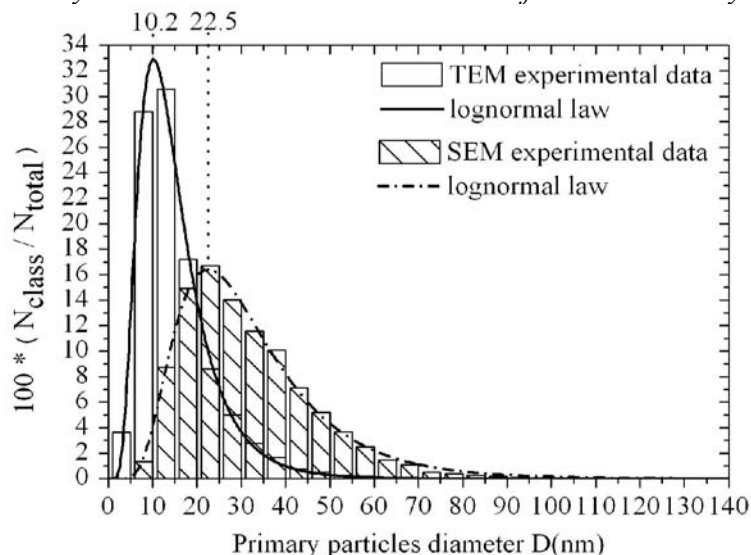


Figure 2. Primary particles size distributions derived from SEM and TEM images. N_{class} is the number of primary particles of a given class and N_{total} is the total number of particles which is equal to 10,007 and 13,494 respectively for the TEM and SEM analyses.

Although both size distributions follow a lognormal law, their maxima are centered at $(10.2 \pm 0.1) \times 10^{-9}$ m and $(22.5 \pm 0.2) \times 10^{-9}$ m when derived from TEM and SEM images respectively. Keeping in mind that soot samples deposited on polycarbonate membranes are coated with an amorphous carbon film prior to the SEM analysis, we attribute the difference in the maxima positions to the amorphous carbon film thickness. We conclude from several set of measurements that TEM is a more suitable technique for determining the primary particles size distribution since, unlike SEM, it does not require a sample preparation which strongly shifts the maximum of the size distribution towards higher values. This latter point will be discussed in another paper. The primary soot particles mean diameter of $(10.2 \pm 0.1) \times 10^{-9}$ m obtained from our TEM measurements is lower than values available in the literature, which are in the range 25 to 50×10^{-9} m for various types of soot (Petzold, 1998 ; Popovicheva *et al.*, 2000 . Popovicheva *et al.*, 2003) but it has to be noted that this work is the first to have been conducted with a commercial aircraft engine in a civil aero-engine bench.

3.2 Microstructure and elemental composition

A TEM image of a soot primary particle is shown in figure 3a. It clearly exhibits a spherical shape made out of concentric, size-limited, graphene layers arranged in an “onion-like” structure. Such structures have already been observed in premixed flames (Grieco *et al.*, 2000) as well as in combustor soot (Popovicheva *et al.*, 2000).

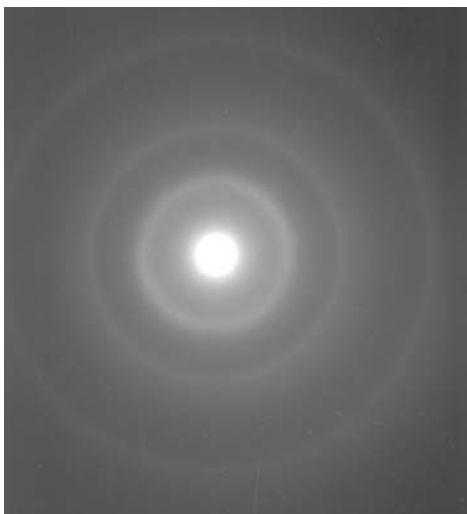


Figure 3a. “Onion-like” structure of a soot primary particle observed by TEM at 200 kV.

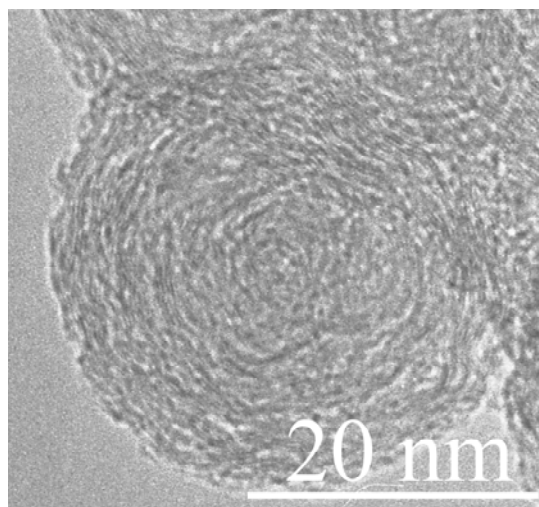


Figure 3b. Diffraction pattern of soot primary particles having an “onion-like” structure.

In addition to the specular reflection, diffraction patterns associated to the observed “onion-like” structures do not exhibit bright diffraction spots but three distinct diffuse rings, as shown in figure 3b, which correspond to real-space values of $d_{(002)} = (3.82 \pm 0.17) \times 10^{-10}$ m, $d_{(10)} = (2.15 \pm 0.07) \times 10^{-10}$ m, and $d_{(11)} = (1.25 \pm 0.02) \times 10^{-10}$ m. These diffuse rings are typical of turbostratic structures and thus support the real-space TEM observations. Numerous EDS analyses on such particles also allow us to determine their mean elemental composition. We find that they are mainly constituted of carbon atoms, 98.3 ± 2.5 % at., with a few oxygen atoms, 1.5 ± 0.4 % at., and traces of sulfur atoms, 0.12 ± 0.05 % at. This elemental composition do not really differ from that determined by Popovicheva *et al.* (2004).

3.3 Infrared spectrum of aircraft engine soot

Soot particles may have surface functional groups that cannot be evidenced by EDS experiments. Thus we have performed FTIR experiments in transmission mode on soot particles deposited onto silicon windows. An infrared spectrum recorded at room temperature and with a resolution of 4 cm^{-1} is shown in figure 4.

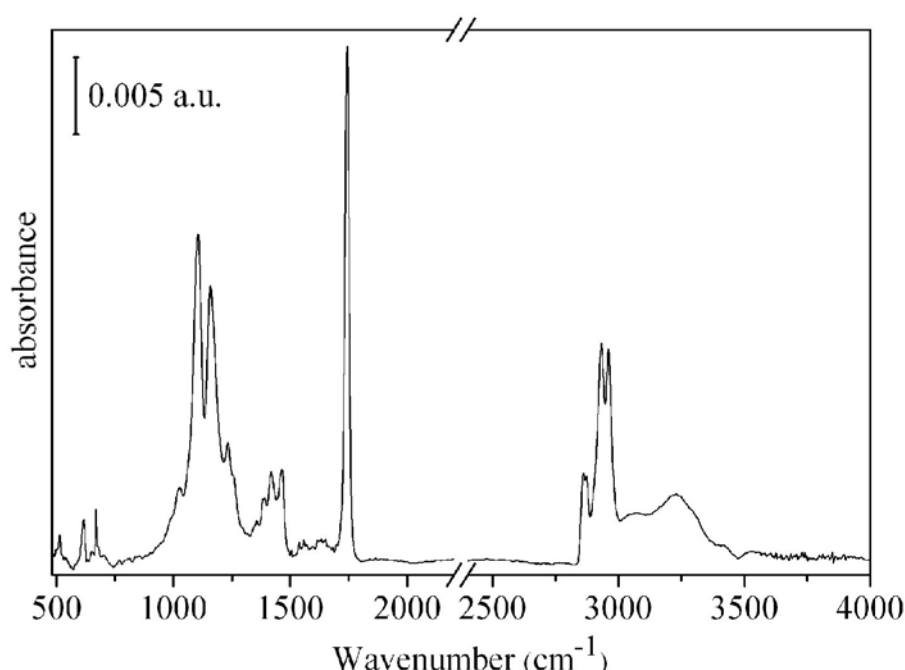


Figure 4. FTIR spectrum of aircraft engine soot recorded at 4 cm^{-1} resolution.

This spectrum is relatively complicated and at this stage, we can not unambiguously assess all the various peaks. The most intense contribution at 1730 cm^{-1} is due to C=O carbonyl groups. Bands between 3000 and 3600 cm^{-1} are attributed to free hydroxyl OH groups and also to associated OH groups such as alcohol and carboxylic functions. The carbon skeleton (-C-C- and -C=C- groups) results in many absorption bands between 1000 and 1600 cm^{-1} whereas CH_2 and CH_3 vibrational modes are detected in the range $2800 - 3000 \text{ cm}^{-1}$. We also note the presence of sulfur and disulfur bands around 500 cm^{-1} . The assessment of several other spectral features is still under investigation and a more detailed analysis will be presented in a forthcoming paper. However, the detected functional groups are consistent with our EDS analyses.

4 CONCLUSION

We have presented here an experimental characterization of the physico-chemical properties of soot particles collected from a commercial aircraft engine. We have performed TEM and SEM experiments that show the spherical morphology of the primary soot particles and allow the determination of their size distribution, which follows a lognormal law centered at $(10.2 \pm 0.1) \times 10^{-9}$ m. The elemental composition indicates that these particles are mainly composed of carbon, with a few

oxygen and traces of sulfur. Various surface functional groups have also been evidenced at the surface of soot particles through FTIR experiments. However, further experiments combining complementary experimental techniques are needed to investigate the reactivity of soot particles in order to reach a better understanding of their ice nucleating properties.

REFERENCES

- Grieco, W.J., J.B. Howard, L.C. Rainey, J.B. Vander Sande, 2000: Fullerenic carbon in combustion-generated soot, *Carbon* 38, 597-614
- Kärcher, B., J. Hendricks, U. Lohmann, 2006: Physically based parameterization of cirrus clouds formation for use in global atmospheric models, *J. Geophys. Res.* 111, D01205
- Lauer, A., J. Hendricks, I. Ackermann, B. Schell, H. Hass, S. Metzger, 2005: Simulating aerosol microphysics with the ECHAM/MADE GCM - part I: Model description and comparison with observations, *Atmos. Chem. Phys.* 5, 3251-3276
- Lohmann, U., B. Kärcher, J. Hendricks, 2004: Sensitivity studies of cirrus clouds formed by heterogeneous freezing in the ECHAM GCM, *J. Geophys. Res.* 109, D16204
- Petzold, A., F. Schröder, 1998: Jet engine exhaust aerosol characterization, *Aerosol Sci. Technol.* 28, 62-77
- Penner, J.E., D.H. Lister, D.J. Griggs, D.J. Dokken, M. McFarland, 1999: *Aviation and the global atmosphere*. A special report of working groups I and III of the Intergovernmental Panel on Climate Change. Cambridge University Press, Cambridge, United Kingdom, ISBN 0-521-66300-8, 373 pages.
- Popovicheva, O.B., N.M. Persiantseva, M.E. Trukhin, G.B. Rulev, N.K. Shonija, Y.Y. Buriko, A.M. Starik, B. Demirdjian, D. Ferry, J. Suzanne, 2000: Experimental characterization of aircraft combustor soot: Microstructure, surface area, porosity and water adsorption, *Phys. Chem. Chem. Phys.* 2, 4421-4426
- Popovicheva, O.B., N.M. Persiantseva, B.V. Kuznetsov, T.A. Rakhmanova, N.K. Shonija, J. Suzanne, D. Ferry, 2003: Microstructure and water adsorbability of aircraft combustor soots and kerosene flame soots: Toward an aircraft-generated soot laboratory surrogate, *J. Phys. Chem. A* 107, 10046-10054
- Popovicheva, O.B., N.M. Persiantseva, E.E. Lukhovitskaya, N.K. Shonija, N.A. Zubareva, B. Demirdjian, D. Ferry, J. Suzanne, 2004: Aircraft engine soot as contrail nuclei, *Geophys. Res. Lett.* 31, L11104
- Schröder, F., B. Kärcher, C. Duroure, J. Ström, A. Petzold, J.F. Gayet, B. Strauss, P. Wendling, S. Borrmann, 2000: On the transition of contrails into cirrus clouds, *J. Atmos. Sci.* 57, 464-480
- Schumann, U., F. Arnold, R. Busen, J. Curtius, B. Kärcher, A. Kiendler, A. Petzold, H. Schlager, F. Schröder, K.H. Wohlfrom, 2002: Influence of fuel sulfur on the composition of aircraft exhaust plumes: The experiments SULFUR 1-7, *J. Geophys. Res.* 107, D15, 4247-4274
- Schumann, U., 2005: Formation, properties and climatic effects of contrails, *Comptes Rendus Physique* 6 4-5, 549-565
- Seinfeld, J.H., 1998: Clouds, contrails, and climate, *Nature* 391, 837-838
- Stier, P., J. Feichter, S. Kinne, S. Kloster, E. Vignati, J. Wilson, L. Ganzeveld, I. Tegen, M. Werner, Y. Balkanski, M. Schulz, O. Boucher, A. Minikin, A. Petzold, 2005: The aerosol-climate model ECHAM5-HAM, *Atmos. Chem. Phys.* 5, 1125-1156
- Van Poppel, L.H., H. Friedrich, J. Spinsby, S.H. Shung, J.H. Seinfeld, P.R. Busek, 2005: Electron tomography of nanoparticles clusters : implications for atmospheric lifetimes and radiative forcing of soot, *Geophys. Res. Lett.* 32, L24811

Development of an Emissions Database to Inform Comparisons of Various Transportation Modes

P.E. Yelvington*, R.C. Miake-Lye, S.C. Herndon, E.C. Wood, T.B. Onasch
Aerodyne Research, Inc.

Keywords: intermodal comparison, transportation emissions, aircraft, on-road, locomotive, shipping

ABSTRACT: While comparison of emissions within a transportation mode (i.e. comparing Car A to Car B) is fairly straightforward using existing data sources, comparison across modes (i.e. comparing Car A to Aircraft B) is more difficult. Appropriate comparisons are challenging because duty cycles, emissions metrics, measurement instrumentation, and other factors differ among transportation modes. In response, a Comparative Emissions DataBase (CEDB) is being designed and implemented to inform comparisons of various transportation modes in terms of potential impact on global climate change. The transportation modes being considered are commercial aircraft, light-duty cars, heavy-duty diesel trucks/buses, locomotives, and marine vessels. Emissions data are being drawn from regulatory certification measurements and research-grade measurements, both from literature and our own studies. While the focus of this project is compiling and organizing measured emissions data rather than inventory development or policy analysis, some basic examples of the modal comparisons facilitated by the CEDB have also been performed.

1. MOTIVATION AND OVERVIEW

Often there are several options for the mode of transportation used by passengers or freight companies. For example, a passenger wishing to travel from Boston to New York can choose to travel by car, airplane, bus, or train. Freight companies make similar choices among heavy-duty diesel trucks, freight trains, cargo ships, and freight aircraft. These decisions are usually based on factors such as cost, travel time, safety, and convenience. However, various modes of transportation also present trade-offs in terms of environmental impact. The objective of this work is to build a database tool, incorporating data from our own measurements, literature and certification sources, that enables a comparison of the potential environmental impact (especially for climate change) of moving passengers and freight via various transportation modes. This tool could potentially be used by policy-makers or urban planners to devise incentives or other programs that would minimize environmental impact by encouraging the use of certain transportation modes for certain routes.

The pollutants considered in the database include traditional long-lived greenhouse gases (CO₂, CH₄, N₂O) that effect climate change directly and shorter-lived urban air pollutants (CO, NO_x, hydrocarbons) that can have an indirect effect on the climate in addition to contributing to smog formation and other environmental effects. In addition, formaldehyde (HCHO) is also included because it is an important air toxic and a major component of the total hydrocarbon emissions from many combustion sources.

The sources of data for the CEDB include measurements performed by Aerodyne Research (ARI) during various measurement campaigns, literature data, and certification data. The individual data sources are too numerous to list, but major sources for each mode include: on-road vehicles (Becker et al. 2000; Shorter et al. 2001; Nam et al. 2004; Davis and Diegel 2006), aircraft (Spicer et al. 1994; Herndon et al. 2004; Anderson et al. 2006; Herndon et al. 2006; ICAO 2006; Wey et al. 2006), locomotives (Fritz and Cataldi 1991; Fritz 1994; U.S. EPA 1998), and marine ships (Corbett and Koehler 2003; Endresen et al. 2003; Eyring et al. 2005; Williams et al. 2005).

* *Corresponding author:* Paul Yelvington, Aerodyne Research Inc., 45 Manning Road, Billerica, Massachusetts, USA. Email: paul@aerodyne.com. This material does not necessarily represent the views or recommendations of the U.S. DOT and its agencies.

2. CHALLENGES OF INTERMODAL COMPARISON

Comparing emissions performance among transportation modes is challenging for several reasons. First, the metrics used by government agencies to regulate emissions from various modes are often different. The metrics used in the USA to regulate gas-phase pollutants and particulate matter or “smoke” are listed in Table 1. The gas-phase certification metrics are based on mass of pollutant per distance travelled for light-duty vehicles or mass of pollutant per unit of work for the other modes. To, for example, compare emissions performance of a car and bus, a conversion to a common metric must first be done. Comparing particulate matter emissions among modes is even more challenging. On-road compression-ignition vehicles are regulated based on a mass-based PM_{2.5} measurement. In addition, buses, heavy-duty trucks, and locomotives are subject to a measurement of percent opacity of the exhaust plume. Aircraft are certified based on smoke number, which measures the amount of light reflected by filter paper that has been exposed to the exhaust. Large marine ships (C3) currently are not regulated for particulate matter or smoke. Some correlations exist for estimating PM emissions from the smoke measurements, but these correlations often involve considerable uncertainty.

Table 1. U.S. Transportation Emission Regulation Metrics

Mode	Basis for Certification (gas-phase)	Measure of particles (or smoke)
Light-duty vehicles	g/mi	PM _{2.5} (CI)
Buses	g/bhp-hr	PM _{2.5} and % opacity (CI)
HDD trucks	g/bhp-hr	PM _{2.5} and % opacity (CI)
Freight locomotives	g/bhp-hr	PM _{2.5} and % opacity
Ships	g/bhp-hr	None (for C3 engines)
Aircraft	g/kN (also report g/kg fuel)	smoke number

bhp = brake horsepower, CI = compression ignition, C3 = Category 3 (displacement/cylinder > 30 L)

Another complication arises because different modes of transportation use different drive cycles (or duty cycles) for emissions testing. In the USA, new light-duty vehicles are measured based on three drive cycles: the FTP drive cycle for emissions, the UDDS drive cycle for “city” fuel economy, and the HWFET cycle for “highway” fuel economy. Heavy-duty vehicles, such as buses, trains, trucks, and ships, have their own duty cycles. Aircraft are regulated based on the ICAO duty cycle, which does not include any emissions above 3000 ft (914 m). As a result of this variability, care must be taken to ensure that the duty cycle used for the emission measurements are representative of the “trip” that was envisioned for the comparison. This issue of duty cycle is somewhat less important for comparison within a single mode because, even if the cycle does not perfectly represent real-world use, the same cycle is used for all measurements in the comparison.

3. CALCULATION OF COMPARATIVE METRICS

The choice of an appropriate comparative metric is necessary to ensure that the intermodal comparisons are meaningful, so several alternatives were considered. The emission index, EI, (mass pollutant per mass of fuel burned) is attractive because it is widely used in the literature. However, the EI only describes how cleanly fuel is consumed and does not address how efficiently that fuel is used to transport passengers or freight. Ultimately, the emission intensity, defined as the mass of pollutant per passenger per distance travelled for passenger travel or the mass of pollutant per tonne per distance travelled for freight, was chosen as the comparative metric. The emission intensity of a passenger vehicle at maximum capacity (units of g/seat-km) is related to the emission intensity of a partially loaded vehicle (units of g/passenger-mi) by the load factor, which is the fraction of seats that are occupied. For passenger cars, the emission intensity of pollutant i , m_i , can be calculated from available data very easily:

$$m_{i,car}[\text{g}/\text{seat-km}] = \frac{EF[\text{g}/\text{km}]}{c[\text{seats}]} \quad (1)$$

where EF is the emission factor and c is the number of seats in the car. For locomotives, literature data for emissions are typically available for each notch, or discrete locomotive power setting. The emission intensity, m_i , can be calculated by summing the product of the emission factor, EF, and the power, P , weighted by the fraction of time spent in each notch and dividing by the number of seats, c , and the average speed (d/t):

$$m_{i,locomotive}[\text{g}_i/\text{seat-km}] = \frac{t[\text{hr}]}{100\% \cdot c[\text{seats}] \cdot d[\text{km}]} \sum_{n=1}^{\text{modes}} EF_{i,n}[\text{g/kW-hr}] \cdot P_n[\text{kW}] \cdot t_{mode,n}[\%] \quad (2)$$

Note that the emission factor for the locomotive is defined based on the power for a particular notch and not the rated power of the engine. For aircraft, ICAO requires measurement of emission indices and fuel flow at four modes: idle, climb-out, approach, and take-off. Using these data and an estimate of emissions at cruise, the emission intensity can be calculated using:

$$m_{i,aircraft}[\text{g}_i/\text{seat-km}] = \frac{n_{engines}}{c[\text{seats}] \cdot d[\text{km}]} \sum_{n=1}^{\text{modes}} EI_{i,n}[\text{g/kg fuel}] \cdot f_{fuel,n}[\text{kg fuel/min}] \cdot t_{mode,n}[\text{min}] \quad (3)$$

where $n_{engines}$ = number of engines per aircraft, c = number of seats, d = trip distance, EI = emission index, f_{fuel} = fuel flow per engine, and t_{mode} = time in mode. Equations 1-3 can be multiplied by load factors to calculate $\text{g}_i/\text{passenger-mi}$ and similar expressions can be used to calculate emission intensities for freight in $\text{g}_i/\text{tonne-mi}$.

4. IMPLEMENTATION OF THE DATABASE

The comparative emissions database (CEDB) was implemented using a relational database structure. Relational databases are linked groups of entities (tables) made up of attributes (columns) and records (rows). The tables are related to each other by use of unique columns called keys. The advantage of using a relational structure over a flat-file structure, such as a spreadsheet, is that the relational database removes the need for entering redundant information and thereby minimizes data entry errors. For example, the data presented in the ICAO emissions databank can be organized into four entities: 1) the engine, which has attributes such as manufacturer and bypass ratio; 2) the measurement, which has attributes such as test date and ambient temperature; 3) power cycle data, which contains the power setting and the emission indices; and 4) landing/take-off (LTO) data, which contains characteristic emissions of each pollutant averaged over the LTO cycle. The four entities are associated through “has one” or “has many” relationships. For example, the Engine entity has one Measurement in the ICAO databank (although in principle an engine could be measured on multiple occasions), and a Measurement has many PowerCycleData (one for each power setting) and LTO-Data (one for each species). The relational database structure used by the CEDB was implemented using the MySQL database management software. MySQL is a popular, open-source, well-documented relational database software package that is capable of efficiently handling large datasets. Queries to the database are performed using the structured query language (SQL), which is a flexible and powerful way to extract useful information from the database.

5. EXAMPLE CASE USING THE CEDB

The focus of this project is compiling and organizing measured emissions data rather than inventory development or policy analysis, yet in order to insure that the CEDB is a useful tool for enabling those types of analyses, its design and scope need to consider the range of queries that may be posed. Thus basic examples of modal comparisons facilitated by the CEDB have been performed.

Figure 1 shows a comparison of the emissions intensity from a light-duty car (2005 Toyota Camry, 4 cylinder, automatic transmission), a passenger locomotive (GM EMD F59PH engine, Amtrak Pacific Surfliner trainset), and a wide-body aircraft (Airbus A320-200) with modern turbofan engines (IAE V2527-A5). Figure 1 compares the emission intensities for the vehicles at full passenger capacity, while Figure 2 shows the comparison for typical passenger load factors (U.S. DOT BTS 2005a; Amtrak 2006; Davis and Diegel 2006). The emission intensities of CO₂, CO, HC, and PM are fairly comparable among modes, and the trend for CO₂ is to be expected. However, cer-

tain observations are immediately obvious from this type of comparison; for example, the fact that the automobile is the only mode using NO_x aftertreatment is evident.

The CO , NO_x and hydrocarbons (HC) data for the Toyota Camry were taken from the EPA Annual Certification Test Data (U.S. EPA OTAQ 2005) for model year 2005. The CO_2 emissions were estimated assuming complete combustion and using the combined city/highway fuel economy (11.9 km/L) reported in the 2005 DOE Fuel Economy Guide. The emission intensities for the EMD locomotive were calculated based on the emission factors and fuel flows reported by Fritz *et al.* (Fritz 1994) and the passenger locomotive duty cycle given in (U.S. EPA 1998). This locomotive engine uses a separate diesel generator to produce “head end power” for the cabin, and the figures presented here include emissions for that generator operating at 60% capacity (300 kW). The emission intensities for the A320 aircraft were calculated from emission indices and fuel flows from the ICAO emissions databank (ICAO 2006). Since ICAO does not include measurements of emissions at cruise, the Boeing Fuel Flow Method 2 (BFFM2) (Baughcum *et al.* 1996) was used to estimate cruise emissions. The fuel flow at cruise inputted to the BFFM2 was taken from the Eurocontrol Base of Aircraft Data (BADA) (Eurocontrol 2004). The PM emissions from the aircraft were estimated using the smoke number (SN) reported in the ICAO database and the FAA first-order approximation. This calculation overestimates PM for two reasons: 1) only the maximum SN was reported in the ICAO databank for this aircraft engine, and this SN was used for the entire flight, and 2) the FAA first-order approximation is intended to give a conservative overestimate of PM emissions. The aircraft emissions depend on the length of the trip because it affects the percent of time the aircraft spends at cruise compared to landing and take-off. A trip length of 440 mi (708 km) was chosen for this comparison, the approximate distance from Boston, MA to Washington, DC. The CO_2 emission intensity calculation used typical values for the C/H ratio of gasoline, diesel, and jet fuel, and assumed complete combustion for all modes.

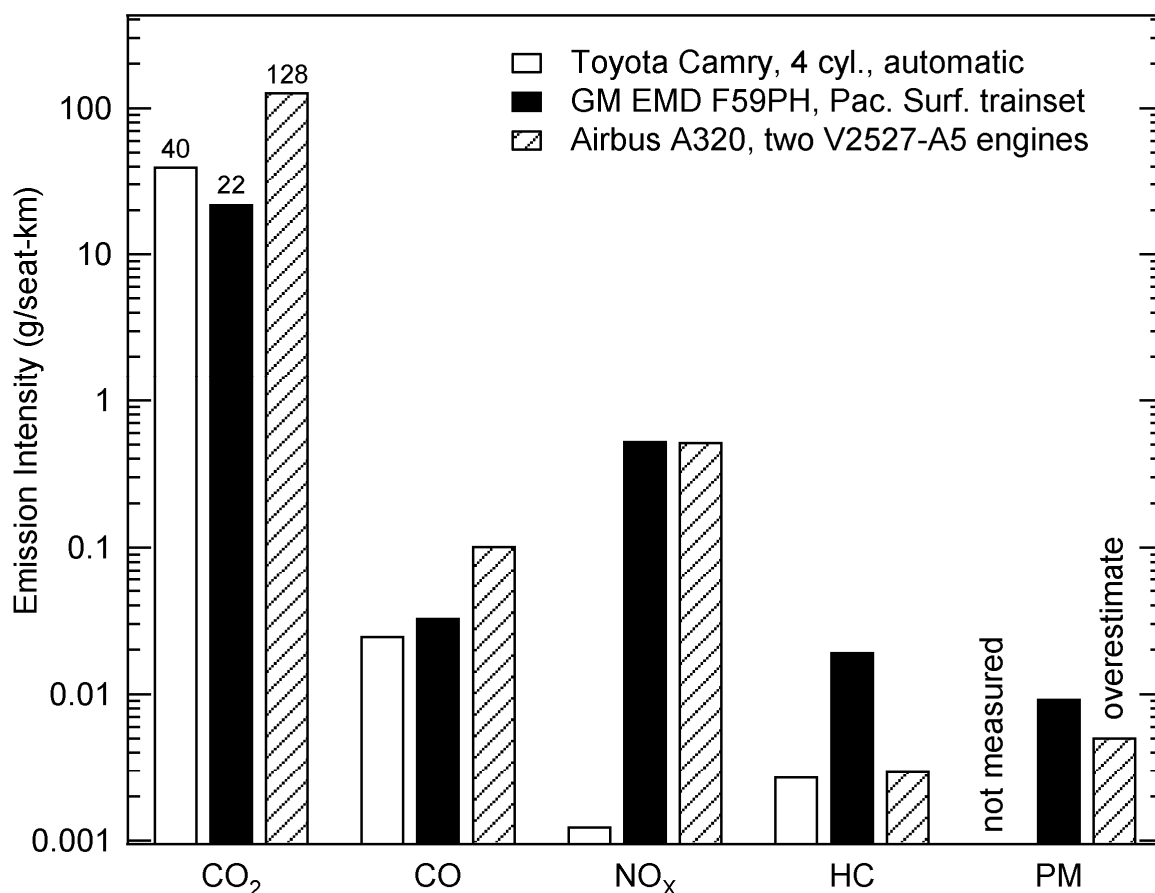


Figure 1. Comparison of emissions from a locomotive, automobile and airplane at full passenger capacity.

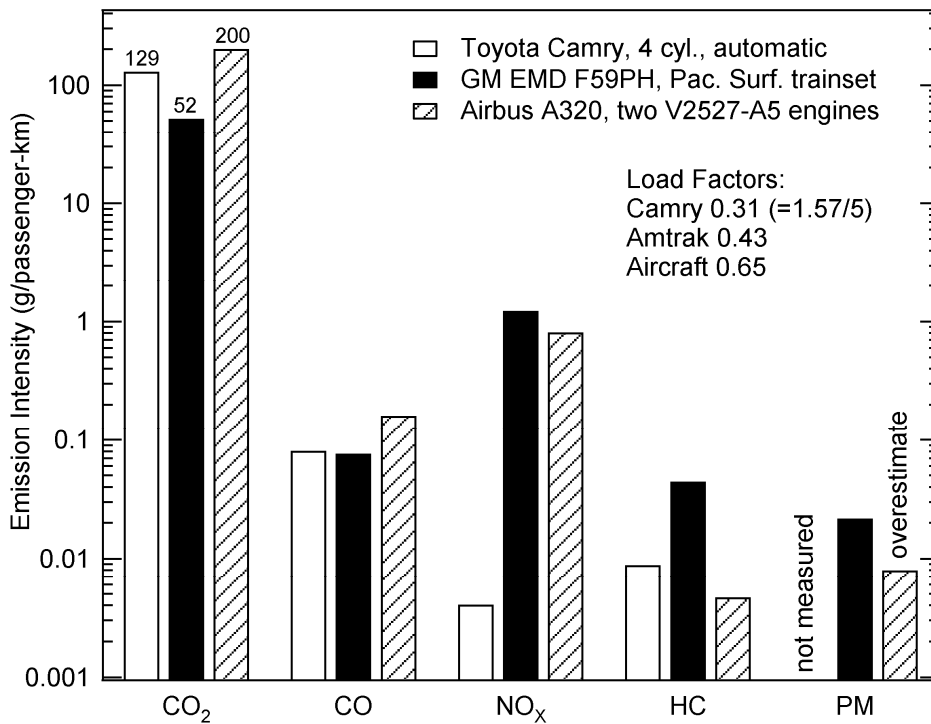


Figure 2. Comparison of emissions from a locomotive, automobile and airplane using typical passenger load factors.

It is important to remember that the vehicles compared in this example case are not necessarily representative of the fleet average emission intensities. This point is demonstrated in Figure 3, which compares the energy intensity (related to m_{CO_2}) of the three vehicles in this example case to the 2001 fleet average (U.S. DOT BTS 2005b). The energy intensity of the A320/V2527 aircraft is quite close to the fleet average although slightly higher, while the energy intensity of the Toyota Camry and EMD locomotive are somewhat lower than their respective fleet averages. The data in the CEDB could easily be used to extend this example case to other vehicles and thereby account for fleet variability.

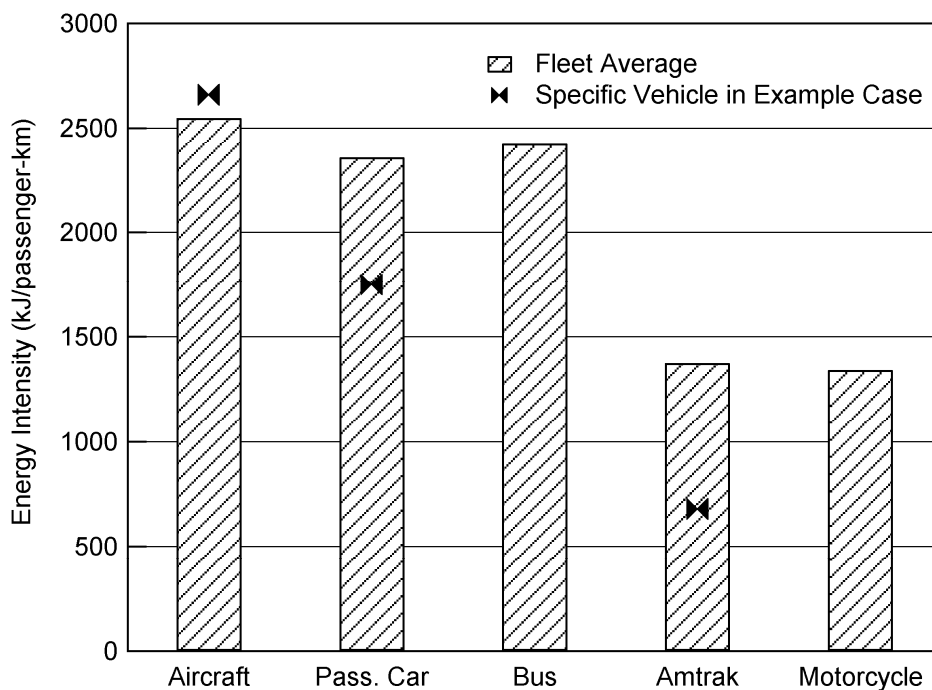


Figure 3. Comparison of energy intensity of specific vehicles used in this example case to fleet average values.

6. SUMMARY

A Comparative Emissions DataBase (CEDB) is being developed to enable comparisons of emissions of greenhouse gases and other pollutants from various modes of transportation. Potential end users of this tool would be policymakers and transportation policy researchers wishing to understand the environmental trade-offs of moving people and goods via different modes. This project is a work-in-progress, so improvements and expansion of the database are ongoing. Planned improvements include, for example, the inclusion of estimated uncertainties for the emissions data to allow propagation of uncertainty through to the final emission intensities.

ACKNOWLEDGEMENTS

We would like to thank the U.S. DOT Center for Climate Change and Environmental Forecasting and the Federal Aviation Administration (Contract No. DTOS59-05-00421) for funding this work. This material, however, does not necessarily represent the views or recommendations of the U.S. Department of Transportation and its agencies.

REFERENCES

- Amtrak, 2006: *Amtrak Monthly Performance Report of February 2006*, Amtrak, 86 pp.
- Anderson, B. E., G. Chen and D. R. Blake, 2006: Hydrocarbon Emissions from a Modern Commercial Airliner. *Atmos. Environ.* 40, 3601-3612.
- Baughcum, S. L., T. G. Tritz, S. C. Henderson and D. C. Pickett, 1996: *Scheduled Civil Aircraft Emission Inventories for 1992: Database Development and Analysis*. NASA/CR—4700, NASA.
- Becker, K. H., J. C. Lorzer, R. Kurtenbach, P. Wiesen, T. E. Jensen and T. J. Wallington, 2000: Contribution of vehicle exhaust to the global N₂O budget. *Chemosphere - Global Change Science* 2, 387-395.
- Corbett, J. J. and H. W. Koehler, 2003: Updated emissions from ocean shipping. *J. Geophys. Res.*, [Atmos.] 108(D20, doi:10.1029/2003JD003751).
- Davis, S. C. and S. W. Diegel, 2006: *Transportation Energy Data Book*. ORNL-6974, Oak Ridge National Laboratory, Center for Transportation Analysis, 332 pp.
- Endresen, O., E. Sorgard, J. K. Sundet, S. B. Dalsoren, I. S. A. Isaksen, T. F. Berglen and G. Gravir, 2003: Emission from international sea transportation and environment impact. *J. Geophys. Res.*, [Atmos.] 108(D17, doi:10.1029/2002JD002898).
- Eurocontrol, 2004: *Aircraft Performance Summary Tables for the Base of Aircraft Data (BADA) Revision 3.6*. EEC Note No. 12/04, 113 pp.
- Eyring, V., H. W. Koehler, J. van Aardenne and A. Lauer, 2005: Emissions from international shipping: 1. The last 50 years. *J. Geophys. Res.*, [Atmos.] 110(D17305, doi:10.1029/2004JD005619).
- Fritz, S. G., 1994: Exhaust emissions from two intercity passenger locomotives. *J. Eng. Gas. Turb. Power* 116(4), 774-83.
- Fritz, S. G. and G. R. Cataldi, 1991: Gaseous and particulate emissions from diesel locomotive engines. *J. Eng. Gas. Turb. Power* 113(3), 370-6.
- Herndon, S. C., T. M. Rogers, E. J. Dunlea, J. T. Jayne, R. C. Miake-Lye and W. B. Knighton, 2006: Hydrocarbon Emissions from In-Use Commercial Aircraft during Airport Operations. *Environ. Sci. Technol.* 40, 4406-4413.
- Herndon, S. C., J. H. Shorter, M. S. Zahniser, D. D. Nelson, Jr., J. Jayne, R. C. Brown, R. C. Miake-Lye, I. Waitz, P. Silva, T. Lanni, K. Demerjian and C. E. Kolb, 2004: NO and NO₂ emission ratios measured from in-use commercial aircraft during taxi and takeoff. *Environ. Sci. Technol.* 38, 6078-6084.
- International Civil Aviation Organization, 2006: ICAO Aircraft Engine Emissions Databank. <http://www.caa.co.uk/default.aspx?categoryid=702&pagetype=90>, accessed April 2006.
- Nam, E. K., T. E. Jensen and T. J. Wallington, 2004: Methane Emissions from Vehicles. *Environ. Sci. Technol.* 38, 2005-2010.
- Shorter, J. H., S. C. Herndon, M. S. Zahniser, D. D. Nelson, Jr., J. T. Jayne and C. E. Kolb, 2001: *Characterization of heavy-duty vehicle exhaust in dense urban environments*. 10th International Symposium "Transport and Air Pollution", Boulder, Colorado.
- Spicer, C. W., M. W. Holdren, R. M. Riggan and T. F. Lyon, 1994: Chemical composition and photochemical reactivity of exhaust from aircraft turbine engines. *Ann. Geophys.* 12(10/11), 944-55.

- U.S. Department of Transportation Bureau of Transportation Statistics, 2005a: *Air Carrier Statistics (Form 41 Traffic Data)*. <http://www.transtats.bts.gov/>, accessed April 2006.
- U.S. Department of Transportation Bureau of Transportation Statistics, 2005b: *National Transportation Statistics*, Washington, DC.
- U.S. Environmental Protection Agency, 1998: *Locomotive Emission Standards: Regulatory Support Document*, 127 pp.
- U.S. Environmental Protection Agency Office of Transportation and Air Quality, 2005: *Annual Certification Test Results & Data for Cars and Light Trucks*. <http://www.epa.gov/otaq/crttst.htm>, accessed April 2006.
- Wey, C. C., B. E. Anderson, C. Hudgins, C. Wey, X. Li-Jones, E. Winstead, L. K. Thornhill, P. Lobo, D. Hagen, P. D. Whitefield, P. E. Yelvington, S. C. Herndon, T. B. Onasch, R. C. Miake-Lye, J. Wormhoudt, W. B. Knighton, R. Howard, D. Bryant, E. Corporan, C. Moses, D. Holve and W. Dodds, 2006: *Aircraft Particle Emissions eXperiment (APEX)*. NASA TM-2006-214382, NASA, Washington, DC, 514 pp.
- Williams, E. J., B. M. Lerner, T. Bates, T. Quinn and J. Johnson, 2005: *Trace Gas and Particle Emission Factors for Marine Vessels*. American Geophysical Union Meeting, San Francisco, CA.

In-Situ Microphysical Measurements In Rocket Plumes With The Cloud And Aerosol Spectrometer (CAS)

D. Baumgardner^{*}, M. Flores

Universidad Nacional Autónoma de México, Mexico City, Mexico

G. L. Kok

Droplet Measurement Technologies, Inc., Boulder, CO

D. Toohey

University of Colorado, Boulder Colorado

R. Hermann

Jet Propulsion Laboratory, Pasadena, Ca.

M. Ross

Aerospace Corporation, Los Angeles, Ca

T. Thompson

NOAA Aeronomy Laboratory, Boulder, CO

L. Avallone, L. Kalnajs

Laboratory for Atmospheric and Space Physics, Boulder, Co.

Keywords: rocket emissions, plume particle properties, particle shape analysis

ABSTRACT: High resolution, single particle measurements have been made in rocket plumes using an optical particle spectrometer that measures diameters from 0.5 to 44 μm . The diameter, shape and composition is derived from bi-directional scattering. The CAS was mounted on the NASA WB-57F aircraft as part of the Plume Ultrafast Measurements Acquisition (PUMA) project to study the chemistry and microphysics of rocket plumes. Measurements were made in plumes generated by an Atlas IAS rocket and the booster of the space shuttle Discovery. The microstructure of the two plumes and the characteristics of their particles were distinctly different. The Atlas particles were on average larger and more irregular in shape. The composition of the Shuttle particles suggests hydrates of nitric acid whereas the Atlas particles were more representative of ice.

1 BACKGROUND

Solid-fueled rockets emit chlorine and alumina particles directly into the stratosphere, thus contributing to the depletion of the ozone layer [Prather et al., 1990; Jackman et al. 1998; Danilin et al, 2003]. Recent analysis of solid-fueled rocket plumes shows almost complete depletion of ozone locally [e.g., Ross et al., 2000]; however, global implications of such sharp local ozone reductions are predicted to be small [Danilin et al., 2001]. On the other hand, the heterogeneous reactions on alumina particles may be important on the global scale by converting emitted and background HCl into short-lived Cl_2 , resulting in ozone depletion depending on the location of emissions and the size distribution and surface area of alumina particles. Previous measurements in rocket plumes have documented the emissions of gases and the average total concentrations of the particles, but were limited to the smallest particle sizes, $< 1 \mu\text{m}$. More recent measurements have been made that document the size distribution of particles $> 1 \mu\text{m}$ at much higher spatial resolutions than previously possible. In addition, the instrument that made these measurements also provides information from which the shape and composition are derived. These measurements were made as part of the *Plume Ultrafast Measurements Acquisition (PUMA)* project. Instruments were mounted on the

^{*} *Corresponding author:* Darrel Baumgardner, Universidad Nacional Autónoma de México, Mexico City, DF 04150 Mexico. Email: darrel@servidor.unam.mx

NASA WB57F to measure water vapor, ozone, CO₂ and particles. The objectives of the particle measurements were to characterize the size, shape and composition of fresh particles found in the rocket exhausts.

2 MEASUREMENT TECHNIQUE

The cloud, aerosol and precipitation spectrometer (CAPS), shown in figure 1, is a combination of three sensors for particle size and liquid water content (LWC) measurements. The cloud and aerosol spectrometer (CAS), circled in white, derives size distributions from the light scattered by individual particles that pass through a focused beam from a diode laser (Baumgardner et al., 2001). Two cones of light, 4 to 12° and 168° to 176°, are measured by separate detectors and the peak amplitudes are classified into size bins to create two frequency histograms, forward and backward, every second. Figure 2 is a schematic diagram of the optical configuration of the CAS. The peak amplitudes of the forward and backward scattering signals are recorded for individual particles. In addition, the time of arrival, i.e. the time between successive particles that arrive in the laser beam, is recorded.

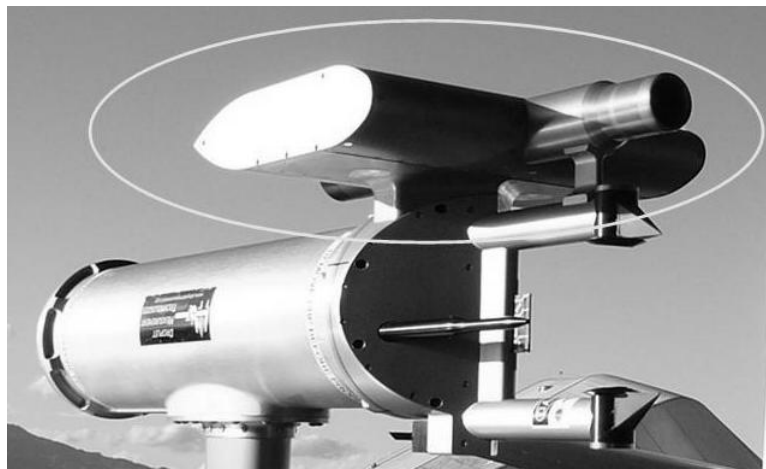
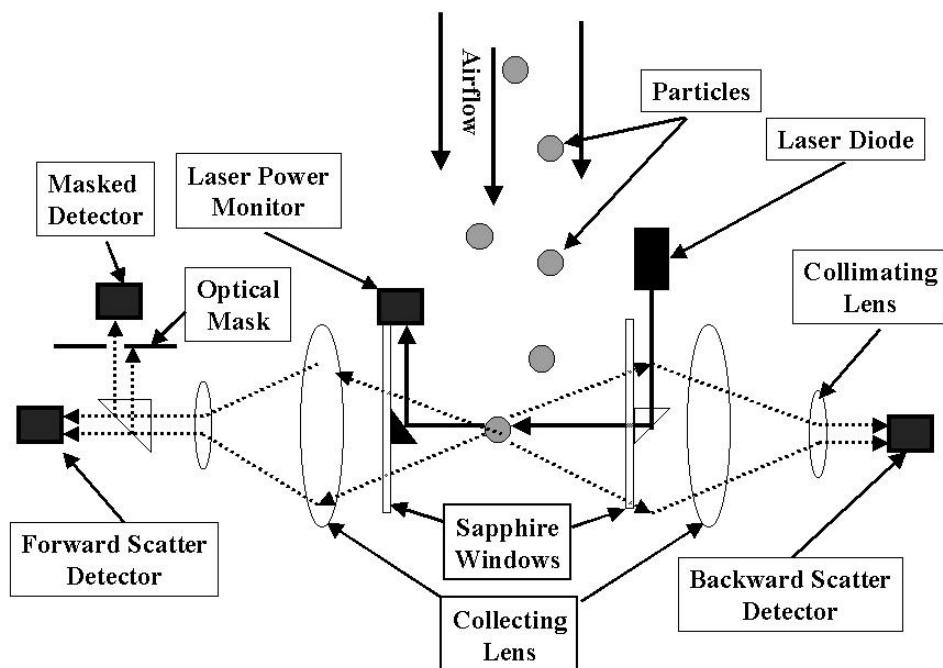


Figure 1. The CAPS probe, mounted on the wing the NASA WB57 F is shown here. The CAS portion of the CAPS is circled in white.



Forward/Backscatter Sensor Optical Path Diagram

Figure 2. This block diagram is a schematic representation of the optical configuration of the CAS

The relationship between the forward and backward scattered light is a function of the particle size, refractive index and shape. This relationship is exploited in the CAS to derive a refractive index or shape factor from the ratio of forward and back scattered signals (*Baumgardner et al.*, 1996; *Baumgardner et al.*, 2005; *Chepfer et al.*, 2005). Figure 3 illustrates the relationship between refractive index and shape in relation to the forward to back ratio (F2BR) as measured by the CAS. The shape is expressed as an aspect ratio of spheroids, calculated using T-matrix scattering theory (Mischenko and Travis, 1998). As shown by the dashed line box, there is a range of F2BR in which the refractive index and aspect ratio cannot be resolved unambiguously.

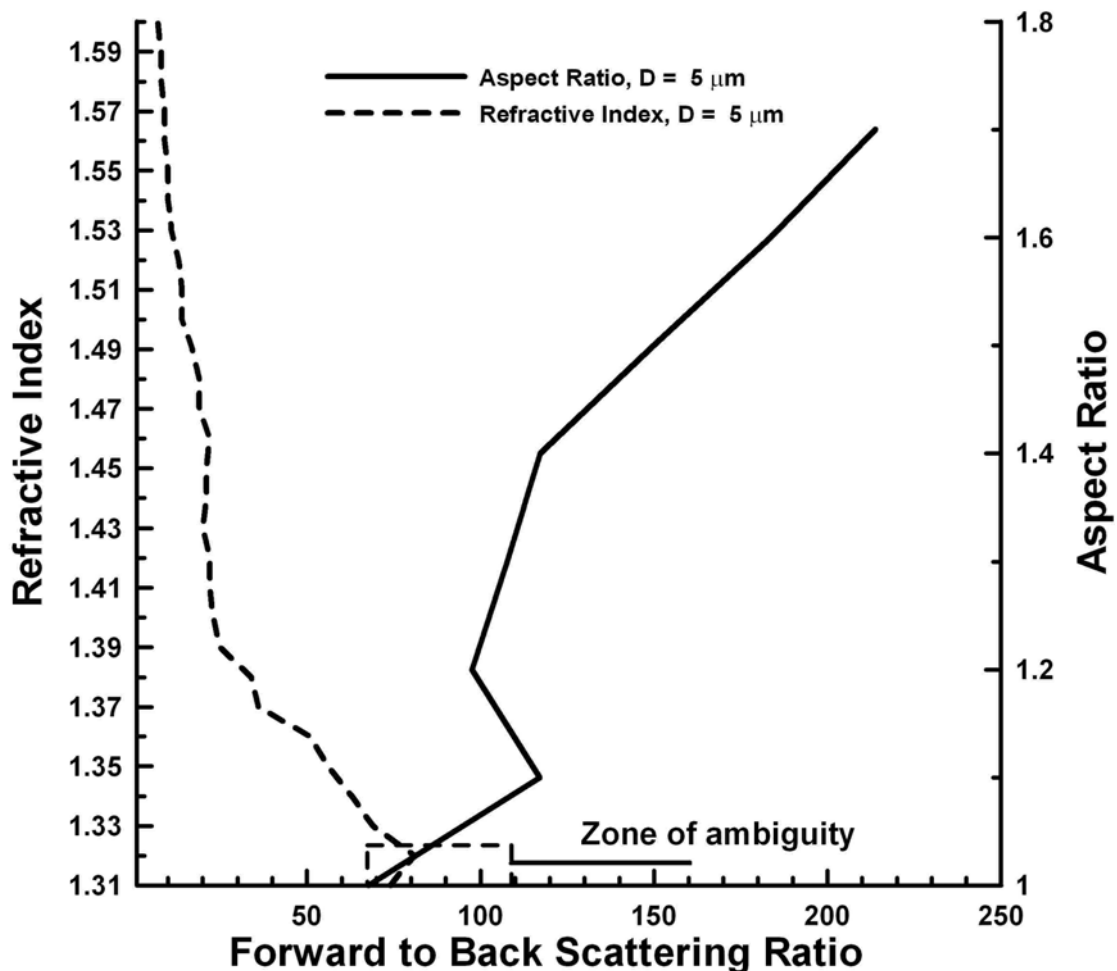


Figure 3. The ratio of light scattered forward and backward from a particle depends on the refractive index (dashed curve) and the shape (solid curve).

3 RESULTS

Measurements were made in the plume from an Atlas IIAS rocket on May 19, 2004 and from the first stage booster rocket of the Space shuttle Discovery on July 26, 2005, both launched from Cape Kennedy Space Center, USA. The Atlas plume was intersected at 18 km, 16.2 km, 14.2 km and 13.6 km, at an environmental temperature of -67°C . The shuttle plume was sampled four times at an altitude of 18 km and a temperature of -67°C . Figure 4 compares the size distributions of the particles in the two plumes. The majority of the particles are less than $5\ \mu\text{m}$ in equivalent optical diameter; however, the size distribution of the Atlas plume is broader than that of the space shuttle, although neither plume has particles larger than $8\ \mu\text{m}$.

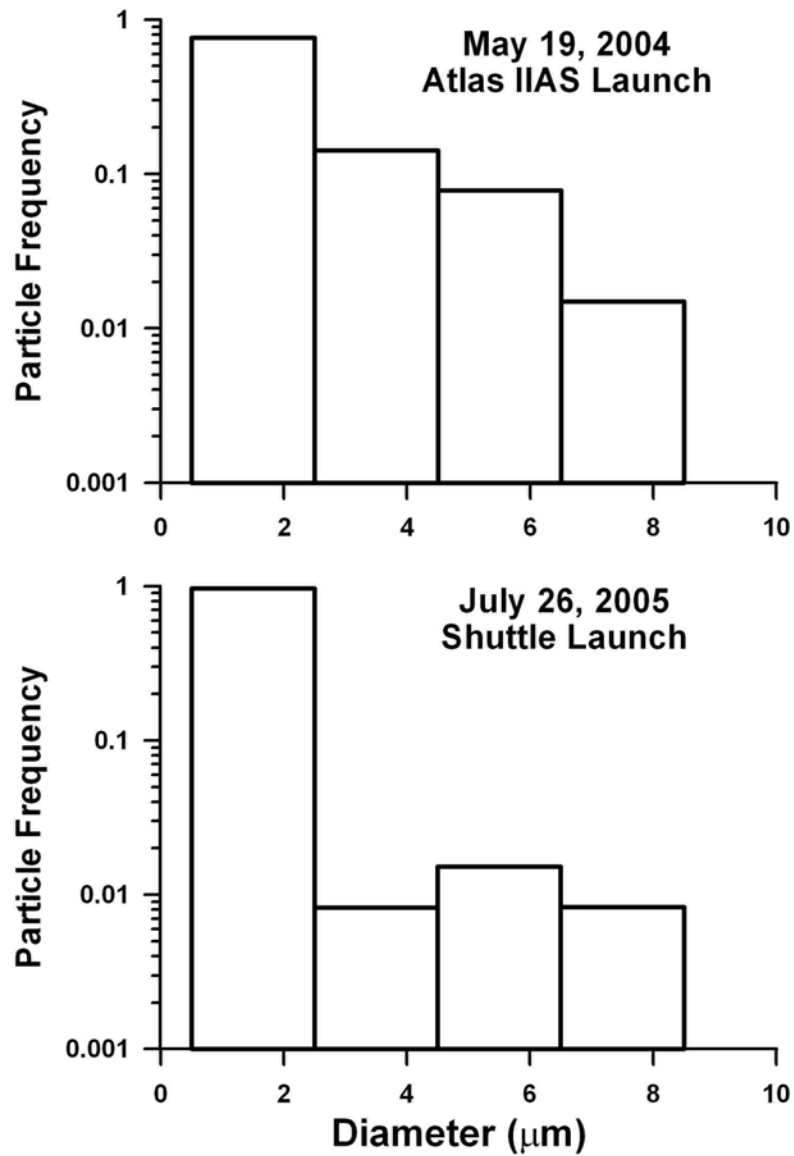


Figure 4. Size distributions of the Atlas and Shuttle particles.

The shape factors are given here in terms of aspect ratios for equivalent spheroids using the model for oblate spheroids as described in Section 3. The frequency distributions of particle aspect ratios, shown in Figure 5, compare the plumes of the Atlas and Space shuttle. In this figure we see that 35% of the particles in the Atlas plume were spherical and the remainder had a variety of shapes with aspect ratios between 1.2 and 1.6. A larger percentage of the Shuttle particles were spherical, 45%, with the remainder between 1.2 and 1.4 aspect ratios.

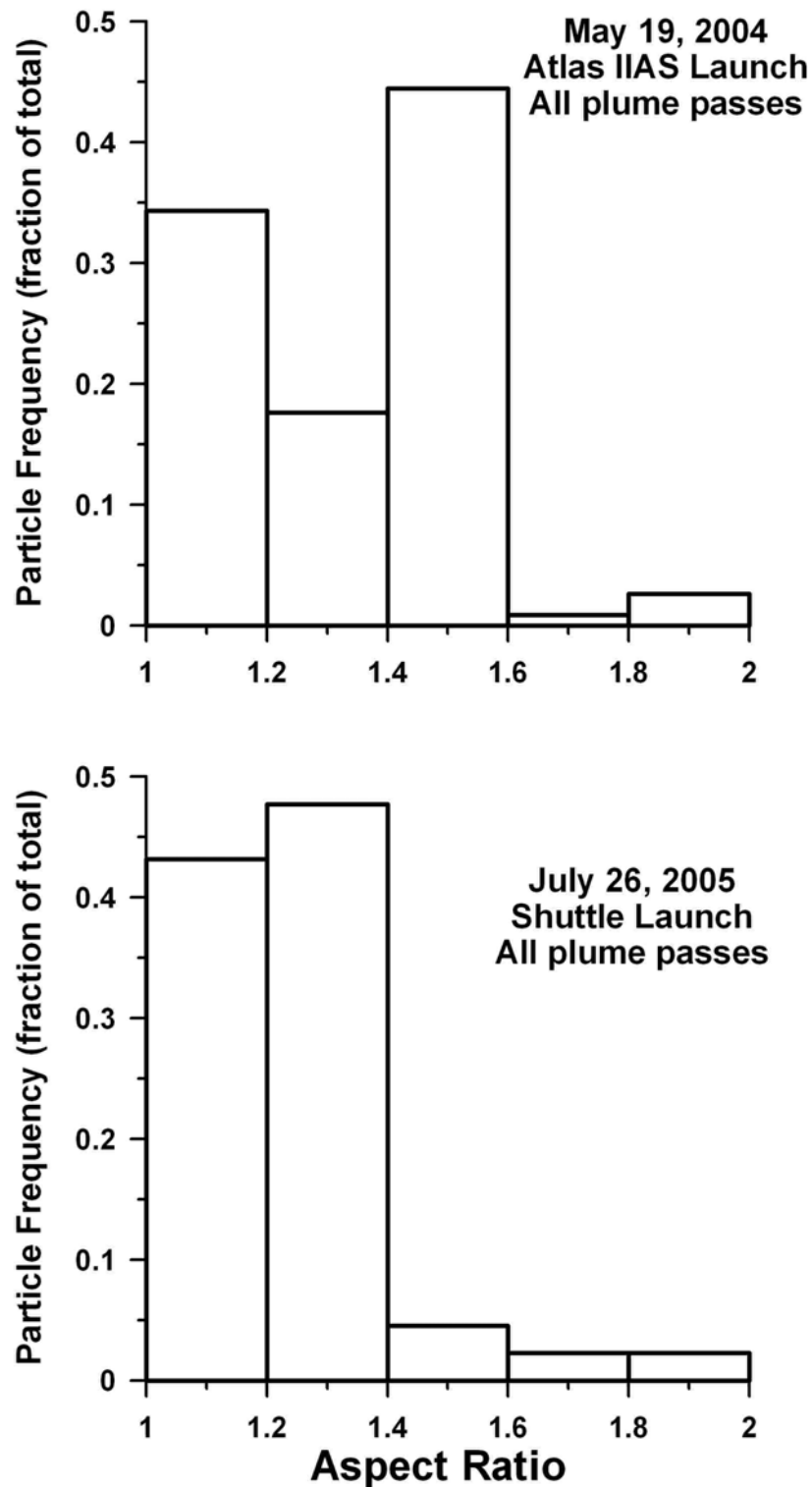


Figure 5. The frequency distribution of particle aspect ratios for the Atlas and Shuttle emissions are plotted in this figure

The composition of the particles, as indicated by the derived refractive indices, was very different, as shown in the frequency distributions in Figure 6. The 35% of particles in the Atlas plume that were near spherical had refractive indices between 1.30 and 1.35, indicative of ice. The majority of the spherical particles in the plume of the shuttle had refractive indices between 1.5 and 1.55. Ice particles with a coating of nitric acid or hydrates of nitric acid have refractive indices in this range.

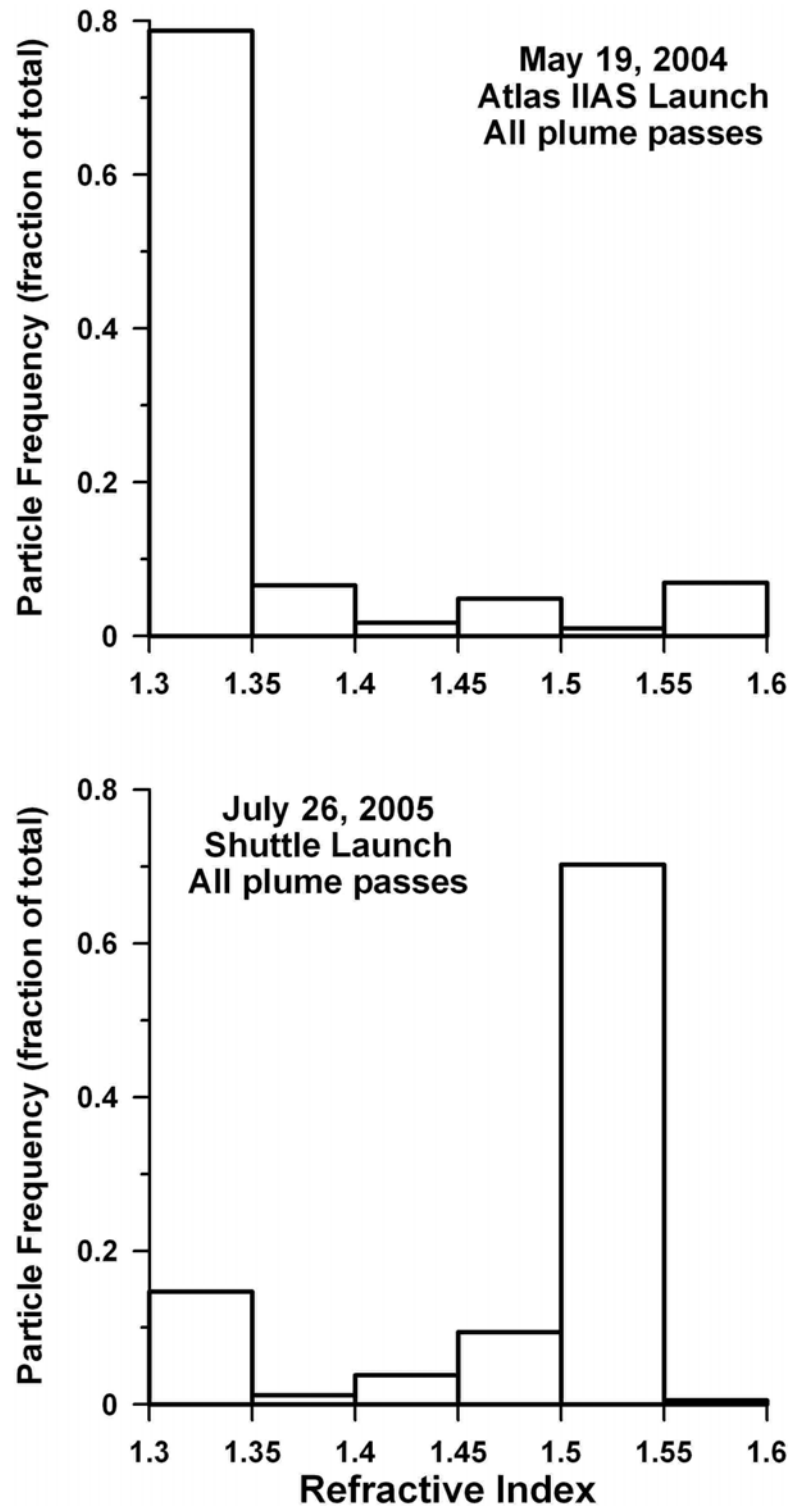


Figure 6. The frequency distribution of particle refractive indices for the Atlas and Shuttle emissions are shown here..

The dispersion of the plumes, as indicated by the spatial distribution of the individual particles, differs between the Atlas and the Shuttle exhausts. Figure 7 shows the frequency of spatial distances between the particles, measured in millimetres. The dashed lines on the figures are the spatial distributions predicted for uniformly, random spacing of particles with different number concentrations. These predicted curves assume Poisson probability distributions to predict the expected frequency of separations. The measured distributions of both plumes indicate that the exhausts are mixtures of high and low concentrations, as indicated by the dashed curves with steep (high concen-

tration) and shallow (low concentration) slopes. The high concentrations were in the central parts of plumes where little dilution by mixing with environmental air has occurred and the low concentrations are at the plume edges where entrainment has diluted the concentrations.

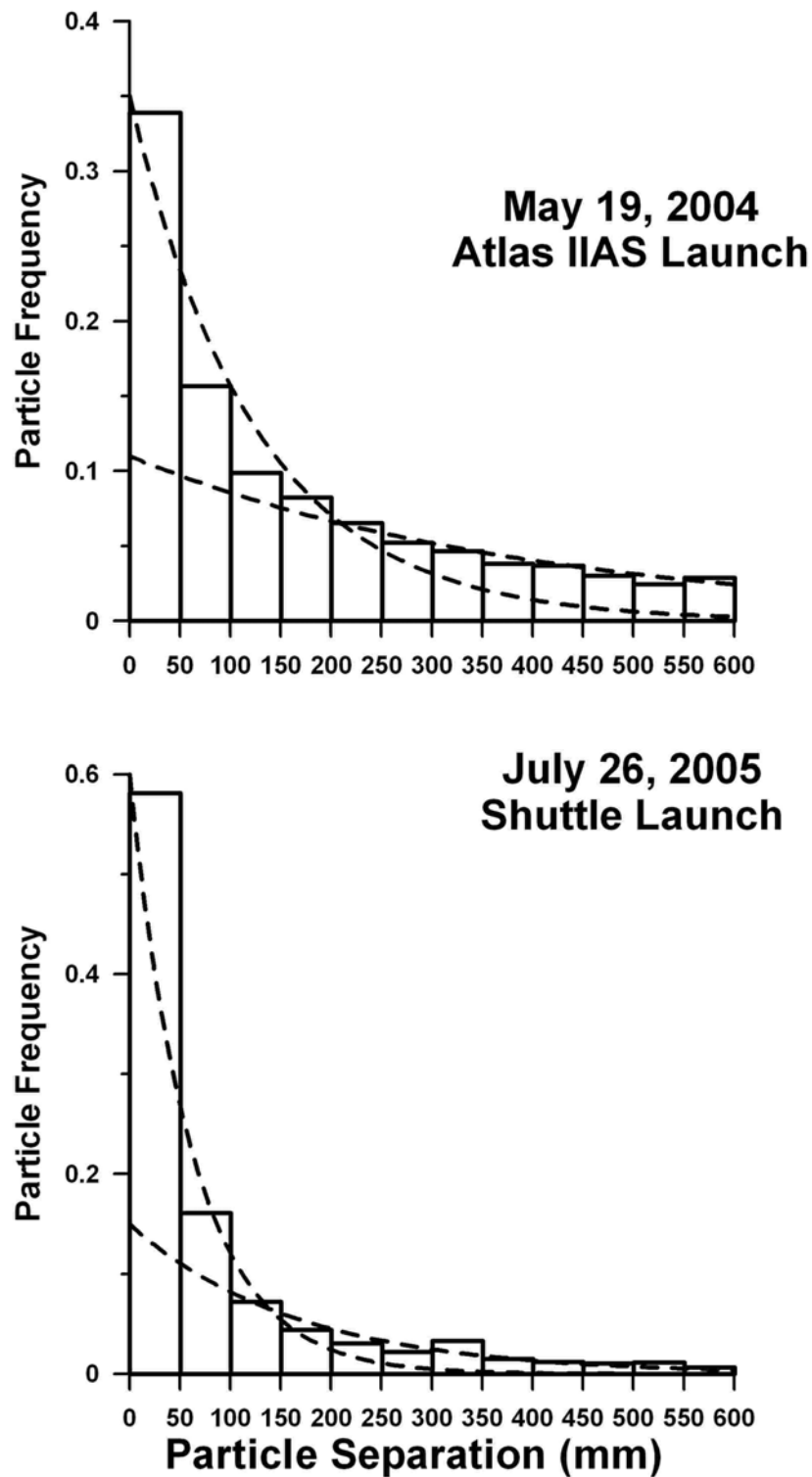


Figure 7. These are frequency distributions of the interarrival times of the particles in the Atlas and shuttle plumes

4 CONCLUSIONS

Measurements of particle size, shape, refractive index and spatial distribution indicate fundamental differences between characteristics of exhaust particles in an Atlas rocket plume and Shuttle booster rocket plume. These differences are related primarily to the type of fuel used in the two systems. The major characteristics that were detected were:

- The majority of particles were $< 5 \mu\text{m}$ in both plumes.
- The particle refractive indices suggest ice as the dominant particle composition in the Atlas plume whereas hydrates of HNO_3 nitric acid coated ice was dominant in the Shuttle plume.
- The particles in the Atlas plume were more aspherical than those in the Shuttle plume but 35% and 45% of the particles were spherical, respectively.
- These results can contribute to the improvement of chemical transport models of rocket plumes with better estimates of particle surface area and dynamics.

ACKNOWLEDGEMENTS

Thanks to NASA JSC, in particular, Andy Roberts, Joe Gerky, Shelley Baccus, Brian Barnett and the WB-57F crew for logistical support, to Anne-Marie Schmoltner and NSF for project funding and to Bruce Doddridge and Chris Cantrell for their early encouragement.

REFERENCES

- Baumgardner, D., B. Baker, and K. Weaver 1993: A technique for the measurement of cloud structure on centimeter scales, *J. Atmos. Oceanic Tech.*, 10, 557-565.
- Baumgardner, D., J.E. Dye, B. Gandrud, K. Barr, K. Kelly, K.R. Chan, 1996: Refractive indices of aerosols in the upper troposphere and lower stratosphere, *Geophys. Res. Lett.*, 23, 749-752.
- Baumgardner, D., H. Jonsson, W. Dawson, D. O'Connor and R. Newton, 2001: The cloud, aerosol and precipitation spectrometer (CAPS): A new instrument for cloud investigations, *Atmos. Res.*, 59-60, 251-264.
- Baumgardner, D., H. Chepfer, G.B. Raga, G.L. Kok, 2005: The Shapes of Very Small Cirrus Particles Derived from In Situ Measurements, *Geophys. Res. Lett.*, 32, L01806, doi:10.1029/2004GL021300.
- Danilin, M. Y., M. K. W. Ko, and D. K. Weisenstein, 2001: Global implications of ozone loss in a space shuttle wake, *J. Geophys. Res.*, 106, 3591-3601.
- Jackman, C. H., D. B. Considine, and E. L. Fleming, 1998: A global modeling study of solid rocket aluminum oxide emission effects on stratospheric ozone, *Geophys. Res. Lett.*, 25, 907-910.
- Mishchenko, M.I. and L. D. Travis, 1998: Capabilities and limitations of a current FORTRAN implementation of the T-matrix method for randomly oriented, rotationally symmetric scatterers, *J. Quant. Spectrosc. Radiat. Transfer*, 60, 309-324.
- Prather, M. J., M. M. Garcia, A. R. Douglas, C. H. Jackman, M. K. W. Ko, and N. Dak Sze, 1990: The space shuttle's impact on the stratosphere, *J. Geophys. Res.*, 95, 18,583-18,590.
- Ross, M. N., M. Y. Danilin, D. K. Weisenstein, and M. K. W. Ko, 2004: Ozone depletion caused by NO and H₂O emissions from hydrazine-fueled rockets, *J. Geophys. Res.*, 109, D21305, doi:10.1029/2003JD004370.

Historical and future development of air transport fuel efficiency

P. M. Peeters*

NHTV University of Applied Sciences Breda, the Netherlands

J. Middel

National Aerospace Laboratory NLR, Amsterdam, the Netherlands

Keywords: air transport, fuel efficiency, piston engines, jet engines, history

ABSTRACT: The historical developments of the average fuel efficiency of both piston and jet powered aircraft are reviewed with the objective to find ways to better forecast future developments. It is argued that the current methods of a constant percentage efficiency improvement per year cannot satisfactorily represent the historical time series. A sigmoidal model is suggested for better fits and more reliable prognoses, leading to less optimistic fuel efficiency gains for 2040 than suggested in current literature.

1 INTRODUCTION TO HISTORICAL ANALYSIS OF FUEL EFFICIENCY

A recent study on the development of energy efficiency of individual new civil aircraft and for the USA fleet shows that the Intergovernmental Panel on Climate Change (IPCC) efficiency assumptions yield too optimistic fuel reductions if extrapolated towards the future (Peeters et al., 2005). Like IPCC, most air transport greenhouse gas emission scenarios assume a constant percentage energy efficiency increase (leading to a near-zero fuel consumption in the long term). The IPCC special Report on aviation and the global atmosphere assumes values between 1.2% and 2.2% efficiency increase per annum (Penner et al., 1999). Also several other authors propose constant percentages, though often assumed to differ between different time periods to fit the result better to the available data (see for example Green, 2003; Lee, 2003; Lee et al., 2001; Pulles et al., 2002). As will be shown in this paper, a constant reduction percentage approach might not be the best model for forecasting purposes.

Operational impacts have not been explicitly included in the analysis. Load factors, efficient routing, holding, weather impacts and delays depend (more) on the efficiency of deployment of the aircraft rather than the aircraft technical characteristics themselves.

2 MATHEMATICAL ANALYSIS OF FUEL EFFICIENCY DEVELOPMENT

Lee et al. (2001) introduced the term Energy Intensity (E_I), the energy consumption per available seat-kilometre (MJ/ASK), as a measure for the technological (transport) performance of individual aircraft or an aircraft fleet. This E_I typically depends on aircraft (technology) parameters:

- Aerodynamic efficiency, specifically the lift-to-drag ratio during climb and cruise.
- Weight efficiency, the ratio of payload to the Maximum Take-off Weight (MTOW) and the ratio between Operating Empty Weight (OEW) and MTOW.
- Engine efficiency in terms of fuel consumption per unit thrust (Specific Fuel Consumption, SFC). The number of seats; Cabin layout has a significant impact on the number of seats, hence seat-kilometres. Seating density may vary by a factor of two between a typical mixed-class layout and single-class high-density layout, while having approximately the same fuel burn per aircraft-kilometre.

* *Corresponding author:* Paul Peeters, NHTV Breda University for Applied Sciences, PO Box 3917, 4800 DX Breda, the Netherlands. Email: peeters.p@nhtv.nl

Many studies present technological trends in terms of a constant annual percentage efficiency gain, as observed from history. Lee et al. (2001), for instance, assert that this ratio will be between 1.2% and 2.2% a year in the future, while Penner et al. (1999) use 1.4% for most future scenarios. This approach can be modelled with the form:

$$E_t = E_{I_b} \cdot (1 - c_a)^{(Y - Y_{ref})} \quad (1)$$

where E_t is the Energy Intensity (unit MJ/ASK) and $(Y - Y_{ref})$ the number of years since a base year Y_{ref} . E_{I_b} is the Energy Intensity at the base year and c_a the annual (fractional) reduction of the Energy Intensity.

Long haul aircraft fuel efficiency

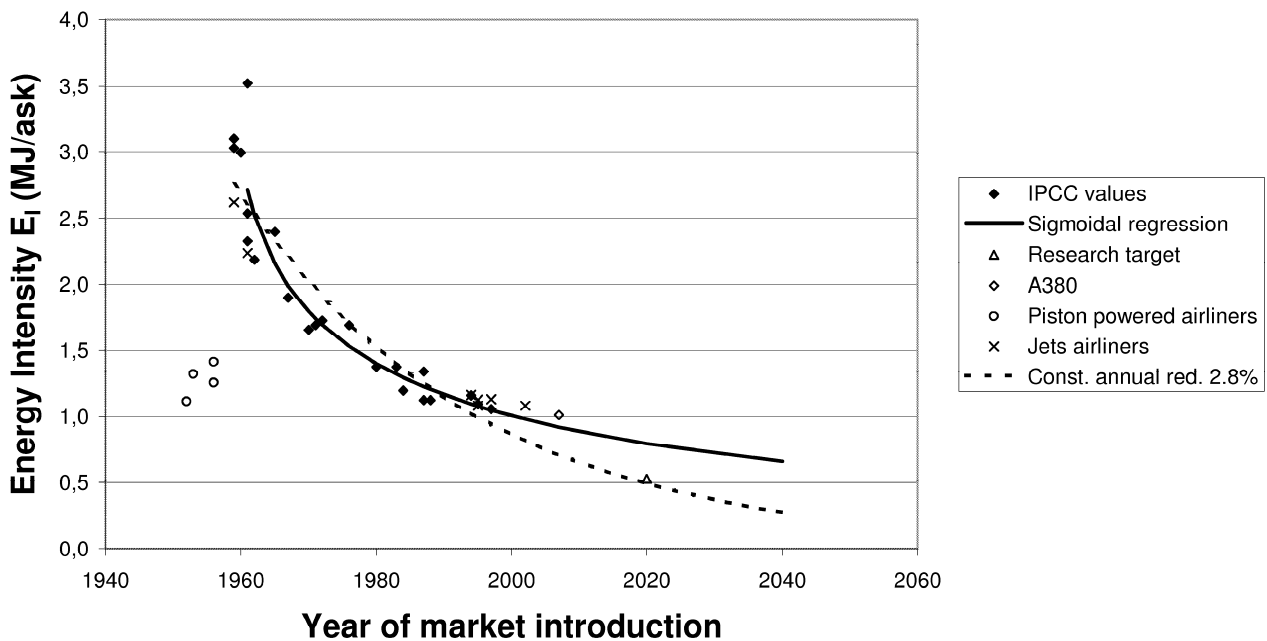


Figure 1: IPCC graph with additional data (see text for references).

The historical data presented in this paper show clearly that the reduction percentage itself is not a constant, but reduces with time (Fig. 1). Hence, the percent-wise fuel reductions observed in the past cannot directly be used for future fuel reduction assumptions. Implicitly, scenarios using this approach neglect several technology limits. Amongst others, these concern the limited energy content per kg fuel and minimum obtainable levels of aircraft drag and weight. Moreover, immediately after market introduction of technology, opportunities for improvement are numerous and relatively cheap, causing improvements initially to be implemented at a high rate. When the technology becomes mature, these opportunities for improvement reduce.

Therefore, this paper proposes an approach that allows strong improvements in the first years after introduction and continuously decreasing improvements over time. Several tests with GraphFirst (Vasilyev, 2002) showed the ‘sigmoidal (logistic 5)’ regression curve resulted in the best fit within the requirements. This curve has been developed to represent biological processes with rapidly slowing down growth rates (see Gottschalk and Dunn, 2005). The curve has the form:

$$E_t = E_{I_0} + \frac{C_{E_t}}{1 + \left(\frac{(Y - Y_{ref}) - C_1}{C_2} \right)^\gamma} \quad (2)$$

where E_t is the Energy Intensity (MJ/ASK) and $(Y - Y_{ref})$ the number of years since a base year Y_{ref} (i.e. the year of introduction of a new technology or the starting year of the data base), E_{I_0} is a

theoretical minimum energy intensity and C_{E_I} , C_1 , C_2 γ are constants defining the initial (maximum) energy intensity and the rate at which the annual gain of Energy Intensity reduces.

The E_I data of individual civil airliners, are taken from two sources (Penner et al., 1999 (IPCC), and Lee et al., 2001). These sources contain only data on jet aircraft since 1957. To complement the history of fuel efficiency, E_I of piston airliners, roughly since the introduction of all-metal fuselages with the DC-2, are added. The exact construction method of the data points by Penner et al., 1999 and Lee et al., 2001 are not published. Therefore we checked the data by first calculating the Energy Intensities for four piston airliners (the L-1049, L1049H and L-1649G version of the Lockheed Super Constellation and the DC-7C), two early jets (Boeing B707-120B B707-320) and five new jets (Boeing B737-800, B777-200 and B777-200IGW and Airbus A330-300 and A340-300). Then we fitted the results using the two early and seven modern jets to fit the same models to the IPCC data. The fuel consumption per ASK of individual aircraft is derived from the harmonic flight distance given by the aircraft's payload-range diagram (assuming still air, ICAO standard takeoff and landing procedures and flying an optimal flight profile). The harmonic flight distance indicates the maximum flight stage length at maximum payload and therefore describes the aircraft best fuel efficiency performance.

Figure 1 shows the data given by IPCC (Penner et al., 1999) plus the results of the sigmoidal model analysis for jets and piston engine airliners. Based on these the sigmoidal regression model has been applied (for parameters see Table 1). The dotted line represents a regression for the best fit of an evolutionary model with constant efficiency improvement of 2.8% per year. The E_I of the new Airbus A380 is based on the 12% reduction with respect to the B747-400, cited by Bickerstaff (2005). Finally the 'typical research target' as mentioned by ATAG (2005) is shown.

3 HISTORIC E_I DEVELOPMENTS OF THE US FLEET

Parallel to the analysis of individual aircraft types, the overall average energy efficiency E_I of a representative fleet of commercial aircraft is investigated as well. Though world-wide aviation traffic statistics are available from several sources (e.g. IATA, 1957-2004; Mitchell, 1999), specific data on world-wide fuel consumption for commercial aviation are not. Only for the US consistent data on both transport volume and fuel consumption could be found from several editions of three sources of data (ATA, 1940; ATA, 1950; ATA, 1980; ATA, 2005, Bureau of Transport Statistics, 2005a; Bureau of Transport Statistics, 2005b and Lerner, 1975). It is presumed that the development in the US is representative for world aviation as historically US originating commercial aircraft and engine technology has dominated the world fleet.

The databases cover various time-periods, definitions, units and parameters. All payload including mail, express and freight, is converted from ton-kilometres to hypothetically available seat-kilometres assuming 160 kg per seat. In this way a E_I time series was created for the period 1930-2005. For further details on the method used see Peeters et al. (2005).

The results are plotted in Figure 2, which clearly shows two general trends of energy intensity (E_I) decrease: one before 1955, the other after 1970. The "discontinuity" coincides neatly with the fast replacement of pistons with jet aircraft between 1957 and 1968 (also shown in the figure marked with **x**). Medium speed, low flying piston-engined aircraft, using (expensive) avgas as energy source, are replaced with high speed, high altitude jet powered aircraft, using (cheap) kerosene. As a result the overall air-transport productivity increased. In terms of transport capacity, energy consumption and energy efficiency, the transition from piston-engined aircraft to jets must have developed at an even higher rate, as the average jet aircraft has a much larger transport productivity as the average piston airliner replaced by the aircraft. Figure 2 also shows the fit of the two fleet sigmoidal (logistic 5) curves for piston and jet.

USA fleet Energy Intensity per ASK @ 160 kg payload/seat conversion

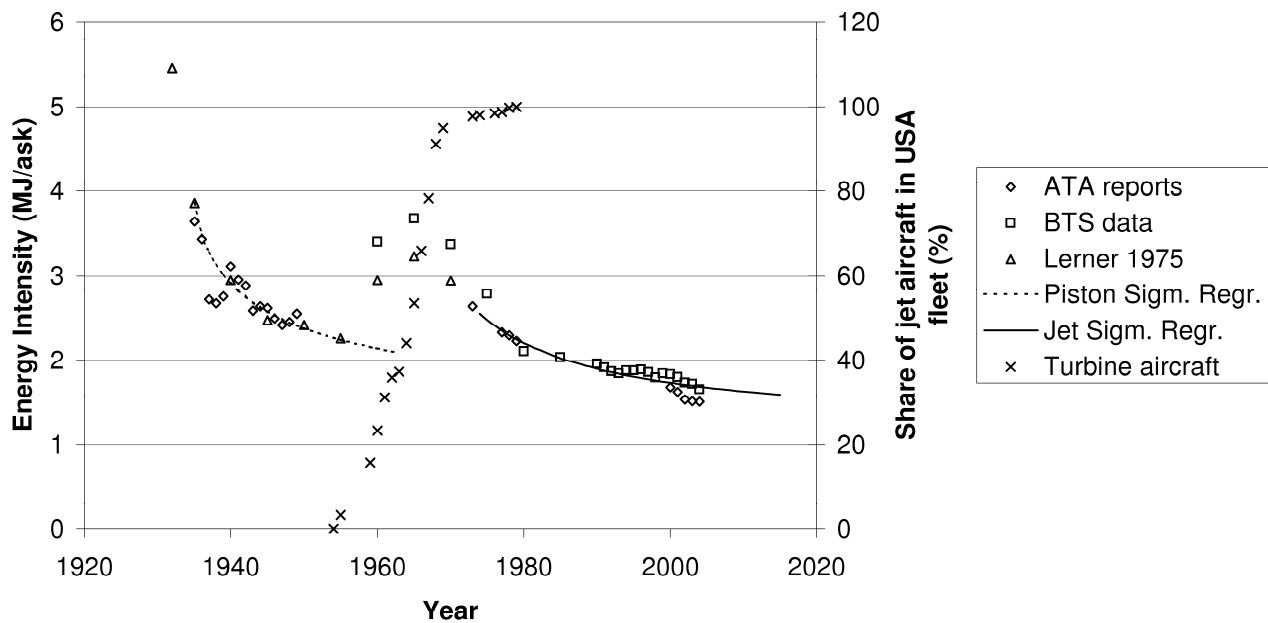


Figure 2: Overall results of the fleet analysis, (data series based on ATA, 1940; ATA, 1950; ATA, 1980; ATA, 2005; Bureau of Transport Statistics, 2005a; Bureau of Transport Statistics, 2005b; Lerner, 1975).

4 FUEL EFFICIENCY FORECASTS

Using the model presented in section 2, the sigmoidal (logistic 5) curve parameters for both individual aircraft types and fleet averaged data sets are obtained. Table 1 and Figures 1 and 2 show the results. The parameters of the graphs are relatively similar, with the exception of the parameters for the jet aircraft fleet data. Figure 2 shows these jet aircraft fleet data to be rather irregular, specifically after 1980. Speculatively this may be caused by an irregular fleet renewal rate by US airlines between 1970 and 2000 and by undefined changes in the measuring method of the data published by ATA.

Table 1: parameters as estimated with FindGraph (Vasilyev, 2002) for equation (2) and the four available time series.

Case	E_{I_0}	C_{E_I}	C_1	C_2	γ	Y_{ref}
IPCC individual long haul aircraft dataset (Albritton et al., 1997; Penner et al., 1999)	-0.2010	3.207	2.214	19.69	0.7183	1958
Lee individual long and short haul aircraft dataset (Lee et al., 2001)	0.0446	2.855	2.213	19.69	0.7183	1958
Piston fleet (ATA, 1940; ATA, 1950)	1.195	2.746	3.916	10.22	0.7186	1931
Jet fleet (ATA, 1980; ATA, 2005; Bureau of Transport Statistics, 2005a; Bureau of Transport Statistics, 2005b)	1.160	1.465	4.051	17.15	0.9976	1969

Using the parameters from Table 1 in the sigmoidal model for the IPCC data (long haul only) yields a 2040 EI of 0.658 MJ/ASK (35% reduction with respect to IPCC value in 2000), the Lee data (short and long haul) yields 0.810 MJ/ASK (28% reduction with respect to the Lee value in 2000) and for the USA jet fleet 1.460 MJ/ASK (16% reduction with respect to the jet fleet value in 2000).

These data contrast with the often cited constant percentage reduction per year ‘best’ fit on the IPCC data yielding 2.8% and $E_{I_b} = 2.84$ MJ/ASK. Extrapolation of “constant percentage reduction approach” results in 0.280 MJ/ASK and a reduction of 72% between 2000 and 2040. A moderate

reduction of 1.4% proposed by Penner et al., 1999 would yield a reduction of 43% in 40 years, which is still significantly higher than the result with the sigmoidal model for the IPCC data.

5 DISCUSSION AND CONCLUSIONS

Figure 1 shows clearly that the common practice of a constant percentage reduction of energy consumption per year is less suitable for prognoses as it probably does not very well represent the economic and physical processes causing the evolutionary development. In many studies this shortcoming is countered by using different 'constants' for different periods of time. This method leaves us with rather arbitrary choices, introducing some extra uncertainty for prognoses. Therefore, one model able to represent the whole historical development with one set of parameters would help to reduce this uncertainty. The proposed sigmoidal model represents such a model.

The main message from the above is the notion that current fuel efficiency forecasts tend to be too optimistic.

The presented data support the idea that most aviation technology developments are clearly driven by cost savings, and productivity increases, safety improvements, increased range and take-off and landing performance. Fuel burn is only one - and commonly not the main - of cost components. The transition from piston engines to gas turbines illustrates this clearly as it was made predominantly to increase aircraft speed and altitude and to some extent range. The transition increased transport efficiency in terms of revenue ton kilometres per year as well as passenger appeal and comfort. As kerosene was much cheaper than avgas, the transition did not significantly raise fuel *cost*. The overall effect at the outset of this transition was higher energy intensity.

Comparing the performance of jet- and piston-powered aircraft in the transition phase between the fifties and the seventies of last century, implies comparing immature, early adoption of gas turbine technology with mature piston engine technology. In general, aircraft size, speed, range and (payload) weight all influence fuel consumption. Today's aircraft differ significantly in these respects from aircraft in the past. Furthermore, load factors do have some influence on fuel consumption per seat-kilometre: extra payload costs extra fuel. As load factors increased between 1970 and 2000, this means that energy consumption per ASK has also been increasing, by several percent. However, this applies only for the jet fleet data, as the individual aircraft data are based on full payload. Finally the introduction of jet engines implied a significant reduction in complexity of the engine, hence, reduced maintenance costs and increased reliability.

In relation to aviation and environment and the piston-jet transition, there is more than just Energy Intensity. From a life-cycle perspective, kerosene is less pollutant to the environment and less costly to produce than avgas (of the fifties). The two fuel types have different fuel combustion quality requirements, due to fundamental differences between the respective engines. Leaded avgas is a high-grade fuel that (in the fifties) included dopes with highly toxic substances such as ethylene bromide. In those years, the use of avgas probably caused significant more damage to the local air quality (and may be even some to radiative forcing) than kerosene.

The following conclusions may be drawn from the study:

- The development of technical fuel efficiency – in terms of fuel consumption per ASK - of civil aircraft shows an S-curve due to the transition from the last fuel efficient piston powered airliners to the less fuel efficient first jets.
- The fuel efficiency development of a time series of a typical aircraft layout is in most studies represented by a model based on one or just a few time periods with a constant increase in fuel efficiency per year. However, a sigmoidal (logistic) model better represents with one set of parameters per dataset the full time series.
- Forecasts on fuel consumption, using the constant percent fuel consumption reductions per year tend to over-predict future gains, compared to the sigmoidal (logistic) model.

REFERENCES

- Albritton, D., G. Amanatidis, G. Angeletti, J. Crayston, D. Lister, M. McFarland, J. Miller, A. Ravishankara, N. Sabogal, N. Sundararaman and H. Wesoky, 1997: *Global atmospheric effects of aviation. Report of the Proceedings of the symposium held on 15-19 April 1996 in Virginia beach Virginia, USA*. NASA, Washington, NASA CP-3351.
- ATA, 1940: *Little known facts about the scheduled air transport industry*. Air Transport Association of America, Chicago, USA, Volume two.
- ATA, 1950: *Air transport facts and figures*. Air Transport Association of America, Washington, USA, 11th edition.
- ATA, 1980: *Air transport 1980. The annual report of the U.S. scheduled airline industry*. Air Transport Association of America, Washington, USA.
- ATA, 2005: *2005 Economic Report. New thinking for a new century*. Air Transport Association of America, Washington, USA.
- ATAG, 2005: *Aviation & environment summit discussion paper*. Air Transport Action Group, Geneva, Switzerland.
- Bickerstaff, C., 2005: Aircraft Technological Developments., *AERONET III Workshop on Air Transportation Systems*, 31 May to 1 June 2005, Stockholm, Sweden.
- Bureau of Transport Statistics, 2005a: *Historical Air Traffic statistics, annual 1954-1980*. Online document at URL http://www.bts.gov/programs/airline_information/indicators/airtraffic/annual/1954-1980.html [24-10-2005].
- Bureau of Transport Statistics, 2005b: *Historical Air Traffic statistics, annual 1981-2001*. Online document at URL http://www.bts.gov/programs/airline_information/indicators/airtraffic/annual/1981-2001.html [24-10-2005].
- Gottschalk, P. G. and J. R. Dunn, 2005: The five-parameter logistic: A characterization and comparison with the four-parameter logistic. *Analytical Biochemistry*, 343, 54–65.
- Green, J. E., 2003: Civil aviation and the environmental challenge. *The Aeronautical Journal*, 107 (1072), 281-299.
- IATA, 1957-2004: *World air transport statistics*, International Air transport Association, Montreal, Canada.
- Lee, J., S. P. Lukachko, I. A. Waitz and A. Schafer, 2001: Historical and future trends in aircraft performance, cost and emissions. *Annual Review Energy Environment*, 26, 167-200.
- Lee, J. 2003: The potential offered by aircraft and engine technologies. IN Upham, P., J. Magham, D. Raper & T. Callum (Eds.) *Towards sustainable aviation*, Earthscan Publications Ltd London, UK, 162-178.
- Lerner, W. 1975: Air transportation (series Q 565-637). *Historical statistics of the United states. Colonial times to 1970*, Bureau of the Sensus, USA, 767-773.
- Mitchell, B. R., 1999: *International historical statistics. The Americas 1750-1993*, ISBN 0-333-726898, USA.
- Peeters, P. M., J. Middel and A. Hoolhorst, 2005: *Fuel efficiency of commercial aircraft. An overview of historical and future trends*. Peeters Advies/National Aerospace Laboratory NLR, Amsterdam, the Netherlands, NLR-CR-2005-669.
- Penner, J. E., D. H. Lister, D. J. Griggs, D. J. Dokken and M. McFarland (Eds.), 1999: *Aviation and the global atmosphere; a special report of IPCC working groups I and III*, Cambridge University Press, Cambridge, UK.
- Pulles, J. W., G. Baarse, R. Hancox, J. Middel and P. F. J. van Velthoven, 2002: *AERO main report. Aviation emissions and evaluation of reduction options*. Ministerie van V&W, The Hague, the Netherlands.
- Vasilyev, S., 2002: *FindGraph*, version 1.491, Uniphiz Lab, Vancouver, Canada.

Contracting UK carbon emissions: implications for UK aviation

K. Anderson, A. Bows*

Tyndall Centre for Climate Change Research, University of Manchester, UK

Keywords: carbon, aviation, energy consumption, UK, emissions

ABSTRACT: Stabilising atmospheric CO₂ concentrations at or below 550ppmv is widely believed to be necessary to avoid ‘dangerous climate change’. However, the latest science suggests that a 450ppmv stabilisation is more likely to achieve the desired goal of ensuring that global mean surface temperatures do not increase by 2°C above pre-industrial levels. Achieving such levels demands industrialised nations make significant emissions cuts, whilst emerging economies adopt low-carbon pathways. This paper focuses on the UK as a typical Annex 1 nation, and demonstrates the severe consequences in meeting its obligations to reduce carbon emissions under the apportionment rules informing both the RCEP’s 22nd report, *Energy the Changing Climate*, and the 2003 Energy White, if the UK Government continues to permit the current high levels of growth within its aviation sector.

1 INTRODUCTION

European nations are in broad agreement that individual States, and the EU as a whole, must tackle the problem of rising CO₂ emissions. In response, some nations have set carbon reduction targets. In theory, many of these targets are chosen to correspond with stabilising CO₂ concentrations at levels that are likely to avoid ‘dangerous climate change’. Although there is no scientific consensus for what is considered to be ‘dangerous’ in relation to climate change, it has been broadly accepted by the policy community that this relates to global mean surface temperatures rising less than 2°C above pre-industrial levels. However, many of the chosen carbon reduction targets omit emissions from the aviation industry. By choosing targets related to global CO₂ concentrations, governments have, often without due consideration or recognition, accepted that such targets must include all CO₂-producing sectors. In this regard, the UK is a clear example, and, as a typical OECD nation with a ‘mature’ aviation industry, it will provide the focus of this paper which addresses the conflict between the UK’s energy and aviation policies. The UK Government set a carbon reduction target in 2003. Its basis for this target was a Royal Commission on Environmental Pollution’s report (RCEP, 2000), which calculated that, for the UK to make its ‘fair’ contribution to stabilising global CO₂ concentrations at 550ppmv, it must cut its carbon emissions by 60% from 1990 levels by 2050. Their calculation used a Contraction & Convergence regime to apportion emissions between nations. However, the UK Government stated that this target does not include emissions from either international aviation or shipping. Furthermore, in the same year that it chose its carbon target, it published a White Paper proposing how the UK could meet the rising demand for air travel.

Selecting which sectors to include and which to omit to meet a particular carbon target essentially negates the choice of basing it on global CO₂ concentrations, unless those sectors contribute negligible amounts of CO₂. This paper clearly demonstrates that this is not the case for the UK’s aviation sector, and illustrates that this sector’s emissions are growing rapidly. The implications for such rapid growth in relation to the UK’s carbon reduction target are highlighted using carbon profiles for stabilising CO₂ concentrations at both 550ppmv and 450ppmv.

* *Corresponding author:* Alice Bows, Tyndall Centre for Climate Change Research, University of Manchester, PO Box 88, M60 1QD, Email: alice.bows@manchester.ac.uk

2 BACKGROUND

Although the UK's national emissions inventory does not include emissions generated by the UK's international aviation or shipping industries, data for these sectors are collected and submitted separately as a memo to the United Nations Framework Conventional on Climate Change (UNFCCC). To estimate the emissions generated by the UK's aviation sector, the National Environment Technology Centre (NETCEN), employ a methodology that takes into account aircraft movements, distances travelled, deliveries of aviation spirit and turbine fuel and the consumption of aviation turbine fuel by the military (Watterson et al., 2004). The data includes both passengers and freight and is plotted in Figure 1. Uncertainties analysis can be found in the Watterson paper.

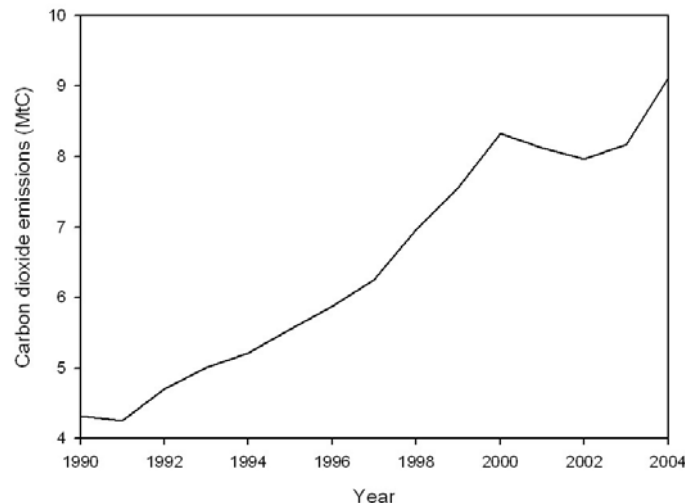


Figure 1. CO₂ emissions from the UK's international aviation industry measured in million tonnes of carbon.

The data indicates that CO₂ emissions from the UK's international aviation industry have increased rapidly since 1991, apart from during the two years following the events of September 11th 2001. On average, emissions increased at an annual rate of 7% between 1990 and 2000. According to these estimates, between 2003 and 2004, CO₂ emissions generated by international aviation increased by 11.7%, and those from domestic aviation increased by 3.8%. Not surprisingly, the figures for the number of passengers passing through UK airports collected by the Civil Aviation Authority follow a similar trend (CAA, 2005). The annual average growth rate between 1990 and 2001 was 7% per year. However, the increase in passenger numbers between 2003 and 2004 was much smaller than the growth in emissions, around 8% compared with 11%. The difference between these two figures has not been explored in detail, but could be due to a range of factors. For example, if there is a larger growth in number of passengers flying long-haul than short-haul, the emissions per passenger averaged over all flights will increase.

To assess whether or not future emissions from the aviation industry will be significant in relation to the UK Government's proposed contracting carbon profile, a combination of Government aviation forecasts, and 'what if' scenarios for the aviation industry are compared with UK CO₂ trajectories for the UK's 60% target trajectory relating to 550ppmv, and for 450ppmv, as it relates more closely to the 2°C temperature threshold.

3 DISCUSSION

3.1 Current and historical CO₂ emissions

Figure 2 illustrates the UK's domestic CO₂ emissions. According to these NETCEN estimates (Eggleston et al., 1998), emissions have been reducing on average at 0.36% per year. However, the period between 1991 and 1995 was significantly affected by a switch from coal to gas, and a relocation of energy intensive industry overseas. Both contributed to the biggest reduction in carbon emissions seen between 1990 and 2004, and are likely to be one-off events that can not be repeated.

CO₂ emissions have not been declining since 1995. When the estimates for CO₂ emissions from international aviation and shipping are added to this profile, it is clear that CO₂ emissions have not shown the same level of reduction since 1990. [Emissions for shipping submitted to the UNFCCC are currently based on UK marine bunker sales. However, unlike aviation, the tax on shipping fuel allows for large discrepancies in price from nation to nation, resulting in a significant amount of 'bunkering'. Assuming that the proportion of total marine bunker fuel is related to a nation's GDP is a crude but more realistic method of apportioning shipping emissions and is employed here. This method will be refined in the future. The uncertainty associated with this method has not been quantified, but will be affected by uncertainty in the global marine bunker fuels sold, for which no figure could be obtained. Assuming this figure, provided by the International Energy Agency, to be appropriate, the fact that the UK is an island state suggests that any apportionment of shipping emissions based on national GDP is more likely to be an underestimate than an overestimate]. The gap between emissions that do not include aviation and shipping, and those that do include these sectors, is widening. This indicates that international aviation and shipping emissions are becoming larger portions of the overall total as time progresses.

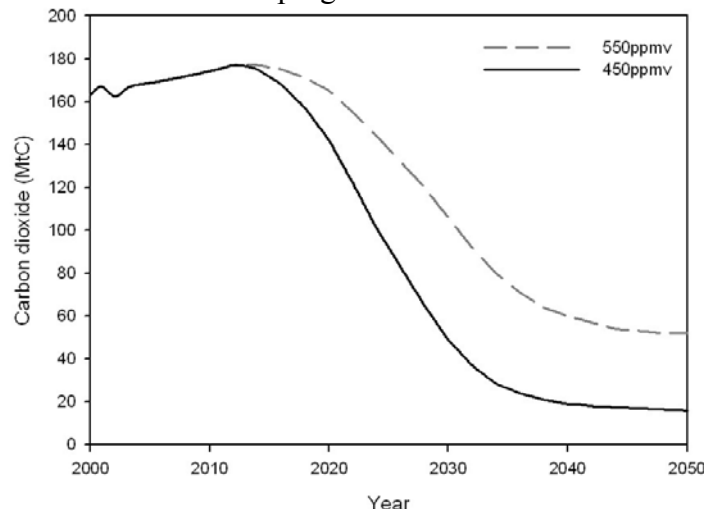


Figure 2. UK domestic CO₂ emissions estimates and those including international aviation and shipping.

3.2 Carbon emission trajectories

To produce total economy future emission trajectories for the UK, the Global Commons Institute (GCI) Contraction & Convergence model was used to reproduce the results of the RCEP report (RCEP, 2000), in line with the UK Government's 60% target. The GCI model, *CCOptions*, essentially calculates a global carbon trajectory based on stabilising atmospheric CO₂ concentrations at a particular level. This global carbon budget is then apportioned between nations as they move towards equal per capita emissions. However, the *CCOptions* model does not include emissions from international aviation and shipping.

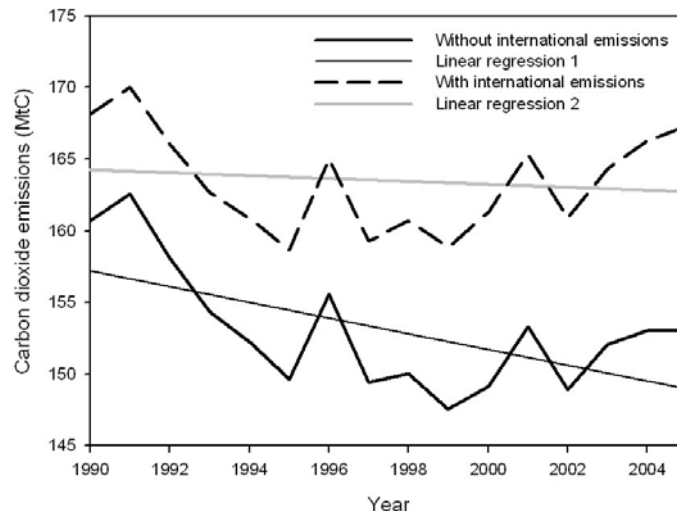


Figure 3. 450ppmv and 550ppmv profiles for UK carbon emissions.

To estimate the impact of including these emissions, the model was modified to incorporate global bunker fuel data available from the CDIAC database (CDIAC, 2005). A trajectory is generated for the UK based on the output of the *CCOptions* model, but modified to produce a scenario reflecting the historical emissions between 2000 and 2004, and their likely trends up until 2012. The resultant trajectory is illustrated in Figure 3. If a similar method is applied to the 450ppmv level, the second profile illustrated in Figure 3, is produced. To investigate the implications of these trajectories for the aviation sector, UK Government aviation forecasts and Tyndall scenarios are compared with the emissions profiles illustrated in Figure 3.

3.3 Future aviation emissions

In 2003, the UK Government published a White Paper (DfT, 2005) including 3 forecasts for aviation industry CO₂ emissions (DfT, 2005) from domestic, international and freight aviation (Table 1).

Table 1: UK Government aviation emission forecasts

Year	DEFRA	DEFRA	DEFRA
	Worst Case	Central Case	Best Case
MtC			
2000	8.8	8.8	8.8
2010	11.4	10.8	10.3
2020	16.5	14.9	13.4
2030	20.9	17.7	15.9
2040	25.1	18.2	16.4
2050	29.1	17.4	15.7

The data for these forecasts begin in the year 2000, but data for 2004 is now available. Furthermore, the methodology used by the NETCEN to estimate emissions has been revised recently and historical figures re-evaluated (Watterson et al., 2004). Comparing the new estimates for 2000 to 2004 (Table 2) with these figures illustrates that the figure for 2004 is already close to the forecasted values for 2010. Emissions would therefore have to grow at extremely low rates between 2004 and 2010 to remain within the upper bound of the ‘worst’ case estimate by 2010.

Table 2. NETCEN aviation emissions data as submitted to the UNFCCC

Year	NETCEN data MtC
2000	9.0
2001	8.8
2002	8.6
2003	8.8
2004	9.8

The very high growth rates experienced by the aviation industry during the past few years have already rendered these UK Government’s forecasts out-of-date. This is a significant limitation when attempting to assess this industry’s impact on the climate. To illustrate how emissions are more likely to evolve if growth rates continue at close to current rates in the short term, two very simple scenarios are presented here.

The first assumes that the average annual rate of growth in emissions of 7% per year, seen between 1993 and 2001, continues from a baseline 2004 figure of 9.8MtC, until the year 2012. This growth rate is somewhat lower than the latest confirmed rate available indicating that emissions from international aviation increased by ~12% between 2003 and 2004. Between 2013 and 2050, emissions are assumed to grow at a much lower rate of 3% per year – similar to the figure suggested by the UK Government forecasts. Assumptions underlying this scenario for 2004 and 2012 include:

no new policies to address growth within the aviation sector; oil prices continue to have a very limited impact on growth; the success of the low-cost airlines continues and grows; fuel efficiency improves at around 1% per year across the fleet

For the period post-2012, it is assumed that: radical policies either in the form of quotas or fiscal measures, are introduced; fuel efficiency improvements are more significant

The second scenario, assumes: rates of growth in emissions seen historically, continue until 2030; fares remain affordable and there is little to no tax on kerosene; airport capacity is increased to adapt to this growth; fuel efficiency of the fleet increases by ~1% per year

Table 3: Aviation emission scenarios

Year	Scenario 1	Scenario 2
	MtC	
2000	9.0	9.0
2010	14.7	14.7
2020	21.4	29.0
2030	28.7	57.0
2040	38.6	76.7
2050	51.9	103.0

3.3.1 Implications of a growing aviation for UK climate policy

To assess the implications of a growing aviation industry within a UK striving to cut emissions, the UK Government aviation forecasts and the Tyndall aviation scenarios are compared with the Contraction & Convergence profiles illustrated in Figure 3. Figure 4 presents the comparison between the UK Government's aviation forecasts and the UK carbon budget. Despite these forecasts being unrepresentative of the true scale of aviation emissions, the results show that for all of the DfT's forecasts, carbon emissions from the aviation industry are accounting for more than the total carbon budget for the 450ppmv profile by 2050. Furthermore, the UK Government's 'worst' case scenario exceeds the 450ppmv profile during the 2030s. This is particularly worrying as recent scientific research (Elzen and Meinshausen, 2006) indicates that stabilising CO₂ concentrations at levels lower than 450ppmv, will be necessary if there is to be a reasonable likelihood of avoiding so-called 'dangerous climate change'. In other words, it will be virtually impossible to reconcile the levels of aviation growth forecast by the UK Government with a 450ppmv stabilisation level, unless dramatic changes are made to the way aircraft consume fuel or indeed the nature of the fuel source itself. This disproportionate allocation of emissions to one sector will inevitably have significant consequences for all other carbon-emitting sectors of the economy (Anderson et al., 2005).

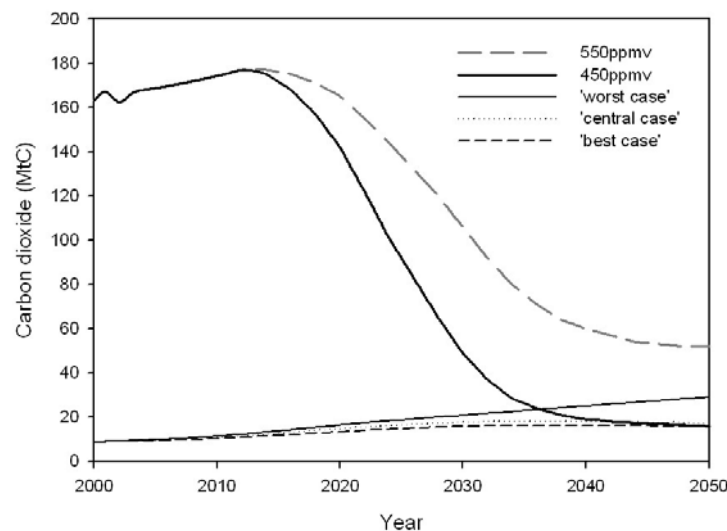


Figure 4. UK carbon emission trajectories vs UK Government aviation forecasts

Considering now the 550ppmv profiles, the DfT's forecasts show aviation emissions representing between 15% and 20% of the carbon budget by 2030, and between 30% and 56% by 2050. For comparison, in 2004, aviation accounted for 7% of the UK's carbon budget (Anderson et al., 2005). The likely shift from a 7% share to these much higher proportions would indicate that other sectors need to decarbonise substantially to compensate for air travel, either through significant reductions in energy consumption or the large-scale adoption of low-carbon energy supply. Consequently, the UK Government's forecasts predict the aviation industry accounting for over 50% of the UK's total carbon budget by 2050 if 550ppmv is the stabilisation target, and exceeding the UK's total 2050 carbon budget for 450ppmv. Whilst it may be argued that the Hadley Centre model, upon which the Contraction & Convergence profiles are based, generates slightly larger carbon-cycle feedbacks than other similar models (Zeng et al., 2004), the forecasts nevertheless clearly highlight the substantial contradictions between the UK Government's Energy White Paper targets for carbon emissions and the same government's Aviation White Paper's airport expansion proposals.

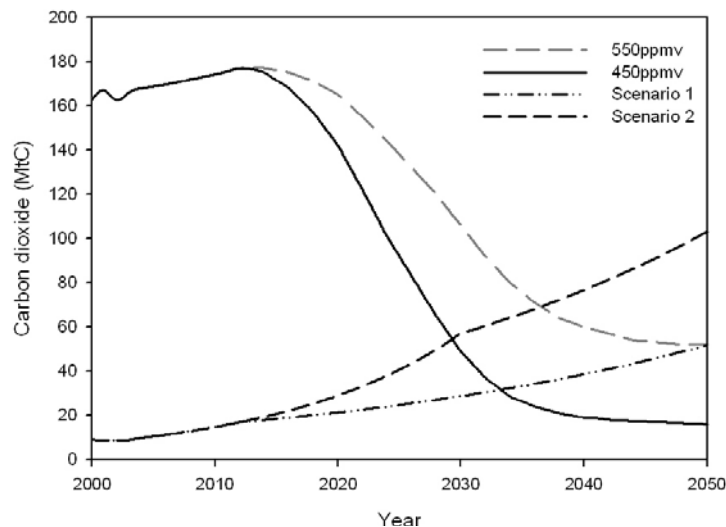


Figure 5. UK carbon trajectories vs aviation scenarios

The aviation scenarios presented in Table 3, and in graphical form in Figure 5 clearly illustrate the outcome of the arguably more realistic growth scenarios for the aviation industry, and what this means for the UK's total carbon budget. Both scenarios exceed the UK's carbon budget under the 450ppmv regime by the early 2030s, with scenario 2 exceeding it prior to 2030. If 550ppmv is the chosen trajectory, only scenario 1 remains within budget by 2050. The rapidly increasing emissions being generated by the aviation industry will likely leave the industry with extremely difficult choices in the future. If the current high rates of growth continue, even for a short period, then emissions growth will need to be curbed to less than 3% per year within the next 6 years, if the UK is to remain within the budget necessary to meet 550ppmv. However, the latest science is suggesting that to have a reasonable chance of avoiding 'dangerous climate change', a 450ppmv target is more appropriate. The corresponding budget would require growth in passenger-kilometres to closely match fuel efficiency per passenger-kilometre over the short to medium-term. In other words, growth in the region of 1 to 2% per year.

The silver bullet for the aviation industry is often cited as its swift incorporation into the EU Emissions Trading Scheme (EU ETS). However, as all of the EU nations are industrialised, they too will be looking to significantly reduce their carbon emissions from all of their sectors year-on-year. The EU Commission intends to include international aviation in the EU ETS by or before 2012 (COMM, 2005). The Commission is also intending for the scheme to include all flights taking off from EU nations, as opposed to a scheme incorporating just intra-EU flights in the first instance; the latter being preferred generally by the aviation industry (Bows et al., 2006). However, given the logistics of incorporating this international sector within the current EU ETS, it is highly unlikely that trading between the aviation industry and other sectors will begin prior to 2010-12.

4 CONCLUSION

By focussing on the UK as an exemplar nation, this paper illustrates a number of key points in relation its aviation industry and climate change targets. Firstly, UK Government forecasts for aviation emissions have quickly become outdated due to the very high rates of growth being seen within the industry. Consequently, these forecasts must be revisited as a matter of urgency. Secondly, that even using these outdated forecasts, this paper illustrates the conflict between the UK Government's Aviation White Paper, which lays out measures to meet the demand for flights, and the UK's Energy White Paper of the same year. Indeed, the UK typifies the EU in actively planning and thereby encouraging continued high levels of growth in aviation, whilst simultaneously asserting that they are committed to a policy of substantially reducing carbon emissions. Thirdly, using aviation emission scenarios that reflect the recent trends in emissions, the conflict between the UK Government's target and this growing industry has serious consequences for other sectors.

If the aviation sector is to be given a larger quota of emissions compared with other sectors, then these other sectors will need to decarbonise to compensate. This could be a reasonable solution to the limitations on technology and alternative fuels unique to the aviation sector, if the room for manoeuvre for other sectors were significant. However, these aviation scenarios suggest that if 450ppmv becomes the new climate target stabilisation level, then aviation emission can not be sustained at current levels, even with significant compensation from other sectors. If 550ppmv is chosen, then it is still possible that the total carbon budget will be exceeded by this one industry by 2050. Furthermore, if the industry were to take up 90% of the carbon budget, the pressure on other industries to decarbonise to 10% of their current levels would likely be too great. Ultimately, the UK and the EU face a stark choice: to permit high levels of aviation growth whilst continuing with their climate change rhetoric; or to convert the rhetoric into reality and substantially curtail aviation growth until it can be balanced by fuel efficiency gains.

REFERENCES

- Anderson, K., S. Shackley, S. Mander and A. Bows, 2005: *Decarbonising the UK: Energy for a climate conscious future*, The Tyndall Centre for Climate Change Research, Manchester.
- Bows, A., K. Anderson and P. Upham, 2006: *Contraction & Convergence: UK carbon emissions and the implications for UK air traffic*, Tyndall Centre Technical Report, Norwich, Tyndall Centre for Climate Change Research, 40.
- CAA, 2005: *Main outputs of UK airports*, CAA.
- CDIAC, 2005: 'Carbon dioxide emission trends', from <http://cdiac.esd.ornl.gov/trends/emis/annex.htm>.
- COMM, 2005: *Reducing the climate change impact of aviation*, Commission of the European Communities, 459.
- DfT, 2005: *Transport Statistics Great Britain*, Transport Statistics Great Britain, TSO, London, Department for Transport.
- Eggleston, H. S., A. G. Salway, D. Charles, B. M. R. Jones and R. Milne, 1998: *Treatment of Uncertainties for National Estimates of Greenhouse Gas Emissions*, Centre, N. E. T., AEA Technology - 2688.
- Elzen, M. G. J. and M. Meinshausen, 2006: *Multi-gas emission pathways for meeting the EU 2C climate target*, in Schellnhuber, H. J., W. Cramer, N. Nakicenovic, T. Wigley and G. Yohe.(ed.), *Avoiding dangerous climate change*, Cambridge University Press, Cambridge.
- RCEP, 2000: *Energy - the changing climate*, 22nd report, CM 4749, The Stationery Office, London.
- Watterson, J., C. Walker and S. Eggleston, 2004: *Revision to the method of estimating emissions from aircraft in the UK greenhouse gas inventory*, Report to Global Atmosphere Division, DEFRA, NETCEN.
- Zeng, N., H. Qian, E. Munoz and R. Iacono, 2004: *How strong is carbon cycle-climate feedback under global warming?*, *Geophysical Research Letters*, 31, (L20203).

Estimates of UK CO₂ Emissions from Aviation Using Air Traffic Data

T. Pejovic, R.B. Noland*, V. Williams

Centre for Transport Studies, Department of Civil and Environmental Engineering, Imperial College London, UK

R. Toumi

Space and Atmospheric Physics Group, Blackett Laboratory, Imperial College London, UK

Keywords: CO₂ Emissions, Aviation

ABSTRACT: The allocation of CO₂ emissions to specific sources is a major policy issue for international aviation. This paper addresses this problem by recommending a possible methodology for calculating air transport carbon dioxide (CO₂) emissions using detailed air traffic data. The basis for the calculations is an air traffic sample for one full-day of traffic for the UK. The results are compared with two of the most widely-used aviation CO₂ emission estimates to have been made for the UK: the SERAS study and NETCEN estimate. Their estimates for the year 2000 are 26.1 Mt and 31.4 Mt, respectively. Our estimate of total aviation CO₂ emissions, using detailed simulations and real air traffic data, is 34.7 Mt for the year 2004. Different methodologies and their implications are also discussed.

1 INTRODUCTION

Carbon dioxide (CO₂) is one of the main causes of climate change and air transport is the fastest growing source. Commercial air transport currently contributes a small but growing share of global anthropogenic CO₂ emissions. This share was estimated at 2% of the worldwide total in 1992 (Intergovernmental Panel on Climate Change (IPCC), 1999). In the UK, reported CO₂ from sales of fuel for international aviation was 2.8% of all CO₂ emissions in 1992 (which includes all international bunker fuels, which are sometimes ignored in assessments of CO₂ emissions). By 2003, this had risen to over 5% (UNFCCC, 2006). With estimated world wide growth in air transport as high as 5% per year, the air transport sector will account for a growing percentage of total CO₂ emissions, despite improvements in efficiency.

In the Kyoto Protocol, anthropogenic greenhouse gas emissions are attributed to individual countries to set targets and monitor performance. Currently, countries only have to include domestic air traffic in the calculation of total national emissions. Total international aviation fuel sales in each country are reported separately (as bunker fuels), but there is no agreed allocation procedure to attribute the associated CO₂ emissions to national totals and bring them within targets for emission reduction. In the context of national progress towards Kyoto targets, it is important to have a clear understanding of the total contribution of aviation, not just domestic flights, to ensure that policy priorities can be fairly assessed.

Several air transport CO₂ emission estimates have been provided for the UK in the past few years. The National Environmental Technology Centre (NETCEN) estimated that in 2000, UK air transport accounted for 31.4 million tonnes (Mt) of CO₂ emissions (DfT, 2003). Figures produced by Halcrow for the UK Department for Transport (DfT) in the South East and East of England Regional Air Services Study (SERAS) estimated total air transport related CO₂ emissions for 2000 at 26.1 Mt (DfT, 2003). Both studies had their limitations and assumptions. Here, in this study, we assess their findings using real air traffic data for one day to develop a new CO₂ emissions estimate.

* *Corresponding author:* Robert B. Noland, Centre for Transport Studies, Department of Civil and Environmental Engineering, Imperial College London, UK. Email: r.noland@ic.ac.uk

2 METHODOLOGY

2.1 Scenario Definition

The Reorganized Air Traffic Control Mathematical Simulator (RAMS Plus) and the Advanced Emission Model (AEM III) were used to analyse fuel burn use and hence CO₂ emissions. The RAMS Plus model simulates the four dimensional profile of each flight, describing the operation of the aircraft at each point, such that the fuel burn for each element of the journey can be calculated. This allows calculation of the emitted CO₂. The AEM has been developed at the EUROCONTROL Experimental Centre to estimate aviation emissions and fuel burn using flight profile information (AEM, 2003).

Simulations were conducted using traffic, route network and sector data provided by National Air Traffic Services in the UK (NATS). A 24-hour air traffic sample for Friday, 3rd September, 2004 was used with 7074 flights, each with specified departure and destination airports and simulation entry times. The simulation area covers the UK airspace. For the region simulated, data describing the location of sector boundaries, airports and navigation aids (navaids), are specified. The ATC sectors are specified in four dimensions and the routes are defined according to the sequence of navaids to be used.

2.2 CO₂ Emissions Calculations

The fuel burn rate, and hence the rate of CO₂ emission, varies with mode of flight. Two flight phases can be considered for emissions calculations: the Landing and Take Off cycle (LTO) which includes all activities below 3000 feet (1000 m) and the Climb, Cruise and Descent cycle (CCD) which is defined as all activities that take place at altitudes above 3000 feet.

Additional emissions occur due to fuelling and fuel handling in general, maintenance of aircraft engines and fuel jettisoning to avoid accidents. These emissions are, however, not included in this analysis. Also, CO₂ emissions from surface access to airports were not within the scope of this estimate.

To calculate the total fuel burn for the traffic sample, fuel burn rates from the performance tables of the Eurocontrol Experimental Centre (EEC) Base of Aircraft Data (BADA) Revision 3.6 were incorporated into RAMS Plus. Flight speed and rate of climb/descent were also defined according to the BADA performance tables.

The configuration of RAMS Plus with the UK air traffic sample has two limitations. Firstly, it only has the capability to calculate emissions above 3000 ft (CCD cycle), as detailed data on airport configurations and ground movements was not available. Secondly, given the limitations of the available air traffic sample and the specific sectors, navaids, and routes as defined for UK airspace, as required by RAMS Plus, it was possible to only calculate emissions within UK airspace. Since one of the objectives of this research was to estimate UK CO₂ emissions which can be allocated to the UK CO₂ budget, using a Flight Schedule Approach (meaning all domestic and traffic departing from UK airports), it was necessary to perform additional calculations using the AEM tool.

The air traffic sample available had detailed information only on flights within UK airspace. For international departures, the AEM completes the flight profile assuming that the aircraft uses the shortest (great circle) distance between the point of departure from UK airspace and the destination airport. On average, journeys are about 10% longer than this great circle route because of airspace constraints and meteorological factors (IPCC, 1999). In addition, the AEM completes the whole flight profile by adding missing LTO legs from departure and arrival airports as well as joining these legs with the first and last known position of the aircraft according to the flight file from RAMS.

3 UK CO₂ EMISSIONS ESTIMATE

The AEM uses flight profile information from the RAMS Plus output to calculate fuel consumption and emissions. Summing the emissions from all flights it was possible to derive total CO₂ emissions for the 24 hr traffic sample. Traffic was separated into three categories: domestic, UK departures to the EU, and UK departures to other international airports. All other traffic, including fly-over

flights and flights arriving to the UK are omitted; emissions are calculated only for departures. This Flight Schedule approach gives a total fuel estimate consistent with the recorded deliveries of aviation fuel to the UK and prevents double counting of emissions allocated to international aviation. Just over half (55.19%) of the UK's total daily traffic movements are domestic (21.11% of total air traffic) or EU departures (22.78%) and international departures (11.30%) and they are used for estimation of the CO₂ emissions inventory.

The daily CO₂ estimates are adjusted to correct for underestimation due to the assumption that the flight trajectory follows the shortest (great circle) route outside of UK airspace. Previous studies (IPCC, 1999; Howell et al., 2003) have estimated that the distance flown is typically 10% longer than the great circle route. As this additional distance occurs in the cruise phase, and only outside UK airspace, the underestimation of the total CO₂ will be less than 10%. Assuming that the great circle portion of the flight underestimates distance flown by 10%, and that the additional CO₂ for the route as flown is proportional to the additional distance, the mean underestimation is 4.9% for EU departures and 6% for other international departures (expressed as a percentage of the total CO₂ for the full flight trajectory). Total daily CO₂ estimates are adjusted accordingly. CO₂ for domestic flights is not adjusted as there is no section outside of UK airspace.

In the absence of detailed data for each day, monthly total estimates for September were obtained by multiplying daily values by 30.

To reflect seasonal variation in air traffic volumes, monthly CO₂ emissions for the three categories of air traffic for the rest of the year were calculated using the reference values for September and weighting for the monthly number of air traffic movements using Civil Aviation Authority statistics for 2004 (CAA, 2004a). CAA monthly airport statistics tables for 2004 do not include records for accession countries admitted into the European Union in May 2004.

Air travel is greater during the week than on weekends and fairly uniform across individual days of the week. For scheduled traffic, a 20% difference between a weekday and a weekend day is not unusual (EUROCONTROL, 2006). Converting from a single weekday to an annual figure overestimates total traffic movements, partly by failing to account for the reduction in traffic at weekends. To correct for this, we assumed that the overestimation can be described by the difference between the number of air transport movements in our sample and those reported by the CAA and that this overestimation of traffic movements corresponds to a proportional overestimation of CO₂ emissions. For domestic traffic, the overestimation of traffic movements is 13.6%; for international (EU and other international departures), it is 9.7%. The annual CO₂ estimates are adjusted to correct for this.

Annual CO₂ emissions estimates for 2004 for the three traffic categories are shown in Table 1. It is assumed that the emissions in each category follow the annual cycle of movements, that is, the mix of aircraft types and route lengths remains constant and changes in frequency of service occur uniformly across the traffic fleet (within each traffic category).

Table 1. UK CO₂ Emissions - 2004

2004 UK CO ₂ Emissions Estimate	CO ₂ (Mt)
Domestic	1.94 – 3.14
EU Departures	7.98 – 9.73
International Departures	16.54 – 22.97
Total	26.46 – 35.85

For domestic traffic, the monthly variation in movements is small and the distribution of routes shows little seasonal variability (CAA, 2004b). EU and International traffic are more variable. Most destinations for EU-bound traffic have a uniform pattern throughout the year, but traffic (in terms of carried passengers) to vacation destinations like Spain and Greece almost doubles during the summer. Within the International (non-EU) routes the largest variation is again for summer vacation destinations, such as Cyprus and Turkey, and for long haul flights to North America and the Far East (CAA, 2004c).

The assumption that the pattern of routes does not show seasonal variability overestimates stage lengths by about four percent for international scheduled services and by 7.5% for non-scheduled services within the 25 EU states. This is based on an analysis of CAA data (CAA, 2004d). There is

a further underestimate of the stage lengths of international non-scheduled, non-charter traffic by 18.3%; however these flights represent only 2.3% of annual UK airlines flights for 2004.

Figure 1 shows the estimated annual cycle of the UK's CO₂ emissions from aircraft. As expected, the biggest polluter group comprises International Departure flights; although the number of movements is roughly half that for domestic or intra-EU flights. Aircraft are typically larger and the average route is much longer for these flights. EU and international departures have similar annual cycles; both groups have the highest emissions occurring in July and August. CO₂ emissions from domestic traffic have only minor variations throughout the year.

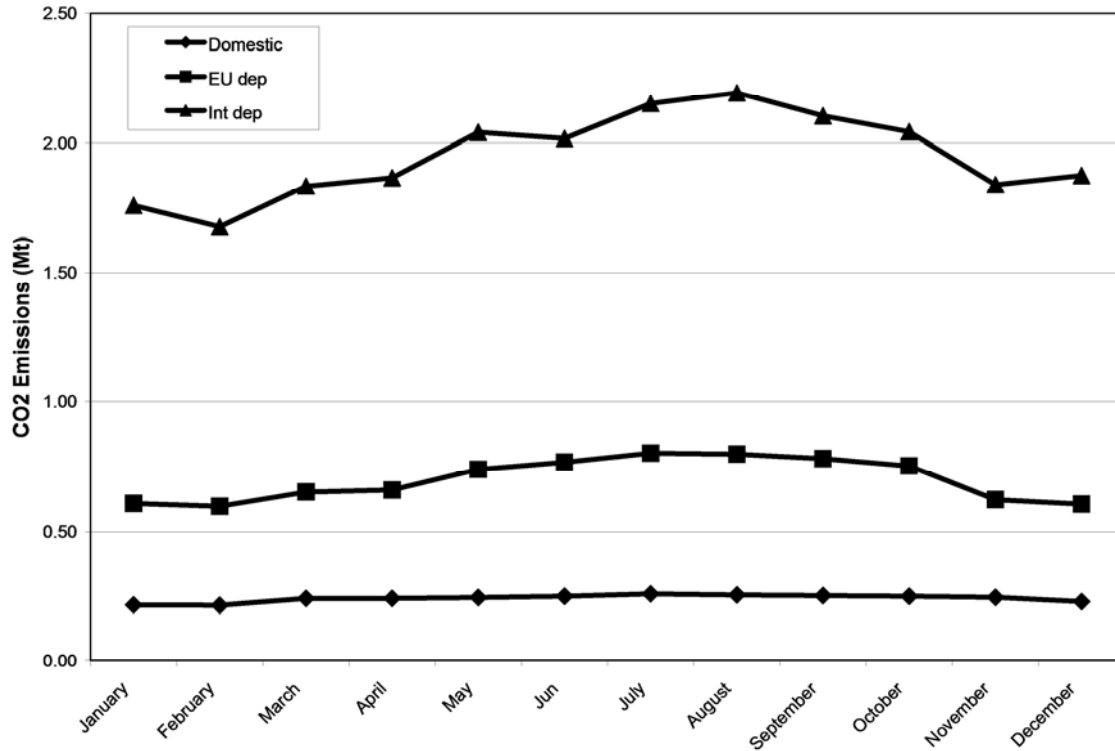


Figure 1. UK's CO₂ Emissions Annual Cycle

In addition to providing a national CO₂ emission estimate, this method allows analysis of those flights and aircraft within the sample that are the largest emitters. This provides an assessment of which flights and associated aircraft account for the bulk of emissions. More detailed analysis can be found in Pejovic *et al.* (in prep).

4 COMPARISON WITH OTHER CO₂ EMISSION ESTIMATES

Findings from this analysis are compared with the NETCEN and SERAS CO₂ estimates for the year 2000 taken from the report *Aviation and the Environment: Using Economic Instruments* (DfT, 2003). Despite the fact that estimates were made using different methodologies and data, there is some consistency between them (Table 2). Our estimate includes the uncertainty associated with the BADA performance data and fuel burn rates and uncertainties in the corrections for the great circle approximation and the overestimation of traffic. More detailed information can be found in Pejovic *et al.* (in prep).

Table 2. Aviation-related CO₂ Emissions, Year 2000 (million tonnes)

Type of traffic	SERAS (2000)	NETCEN (2000 old)	NETCEN (2000 new)	NETCEN (2004 new)	This analysis (2004)
Domestic	1.5	2.9	1.97	2.30	1.94 - 3.14
International	24.6	28.5	30.24	33.12	24.52 - 32.71
Total	26.1	31.4	32.21	35.42	26.46 - 35.85

NETCEN estimated that in 2000, UK air transport accounted for 31.4 Mt of CO₂ emissions, of which 2.9 Mt CO₂ were emitted by domestic flights (DfT, 2003). In addition, NETCEN's updated UK Greenhouse Gas Inventory 1990 to 2003, records that the UK aviation sector, including all domestic flights plus international passenger departures and freight air traffic movements produced 32.2 Mt of CO₂. Of this total, UK civil passenger aviation produced 30 Mt of CO₂ (Baggot *et al.*, 2005). Using a new methodology, their just released UK Greenhouse Gas Inventory 1990 to 2004, suggests that CO₂ emission estimates for international traffic in 2000 and 2004 were 30.2 and 33.1 Mt respectively (Baggott *et al.*, 2006).

The NETCEN figures take into account the fact that international and domestic flights have a different proportion of emissions at altitude and in the LTO cycle. However, NETCEN calculates estimates of aviation CO₂ emissions at cruise altitudes based on aviation fuel sales data. Therefore NETCEN's estimate of the UK's CO₂ emissions is an approximation since NETCEN estimates the total fuel uplifted by aircraft in the UK as the UK's CO₂ emissions from aviation. In practice, part of the uplifted fuel could be used on flights not departing from the UK but used, for example, on a return flight back to the UK from a different country (or vice versa).

The SERAS study gave slightly different results. In the SERAS study total air transport related CO₂ emissions were estimated at 26.1 Mt for the year 2000 (DfT, 2003). SERAS produced estimates, which are over 10% lower than those estimated by NETCEN, assuming that aircraft use "great circle" routes. In addition, the SERAS estimates were based on the assumption that the UK's share of international flights is one-half of the total traffic. Apart from smaller coverage of UK airports by SERAS (29 UK airports), the likeliest reason for the discrepancy is that the modelling for the SERAS estimate assumed that all aircraft fly great circle distances. Our use of the RAMS simulation with real air traffic data allows actual flight paths to be modelled.

5 DISCUSSION AND CONCLUSIONS

The international air traffic emissions, calculated in this study (31.8Mt), appear to be slightly higher than those given by NETCEN for 2000 (30.2 Mt). However, looking at the NETCEN figures for the CO₂ emissions of international traffic in 2004 (33.1 Mt) and with respect to traffic growth between 2000 and 2004 which is in the range of 2-6% per year (CAA, 2004e), these estimates match well. Moreover, the latest UNFCCC records show that the UK's reported emissions resulting from fuel use for aircraft engaged in international transport were 30.24 Mt and 29.66 Mt in 2000 and 2003 respectively (UNFCCC, 2006).

There is a possibility, though, that NETCEN figures for emissions of international traffic are overestimated, since the metric used by NETCEN to measure the CO₂ emissions in cruise phase is an approximation. Furthermore, the high uncertainty in NETCEN's aviation fuel consumption reflects the uncertainty in the split between domestic and international aviation fuel consumption taken from DUKES. On the other hand, the SERAS study produces under-estimates and their approach uses assumptions which do not represent realistic assumptions about air traffic in the UK.

Nevertheless, both the NETCEN and the SERAS study provide a good basis for evaluation of our results. The results presented here indicate that by using real traffic profiles to calculate CO₂ emissions, by means of the Flight Schedule Approach, and applying different emission factors for each different mode of flight, it is possible to calculate a CO₂ emissions inventory consistent with other estimates. This approach also allows better disaggregation of domestic and international flights and their emissions as well as disaggregation into aircraft groups and route profiles that can serve as a basis for analysis of various policy effects, which the other estimates cannot provide.

Understanding of the total contribution of aviation, not just domestic flights, can ensure that policy priorities can be fairly assessed. Even if national targets for CO₂ emission reduction are met, a very small proportion of international departures can consume a large amount of the national allowances. This has implications for how the associated CO₂ emissions of international aviation can be brought within national targets for emission reduction.

Overall, this method for calculating a CO₂ emissions inventory based on actual flight paths, allows a better disaggregation of domestic and international flights and their emissions. CO₂ emissions of international traffic are calculated using real traffic profiles within UK airspace, and applying different emission factors for each different mode of flight, which results in a higher accuracy of

the method. This approach also provides an assessment of which flights and associated aircraft account for the bulk of emissions. Furthermore, with availability of different traffic samples, to reflect seasonal and weekend traffic changes, it is evident that this approach can give us even more realistic and accurate estimates.

ACKNOWLEDGEMENTS

This work was supported by the UK Engineering and Physical Sciences Research Council. Assistance from the RAMS Plus support group at ISA Software is gratefully acknowledged. National Air Traffic Services supplied the one day UK air traffic sample. Advanced Emission Model III was provided by the EUROCONTROL Experimental Centre.

REFERENCES

- AEM, 2003: *AEMIII User Guide*. Eurocontrol Experimental Centre – SEE: Society Environment Economy. Bretigny-sur-Orge, France
- Baggott, S.L., R. Milne, T.P. Murrells, N. Passant, G. Thistlethwaite, J.D. Watterson, 2005: UK Greenhouse Gas Inventory, 1990 to 2003: Annual Report for submission under the Framework Convention on Climate Change, AEAT/ENV/R/1971, 29/04/2005. Available at: http://www.airquality.co.uk/archive/reports/cat07/0509161559_ukghgi_90-3_Issue_1.1.doc
- Baggott, S.L., R. Milne, T.P. Murrells, N. Passant, G. Thistlethwaite, J.D. Watterson, 2006: UK Greenhouse Gas Inventory, 1990 to 2004: Annual Report for submission under the Framework Convention on Climate Change, AEAT/ENV/R/1971, 14/04/2006. Available at: http://www.airquality.co.uk/archive/reports/cat07/0605031644_ukghgi_90-04_v1.0.pdf
- CAA, 2004a: UK Airport Statistics: Air Transport Movements 2004. Available at: <http://www.caa.co.uk/default.aspx?categoryid=80&pagetype=88&pageid=3&sglid=3>
- CAA, 2004b: UK Airport Statistics: Domestic Air Passenger Traffic To and From UK Reporting Airports for 2004. Available at: http://www.caa.co.uk/docs/80/airport_data/2004Annual/Table_12_2_Domestic_Air_Pax_Traffic_Route_Analysis.csv
- CAA, 2004c: UK Airport Statistics: International Passenger Traffic to and from UK Reporting Airports by Country 1993-2004. Available at: http://www.caa.co.uk/docs/80/airport_data/2005Annual/Table_11_International_Air_Pax_Traffic_to_from_UK_by_Country.csv
- CAA, 2004d: UK Airlines Statistics. Available at: <http://www.caa.co.uk/default.aspx?categoryid=80&pagetype=88&pageid=1&sglid=1>
- CAA, 2004e: UK Airport Statistics: 2004 – annual. Available at: http://www.caa.co.uk/docs/80/airport_data/2004Annual/Table_04_2_Air_Transport_Movements_1994_2004.pdf
- DfT, 2003: *Aviation and the Environment: Using Economic Instruments*, Department for Transport, London, Available at: http://www.hm-treasury.gov.uk/documents/taxation_work_and_welfare/tax_and_the_environment/aviation/tax_avi_index.cfm
- Eurocontrol, 2006: Trends in Air Traffic, Volume 1, Getting to the Point: Business Aviation in Europe. Available at: http://www.eurocontrol.int/statfor/public/site_preferences/Business%20Aviation%20Study%20Doc176%20v1.0%20FINAL.pdf
- IPCC, 1999: *Aviation and the Global Atmosphere*. A Special Report of IPCC Working Groups I and III in collaboration with the Scientific Assessment panel to the Montreal Protocol on Substances that Deplete the Ozone Layer, J. E. Penner, D. H. Lister, D. J. Griggs, D. J. Dokken and M. McFarland (eds). Cambridge University Press, UK.
- Howell, D., M. Bennett, J. Bonn, D. Knorr, 2003: Estimating the en-route efficiency benefits pool. 5th USA/Europe R&D Seminar, June 2003, Budapest.
- Pejovic, T., R. B. Noland, V. Williams, R. Toumi (in prep) Estimates of UK CO₂ Emissions from Aviation Using Air Traffic Data, submitted to the Annual Meeting of the *Transportation Research Board*.
- UNFCCC 2006: United Nations Framework Convention on Climate Change, Greenhouse Gas Inventory Data, Aviation Emissions - CO₂, Available at: http://ghg.unfccc.int/tables/a3_aviation.html

Global road transport's emission inventory for the year 2000

H. Steller^{*}, J. Borcken

DLR – Verkehrsstudien Berlin-Adlershof, Germany

Keywords: emission inventory, road transport, gridding

ABSTRACT: Emission inventories are needed to determine the impact of different sectors and trace species on environment and health. We have calculated a highly differentiated emission inventory for road passenger and freight transportation worldwide, with a resolution of 1°x1° longitude/latitude, for CO₂, CO, NMVOC, CH₄, NO_x, primary PM and SO₂. Our bottom-up country by country calculation agrees to 2% with global fuel sales. We compare our results to other inventories, which have used a less differentiated approach or only cover certain world regions.

1 INTRODUCTION

Atmospheric research needs emission inventories to determine the impact of different sectors and trace species on the atmospheric composition and consequently on environmental and health impacts, among others climate change. Transportation has received increasing attention because it contributes about 15 to 20% of global anthropogenic emissions of carbon dioxide, carbon monoxide, nitrogen oxides, volatile organic hydrocarbons and primary particulate matter (EDGAR 32FT2000 Emission data, 2005). Furthermore, road transportation runs almost exclusively on oil products and combustion engines. With high growth rates for the transport volume in most parts of the world it is set to stay a major emitter of atmospheric pollutants, even if exhaust emission standards become more tightened and fuel quality improves.

This paper presents an inventory of road transport's fuel consumption and emissions of air pollutants on a 1°x1° grid for the whole world for the year 2000. We differentiate by vehicle category and fuel type on a country by country level. With this differentiation and scope of pollutants we go substantially beyond current knowledge (EDGAR 32FT2000 Emission data, 2005; Olivier et al., 2002; Schafer and Victor, 1999). Such a technology based approach is necessary for a more accurate estimate of current pollutant emissions.

Section 2 summarizes system boundaries and explains our calculation method, section 3 discusses validation, section 4 presents the emission results, and section 5 gives conclusions.

2 APPROACH

For the purposes of this inventory, road transport is any movement with motorized vehicles on public roads, for passenger or freight transportation. Excluded are movements by agricultural, forestry, building or construction machinery and with sports, pleasure or museum vehicles. Road vehicles are split up in five categories: mopeds, motor-cycles and three-wheelers (later referred to simply as two-wheelers); passenger cars; busses and coaches (later referred to simply as busses); light duty trucks below 3.5 tons gross weight; heavy duty trucks above 3.5 tons gross weight.

We consider consumption of motor gasoline, diesel, ethanol, biodiesel, LPG and CNG (the last four only for cars). We calculate exhaust emissions of CO₂ (from fossil fuels and non-fossil fuels separately), CO, NMVOC, CH₄, NO_x, primary PM and SO₂. Not included are evaporative losses, brake, tyre or clutch wear, resuspension, or discharges during maintenance, accidents or at the end-of-life.

^{*} *Corresponding author:* Heike Steller, DLR – Verkehrsstudien, Rutherfordstr. 2, 12489 Berlin, Germany. Email: Heike.Steller@dlr.de

All emissions and the fuel consumption are calculated separately for 216 countries and territories, which are grouped in twelve world regions. For each country and vehicle-fuel combination, transport volumes (expressed as vehicle-kilometers) were estimated as described in Vanhove and Franckx (2006) and Borken et al. (submitted). Specific fuel consumption and exhaust emission factors (in g emitted substance per vehicle-kilometer) were estimated for each world region (Merétei, 2006; Borken et al., submitted). The sum-product of specific fuel consumption and transport volumes gives the total fuel consumption in a region. This calculated fuel consumption is compared to fuel sales data in road transport (IEA/OECD, 2003). The comparison is made separately for gasoline and diesel in each world region. Comparing on the level of world regions instead of countries has the advantage that fuel tourism does not distort the picture.

Our transport volumes are scaled such that the resulting fuel consumption matches the fuel sales data. Emissions are then calculated as the product of emission factor and transport volume, per vehicle-fuel combination and country.

2.1 *Uncertainties*

Emission factors have a high uncertainty even for OECD countries. This is because of the large number of factors influencing emissions, about which little data are available. Emission regulations provide some help, but they vary even between countries belonging to the same world region. Measurement data are often not representative of the fleet average. Also, so-called super-emitters have a high share in the overall emissions, despite their small number, and little data are available on them.

Inaccuracies in the mileage distribution over vehicle types affect both the overall level of emissions and the relative amount of particular substances. Especially uncertain is the distribution of freight vehicle mileage over light duty trucks and heavy duty trucks, as often only total ton-kilometers are given in statistics.

It is also known that some fuel is misallocated in the IEA data (e.g. fuel consumed in road transport is reported as fuel consumed in agriculture), notably in non-OECD countries. After comparison with other sources, we assumed different fuel sales for road transport than IEA in China, South Korea and India. This uncertainty affects the overall level of emissions in the respective world region.

3 VALIDATION

3.1 *Comparison of calculated fuel consumption with fuel sales data*

A first plausibility check for transport volumes, fuel consumption factors and fuel sales data is given by the comparison of our calculated fuel consumption with the fuel sales data (mostly IEA data). Globally, they are in good agreement; the total calculated gasoline consumption is lower than the sales data by 3% and the total calculated diesel consumption by 1%. In individual world regions, the discrepancy is sometimes much higher, but usually where gasoline consumption is underestimated, diesel consumption is overestimated, which means the discrepancy of total fuel sales is lower and the problem is partly due to difficulties with the distribution of mileage over fuel types (probably mostly freight mileage). The notable exception is the Middle East, where we underestimate both gasoline and diesel consumption by more than 40% compared to IEA sales data. We are therefore in the process of revising our transport volumes for this region and have also identified problems with the IEA sales data.

As discussed above, our raw data are adjusted according to the fuel sales data for each region and fuel separately. The following presents adjusted data only.

3.2 *Comparison with global and regional emission inventories*

As measurements of real world emissions are so far limited either in driving conditions or in the representativeness of the fleet, our best possibility of comparison are other global or regional emission inventories. Here we compare road transport's emissions globally, for North America, Western Europe and Asia. Comparison data are taken from one global, but regionally disaggregated inventory (EDGAR 32FT2000 Emission data, 2005) and one region specific inventory each (National Transportation Statistics 2004, 2005; De Ceuster et al., 2006; RAINS ASIA, 2001).

Table 1. Comparison of inventory data for road transport's emissions in the year 2000 globally, in North America, Western Europe and Asia; percentages denote differences to this work.

	CO ₂ [Mt]	CO [Mt]	VOC [Mt]	NO _x [Mt]	PM [Mt]	SO ₂ [Mt]
World						
this work	4223	111	15.6 ¹	29.2	1.33	1.79
EDGAR	4276 [+1%]	186 [+68%]	35.4 [+127%]	28.5 [-2%]		3.66 [+104%]
North America						
this work	1570	41	4.0 ¹	7.9	0.18	0.19
EDGAR	1639 [+4%]	64 [+56%]	8.4 [+110%]	7.5 [-5%]		0.33 [+74%]
NTS (only USA)	1407 [-10%] ²	62 [+51%]	4.8 [+20%]	7.6 [-4%]	0.21 [+17%] ³	0.24 [+26%]
Western Europe						
this work	800	12	1.7 ¹	5.4	0.28	0.09
EDGAR	819 [+2%]	17 [+42%]	4.4 [+159%]	4.6 [-15%]		0.27 [+200%]
REMOVE	842 [+5%]	21 [+75%]	3.7 [+118%]	4.4 [-19%]	0.20 [-29%]	0.10 [+11%]
Asia						
this work	608	21	4.7 ¹	6.2	0.45	0.53
EDGAR	589 [-3%]	37 [+76%]	9.4 [+100%]	5.6 [-10%]		1.53 [+189%]
RAINS ASIA						0.78 [+47%]

¹ without evaporative emissions

² derived from fuel consumption

³ PM₁₀ (PM_{2.5}: 0.15 Mt)

The variation is small for CO₂ emissions, which means that the assumptions for road transport's fuel consumption are in close agreement. Therefore, differences in the other pollutants must result from different fleet average emission factors, i.e. due to different assumptions about the shares of the various vehicle-fuel combinations and the respective vehicle emission factors. E.g. EDGAR 32FT2000 values are calculated with emission factors for the year 1995. These do not capture the subsequent reductions in specific vehicle emissions and hence EDGAR has higher total emissions throughout than our work. One notable exception is the emission factor for NO_x: It has recently been discovered in EU15 that real world emissions from heavy duty vehicles are about 30% higher than the limit values (Hausberger et. al, 2003). This is already reflected in our emission factors, contrary to all other data.

Concerning VOC emissions it must be noted that we calculated tail pipe emissions only, and therefore our data are not directly comparable to other inventories which include evaporative emissions as well.

4 RESULTS

4.1 Total global and regional pollutant emissions from road transport

Road transportation emits about 4223 Mt CO₂, 111 Mt CO, 15 Mt NMVOC, 0.8 Mt CH₄, 29 Mt NO_x, 1.33 Mt primary PM and 1.8 Mt SO₂ worldwide in the year 2000 (Table 2).

The OECD regions (North America, Western Europe, Japan, Oceania) emit almost two-thirds of fossil CO₂, more than half of which is from North America. Asia and the Middle East account for one fifth of CO₂ emissions. Road transportation in the Former Soviet Union and in Central and Eastern Europe accounts for about 5% of CO₂ emissions, while Africa's share is about 3%. This reflects the regional shares in fuel consumption.

The shares are different for the other exhaust gases due to the regional differences in the vehicle fleet composition, fuel usages, in exhaust emission controls and technology: The OECD regions, which have started to implement vehicle exhaust emission controls long before the year 2000, account for 54% of CO, 41% of NMVOC, 38% of CH₄, 52% of NO_x, 39% of primary PM and only 18% of SO₂ emissions globally, with the US again providing the lion's share except for PM. Vice versa, all Asian regions have higher shares of exhaust pollutants than their respective share in fuel consumption. There, an exhaust emission control began only recently and many two-wheelers were

still powered by two-stroke engines. Due to the high sulphur contents in their fuels, Africa, Latin America and the Middle East account for about half of global sulphur dioxide emissions.

Table 2. Emissions from road transportation in the year 2000 differentiated by region, in decreasing order of fuel consumption and CO₂ emissions, in absolute numbers and as shares of the global total.

	Fuel [Mtoe]	CO ₂ [Mt]	CO [Mt]	NMVOG [Mt]	CH ₄ [Mt]	NO _x [Mt]	PM [Mt]	SO ₂ [Mt]
NAM	533 [37%]	1570 [37%]	40.9 [37%]	3.85 [26%]	0.18 [23%]	7.87 [27%]	0.18 [14%]	0.19 [11%]
EU15	268 [19%]	800 [19%]	12.2 [11%]	1.66 [11%]	0.08 [10%]	5.35 [18%]	0.28 [21%]	0.09 [5%]
LAM	130 [9%]	369 [9%]	9.3 [8%]	1.16 [8%]	0.06 [8%]	2.89 [10%]	0.13 [10%]	0.46 [26%]
EAS	101 [7%]	301 [7%]	10.1 [9%]	1.85 [12%]	0.11 [14%]	2.81 [10%]	0.15 [11%]	0.15 [8%]
JPN	78 [5%]	233 [6%]	4.6 [4%]	0.47 [3%]	0.03 [4%]	1.53 [5%]	0.04 [3%]	0.02 [1%]
MEA	71 [5%]	211 [5%]	8.5 [8%]	1.33 [9%]	0.07 [9%]	1.95 [7%]	0.10 [8%]	0.22 [12%]
SEA	59 [4%]	175 [4%]	7.1 [6%]	1.39 [9%]	0.08 [10%]	1.68 [6%]	0.15 [11%]	0.21 [12%]
CIS	47 [3%]	140 [3%]	6.6 [6%]	0.92 [6%]	0.04 [5%]	1.15 [4%]	0.06 [5%]	0.05 [3%]
AFR	44 [3%]	131 [3%]	3.3 [3%]	0.48 [3%]	0.02 [3%]	1.01 [3%]	0.05 [4%]	0.19 [11%]
SAS	43 [3%]	131 [3%]	4.0 [4%]	1.19 [8%]	0.08 [10%]	1.75 [6%]	0.14 [11%]	0.17 [9%]
CEC	29 [2%]	87 [2%]	2.2 [2%]	0.34 [2%]	0.02 [3%]	0.71 [2%]	0.03 [2%]	0.02 [1%]
OCN	25 [2%]	73 [2%]	2.2 [2%]	0.22 [1%]	0.01 [1%]	0.53 [2%]	0.01 [1%]	0.02 [1%]
World	1429	4223	110.9	14.86	0.78	29.23	1.33	1.79

NAM: North America; EU15: Western Europe; LAM: Latin America; EAS: East Asia; JPN: Japan; MEA: Middle East; SEA: South East Asia; SAS: South Asia; CIS: Commonwealth of Independent States; AFR: Africa; CEC: Central and Eastern Europe; OCN: Oceania

4.2 Gridded pollutant emissions from road transport

Emissions are distributed from a country level to a 1°x1° grid using rural and urban population densities, which are available for 1990 from EDGAR (Olivier et al., 2002). Depending on the vehicle category and world region, urban and rural populations are weighted differently in the gridding. The emissions of every vehicle category are split in two shares: one is distributed according to the density of the rural population, the other according to the density of the urban population. The shares are detailed in Table 3. This approach is a better approximation than distributing the traffic volumes according to the total population, because it takes into account the differences in the transport structure of rural and urban areas, e.g. individual motorized passenger transport in developing countries is available primarily in urban areas and heavy duty trucks drive more in rural areas compared to light duty trucks.

Figures 1 and 2 show as examples maps for emissions of CO₂ and NMVOG. Remarkable are especially the high NMVOG emissions in parts of India, China and South East Asia. These are due to the relatively low emission control standards and high share of two-wheelers, often still with two-stroke engines.

Table 3. Weighting of rural and urban population for gridding of emissions per vehicle category and region.

	Car		Bus		Two-wheelers		Light duty truck		Heavy duty truck	
	Rural	Urban	Rural	Urban	Rural	Urban	Rural	Urban	Rural	Urban
AFR+MEA	10%	90%	30%	70%	20%	80%	50%	50%	50%	50%
CEC	61%	39%	57%	43%	60%	40%	63%	37%	66%	34%
CIS	20%	80%	30%	70%	10%	90%	50%	50%	75%	25%
EAS+SAS+SEA	25%	75%	75%	25%	10%	90%	20%	80%	90%	10%
EU15+JPN	50%	50%	49%	51%	53%	47%	59%	41%	64%	36%
LAM	20%	80%	50%	50%	10%	90%	25%	75%	90%	10%
NAM+OCN	37%	63%	61%	39%	42%	58%	39%	61%	58%	42%

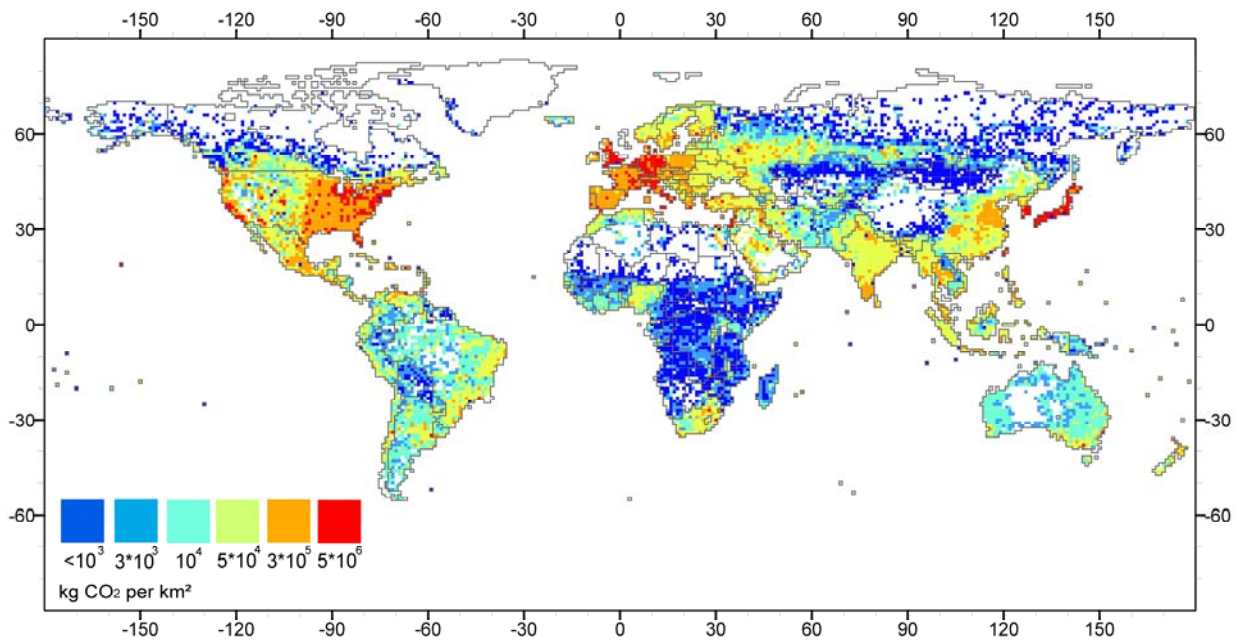
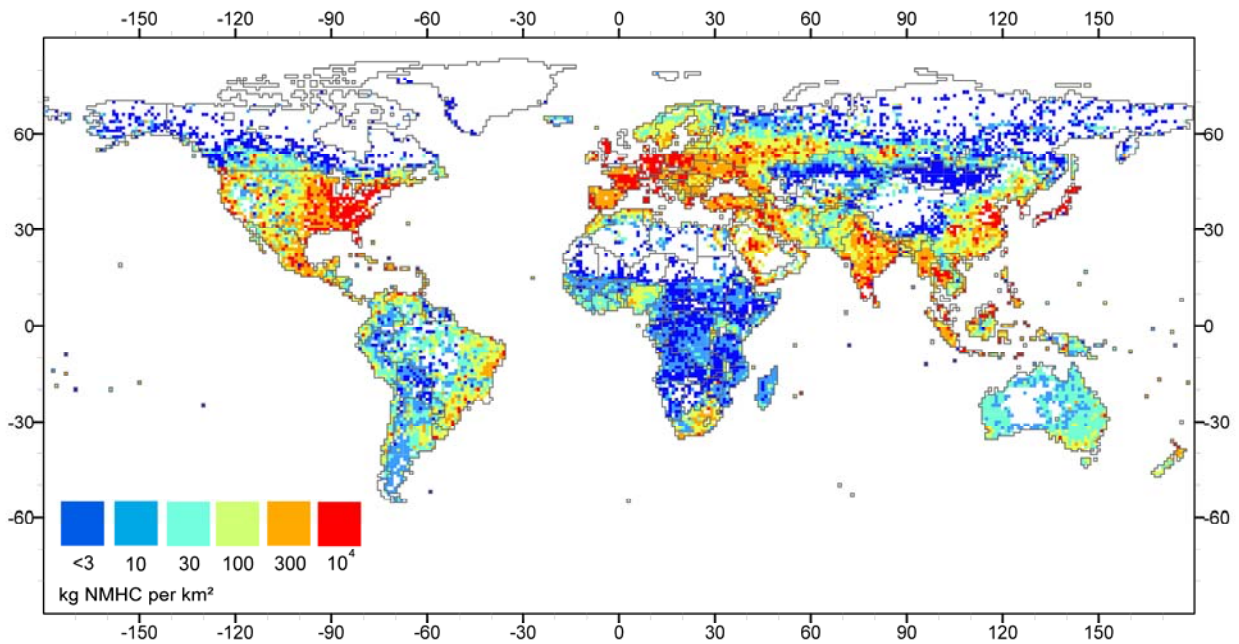
Figure 1. CO₂ emissions from road transportation in the year 2000

Figure 2. NMVOC emissions from road transportation in the year 2000

5 CONCLUSIONS

The work presented here is a major step towards a detailed and consistent global emission inventory for transportation (cf. QUANTIFY Homepage: <http://www.pa.op.dlr.de/quantify/>). Emissions of road passenger and freight transport are available separately, and if needed, emissions by vehicle category and by fuel type can be provided. Road transport's exhaust emissions have been calculated for the first time for many non-OECD regions at this level of detail. Fuel sales data have been cross-checked for some important non-OECD countries, which improves the reliability of the emission estimates for those countries.

The largest source of uncertainty remain the emission factors, especially in non-OECD regions. Also important are the uncertainties resulting from the lack of knowledge about the distribution of total ton-kms over the different vehicle and fuel types, and the associated load factors. A sensitivity analysis is planned to estimate the magnitude of the uncertainties. We also develop scenarios for future emissions from road transportation, analyzing the potential of different mitigation measures.

Similar inventories are being prepared for rail and inland waterways emissions. Together with the maritime shipping emission inventory produced by Det Norske Veritas and the aviation emission inventory produced by the Manchester Metropolitan University, the whole transport sector will be covered in much detail.

ACKNOWLEDGEMENTS

We gratefully acknowledge the financial support as part of the Integrated Project "QUANTIFY – Quantifying the Climate Impact of Global and European Transport Systems" funded under the 6th Framework Programme for Research of the European Union (Contract no. 003893) as well as the support from DLR. We particularly thank the coordinator, R. Sausen, and our colleagues T. Merétei and F. Vanhove for the good cooperation and S. Baidya, K. Rypdal and J. van Aardenne for helpful discussions.

REFERENCES

- Borken, J., H. Steller, T. Merétei, and F. Vanhove, submitted: Global and country inventory of road passenger and freight transportation, their fuel consumption and their emissions of air pollutants in the year 2000. *Transportation Research Record*.
- De Ceuster, G., B. van Herbruggen, and S. Logghe, 2006: *TREMOVE – Description of model and baseline version 2.41*. Draft report for the EC – DG ENV.
- EDGAR 32FT2000 Emission data. Netherlands Environmental Assessment Agency. 16 Aug 2005. <http://www.rivm.nl/edgar/model/v32ft2000edgar/edgv32ft-ghg/>. Accessed February 21, 2006.
- Hausberger, S., D. Engler, M. Ivanisin, M. Rexeis, 2003: *Update of the Emission Functions for Heavy Duty Vehicles in the Handbook Emission Factors for Road Traffic*. Federal Environment Agency Austria, Spittelauer Lände 5, 1090 Vienna, Austria. BE-223.
- IEA/OECD, 2003: *Energy balances of OECD and Non-OECD countries, 2003 edition*.
- Merétei, T. (with contributions of A. Szirányi, J. Kis), 2006: *Specific Emission Factors for Road Transport regarding the year 2000*. Unpublished QUANTIFY Deliverable 1.1.3.3. KTI – Institute for Transport Sciences, Budapest, Hungary.
- National Transportation Statistics 2004*. U.S. Department of Transportation, Bureau of Transportation Statistics. Washington D.C., U.S. Government Printing Office, Feb. 2005, 640 pp.
- Olivier, J.G.J., J.J.M. Berdowski, J.A.H.W. Peters, J. Bakker, A.J.H. Visschedijk, and J.P.J. Bloos, 2002: *Applications of EDGAR. Including a description of EDGAR 3.2: reference database with trend data for 1970-1995*. RIVM report 773301001 / NRP report 410200051. RIVM, Bilthoven, Netherlands, 155 pp. Available from: <http://www.rivm.nl/bibliotheek/rapporten/410200051.html>.
- RAINS ASIA. CD-ROM. Version 7.52. International Institute for Applied Systems Analysis (IIASA), Laxenburg, Austria, 2001.
- Schafer, A., and D.G. Victor, 1999: Global Passenger Travel: Implications for carbon dioxide emissions. *Energy, Vol. 24*, 657-679.
- Vanhove, F., L. Franckx, 2006: *Global transport volumes for the year 2000*. Unpublished QUANTIFY Deliverable D1.1.3.5. Transport & Mobility Leuven, Belgium.

Forecasted Maritime Shipping Emissions for Belgium with an Activity Based Emission Model

L. Schrooten*, I. De Vlieger, L. Int Panis, R. Torfs
VITO - Flemish Institute for Technological Research, Belgium

Keywords: sea-going vessels, emission model, activity based, technological improvements, scenarios

ABSTRACT: In this paper we demonstrate the forecasting of maritime shipping emissions for Belgium with an activity based emission model. The activity based emission model made it possible to forecast the emissions from maritime shipping for the near future (2010). Emissions for the year 2010 are calculated by using activity growth factors, fleet evolution, existing legislation and detailed data from a statistical year (2004). To compute the effect of the existing IMO and EU legislation, we defined on the one hand an autonomous growth scenario and on the other hand a current legislation scenario. The IMO regulation decreases the NO_x emissions of the main engines with merely 1 % in 2010. The IMO and EU regulation on the sulphur content in maritime fuels has a large effect on the SO₂ emissions (decrease of 50 - 53 %).

1 INTRODUCTION

As in many other countries, the current emission estimation methodology for maritime shipping in Belgium is based on bunker fuels allocated to the country. VITO developed an alternative approach based on traffic related data. The activity based emission model for maritime shipping calculates the carbon dioxide (CO₂), sulphur dioxide (SO₂), nitrogen oxides (NO_x), carbon monoxide (CO), hydrocarbons (HC) and particulate matter (PM) emissions from sea-going vessels within Belgian jurisdiction. The activity based emission model made it possible to forecast the emissions from maritime shipping for the near future (2010), taking into account the effect of the current IMO and EU legislation.

2 OBJECTIVES

In this paper we want to demonstrate an activity based emission model to map historical emissions from maritime shipping and to make emission projections for the near future (2010). Therefore, we have defined the following subsidiary aims:

- To present briefly the activity based bottom-up approach for the calculation of an emission inventory of maritime shipping within Belgian jurisdiction.
- To describe the methodology used for forecasting maritime shipping emissions for Belgium, taking into account the IMO and EU legislation.
- To forecast the CO₂, SO₂, NO_x, CO, HC and PM emissions from maritime shipping in Belgium for the year 2010 under a well-defined current legislation scenario.
- To analyse the effect of the current IMO and EU legislation on the emissions of sea-going vessels in the year 2010.

* *Corresponding author:* Liesbeth Schrooten, VITO – Vlaamse Instelling voor Technologisch Onderzoek, Boeretang 200, 2400 Mol, Belgium. Email: Liesbeth.Schrooten@vito.be

3 ACTIVITY BASED MARITIME SHIPPING EMISSION MODEL

We have evaluated different European activity based methodologies MEET (1999), ENTEC (2002), ENTEC (2005), EMS (2003) and TRENDS (2003) used to estimate emissions for maritime transport. We screened the utility of the different methodologies for mapping emissions from sea-going vessels in Belgium on the basis of a list of strengths and weaknesses. Transparency, reproducibility, the integration of technical aspects of the sea-going vessels and the amount of detail were important selection criteria for the methodology. Therefore, we finally decided upon an approach similar to the one used in EMS (2003), but with specific adaptations to the Belgian situation.

We developed an activity based maritime shipping emission model for six different geographical areas in Belgium: four harbours, the river Scheldt and the North sea (12 mile zone). The model contains data on all shipping activities of sea-going vessels for the year 2004, originated from:

- each of the Belgian harbours (Antwerp, Ghent, Ostend and Zeebrugge) for the activities in the different harbours and the Belgian part of the river Scheldt;
- the Belgian/Dutch Vessel Traffic System for the activities in the Belgian jurisdiction of the North Sea (12 mile zone).

The information systems where the activity data for the year 2004 were extracted from are not modelled for the emission inventory purpose. It was a time consuming job to transform the information into appropriate input files.

We extracted for the year 2004 all Lloyd's numbers for sea-going vessels that called in at a Belgian harbour (or travelled in the 12 mile zone of the North sea). VITO then purchased the following characteristics of those sea-going vessels from Lloyd's Register Fairplay:

Ship Type	RPM
Length	TEU
Date of building	Refrigerated containers
Main engine type	Speed
Power main engine	Flag

The model determines CO₂, SO₂, NO_x, CO, HC and PM exhaust emissions through the energy use (power and fuel consumption), taking into account the length, building year and other technical aspects (e.g. engine type, RPM, fuel type, ...) of the sea-going vessels, and the power use during each stage of navigation (cruise speed, reduced speed, manoeuvring, hotelling and anchoring). A distinction is made between the exhaust emissions of auxiliaries (e.g. for on board electricity production) and the main propulsion engines. For the latter, we distinguish three types of main engines, namely 2-stroke engines, 4-stroke engines and steam turbines.

The model is provided with technology-related emission factors from EMS (2003) to compute the NO_x, CO, HC and PM emissions. These emission factors depend on the building year of the vessel and the percentage of the maximum continuous rate. The emission factors for CO₂ correspond with the IPCC (1997) CO₂ emission factors for the different maritime fuels. The model also takes into account the EC (2002, 2005) and IMO (2005) regulations for the sulphur content of maritime fuels (Table 1).

Table 1. Overview of the CO₂ and SO₂ emission factors (kg/ton fuel).

Emission Factor [kg/ton]		Heavy fuel oil	Diesel & gas oil	Gas boil off
CO ₂	-	3110	3100	2930
SO ₂	(... - 18/05/2006)	54	4	~0
SO ₂	(19/05/2006 - 2009)	30	4	~0
SO ₂	(2010 - ...)	30	4 or 2 ¹	~0

¹ 2 kg SO₂/ton diesel or gas oil at berth (minimum duration of 2 hours)

Energy for loading and unloading can either be supplied from the vessel engines or from the harbour energy facilities. Currently, the energy consumption and the emissions resulting from it for loading and unloading are not included into the model.

4 FORECASTS

The activity based emission model made it possible to forecast the emissions from sea-going vessels for the near future. To compute the effect of the current IMO and EU legislation, we defined on the one hand an autonomous growth scenario and on the other hand a current legislation scenario.

4.1 *The autonomous growth scenario*

In the autonomous growth scenario, we only take into account the traffic and fleet evolution, based on activity growth rates per harbour and techno-economic improvements (fuel, ship size, engine management). So, no environmentally-friendly legislation was included.

The determination of the activity growth factors is exogenous to the model. We use economic growth rates to model future activities. The bases for the merchant vessels are the transported freight tonnes by sea-going vessels per harbour in the year 2004 and projected tonnages for the year 2010 according to a low and high autonomous growth scenario. From 2004 until the year 2010 and for each harbour, we implemented for passenger ships an annual growth rate of 1 % in a low autonomous scenario and 2 % in a high autonomous scenario (DG Environment, 2005).

In consultation with an expert committee, we assumed that the increase in traffic of merchant vessels will be filled in by newly built sea-going vessels. The extra tonnages have to be transported to the different harbours with those new ships. We determined how many extra visits the new ships will have to make by taking into account the gross tonnage of the new ships. For passenger ships and negative growth of merchant vessels, we assumed that the growths between the year 2004 and 2010 will have an effect on all ship categories (lengths). Therefore, we decreased the activity data of the different ship types with accumulated growth rates over 6 years.

We made the following assumptions to define the ship characteristics of the new sea-going vessels and this for each harbour and each ship type to take into account geometry of the harbours and the docks:

- new ships have the length of the largest ship visiting in 2004;
- the characteristics of a new ship are based on average ship characteristic from all available ships in the Lloyd's Register Fairplay database with the corresponding length that were built from 2000 on.

4.2 *The current legislation scenario*

We implemented extra measures in the current legislation scenario compared to the autonomous growth scenario to meet the IMO and EU regulations.

On the 19th of May 2005, the MARPOL Annex VI convention came into force. The NO_x Technical Code, developed by IMO, defines mandatory procedures for the testing, survey and certification of marine diesel engines to ensure that all applicable engines comply with the NO_x emission limits defined in it. The requirements for the control of emissions apply to all engines > 130 kW installed on ships constructed after 1st of January 2000 and all engines that undergo a major conversion after 1st of January 2000 (Table 2).

Table 2. NO_x-standard for sea-going vessels according to Annex VI of MARPOL.

Engine speed - n [rpm]	n < 130	130 ≤ n < 2000	n ≥ 2000
Limit Value [g/kWh]	17.0	45 * n ^{-0.2}	9.8

Apart from standards for NO_x, Annex VI also includes limit values for SO₂. In the Annex, a global upper limit of 4.5 mass % on the sulphur content of fuel oil for sea-going vessels is set as well as two emission control areas (SO_x Emission Control Areas – SO_xECA's) with more stringent controls on sulphur emissions. Ships in these areas can only use fuel oil with a sulphur content lower than 1.5 mass %. Alternatively, ships must fit an exhaust gas cleaning system or use any other technological method to limit SO_x emissions. In the original protocol, the Baltic Sea area has been designated as SO_xECA, the North Sea and the English Channel have been appointed in 2000 after negotiations with the EU-member states. This required the implementation of:

- a NO_x correction factor in the emission model for all vessels built from 2000 on;

– a sulphur content of 1.5 mass % for heavy fuel oil.

The sulphur content of 1.5 mass % for heavy fuel oil is also prescribed by the 2005/33/EC Directive. This Directive also imposes the use of 0,1 mass % sulphur for vessels at berth with a minimum berth duration of 2 hours. We assumed the use of diesel oil with a sulphur content of 0.1 mass % for all vessels at berth because the duration at berth is in most cases (> 97 %) longer than two hours.

5 EMISSION RESULTS

Table 3 presents the emission results for the historical year 2004 and the future year 2010 in the low and high current legislation scenario.

Table 3. Emissions of sea-going vessels in the historical year 2004 and the future year 2010 (Belgium) in a low and high current legislation scenario.

Emission [kton]	2004	2010 (low)	2010 (high)
CO ₂	720	735	783
SO ₂	10.9	5.16	5.48
NO _x	16.9	17.1	18.1
PM	1.28	1.25	1.34
CO	2.77	2.89	3.11
HC	0.569	0.579	0.614

Depending on a low or high economic growth, the CO₂ emissions increase with respectively 2 % and 9 % in the current legislation scenario over the period 2004-2010 due to an increase in activity.

The NO_x emissions rise slightly (1 %) in the low current legislation scenario, the increase in activity offsets the reductions of the IMO and EU regulations. An increase of 8 % of the NO_x emissions takes place in the high current legislation scenario between the years 2004 and 2010.

The IMO and EU regulations are most effective for the reduction in SO₂ emissions. A decrease of 53 % (low) and 50 % (high) in SO₂ emissions is accomplished despite to the increase in activity between the years 2004 and 2010.

6 THE EFFECT OF THE IMO AND EU LEGISLATION

Figure 1 shows the regulated emissions SO₂ and NO_x of sea-going vessels in Belgium for the years 2004 and 2010 in the autonomous growth and current legislation scenarios.

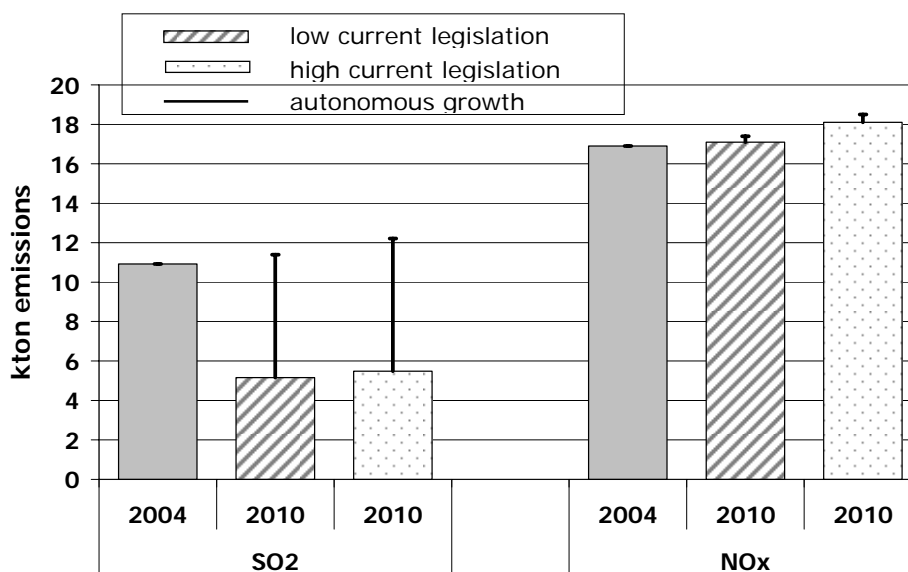


Figure 1. SO₂ and NO_x emissions of sea-going vessels in the reference and baseline scenarios.

The IMO regulation results in a reduction of merely 1 % of the NO_x emissions of main engines in the year 2010. The total reduction of 55 % in SO₂ emissions is due to both the IMO and EU regulations:

- a decrease of the sulphur content for heavy fuel oil;
- a decrease of the sulphur content for fuels used at berth, which also implies a switch from heavy fuel oil to diesel oil for vessels at berth built after 1984.

The switch from heavy fuel oil to diesel oil for vessels at berth results for the auxiliaries in a large emission reduction (33 %) for PM and small emission reductions for CO₂ (5 %), NO_x (5 %), CO (4 %) and HC (4 %).

7 CONCLUSIONS

The transformation of the activity data for historical years into the activity based emission model for maritime shipping is a time consuming job. The activity based emission model however, makes it possible to forecast the emissions from sea-going vessels for the near future by taking into account various legislations.

The technological evolution of sea-going vessels is slower than that of other transport modes. An increase in activity between 2004 and 2010 offsets the technological improvements for most pollutants. CO₂ emissions increase with 2 - 9 % between 2004 and 2010. The IMO and EU legislation have the largest effect on the SO₂ emissions. A decrease of 50 -53 % between 2004 and 2010 was calculated in the current legislation scenario. The IMO regulation has only a small reducing effect on the total NO_x emissions of sea-going vessels in the year 2010.

ACKNOWLEDGMENTS

The paper is based on the “MONitoring Programme on air pollution from SEA-going vessels (MOPSEA)” research project, commissioned by the Belgian Science Policy under the SPSDII programme. VITO performed this study in cooperation with Resource Analysis.

REFERENCES

- DG Environment, 2005: *Key assumptions for subsequent calculation of mid and long term green gas emission scenario's in Belgium*. Federal Public Service of Public Health, Food Chain Safety and Environment - DG Environment, VITO-ECONOTEC, Belgium, 63 pp.
- EC, 2002: *Commission launches strategy to reduce air pollution from ships IP/02/1719*. European Commission, Brussels, Belgium.
- EC, 2005: *Official journal of the European union: Directive 2005/33/EC of the European parliament and of the council of 6 July 2005 amending Directive 1999/32/EC*. European Commission, Brussels, Belgium.
- EMS, 2003: *AVV, TNO-MEP, RIZA, MARIN, CE-Delft, Haskoning, Emissieregistratie en –Monitoring Scheepvaart*, DGG, the Netherlands.
- ENTEC, 2002: *Quantification of emissions from ships associated with ship movements between ports in the European Community*. ENTEC Limited, Final report for the European Commission, England, 48 pp.
- ENTEC, 2005: *Service Contract on Ship Emissions: Assignment, Abatement and Market-based Instruments*. ENTEC Limited, Final report for the European Commission, England, 513 pp.
- IMO, 2005: http://www.acidrain.org/pages/policy/sub6_4.asp
- IPCC, 1997: *Greenhouse gas inventory reference manual (IPCC 1996 Revised Guidelines for national greenhouse gas inventories, Volume 3)*. France.
- MEET, 1999: *Methodology for calculating transport emissions and energy consumption, Transport research*. Fourth Framework Programme, Strategic Research, DG VII, ISBN 92-828-6785-4, Luxembourg, 362 pp.
- TRENDS, 2003: *Calculation of Indicators of Environmental Pressure caused by Transport, European Commission*, Luxembourg, 91 pp.

Measurement method for emissions from inland navigation

A. Kraai*, A. Hensen, G.P.A. Kos, H.P.J. de Wilde
Energy research Centre of the Netherlands, the Netherlands

J.H. Duyzer, H. Weststrate, J.C.Th. Hollander
The Netherlands Organisation for Applied Scientific Research TNO, the Netherlands

Keywords: Ship emissions, emission factor, NO_x, PM

ABSTRACT: Transport over water is more efficient and cleaner than transport over land. But the standards for exhaust gas emissions from diesel engines from inland vessels lag 5 to 10 years behind the standards for emissions from road transport. With unchanged policy, this will result in more nitrogen oxides and particle matter to the transport performance (in kilometres) for inland vessels than for trucks.

However, the emissions from the inland navigation are based on only a few experiments with a few vessels whereas the emissions from road transport are much better known.

This measurement method is based on remote measurement of the exhaust plumes from vessels that pass by on a canal/river. In a two-day campaign, 20 km east of Rotterdam, emissions from about 150 ships were obtained. The gasses, which were measured are CO₂, NO, NO₂. For particulate matter, total particle numbers and particle size distribution were determined. High time resolution made it possible to see the different ship passages. The observed plumes for NO_x and particles were linked to those observed for CO₂. The latter is linked to the amount of diesel used and to the engine power. In this way we obtained an average emission factor for NO_x of 11±4 g NO_x/kWh (n=132 vessels).

The same procedure was used for particle numbers. For particle mass the uncertainty is significantly larger but the measurements seem to indicate that ships are slightly cleaner than expected. The average emission factor was in the range of 0.1-0.3 g/kWh.

These experiments can give a better understanding of the ship emissions and may facilitate effective policy on reduction of emissions from inland shipping

1 INTRODUCTION

Cargo transport by inland navigation will be more important in Europe in the future. Navigation is considered to be a durable option for long and middle-long distances compared to cargo trucks (Schilperoord, 2004).

Because of the current policy in the Netherlands, NO_x emissions from mobile sources are decreasing, but this is mostly through cleaner techniques for road traffic. The use of these techniques in sea and inland navigation takes more time, also because ship engines can last for 25 years. The contribution of these sources is increasing both in absolute sense and relatively compared to road traffic emissions. NO_x-data from the central bureau of statistics (CBS) in the Netherlands for the years 1990-2003 show decrease of NO_x for total of mobile sources, but an increase for inland navigation and total navigation (Fig. 1). The emission factors are relatively uncertain, because these are based on scarce data from a limited number of experiments that were not specific for the Dutch fleet (Klein et al., 2004).

* *Corresponding author:* Aline Kraai, Energy research Centre of the Netherlands, P.O.Box 1, 1755 ZG, Petten, The Netherlands. Email: kraai@ecm.nl

At this moment, with the available emission data and with measurement techniques used so far, it is difficult to quantify the total emission of the total Dutch fleet. CBS calculates the emission from vessel kilometres. These are transformed with an assumed average speed into sailinghours to calculate kilowatt-hour (Klein, 2004). Emission ceilings for NO_x emissions from inland vessels vary between 9.3 and 13 g/kWh, depending on the engine rotations (Schilperoord, 2004). The emission factors which are registered in the Netherlands are between 8 and 16 g NO_x /kWh and 0.3 and 0.6 g PM/kWh (Oonk et al., 2003)

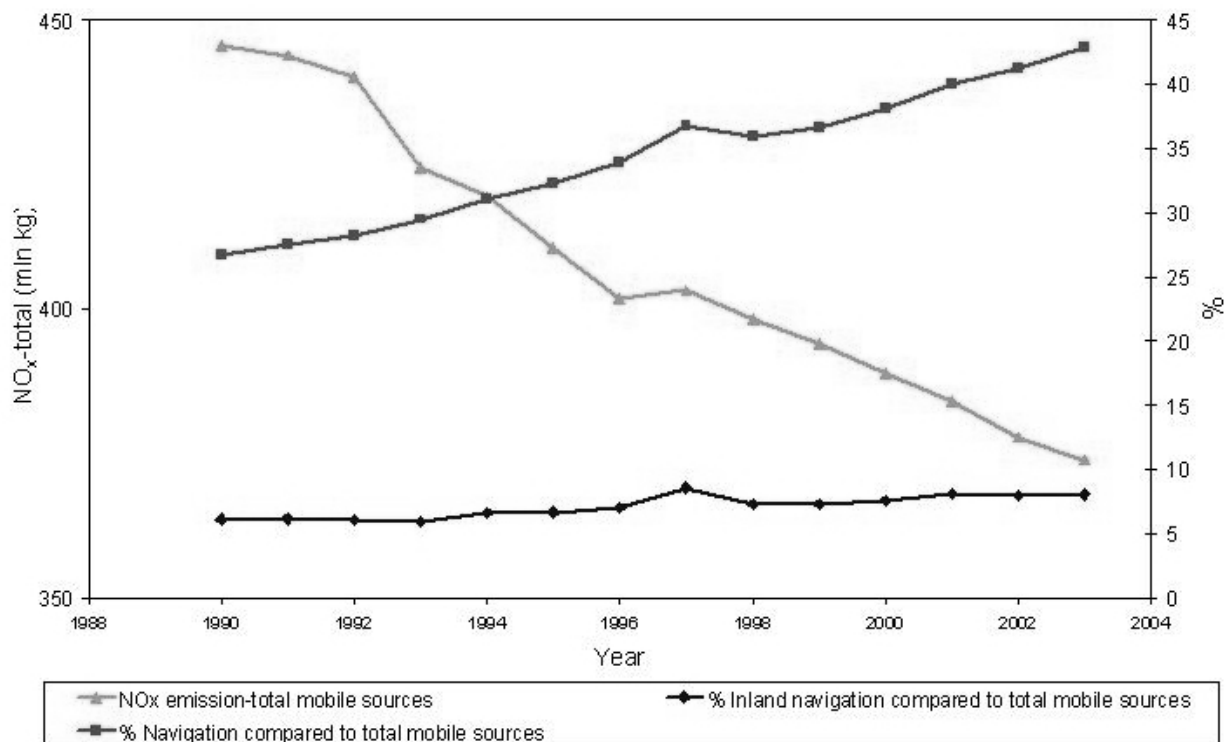


Figure 1. NO_x emissions for the total mobile sources in millions of kg (left axis) by CBS, the Netherlands for the years 1990-2003. The right axis shows the percentage of the total navigation (including sea navigation) and the inland navigation against the total mobile sources emissions.

2 MEASUREMENT METHOD

The exhaust gas of diesel engines in vessels is a mix of gasses and particles among which are carbon dioxide (CO_2), nitrogen oxides (NO_x), particulate matter (PM) and sulphur dioxide (SO_2). Once in the atmosphere the emitted gasses and particles are carried along with the wind in a (smoke) plume.

2.1 Plume measurements

Emission measurements for vessels are possible at the lee side of the wind using high time resolution instruments that analyse the gasses or particles in the air. In this experiment a mobile van was used to house all the instruments. (Fig. 2).

Ambient air was analysed using a chemiluminescence NO/NO_x analyzer (Eco-physics CLD 700 AL), a $\text{CO}_2/\text{H}_2\text{O}$ analyzer (Licor Li-6262), and a pulsed Fluorescence SO_2 analyzer (Thermo Electron Model 43A). These systems used a 2 m $\frac{1}{4}$ inch inlet hose that was flushed at 7 l/minute. NO_x calibration took place in the lab after the experiments. The CO_2 monitor was calibrated each day before and after the experiments using N_2 for zero calibration and 450 ppm CO_2 in an N_2/O_2 mixture.

A range of different instruments were used to measure particulate matter. A PM10-TEOM (model 1400) was used to obtain PM mass data. This instrument is too slow to enable measurements of individual plumes but the whole day timeseries was used to determine a proper conversion factor for the optical particle instruments into mass level. A Condensation Particle Counter (TSI-3022A)

was used for particle numbers. The CPC has a high resolution in time, but only provides particles numbers and can't be used to determine the particle size. Particle size distribution data was obtained using a LAS-x. This instrument also counts the number of particles and classifies each particle in one of the 16 different size channels (from 120 nm – 10µm). These distributions are transferred into mass. This was done assuming all particles are spheres with a uniform density. The density is dependent on the aerosol composition. Diesel exhaust mainly contains elemental carbon (40 %), organic carbon (30%), sulphate and water (14%) and remaining elements (13%) (Burtcher, 2005). The LAS-x was not specifically calibrated for ship diesel exhaust during this experiment. Experiments in the lab were done that showed that for this instrument a density of 1.65 g cm⁻³ provides an accurate mass number as compared to a filter collection system.

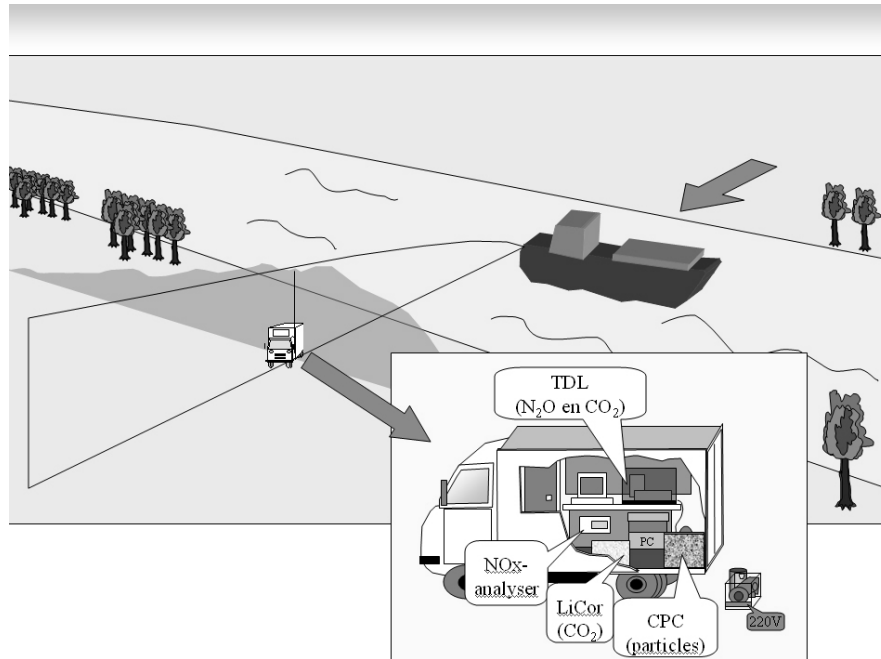


Figure 2. Schematic overview of the measurement set-up.

2.2 Tracer use

The measured concentration at a certain distance of the source is a function of both the released amount of gas/particles and the dilution or dispersion that occurs in the atmosphere. This dilution depends on many variables like wind speed, wind direction, stability of the atmosphere, the distance between source and measurement location and speed of the vessel. The dilution factor can be determined with a Gaussian plume model, but there are many uncertainties because of all the different input parameters. A way to determine the dilution factor is to release a tracer gas with a known source strength from a ship and determine the concentration of that constituent. (Fig. 3)

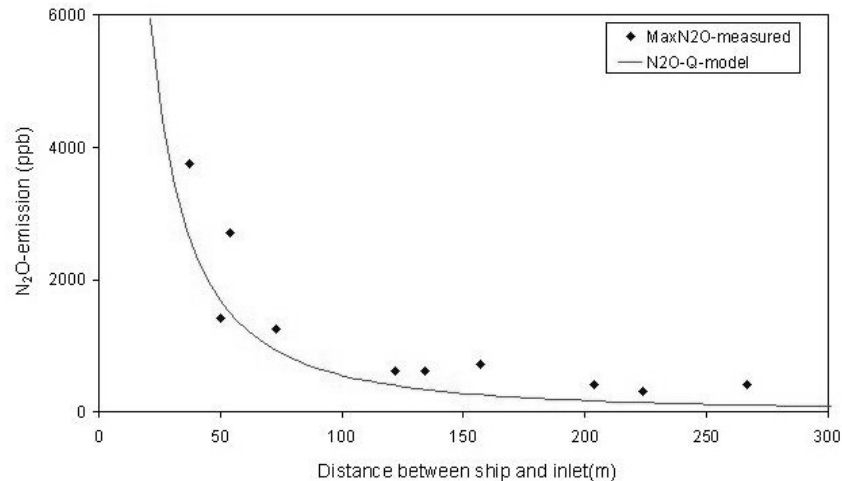


Figure 3. Experiment with release of tracer gas (N₂O). The plume model and the measurements are in one line also with different distances from the source.

In this experiment the CO₂ released from the ship itself was used as tracer. Doing so the absolute quantity of the emitted gas is not obtained but the emission factor can be still be determined. The measured concentration equals the emission multiplied with an unknown dilution factor. Dividing

$$\frac{\text{ConcentrationNO}_x}{\text{ConcentrationCO}_2} = \frac{\text{EmissionNO}_x}{\text{EmissionCO}_2}$$

two equations for two components eliminated the dilution factor and provides:

The concentration measurements are used to obtain the concentration ratio in the plume. This is done by integration of the concentration above the background level. The integrated values for NO_x and CO₂ are divided to obtain a gNO_x/gCO₂ emission factor. Since the emission standards are defined used in gNO_x per kWh. The CO₂ emission is transferred into the amount of fuel used. With the carbon fraction in diesel and the combustion value of diesel this provides a conversion factor of 73.3 g CO₂ MJ⁻¹. Finally the emission factor is obtained assuming an engine efficiency of 38% (Schilperoord, 2004) for the ship engines.

3 RESULTS

Two projects were done on inland navigation. On 18 march 2005 at the Amsterdam-Rijn canal and on 6 and 7 February 2006 at the Dordtse Kil, a river east of Rotterdam. The distance between source and inlet to the instruments was between 25 and 200 m. On a single day about 100 ships pass by and 60 to 70 ships were analysed. At the measurement location a typical plume passage lasts for about 40 seconds per ship. A time series obtained with several passing vessels shows how the different components increase simultaneously when a ship is passing. (Fig. 4) The difference in concentration peaks height is caused either by difference in emissions or difference in dilution. The correlation between peak levels of CO₂ and NO_x or particles counts is good.

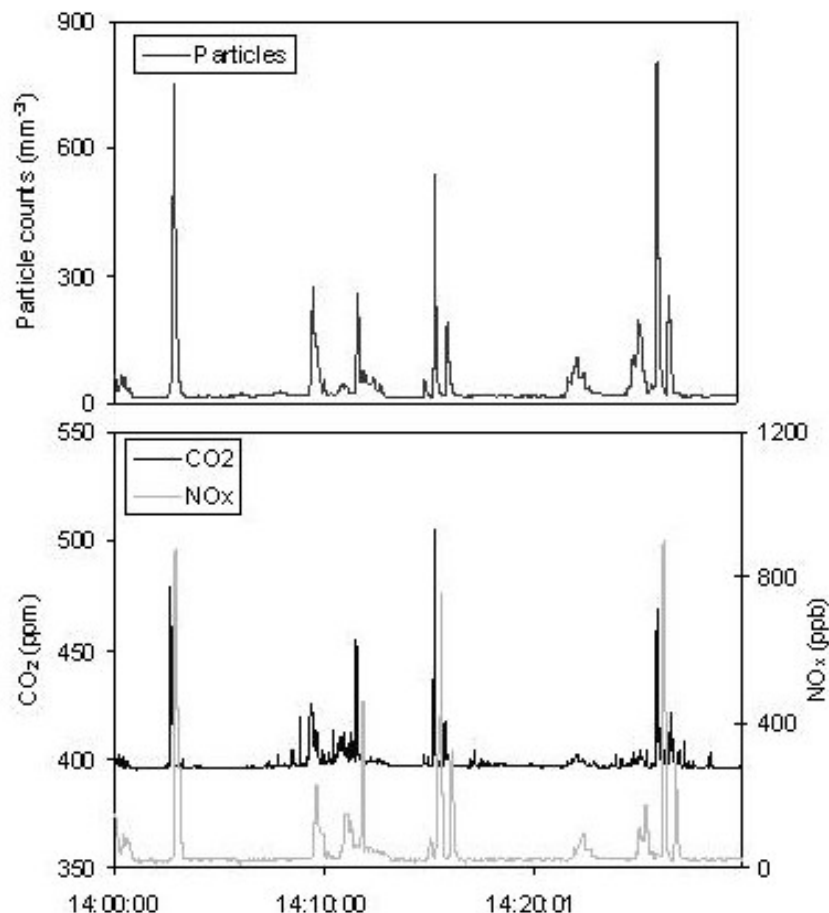


Figure 4. Time series with a set of passing vessels. Simultaneous concentration peaks occur for the different components. The concentrations of the gasses CO₂ and NO_x are shown in the lower part of the graph and particle counts in the upper graph.

3.1 NO_x

The emission factors obtained with the method described here provided a consistent dataset. Table 1 gives the statistics for the measurements at the Dordtse Kil, the data is also shown Figure 5. The average emission factor for NO_x is in the expected range.

Table 1. Statistics of emission factors for NO_x in g/kWh

	g NO_x /kWh
Average	10.7
Median	10.7
Standard deviation	3.6
Relative standard deviation	33%
Plume counts	132

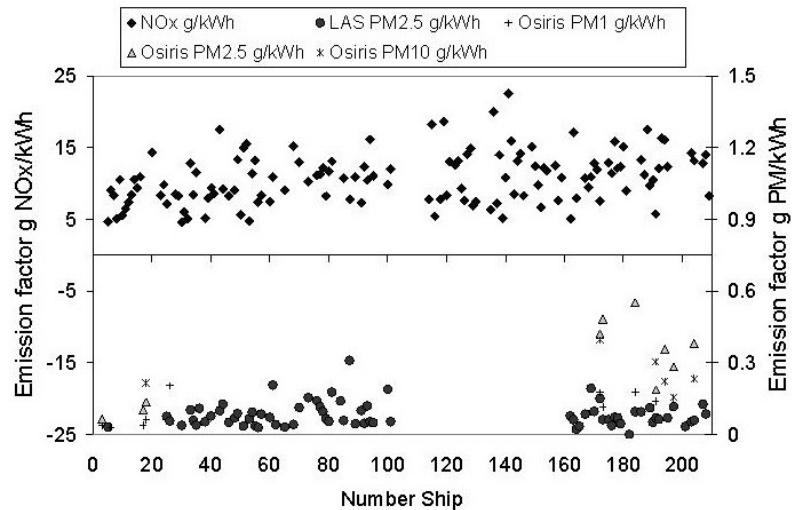


Figure 5. Emission factors of NO_x and PM (measured with LAS-x and Osiris)

3.2 PM

Figure 5 shows the emission factors of particulate matter that were obtained. These are all low emissions compared to what is used in the Netherlands until now. An example of the size distribution obtained on a single day is shown in Figure 6. The patterns show an average particle size distribution for 25 plumes both using the data in the plume and in the background data in between these plumes. The difference of these two distributions represents the PM added to the background level by the plume. About 80 % of this mass is below $1 \mu m$ with the peak around $0.5 \mu m$.

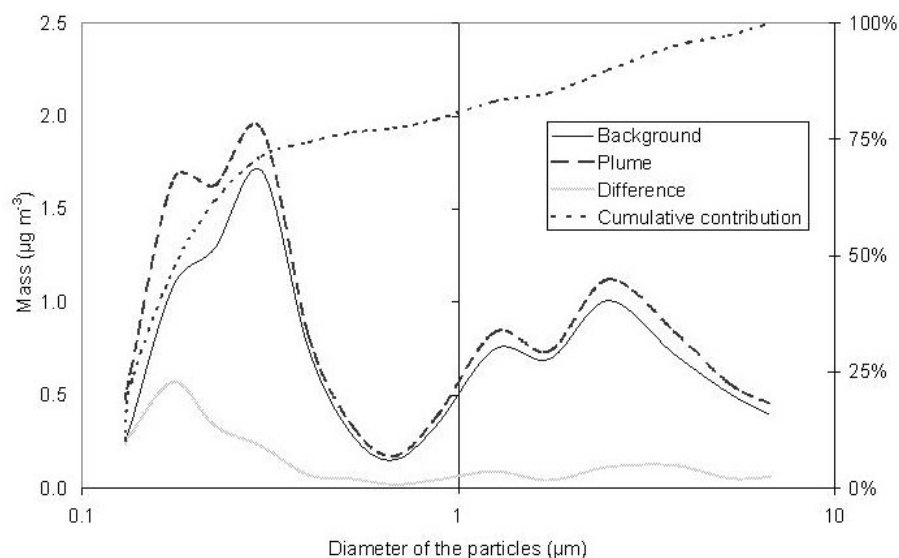


Figure 6. The particle size distribution downwind of the river in and outside a set of 25 plumes as measured with the LASx.

During part of the measurements we used an inlet to the LAS-x which was relatively long (1 m steel tube), this might have caused an underestimation of the emission level. The average emission factor was in the range of 0.1-0.3 g PM/kWh.

4 DISCUSSION AND CONCLUSIONS

This method provides emission factors for a large number of vessels per day especially as compared to tailpipe measurements. Another advantage of this method is that the emission factors of the fleet can be determined in a realistic situation instead of a laboratory setting. The flexibility of a moving laboratory enables experiments on various locations and eventually also the evaluation of actual exposure levels for people living close to the waterways.

The use of CO₂ as internal tracer works well. This means that the emission factor of the vessels can be determined directly instead of indirectly using an atmospheric transport model. The model is still needed when an absolute emission of NO_x is required.

The emission factors of NO_x obtained with this plume method had an average level of 11±4 g NO_x/kWh which was obtained (n= 136). The range in the emission factors obtained was relatively small which results in a 95% confidence level of 0.7 for the average emission factor. This factor is within the range of the emission factors used by the Dutch emission registration.

The particle size distribution for ship emissions peaks below 1 µm. An instrument that can detect smaller particles compared to the LAS-x used here (below 120 nm) would be an advantage for the next measurements to evaluate the mass in the plume below this size level. According to Burtcher (2005) the particle emissions of (car) diesels have an average diameter from 60-100 nm that is nearly independent from motor type or running circumstances. These small particles might add 10-20% to the mass. This cannot explain why the emission factors measured for PM during these experiments were about 5 times below the level used in the emission inventory. This difference was larger than expected even if we assume our data has an uncertainty of a factor of 2. For this reason experiments are still ongoing with a focus on additional experiments that can narrow down the uncertainty in the PM emission levels.

ACKNOWLEDGEMENTS

Initial development of this method was funded by the Netherlands Ministry of Housing Spatial planning and the Environment. Further development and the measurement campaign along the Dordtse Kil were funded by the Ministry of Transport, Public Works and Water Management. We acknowledge our colleagues Alex Vermeulen, Pim van der Bulk and Theo Schrijver for software logistics and technical support respectively.

REFERENCES

- Burtscher, H., 2005: Physical characterization of particulate emissions from diesel engines: a review. *Journal of Aerosol Science*, vol. 37, pp. 896-932.
- Germanischer Lloyd, 2001: Erarbeitung von verfahren zur ermittlung der luftschadstoffemissionen von in betrieb befindlichen Binnenschiffsmotoren.
- Klein, J., R. van den Brink, A. Hoen, J. Hulskotte, N. van Duynhoven, E. van de Burgwal, D. Broekhuizen, 2004: Methoden voor de berekening van emissies door mobiele bronnen in Nederland t.b.v. emissiemonitor, jaarcijfers 2001 en ramingen 2002.
- Oonk, J.A., J. Hulskotte, R. Koch, G. Kuipers, J. van Ling, 2003: Emissiefactoren voor de binnenscheepvaart TNO-MEP Rapport R2003/437.
- Schilperoord, H.A., 2004: Environmental Performance of inland shipping. www.royalhaskoning.com
- CBS: <http://statline.cbs.nl>

Particle Emissions from Ship Engines: Emission Properties and Transformation in the Marine Boundary Layer

A. Petzold*, B. Weinzierl, M. Fiebig, M. Lichtenstern
DLR-Institute of Atmospheric Physics, Oberpfaffenhofen, Germany

P. Lauer
MAN Diesel SE, Augsburg, Germany

C. Gurk
Max-Planck-Institute for Chemistry, Mainz, Germany

K. Franke
University of Bremen, Bremen, Germany

E. Weingartner
Paul Scherrer Institute, Villigen PSI, Switzerland

Keywords: Ship Emissions, Combustion, Marine Aerosol, Marine Boundary Layer

ABSTRACT: In the framework of a combined effort ship emission studies were conducted in 2004. Detailed aerosol microphysics and chemistry was measured in the raw exhaust gas of a single-cylinder test bed engine. The emission studies were complemented by airborne aerosol transformation studies in the marine boundary layer using the DLR aircraft Falcon 20 E-5. In this experiment a single plume of a large container ship was extensively investigated. Observations from emission studies and plume studies combined with a Gaussian plume dispersion model yield a consistent picture of particle transformation processes from emission from a ship engine to atmospheric processing in the marine boundary layer during plume expansion. The results are used for the determination of emission indices of particulate matter from ships and for the estimation of life times of ship exhaust particles in the marine boundary layer.

1 INTRODUCTION

Currently, gaseous and particulate matter emissions from ship engines are gaining increasing attention because of possible environmental and climate impacts (Eyring et al., 2005a, b). Emitted species can considerably influence the atmospheric composition and in particular the ozone chemistry in the troposphere (Endresen et al., 2003). As for any combustion source, ship engine exhaust also contains particulate matter. Ship engine exhaust particles are composed of combustion aerosol particles consisting of elemental and organic carbon, sulphate and ash (Petzold et al., 2004), and of volatile particles forming outside the combustion process in the expanding plume.

Elemental or black carbon (BC) is the most efficient particulate absorber of atmospheric solar radiation and has therefore a strong impact on the atmospheric radiation balance. Additionally, combustion particles can act as nuclei for the formation of cloud droplets and affect by that means the life cycle and radiative properties of marine stratus clouds at the top of the marine boundary layer (Durkee et al., 2000).

In particular the emission of particles and their fate in the marine environment are however widely unknown. Until today, observations reported mainly bulk aerosol properties like mass concentrations (Cooper, 2003), while detailed chemical analyses and aerosol microphysical data are missing.

In the framework of a combined effort, ship emission studies were conducted in 2004 as part of the European Integrated Project HERCULES (**H**igh **E**fficiency **R**&**D** on **C**ombustion with **U**ltra

* *Corresponding author:* Andreas Petzold, DLR Institute of Atmospheric Physics, Oberpfaffenhofen, 82205 Wessling, Germany Email: andreas.petzold@dlr.de.

Low **E**missions for **S**hips). Detailed aerosol microphysics and chemistry were measured in the exhaust gas of a single-cylinder test bed engine, which was operated at various load conditions, running on fuel with a sulphur content of 3.45 wt.-%.

The emission studies were complemented by airborne aerosol transformation studies in the marine boundary layer as part of the ICARTT-ITOP (**I**ntercontinental **T**ransport of **O**zone and **P**recursors) experiment in 2004. Research flights using the DLR aircraft Falcon 20 E-5 were conducted in the English Channel and in a single plume of a large container ship.

2 METHODS AND RESULTS

On board of the DLR research aircraft Falcon, a comprehensive set of instruments was operated for measuring aerosol microphysical properties of both the secondary volatile aerosol, the primary combustion aerosol and trace gases H_2O , NO , NO_x , O_3 , CO , CO_2 , and SO_2 . The excess CO_2 , or ΔCO_2 respectively, was calculated from the total CO_2 time series by subtracting the average background value from the full CO_2 signal. Since there is no additional source for CO_2 in the vicinity of the investigated ship plume, the value of ΔCO_2 is a very good indicator for combustion emissions. Using a calculated value of 40000 ppm CO_2 in the raw exhaust gas of the investigated vessel, the plume dilution can be determined from ΔCO_2 .

Figure 1 shows the flight track of the aircraft during the plume study in the exhaust of the container ship. The colour of the symbols represents the black carbon mass concentration in the plume. Close to the source, ΔCO_2 exceeded a value of 10 ppm, ranging up to > 100 ppm. Simultaneously, the BC mass concentration reached values of close to $10 \mu\text{g m}^{-3}$, while the Condensation Particle Counters (TSI 3760A) were above their upper detection limit of $20,000 \text{ cm}^{-3}$.

The plume encounters observed during the Single Plume Study are shown in Figure 2. The strength of the plume event was rated according to the CO_2 measured above the background signal (excess CO_2 , ΔCO_2).

The analysis of the measured DMA size distributions in the fresh plume yielded a count median diameter of the combustion particles of 70 nm. Comparable data from emission studies yield a count median diameter of 52 nm. For aged plumes the count median diameter of the combustion particle mode was found at approx. 100 nm. These values reflect a considerable size shift in the particle size distribution by coagulation during the plume expansion from exhaust conditions to an aged plume embedded in the marine boundary layer.

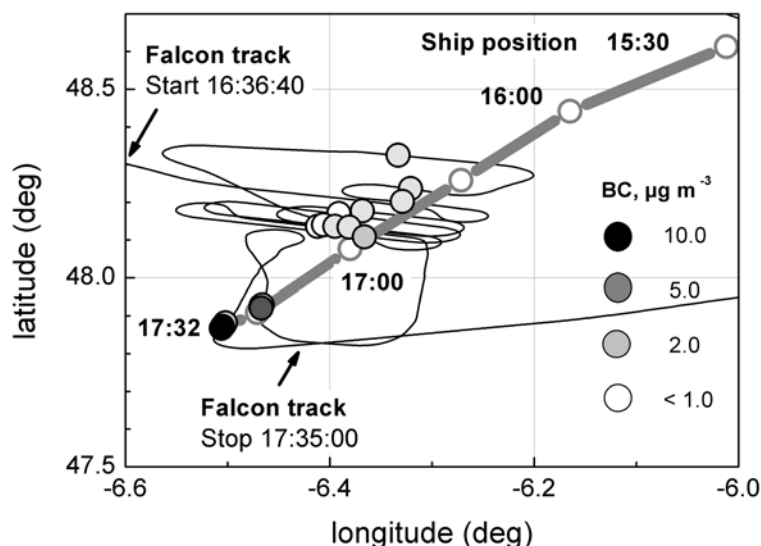


Figure 1. Tracks of the source ship and the research aircraft Falcon during the Single Plume Study; symbol colours represent Black Carbon mass concentrations in the plume.

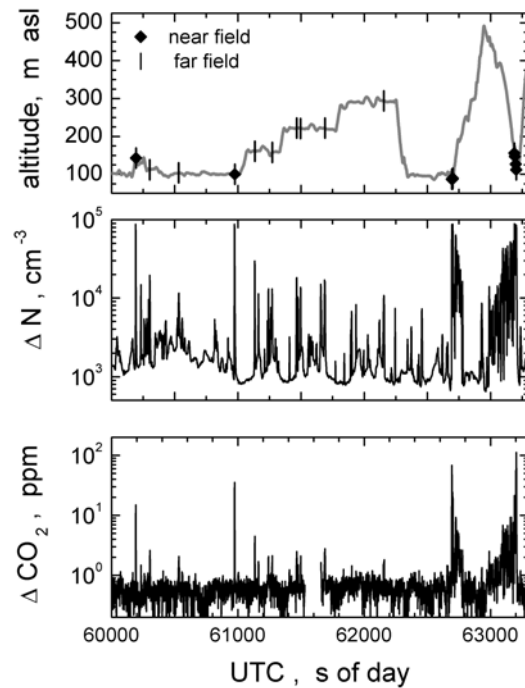


Figure 2. Time series of flight altitude in m above sea level (asl), excess CO_2 (ΔCO_2) and excess number concentration ΔN during the Single Plume Study.

As is shown in Figure 3a, the exhaust particle mode inside the ship plume exceeds the background aerosol in the size range from 20 to 200 nm by max. two orders of magnitude. In the size ranges below and above this range of particle diameters, no deviation from the background aerosol was found. The ship exhaust particle mode was still detectable in polluted air masses outside the single plume. This observation is in agreement with data reported by Osborne *et al.* (2001). For comparison, Figure 3b shows the size distribution measured on the test bed in the exhaust of an engine which operated at 100% load.

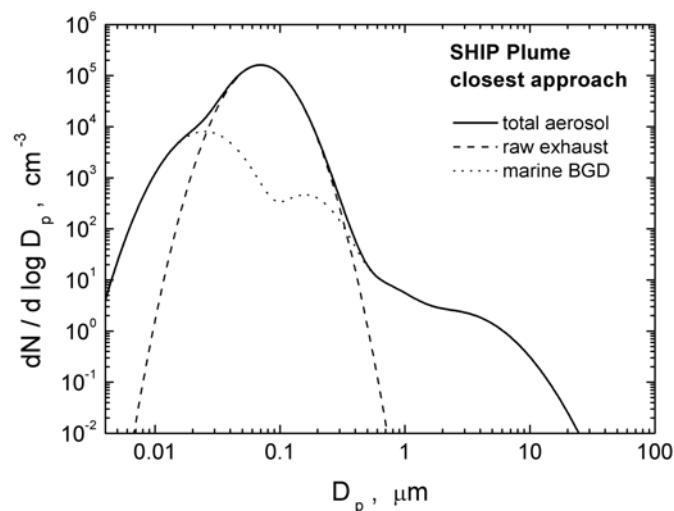


Figure 3a. Composite size distributions from data from DMA, PCASP 100X and FSSP 300 for a strong plume encounter and for a marine background case; the log-normal size distribution represents the exhaust particle mode.

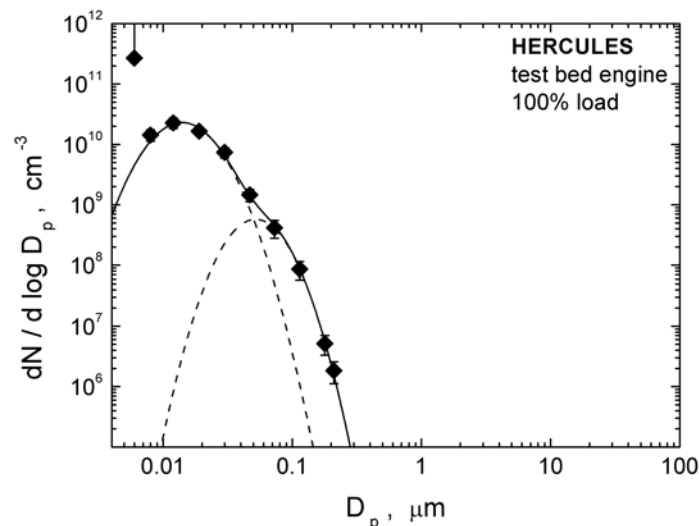


Figure 3b. Size distributions of raw particle emissions measured in the test bed studies.

The plume age during the Single Plume Study was calculated from trajectory analyses of the ship plume with respect to the aircraft flight track and from the geometrical distance from the probing aircraft to the source ship at the time of emission. The CO_2 data measured during the Single Plume Study were then used for the determination of the plume diffusion coefficients according to the plume dispersion model of Glasow et al. (2003). Glasow et al. report best estimates for horizontal and vertical diffusion coefficients of 0.75 and 0.6, while a plume model fitted to the CO_2 measurements yields values of 0.74 and 0.7. When using ΔCO_2 as an indicator for the plume age, plume observations extended from very young plumes in the Single Plume Study ($t \cong 60$ s) to well aged plumes in the English Channel ($t \cong 10,000$ s).

Comparing Figures 3a and 3b, a strong mode of particles with diameters around 10 nm is visible in the raw exhaust data (Figure 3b) while only very few particles are observed in the young plume (Figure 3a). A detailed analysis yielded a ratio $N(D > 4 \text{ nm}) / N(D > 10 \text{ nm})$ of 1.25 at plume ages of about 600 s while this ratio decreased to 1.0 ± 0.1 after about 100 s. Hence nucleation mode particles are expected to live no longer than about 1 h.

Assuming an estimated precision of 0.2 ppm for the determination of ΔCO_2 , the ΔCO_2 signature of a ship plume becomes indistinguishable from the CO_2 background after about 10 h. This value can be used as an average ship plume life time when plume dispersion is the only active dilution process. As soon as turbulent mixing comes into play the life time can be much shorter.

3 CONCLUSIONS

The adapted Glasow plume dispersion model in combination with the observations from emission studies and plume studies yields a consistent picture of particle transformation processes from emission from a ship engine to atmospheric processing in the marine boundary layer during plume expansion:

- Black carbon mass and ΔCO_2 are well correlated for emission and young plume conditions.
- Extensive transformation of particle size distribution properties from exhaust to aged plume observed: count median diameter of the size distributions shifts from 52 nm (raw exhaust) to 70 nm (young plume) and to approx. 100 nm (aged plume).
- Strong nucleation particle mode in raw exhaust; nucleation mode is almost completely depleted in the single plume far field (plume age $> 10^3$ s).
- High abundance of volatile Aitken mode particles in raw exhaust, increased fraction of volatile particles in ship plumes is still visible at plume ages $> 10^4$ s.
- Ship plume reaches top of MBL after approx. 1000 s, earliest onset of ship track effects.
- ΔCO_2 plume signature disappears latest after approx. 10 h.

A detailed analysis of the SHIP Plume Study is under way. Quantitative results on emission factors in terms of mass and number and particle life times will be reported soon in a publication in preparation for *Atmospheric Chemistry and Physics*.

REFERENCES

- Capaldo, K., Corbett, J.J., Kasibhatla, P., Fischbeck, P.S. and Pandis, S.N., 1999: Effects of ship emissions on sulfur cycling and radiative climate forcing over the ocean, *Nature*, 400, 743-746.
- Cooper, D.A., 2003: Exhaust emissions from ships at berth, *Atmos. Environ.*, 37, 3817-3830.
- Durkee, P.A., K.J. Noone, and R.T. Bluth, 2000: The Monterey Area ship track experiment, *J. Atmos. Sci.*, 57, 2523-2541.
- Endresen, Ø., E. Sørsgård, J.K. Sundet, S. B. Dalsøren, I.S.A. Isaksen, T. F. Berglen, and G. Gravir, 2003: Emission from international sea transportation and environmental impact, *J. Geophys. Res.* 108, 4560, doi:10.1029/2002JD002898.
- Eyring V., H. W. Köhler, J. van Aardenne, A. Lauer, 2005a: Emissions from international shipping: 1. The last 50 years, *J. Geophys. Res.*, 110, D17305, doi:10.1029/2004JD005619.
- Eyring V., H. W. Köhler, A. Lauer, B. Lemper, 2005b: Emissions from international shipping: 2. Impact of future technologies on scenarios until 2050, *J. Geophys. Res.*, 110, D17306, doi:10.1029/2004JD005620.
- Osborne, S.O., et al., 2001: Modification of the aerosol size distribution within exhaust plumes produced by diesel-powered ships, *J. Geophys. Res.*, 106, 9827-9842.
- Petzold, A., et al., 2004: Particle emissions from ship engines, *J. Aerosol Sci., Abstracts of the European Aerosol Conference*, S1095-S1096.
- Von Glasow, R., et al., 2003: Modelling the chemical effects of ship exhaust in the cloud-free marine boundary layer, *Atmos. Chem. Phys.*, 3, 233-250.

Part of this work was funded by the EC within the I.P. HERCULES under Contract No. TIP3-CT-2003-506676. The collaboration of the MAERSK shipping company during the SHIP Plume Study is gratefully acknowledged.

Aircraft-based Trace Gas Measurements in a Primary European Ship Corridor

H. Schlager*, R. Baumann, M. Lichtenstern, A. Petzold
DLR-Institut für Physik der Atmosphäre, Oberpfaffenhofen, Germany

F. Arnold, M. Speidel
Max-Planck-Institut für Kernphysik, Heidelberg, Germany

C. Gurk, H. Fischer
Max-Planck-Institut für Chemie, Mainz, Germany

Keywords: ship emissions, ship exhaust plumes, nitrogen oxides, sulphur dioxide

ABSTRACT: Aircraft measurements of gaseous ship emissions were performed in the vicinity of the heavily travelled ship lanes through the English Channel and in the exhaust trail of a major sea-going container ship. In the single ship plume experiment the concentration and dilution of major emissions (CO_2 , NO , NO_y , SO_2) were measured up to a distance to the source ship and plume age of 25 km and 1650 s, respectively. Emission factors for NO_x and SO_2 were determined from individual plume encounters. The inferred NO_x emission indices compare well with calculated emission indices from the engine emission model of the manufacturer. The deduced SO_2 emission indices from the SO_2 enhancements in the plume are smaller than calculated emission indices based on the analysed sulphur content in the fuel sample. However, the difference is still within the estimated error limits for the SO_2 emissions factor measurements. A survey flight in the ship corridor through the English Channel revealed the presence of a multitude of ship plumes aged between 0.5 and several hours. Many of the observed concentration enhancements in the ship corridor are due to the superposition of several plumes with different ages.

1 INTRODUCTION

Shipping represents a major element of international transportation. Combustion from ships produces gaseous species and aerosols that contribute to anthropogenic pollution and climate change (e.g. Corbett and Fischbeck, 1997, Lawrence and Crutzen, 1999, Endresen et al., 2003). A number of model studies have been performed to investigate the local, regional and global impact of gaseous ship emissions on photochemistry (Capaldo et al. 1999, Lawrence and Crutzen 1999, Kasibhatla et al. 2000, Davis et al. 2001, Glasow et al. 2002, Endresen et al. 2003, Song et al. 2003). These studies revealed that photochemical and heterogeneous processes in the ship exhaust plumes and the ship corridors are important but not well parameterized in the chemistry transport models. Experimental data to investigate these processes, however, are very sparse. Chen et al. (2005) performed aircraft measurements in the exhaust trail of two ships off the coast of California in 2002 and found that models underestimate NO_x and SO_2 losses and largely overestimate HNO_3 abundances in the plumes. Recently, Williams et al. (2005) reported observations in exhaust plumes of several small marine ships off the coast of New England performed on board the research vessel Ron Brown in summer 2004. Here we report on first aircraft measurements in a major European ship traffic corridor including detailed observations in the exhaust trail of a large container ship. The objectives of these investigations are to provide data for analysis of plume dilution and mixing, determination of ship emission factors, and validation of plume box and chemistry transport models. This paper presents the measurements of chemical compounds, observations of particulate ship emissions are described in the proceedings contribution of Petzold et al. (this issue).

* *Corresponding author:* Hans Schlager, DLR-Institut für Physik der Atmosphäre, Oberpfaffenhofen, D-82224 Wessling, Germany. Email: hans.schlager@dlr.de

2 EXPERIMENT

The measurements were performed on 23 and 30 July 2004 as part of the DLR research program Transport and Environment. The DLR research aircraft Falcon was used based from Creil in northern France. The objective of the flight on 23 July 2004 was to survey the English Channel at the western exit and search for corridor effects of ship emissions. The English Channel is one of the most travelled ship corridors in the world. About 500 ships per day use the east- and westbound shipping lanes in the English Channel. The objective of the flight on 30 July 2004 was to sample the exhaust trail of a designated source ship, a very large container ship. The sampling of the container ship plume was performed off the coast of north-western France near 48.2°N/ 6,5°W. Information on the operating conditions of the ship and the engine as well as a sample of the fuel burnt were provided by the ship operator.

Measurements presented here include CO₂, NO, NO_y, O₃ and SO₂. A NDIR absorption spectrometer was used for fast CO₂ measurements (modified LI-COR 6262) with an accuracy of ±0.8 ppmv for a time resolution of 1 s. (Fischer *et al.*, 2002). NO and NO_y were detected using chemiluminescence technique (Schlager *et al.*, 1997, Ziereis *et al.*, 1999). Individual NO_y compounds were catalytically reduced to NO on the surface of a heated gold converter with addition of CO. The inlet tube for air sampling was oriented rearward and heated to 30°C to avoid sampling of NO_y in particles and adsorption of nitric acid on the wall of the sampling tube, respectively. The accuracy of the NO and NO measurements is 8 and 15 % for a time resolution of 1 s. Detection of O₃ was by UV absorption technique (Thermo Electron Corporation, Model 49) with an accuracy of 5 % for a time resolution of 5 s. SO₂ was measured using an ion trap mass spectrometer and chemical ionization technique (Speidel *et al.* 2006).

3 RESULTS

3.1 Individual plume measurements

Figure 1 shows the route of the container ship and the Falcon flight track during the exhaust trail measurements on 30 July 2004. The detailed sampling of the plume was performed between 16.30 – 17.30 UTC at flight levels between 93 and 266 m asl. The wind direction was east/southeast with a mean wind velocity of 2.5 ms⁻¹. Besides the exhaust plume of the container ship additional plumes were present of other ships cruising west (downwind) of the container ship on similar routes.

Table 1 summarises the observations during ten successful plume penetrations. Given are the measured enhancements of mixing ratios of CO₂, NO, and NO_y in the plume. Also included is time, altitude, and estimated plume age for each encounter. NO and NO_y values are missing for the encounters at small plume ages due to concentrations in the plume outside the measurement range of the instruments. A device for dilution of the sample air prior to detection was not used during these first measurements of ship plumes.

Figure 2 (right panel) shows the measured peak mixing ratios of CO₂, NO, and NO_y for the plume encounters as a function of plume age. After a plume age of 1000 s the exhaust plume is diluted by a factor of $3.5 \cdot 10^{-5}$ considering the initial CO₂ mixing ratio at the engine exit of 40.000 ppmv. Observed $\Delta\text{NO}_y/\Delta\text{CO}_2$ ratios versus plume age are shown in the right panel of Figure 2. The NO_y/ΔCO₂ ratios for the plume encounters #6 and #10 agree within error estimates with the initial NO_x/CO₂ ratio at the engine exit indicating no NO_y loss for plume ages up to 1300 s for the meteorological conditions in the boundary layer during the measurements. The NO_y/ΔCO₂ ratio of plume encounter #3 is slightly smaller than the initial NO_x/CO₂ ratio at the engine exit suggesting onset of reactive nitrogen loss.

3.2 Ship traffic corridor measurements

Figure 3 depicts the Falcon flight track on 23 July 2004. The flight section in the ship corridor was from Brest (48.5°N, 4.2°W) to the northwest (50°N, 7°W) at a constant altitude of 200 m asl. Figure 4 shows observed mixing ratios of NO_y, NO, SO₂, and CO₂ along the Falcon flight track in the ship

corridor (right panel). Coincident enhancements in the mixing ratios of NO_y , NO and SO_2 were found caused by a multitude of ship exhaust plumes aged between about 0.5 and 5 hours. In many cases measured concentration peaks are due to superposition of several ship plumes. For some of the exhaust plumes enhancements of the CO_2 mixing ratios were also detected. An example is shown in the right panel of Figure 3. Observations in this multiple plume were used to infer emission factors for NO_x (see below).

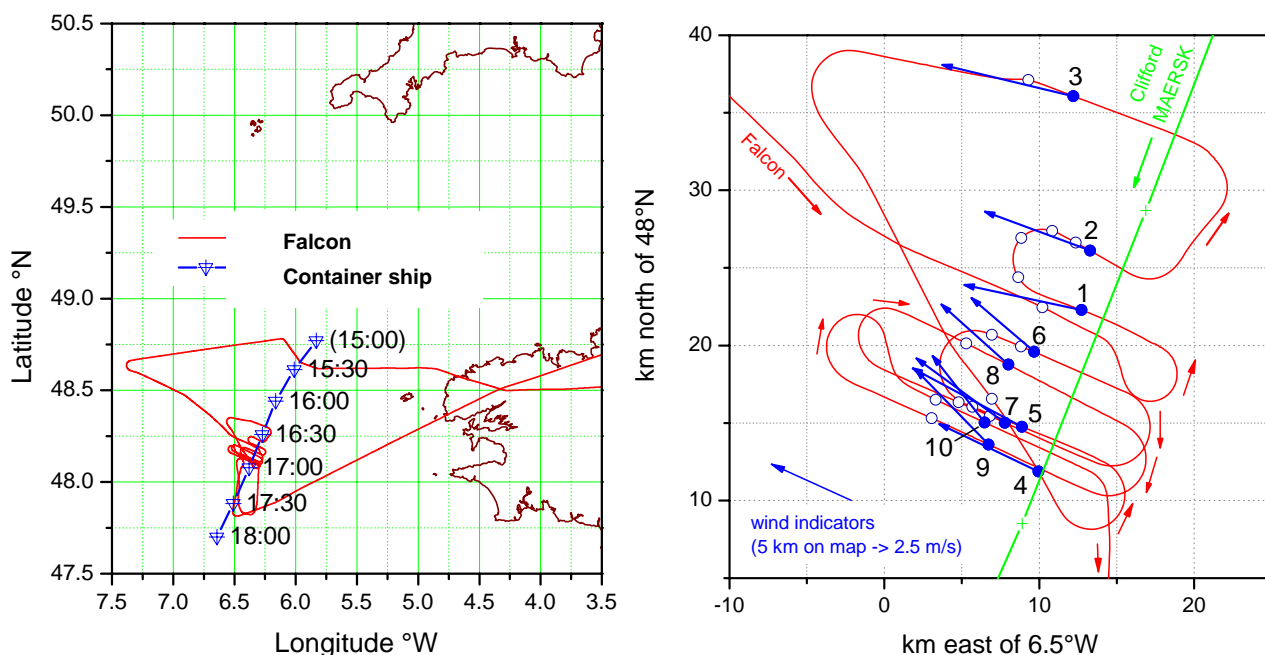


Figure 1. Sampling strategy of the exhaust plume of the large container ship. Routing of the Falcon and container ship (left panel). Falcon encounters (solid circles) of the container ship plume are labelled from 1-10 (right panel). The wind direction and velocity are also indicated. Plumes from other nearby ships were also penetrated (open circles).

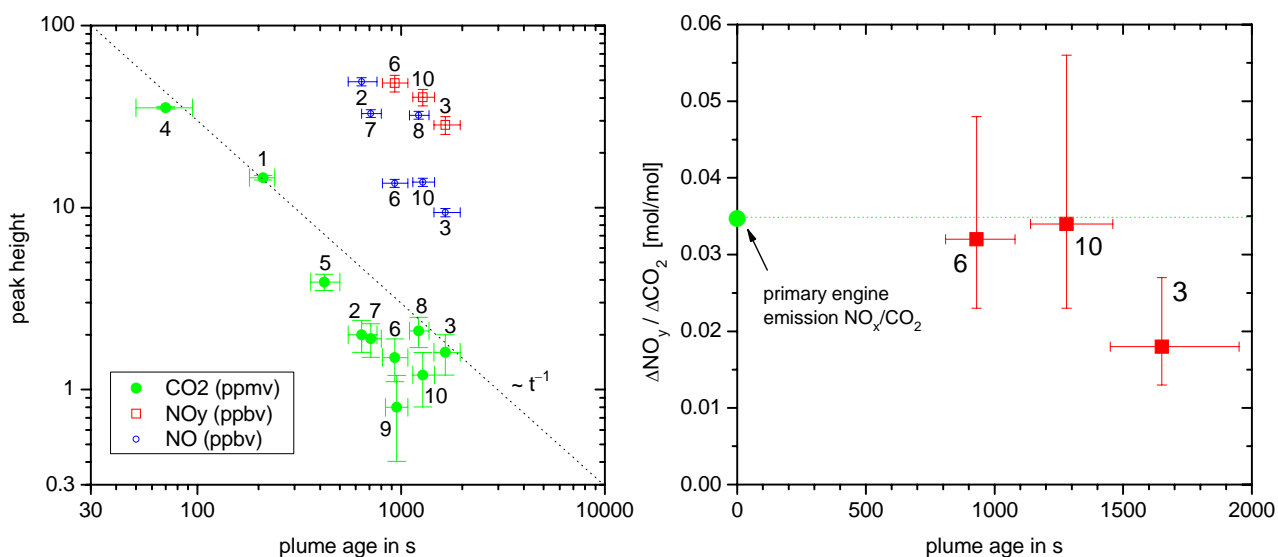


Figure 2. Observed peak concentrations of CO_2 , NO_y , and NO for the container ship plume transects versus estimated plume age (left panel). Measured NO_y/CO_2 ratios of the plume encounters #3, #6, and #10. Also included is the initial emission NO_x/CO_2 ratio at the engine exit (right panel).

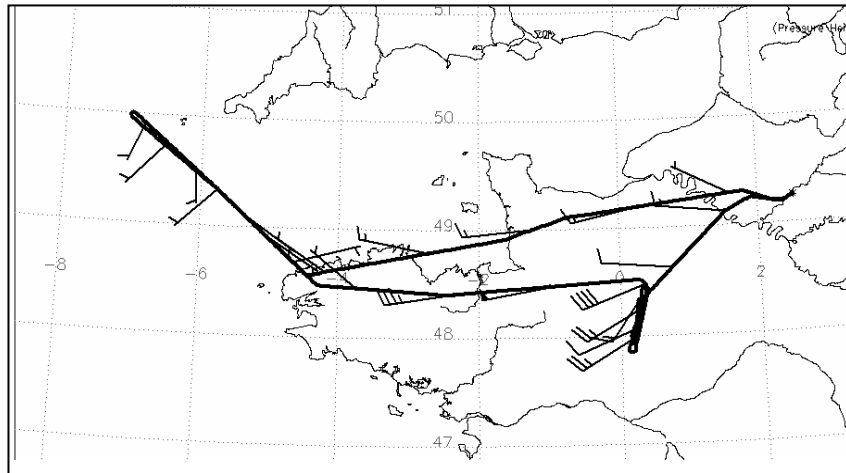


Figure 3. Falcon transect through the ship corridor at the exit of the English Channel at a constant altitude of 200 m asl on 23 July 2004.

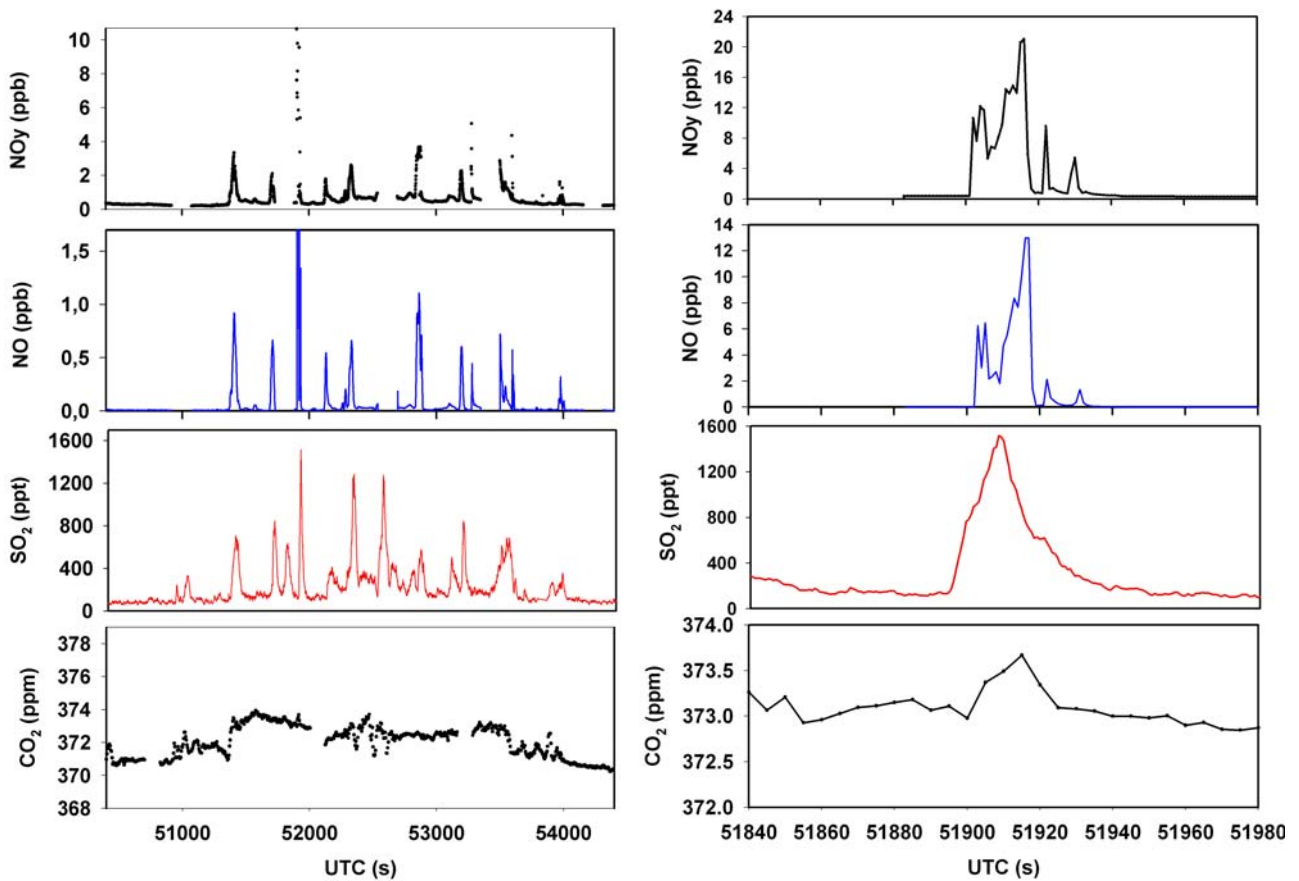


Figure 4. Time series of observed NO_y , NO , SO_2 , and CO_2 for the ship corridor transect (left panels). Observed concentration enhancements in the multiple plume sampled at about 51910 s (UTC) in the ship corridor (right panels).

Table 1. Observed differences of trace gas mixing ratios for the individual plume encounters relative to ambient concentrations in the boundary layer. Plume ages are calculated using the wind measurements from the Falcon

#	UTC Sec	Alt m	plume age S	ΔCO_2 $\mu\text{mol} / \text{mol}$	ΔNO nmol / mol	ΔNO_y nmol / mol	$\Delta\text{NO}_y / \Delta\text{CO}_2$ mmol / mol
1	60194	134	210 ±30	14.6±0.4	-	-	-
2	60307	105	640 -90/+120	2.0±0.4	49.2±2.5	-	-
3	60536	95	1650 -200/+300	1.6±0.4	9.4±0.5	28.4±3.2	18(-5/+9)
4	60977	93	70 -20/+25	35.3±0.5	-	-	-
5	61136	150	420 -60/+80	3.9±0.4	-	-	-
6	61274	149	930 -120/+150	1.5±0.4	13.6±0.7	48.3±5.1	32(-9/+16)
7	61470	194	710 -70/+90	1.9±0.4	32.9±1.6	-	-
8	61689	195	1220 -120/+150	2.1±0.4	32.2±1.6	-	-
9	61903	263	950 -110/+130	0.8±0.4	-	-	-
10	62157	266	1280 -140/+180	1.2±0.4	13.8±0.7	40.4±4.2	34(-11/+22)

3.3 Determination of emission factors

Emission factors for NO_x were derived from the plume encounters #3, #6, and #10 during the flight on 30 July 2004 (see Table 1) and the multiple plume observed in the ship corridor during the flight on 23 July 2004 (Figure 3, right panel). Emission factors for SO_2 were inferred from the plume encounters #3 and #10. Emission indices (emitted mass per kg fuel burnt) for NO_x (as NO_2 mass) were calculated using (e.g. Schulte & Schlager, 1996)

$$\text{EI}(\text{NO}_x) = \text{EI}(\text{CO}_2) 46/44 \Delta[\text{NO}_x]/\Delta[\text{CO}_2] \quad (1)$$

where $\text{EI}(\text{CO}_2)$ denotes the CO_2 emission index, 46 and 44 the mole masses of NO_2 and CO_2 , respectively. $\Delta[\text{NO}_x]$ and $\Delta[\text{CO}_2]$ are the observed enhancements of the mixing ratios in the plumes relative to ambient background concentrations. For $\Delta[\text{NO}_x]$ we used the measured $\Delta[\text{NO}_y]$ and assumed no loss of reactive nitrogen in the plumes. The CO_2 emission index is known with high accuracy ($3070 \pm 20 \text{ g CO}_2 / \text{kg fuel}$) from the carbon mass fraction in ship fuel (85.1%) and the fraction of carbon that is converted to CO_2 for cruise conditions (98.5%). The calculated NO_x emission indices are given in Table 2.

Emission factors for SO_2 were derived from the ratios of the integrals of the corresponding plume enhancements

$$\text{EI}(\text{SO}_2) = \text{EI}(\text{CO}_2) 64/44 \int[\text{SO}_2] / \int[\text{CO}_2]. \quad (2)$$

Integral ratios needed to be used because of the different time responses of the CO_2 and SO_2 measurements. The calculated SO_2 emission indices are also summarized in Table 2.

Table 2. Summary of emission indices derived from the plume observation. For comparison calculated values are also given.

Date, Plume encounter	$\text{EI}(\text{NO}_x)$ measured (g NO_2 / kg fuel)	$\text{EI}(\text{NO}_x)$ calculated (g NO_2 / kg fuel)	$\text{EI}(\text{SO}_2)$ observed (g SO_2 / kg fuel)	$\text{EI}(\text{SO}_2)$ calculated (g SO_2 / kg fuel)
30 July, #3	96 ± 14	112 (a)	46 ± 12	49 (c)
30 July, #6	103 ± 15	112 (a)	-	49 (c)
30 July, #10	109 ± 16	112 (a)	40 ± 10	49 (c)
23 July, corridor	98 ± 15	86 (b)	-	

(a) engine model of manufacturer for measurement conditions, (b) mean all cargo ships (Eyring et al. 2005), (c) from analysis of sulphur content in the fuel sample of the container ship (2.45% by mass), (d) from mean sulphur content of cargo ship fuel (Eyring et al., 2005).

The inferred $\text{EI}(\text{NO}_x)$ values compare well with calculated emission indices for the container ship using the engine emission model of the manufacturer and the known engine operating conditions during the measurements. The SO_2 emission factors derived from the integrals of the CO_2 and SO_2 enhancements observed in the plume are lower by 6% and 19% compared to the values calculated

from the known sulphur content in the fuel burnt by the container ship. Considering the estimated errors, however, the emissions factors are still consistent with the values derived from the analysis of the sulphur in the fuel.

4 CONCLUSIONS

The measurements in the exhaust trail of a designated source ship and in the ship corridor revealed that aircraft-based observations in ship plumes are possible for plume ages up to about 5 hours. The inferred emission factors for NO_x are consistent with reported mean values for the fleet of large container ships. Observed SO₂ enhancements in the plumes relative to the CO₂ enhancements as a dilution tracer are smaller than calculated values from the known sulphur content in the fuel but still agree within error limits. In order to study SO₂ losses in the exhaust plumes further measurements with higher accuracy and for larger plume ages are needed. During the flight transects in the ship corridor very inhomogeneous concentration field were found for trace gasses related to ship emissions due to multiple aged plumes. Next year a large aircraft campaign on ship emission will be performed in the frame of the EC project QUANTIFY with an extended set of instruments.

REFERENCES

- Capaldo, K., J.J. Corbett, P. Kasibhatla, S.N. Pandis, 1999: Effects of ship emissions on sulphur cycling and radiative climate forcing over the ocean, *Nature* 400, 743-746.
- Corbett, J.J., and P.S. Fischbeck, 1997: Emissions from ships, *Science* 278, 3723-3731.
- Chen, G., et al. 2005: An investigation of the chemistry of ship emission plumes during ITCT 2002, *J. Geophys. Res.* 110, doi:10.1029/2004JD005236.
- Davis, D.D., G. Grodzinsky, P. Kasibhatla, J. Crawford, G. Chen, S. Liu, A. Bancy, D. Thornton, H. Guan, S. Sabdholm, 2001: Impact of ship emissions on marine boundary layer NO_x and SO₂ distributions over the Pacific Basin, *Geophys. Res. Lett.* 28(2), 235-238.
- Eyring, V., H.W. Köhler, J. van Aardenne, A. Lauer, 2005: Emissions from international shipping: 1. The last 50 years, *J. Geophys. Res.* 110, doi:10.1029/2004JD005619.
- Endresen, O., et al., 2003: Emissions from international sea transportation and environmental impact, *J. Geophys. Res.* 108, doi: 10.1029/2002JD002898.
- Fischer, H., et al., 2002: Synoptic tracer gradients in the upper troposphere and lower stratosphere over central Canada during the Stratosphere-Troposphere Experiment by Aircraft Measurements 1998 summer campaign, *J. Geophys. Res.* 107, doi:10.1029/2000JD000312.
- Glasow, V., M. Lawrence, R. Sander, P.J. Crutzen, 2003: Modeling the chemical effects of ship exhaust in the cloud-free marine boundary layer, *Atmos Phys. & Chem, Vol 3*, 233-250.
- Kasibhatla, P., et al., 2000: Do emissions from ships have a significant impact on concentrations of nitrogen oxides in the marine boundary layer? *Geophys. Res. Lett.* 27, 2229-2232.
- Lawrence, M.G., P.J. Crutzen, 1999: Influence of NO_x emissions from ships on tropospheric photochemistry and climate, *Nature* 402, 167-170.
- Schlager, H., P.Konopka, P. Schulte, U. Schumann, H. Ziereis, F. Arnold, M. Klemm, D. Hagen, P. Whitefield, J. Ovarlez, 1997: In situ observations of air traffic emission signatures in the North Atlantic flight corridor, *J. Geophys. Res.* 102, 10739-10750.
- Schulte, P. and H. Schlager, 1996: In-flight measurements of cruise altitude nitric oxide emission indices of commercial jet aircraft, *Geophys. Res. Lett.* 23, 165-168.
- Song, C.H., G. Chen, S.R. Hanna, J. Crawford, D.D. Davis, 2003: Dispersion and chemical evolution of ship plumes in the marine boundary layer: Investigation of O₃/NO_y/HO_x chemistry, *J. Geophys. Res.* 108, doi: 10.1029/2002JD002216.
- Speidel, M, R. Nau, F. Arnold, H. Schlager, A. Stohl, 2006: Aircraft-based atmospheric sulfur dioxide measurements during ITOP 2004, *J. Geophys. Res.* (in preparation).
- Williams, E., B. Lerner, P. Quinn, T. Bates, 2005: Measurements of gas and particle emissions from commercial marine vessels, American Geophysical Union, Fall Meeting 2005, Abstract A51E-0130.
- Ziereis, H., H. Schlager, P. Schulte, I. Köhler, R. Marquardt, C. Feigl, 1999: In situ measurements of the NO_x distribution and variability over the eastern North Atlantic, *J. Geophys. Res.* 104, 16,021-16,032.

Airport Emission Studies of Gaseous and Particulate Emissions

S.C. Herndon, E.C. Wood, M.J. Northway, T.B. Onasch, P.E. Yelvington, R.C. Miake-Lye*
Aerodyne Research, Inc., 45 Manning Road, Billerica, MA 01821 USA

W. Berk Knighton
Department of Chemistry, Montana State University, Bozeman, MT 59717, USA

Keywords: Airport, runway, NO_x, CO, formaldehyde, particles, gaseous, hydrocarbon, emissions

ABSTRACT: Dedicated tests to measure the emissions from aircraft engines are costly due to high fuel and equipment costs, require specialized probes and support structures, and are generally logistically complex. On the other hand, in-service aircraft are routinely being operated using normal procedures at any active airport. Several recent studies have used the transport of prevailing winds to carry the airplane emissions to a suite of sensitive, fast time response measurement instruments. By identifying individual aircraft tail numbers, the measured emissions can be tied to the specific engines being operated, without interfering with airport operations. A description of such airport tests and the type of results obtained from advected plume studies using a suite of measurement instruments are presented. Distinct differences in emission quantities can be discerned for differing aircraft types, especially notable in particle property signatures of older versus newer airplanes.

1 MEASURING IN-SERVICE AIRCRAFT EMISSIONS AT AIRPORTS

While dedicated engine tests are very useful for obtaining detailed emissions measurements at precisely defined engine operation conditions, making measurements of in-service airplanes as they carry out their routine operations has several significant advantages. The measurement of aircraft engine plumes advected by the wind to strategically placed instruments allows data during actual operation to be obtained with no cost or burden on the normal operations of the airplanes or airport. Not only are the planes being operated as they are normally but the emissions are also captured at downwind locations in ways that account for the mixing, dilution, and emission evolution that occur as the emissions are processed in the atmosphere.

In order to make such advected plume emission measurements, the instrumentation must be sensitive enough to measure the diluted species concentrations and must have sufficient time resolution to capture a reliable signal during the time while the plume concentrations are elevated. Positioning the instrumentation must be planned based on the prevailing wind direction and an understanding of where the emissions are released from the airplane during the various aircraft operational modes. In tests to date, measurements during idle, taxi, take-off, and landing have all been obtained.

Several advected plume airport emission measurements have been made in the past several years (Herndon et al., 2004, 2005, 2006, ARB 2006). Most recently in August 2005, the JETS/APEX2 series of tests were performed at Oakland International Airport by a consortium of measurement teams, with significant support and interaction with the Port of Oakland and Southwest Airlines, supported by the California Air Resources Board, NASA, FAA, EPA, and DoD. Both dedicated engine tests (not discussed here) and advected plume studies were performed. The latter were carried out by The University of Missouri, Rolla's Center of Excellence on PM Reduction Research, and included personnel from UMR, Aerodyne, and NASA. Figure 1 indicates the general arrangement used for advected plume studies in that series of measurements. The prevailing winds were at a shallow angle to the axis of the primary runway, which allowed a measurement site to be identified

* Corresponding author: R.C. Miake-Lye, Aerodyne Research, Inc., 45 Manning Road, Billerica, MA 01821 USA.
Email: rick@aerodyne.com

that would allow plumes to be captured for airplanes taxiing to the runway, for idling prior to take-off, during take-off itself, and for airplanes landing on that same runway.

Oakland International Airport 8/2005 Measurements JETS/APEX-2

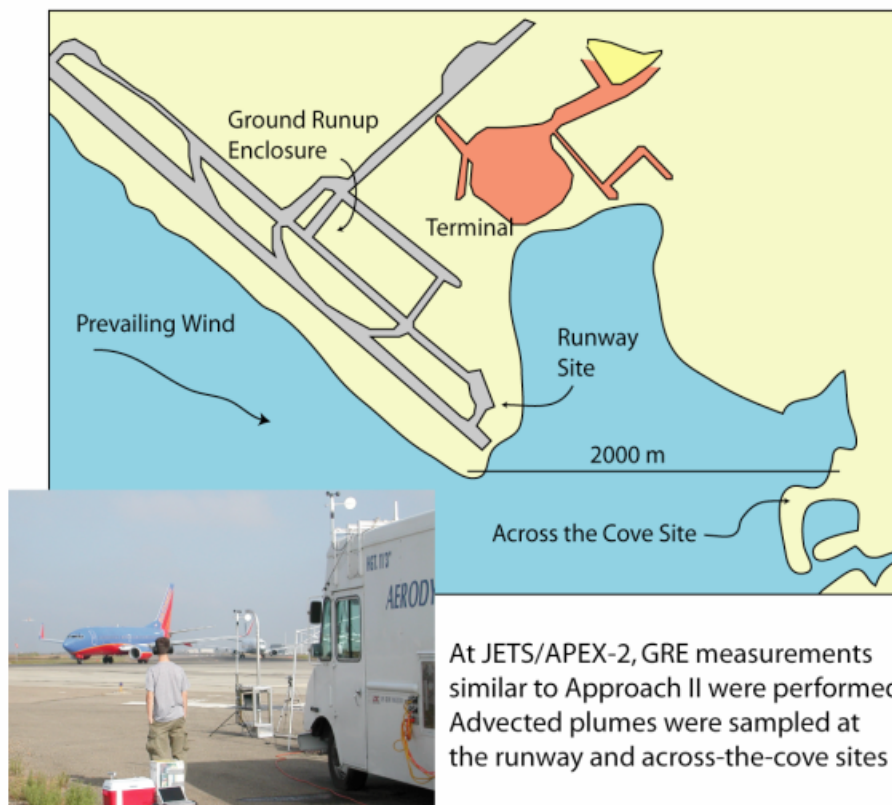


Figure 1. Measurements were made at the Oakland International Airport in JETS/APEX2. Dedicated engine tests (not presented here) were performed in the Ground Run-up Enclosure (GRE) with support of Southwest Airlines and the Port of Oakland. Runway tests on advected plumes as reported here were performed at the southeast end of the primary runway.

By recording the aircraft identifying tail number, specific airframe and engine information for the emitting aircraft could be obtained. The wind direction and speed, in concert with video recordings of the upwind field of view, were used to unambiguously identify the timing and source of any individual plume. Each arriving plume was measured by fast time response instruments to record both gaseous and particle emissions from the subject aircraft. The measured emissions include NO_x , CO, several hydrocarbon species, and a variety of particle parameters. Particle measurements by AeroDyne include black carbon (using Multi-Angle Absorption Photometry, MAAP), particle number (using a Condensation Particle Counter, CPC), and non-refractory aerosol composition and size (using an Aerosol Mass Spectrometer, AMS).

2 EI ANALYSIS BASED ON TIME RESOLVED CONCENTRATION MEASUREMENTS

Advected aircraft engine plumes are swept by the measurement station, lasting seconds to minutes with varying concentration histories that depend on the plume dilution and how the plume is transported past the sampling probe. In order to determine the relationship between the measured species and the emissions performance of the engine, Emission Indices (EIs) are determined. These are calculated using the correlation between any individual measurement and the CO_2 concentration measured for the sample exhaust sample. CO_2 provides a direct indication of the amount of fuel consumed in generating those emissions, where ideal combustion can be assumed or correction can be applied to account for combustion inefficiencies, usually very small for aircraft gas turbine engines. Thus by plotting the species of interest versus CO_2 , EIs can be obtained from the slope of their correlation, independent of the dilution history or plume structure.

Figure 2 demonstrates the basis of determining EIs for gaseous species in a plume. The top panel includes time series for CO_2 , CO , NO_2 , and NO , which are all put on the same time basis to generate the correlations in the bottom panel. Linear fits to each of the concentration histories provide EIs for the pronounced peak in the emissions curves. Some of the scatter in the correlation plots at lower CO_2 values can be attributed to overlap of an idle plume (at 11:55:300) overlapping with the more pronounced take-off plume. This type of analysis allows such interference to be identified and removed during data processing. In addition, such correlative analysis also automatically accounts for varying background levels in all species of interest as long as that variation is slow compared to the plume passage times.

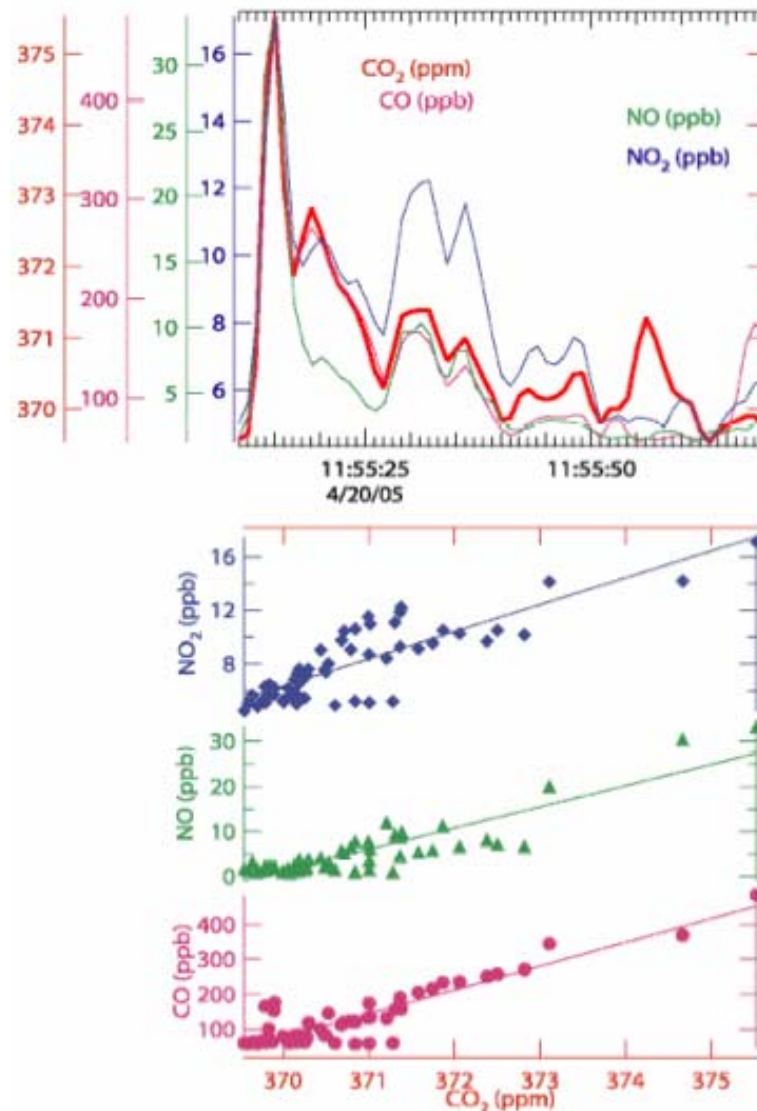


Figure 2. EIs are determined by plotting the species of interest against CO_2 , and using the slope of the linear fit to calculate an EI. The species and CO_2 must both be analyzed on the same time basis, accounting for different instrument response times and any time shifts due to instrument or line delays.

Similar analysis is performed on the particle data. Figure 3 shows correlations for both MAAP (black carbon mass) and CPC data (particle number), for two overlapping plumes. While the distinct nature of the two events (full versus open symbols) is more apparent in the CPC data, the MAAP fit would also be affected if that bimodal nature of the combination of two plumes were not properly taken into account. Such overlapping plumes were not very frequent during JETS/APEX2, since Oakland is a smaller hub that primarily uses a single runway. However, examination of the data in this manner is important to exclude such interferences when they occur and also to be sure that a linear correlation is obtained, indicating that time shifts and instrument effects are properly included and a reliable EI has been obtained.

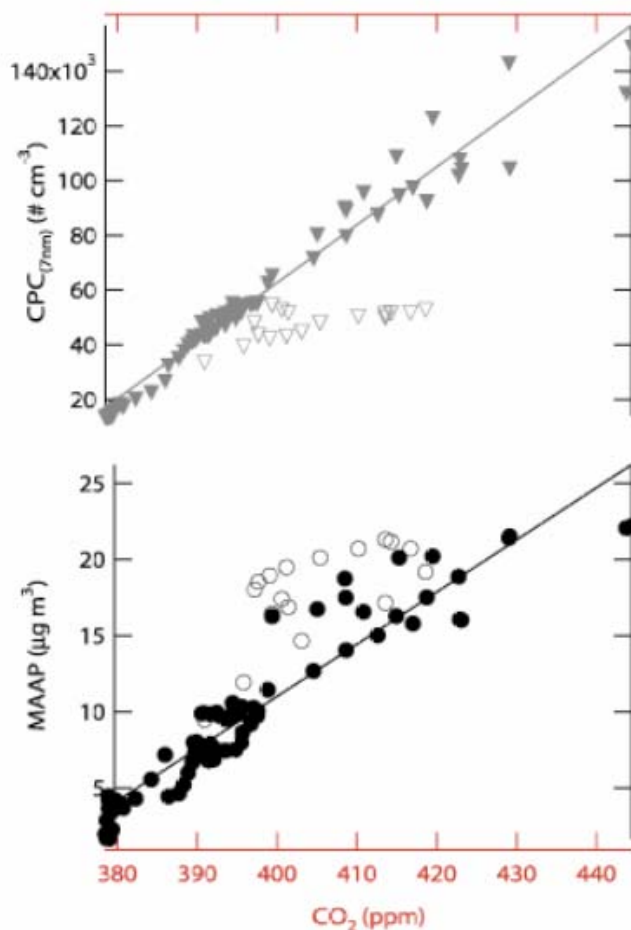


Figure 3. Particle parameter EIs are obtained from plots versus CO_2 , here showing a two-plume event. The bimodal nature is most obvious in the CPC data (open versus closed symbols), but even the MAAP data would be affected if the entire data set were fit as a single plume event.

3 RESULTS

Figure 4 shows a time series that includes both an idle plume and a take-off plume. The idle plume (left event) is enhanced in CO, formaldehyde, and ethylene relative to the take-off plume (right event), in both cases accounting for CO_2 levels. Also of interest is that most of the NO_x is present as NO_2 in the idle plume, while more NO_x is present as NO in the take-off plume.

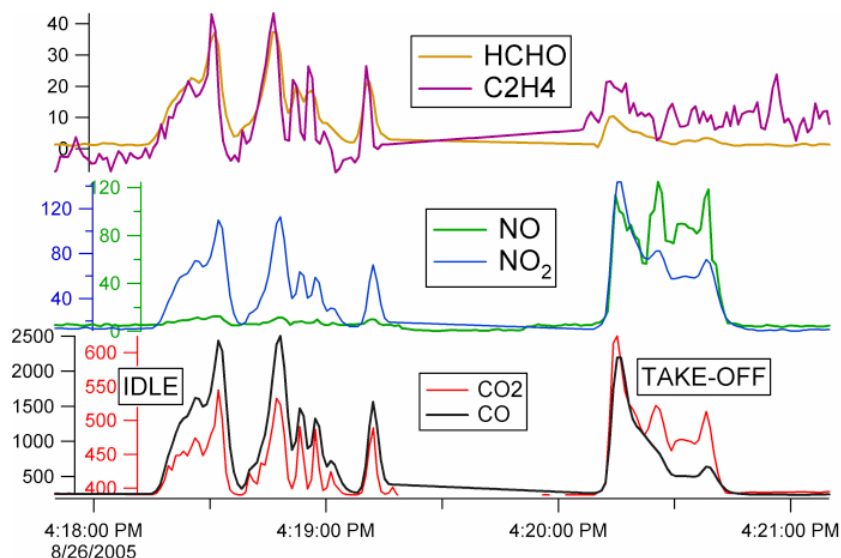


Figure 4. Time traces for gaseous species are presented for both an idle plume event (4:18:00 to 4:19:30) and a take-off plume event (4:20:00 to 4:21:00). The composition is enhanced in HCs for idle and the NO_2/NO ratio is significantly higher (shifted to NO_2) for idle conditions.

Figure 5 presents two take-off plumes that occurred close together. The earlier (left event) plume shows higher MAAP signals relative to the later (right event) plume, while the earlier plume has lower CPC signals than the later event. So on a relative basis, the first plume has fewer, more massive particles being emitted, while the later plume has more numerous less massive particles. This isolated comparison has been borne out in other cases analyzed, and the earlier plume is more characteristic of some older technology engines, while newer technology engines tend to have emissions more consistent with the later plume in this figure.

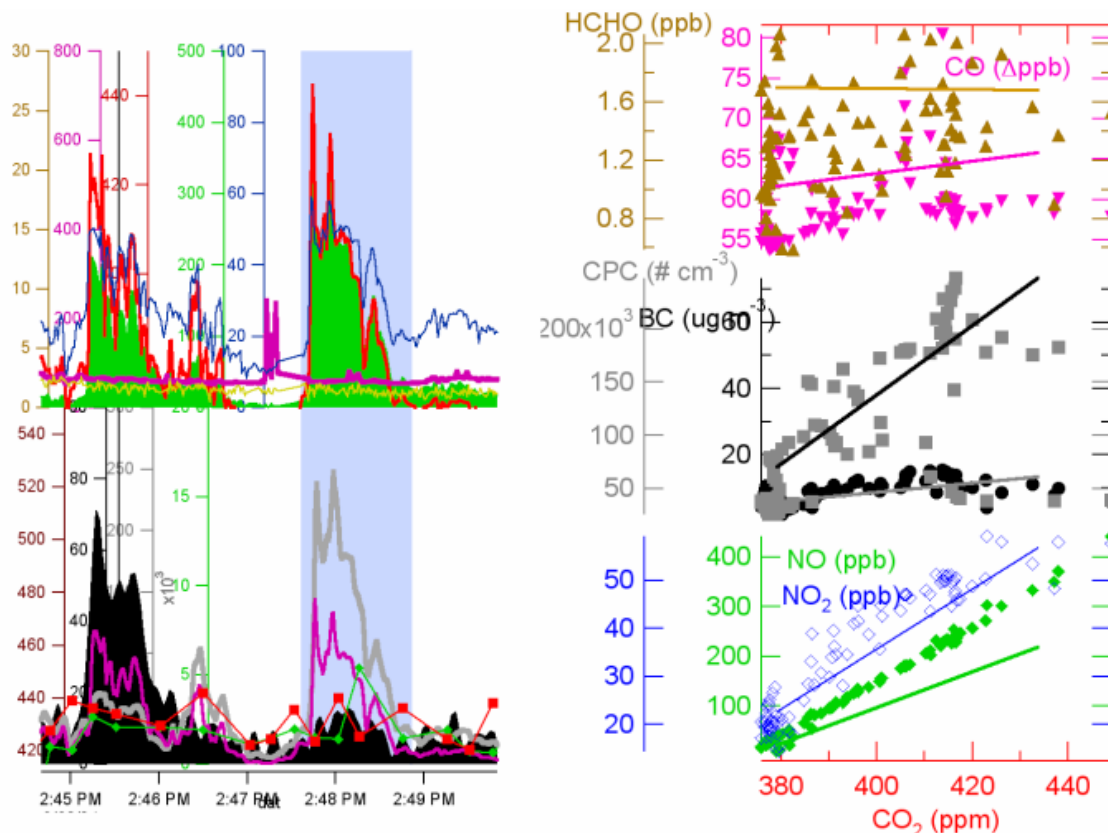


Figure 5. Two take-off plumes are presented, with the concentrations time series on the left panels and the EI analysis for the later (rightmost) plume presented in the right panels. The MAAP data is the filled-in curve in the lower left panel, while the CPC data is the thick (grey) shaded line in the same panel. The EIs for HCs

are very small for these take-off plumes, while NO_x and particle EIs are significant and different for each plume. The top curves in the left panel show several gaseous species.

4 CONCLUSIONS AND NEXT STEPS

A comprehensive emissions suite has been effectively employed in non-interfering runway studies and individual engine/airframe combinations have been identified for the specific emissions events that were captured. Multiple analyses are possible using the EIs that have been obtained using correlation between the species of interest and the measured CO₂ concentration in the sampled exhaust. Because the airframe/engine combination was determined, through the subject aircraft's tail number, the emissions values can be compared to the ICAO databank. Further, individual signatures for particular engine types may be determined, and statistical information on the emissions performance for specific engine/airframes and on averages, variation, and correlation of emissions with maintenance history may all be possible with sufficient airport emissions data.

ACKNOWLEDGMENTS

Sponsorship of NASA, CARB, FAA and the UMR Center of Excellence for Aerospace Particulate Emission Reduction Research is gratefully acknowledged. Support and interaction with the various mission team members, including airports, airlines (notably Port of Oakland and Southwest Airlines for JETS/APEX2 results) and other research teams contributed greatly to the overall missions' successes.

REFERENCES

- ARB, 2006 The Development of Exhaust Speciation Profiles for Commercial Jet Engines, Final report in press.
- Herndon, S.C., J.H. Shorter, M.S. Zahniser, D.D. Nelson, J.T. Jayne, R.C. Brown, R.C. Miake-Lye, I.A. Waitz, P. Silva, T. Lanni, K.L. Demerjian, and C.E. Kolb, 2004: NO and NO₂ emission ratios measured from in-use commercial aircraft during taxi and takeoff, *Environ. Sci. Technol.* 38, 6078-6084.
- Herndon, S.C., T.B. Onasch, B.P. Frank, L.C. Marr, J.T. Jayne, M.R. Canagaratna, J. Grygas, T. Lanni, B.E. Anderson, D.R. Worsnop, and R.C. Miake-Lye, 2005: Particulate emissions from in-use commercial aircraft, *Aerosol. Sci. Technol.* 39, 799-809.
- Herndon, S.C., T. Rogers, E.J. Dunlea, J.T. Jayne, R.C. Miake-Lye, and B. Knighton, 2006: Hydrocarbon emissions from in-use commercial aircraft during airport operation, *Environ. Sci. Technol.* 40, 4406-4413.

PM Emissions from Advected Aircraft Plumes at the Oakland International Airport

P.D. Whitefield*, P. Lobo, D.E. Hagen

University of Missouri – Rolla Center of Excellence for Aerospace Particulate Emissions Reduction Research, Rolla, MO, USA

Keywords: Aircraft, PM emissions, plumes, Oakland

ABSTRACT: At an airport study conducted at the Oakland International Airport (OAK) in August 2005, aircraft PM emissions data was gathered during a twelve hour period of normal daylight taxi and run- way operations. The prevailing wind was from the W/NW and the sampling location was situated downwind of the eastern end of the runway at OAK. The location selected for sampling the advected plumes was unique in the sense that it provided an opportunity to measure emissions as aircraft taxied to departure, departed, and landed on the single runway. Real-time PM and emission gas measurements, provided emission factors, size distributions and chemistry for over 300 aircraft under normal operating conditions. Aircraft tail numbers were also recorded for identification of the airframe and engine. This paper discusses the physical characteristics of the PM detected for the most common aircraft type operating at OAK, the B737.

1 INTRODUCTION

Project JETS APEX2 was a multi-agency funded study to measure PM emissions from in-service commercial aircraft at the Oakland International Airport (OAK) in August 2005. There were two components of this project –dedicated engine emissions testing performed at the Ground Runup Enclosure (GRE) and an airport runway study. A detailed account of the dedicated engine emissions results is provided in Hagen et al. (2006). This paper focuses on the airport runway study results associated with measurements of B737 type aircraft emissions during normal Landing and Take-Off (LTO) operations. It demonstrates the potential of downwind emissions monitoring adjacent to active taxi- and run- ways as a means to rapidly acquire evolving aircraft PM characteristics from in-service commercial aircraft. Emissions were monitored during a twelve hour period of daylight aircraft operations along a single runway where the advected exhaust plumes for over 300 aircraft were sampled. An aerial view of the test venue is shown in Figure 1. Mobile laboratories from UMR and Aerodyne Research Inc. (ARI) were co-located downwind on the eastern end of the runway with the prevailing wind direction coming from the W/NW. The UMR laboratory focused on the physical characterization of the advected PM and the measurement of CO₂. The ARI laboratory focused on PM speciation, CO₂, and additional combustion gases (Miake-Lye et al., 2006)



Figure 1.
Aerial view of the OAK test venue for advected plume monitoring

* *Corresponding author:* Philip D. Whitefield, UMR Center of Excellence for Aerospace Particulate Emissions Reduction Research, G-11 Norwood Hall, University of Missouri – Rolla, Rolla, MO 65409, USA. Email: pwhite@umr.edu

2 INSTRUMENTATION SUITE

UMR has developed a state-of-the-art mobile diagnostic facility and a sophisticated sampling methodology for nanometre scale PM optimized for jet engine exhaust characterization (Schmid et al., 2004; Lobo et al. 2006). The instrumentation consists of a state-of-the-art fast particulate spectrometer (Cambustion DMS500) to gather real-time size distribution information and total concentration of engine exhaust PM; a differential mobility analyzer (DMA) (TSI model 3071), a more traditional tool for particle size measurement, sacrificing speed for greater sensitivity when compared to the DMS500; Condensation Particle Counters (CPCs) (TSI models 3022 and 3025) to measure total number concentration; a fast response carbon dioxide (CO₂) detector (Sable Systems model CA-2A) to monitor sample dilution and establish emission factors; and a weather station to monitor the ambient conditions of temperature, relative humidity, pressure, and wind speed and direction.

3 RUNWAY STUDY RESULTS

A total of 300 aircraft landings and departures were detected and monitored during the period from 7am – 7pm on Friday, August 26, 2005. The distribution of landings and departures as a function of time is presented in Figure 2a. Aircraft tail numbers and operational status (i.e. taxi, takeoff, and landing) were acquired through visual observation including video recordings. Aircraft specific airframe and engine data were obtained by correlating these tail numbers with a Federal Aviation Administration (FAA) database. Figure 2b. illustrates the distribution of aircraft types operating at OAK on that day. 15 different airframe types were operating, of which approximately 63% of the aircraft were B737 type. The analysis in this paper will be limited to B737 airframes only.

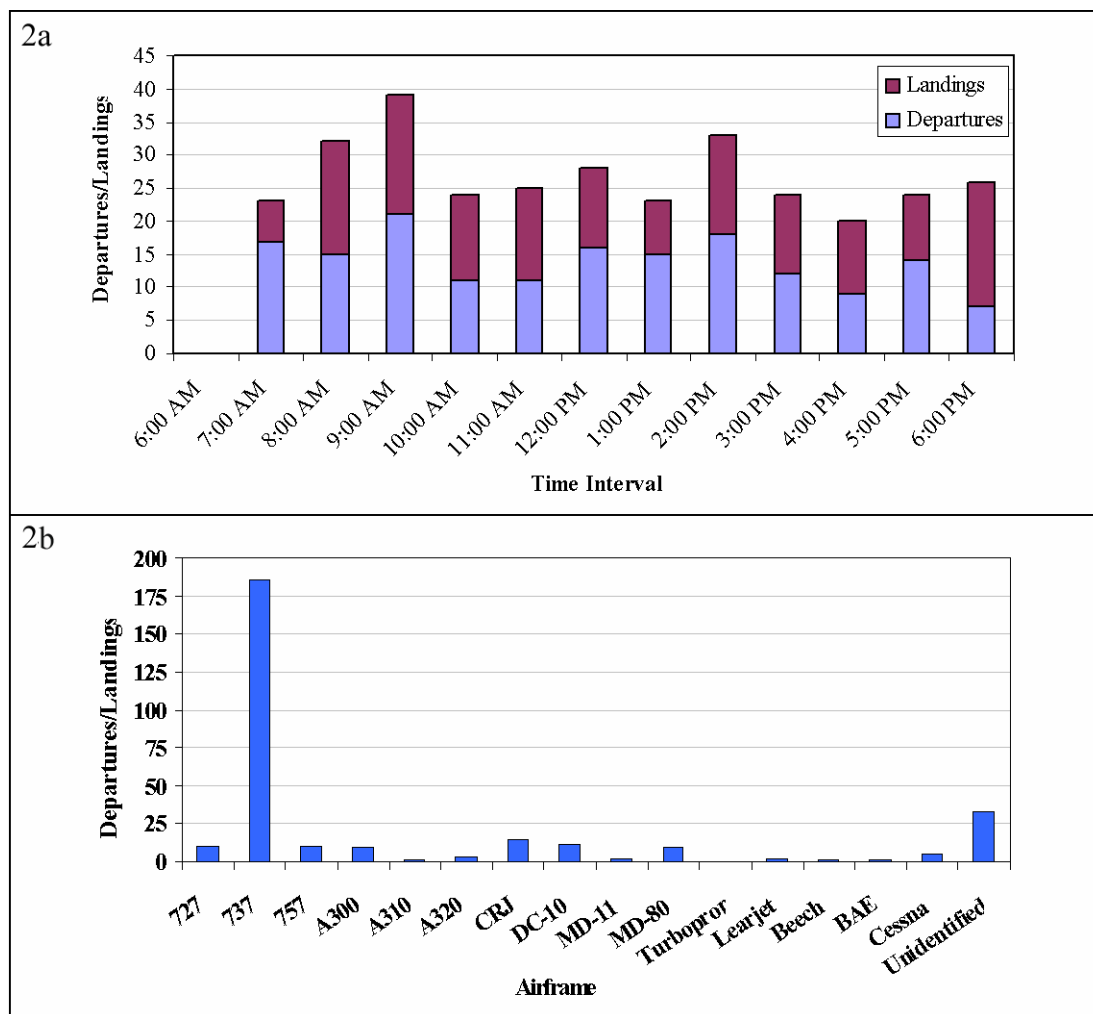


Figure 2a and 2b. Distributions of aircraft activity as a function of time (2a) and airframe (2b)

Distinguishing aircraft emissions from ambient PM is a significant component of the analysis task for sampling downwind of a runway. The ratio of plume PM concentrations to ambient levels was found to always exceed 50:1 and was found to vary significantly from plume to plume. The OAK runway is located on the eastern shore of San Francisco Bay, downwind of the conurbation of the western Bay Area, and upwind of the OAK terminal. Figure 3. illustrates the time-dependent ambient PM levels recorded during the study. Each data point represents a 60 sec. average of the integrated size distributions, centred on periods where no aircraft activity occurred. Peaks at ~9am and ~4pm in the ambient PM levels can be attributed to rush hour activity in the Bay Area. These time-dependent ambient PM levels have been subtracted from the operational plume data presented below. The ambient CO₂ values were also measured and subtracted from the respective plume values.

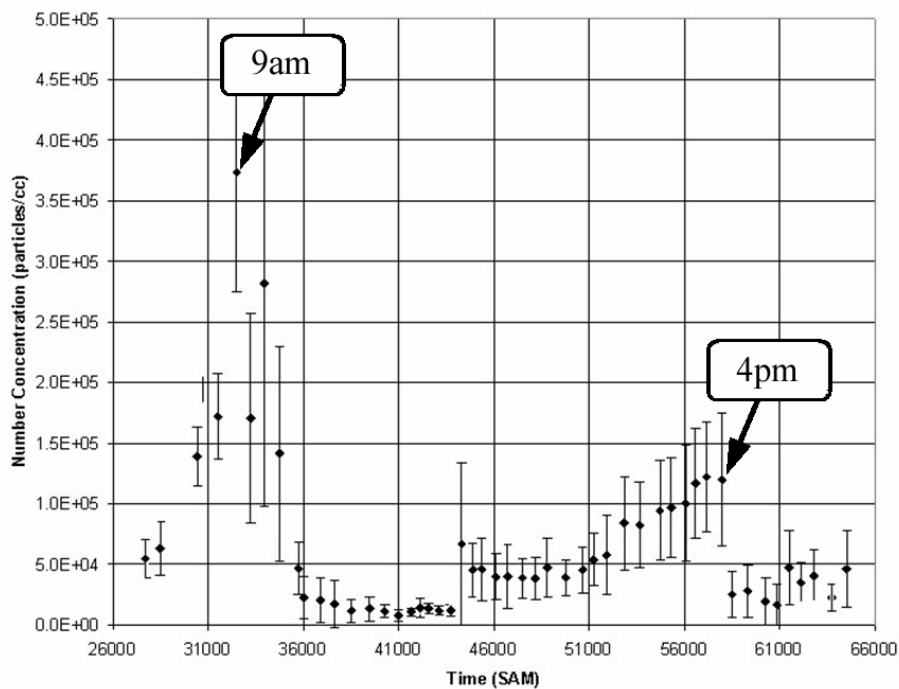


Figure 3. Time dependent ambient PM concentration during the test period (August 26, 2005)

Figure 4a shows emission profiles for CO₂, PM number and volume concentrations for a typical isolated aircraft taxi followed by take-off event involving a B737-300 aircraft with CFM56-3B1 engines. By comparison, Figure 4b. demonstrates a non-isolated series of events involving 3 aircraft, 2 landings in close succession followed by a taxi event. In this case, the PM emissions profiles are more complex and require combining PM data with concomitant speciation data to associate the emissions with specific aircraft. The latter example is more representative of the sampling environment in this one-day campaign. In this paper, where the intent is to demonstrate the practicality of downwind sampling, the analysis will focus on isolated events such as those observed in Figure 4a. Time-dependent number-based and volume-based size distributions corresponding to these events are presented in Figures 5a and 6a for the taxi, and Figures 5b and 6b for the take-off event, respectively. Table 1 lists the physical PM characteristics derived for these events where Dgeom is the number-based geometric mean diameter, Sigma is the geometric standard deviation, DgeomM is the mass-based geometric mean diameter, and EIn and EIm are the number and mass-based emission indices, respectively. EIn and EIm are derived from the ratio of the ambient subtracted PM parameter to its CO₂ concentration.

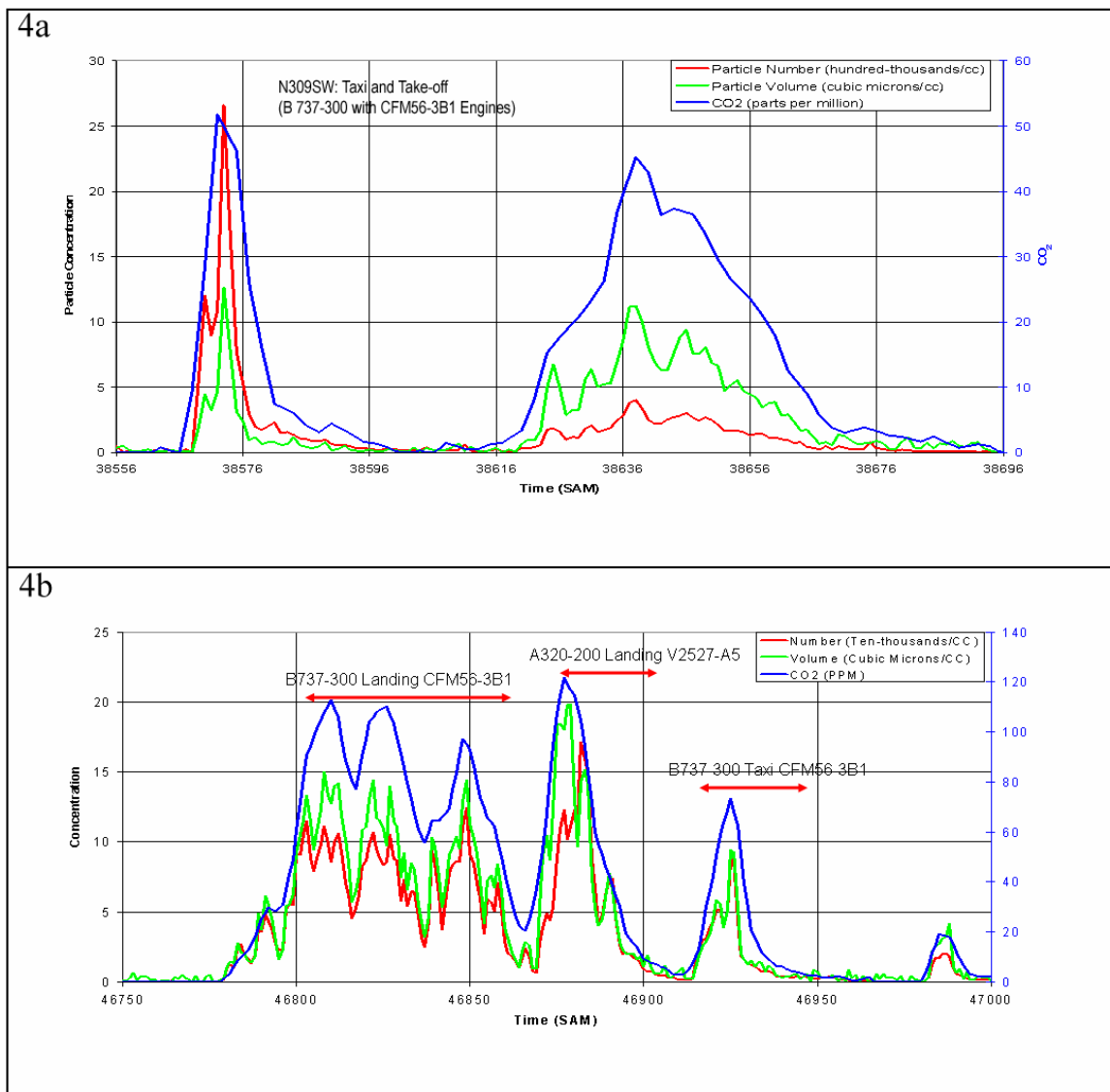


Figure 4a and 4b. Emissions profiles (CO₂, PM-number, PM-volume) for the taxi and take-off of plumes for one aircraft (4a), and for two landings and one taxi event occurring in rapid succession (4b)

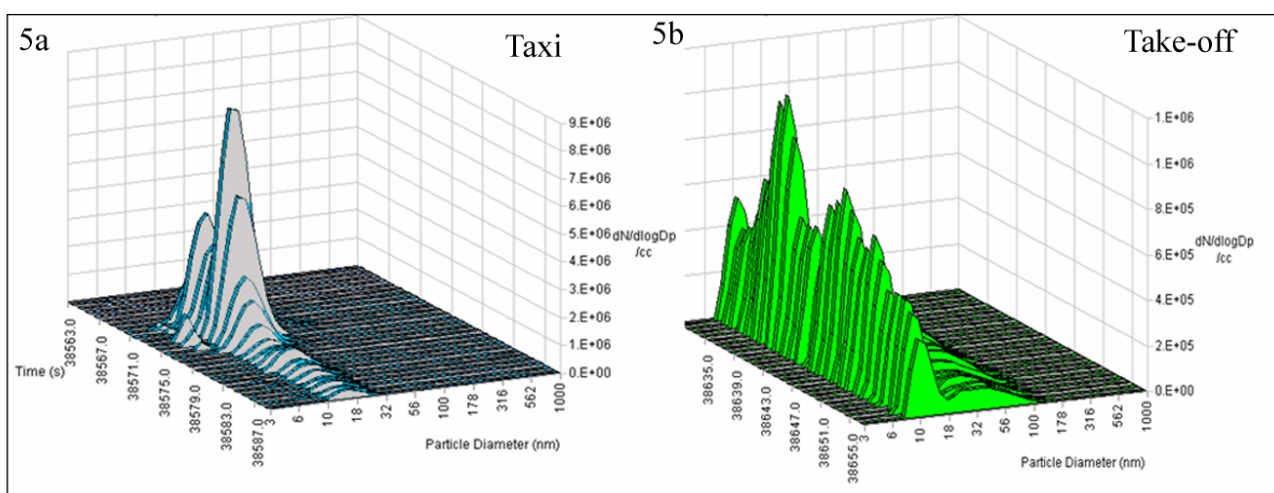


Figure 5a and 5b. Time dependent number-based size distributions for the events shown in Figure 4a

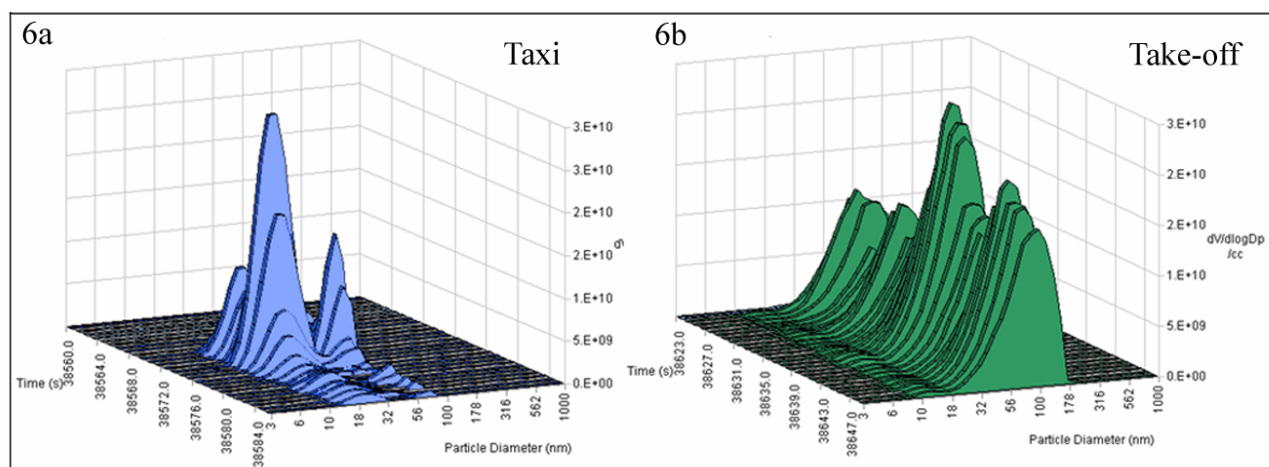


Figure 6a and 6b. Time dependent volume-based size distributions for the events shown in Figure 4a

Table 3. Physical PM Characteristics for an isolated taxi and take-off event

Event	Parameters				
	Dgeom (nm)	Sigma	DgeomM (nm)	EIn (1e15/kg fuel)	EIm (g/kg fuel)
Taxi	15.90 ± 0.82	1.38 ± 0.09	34.65 ± 15.29	38.37 ± 16.55	0.18 ± 0.09
Take-off	16.69 ± 1.57	1.99 ± 0.09	73.93 ± 6.16	12.42 ± 3.36	0.36 ± 0.10

4 DISCUSSION

Plume processing in the exhaust plume results in the production of a large number of small particles not present at the engine exit plane. The production of these small particles serves to shift D_{geom} to smaller values and results in at least an order of magnitude increase in E_{In} when the plume data are compared to those acquired at the engine exit plane (Hagen et al. 2006). These new particles do not significantly contribute to the mass dependent parameter values and no significant changes are observed in D_{geomM} and E_{Im} .

In this paper, the intent is to demonstrate the practicality of downwind sampling, and the analysis has focused on isolated events where detailed characterizations of the taxi and take-off plumes for the same aircraft have been achieved. In some cases, because of the unique aircraft traffic patterns, sampling location, and prevailing wind direction at OAK, take-off and taxi plumes for different aircraft are found to mix prior to sample extraction, greatly complicating data interpretation. The PM data from these mixed plumes can be deconvolved to yield single aircraft specific information and such analysis is currently underway.

For the subset of plumes that have been assigned to specific airframes and engines, another demonstration of the power of this measurement and analysis approach is presented in Figures 7a and 7b. Here the average taxi and take-off E_{In} and E_{Im} are compared for the B737-300 and B737-700 series of aircraft, having CFM56-3B and CFM56-7B series engines, respectively. To the limit of the number of plumes analyzed at this time (-300 taxi: 14, take-off: 4; -700 taxi: 9, take-off: 4), the following observations can be drawn. For E_{In} , no statistically significant differences were found between taxi and take-off and engine type. However for E_{Im} , the -300 series take-off emissions were significantly greater than those for its taxi emissions and for both take-off and taxi emissions for the -700 series. On average for the -700 series, a newer technology engine, E_{Im} is less than half that for the older technology -300 series.

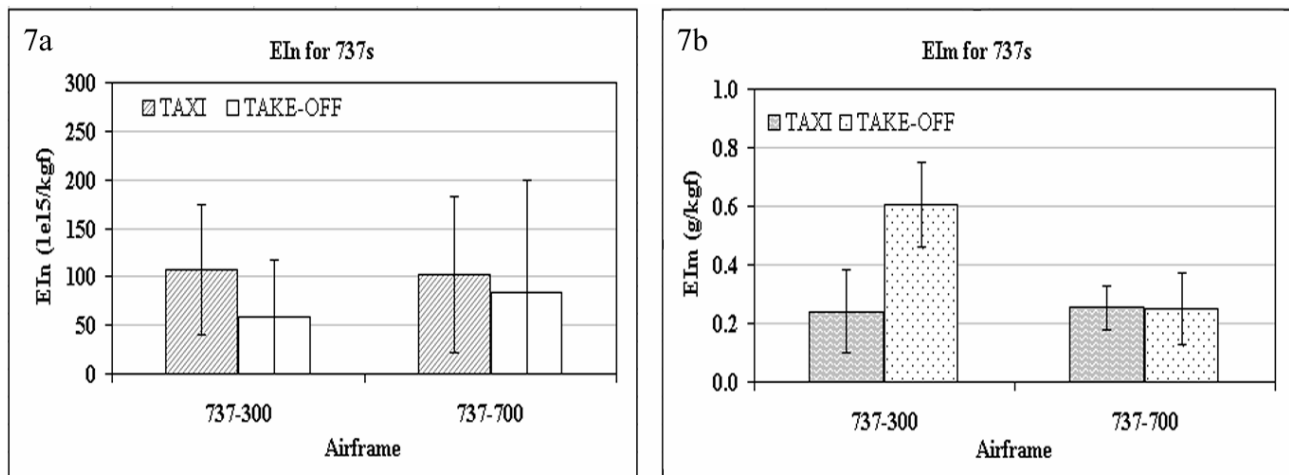


Figure 7a and 7b. Averaged taxi and take-off EIns (7a) and EIms (7b) for B737-300 and B737-700 aircraft monitored

5 CONCLUSION

The work described in this paper clearly demonstrates the potential of downwind emissions monitoring adjacent to active taxi- and run- ways as a means to rapidly acquire detailed and aircraft specific information related to the evolving plumes advected from in-service commercial aircraft under normal operational conditions.

ACKNOWLEDGEMENTS

The authors would like to acknowledge the sponsorship of California Air Resources Board, National Aeronautics and Space Administration, Federal Aviation Administration and the UMR Center of Excellence for Aerospace Particulate Emission Reduction Research throughout the work described in this paper.

REFERENCES

- Hagen, D., Lobo, P., and Whitefield, P. (2006). "Physical Characterization of PM emissions from In-Service Commercial Gas Turbine Engines – Projects APEX and JETS APEX2". *2006 TAC Conf Proc.*
- Lobo, P., Hagen, D.E., and Whitefield, P.D. (2006). Physical characterization of aerosol emissions from a Commercial Gas Turbine Engine – Project APEX. submitted to the *Journal of Propulsion and Power.*
- Miake-Lye, R.C., Herndon, S.C., Knighton, W.B., Onasch, T.B., Jayne, J.T., Northway, M.J., and Wood, E.C. (2006). "Airport Emission Studies of Gaseous and Particulate Emissions". *2006 TAC Conf Proc.*
- Schmid, O., Hagen, D., Whitefield, P., Trueblood, M., Rutter, A., and Lilenfeld, H. (2004). "Methodology for particle characterization in the exhaust flow of gas turbine engines", *Aerosol Sci. & Technol.*, 38:1108-1122.

Water- H₂SO₄- soot interaction in aircraft plume

O.B. Popovicheva^{*}, N.M. Persiantseva,
Institute of Nuclear Physics, Moscow State University, Moscow, Russia

A.M. Starik
Central Institute of Aviation Motors, Moscow, Russia

N.K. Shonija
Chemical Department, Moscow State University, Moscow, Russia

Keywords: Aircraft exhaust soot, Soot properties, Water uptake, CCN

ABSTRACT: This report presents the review of results obtained from 1) laboratory studies of water uptake by original aircraft –generated soot at the conditions of cooling and saturated plume, 2) modeling studies of H₂SO₄ accumulation on the surface of exhaust soot particles due to coagulation with sulfate aerosols and H₂SO₄/H₂O heterogeneous nucleation, and 3) laboratory studies of H₂SO₄ chemical processing of soot particles toward their hygroscopicity.

1 INTRODUCTION

A major source of uncertainties in assessing of aircraft impact on climate change is the emission of aerosols which may induce significant perturbations in cloudiness and the Earth's radiation balance. Aviation-produced soot aerosols are suspected to enhance the contrail and cirrus cloud formation (Schumann et al., 2002; Hendricks et al., 2005). Analysis of ice residuals in contrails (Petzold et al., 1998) and the properties of ice-nucleating aerosols from aircraft plume (Chen et al., 1998) exhibits that soot particles facilitate the contrail formation. Optical observations of an internal mixture of ice-BC aerosols in the plume (Kuhn et al., 1998) directly confirm theoretical model predictions showing (Kärcher et al., 1996) that the exhaust soot particles can serve as cloud condensation nuclei (CCN). The quantification of this impact has been advanced but the state of scientific understanding is still poor, mainly because of the lack of explanations for a number of observations such as 1) why the supersaturation with respect to water is needed for visible contrail formation (Kärcher et al. (1998), 2) is it true that ~ 1/3 proportion of exhaust soot particles (but not all) acts as ice nuclei in contrails (Schroder et al., 1998), and 3) why the changes in the value of Fuel Sulfur Content (FSC) have a small impact on the contrail formation threshold (Schumann et al., 2002).

The main reason for this disadvantage is insufficient studies of the water uptake and ice nucleating ability of exhaust soot aerosols. The lack of experimental data on hygroscopic properties of soot particles produced by aircraft engines led some investigators (Kärcher et al., 1996; Gleitsmann and Zellner, 1998) to assumption about hydrophobic nature of the surface of engine-generated soot particles. Various activation pathways were proposed to facilitate the ice particle formation on a hydrophobic soot particle surface (Kärcher et al., 1996, 1998). Numerical modeling demonstrated that coagulation of homogeneously nucleated sulfate aerosols with soot particles, binary H₂SO₄/H₂O heterogeneous nucleation, and direct deposition of sulfuric acid molecules may have a pronounced effect on the activation of soot particles by creating a liquid solution coating on their surface. However, no visible difference in the appearance of contrail was found at low and normal FSC (Schumann et al., 1996). Moreover, there is no any explanation of the existence of the fraction of exhaust soot particles acting as ice nuclei in contrails (Schroder et al., 1998). This is why it is more reasonable to assume the initial heterogeneities of emitted soot particles in respect to their ability to uptake water molecules and to consider the ways for natural water condensation on the hydrophilic fraction of soot particles.

^{*} *Corresponding author:* Olga B. Popovicheva, Institute of Nuclear Physics, Moscow State University, 199 992, Moscow, Russia. Email: polga@mics.msu.su

To prove such a suggestion the sampling campaigns was conducted to collect original soot behind the combustion chamber of a Russian gas turbine engine D30KU (Popovicheva et al., 2003; 2004). To simulate the cruise conditions the engine was operated with an average air/fuel equivalence ratio of ~ 4 and a pressure up to 7 atm. Aviation kerosene TC1 containing 0.11 wt% sulphur was used as a fuel. Aircraft Engine Combustor soot (AEC) was collected on a specially made copper probe being placed as close as possible to the combustor exit (at 12 cm distance behind it) to minimize the contact time for soot particles with hot exhaust gases.

2 TWO FRACTIONS OF EXHAUST SOOT

AEC soot was characterized in respect to a number of physico-chemical properties such as the particle size, microstructure, surface area, and chemical composition (Popovicheva et al., 2004). Two fractions in engine-generated soot were clearly observed: a main fraction containing essentially amorphous carbon and a fraction of impurities which is characterized by a complex structure and by a large amount of impurities such as oxygen, sulfur, iron, and potassium. Comprehensive chemical analysis exhibited a high amount of water soluble compounds (near 13.5 wt%) including sulfates, organics, and inorganic species which were deposited on soot particles within an engine. Moreover, a strong heterogeneity in the distribution of soluble impurities over the soot surface was found, this is why we assume to address all water soluble compounds to the fraction of impurities. Such an approach allows us to perform the water uptake measurements on AEC soot which itself may represent the fraction of impurities and on laboratory-made kerosene TC1 flame soot, which due to high similarity in microstructure and composition (Popovicheva et al., 2004) can represent the main fraction of exhaust soot.

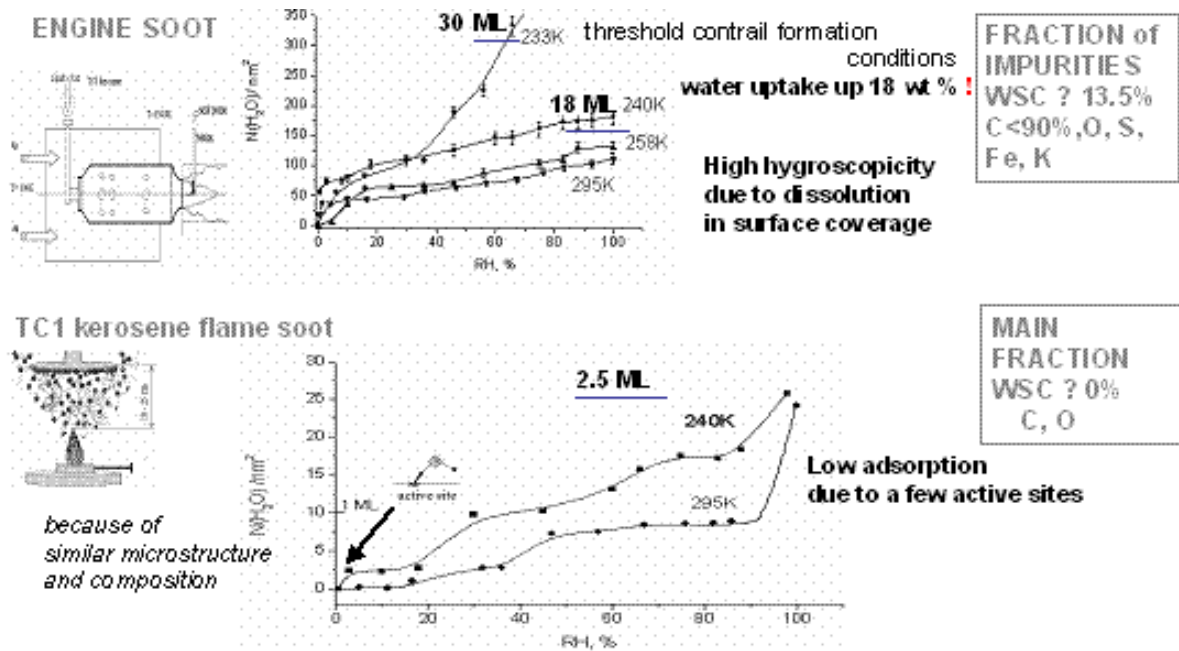
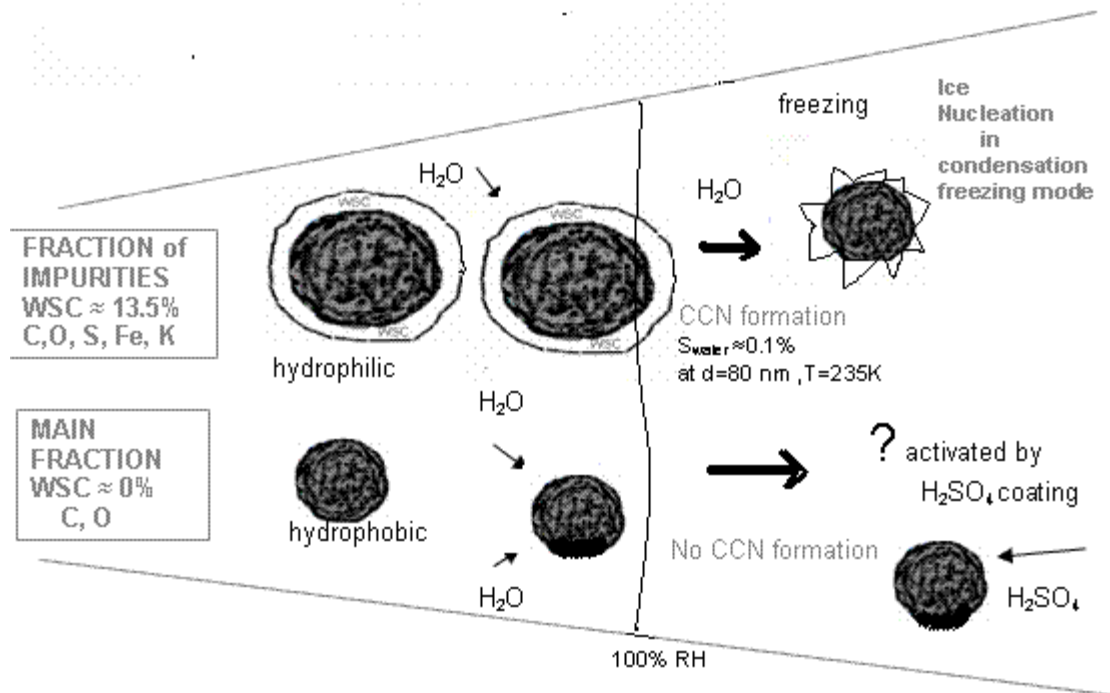


Figure.1. Water uptake of fraction of impurities and of main fraction of AEC soot

A series of water uptake measurements were performed by conventional gravimetric method in the wide range of RH and temperatures down to threshold contrail formation conditions. Figure 1 presents the findings for AEC and TC1 soot samples. As much as 30 statistic monolayer of water molecules (ML) may be absorbed by the soot belonging to the fraction of impurities at 233K that corresponds to $\sim 18\%$ of a total soot mass. Such high hygroscopicity relates with the bulk dissolution of water into the water soluble surface coverage. Low temperature facilitate the water uptake by AEC soot. In opposite, the main fraction of AEC soot is found to be hydrophobic due to low adsorption on active sites of TC1 soot surface (see Figure 1). Even at low temperature of $\sim 240K$ it adsorbs only 2.5 ML of water molecules.

3 UPDATE MODEL OF WATER-SOOT INTERACTION

The concept of separation of emitted soot particles into two fractions: fraction of impurities with high hygroscopicity and main fraction with low water uptake ability allow us to build the update model for interaction of water molecules with soot particles in aircraft plume presented in Scheme 1.



Scheme 1. Update model of water –soot interaction in aircraft plume.

Water molecule uptake by the fraction of impurities leads to formation of the liquid solution on the soot surface that is a prerequisite for the CCN formation at the reaching the conditions of water vapor supersaturation in the cooling plume. The following freezing of solution coverage facilitates the ice nucleation on this fraction of exhaust soot particles in the condensation - freezing mode. However, the soot particles of the main fraction are likely to be remained inactivated due to low water molecule uptake and can not act as CCN if they do not contain some hygroscopic gaseous compounds (like a sulfuric acid), which may be accumulated on the soot surface due to gas- to –surface interaction. To address the question arising how H₂SO₄ activation for hydrophobic soot particles may be effective due to plume proceeding, the additional theoretical and experimental studies have been carried out.

4 MODEL OF H₂SO₄ – SOOT INTERACTION

A quasi-one dimensional model (Starik et al., 2004) for a B-747 aircraft plume at cruise was used with emission parameters described in Savel'ev et al., 1999. At RH>50% in the ambient atmosphere the threshold contrail formation conditions are reached at 100-200 m distance from the nozzle exit when the aircraft plume is cooled down to temperatures of ~ 240-233K. Chemical transformation of 70 gaseous species, binary H₂O/H₂SO₄ homogeneous nucleation, condensation growth of sulfate aerosols, their coagulation with soot particles, and heterogeneous nucleation of H₂O and H₂SO₄ on the soot particle surface were addressed. Measurements of the contact angle, θ , of a sulfuric acid droplet on TC1 soot surface were accompanied the theoretical studies to provide the parameters needed for the classical theory of heterogeneous nucleation. The variation of θ for sulfuric acid with weight percent, wt%, can be approximated by the expression

$$\theta = \theta_0 - B \cdot \text{wt}\% + C \cdot \text{wt}\%^2 - D \cdot \text{wt}\%^3$$

where θ_0 is the water droplet contact angle, $\theta_0=67.67^\circ$. B, C, D are coefficients: $B=0.068$, $C=0.018$, $D=3.6 \cdot 10^{-4}$. We did not take into account the direct deposition of gaseous H_2SO_4 on soot particle surface in our model because our additional experiments have shown the negligible amount of sulfuric acid molecules adsorbed on TC1 soot at the H_2SO_4 concentration of $\sim 10^{12} \text{ cm}^{-3}$ in the young plume.

It was found that the amount of sulfuric acid accumulated on the unit area of the soot particle surface due to both heterogeneous binary H_2O/H_2SO_4 nucleation and coagulation of soot particles with sulfate aerosols strongly depends on the particle radius. The evolution of the total amount of sulfuric acid accumulated on the surface of the whole ensemble of exhaust soot particles, $\varepsilon'_{H_2SO_4}$, along the plume for medium and high FSC is shown in Figure 2. The size distribution of soot particles was assumed to be lognormal with median radius of 25 nm and geometric standard deviation of 1.56. The total concentration of soot particles at the engine exit was assumed to be equal $4 \cdot 10^6 \text{ cm}^{-3}$. The maximum value of $\varepsilon'_{H_2SO_4}$ at high FSC at the contrail formation threshold corresponds to $\sim 0.2 \text{ wt\%}$ of the soot mass if we take into account the surface area of $\sim 30 \text{ m}^2/\text{g}$ for the whole ensemble of exhaust soot particles (Popovicheva et al., 2004). A simple close-packed sphere model for H_2SO_4 molecules, assuming its effective molecular cross-section of 0.246 nm^2 , gives one static monolayer $\approx 4 \text{ H}_2\text{SO}_4$ molecules per nm^2 . With this assumption, we estimate a maximum H_2SO_4 coverage of 0.1 ML for soot particles due to sulfur-induced processing in the young plume.

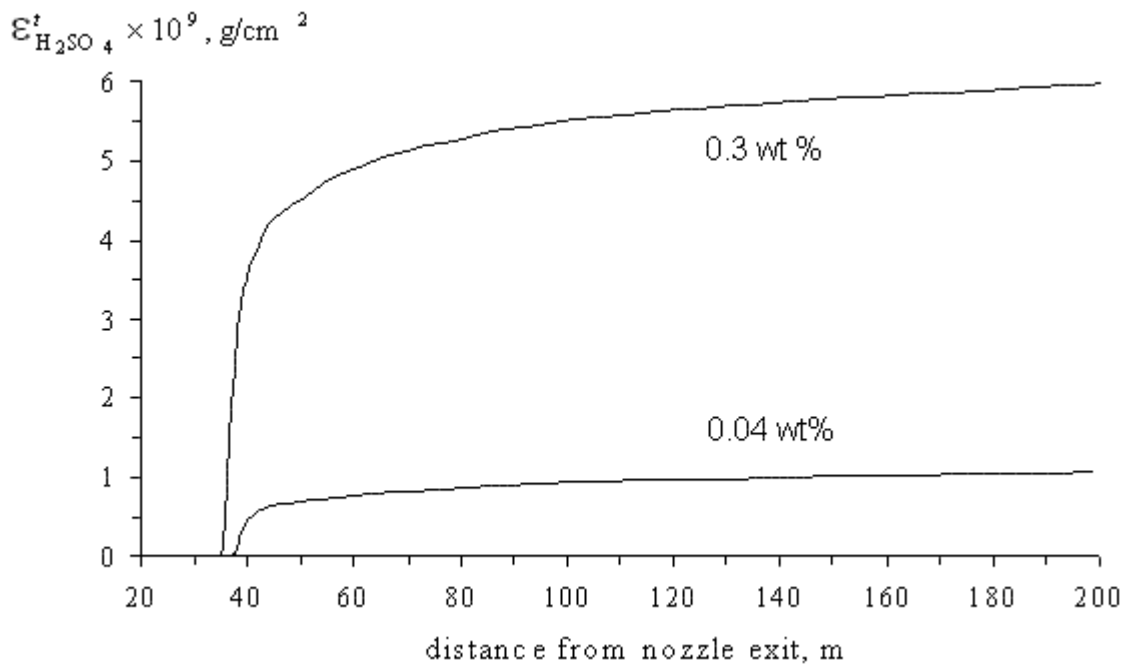


Figure 2. Evolution of the total amount of H_2SO_4 accumulated on the surface of exhaust soot particles along the plume for medium and high FSC. $N_s=4 \cdot 10^6 \text{ cm}^{-3}$.

5 EXPERIMENTAL SIMULATIONS

The TC1 soot treatment conditions were chosen to provide an amount of H_2SO_4 on the surface close to $\varepsilon'_{H_2SO_4} \approx 0.2 \text{ wt\%}$. It was accomplished by the gaseous H_2SO_4 deposition at $T=413\text{K}$ for 3 h. The isotherms of the water adsorption on TC1 soot modified by H_2SO_4 at $T=295\text{K}$ and 240K are shown in Figure 3. At 80% RH treated soot adsorbs water by a factor of 3 larger than untreated soot increasing its mass up to 3.2%. One sees that treated soot with 0.2 wt% of H_2SO_4 can uptake 8 ML of water molecules at the threshold conditions of the contrail formation.

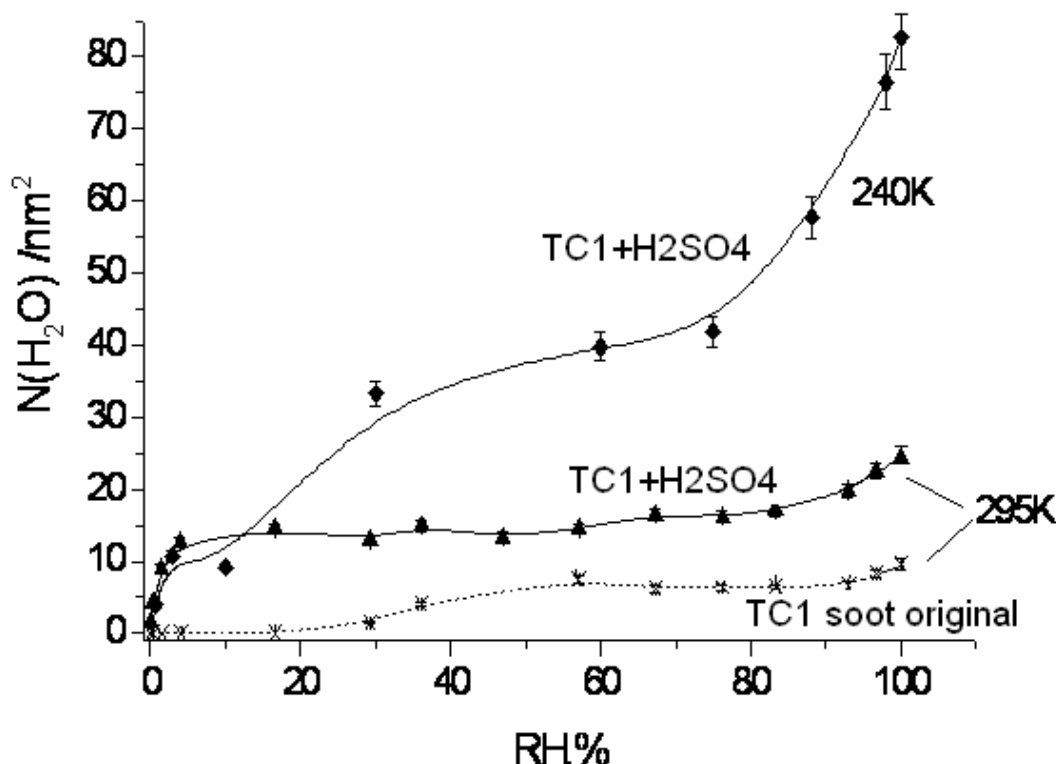


Figure 3. Amount of adsorbed water molecules per surface unit of original TC1 soot (crosses) for $T=295\text{K}$; TC1 soot with maximum value of H_2SO_4 coverage (~ 0.2 wt%) for $T=295\text{K}$ (triangles) and for $T=240\text{K}$ (diamonds).

6 DISCUSSIONS AND CONCLUSION

Treatment of TC1 soot by sulfuric acid (0.2 wt% of H_2SO_4) increases the original amount of SO_4^{2-} by three orders of magnitude. However, it is still much smaller than original one on AEC soot (~ 3.5 wt%). AEC soot exhibits a much higher hygroscopicity than TC1 soot modified by H_2SO_4 in the whole RH range (see Fig.1). Therefore, we conclude that the hydrophilic fraction of engine-generated soot does not require any water activation; its own original amount of sulfates is much larger than the maximal amount of H_2SO_4 which may be accumulated from the gaseous and particulate aircraft exhaust. In opposite, the hydrophobic fraction of engine soot is sensitive to surface-adsorbed acid and may be activated by the sulfur-induced processing.

Our results make it possible to clarify the key question, which had raised in observations: how soot particles could acquire a liquid soluble coating under plume conditions to act as CCN. When the plume reaches water vapor supersaturation, the most hydrophilic fraction of engine-generated soot particles will be activated firstly. If assigning all water soluble (~ 13.5 wt%) measured in AEC soot to the fraction of impurities we should report that this fraction will uptake water constituting of 18% of its mass. It is a fine prerequisite for the CCN formation on such soot particles at water supersaturations. Therefore, we may apply the classical Koehler theory to estimate the critical supersaturation, S_w , needed for CCN activation on the fraction of impurities for engine-generated soot particles. We calculated $S_w \approx 0.08\%$ for soot particles of 80 nm diameter. Such a small value of S_w is definitely reached in the plume. Therefore, we may reasonably conclude about the CCN formation on the hydrophilic fraction of engine soot particles. Since strong evidence is found by in-situ observations (Schröder et al., 1998), which showed that $\sim 1/3$ of exhaust soot particles must be involved in the contrail formation, we believe that this results from the hydrophilic fraction of impurities. After initial liquid stage in the cooled plume, ice nucleation should occur in a condensation-freezing mode.

The same process would require much higher S_w for the activation of the hydrophobic main fraction of engine-generated soot particles, which originally is assumed being not containing water soluble coverage. It may acquire near 0.2 wt% of H_2SO_4 at high FSC in the exhaust plume.

However, such a small value of H_2SO_4 is not enough for CCN activation following the Koehler theory. It is unclear whether this is enough to allow the growth of water droplets in order to overcome the Kelvin barrier. With the assumption that the main fraction of engine soot particles becomes wettable due to H_2SO_4 processing the Kelvin theory makes it possible to estimate the water supersaturations needed for the CCN formation on such particles. At 235K we find $S_w \approx 8\%$ and 3% for particles of 40 and 100 nm diameters, respectively. Hence, whether such particles participate in contrail formation depends on water supersaturations attained in the plume at given ambient conditions. Therefore, the principal role in the contrail formation belongs to the fraction of impurities which may induce the CCN formation due to original presence of water soluble organic and inorganic compounds on the soot surface.

ACKNOWLEDGMENTS

This research was funded by the grants of Council of President of Russian Federation for support of Young Russian scientist and Leading Scientific School SS-9330.2006.8 and SS-7101.2006.02. The authors thank Prof. J.Suzanne, Dr.D.Ferry and Dr. B. Demirdjian (CRMC-N/CNRS, Marseille) for long-time cooperation in this field.

REFERENCES

- Chen et al., Chen, Y.L., Kreidenweis, S.M., McInnes, L.M., Rogers, D.C., and DeMott, P.J., 1998: Single particle analyses of ice nucleating aerosols in the upper troposphere and lower stratosphere, *Geophysical Research Letters* 25, 1391-1394.
- Hendricks J., Karcher B., U.Lohmann, and M.Ponater, 2005: Do aircraft black carbon emissions affect cirrus clouds on global scale? *Geophysical Research Letters*, 32, L12814,doi:10.1029/2005GL022740.
- Gleitsmann, G. and Zellner R., 1998: A modeling study of the formation of cloud condensation nuclei in the jet regime of aircraft plumes, *Journal of Geophysical Research* 103, 19543-19555
- Kärcher, B., Peter, T., Biermann, U.M., and Schumann, U., 1996: The initial composition of jet condensation trails, *Journal of Atmospheric Science* 53, 3066-3083.
- Kärcher, B., Busen, R., Petzold, A., Schröder, F., Schumann, U., and Jensen, E.J., 1998: Physicochemistry of aircraft-generated liquid aerosols, soot, and ice particles - 2. Comparison with observations and sensitivity studies, *Journal of Geophysical Research* 103, 17129-17147.
- Kuhn, M., Petzold, A., Baumgardner, D., and Schröder, F., 1998: Particle composition of a young condensation trail and of upper tropospheric aerosol, *Geophysical Research Letters* 25, 2679-2682.
- Petzold, A., Strom, J., Ohlsson, S., and Schröder, F., 1998a: Elemental composition and morphology of ice-crystal residual particles in cirrus clouds and contrails, *Atmospheric Research* 49, 21-34.
- Popovicheva O.B., Persiantseva N.M., Shonia N.K., Zubareva N.A., Starik A.M., Secundov A.N., Usenko D.A., Zakharov V.M., Suzanne J., Ferry D., and B. Demirjian, 2003: Aircraft engine soot :characteristic properties as CCN in upper troposphere. Combustion and atmospheric pollution. Torus Press, RF, 444-449.
- Popovicheva, O.B., Persiantseva, N.M., Lukhovitskaya, E.E., Shonija, N.K., Zubareva, N.A., Demirdjian, B., Ferry, D., and Suzanne, J., 2004: Aircraft engine soot as contrail nuclei, *Geophysical Research Letters* 31, Art. No. L11104.
- Savel'ev, A.M.; Starik, A.M.; Titova, N.S., 1999: Investigation of the dynamics of formation of environmentally harmful gases in elements of gas turbine engine, *High Temperature* 37, 3, 470-478.
- Schröder, F., Kärcher, B., Petzold, A., Baumann, R., Busen, R., Hoell, C., and Schumann, U., 1998: Ultrafine aerosol particles in aircraft plumes: In situ observations, *Geophysical Research Letters* 25, 2789-2792.
- Schumann U., Arnold F., Busen R., et al. 2002: Influence of fuel sulfur on the composition of aircraft exhaust plume: The experiments sulfur 1-7, *Journal of Geophysical Research*, 107, D15, 10.1029/2001JD00813.
- Starik, A.M.; Savel'ev, A.M.; Titova, N.S.; Loukhovitskaya, E.E.; Schumann, U., 2004: Effect of aerosol precursors from gas turbine engines on the volatile sulfate aerosol and ion clusters formation in aircraft plumes, *Phys.Chem.Chem.Phys.* 6, 3426-3436.

Numerical simulation of aircraft plumes using a mesoscale code

R. Paugam^{*}, R. Paoli, D. Cariolle, B. Cuenot
CERFACS France

Keywords: contrail, mesoscale, numerical simulation

ABSTRACT: This study describes high-resolution three-dimensional simulations of an aircraft exhaust plume and represents a first step towards the simulation of a complete contrail evolution in an aircraft wake. The baseline configuration used for the simulations is an aircraft vortex pair descending in a stratified atmosphere. The numerical tool is the Météo-France meteorological code MesoNH used in its LES version. Focus is laid on the three-dimensional vortex dynamics and the effects of stratification on the development of vortex instabilities as well as on the dispersion of (passive) exhaust species in the atmosphere. Comparisons with previous works on the subject are provided. A first study of the coupling process between vortex dynamics and ice microphysics is also presented for a simple two-dimensional contrail simulation. The extension to full three-dimensional dynamics/ice microphysics coupling and its application to mesoscale simulations of contrails are finally discussed.

1 INTRODUCTION

Condensation trails (“contrails”) are the thin clouds which are commonly visible as white streaks behind aircrafts in otherwise clear sky. Due to the rapid growth of the commercial aircraft traffic, aircraft emissions became an important subject of academic research and practical interest because of their potential environmental impact as indicated in the Intergovernmental Panel on Climate Change (IPCC) Penner et al. (1999). It is known for example that for suitable atmospheric conditions, contrails trigger the formation of cirrus clouds, thus altering the radiative balance of the atmosphere. Furthermore, NO_x emissions perturb the Earth chemical cycle, resulting in the production or destruction of ozone according to the local thermodynamic conditions, while emissions of CO_2 and H_2O contribute to greenhouse effect.

This work is part of a research effort made in the Aviation & Environment Team at Cerfacs in the framework of the European project QUANTIFY (<http://www.pa.op.dlr.de/quantify>). The main objective is to develop a modelling and computational strategy that allows one to simulate the aircraft plume evolution up to some hours after the release of exhausts, and to provide parameterisations to Global Circulation Models (GCM).

Simulations of aircraft plumes have been mostly carried out in the literature using LES formulations, see e.g. Gerz et al. (1999), and Lewellen et al. (2001), and focused on one specific stage (vortex regime) of the plume evolution. The originality of our research is to simulate a complete contrail evolution since the beginning of the vortex regime to the scales of GCM (i.e. a few hours from emission time). The dynamical, microphysical and chemical processes are then solved by coupling a LES model (MesoNH-LES) for the early plume stages, with an atmospheric mesoscale model (MesoNH) for late dispersion and diffusion regimes, see Lafore et al. (1998).

A brief description of contrail physics is presented in section 2, an overview of the computational strategy is given in section 3. The MesoNH code is described in section 4. Section 5 reports the first results of the wake dynamics vortex simulations. Section 6 shows the first implementation of a dedicated microphysical scheme for aircraft plume. Conclusions are given in Section 7.

^{*} *Corresponding author:* Ronan Paugam, CERFACS 42 avenue Gaspard Coriolis 31057 TOULOUSE cedex 01 FRANCE. Email: paugam@cerfacs.fr

2 THE EVOLUTION OF AN AIRCRAFT PLUME

The evolution of an aircraft plume in the atmosphere includes several physical phenomena such as jet, vortex dynamics, and atmospheric turbulence which have different characteristic scales. This makes its modelling and simulation a challenging task in atmospheric science. According to Gerz *et al.* (1998), Lewellen *et al.* (2001), and Sussmann *et al.* (1999), the evolution of a plume can be qualitatively described in four successive regimes.

In the jet regime, the two counter rotating vortices are formed around the wing tips, while hot exhaust released from the engines are trapped around vortex cores. (Typically for a B747, the vortices are initially separated by 50 m, and the cores are about 5 m wide). This regime ends after 20 seconds when the peak absolute temperature T_{\max} gets to a minimum and the peak concentration c_{\max} of an inert gas (e.g. CO₂) attains some asymptotic steady value. During the next minute (vortex regime), the vortices move downward by mutual induction. The exhaust is then entrained by the vortices and propagates down from flight level to 150 to 250 m. As the primary wake falls down in a stratified environment, it leaves back a vertical curtain which forms a secondary wake at the flight level, Spalart(1996). A significant part of exhaust (around 30 per cent according to Gerz *et al.* (1998)) is then detrained from the primary wake, and experiences different microphysical and chemical processes. The vortex regime ends after the collapse of the two vortex, typically by a long-wave sinusoidal instability Crow(1970). The time scale of instability is mainly controlled by the atmospheric turbulence, and the vortex regime persists until 80 s. (120 s.) for calm (weak turbulent) atmosphere conditions. During this regime temperature T_{\max} increases by adiabatic heating of the exhaust in the sinking vortex, and the concentration c_{\max} remains almost constant. Actually a maximum of exhaust is still caught in the vortex cores. Note that during this phase, the formation of a visible secondary wake (ice particle formation) is controlled by the relative humidity with respect to ice RH_i of the surrounding atmosphere, see Sussmann *et al.* (1999). If RH_i < 100 %, no visible secondary wake appears, if RH_i ≥ 100 %, a gap forms between the two wakes, and finally if RH_i >> 100 %, a plume of ice particles persists. In the following dispersion regime the vortices break up and generate turbulence, which is later dissipated to background level where the dynamics is controlled by positive buoyancy acquired from hot exhaust and ambient stratification. The temperature T_{\max} and the concentration c_{\max} decrease due to mixing with the atmosphere, whereas the entrainment rate $\omega = -d/dt \ln(c_{\max})$ increases (this parameter is a measure of the plume expansion rate which is valid for both the primary and the secondary wake). Then the plume expands and mixes in the atmosphere within one or two Brunt Väsälä frequency, typically until a contrail age of 600 or 1200 s. Then the diffusion regime starts where no aircraft induced motion exists anymore, and the plume is only controlled by interaction with the atmosphere. Shear and stratification act on the plume up to a complete mixing, basically within 2 to 12 hours. For suitable conditions, the plume can reach a cross stream extension of 1 x 4 km respectively in the vertical and horizontal direction, see Dürbeck *et al.* (1996).

Hence, the evolution of a contrail is characterized by different lengths scale, from centimeter -to-meters in the jet and vortex regimes, to tens of meters in the diffusion regime. The dispersion regime is a transition phase between these two main regimes of the contrail lifetime, where dynamical scales change from wake-controlled scales to the atmospheric scales.

3 DESCRIPTION OF THE NUMERICAL CODE

The MesoNH Atmospheric Simulation System is a joint effort of Centre National de Recherches Météorologiques (Météo-France) and Laboratoire d'Aérodynamique (CNRS). The detailed scientific documentation of the code is available at <http://www.aero.obs-mip.fr/mesonh/index2.html>, see also Lafore *et al.* (1998). It is a non-hydrostatic mesoscale atmospheric model with a horizontal resolution ranging from 1 m to 1 km, allowing simultaneously up to 8 nested models to run. The basic prognostic variables are the velocity field (u,v,w) and the potential temperature θ . According to the required resolution, the code can run in real mesoscale mode where all scales of turbulence are parameterized; or in a LES mode typical of small-scale simulations meaning that the transported turbulent kinetic energy (TKE) is used to model the sub-grid scale fluxes (to that end a homogeneous resolution of less than ten meters is needed), see Cuxart *et al.* (2000).

Scalar transport is obtained via a second order centred finite difference scheme for both advection and diffusion operators, and is coupled to a chemical kinetics module to treat species chemical reactions.

A complex cloud microphysics module is also available for both warm and cold cloud, carrying up to seven water mixing ratios, according to the different physical transformations: vapor, cloud liquid water, rain water, cloud ice, snow, graupel, and hail. For example, warm liquid clouds are mainly involved in marine stratocumulus (see Sandu *et al.* (2005)) and ship track simulations. To that end, the code has its own radiative scheme although it could in principle use other external scheme as well. Furthermore, a dry aerosol module, based on a lognormal representation of size distribution, has been recently implemented in the code, Tulet *et al.* (2005).

The code MesoNH has been installed at CERFACS and validated on the Cray supercomputer for tri-dimensional test cases such as contrails and marine boundary layer simulations.

4 OVERVIEW OF A COMPLETE SIMULATION

As explained in Sec. 2, the vortex regime is of primary importance for the simulation of an aircraft plume because of the strong impact that it has on the evolution of the wake. The main dynamical processes of interest in this regime are the Crow instability and the induced secondary wake (see section 2). To the authors' knowledge, no simulations of the late dispersion and the diffusion regime have been investigated with realistic initial conditions from the vortex regime. The originality of our work is the simulation of the complete plume evolution where chemical and microphysical processes from both primary and secondary wake are solved up to the diffusion regime. To that end, an integrated simulation strategy has been developed (see the sketch in Fig. 1) to resolve all relevant dynamical and chemical scales of the aircraft plume, from the near-field wake to the mesoscales representative of grid boxes of global models (i.e. a few hundred kilometers).

Small-scale simulations using accurate high order LES code see Paoli *et al.* (2004), provide the initial wind field, the particles distributions and the aircraft-generated turbulence from the earlier jet regime. Then these fields are filtered and interpolated on a coarser mesh to start the simulations of the vortex regime. Then simulations start with MesoNH in its LES version with a resolution of 1 meter over the cross sectional plan. The resolution is then reduced and the domain enlarged accordingly. Interpolation and filtering are applied at each swap from one domain to the larger one.

The switch from the LES version of MesoNH to its "standard" mesoscale version is imposed when the resolution is coarser than tens of meters, implying that the horizontal turbulent fluxes are assumed to be homogeneous. When starting the mesoscale simulation, a stretched mesh is used in the vertical direction from the ground to the tropopause, with maximum resolution at the aircraft altitude. Such a grid should then allow one to account for radiation in a dedicated following study.

Coupling processes based on the LES version of MesoNH :

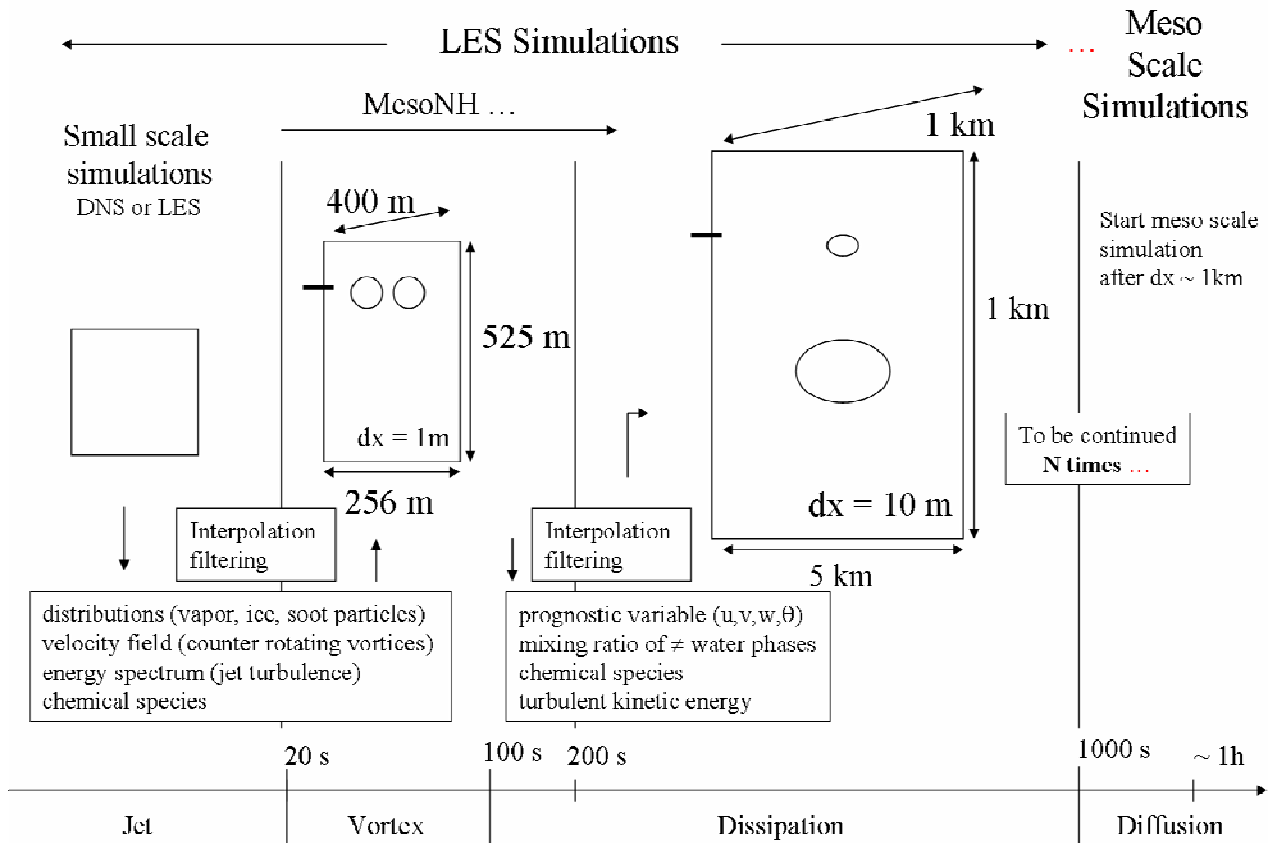


Figure 1: Sketch of the computational strategy adopted to swap from small-scale to mesoscale simulations. Note that the numerical box is advected by the aircraft velocity so that cyclic boundary conditions are applied in the axial direction.

5 THE FIRST RESULTS OF WAKE VORTEX SIMULATIONS

This section details the first step of the integrated approach presented above, i.e. the simulation of the vortex regime which corresponds to a wake lifetime of 20 s. up to 100 s. Note that in the following, the starting time of our simulations ($t=0$) corresponds to a plume age of 20 seconds. The main physical processes occurring during the vortex regime are the break up of the vortices by the Crow instability and the formation of the so called secondary wake (see section 2). In order to well resolve the break up of the vortices, the simulation is integrated over 125 s.

To validate the MesoNH code in simulation of vortex, we first used analytical initial conditions of the beginning of the vortex regime based on the work by Gerz et al. (1999). They consist of two counter rotating vortices corresponding to a B747 flying at cruise altitude (11,000 m.) in an ambient stratified atmosphere. The vortices are initially separated by $b_0 = 47$ m., the cores are 5.8 m. wide, and an initial circulation of $\Gamma_0 = 600 \text{ m}^2 \text{ s}^{-1}$. The computational domain of the simulation is $400 \times 256 \times 525$ m., in flight (x), cross (y), and vertical (z) directions, respectively (with $1 \times 1 \times 8$ m. resolution). For numerical stability of MesoNH, a time step of 25 msec. is required. A preliminary grid-independence analysis in 2D simulations shows that after a time of 50 seconds the vortices reach the same altitude for 1 m. or 2 m. resolution, and that the formation of the secondary wake is almost of the same amplitude (see left panel of Fig. 2). Though peak value of the vertical velocity exhibits a weak grid dependence (see right panel of Fig. 2), the 1 m. resolution in the cross-section has been chosen for compromise between accuracy and CPU time.

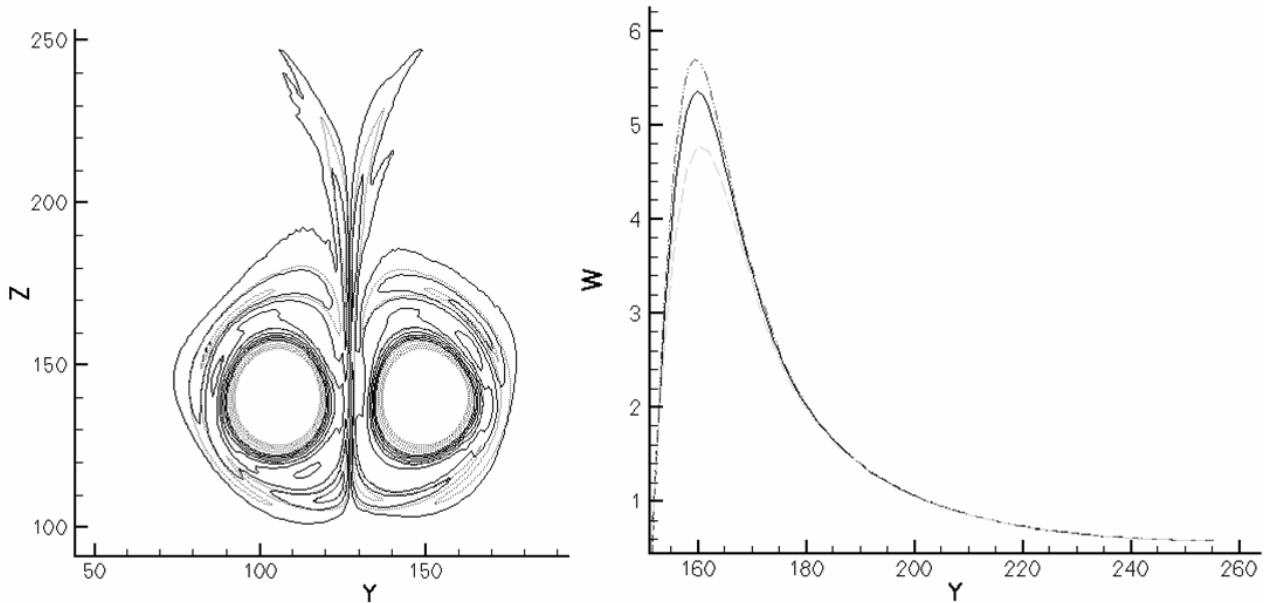


Figure 2: Left panel: Iso-contours of vorticity at time $t = 50$ s. for $dy = dz = 0.5$ (dot), and 1.0 m. (solid). Right panel: Profile of the vertical velocity at vortex location at $t = 50$ s (for simplicity, only the right vortex is shown, $y > 150$ m), for different cross-sectional resolutions: $dy = dz = 0.5$ (dot and dash), 1.0 (solid), and 2.0 m. (dash).

Three dimensional simulations were performed using a temporal approach and Taylor approximation, i.e. the computational box is supposed to be convected by the aircraft velocity ($\sim 250 \text{ m.s.}^{-1}$); periodic boundary conditions are used in the axial direction. The length of the flight direction is chosen to contain one Crow length. Cyclic boundaries are used over the cross directions and the vortices are supposed to be at sufficient distance from the boundaries to neglect the effect of their images. Furthermore they are located far enough from the bottom of the domain to break up before touching it. Top and bottom boundary conditions are free slip and rigid lid, respectively. The initial vortices are solution of the Navier-Stokes equations (see Garten et al. (1998) for the analytical expression), and the initial atmospheric conditions are typical of the upper troposphere with ambient stratification of $N=0.0108$. We assume that the atmosphere is steady, and an initial perturbation on the potential temperature field is added to force the Crow instability (see Robins et al. (1998)).

Results of the simulations are shown in Figure 3 in terms of the λ_2 criterion. The minimum of λ_2 shows the minima of the pressure field that gives an information on the structure of the flow (see Jeong et al. (1995)). The induced secondary wake and the break up of the primary vortices structure can be easily observed during the 125 seconds of the simulation. For the sake of validation of MesoNH for vortex simulation, we also compare the descent rate of the primary vortices to that obtained by Holzäpfel et al. (2001) for approximately the same stratification, $N=0.01$. Figure 4 shows the descent of the vortex for 2D and 3D simulations respectively. In the 3D simulation the descent is tracked in the cross plan where the spacing between the two counter-rotating vortices is maximum. As in Holzäpfel et al. (2001), a late acceleration is observed in the 2D simulation, although a deceleration occurs in the 3D simulation.

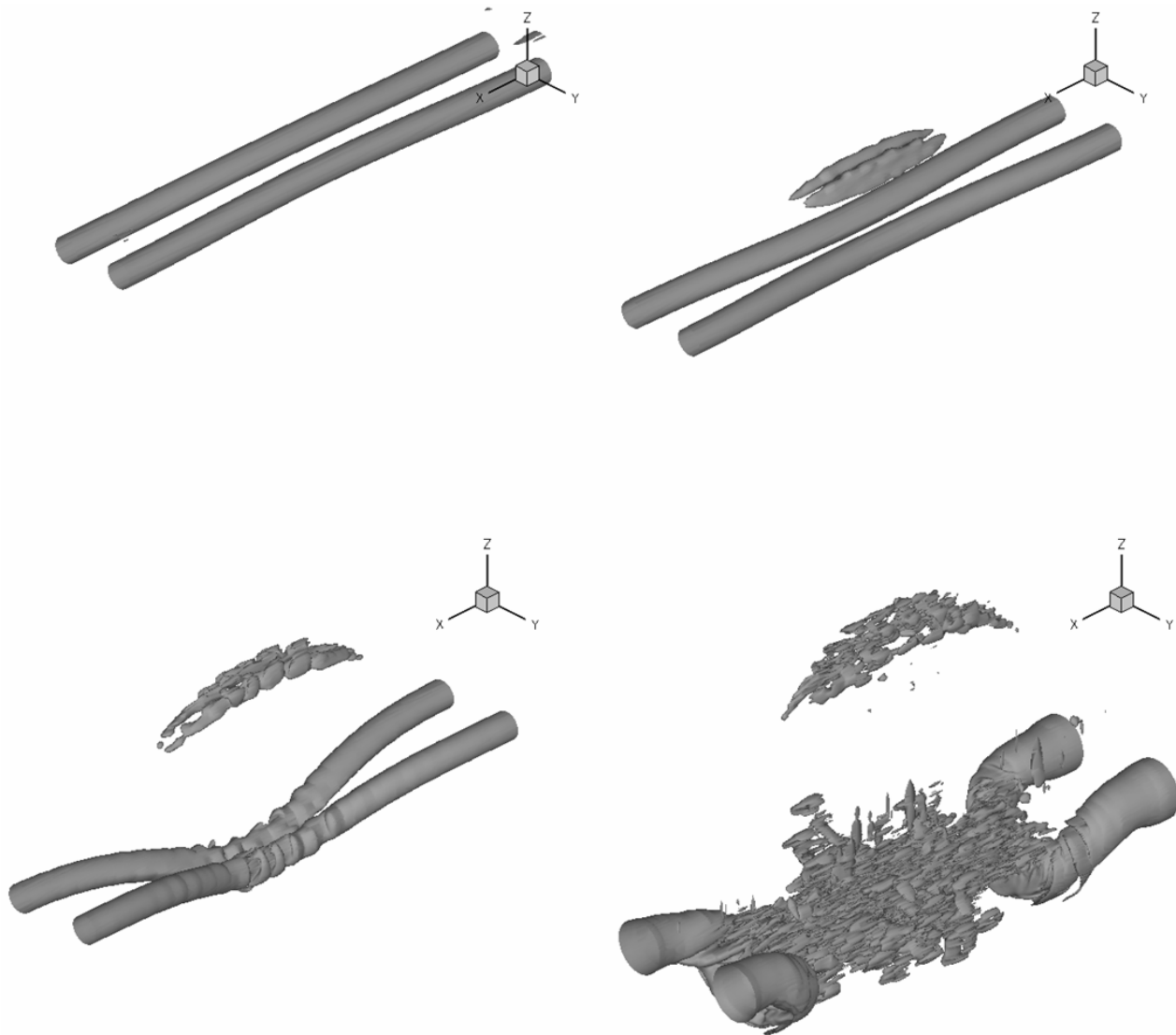


Figure 3: Perspective view of the iso-surface $\lambda_2 = -0.003$ identifying the vortex structure at $t = 0, 30, 60, 90,$ and 125 s

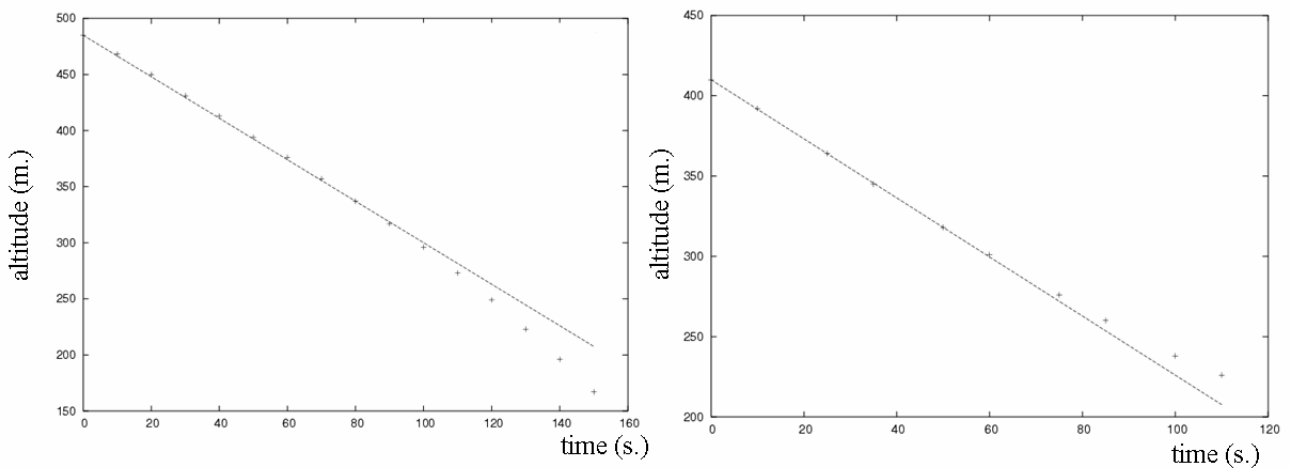


Figure 4: Plot of the vertical position of the vortices in 2D (left) and 3D (right) simulations. The points correspond to the numerical simulations, while dashed lines indicate the uniform vortex descent in a non stratified environment, i.e. with constant velocity $v = v_0 = \Gamma_0/2\pi b_0$.

6 A SIMPLE MICROPHYSICAL SCHEME

So far we have described the dynamics of the vortex evolution. This section presents the first 2D simulation of the microphysical processes obtained by integrating the simplified ice growth model by Kärcher(1996) in MesoNH. Ice crystal is the only class of particles present, and microphysics reduces to condensation / evaporation. Neither coagulation nor sedimentation is presently accounted. The condensation growth law is given by Kärcher(1996),

$$\frac{d}{dt} r = D G_{\alpha}(r) \frac{S_I}{r} \quad (1)$$

where r is the mean radius, S_I is the ice supersaturation, D stands for the molecular vapour diffusivity and $G_{\alpha}(r)$ is a model function. A bulk approach was first investigated as in Lewellen et al. (2001), where the number of particles, the ice mixing ratio and the vapor mixing ratio are transported. This yields to the following set of equations,

$$\begin{cases} \frac{d}{dt} r_I = \left[\frac{4\pi N_{particles}}{\rho_{air}} \right]^{2/3} D G(r) (r_w - r_{wSi}) \left[\frac{3 r_I}{\rho_{ice}} \right]^{1/3} \\ \frac{d}{dt} r_w = -\frac{d}{dt} r_I \\ \frac{d}{dt} N_{particles} = 0 \end{cases} \quad (2)$$

where r_I is the ice mixing ratio, r_w the vapor mixing ratio, r_{wSi} the vapor mixing ratio at ice saturation, $N_{particles}$ the number density of particles, ρ_{ice} the density of ice, and ρ_{air} the density of the dry air. The mean radius r is obtained by the definition of the ice mixing ratio,

$$r_I = \frac{4/3 \pi r^3 N_{particles} \rho_{ice}}{\rho_{air}} \quad (3)$$

The results of a 2D simulation using this microphysical scheme are shown in Figure 5 for the supersaturation field. The initial background conditions for S_I are deduced from the scenario 2 of Sussmann et al. (1999). This corresponds to a weak supersaturation at the flight level and a subsaturated air 200 meters below. Note that initially, the supersaturation is not balanced with the temperature perturbation induced by the vortices. For simplicity, tangent hyperbolic distribution of particles are inserted inside the core vortices with a maximum of number density $N_{particles}^{max} = 2.8 \text{ e}+9$ and a corresponding mean radius $r_{max} = 1. \text{e}-6 \text{ m}$. These values are extrapolated from exhaust values using a dilution factor to account for the expansion of the plume in the jet and vortex regime. Note that we assume that all the ice particles are formed during the jet regime.

From Figure 5, we observe at a $t = 12 \text{ s}$. the formation of subsaturated air at the bottom of the vortices, and their final wrapping around them at $t = 70 \text{ s}$. This is due to the adiabatic compression of the primary wake during its descent in the stratified fluid. Mean radius contour plots are shown in Figure 6. As initially the particles are trapped inside the vortices, and since the simulations are two-dimensional so that vortex instabilities cannot develop, there is no break up of the vortices and particles stay trapped inside the cores. Then the system gets to an equilibrium state where vapor reaches saturation conditions.

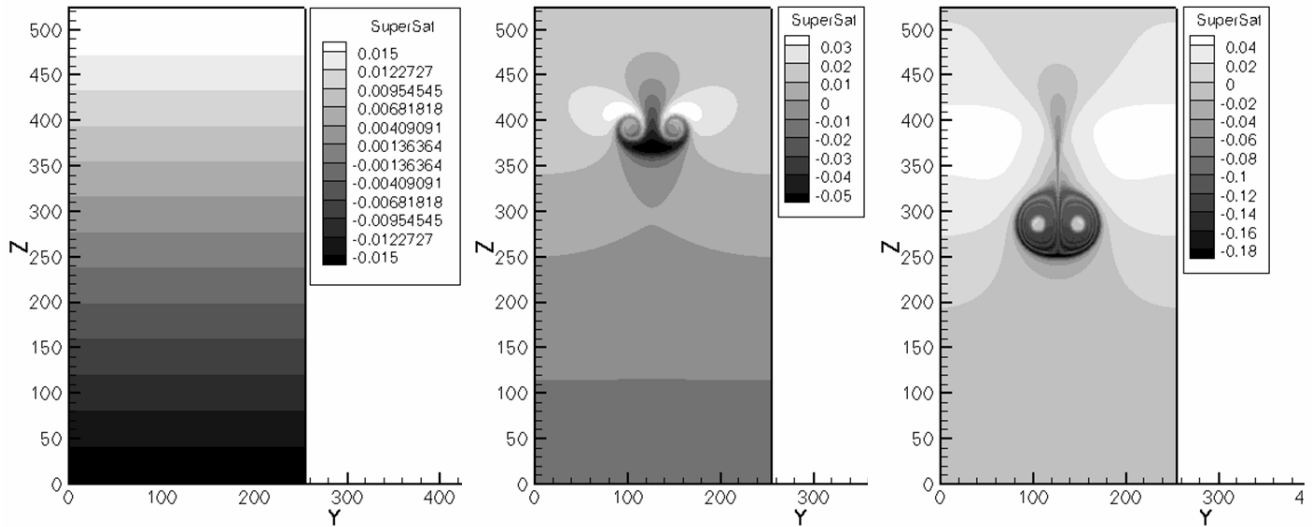


Figure 5: Plots of the supersaturation field at time $t = 0, 10, 70$ s. Note that at the first time step the vapor mixing ratio is not in equilibrium with temperature.

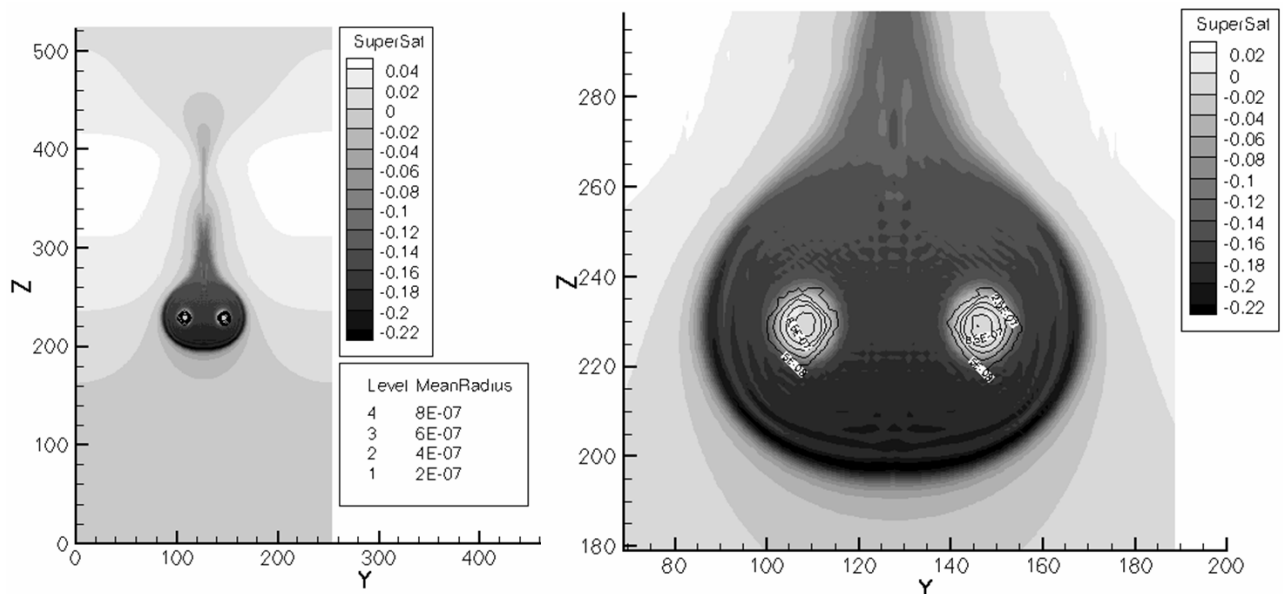


Figure 6: Plots of supersaturation field (flood contour) and mean radius (iso-contour) at $t = 100$ s. The right panel is a zoom around the two vortex cores.

7 CONCLUSION

High-resolution three-dimensional simulations of an aircraft wake were carried out using the Météo-France meteorological code MesoNH for applications to the evolution of a contrail in the far-field wake. The code was run in its LES version with a resolution of 1 meter. The dynamics of the wake vortex and the dispersion of aircraft plume were in agreement with previous studies from the literature. A microphysics model for the growth of ice crystals has been integrated in the MesoNH and validated in 2D simulations. Ongoing actions include the extension of the dynamics-microphysics coupling to three-dimensional wakes, and the simulations of the dispersion and diffusion regimes on larger computational domains.

ACKNOWLEDGEMENTS

This work was supported by the European Union Integrated Project QUANTIFY (<http://www.pa.op.dlr.de/quantify>).

REFERENCES

- Crow, S. C., 1970: Stability Theory for a Pair of Trailing Vortices. *AIAA Journal*, Vol. 8 no. 12, 2172-2179
- Cuxart, J., P. Bougeault, and J.-L. Redelsperger, 2000: A turbulence scheme for mesoscale and large-eddy simulations. *Q.J.R. Meteorol. Soc.*, Vol. 126, pp. 1-30
- Dürbeck, T. and T. Gerz, 1996: Dispersion of aircraft exhaust in the free atmosphere. *J. Geophys. Res.* Vol. 101 no. D20, pp. 26,007-26,015
- Garten, J.F., S. Arendt, D. C. Fritts, and J. Werne, 1998: Direct numerical simulations of the Crow instability and subsequent vortex reconnection in a stratified fluid. *J. Fluid Mech.* Vol. 361, pp. 189-236
- Gerz, T., T. Dürbeck, and P. Konopka, 1998: Transport and effective diffusion of aircraft emission. *J. Geophys. Res.* Vol. 103 no. D20, pp. 25,905-25,913
- Gerz, T., and F. Hozapfel, 1999: Wing Tip Vortices, Turbulence, and the Distribution of Emissions. *AIAA Journal* vol. 37, pp. 1270-1276
- Holzäpfel, T., T. Gerz, and R. Baumann, 2001: The turbulent decay of vortex pairs in stably stratified environment. *Aerosp. Sci. Technol.* Vol. 5, pp. 95-108
- Jeong, J., and F. Hussain, 1995: On the identification of a vortex. *J. Fluid Mech.* Vol. 285, pp. 69-94
- Kärcher, B., 1996: The initial Composition of the Jet Condensation Trails. *J. Atmos. Sci.* Vol. 53, pp. 3066-3082
- Lafore, J.-P., J. Stein, N. Asencio, P. Bougeault, V. Ducrocq, J. Duron, C. Fischer, P. Hérel, P. Mascart, V. Masson, J.-P. Pinty, J.-L. Redelsperger, E. Richard, and J. Vilà-Guerau de Arellano, 1998. The MesoNH Atmospheric Simulation System. Part I: adiabatic formulation and control simulations. *Scientific objectives and experimental design*, *Ann. Geophys.* Vol. 16, 90-109
- Lewellen, D.C., and W.S. Lewellen, 2001: The Effect of Aircraft Wake Dynamics on Contrails Development. *J. Atmos. Sci.* Vol. 58, pp. 390-406
- Paoli, R., J. Hélie and T. Poinso, 2004: Contrails formation in aircraft wake. *J. Fluid Mech.* Vol. 502, pp. 361-373
- Penner J. E., 1999: *Aviation and the Global Atmosphere*, Cambridge University Press.
- Robins, R. E., and D. P. Delisi, 1998: Numerical Simulation of Three-Dimensional Trailing Vortex Evolution in Stratified Fluid. *AIAA Journal* Vol. 36, pp. 981-985
- Sandu, I, P. Tulet, and J.-L. Bringuier, 2005: Parametrisation of the Cloud Droplet Single Albedo Based on Aerosol Chemical Composition for LES modelling of boundary layer clouds. *Geophys. Res. Lett.* Vol. 32, L19814
- Spalart, P. R., 1996: On the motion of laminar wing wakes in a stratified fluid. *J. Fluid Mech.* Vol. 327, pp. 139-160
- Sussmann, R., and K. Gierens, 1999: Lidar and numerical studies on the different evolution of vortex pair and secondary wake in a young contrails. *J. Geophys. Res.* Vol. 104, no D2, pp. 2131-2142
- Tulet, P., V. Crassier, F. Cousin, K. Suhre, and R. Rosset, 2005 : ORILAM, a three-moment lognormal aerosol scheme for mesoscale atmospheric model : Online coupling into the MesoNH-C model and validation on the Escompte campaign. *J Geophys. Res.* Vol. 110, D18201

Gas Turbine (Turbo Fan Engine) and IC Engine Emissions

H.-J. Bauer*

Institut fuer Thermische Stroemungsmaschinen, Universitaet Karlsruhe (TH), Germany

U. Spicher

Institut fuer Kolbenmaschinen, Universitaet Karlsruhe (TH), Germany

Keywords: Gas Turbine, Turbofan, IC Engine, Emissions

ABSTRACT: Turbofan engines dominate civil aviation. The need for high efficiency and low weight has led to a continuous increase in their overall pressure ratio and turbine inlet temperature. Combustion at high pressures and near stoichiometric conditions promotes the formation of nitrogen oxide. Several principles for NO_x abatement have been developed and gone into service like RQL and DAC combustors or are under investigation such as LDI or LPP technology. The major challenge is to reduce NO_x emissions without jeopardizing safe operability of the propulsion system or increasing other pollutants like CO, UHC or smoke. NO_x emissions from IC engines have a major impact on local airport air quality. Primary measures influencing the combustion process as well as exhaust gas treatment has led to a substantial reduction of pollutant emissions of Diesel and SI engines. Recent developments like direct injection engines and upcoming technologies such as HCCI engines aiming at improved fuel efficiency offer both challenges as well as opportunities to further tackle engine emissions.

1 INTRODUCTION

Whereas the majority of the presentations given at the TAC conference concentrated on the properties of pollutant emissions and their effects on the environment this paper intends to summarise the mechanisms that are related to pollutant formation in aircraft propulsion systems and, briefly, in internal combustion (IC) engines.

2 TURBOFAN ENGINES

Based on gas turbine technology (Saravanamuttoo, 2001) turbofan and, to a lesser degree, turbo-prop engines have become the single propulsion systems for civil aviation. This is due to their high economy combined with exceptional reliability and comfort and the capability to transport people and cargo at high speeds close to the speed of sound across long distances. However, they also affect the environment by emitting noise and pollutant emissions such as nitric oxides (mainly NO and NO₂ referred to as NO_x), carbon monoxide (CO), unburnt hydrocarbons (UHC) or soot. Huge efforts have been undertaken at industry and academia to reduce the environmental impact of jet engines. These efforts will have to be even intensified in the future in order to achieve the ambitious targets as set e.g. by ACARE in its vision 2020 (N.N., 2001). Particularly NO_x has turned out to be extremely difficult to be addressed appropriately due to its interdependence with the measures to improve overall engine efficiency as will be discussed in the following.

2.1 *Combustor Requirements*

Turbofan engine combustors need to comply with many requirements besides the demand for low emissions and within emissions NO_x is not the only species which needs to be considered. But in order to assess potential technologies to achieve the envisaged NO_x reduction targets, all the other requirements need to be taken into account in an appropriate manner as well. Amongst others these

* *Corresponding author:* Hans-Joerg Bauer, Institut fuer Thermische Stroemungsmaschinen, Universitaet Karlsruhe (TH), Kaiserstr. 12, D-76128 Karlsruhe, Germany. Email: hans-joerg.bauer@its.uni-karlsruhe.de

requirements comprise safe operability (Ground and altitude ignition and pull away capability, weak extinction capability - particularly during slam deceleration of the engine at inclement weather conditions - as well as the suppression of any significant thermo-acoustic pressure oscillation), compatibility (with the engine cycle in terms of pressure, temperature, overall air-fuel ratio and capacity, with the mechanical and aerothermal compressor and turbine interfaces, with the employed fuel and with the weight and size requirement of the engine), economy (development and unit costs, fuel consumption in terms of pressure loss and combustion efficiency, maintainability and reparability and life) and emissions (besides NO_x : CO, UHC, Smoke and even H_2O and CO_2). From all requirements safe operability has the highest priority!

2.2 Gas Turbine Combustion – Joule-Brayton Cycle

Turbofan Engines work according to the thermodynamic Joule-Brayton cycle (Saravanamuttoo, 2001), i.e. air is compressed in a compressor. Heat is added to the compressed air by means of continuously burning fuel at constant pressure. The hot gases are then expanded in a turbine, which drives the compressor. Due to the divergence of the isobars in the enthalpy entropy diagram more work can be gained in the expansion process of the hot gases than is needed for the compression of the air. Hence a stationary gas turbine expands the hot gases in the turbine to ambient pressure and uses the excess work to drive an electric generator.

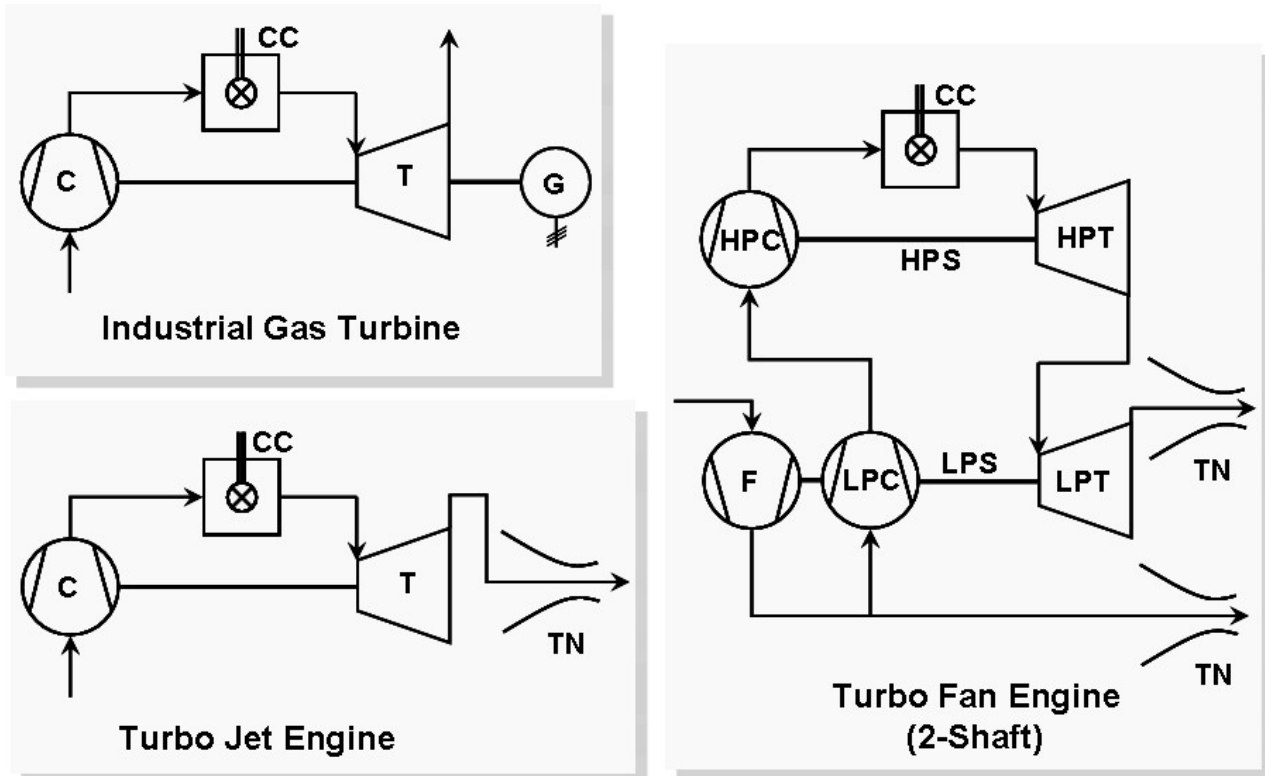


Figure 1: Gas Turbine and jet Engine Set-Up

The Turbo Jet Engine, which was the first jet engine used for aircraft propulsion expands the hot gases in the turbine to drive the compressor only. The remnant enthalpy is then used to expand and accelerate the hot gases in a nozzle and generate a thrust force according to the momentum principle. As will be shown later this is not the most efficient way to generate thrust. Therefore, modern Turbofan Engines as depicted in Figure 2 use the energy gained in the expansion process to drive a so-called fan and split the air afterwards into a bypass flow, which amounts to up to 80 % of the overall air mass flow and beyond and a core mass flow (Rolls-Royce, 2005). The fan is driven by a low pressure turbine through a separate shaft, which also drives an optional low pressure compressor. Bypass air and the hot gases are expanded either in separate thrust nozzles as indicated in Figure 1 or are mixed in a forced mixer as shown in Figure 2 and then jointly enter a common thrust nozzle.

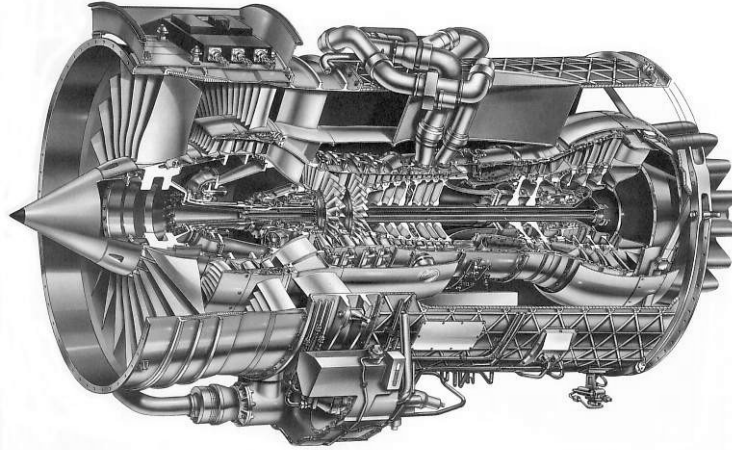


Figure 2: Modern Turbofan Engine (Rolls-Royce BR715)

In contrast to IC engines the processes of air intake, compression, combustion and expansion are continuous and non-intermittent. This is of particular importance for the combustion process, which is conducted at constant pressure, whereas IC engines, especially SI engines, feature to a certain degree constant volume combustion, which leads to an additional internal compression. Modern Turbofan Engines typically have annular combustors as depicted in Figure 3. Air from the last compressor stages is first decelerated in a diffuser in order to minimise aerodynamic losses. The air enters the annular combustor liner where the combustion process takes place through several orifices. Liquid fuel is injected by means of a number of fuel injectors. In modern combustors a part of the combustion air is used to atomise the fuel into a spray with very fine droplets and simultaneously generate a combustible mixture of fuel and air. Additionally the air which is used for atomisation has a high swirl in order to generate a flow recirculation, which is needed to permanently stabilise combustion. The igniter is only needed to start up the combustion process once. The purpose of the primary zone is to stabilise the combustion process over the entire range of operation from idle to take-off. Similar to a Diesel Engine the power of a Turbofan Engine is controlled by the amount of fuel injected into the combustor. Hence the leanest overall fuel air ratio determines the fraction of air which is allowed to enter the primary zone, through the air assisted fuel injector and the primary air injection ports at the outer and inner barrel of the combustor liner. The majority of the remaining air is then added through subsequent rows of holes in the liner into the secondary/mixing zone. This part of the combustor is needed in order to achieve a complete conversion of the combustion products exiting the primary zone and to tailor a radial temperature profile suited for the first turbine stage. It is obvious that the temperature in the primary zone is much hotter than the required turbine inlet temperature. This is of particular importance for the formation of NO_x as will be discussed later on. A considerable amount of the air is needed to cool the liner material.

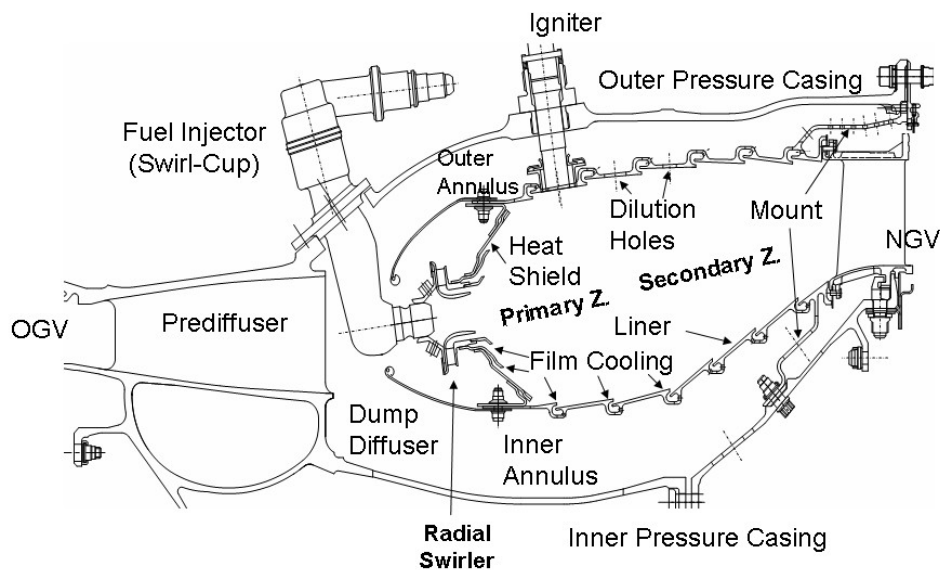


Figure 3: Annular Combustor (General Electric CF6-80)

In the ideal Joule-Brayton Cycle, compression and expansion are isentropic processes. In real engines polytropic compression and expansion is encountered and additional losses, e.g. a loss in total pressure during combustion, have to be accounted for as well. For the ideal process the thermal efficiency, i.e. the net power output related to the added heat, is solely depending on the overall pressure ratio (OPR) according to

$$\eta_i = 1 - \frac{1}{\left(\frac{p_2}{p_1}\right)^{\frac{\kappa-1}{\kappa}}} \tag{1}$$

where p_1 and p_2 are the pressures prior to and after compression, respectively, and κ is the isentropic coefficient. In real engines thermal efficiency increases for a given pressure ratio with increasing turbine inlet temperature T_3 and there is an optimal pressure ratio for a given turbine entry temperature, as indicated in Figure 4. The strong impact of the pressure ratio on thermal efficiency has led to a continuous rise in overall pressure ratio over the last decades, see Figure 5.

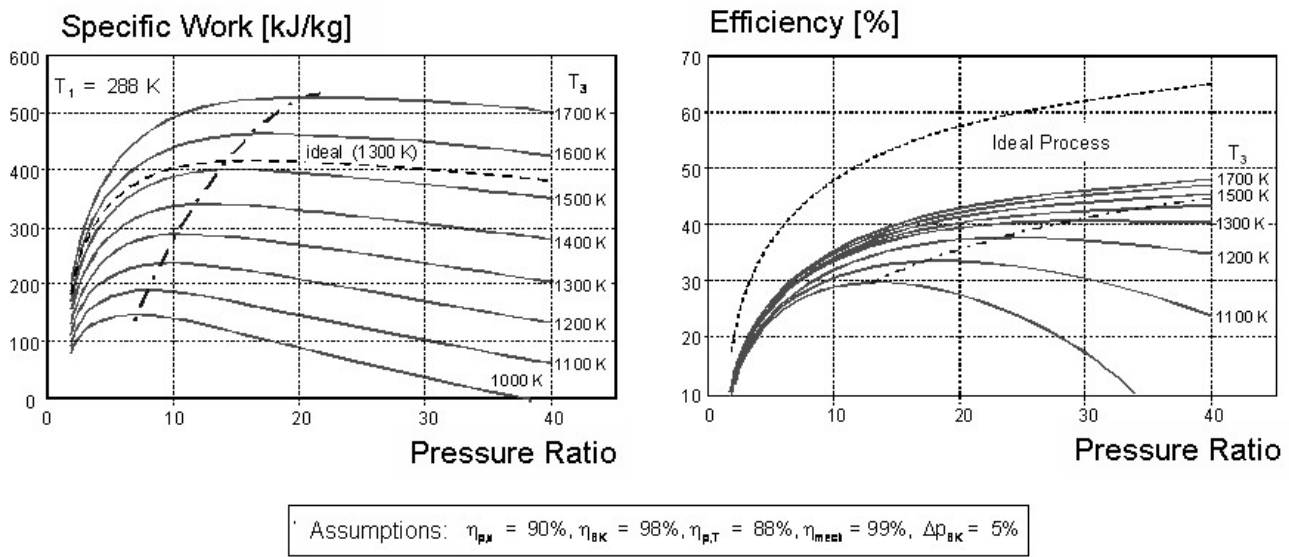


Figure 4: Specific Work and Thermal Efficiency of the Joule-Brayton Cycle

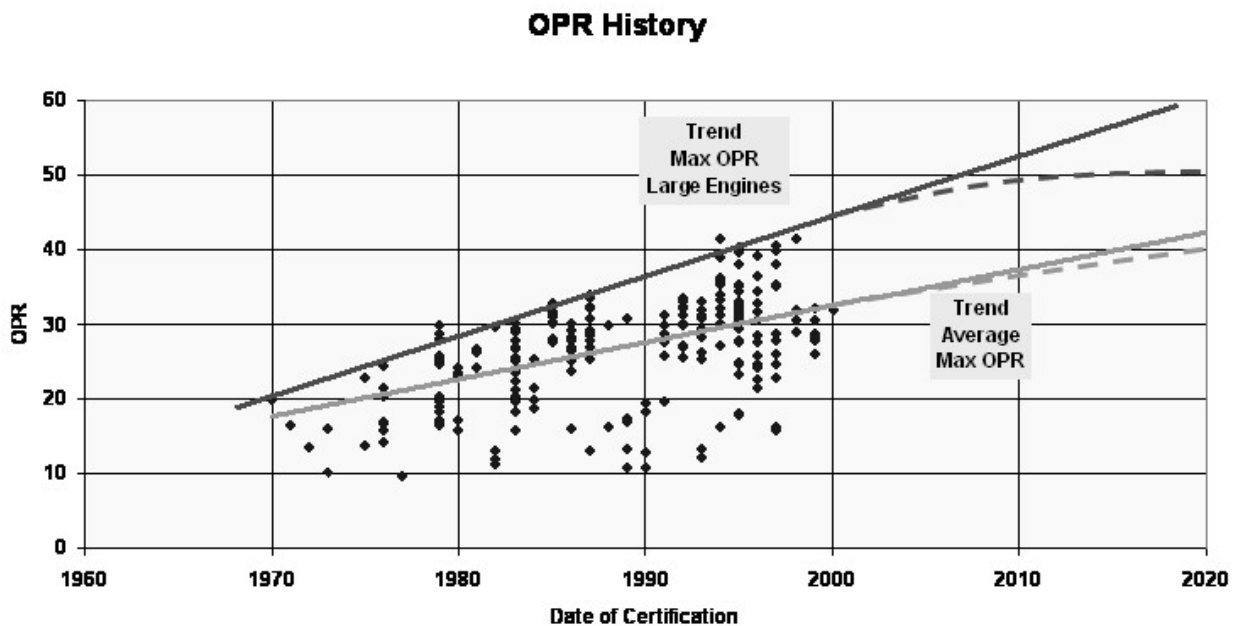


Figure 5: Past, Current and Future OPRs

It is obvious that the thrust to weight ratio is another important property of a propulsion system. This ratio is directly linked with the specific work, i.e. net power output divided by the air mass flow through the core engine. As depicted in Figure 4 the specific work strongly increases with the turbine inlet temperature. Another driver for increasing turbine inlet temperature, at least for certain flight conditions, is the so called propulsive efficiency, which determines how much of the power generated by the gas turbine process is actually used to propel the aircraft. If we consider the thrust of an engine F_t , which can be derived from a momentum balance under the assumption that the fuel mass flow is much smaller than the air mass flow \dot{m}_a

$$F_t \approx \dot{m}_a \cdot (w_a - w_f) \quad (2)$$

with w_a and w_f being the velocity of the hot gases leaving the thrust nozzle and the flight velocity, respectively, it is evident that the thrust can either be generated by slightly accelerating a huge amount of air passing through the engine or by strongly accelerating a smaller air mass flow rate. However, the propulsive efficiency plotted in Figure 6 suggests that the jet velocity should not exceed the flight velocity too much in order to avoid an efficiency penalty. The reduction of the jet velocity has been accomplished by introducing the Turbofan Engine, compare Figure 1 and Figure 2, featuring a core and a bypass air mass flow.

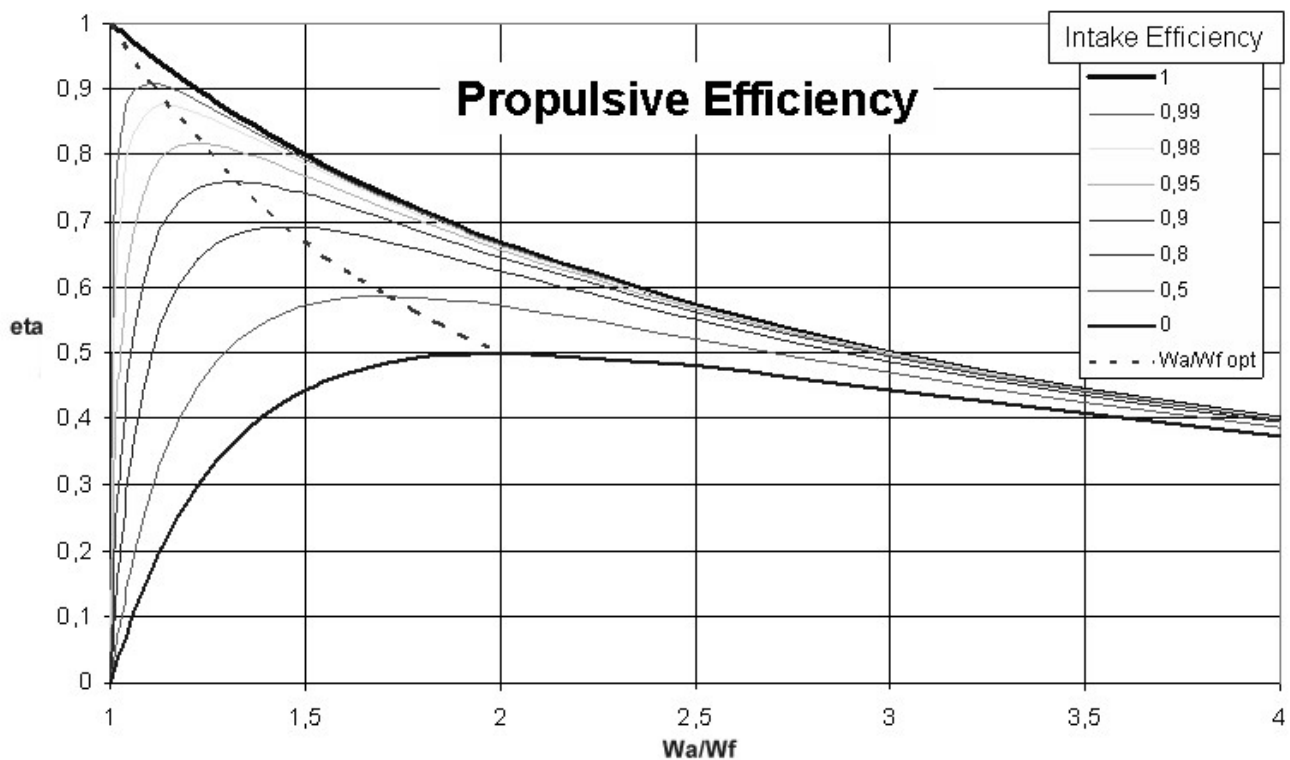


Figure 6: Propulsive Efficiency of a Jet Engine

2.3 Pollutant Formation

Besides CO_2 , H_2O and heat, which are the main products resulting from the combustion of fossil fuel pollutants are generated. Unburned hydrocarbons and CO are emitted during low power operation at low combustor inlet temperatures and pressures. They are directly linked with the combustion efficiency. Lefebvre (Greenhough and Lefebvre, 1957) introduced a loading parameter that characterises combustion in-efficiency and therefore CO and UHC emissions, Figure 7. The loading parameter is proportional to a global Damkoehler number, which relates the residence time in the combustor to the time required for complete chemical reaction. High Loading parameters can be achieved by high pressures and inlet temperatures and/or high combustor volumes.

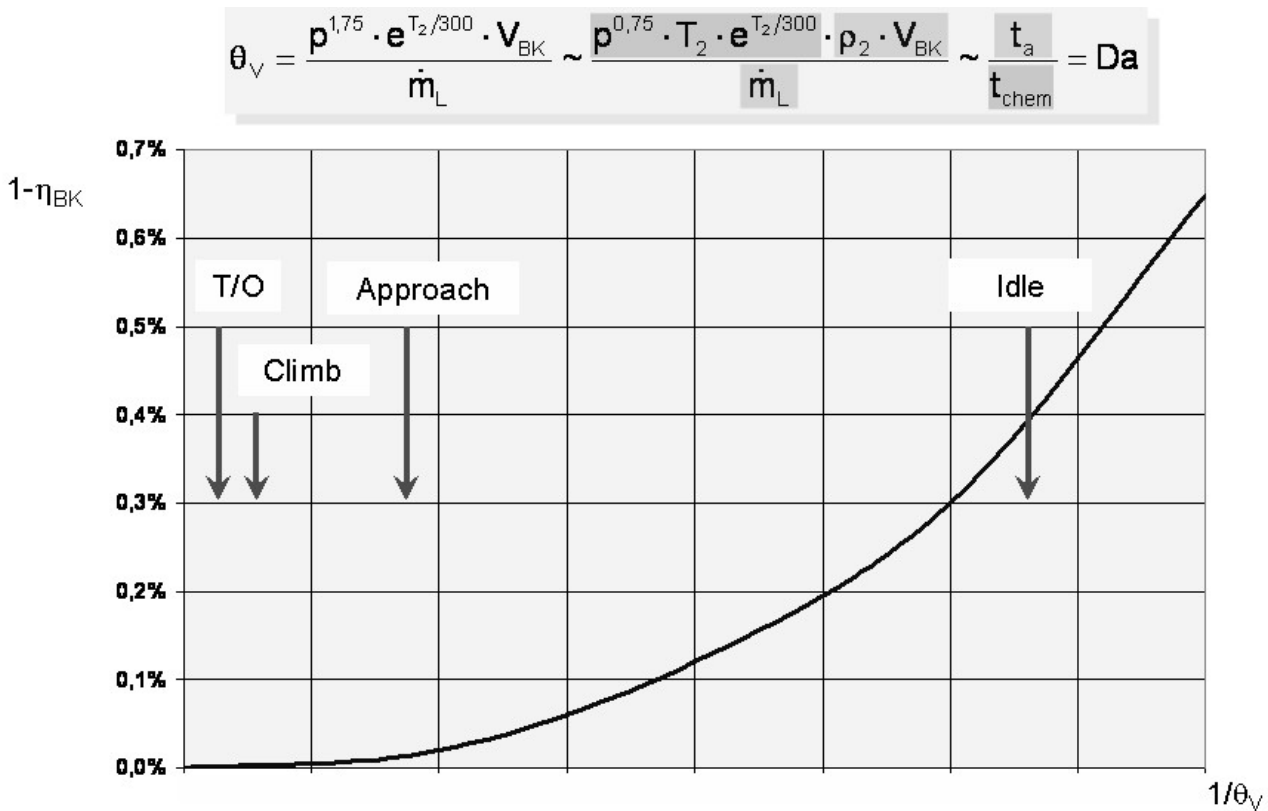


Figure 7: Combustion Efficiency (CO, UHC)

For modern Turbofan Engine combustors CO and UHC emissions are no concern as they have significantly decreased as compared to former engine generations. This is partly due to the effect that the overall pressure ratio has continuously increased in order to achieve higher thermal efficiencies, compare Figure 5. This led to an increase of combustor pressure and inlet temperature also for low power conditions. However, a substantial contribution is owed to an improvement of the fuel preparation process by the replacement of pressure atomisers with air blast atomisers. This is an additional effect that cannot be correlated with the loading parameter, which considers only chemical kinetics.

Soot and NO_x are pollutants which are mainly emitted at high power conditions. Soot is formed at elevated temperatures and very rich stoichiometry (Kellerer et al., 1995) existing in the primary zone close to the fuel injector. The majority of the soot is oxidised in the secondary zone of the combustor at lean conditions and high temperatures. However, a part of the soot generated leaves the combustor having been not fully oxidised particularly in very lean areas where the oxidation reactions have been quenched due to low temperatures. The introduction of airblast atomisers also had a tremendous effect on the reduction of soot emissions.

However, NO_x is the species which has not been significantly reduced until the last one and a half decades, where significant efforts have started to tackle this issue. The challenges of NO_x reductions will mark the focus of this publication.

Turbofan engine emissions are characterised according to the ICAO Landing and Take-Off Cycle (LTO) which directly accounts mainly for the local effect in the airport environment. Four typical thrust settings are considered corresponding to approach (30%), taxi (7%), take-off (100%) and climb (85%). Engine emissions are measured for these load conditions on static test beds, weighted with the respective times and normalised with their take-off thrust F_∞ in order to be able to compare engines of different size. The resulting engine emissions in terms of Dp/ F_∞ have to comply with legislative limits as defined by the International Civil Aviation Organisation (ICAO) (N.N. 1993). In some engine NO_x emission data are plotted versus their overall pressure ratio at take-off and compared with the respective ICAO CAEP (Civil Aviation Environmental Protection) limits.

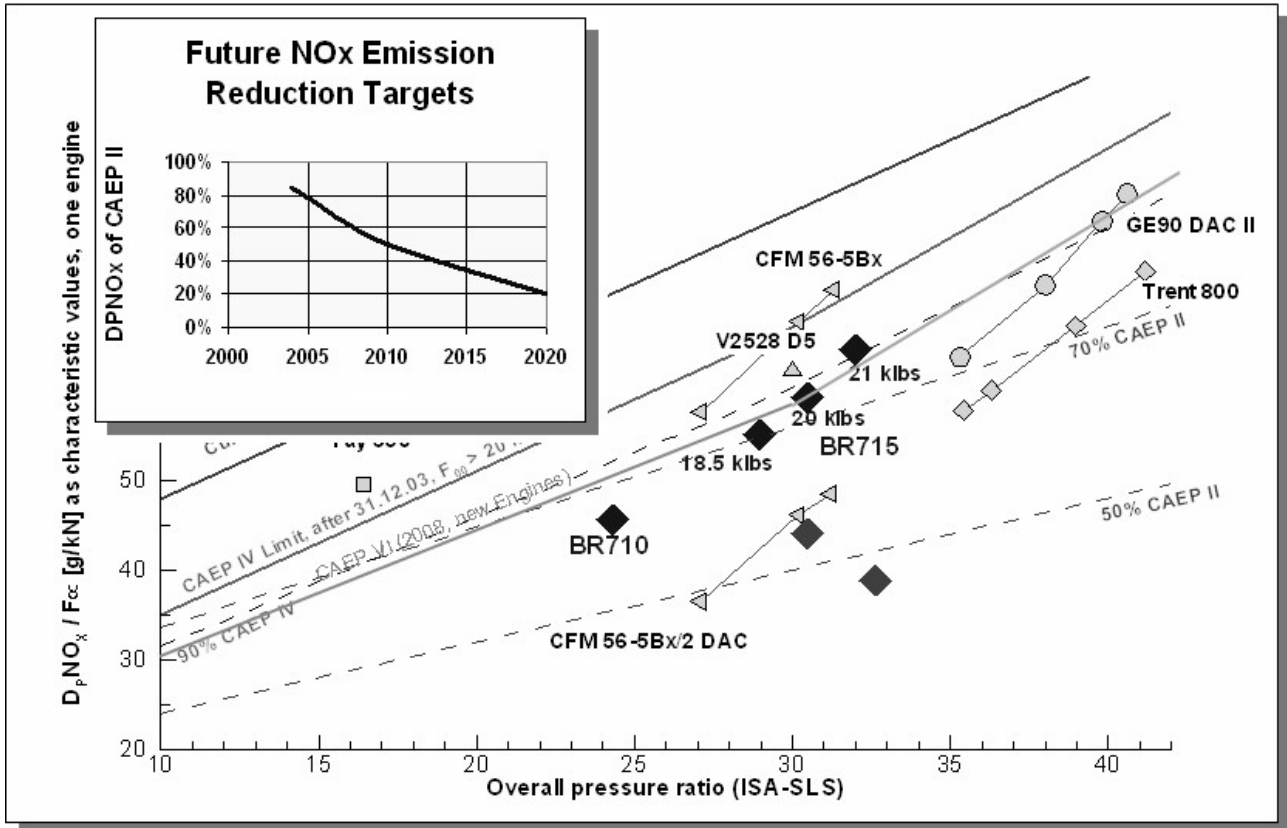


Figure 8: Current and Future NOx Emissions Requirements

NO_x is the only regulated species for which the limits account for the dependence of its formation rates on the overall pressure ratio (OPR) of the engine cycle. In Jet Engine combustors NO is mainly formed by the thermal mechanism as found by Zeldovich (1946) and extended by Baulch et al. (1991):



and then partly further oxidized to NO₂. The mechanism is called “thermal” because of the high activation energy required to break the triple bond of the Nitrogen molecule.

With first order accuracy the processes leading to NO formation in jet engine combustors as well as possible remedies can be investigated by means of a perfectly stirred reactor (PSR) calculation using a complex chemical mechanism for Iso-Octane (Behrendt, 1989) which also includes the NO formation reactions (3) as depicted in Figure 9. In this calculation the stoichiometry and pressure are varied at a fixed air inlet temperature and residence time.

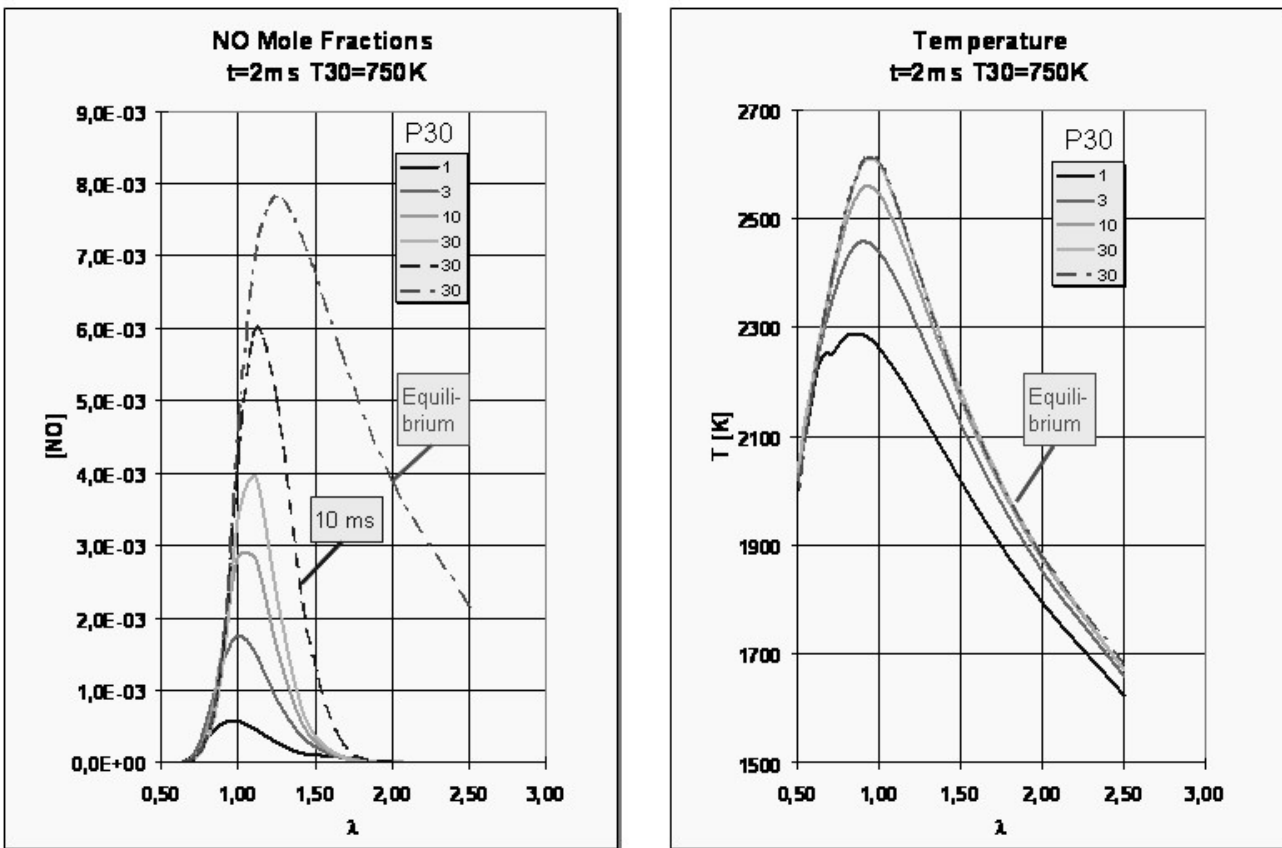


Figure 9: PSR Calculation: NO Formation and Possible Remedies

As expected the highest temperatures are encountered at conditions close to stoichiometric values, i.e. $\lambda=1$, with λ being the normalised air fuel ratio (AFR) or the inverse equivalence ratio ϕ . With an increase in pressure the maximum temperature increases as well due to the suppression of endothermic dissociation reactions. For a pressure of 30 bars the primary combustion reactions determining the flame temperatures, being almost identical with the equilibrium values, are very fast. Due to the exponential dependence of the NO formation rate on temperature the pressure dependence of the amount of NO formed in the PSR is even more pronounced. It needs to be considered, that in gas turbines the combustor inlet temperature is linked with the overall pressure ratio through the polytropic nature of the compression process. Hence an increase in combustor pressure will additionally increase the combustor inlet temperature and lead to an even stronger increase in NO formation than obvious in this consideration.

Projecting the development of the past into the future it is very likely that the pressure ratios will continue to rise, maybe with reduced rates than so far. Hence any future reduction in NO_x emission by x % relative to the CAEP II limit will result in a lower reduction in absolute numbers due to the slope of the limit and the tendency towards higher OPRs.

On the positive side it can be observed that NO formation is a significantly slower process than the mere combustion reactions. Even for an increased residence time of 10 ms the NO values are significantly lower than equilibrium at high pressures. Additionally NO formation is low at very rich and very lean conditions. Possible remedies are therefore to i) reduce the residence time in the combustor ii) stabilise combustion at very rich conditions and then switch to lean conditions by quickly adding a substantial amount of mixing air (RQL = Rich burn – Quick quench – Lean burn) or iii) burn the fuel at lean conditions. These possibilities will be briefly discussed in the following.

2.4 Low NO_x Concepts

2.4.1 Rich Concepts

Present aeroengine single annular combustors have achieved NO_x reductions relative to earlier designs operating at the same thermodynamic parameters (P, T, AFR) using the RQL principle. Besides their characteristic to produce lower amounts of Nitrogen oxides than former combustor generations, their generally rich primary zone has the advantage that combustion is very stable, even at

low power conditions when the overall stoichiometry of the combustor is much leaner. Theoretical and experimental investigations have revealed that a primary zone equivalence ratio of 1.4 results in the lowest NO emissions (Meisl et al., 1995). The highest temperatures and NO formation rates, respectively, appear in the quench zone during the transition from rich to lean mixtures. High temperatures can also be observed in the primary zone in the vicinity of the liner film cooling.

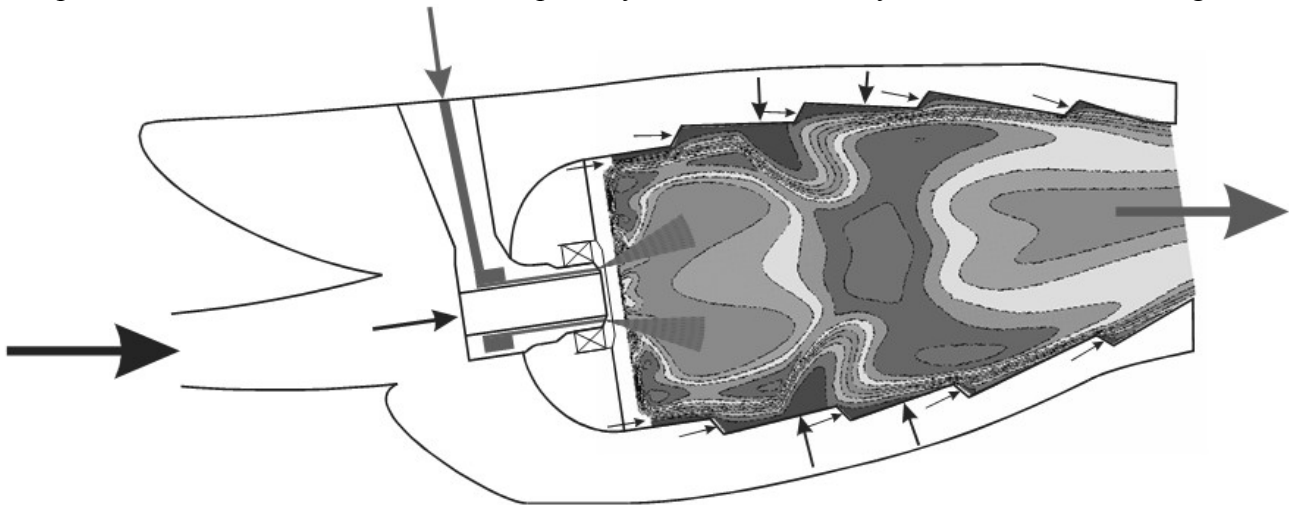


Figure 10: RQL combustor

What is mostly limiting the NO reduction potential of RQL combustors is the NO_x -smoke trade-off, which has to be encountered. Although the airblast atomisers employed in modern combustors generate a much more homogeneous fuel air mixture than the former pressure swirl atomisers there are still comparatively rich zones in the vicinity of the injector. Rich equivalence ratios in conjunction with elevated pressures and fairly high temperatures support the formation of soot, (Kellerer et al., 1995). This mechanism limits the primary zone stoichiometry to the rich side. On the other hand the rapid quenching of the NO formation by a quick transition from the rich to lean condition simultaneously tends to quench the soot oxidation reactions. Therefore, the optimisation of an RQL combustor needs careful consideration of both NO and smoke and the thermodynamic cycle of the engine and the OAFR at T/O have to be taken into account as well.

In summary the RQL concept has proven very successful for Turbofan Engine combustor applications so far. For the highest thrust range thoroughly optimised RQL combustors could even achieve lower NO emission levels in the ICAO LTO cycle than fuel staged combustor concepts, which will be discussed below. By optimisation of the primary zone and quench zone further NO_x reduction should be feasible. No detrimental effect on the emissions of other species, weight and operability are expected nor for smoke, provided that enough homogenisation can be achieved. However, the potential of RQL combustors to further decrease NO emissions to the ACARE targets set for 2020 seems to be rather limited.

Whereas RQL combustors are often called air staged combustors fuel staging aims at a different principle. This approach satisfies the demand for low emissions and appropriate operability by means of the introduction of two separate burning zones. The so called “Pilot stage” is designed for operability, i.e. light-up, altitude relight and pull-away, weak extinction stability, good combustion efficiency at low power settings and hence low emissions of carbon monoxide and unburned hydrocarbons. The “Main Stage” is purely optimised for low NO_x emissions. Low NO formation is achieved by reduced residence times and frequently by an overall lean stoichiometry of this zone.

All major aeroengine manufacturers have been investigating staged combustor concepts or are still doing so with two engine families in service using staged combustor architecture. The concepts comprise radially staged architectures, dubbed double annular combustors (DAC) (Bahr and Gleason, 1975), axially staged concepts (Sturgess et al., 1993) or mixtures thereof. Staged combustion has clearly demonstrated a significant reduction in NO emissions whilst maintaining the level of CO and HC emissions of RQL combustors (Brehm et al., 1999). However, it needs to be mentioned that the distinct but limited NO_x reduction achieved has to be traded with higher costs, higher weight and increased complexity of the combustor and of the fuel and control system. Additionally the liner wall surface area, which needs to be cooled is much larger than for a conventional single

annular combustor and requires more cooling effort and/or the use of more expensive materials. It is therefore unlikely that this concept will be further pursued.

2.4.2 Lean Concepts

Reducing the combustion temperature can also be achieved by burning the fuel at overall lean conditions. Lean Direct Injection (LDI) is working according to this principle. Depending on the engine cycle at least 60% of the air needs to be directed through the injection system, see Figure 11. In order to avoid autoignition and flashback no/minor fuel/air mixing or fuel prevaporisation external to the combustor takes place. The challenge to achieve low combustion temperatures and hence low NO formation lies in the generation of a homogeneous lean mixture within the combustor but prior to combustion. Experimental investigations in model combustors working under engine like conditions have shown that low NOx values can be achieved, Figure 12 (Bauer, 2004). However, the leaner conditions for part load, idle and particularly transient engine operation require measures to establish stable combustion and limit the emissions of CO and UHC. Pilot diffusion flames and staging of the LDI injection systems are suited remedies.

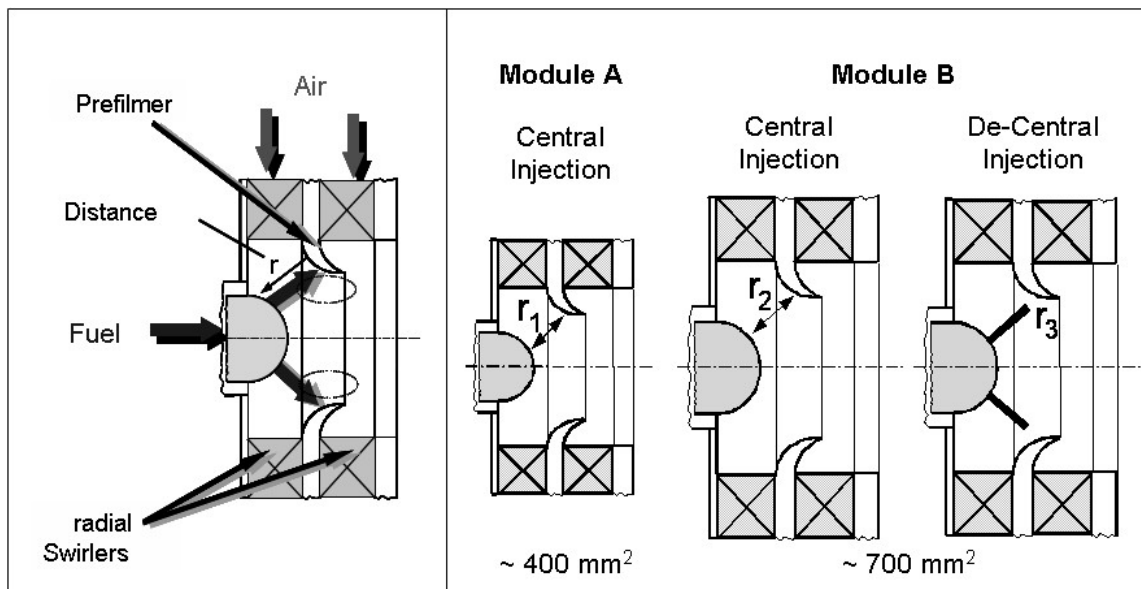


Figure 11: LDI Injectors Featuring Radial Air Swirlers

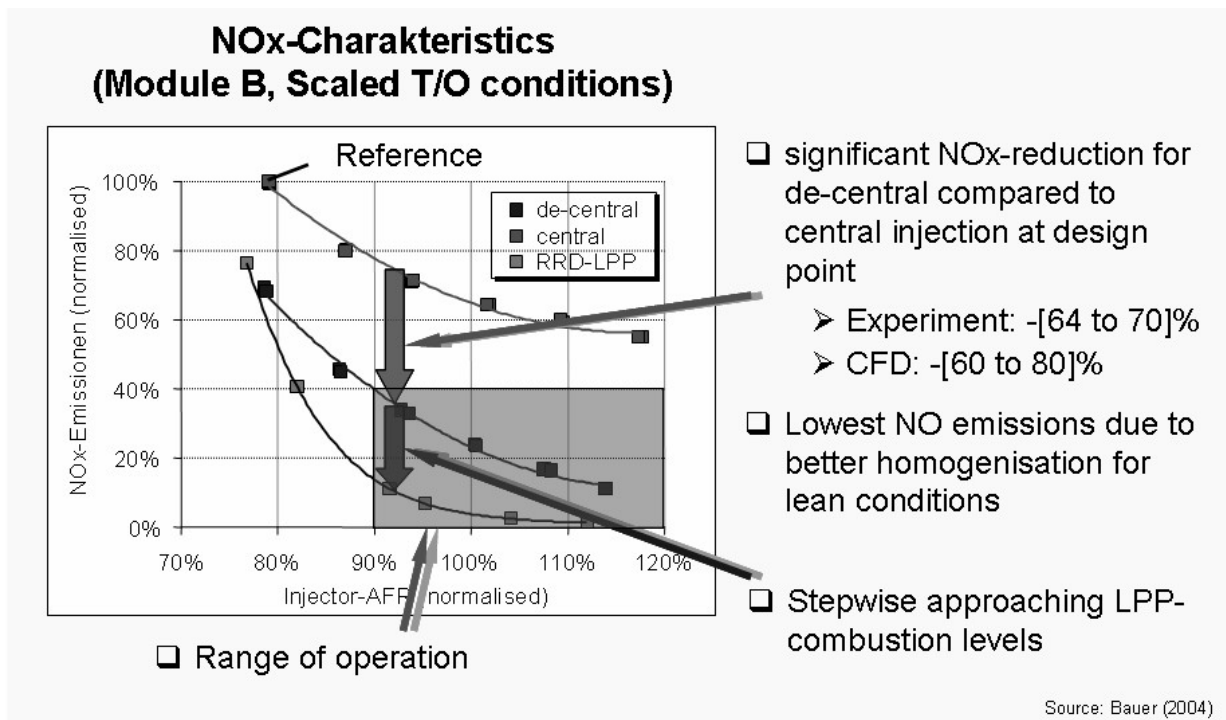


Figure 12: NOx Emission Performance of LDI Systems

However, pilot flames partially compromise the NO_x reduction capabilities of LDI modules (Hassa et al., 2005). Close to the staging points CO emissions still can reach very high levels. Thermal management is required to avoid coking of residual fuel in those injectors which are switched off during staging. The injection systems are bulkier due to their higher air flow areas, therefore their stems tend to be thicker and heavier compared to present designs. Additional fuel lines and valves for staging purposes further add to weight and complexity.

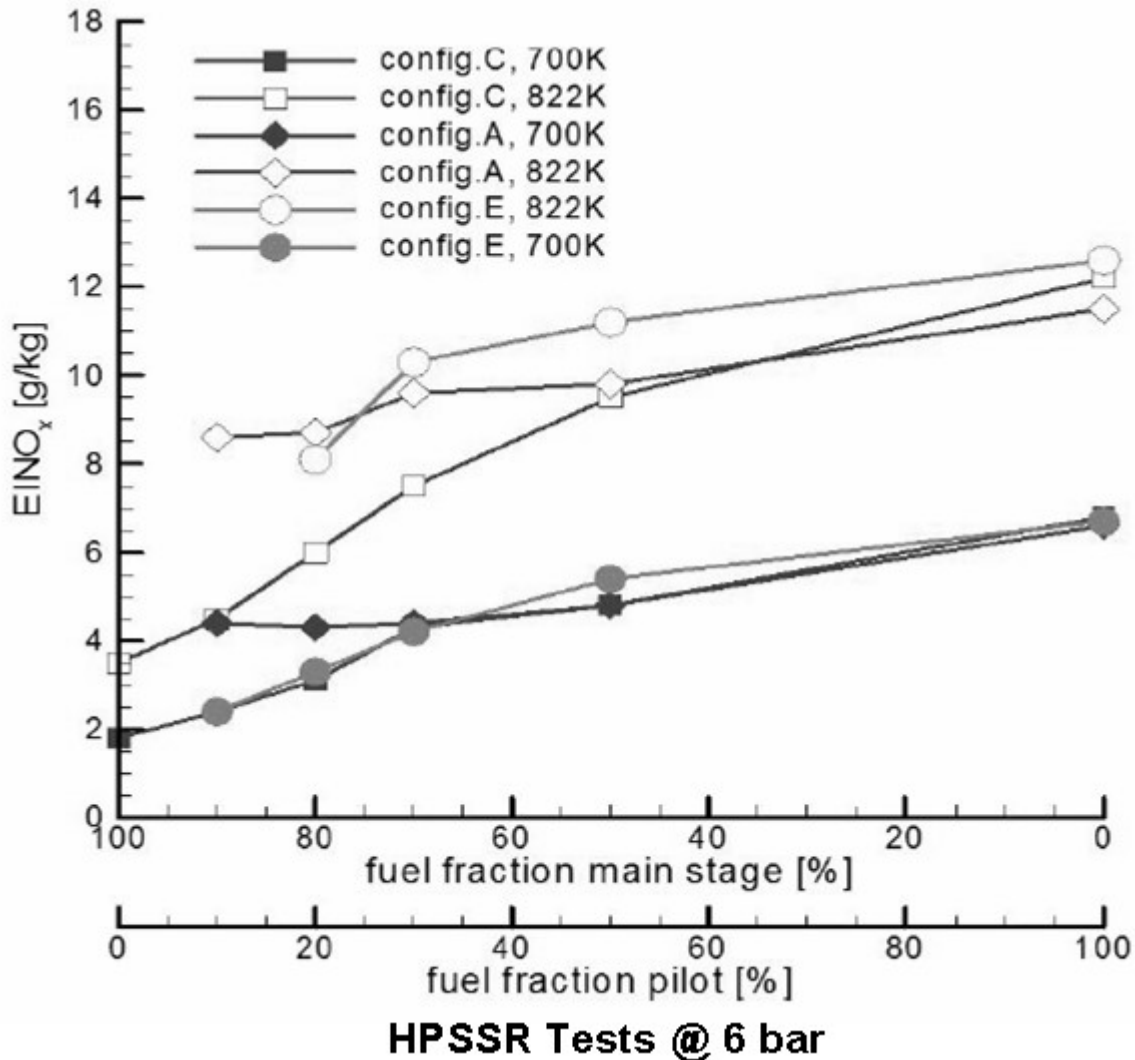


Figure 13: Pilot Effect on NO_x Emissions

Experience from the stationary gas turbine engines imply that thermoacoustic combustion oscillations are likely to appear (Lieuwen and Yang, 2005). The related pressure oscillations impose a risk on combustor and engine integrity. If the inherent damping capability of the combustor (e.g. the liner cooling) is not sufficient to suppress the oscillations additional damping devices have to be employed (Macquisten et al. 2006), further adding to weight and complexity.

Partial or complete premixing and prevaporisation of fuel and air in the lean combustion regime (LPP, Lean Premixed Prevaporised Combustion) can lead to very low NO_x levels, which has been successfully demonstrated on a laboratory scale for operational conditions corresponding to present mid size / large turbofan engines (Von der Bank, 2005). However, similar to the LDI concept staging and piloting is required to achieve stability and low levels of CO / HC emissions considerably compromising the NO_x reduction potential. The remarks concerning thermoacoustic oscillations, fuel coking, weight and complexity made for the LDI concept apply even more for LPP. Operability can be even more compromised by very short autoignition delay times for engines with an OPR > 40 (Cano-Wolff et al., 2001). For these applications the level of premixing and prevaporisation in a separate mixing device will have to be reduced in order to provide sufficient margin against autoignition. The potential remedy to externally prevaporise Kerosene (supercritical pressure) before in-

jecting it into the mixing chamber needs to be investigated in order to better assess its applicability. Flashback into the premixing device either through the boundary layer (Schaefer et al., 2003) or by combustion induced vortex breakdown (Fritz et al., 2004) is another concern.

The NO_x emission reduction potential of LPP systems is very high, while CO and HC emissions are likely to be higher than present values. PM emissions from the pilot injector are expected. The challenge will be to simultaneously achieve low NO_x levels and ensure safe operability.

There are other concepts in discussion with either a very long term perspective like catalytic combustion (Griffin et al., 2004), FLOX® technology (Schuetz et al., 2005), alternative fuels e.g. hydrogen (Contreras et al., 1997) or liquified natural gas (LNG) or which address only local airport quality like water injection (Dagett, 2005). Another approach to reduce NO_x by avoiding the OPR – NO_x trade-off is the consideration of intercooled recuperative engine cycles (Broichhausen et al., 2000).

3 IC ENGINES

While IC engines only play a minor role in commercial aviation they have a major impact on local airport air quality due to their dominance in ground transportation. According to their different combustion principle spark ignition (SI) Engines and Diesel Engines have different levels of pollutants as indicated in Figure 14 for high load conditions. It is obvious that besides NO_x SI engines emit considerable amounts of CO and moderate amounts of UHC whereas Diesel engines have high NO_x and Soot emissions. It should also be mentioned that for part load conditions the raw NO_x emissions of Diesel engines are considerably lower than for SI engines. As in jet engine combustors, formation of NO_x primarily occurs via the Zeldovich mechanism in both SI and Diesel engines. The introduction of effective exhaust gas treatment as well as primary measures to control the combustion process has led to a significant reduction of all relevant species. New combustion technology is expected to further decrease the pollutant emissions from ground transportation in relative as well as in absolute numbers.

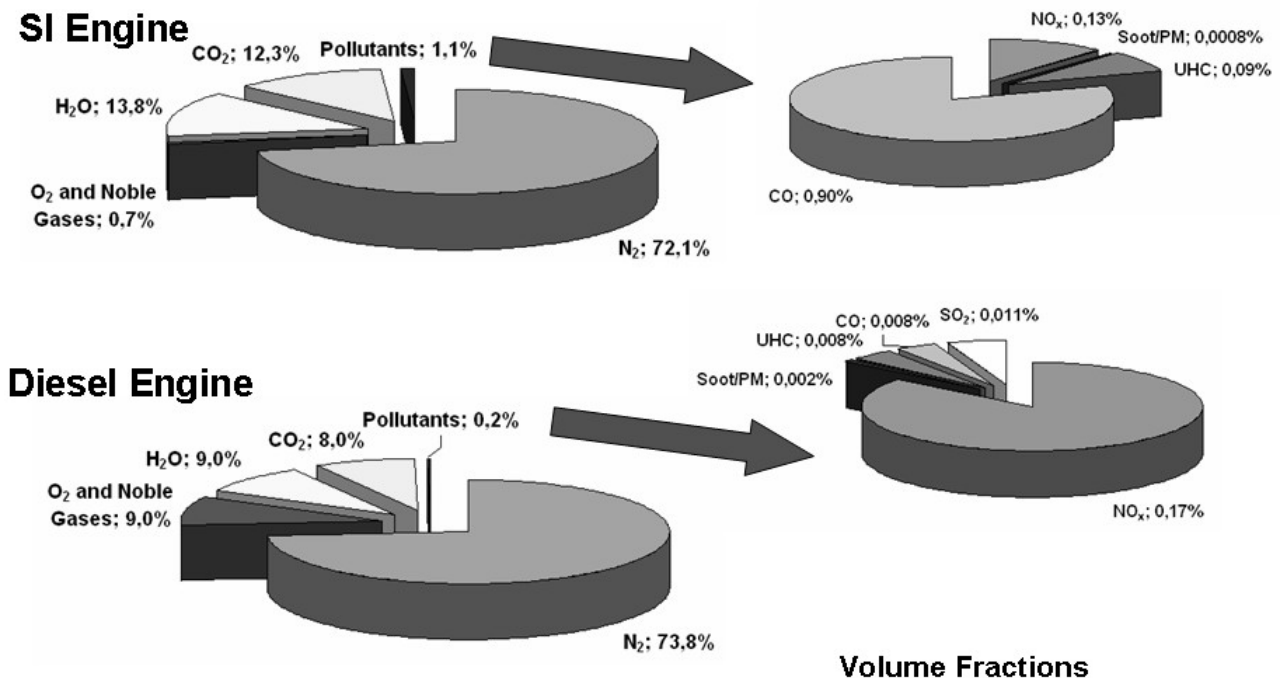


Figure 14: Raw emissions of SI and Diesel Engines

3.1 SI Engines

For port injection engines working at stoichiometric conditions over the entire range of operation a three way catalyst can be used to effectively reduce NO to N_2 and simultaneously oxidise CO and UHC to CO_2 and H_2O . In order to accomplish a high rate of NO conversion λ needs to be tightly controlled within a range of $0.99 < \lambda < 1.002$ (Heywood, 1988), see Figure 15. This control is es-

tablished by a probe measuring the oxygen content in the exhaust gases and a feedback loop to the engine management system controlling the amount of fuel injected.

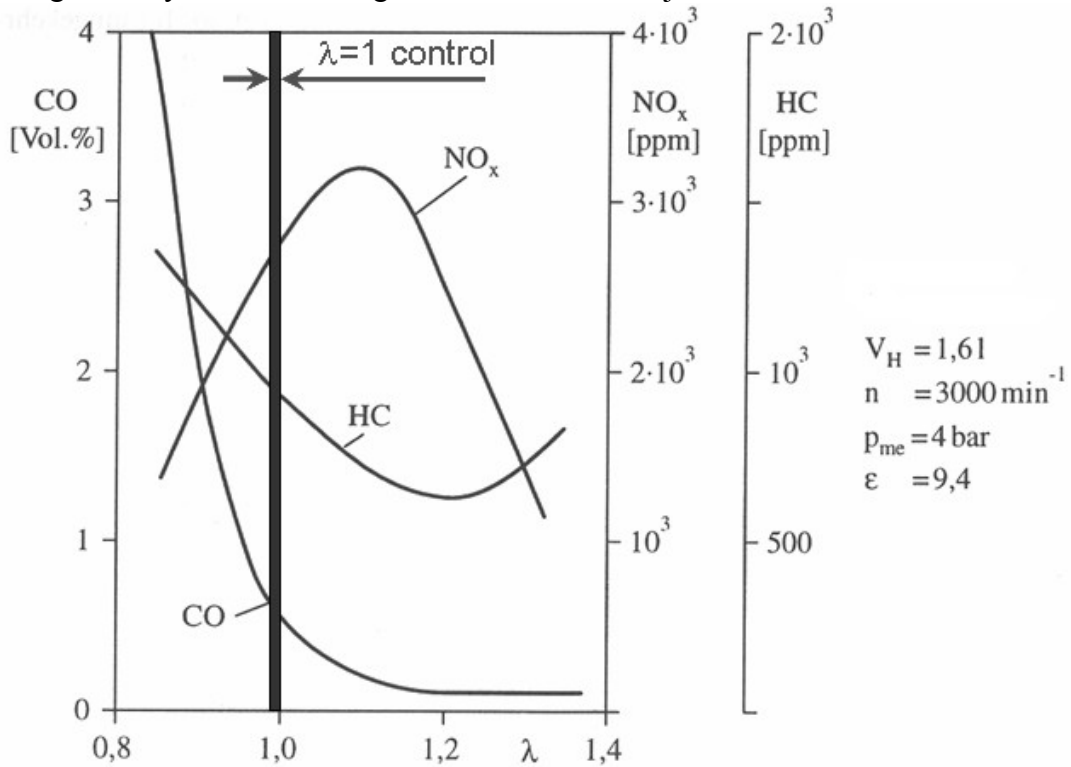


Figure 15: Pollutant Formation in SI Engines (Port Injection) according to Merker et al. (2005)

The need to increase efficiency of SI engines has led to the development of gasoline direct injection engines (GDI) (Spicher et al., 2001). The homogeneous charge GDI engine still runs at $\lambda = 1$ like the port injection engines and uses a throttle valve to achieve the required power output. Fuel is injected during the intake stroke which allows a homogeneous mixing of fuel and air prior to combustion. The advantage of this system is thanks to the fuel evaporation within the cylinder, which reduces the temperature and subsequently the susceptibility to knocking combustion. Hence, a higher compression ratio is possible yielding better efficiency and performance. For this type of engines the same exhaust gas treatment as for port injection engines is possible.

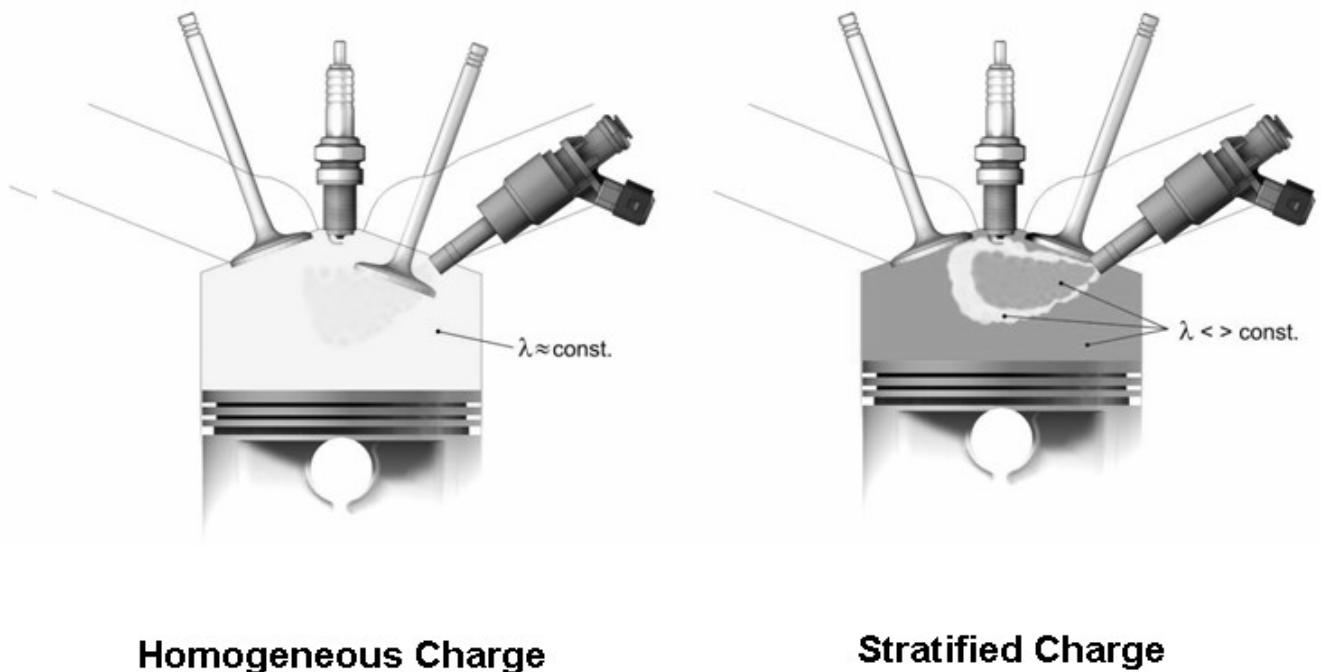
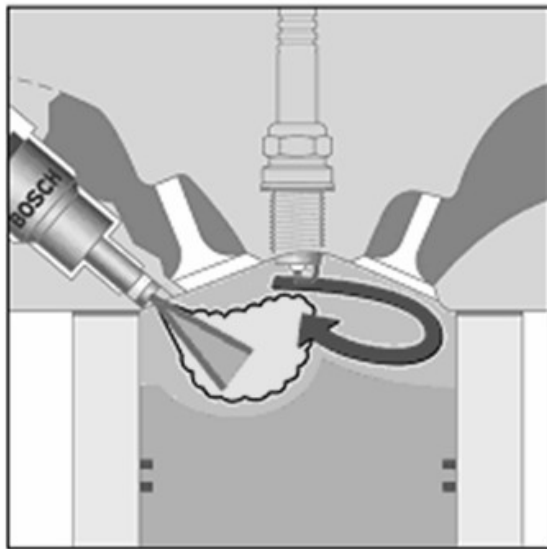
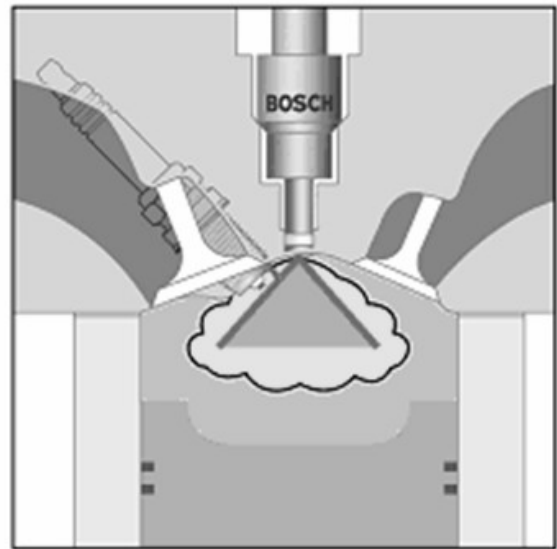


Figure 16: GDI Engines

The more advanced GDI engine controls the power output by a variation of the combustion stoichiometry. This concept avoids throttling losses at part load and yields a considerable efficiency benefit. At part load the fuel air ratio becomes too lean for stable combustion if fuel and air are homogeneously mixed. For these conditions fuel stratification is required to stabilise combustion as indicated in Figure 17. Amongst the different possibilities of stratification, wall guided stratification has found the widest distribution so far. Its major drawbacks are comparatively high emissions of unburned hydrocarbons and particles.



Wall-Guided Stratification

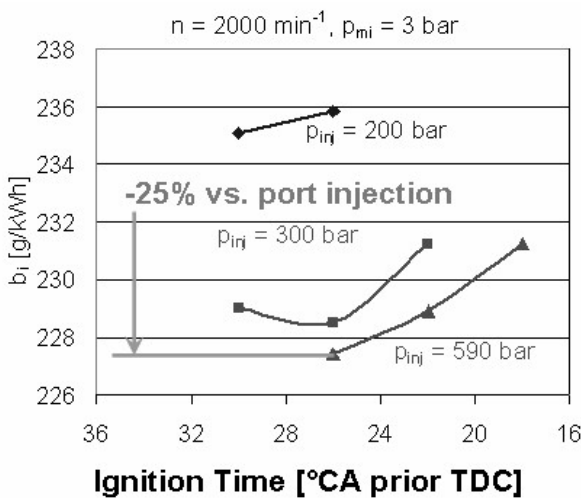


Spray-Guided Stratification

Figure 17: Fuel Stratification

Spray guided stratification, which concentrates the fuel close to the igniter plug is the most promising GDI concept and has recently gone into production in first passenger cars. Through improved fuel atomisation fuel savings in the order of 25% relative to port injection engines can be accomplished. Finer sprays generated by increased fuel injection pressures also significantly reduce the amount of soot emitted.

Specific Fuel Consumption



Soot Emissions

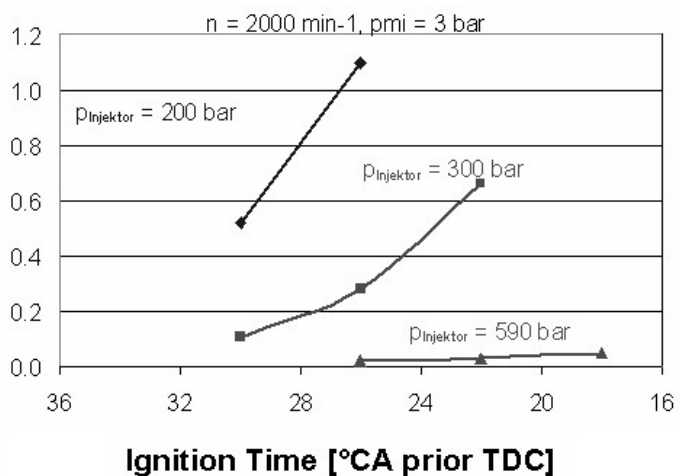


Figure 18: Impact of Spray Quality on SFC and Soot Emissions

NO emissions can either be addressed by means of storage catalysts, which need to be regenerated from time to time. Another principle is exhaust gas recirculation (EGR). Introduction of stratified EGR promises a reduction of NO_x raw emissions by up to 99%.

3.2 Diesel Engines

For Diesel Engines direct fuel injection has become state of the art. Power output is controlled by varying the combustion stoichiometry, with $\lambda > 1.8$. There are no throttling losses at part load, which partly accounts for their efficiency advantage over current SI engines. From an emissions point of view NO_x and soot emissions at high power conditions are of major concern.

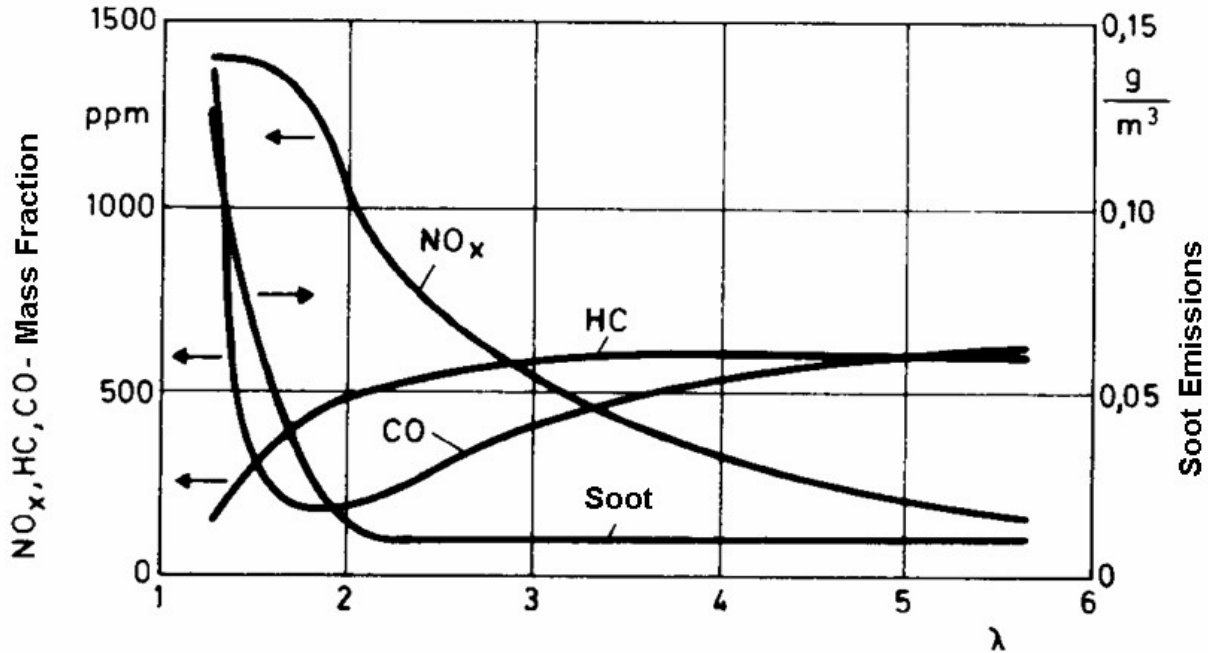


Figure 19: Pollutant Formation in Diesel Engines

There are many remedies to tackle these pollutants either by internal measures controlling the combustion process like improved fuel atomisation and injection timing and exhaust gas recirculation or by external exhaust gas cleaning. However, it is extremely challenging to accomplish low NO_x and soot emissions and low fuel consumption at the same time.

Filters which retain soot particles are presently introduced for new passenger cars and trucks. The filters have to be regenerated in time in order to avoid excessive pressure losses in the exhaust systems. Regeneration is achieved, e.g. by periodically increasing the exhaust gas temperature to a level where soot can be completely converted into CO₂.

Selective catalytic reduction of NO_x is presently developed in order to comply with future emissions regulations. Trucks equipped with SCR systems are on the market since 2005. One approach is to inject urea into the hot exhaust gases which is thermally converted into ammonia in a first step. Subsequently the ammonia generated is used to reduce NO and NO₂ into Nitrogen inside a catalyst (Mueller et al., 2003).

3.3 HCCI

The Homogeneous Charge Compression Ignition concept is presently investigated. It is intended to combine the advantages of Diesel and SI engines. It offers both high thermal efficiency and low emissions of NO_x and soot particles (Assanis et al., 2003).

A HCCI engine uses a homogeneous lean mixture of fuel and air which is compressed until autoignition appears. Combustion is initiated at moderate temperatures of 800 to 1100 K. Due to the low temperature of the combustion process and the lean stoichiometry NO and particle formation is extremely low.

However, there are severe challenges to be faced such as control of the combustion process over a wide load range as well as the level of CO and HC emissions.

4 CONCLUSIONS

Whereas CO and UHC emissions of Turbofan Engines have been substantially reduced in the past advances in reductions of NO_x emissions have been partially compensated by the interdependence of NO formation and the engine pressure ratio. The latter has been increased in order to improve fuel efficiency. Amongst the different approaches the RQL concept has found the widest application and still holds some potential to further limit NO formation. However, the soot NO_x trade-off has to be considered thoroughly. In order to achieve the ambitious ACARE NO_x reduction targets set for the year 2020 a step change in combustion technology needs to be made. Lean concepts such as lean direct injection and lean premixed prevaporised combustion are the most promising concepts albeit their introduction has been prevented so far due to operability concerns. While LDI features the lower risk even for this concept fuel staging and piloting will be required to ensure safe operability. Rich pilot flames are expected to emit soot particles.

NO_x emissions from IC engines have a major impact on local airport air quality. For Diesel engines also soot emissions are of concern. In contrast to jet engines not only internal measures but also exhaust gas treatment can be applied in order to reduce the environmental impact of IC engines. The superior fuel economy of gasoline direct injection engines needs yet to be fully explored. Improvement of fuel preparation additionally offers reductions in raw emissions for this concept. The HCCI technology simultaneously promises low NO_x and soot emissions and outstanding efficiency provided that operability issues and CO and HC emissions will be adequately addressed.

REFERENCES

- N.N., 2001: *European Aeronautics: A Vision for 2020, Meeting society's needs and winning global leadership*. Office for Official Publications of European Communities, Luxembourg, ISBN 92-894-0559-7
- N.N., 1993: *ICAO Annex 16, International Standards and Recommended Practices, Environmental Protection*. Volume II, Aircraft Engine Emissions, 2nd ed. including *Amendment 5* (Nov. 11, 2005)
- Assanis, D.N., P.M. Najt, J.E. Dec, T.N. Asmus, F. Zhao, 2003: *Homogeneous Charge Compression Ignition (HCCI) Engines*. SAE 2003
- Bahr, D.W. and C.C. Gleason, 1975: *Experimental Clean Combustor Program Phase I Final Report*. NASA CR-134732, June 1975
- Bauer, H.-J., 2004: New Low Emission Strategies and Combustor Designs for Civil Aeroengine Applications. *Progress in Computational Fluid Dynamics*. Volume 4, Nos. 3-5, pp 130-142
- Baulch, D.L., C.J. Cobos, A.M. Cox, P. Frank, G. Haymann, T. Just, J.A. Kerr, T. Murrels, M.J. Pilling, J. Tse, R.W. Walker and J. Warnatz, 1991: *Compilation of Rate Data for Combustion Modelling*. Supplement I.J. *Phys. Chem. Ref. Data*. p. 847.
- Behrendt, F. (1989): *Simulation laminarer Gegenstromdiffusionsflammen unter Verwendung detaillierter Reaktionsmechanismen*. PhD Theses, Universität Stuttgart.
- Brehm, N., T. Schilling, H.-J. Bauer, G. Bittlinger, G. Kappler, L. Rackwitz, A. Chatziapostolou, K.-J. Schmidt 1999: *Development of an Annular Combustor with Axially Integrated Burning Zones and Demonstration in a BR700 Core Engine*. 14th International Symposium on Airbreathing Engines, Florence, Italy, 5-10 Sept. 1999.
- Broichhausen, K., H. Scheugenpflug, Ch. Mari, A. Barbot, 2000: *CLEAN The European Initiative Towards Ultra Low Emissions Engines*. ICAS 2000, Harrogate, UK, Aug 27 – Sept 1
- Cano-Wolff, M., R. Koch, and S. Wittig, 2001: *Experimental and Numerical Investigation of the Autoignition of Fuel Sprays in Preheated Flows*. 20. Deutscher Flammentag, VDI Berichte, Vol. 1629, pp. 301-306
- Contreras, A., S. Yigit, K. Oezay and T.N. Veziroglu, 1997: Hydrogen as Aviation Fuel: A Comparison With Hydrocarbon Fuels. *Int. J. Hydrogen Energy*, Vol. 22, No. 10/11, pp. 1053-1060
- Daggett, D., 2005: *Water Injection Feasibility for Boeing 747 Aircraft*. NASA/CR-2005-213656
- Fritz, J., M. Kroener, T. Sattelmayer, 2004: Flashback in a Swirl Burner With Cylindrical Premixing Zone, *ASME Journal of Engineering for Gas Turbines and Power*, Vol. 126, Issue 2, pp. 276-283
- Greenhough, V.W. and A.H. Lefebvre, 1957: *Some Applications of Combustion Theory to Gas Turbine Development*. Sixth Symposium (International) on Combustion, Reinhold, New York, pp. 858-869
- Griffin, T., D. Winkler, M. Wolf, C. Appel, and J. Mantzaras, 2004: *Staged catalytic combustion method for the advanced zero emissions gas turbine power plant*. ASME paper GT2004-54101

- Hassa, C., J. Heinze, L. Rackwitz, and T. Doerr, 2005: *Validation Methodology for the Development for Low Emission Fuel Injectors for Aero-Engines*. XVII International Symposium on Air Breathing Engines (ISABE), 4-9 September 2005, Munich, Germany
- Heywood, J.B., 1988: *Internal Combustion Engine Fundamentals*. McGraw-Hill Inc.
- Kellerer, H., A. Mueller, H.-J. Bauer and S. Wittig, 1995: *Soot Formation from Rich Hydrocarbon Oxidation under Elevated Pressure Conditions*. 20th International Symposium on Shock Waves, Pasadena, CA, USA, July 23 – 28
- Lieuwen, T.C., V. Yang (Eds.), 2005: *Combustion Instabilities in Gas Turbine Engines – Operational Experience, Fundamental Mechanisms, and Modelling*. AIAA, Volume 210, Progress in Astronautics and Aeronautics
- Macquisten, M.A., A. Holt, M. Whiteman, A.J. Moran, and J. Rupp, 2006: *Passive Damper LP Tests For Controlling Combustion Instability*. ASME paper GT2006-90874, 51st ASME Turbo Expo, Barcelona, Spain, May 8-11
- Meisl, J., H.-J. Bauer and S. Wittig 1995: *NOx Emissions Reduction through Staged Combustion at Elevated Pressures*. DGLR German Aerospace Congress, Bonn, 26.-29. September (German Language)
- Merker, G.P., C. Schwarz, G. Stiesch, F. Otto, 2005: *Simulating Combustion: Simulation of Combustion and Pollutant Formation for Engine-Development*. Springer
- Mueller, W., H. Oelschlegel, A. Schaefer, N. Hakim, K. Binder, 2003: *Selective Catalytic Reduction – Europe's NOx Reduction Technology*. SAE paper 2003-01-2304
- Rolls-Royce, 2005: *The Jet Engine*. ISBN 0 902121 2 35
- Saravanamuttoo, H.I.H., G.F.C. Rogers, H. Cohen, 2001: *Gas Turbine Theory*. 5th edition, Prentice Hall
- Schaefer, O., R. Koch and S. Wittig, 2003: Flashback in Lean Premixed Prevaporized Combustion: Non-swirling Turbulent Pipe Flow Study. *ASME Journal of Engineering for Gas Turbines and Power*, Vol. 125, pp. 670-676
- Schuetz, H., R. Lueckerath, T. Kretschmer, B. Noll and M. Aigner, 2005: *Complex chemistry simulation of FLOX® - 'Flameless Oxidation' – Combustion*. 8th International Conference on Energy for a Clean Environment, Cleanair 2005, Lisbon, Portugal
- Spicher, U., A. Koelmel, H. Kubach, G. Toepfer, 2001: *Combustion in Spark Ignition Engines with Direct Injection*. SAE paper 2001-01-0649
- Sturgess, G., R. McKinney and S. Morford, 1993: Modification of Combustor Stoichiometry Distribution for Reduced NOx-Emissions from Aircraft Engines. *Journal of Engineering for Gas Turbines and Power*, Vol. 115, July 1993, pp. 570-580
- Von der Bank, R., T. Doerr, M. Linne, A. Lindholm, and C. Guin, 2005: *Investigations on Internally Staged LP(P) Kerosene Injection Systems*. XVII International Symposium On Air Breathing Engines (ISABE), 4-9 September 2005, Munich, Germany
- Zeldovich, Y.B., 1946: The Oxidation of Nitrogen in Combustion and Explosions. *Acta Physicochim.* USSR 21

Aerosol Evolution from a busy Road in North-West England

B. Davison*

Environmental Science Department, Faculty of Science and Technology, Lancaster University, Lancaster, LA1 4YQ

D. Whyatt

Geography Department, Faculty of Science and Technology, Lancaster University LA1 4YB

C Boardman

Department of Earth Sciences, The Open University, Walton Hall, Milton Keynes. MK7 6AA

Keywords: aerosol vehicle emissions, nano-particles, horizontal profile

ABSTRACT: Motor vehicle emissions are the most significant source of particulate matter (PM) in urban environments (Morawska et al., 1999). This study was undertaken to observe the evolution of aerosols from a busy road, concentrating specifically of the aerosol total number maximum and number size distribution. A Grimm Aerosol Technik (5.400) CPC and DMA 5.5-900 classifier was used to measure ultra-fine particles from 9.8 nm to 1.1 μm at varying distances up to 100 m from the kerbside. Particles number concentration was observed to rise with increasing horizontal distance from the road up to about 100 m. As this occurred the number of fine particle was seen to increase as numbers of larger particles declined. Under stable atmospheric conditions the highest particles number density was found to occur at 40 m from the road (see Figure 1). These findings are discussed and suggested mechanisms considered.

1 INTRODUCTION

Air pollution is responsible for hundreds of thousands of premature deaths around the world each year. The control of atmospheric particulate matter (PM) through the National Air Quality Strategy (NAQS) only legislates for a small fraction of particulate matter, which leaves the majority of particles within the atmosphere unregulated. Epidemiological data from air pollution studies has shown that particulate matter represents a significant risk to human health with prolonged exposure to atmospheric PM particularly the unregulated fine and ultra fine particles (within the ranges of <1 and <0.1 μm , respectively) having a detrimental effects on human health (Dockery et al., 1993; Laden et al., 2000).

In urban environments, motor vehicle emissions are the most significant source of PM. Schwartz et al. (1996) suggested fine and ultra fine particles emitted from combustion sources may pose a major health risk for humans as they are more readily transported deeper into the respiratory system.

This study was undertaken to observe the evolution of PM from a busy road, concentrating specifically on the total number maximums and number size distributions.

2 OBSERVATIONS

Using a busy main road in north-west England with a prevailing wind direction originating from the nearby Irish Sea measurements were collected downwind at varying distance from the road side during crosswinds. Temperature, wind speed and traffic flow were also monitored during sampling. The sampling stations were not screened by vegetation or hedges from the section of road used. Such vegetation barriers are commonly used alongside roads in the UK to screen the road from

* *Corresponding author:* B. Davison, Environmental Science Department, Faculty of Science and Technology, Lancaster University, Lancaster, LA1 4YQ . Email: b.davison@lancaster.ac.uk

nearby dwellings and help cut down noise. This also has the effect of filtering gases and aerosols emitted from the vehicles. The road ran perpendicular to the prevailing wind which originated from a clean maritime sector. This site offers an ideal opportunity to study the emissions of road vehicles and their transformations with distance from the road source.

Sampling was conducted under westerly winds to avoid possible contamination from other sources. Sampling was undertaken from mid morning until mid afternoon (approximately 10am to 4pm local time) to maintain a constant traffic flow and avoid possible increases in flow due to rush hour. In general about 1200 vehicles an hour past the site with around 20% being diesel powered vehicles.

At each sampling site five sample spectra were collected using the aerosol equipment and these were averaged. Sampling took approximately 30 minutes per site. Downwind sites were located at 3, 6, 10, 15, 25, 40, 60 and 100 m from the road side. Measurements were also taken at a background site 20 m upwind of the road. Results from this site were lower than those from the downwind sites.

3 RESULTS

At each site total particle numbers were summed across the size range of the instrument. Figure 1 shows the total particle maximum occurred at a distance of approximately 40 m from the road side.

Particles numbers were summed over selected size bands. This and the aerosol size distribution data showed an increase in the number of ultra fine particle (<100nm) some distance from the road side as shown in Figure 2.

These findings are not easily explained by conventional aerosol dynamic and dispersion models and could not be reproduced using the ADMS road dispersion model. Such models tend to consider aerosols to behave in a simplified standard manner at ambient temperatures with a reduction in particle number with distance travelled from the source due to dilution and deposition (Carruthers *et al.*, 2003). Particle growth is assumed to occur due to condensation and coagulation processes.

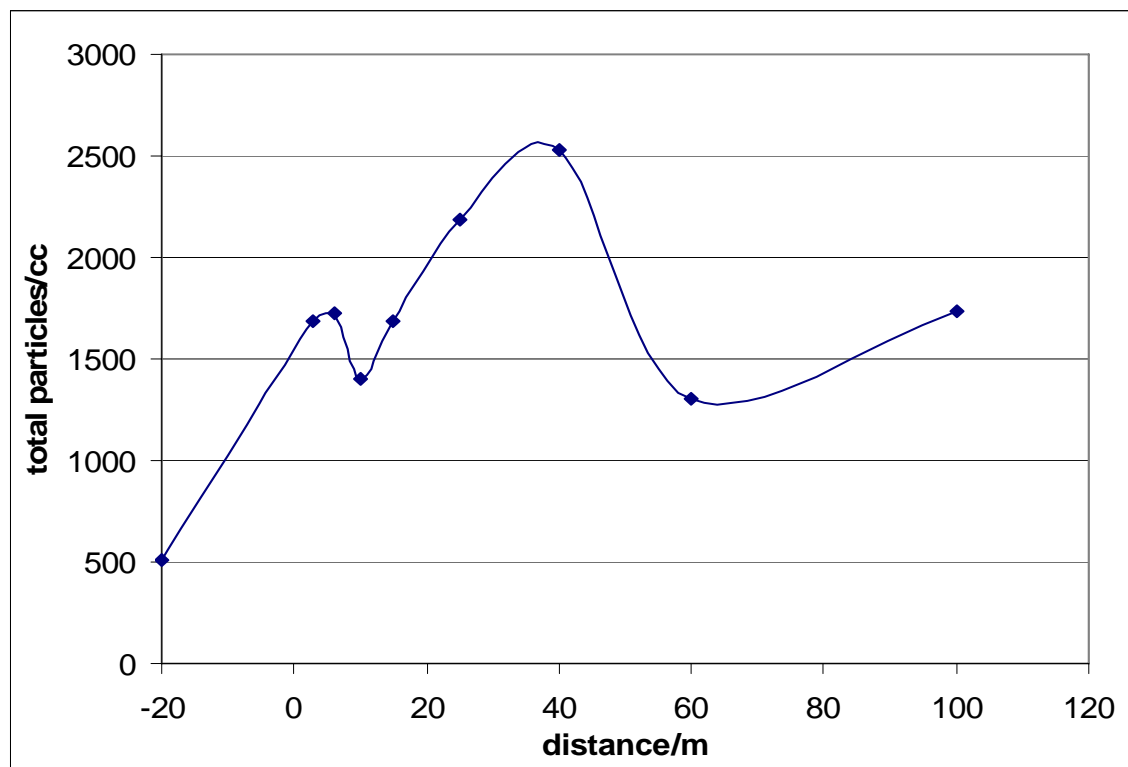


Figure 1. Change in total particle number density with distance from the road showing the maximum in particle numbers occurring at 40m.

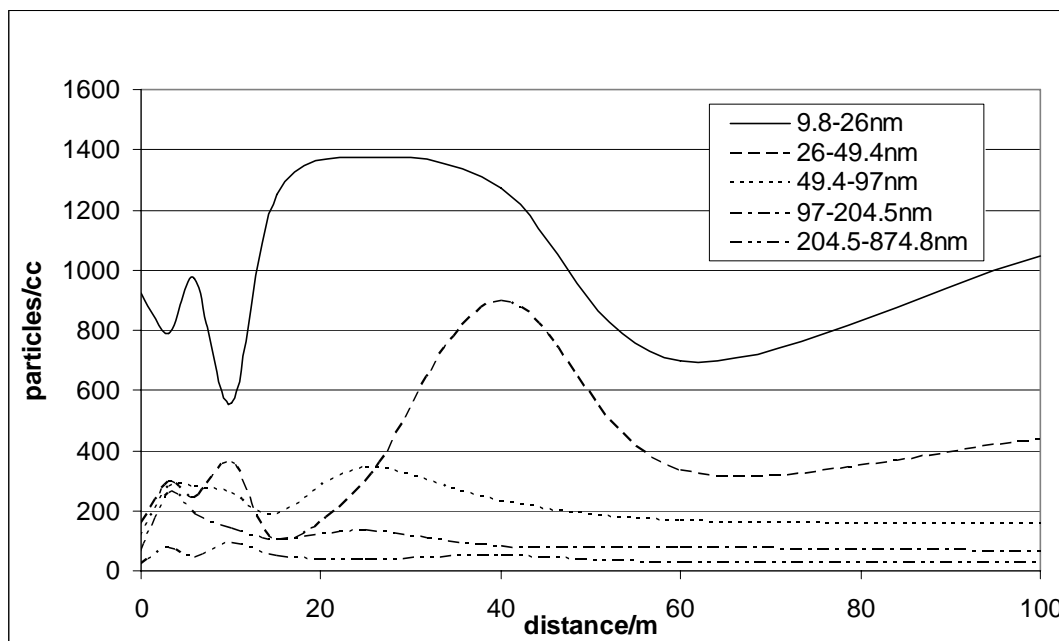


Figure 2. Particles number summed over selected sizes showing an increase in ultra fine (<100nm) particles at 20 to 40m from the road side.

4 MECHANISM

The observations from this study are in agreement with those presented by Gramotnev and Ristovski (2004). In Gramotnev and Gramotnev (2005) a mechanism of thermal fragmentation is proposed to explain the observed particle number increase with distance from the road.

The releases from vehicle exhausts are composed primarily of small carbon/graphite particles (Wentzel *et al.*, 2003). This non-spherical shaped soot particles released at elevated temperatures will be surrounded with a layer of volatile vapour on leaving the fuel rich atmosphere of the vehicle exhaust pipe. The exhaust plume will be cooled as it is transported away from the vapour rich environment vehicles exhaust pipe. As the plume disperses the ambient concentration of hydrocarbons will decline and the volatile vapours surrounding the particle begin to evaporate so causing a decrease in the particle size. Gramotnev and Gramotnev (2005) suggested that this evaporation weakens the bonds within the particle so leading to thermal fragmentation of the particle and an increase in particle number.

It is known however that aspherical soot agglomerates do undergo collapse due to a capillarity effect as they increase in size and this may be an alternative mechanism to explain the particle fragmentation and an increase in particle number.

5 DISCUSSION

Particle size spectra have been measured at increasing distances from a busy road in North-West England. Unexpectedly the maximum of total particle was found some distance (40 m) from the road side rather than close to the source of particles. An increase in nano-particles (<50 nm) was also observed to occur around this distance from the road so causing the observed maximum in total particle numbers. Such observations cannot be accounted for by the current generation of aerosol dispersion models and the exact mechanism causing this phenomenon is under investigation.

Further study of this is necessary in order to evaluate the extent and significance of these increases in particle numbers and their potential effect on human health. Only then can the scale and significance of these particle increases be assessed and a decision on their inclusion into regulative aerosol dispersion models be made.

REFERENCES

- Carruthers, D., J. Blair, and K. Johnson, 2003 *Comparison of ADMS-Urban, NETCEN and ERG Air Quality Predictions for London*, DEFRA, Editor. Cambridge Environmental Research Consultants Ltd.
- Dockery, D.W., A. Pope, X. Xu, J.D. Spengler, J.H. Ware, M.E. Fay, B.G. Ferris, F.E. Speizer, 1993: An association between air pollution and mortality in six US Cities. *New England Journal of Medicine* 329, 1753–1759.
- Gramotnev, D.K. and G. Gramotnev, 2005: A new mechanism of aerosol evolution near a busy road: fragmentation of nanoparticles. *Journal of Aerosol Science*, 2005. 36(3), 323-340.
- Gramotnev, G. and Z. Ristovski, 2004: Experimental investigation of ultra-fine particle size distribution near a busy road. *Atmospheric Environment*. 38(12), 1767-1776.
- Laden F, L.M. Neas, D.W. Dockery, J. Schwartz, 2000: Association of fine particulate matter from different sources with daily mortality in six US cities. *Environmental Health Perspectives* 108, 941-947
- Morawska, L., S. Thomas, D. Gilbert, C. Greenaway, E. Rijnders, 1999: A study of the horizontal and vertical profile of submicrometer particles in relation to a busy road. *Atmospheric Environment* 33, 1261–1274.
- Schwartz, J., D.W. Dockery, L.M. Neas, 1996: Is daily mortality associated specifically with fine particles? *Journal of the Air and Waste Management Association* 46, 927–939.
- Wentzel, M., H. Gorzawski, K-H. Naumann, H. Saathoff, and S. Weinbruch, 2003: Transmission electron microscopical and aerosol dynamical characterization of soot aerosols. *Journal of Aerosol Science*, 34, 1347–1370.

Investigation of road traffic and wood burning emissions in Switzerland using a mobile laboratory

S. Weimer*, C. Mohr, A.S.H. Prévôt
Laboratory of Atmospheric Chemistry, PSI, Switzerland

M. Mohr
Laboratory for internal combustion engines, EMPA Switzerland

Keywords: traffic emissions, wood burning, mobile laboratory

ABSTRACT: On occasion of the project Aerowood (Aerosols from wood burning versus other sources) the spatial and temporal variation of selected aerosol parameters were assessed for two valleys in Southern Switzerland using a mobile laboratory. Results showed that the number concentration for smaller particle diameter (< 30 nm) increased with the proximity to the highway whereas larger particles played the dominant role in villages.

1 INTRODUCTION

For the assessment and understanding of the atmospheric processes that involve aerosols, it is necessary to study more aerosol properties than just the particulate mass.

On the one hand number concentration measurements for example from traffic emissions are in addition to mass measurements very important since the small particles (< 30 nm) have an potential high health effect as well as larger particles but do not contribute a lot to mass emissions. Since the last years engine technology is being improved to remove larger particles (> 30 nm) more efficiently (Kittelson 1998). However, smaller particles are still being detected depending on various parameters such as dilution, weather conditions etc.

On the other hand sources as wood burning seem to play a role concerning mass emissions since wood burning is still commonly used for domestic heating during winter time in some alpine valleys in Southern Switzerland. The goal of this study was to investigate the contribution of road traffic to wood burning emissions in two alpine valleys.

2 METHOD

2.1 *The mobile laboratory*

An IVECO Turbo Daily Transporter was selected as a rolling platform for the measuring equipment. More information concerning the vehicle can be found in Bukowiecki et al. (2002). The instruments inside the mobile laboratory included a Condensation Particle Counter (CPC), a Scanning Mobility Particle Sizer (SMPS), a Diffusion Charger (DC), a Fast Mobility Particle Sizer (FMPS) as well as a CO₂ gas analyzer (Table 1).

2.2 *Measurement site*

In winter 2005/06 mobile measurements were performed in Roveredo in the Mesolcina Valley alongside the San Bernadino route and in the Riviera Valley alongside the San Gotthardo route. Both highways are the main transit route of the Swiss Alps. From November 30th 2005 until December 14th 2005 specific routes were selected including highways, rural roads and residential areas in villages. Every trip was done at least three times. At defined points the engine of the mobile plat-

* *Corresponding author:* Silke Weimer, Dept. 137, EMPA, Ueberlandstrasse 129, CH-8600 Duebendorf, Switzerland. Email: silke.weimer@empa.ch

form was turned off and stationary measurements were performed. Using the geographical information (GPS, Garmin IIplus) the data could be assigned to the specific area. Since the measurements were performed in winter time the average ambient temperature was around $-5\text{ }^{\circ}\text{C}$.

Table 1: Instrumentation of the PSI mobile measurement laboratory

Parameter	Instrument	Time resolution	Detection limit
number conc. $> 10\text{ nm}$	CPC 3010 TSI	1 s	0.0001 cm^3
size distribution 7 – 310 nm	SMPS; DMA, CPC 3010 TSI	2 min	Not defined
active surface area	DC / Matter engineering LQ1-DC	1 s	$10\text{ }\mu\text{m}^2\text{ cm}^{-3}$
size distribution 5.6 – 560 nm	FMPS / TSI	1 s	Not defined
CO_2	CO_2 -Monitor (IR absorption), LI-COR	1 s	0.1 ppm

3 ROAD TRAFFIC VERSUS WOOD BURNING EMISSIONS IN AN ALPINE VALLEY

Compared to road traffic emissions which contribute to particulate matter on highways, roads and play an important role in villages as well, wood burning emissions contribute mainly in villages. For Roveredo, for example around 70 – 80 % of the households use wood for their heating system. In addition to these emissions atmospheric temperature inversions contribute to enhanced levels of particle concentrations throughout winter time in the Mesolcina valley. Almost no dilution takes place.

Average values for number and volume concentrations were calculated by assigning parts of the driven routes to “rural”, “highway” and “village”. Figure 1 shows two bar plots for the Mesolcina Valley. On the left hand side number concentration versus “Rural”, “Highw.” and “village” is presented. The total concentration from FMPS measurements is indicated in black, total concentration for particle diameter larger than 10 nm is shown in white. Highest number concentrations are detected for highways whereas the lowest concentrations are measured for the village. Comparing total concentration of FMPS and FMPS ($> 10\text{ nm}$) demonstrates that the number concentration is dominated by small particle diameters mainly on the highway. On the right hand side one can observe that the concentration for the volume is higher for the village compared to rural road and highway. It seems that mass emissions are higher in villages.

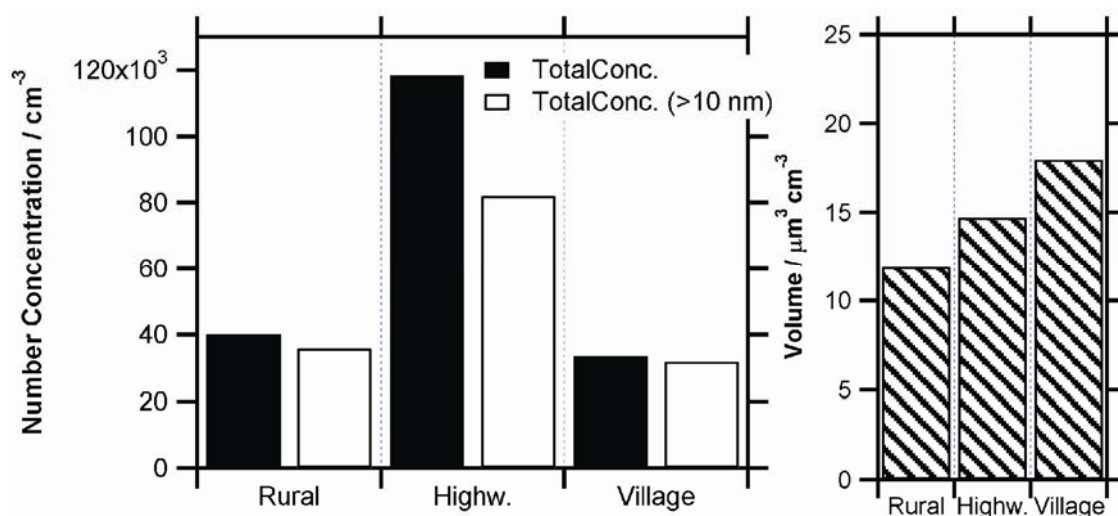


Figure 1. Bar plot for number concentration and volume concentration for rural road, highway and village in the Mesolcina Valley

Size distributions for number and volume concentrations in the Riviera Valley are shown in Figure 2 and 3, respectively. A distinctive mode is found at a particle diameter around 10 nm for the highway. An additional mode is found at around 80 nm particle diameter and is seen for both the villages and the highways. However, the volume size distribution in Figure 3 indicates a mode at around 150 nm particle diameter. The “village” volume size distribution exceeds the volume distribution for the highway.

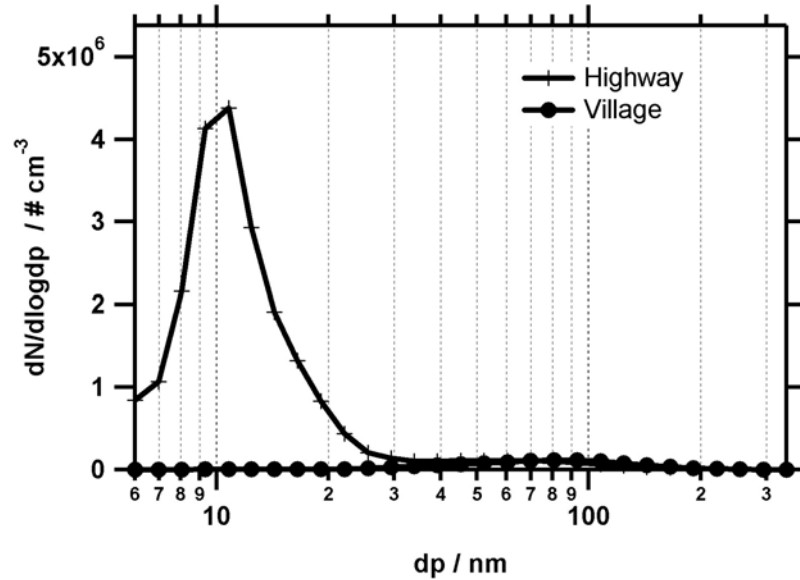


Figure 2. Number size distribution for the Riviera Valley.

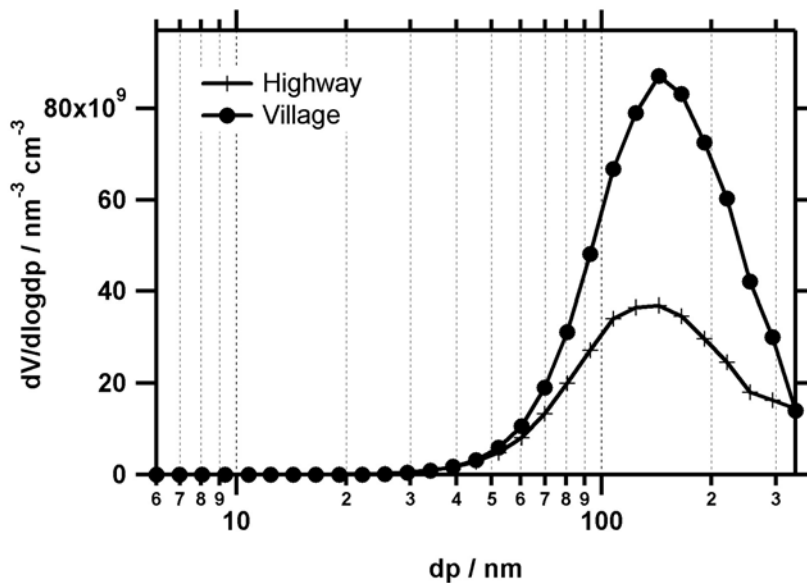


Figure 3. Volume size distribution for the Riviera Valley.

As stated above the aerosol number concentration is very high on the highway. This is due to heavy traffic emissions which favour nucleation if there is little surface area to absorb on for cold temperatures (Bukowiecki et al. 2003, Kreyling et al. 2003). With distance from the highway this nucleation mode disappears in the number size distribution and an accumulation mode dominates the volume size distribution while approaching villages.

4 CONCLUSION

Mobile measurements were performed during the Aerowood campaign in Southern Switzerland in winter 2005/06. The investigations demonstrated that wood burning in villages are more important for the aerosol mass emissions in these valleys than the road traffic emissions.

But the road traffic emissions play the dominant role for the number concentration, especially for smaller particles around 10 nm.

REFERENCES

- Bukowiecki N., J. Dommen, A.S.H. Prévôt, R.Richter, E. Weingartner, U. Baltensperger (2002): A mobile pollutant measurement laboratory – measuring gas phase and aerosol ambient concentrations with high spatial and temporal resolution. *Atmospheric Environment* 36, 5569 – 5579.
- Bukowiecki, N., J. Dommen, A.S.H. Prévôt, E. Weingartner, and U. Baltensperger (2003): Fine and ultrafine particles in the Zuerich (Switzerland) area measured with a mobile laboratory: an assessment of the seasonal and regional variation throughout a year. *Atmos. Chem. Phys.*, 3, 1477 – 1494.
- Kittelson D., 1998: Engines and nanoparticles: a review. *Journal of Aerosol Science* 25, 575-588.
- Kreyling W.G., T. Tuch, A. Peters, M. Pitz, J. Heinrich, M. Stölzel, J. Cyrys, J. Heyder, H.E. Wichmann (2003): Diverging long-term trends in ambient urban particle mass and number concentrations associated with emission changes caused by the German unification. *Atmospheric Environment* 37, 3841 – 3848.

Results of the SCENIC project: impacts of supersonic aircraft emissions upon the atmosphere

Dessens O. *, H. L. Rogers, J.A. Pyle
Department of Chemistry, University of Cambridge, United Kingdom.

C. Marizy
EADS, Airbus France, France.

M. Gauss
University of Oslo, Norway.

G. Pitari
University of L'Aquila, Italy.

Keywords: aviation impact / supersonic aircraft / stratospheric ozone / cross-over point.

ABSTRACT: The EC funded SCENIC project (Scenario of aircraft emissions and impact studies on chemistry and climate) was aimed at quantifying the environmental impact of emissions produced by a supersonic fleet. This paper presents the chemical impact of supersonic aircraft on the stratospheric ozone background concentration and the possible mitigation of this impact due to changes in aircraft / fleet design. The results of supersonic aircraft emissions is a reduction of ozone in the middle stratosphere (-50 ppbv in 2050). Within the UTLS area different behaviours emerge in the model results. The paper focuses on the crossover-point in the ozone net-production between the "stratospheric" chemistry and the "tropospheric" chemistry and the implication upon the aircraft impact calculations. The mitigation study shows that a reduction of speed and reduction of cruise altitude, those two factors are correlated in a supersonic fleet configuration, gives the weakest impact on the ozone in all the model calculations.

1 INTRODUCTION

Aircraft engines emit a range of trace species in the atmosphere: NO_x, water vapor, sulfur, soot or CO₂. The species are directly emitted in the UTLS where they can be chemically active particularly on the ozone, an important constituent of the stratosphere. Since the beginning of the 70's, when aircraft became a mass transport with traffic increase about 10% a year and the possible development of supersonic fleet, the impact of aircraft on the atmosphere have been studied (Crutzen, 1970; Johnston, 1971).

The European commission has taken the decision to found the SCENIC project under the EU Framework 5 RTD Program. The project started in 2002 for 3 years. It regroups several European atmospheric research centres and relevant European aeronautical industry representatives. The aim of the SCENIC project was to study the atmospheric impact of possible future fleets of supersonic aircraft using atmospheric models and realistic supersonic fleet scenarios proposed by the industry partners. The major points evaluated by the SCENIC modelling team are: change in ozone, influence of aerosol and contrail, change in water vapour concentration and finally change in radiative forcing of the atmosphere taking into account of all the previous impacts.

This paper concentrates only on the impact of NO_x and water vapour emissions of supersonic fleets on the ozone concentration.

* *Corresponding author:* Olivier Dessens, Department of Chemistry, Lensfield road, Cambridge, United Kingdom.
Email: olivier.dessens@atm.ch.cam.ac.uk

2 MODEL AND SUPERSONIC FLEET PRESENTATION

Three models are involved in this paper: the Oslo-CTM3 model (Bernsten et al., 1997), the SLIMCAT model (Chipperfield et al., 1999) and the ULAQ model (Pitari et al., 1993). The first two models are chemistry transport models, the ULAQ model has been use in its CTM form for this study.

The Airbus consortium has developed fleet scenarios for 2025 and 2050 as part of the SCENIC project. For each period two data sets are produced: a subsonic scenario with only subsonic aircraft and a mixed scenario with both subsonic and supersonic aircraft. The impact of the supersonic fleet is calculated as the difference between simulations with the mixed fleet and simulations with the subsonic fleet only. The standard supersonic aircraft considered operates at Mach 2, with 250 passengers, a maximum range of 5500 NM and a cruise altitude from 17 to 20 km.

The background scenario developed to represent the mixed fleet emission distributions for the year 2050 (scenario S5) has been used as a reference to determine the best option for an environmentally friendly supersonic aircraft. The development of perturbation scenarios (P2-P6) has been made by the modification of parameters characterising the supersonic aircraft or the supersonic fleet (Fig. 1). Scenario P2: the EI(NO_x) calculated throughout the supersonic mission duration has been increased by a factor of 2. Scenario P3: the total number of supersonic aircraft is doubled. Scenario P4: the cruise speed is fixed to Mach 1.6. Scenario P5: the reference ESCT configuration has been modified to increase its range. Scenario P6: the design of the aircraft scenario P4 has been slightly modified to optimise the performance at a lower cruise altitude.

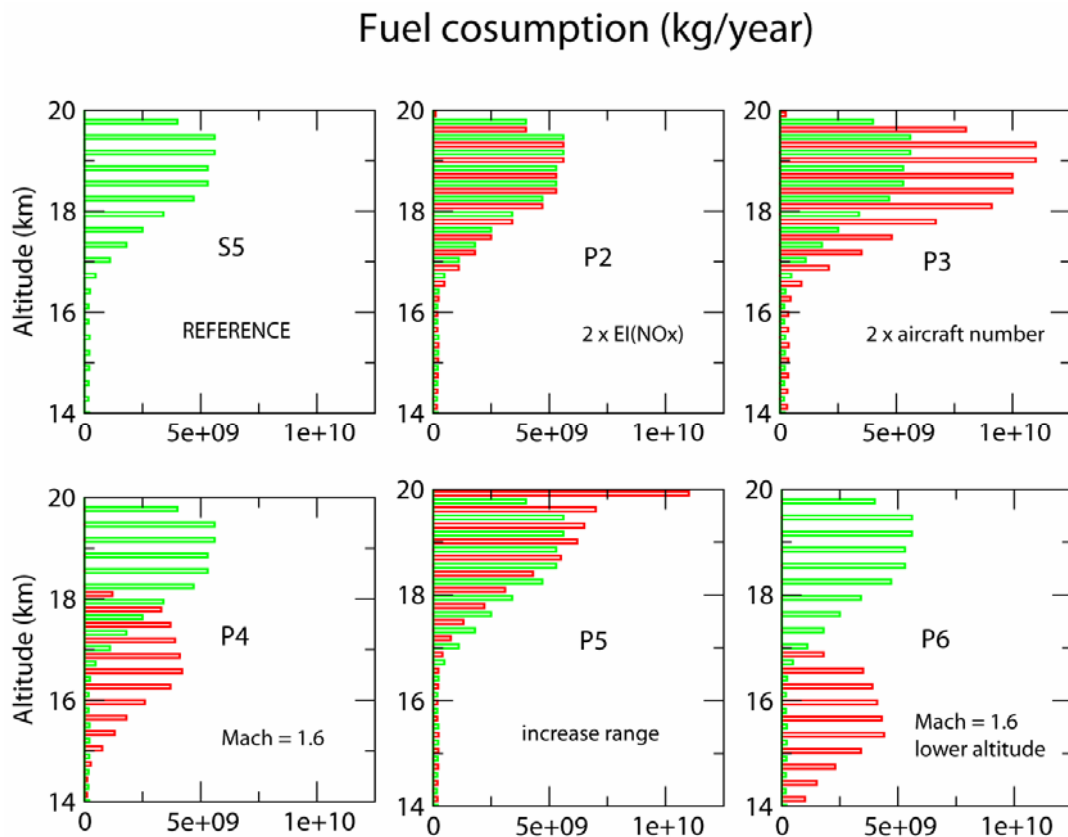


Figure 1. Profile of the fuel consumption for the 2050 supersonic fleet in the S5 and P2 to P6 scenarios.

3 REFERENCE FLEET IMPACT

Figure 2 shows in term of annual-zonal mean, the impact of the supersonic fleet emissions, for the 2050 S5 scenario, on NO_y, H₂O and ozone concentrations. The emissions occur mainly over the North Hemisphere mid-latitude at 18–20 km altitude, it is the place of the maximum impact for H₂O and NO_y. The water vapor impact reaches 293 to 513 ppbv depending on the model. The NO_y increase is ranging from 0.42 to 0.75 ppbv. From the area of release, the species are transported in the

models by the general circulation. The extension of the area impacted by the emissions depends of the efficiency of the transport. Two transport schemes are important according the supersonic tracers: the inter-hemispheric exchange along the isentropic level in the UTLS and the vertical transport reaching the middle stratosphere from the UTLS.

The ULAQ model shows confinement of the NO_y within the Northern Hemisphere UTLS, with some transport in the tropical pipe to the tropical middle stratosphere. The water vapour has a vertical barrier between the two hemispheres also. The ULAQ model has the lowest resolution within the three models and it has been shown by Rogers et al. (2002) that a higher vertical resolution produce an enhancement of the spread of a stratospheric aircraft emission tracer, this explains, with the weaker maximum reached in the emissions area, why the ULAQ model presents the weakest spreading of the emissions. The SLIMCAT model present a strong transport from the emission area to the stratosphere by the tropical upward, but also a exchange of material between the two hemisphere. In consequence a big part of the middle stratosphere and the Southern Hemisphere UTLS are reached by NO_y as well as H_2O . Finally the Oslo model shows an exchange mechanism between the two hemispheres weaker than the UCAM one.

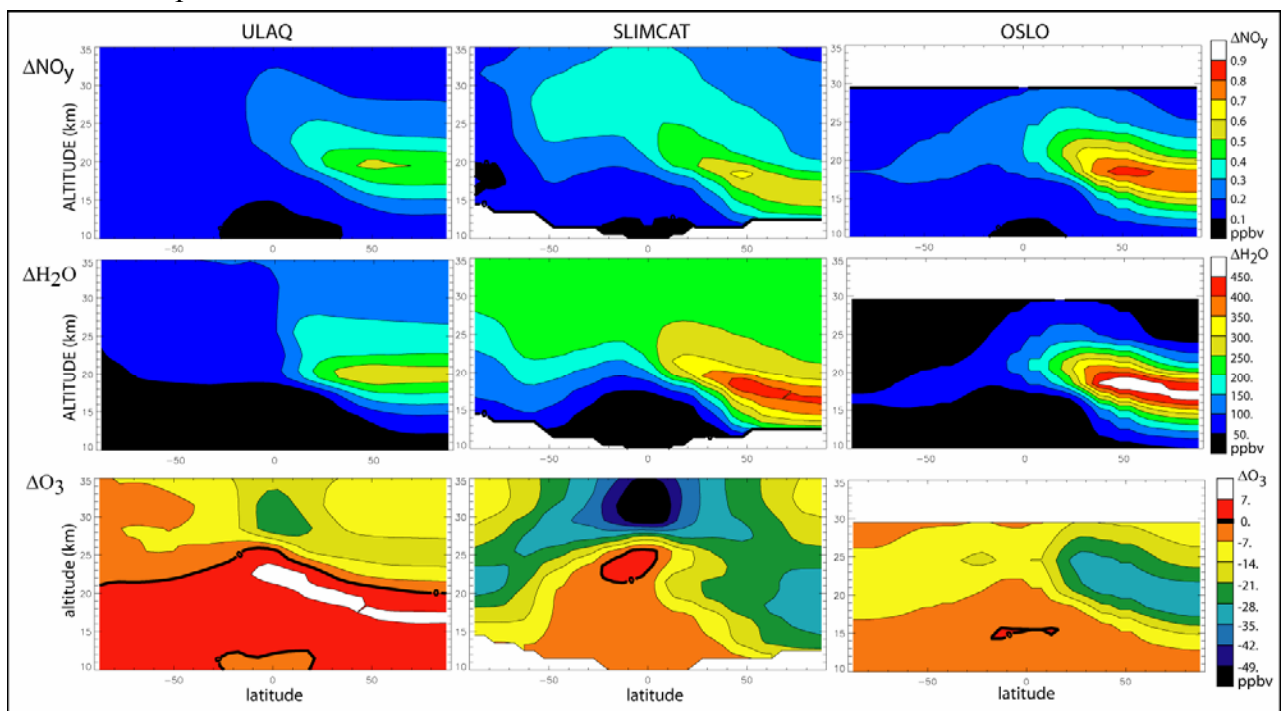


Figure 2. Zonal annual mean of the impact of the 2050 supersonic reference fleet on NO_y , H_2O and ozone field calculated by the tree models..

In term of ozone impact we have to differentiate the middle stratosphere and the UTLS impacts. For the stratosphere a reduction in the ozone concentration has been found. The SLIMCAT and ULAQ models transport the emissions within the middle stratosphere (not represented in the Oslo model with at top level at 30 km). Then the ozone NO_x catalytic destruction in this area is increased; the maximum destruction reaches -50 ppb at 35 km. In the UTLS different behaviours emerge from the figure. The Oslo and SLIMCAT models give a destruction of ozone that follows the area of the supersonic emissions, the destruction reach -29. ppb over the high latitude of the Northern Hemisphere and are mainly due to the direct effect of the NO_x emissions on ozone. For the ULAQ model a net production in ozone occurs below 25 km. These different behaviours could be explained by the difference in the background between the models. Figure 3 gives the 45N profile between 15 and 30 km of the ratio $\text{NO}_x / \text{HO}_x$; it is five time weaker in ULAQ background UTLS than in SLIMCAT or Oslo. This low UTLS ratio between NO_x and HO_x allows the supersonic NO_x emissions to react according to a mechanism producing ozone (as seen in the troposphere) in the ULAQ model.

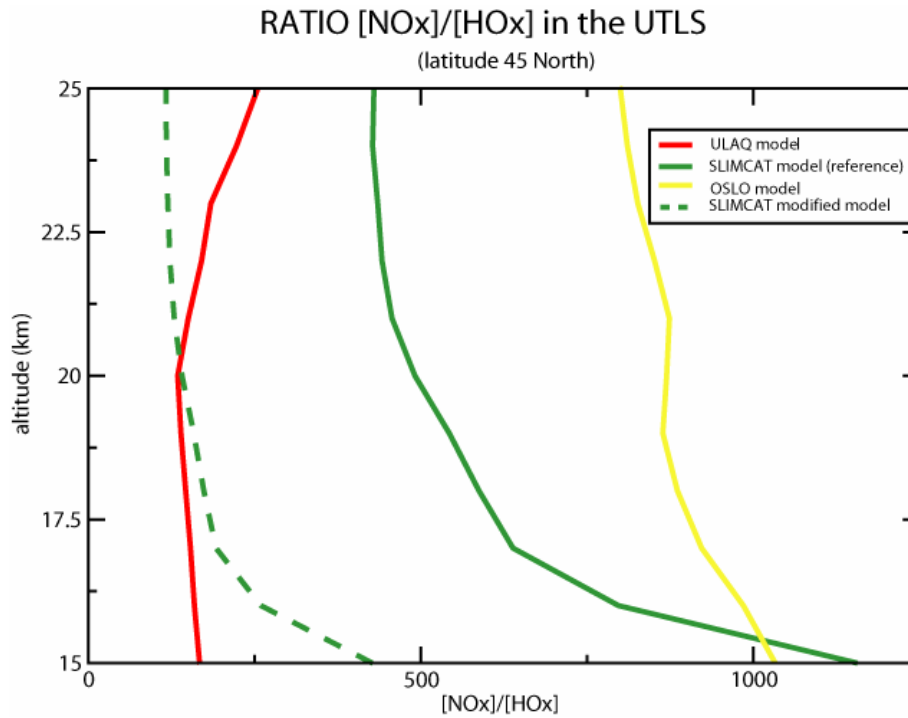


Figure 3. Zonal annually means profile at 45°N of the $\text{NO}_x / \text{HO}_x$ ratio in the UTLS calculated by ULAQ, Oslo and SLIMCAT model.

4 CROSS-OVER POINT STUDY

In order to investigate the cross-over point between the production and the destruction of ozone due to supersonic emissions found in the ULAQ simulations and its relation with the $\text{NO}_x / \text{HO}_x$ ratio of the background UTLS, further studies have been conducted to compare the UCAM and the ULAQ results. The UTLS background of the UCAM model has the ability to be modified according different forcing files. This region is bordered by the bottom level of the model (8 km altitude). This level is constantly overwritten during the simulation to reproduce the mechanism of production or sink of species within the troposphere. The values used are those from the initialisation file of the model. The ULAQ background atmosphere has been interpolated to initialise the UCAM model and the bottom level of the model the simulation is forced by the ULAQ values. Only the NO_y and HO_x families from the ULAQ simulation are prescribed, the other species come from the usual initialisation file of SLIMCAT. After the 6 years spin up the results are comparable in term of mixing ratio of NO_x and HO_x between the ULAQ and the SLIMCAT modified model (Fig. 3). Moreover the impact of the supersonic fleet emissions is radically changed in the SLIMCAT's UTLS as seen on the zonal mean annual mean ozone impact due to the supersonic 2050 fleet plotted in Figure 4. UCAM model, under the ULAQ chemical background conditions for its lower level, is producing a cross-over point at 20/25 km altitude as it has been found in the ULAQ model. The $\text{NO}_x / \text{HO}_x$ ratio is now similar between the two models and the ozone production at 45N reach the same amount between the two calculations indicating the importance of this ratio when it comes to study supersonic aircraft impact on the UTLS area.

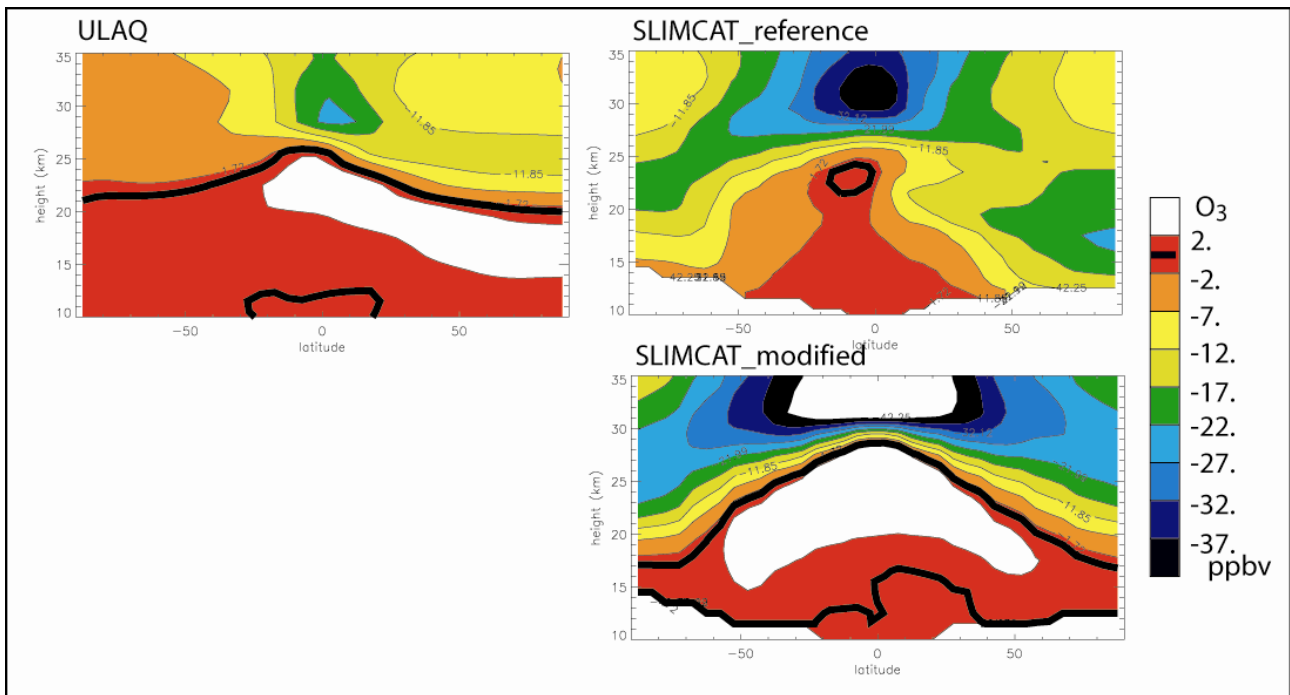


Figure 4. zonal-annual mean of the impact of 2050 supersonic fleet (mixed – subsonic) ozone field calculated by the SLIMCAT model: initialised with ULAQ fields (left) and forced by the ULAQ aircraft-perturbed fields of NO_x and HO_x (right).

5 MITIGATION TO REDUCE THE SUPERSONIC IMPACT

Figure 5 presents the ratio of stratospheric ozone change induced by the supersonic fleet in the perturbation scenarios (P2 to P6) relative to the reference scenario. The P4 and P6 scenarios (lower Mach number and cruise altitude) minimize the impact on stratospheric ozone by a factor 2. The reduction of altitude and speed may increase the EI(NO_x) number, but the lower fuel consumption reduces the NO_x and H₂O emissions and therefore their overall impact on stratospheric ozone. Increase in the NO_x emission (P2), in the number of aircraft (P3), or in the aircraft maximum range (P5) increase the ozone destruction in the stratosphere. In term of ozone destruction, the results of P2 scenario (only the NO_x emissions are increased) and P3 scenario (all the emissions are increased due to the increased number of aircraft) highlight the importance of NO_x emissions on stratospheric ozone over the water vapour emissions as seen in Dutta et al. (2004).

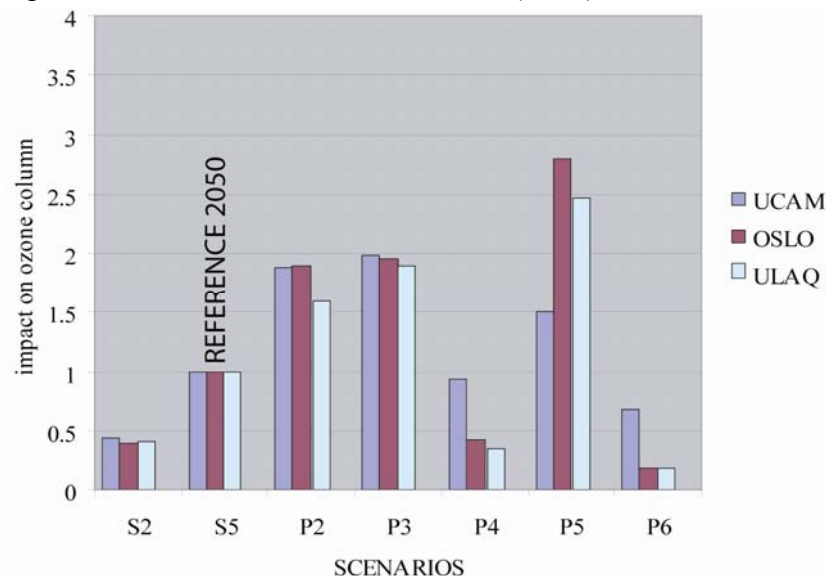


Figure 5. Ratio of the stratospheric ozone impact induced by a supersonic fleet in the perturbed scenario (P2 to P6) relative to the impact of the reference supersonic fleet in 2050 (scenario S5).

6 CONCLUSION

The impact of supersonic aircraft on the ozone has been quantified for several design of supersonic aircraft or fleet. Some differences can be found between the model reactions to the emissions. The main divergence in the ozone behaviour occurs in the UTLS below 25 km altitude. Above this level, in the middle stratosphere, the response to the emissions from the supersonic aircraft fleet is a reduction of ozone due to the preponderance of the NO_x cycle in the ozone destruction cycles at these altitudes. The emissions occur lower in the atmosphere, the strength of this stratospheric ozone reduction is directly related to the strength of the emitted species transported there. The reduction of ozone in the tropical middle stratosphere can reach 1 to 1.5 % compare to the background for the 2050 fleet. For the direct effect of a supersonic fleet on ozone in the UTLS and middle stratosphere, lowering the cruising altitude of the aircraft (and consequently reducing the Mach number and the fuel consumption) is the best option as seen in the perturbation scenarios.

In the UTLS region it has been proved that the background ratio between the NO_x and the HO_x species are determining the sign of the impact. The more stratospheric character the background atmosphere has, such as found in the OSLO or SLIMCAT model, the more ozone depletion occurs from supersonic emission; but under low NO_x, high HO_x conditions the ozone chemistry turns to the tropospheric scheme, producing an increase of ozone driven by the local increase of NO_x due to the emissions, that happens in the ULAQ simulation. This fact can be reproduced with the UCAM model under the UALQ background conditions for NO_x and HO_x families.

That last point highlights the importance of the UTLS knowledge to quantify the impact of a supersonic fleet on the atmospheric composition. The position of this cross over point between the production and the destruction of ozone is crucial in order to investigate the impact on the global atmosphere of a supersonic fleet.

REFERENCES

- Berntsen T. and I.S.A. Isaksen, 1997: A global 3-D chemical transport model for the troposphere, 1, Model description and CO and Ozone results, *Journal of Geophysical Research*, vol. 102, , 21.239-21.280.
- Chipperfield, M.P., 1999: Multiannual simulations with a three-dimensional chemical transport model, *Journal of Geophysical Research*, vol. 104, 1781-1805.
- Crutzen, P., 1970: The influence of nitrogen oxides on the atmospheric ozone content, *Q. J. Roy. Meteorol. Soc.*, 96, 320-325.
- Dutta, M., K. Patten, and D. Wuebbles, 2004: Parametric analyses of potential effects on stratospheric and tropospheric ozone chemistry by a fleet of supersonic business jets projected in a 2020 atmosphere, *National Aeronautics and Space Administration report NASA/CP-2004-213306*.
- Johnston, H. S., 1971: Reduction of stratospheric ozone by nitrogen oxide catalysts from supersonic transport exhaust, *Science*, vol. 173, 517-522.
- Pitari, G., V. Rizi, L. Ricciardulli and G. Visconti, 1993: High speed civil transport impact: role of sulfate, nitric and trihydrate, and ice aerosol studied with a two-dimensional model including aerosol physics, *Journal of Geophysical Research*, vol. 98, 23141- 23164.
- Rogers, H.L., H. Teyssedre, G. Pitari, V. Grewe, P. van Veltoven, and J. Sundet, 2002: Model intercomparison of the transport of aircraft-like emissions from sub- and supersonic aircraft, *Meteorologische Zeitschrift*, vol. 11, 151-159.

Response in ozone and methane to small emission changes and dependence on cruise altitude

M.O. Köhler*, O. Dessens, H.L. Rogers, O. Wild, J.A. Pyle

Centre for Atmospheric Science, Department of Chemistry, University of Cambridge, United Kingdom

Keywords: Aircraft NO_x, ozone, methane, UTLS chemistry, cruise altitude, parameterisation

ABSTRACT: Within the scope of the LEEA (Low Emissions Effect Aircraft) project the effects of small changes in aircraft NO_x emissions on CH₄-NO_x-O₃ chemistry were systematically investigated with the ultimate objective to develop a parametric relationship between the amount / altitude / location of emissions and their effect on the climate system. A large number of sensitivity experiments were carried out with the global 3D CTM p-TOMCAT. Aircraft emission data was used from the European AERO2k Global Aviation Emissions Inventory for 2002. In the experiments the standard emission profile was altered such that, within discrete cruise altitude bands in the altitude range 5–15 km, emissions were globally increased by 5–20%. Investigation of ozone precursor concentrations, ozone production efficiency and methane lifetime has shown both highly linear and additive behaviour in the atmospheric response to the emission perturbations that were applied. This suggests that in future a linear parameterisation can be used to predict the effects of small emission changes on the chemistry in the UTLS region. The LEEA project was funded by Airbus UK and the Department for Trade and Industry.

1 INTRODUCTION

We have used 3D chemistry transport models to study the impact of aircraft nitrogen oxide (NO_x) emissions on ozone (O₃) and methane (CH₄). Both O₃ and CH₄ are important greenhouse gases (IPCC, 2001) and changes in their abundance due to aircraft emissions can contribute to climate change (IPCC, 1999). The principal objective of this study was to investigate the atmospheric response to small perturbations in the emissions as a function of the size of perturbation, cruise altitude, and location. The perturbations were applied in form of local scaling of the background emission distribution at different cruise altitude bands. Small increases in emissions could represent the introduction of a new aircraft to the existing commercial fleet or small changes in air traffic demand. Of particular interest was the question whether it would be possible to find a parametric relationship between the changes in emissions and the atmospheric composition of ozone and methane. Were such a relationship found, this could then be used to predict the atmospheric impact of future changes within the range of these experiments without the need to conduct costly model experiments.

2 MODEL DESCRIPTION

The experiments were carried out using the p-TOMCAT chemistry transport model (O'Connor et al., 2005). This model is an improved and parallelised version of the earlier TOMCAT model (Savage et al., 2004) and its gas-phase chemistry scheme focuses on processes relevant to the troposphere and lower stratosphere. For the experiments in this study the vertical resolution was enhanced to 35 hybrid-pressure levels between 10 hPa and the surface. For each experiment the p-TOMCAT model was integrated for a time period of 2 years and forced by ECMWF operational analyses for the years 2001 and 2002. Aircraft NO₂ emission data for 2002 was used from the

* *Corresponding author:* Marcus Köhler, Department of Chemistry, Lensfield Road, Cambridge, United Kingdom.
Email: marcus.koehler@atm.ch.cam.ac.uk

European FP5 Project AERO2k (Eyers et al., 2004). A subset of the experiments described below was also carried out by the SLIMCAT chemistry transport model (Chipperfield, 1999) to investigate the impact of emission perturbations specifically in the stratosphere. SLIMCAT is forced by UKMO analyses and integrates a stratospheric chemistry scheme on 18 isentropic levels between 335 K and 2700 K (10–55 km). SLIMCAT treats water vapour as a prognostic variable which allows for the additional consideration of aircraft H₂O emissions and their effects on the stratosphere. A spin-up integration of 6 perpetual years of 2001 meteorology prior to one year of 2002 meteorology ensured the appropriate representation of transport timescales within the stratosphere.

3 EXPERIMENT DESIGN

The original monthly aircraft emission data, which is provided at 500 ft vertical resolution, was merged to a 1000 ft vertical grid (Eyers et al., 2004) before being included into the models. The altitude range between 5 and 15 km was subsequently divided into 16 equally spaced cruise altitude bands of 2000 ft (610 m) thickness, from here on referred to as perturbation levels (PL). In a first set of experiments (A) we increased the aircraft emissions locally by 5% for each experiment on one PL at a time. Further experiments (B) with an increase of emissions by 10% and 20% were carried out, however only on four selected PLs at approximately 6 km, 7.8 km, 9.5 km, and 11.5 km altitude. The restriction to these four levels was necessary due to the computational costs associated with each experiment. In a third set of experiments (C) emissions were increased simultaneously by 5% on one of these four PLs from (B) and its neighbouring level underneath, resulting in an emission increase over an altitude band of 4000 ft. Figure 1 shows on the left the zonally and annually integrated AERO2k aircraft emissions in colour. The altitude range covered by the 16 PLs for experiment (A) is shaded in light grey, the four principal PLs for experiment (B) and (C) are highlighted by darker shading. The emission perturbations are applied as a local percentage of emissions in each grid box and therefore the regional distribution of the perturbations reflects the geographical flight routing pattern at the respective cruise altitude band for each PL. Figure 1 shows on the right the horizontal model domain coverage of the perturbations in percent for each PL. Emission perturbations below the dashed line (PL 1–11) are located mainly within the troposphere, those above the dashed line (PL 12–16) are located mainly within the stratosphere. The regional coverage of perturbations is approximately 60% or more of the horizontal model domain within the troposphere. Within the stratosphere the coverage becomes rapidly smaller with increasing altitude.

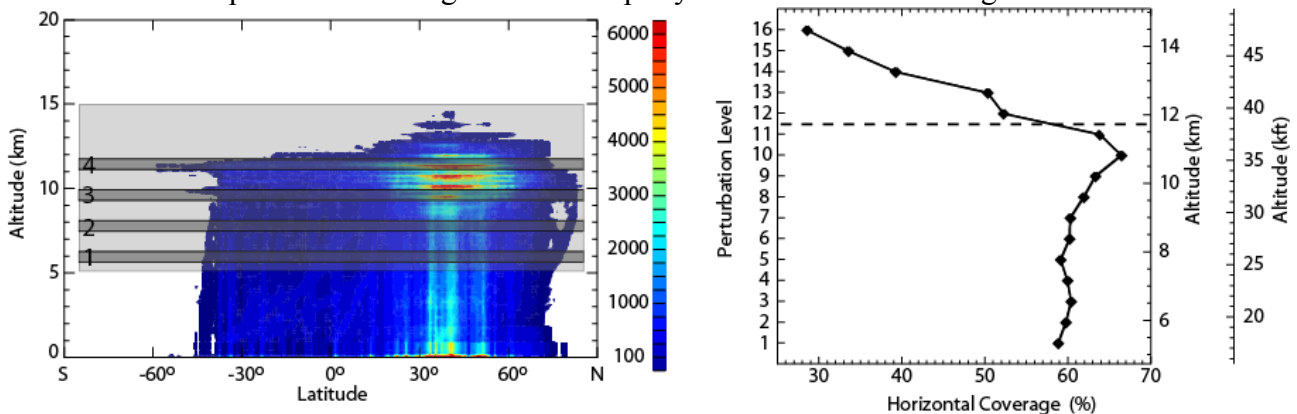


Figure 1. Left: AERO2k aircraft emissions for 2002 in kg NO₂ per year at $1^\circ \times 1^\circ \times 500$ ft. Grey shading indicates the vertical domain of the perturbation levels, the four perturbation levels of experiment B are highlighted. Right: Horizontal coverage of the emission perturbation for each perturbation level expressed as a percentage of the model domain. The altitude of the tropopause is shown as a dashed line.

4 IMPACT OF THE GLOBAL AIRCRAFT FLEET ON OZONE AND METHANE

During initial experiments the p-TOMCAT and SLIMCAT models were used to determine the total impact of global air traffic on ozone levels and the lifetime of methane. Both models calculate an increase of ozone in the troposphere and lower stratosphere with a maximum in the northern hemi-

sphere of 6–9 ppbv and a slight ozone decrease in the middle stratosphere. This is in good agreement with earlier assessment studies (see e.g. IPCC, 1999; Isaksen *et al.*, 2003; Köhler *et al.*, 2004). A more detailed study of the chemical processes in the p-TOMCAT model shows that net ozone production occurs only above 5 km altitude and exhibits a maximum at approximately 10 km altitude where the highest amounts of NO_x are emitted. The stratospheric ozone decrease, caused by catalytic destruction following the upward transport of aircraft NO_x into the middle stratosphere, is less pronounced in the p-TOMCAT model due to the proximity of its upper boundary at 10 hPa where O₃ values are overwritten. Additionally, the timescales of transport of aircraft emissions into the middle stratosphere are represented more appropriately by the SLIMCAT model due to the longer spin-up integration.

An increase in aircraft NO_x emissions will lead to an increase in the abundance of hydroxyl radicals (OH), principally through increased O₃ formation and by shifting the HO_x ratio in favour of OH (Poppe *et al.*, 1993). This increase in OH will lead to CH₄ perturbations which in turn influence the abundance of OH in the form of a “feedback” effect as discussed by Fuglestedt *et al.* (1999), Karlsdóttir and Isaksen (2000), IPCC (2001) *et cetera*. The response time of methane to a change in its abundance is significantly longer than its lifetime (Prather, 1994; 1996) and in order to reach steady state model integrations would have to be carried out over a time scale of decades. Fuglestedt *et al.* (1999) have described a method to calculate the steady state perturbation in CH₄ for short model integrations with altered NO_x emissions and we adopt their method for this study. In all experiments global CH₄ levels were kept constant at all times by applying a globally fixed 3-dimensional CH₄ reference distribution obtained from a long-term integration (Warwick *et al.*, 2002). The model calculates explicitly the methane loss due to tropospheric OH. Losses due to soil uptake and stratospheric sinks were assumed to have lifetimes of 160 years and 120 years, respectively (IPCC, 2001). The feedback factor of 1.30 for the p-TOMCAT model was calculated from the OH perturbation between two reference experiments with normal and with 5% increased methane levels. After steady state in CH₄ is reached global aircraft NO_x emissions from the AERO2k project have reduced the methane lifetime in the p-TOMCAT model by 2.25% with respect to tropospheric OH loss and by 1.88% with respect to all losses. This compares well with values from IPCC (1999) which calculate a reduction of 1.2–1.5% for 1992 and estimate a reduction for 2015 in the range of 1.6–2.9%. This translates into surface mixing ratios being reduced by 44–47 ppbv in the northern hemisphere and by 40–43 ppbv in the southern hemisphere. Moreover, this reduction in methane leads also to a slight decrease in ozone levels (Stevenson *et al.*, 2004), which we assume to be uniformly distributed given the long time scale for steady state to be reached. The ozone burden will be reduced by approximately 0.07% (typically 0.1–0.3 ppbv reduction in ozone in the troposphere).

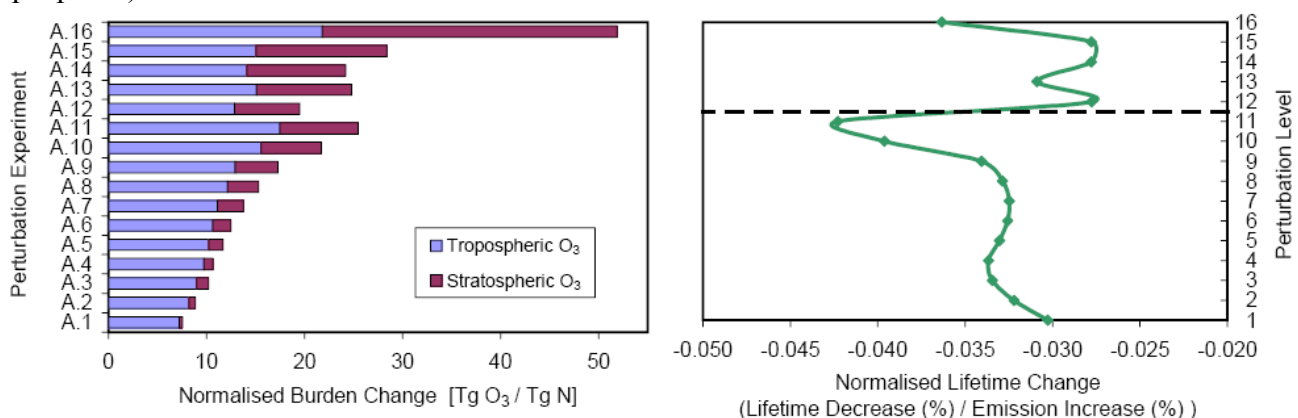


Figure 2. Global values of changes in O₃ burden (left) and CH₄ lifetime (right) due to a 5% emission increase for each perturbation level in experiment A. Values are normalised by the size of the emission perturbation.

5 CRUISE ALTITUDE SENSITIVITY OF EMISSION CHANGES

In experiment (A) emissions were locally increased by 5% on 16 PLs between 5 and 15 km altitude. This is the range where aircraft NO_x emissions were found to cause net ozone production and on all perturbation levels the emission increase resulted correspondingly in an increase of the global

ozone burden. Figure 2 (left) shows the global ozone burden change, normalised by the total amount of the emission increase. Between PL 1 and 11 the ozone burden increase becomes larger with increasing altitude of the emission perturbation, with an increasingly larger proportion of the stratospheric ozone burden being perturbed. More detailed investigations showed an increase in ozone production efficiency (Lin *et al.*, 1988) with altitude due to the increasing lifetime of NO_x at higher altitudes in the troposphere. Above PL 11 in experiments A.12–A.16 the normalised ozone burden change shows significant variation which is predominantly caused by the change in the regional distribution of the background emissions at altitudes above 12 km. At PL 1–11 the distribution of the perturbations covers a comparable geographical region, approximately 60% of the horizontal global model domain (Fig. 1). This geographical coverage becomes significantly smaller with increasing altitude for experiments above PL 11 with merely 28% coverage remaining in PL 16. Further test experiments, in which the geographical distribution of the emission perturbations is kept constant above PL 11, have shown that the normalised ozone burden continues to increase with altitude.

The impact of emission perturbations on methane lifetime has a clear dependency on the altitude where the additional NO_x is released (Figure 2, right). For perturbations applied within the upper troposphere (PL 8–11) the reduction in CH_4 lifetime is largest. Calculations of ozone production efficiency show a local maximum at this altitude range, reflecting the increase of NO_x lifetime with altitude within the troposphere. Ozone produced here is transported to lower altitudes where ambient H_2O levels are higher, such that the impact on the OH abundance and, hence, the lifetime of CH_4 is largest. For emission increases on PL 12–15 the majority of the perturbation is located within the stratosphere. Ozone produced within the lower stratosphere is inhibited from downward transport by the stability above the tropopause, moreover H_2O levels in the lower stratosphere are much smaller than in the lower troposphere. Therefore the impact on the CH_4 lifetime decreases rapidly when the emission perturbations are located within the stratosphere. On PL 16 the impact on CH_4 lifetime becomes larger. This however is an artefact of the geographical location of the emission perturbations. The local emissions increase occurs predominantly at low latitudes and a larger proportion is again released just below the tropical tropopause. Convective activity leads to more effective downward transport of ozone which explains the increased effect on CH_4 lifetime.

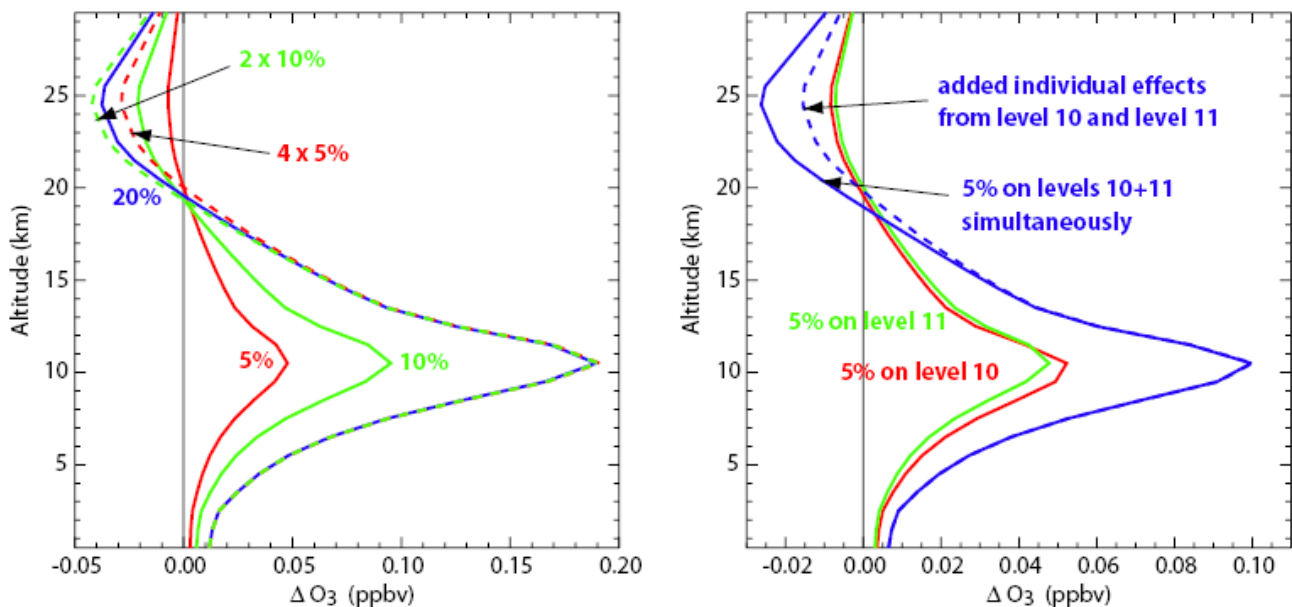


Figure 3. Changes in the vertical ozone profile near 60°N in p-TOMCAT due to a local emission increase. Emissions were scaled on PL 11 by 5%, 10%, and 20% to investigate linearity (left) and on PLs 10 and 11 to investigate additivity (right).

6 LINEAR AND ADDITIVE RESPONSE TO EMISSION CHANGES

In experiments (B) emissions were increased by 10% and 20% and the changes in ozone were compared with those from experiments (A) (5%). Figure 3 (left) shows the change in the vertical ozone profile (zonal average) at 60° N with respect to the reference experiment. The graph shows an entirely linear response of ozone levels in the troposphere and lower stratosphere from the surface to approximately 15 km. Above this threshold the lines begin to diverge which is caused by a combination of the length of the model integration and the proximity to the model's upper boundary. Note that model integrations over two years are likely to be insufficient to represent stratospheric transport timescales. Moreover the downward transport of ozone, which is kept at a constant mixing ratio at the upper model boundary, prevents the emission perturbation signal from propagating undisturbed into the middle stratosphere. In the SLIMCAT model, where the integration time was sufficiently long, linearity in the ozone response is diagnosed throughout the stratosphere. This linearity in the ozone response for emission increases between 5–20% was investigated in vertical ozone profile changes at various latitudes and globally on all model levels. At lower latitudes the point of divergence from linearity was found to be at higher altitudes compared with higher latitudes, which is attributed to more effective vertical transport of the emissions in the tropics and also to the tropopause being located at higher altitude in this region. It was found that linearity in the ozone response can be assumed with confidence between 60° N and 60° S. At higher latitudes occasional outliers of $\pm 10\%$ were found, an issue which is still under investigation. In addition to linear scaling of emissions we also investigated whether the atmospheric response is vertically additive with respect to emissions released at different cruise altitude bands (experiment C). Figure 3 (right) shows that the sum of vertical profile changes due to neighbouring perturbation levels is consistent with the profile changes caused with simultaneous emissions perturbations on both levels. Again, this consistency can be seen from the surface to 15 km. At higher altitudes the atmospheric response is no longer additive for the same reasons described above in the linearity experiments B. The response of the global ozone burden and methane lifetime to local emission scaling on all four altitude bands is shown in Figure 4. It can be clearly seen that the response in both instances is linear with the local scaling of emissions at these altitude bands in the range of 5–20%. Further experiments with a local emission increase of 200% at PL 11 have shown that to a first order approximation the ozone burden still responds linearly. This indicates that the $\text{CH}_4\text{-NO}_x\text{-O}_3$ system may respond linearly to emission increases well beyond 20%. Currently investigations are still in progress as to the extent of the linearity.

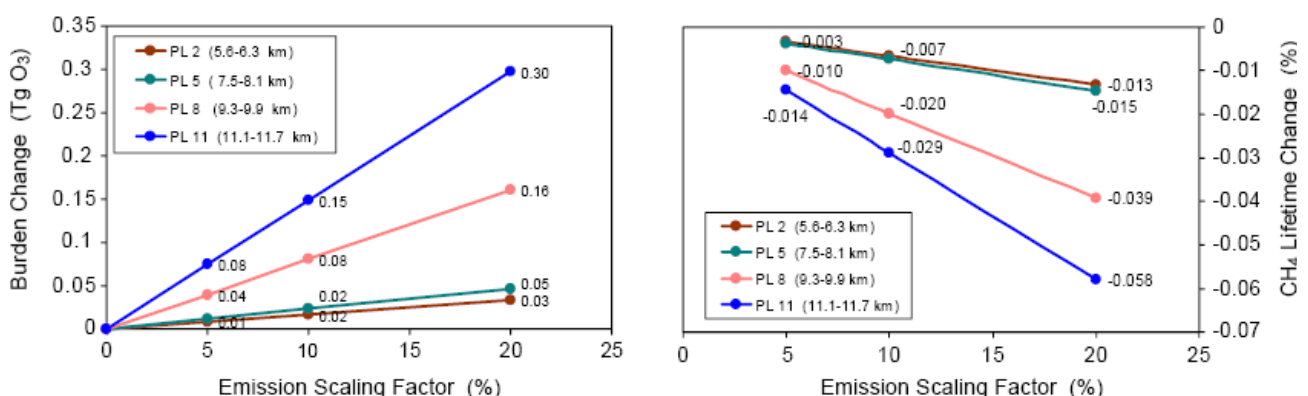


Figure 4. Global changes in ozone burden (left) and methane lifetime (right) due to a local increase in aircraft emissions by 5%, 10%, and 20% on perturbation levels 2, 5, 8, and 11.

7 CONCLUSIONS

A large number of sensitivity experiments were carried out with the 3D chemistry transport models p-TOMCAT and SLIMCAT to investigate the effects on atmospheric composition of small perturbations to aircraft emissions. The AERO2k Global Emissions Inventory has provided one of the

most realistic emission data sets available to date. The resulting impact of global NO_x and H₂O emissions on atmospheric ozone and methane was found to be within the range of results from earlier studies, specifically an increase of 6–9 ppbv in O₃ in the UTLS region and the reduction of the CH₄ lifetime by approximately 2%. With increasing altitude the ozone burden becomes more sensitive to changes in aircraft NO_x emissions. The largest increase in ozone from subsonic aircraft is found in the northern hemisphere near the tropopause. At the same time NO_x emission increases in the upper troposphere were found to result in a particularly strong decrease in the lifetime of methane. The radiative impacts of O₃ and CH₄ are opposite in sign and work on quite different regional and temporal scales due to their different atmospheric lifetimes. A companion paper by Rädcliff *et al.* (this issue) investigates further the radiative aspects of this work.

In further experiments our study has shown that the ozone and methane concentrations respond in both a linear and an additive way to local changes in emissions for the examined perturbation range of 5–20%. This linearity might apply for even larger emission perturbations, an issue which is currently still under investigation. Small inconsistencies seen in the p-TOMCAT results above the tropopause are caused by the proximity of the upper boundary and the insufficient length of the model integration to accurately represent stratospheric processes. SLIMCAT results however showed good linear behaviour also in the stratosphere. The linear relationship established by this study can be used in future work to develop a simplified parameterisation to predict changes in atmospheric composition caused by small emission changes without the need for costly model experiments. As an industrial application this parameterisation could also provide a tool to facilitate the environmental impact assessment of new aircraft during the design phase and help with the characterisation of the environmental performance of existing aircraft.

REFERENCES

- Chipperfield, M.P., 1999: Multiannual simulations with a three-dimensional chemical transport model, *J. Geophys. Res.* **104**, 1781–1805.
- Eyers, C.J., P. Norman, J. Middel, M. Plohr, S. Michot, K. Atkinson, R.A. Christou, 2004: *AERO2k Global Aviation Emissions Inventories for 2002 and 2025*. Report number QinetiQ/04/01113, QinetiQ, Farnborough, Hampshire, United Kingdom.
- Fuglestad, J.S., T.K. Berntsen, I.S.A. Isaksen, H. Mao, X.-Z. Liang, W.-C. Wang, 1999: Climatic Effects of NO_x Emissions through Changes in Tropospheric O₃ and CH₄ – A Global 3-D Model Study, *Atmos. Environ.* **33**, 961–977.
- IPCC, 1999: *Aviation and the Global Atmosphere. A Special Report of Working Groups I and III of the Intergovernmental Panel on Climate Change* [Penner, J.E., *et al.* (eds.)] Cambridge University Press, Cambridge, United Kingdom, ISBN 0-521-66404-7, 373 pp.
- IPCC, 2001: *Climate Change 2001: The Scientific Basis. Contribution of Working Group I to the Third Assessment Report of the Intergovernmental Panel on Climate Change* [Houghton, J.T. *et al.* (eds.)]. Cambridge University Press, Cambridge, United Kingdom and New York, NY, USA, ISBN 0-521-01495-6, 881 pp.
- Isaksen, I.S.A., R. Sausen, J.A. Pyle, *et al.*, 2003: The EU project TRADEOFF – Aircraft emissions: Contributions of various climate compounds to changes in composition and radiative forcing – tradeoff to reduce atmospheric impact, Project Final Report, Contract No. EVK2-CT-1999-0030, 158 pp. (available from the Department of Geosciences, University of Oslo, Oslo, Norway)
- Karlsdóttir, S., I.S.A. Isaksen, 2000: Changing methane lifetime: Possible cause for reduced growth, *Geophys. Res. Lett.* **27**, 93–96.
- Köhler, M.O., H.L. Rogers, J.A. Pyle, 2004: Modelling the Impact of Subsonic Aircraft Emissions on Ozone: Future Changes and the Impact of Cruise Altitude Perturbations. Proceedings of the European Conference on Aviation, Atmosphere and Climate (AAC), Friedrichshafen, Germany, 30 June – 3 July 2003, in: *Air pollution research report 83*, European Commission, EUR 21051, pp. 173–177.
- Lin, X., M. Trainer, S.C. Liu, 1988: On the Nonlinearity of the Tropospheric Ozone Production, *J. Geophys. Res.* **93**, 15,879–15,888.
- O'Connor, F.M., G.D. Carver, N.H. Savage, J.A. Pyle, J. Methven, S.R. Arnold, K. Dewey, J. Kent, 2005: Comparison and visualisation of high-resolution transport modelling with aircraft measurements, *Atmos. Sci. Lett.* **6**, 164–170.
- Poppe, D., M. Wallasch, J. Zimmermann, 1993: The Dependence of the Concentration of OH on its Precursors under Moderately Polluted Conditions: A Model Study, *J. Atmos. Chem.* **16**, 61–78.

- Prather, M.J., 1994: Lifetimes and eigenstates in atmospheric chemistry, *Geophys. Res. Lett.* 21, 801–804.
- Prather, M.J., 1996: Time scales in atmospheric chemistry: Theory, GWPs for CH₄ and CO, and runaway growth, *Geophys. Res. Lett.* 23, 2597–2600.
- Savage, N.H, K.S. Law, J.A. Pyle, A. Richter, H. Nuss, J.P. Burrows, 2004: Using GOME NO₂ satellite data to examine regional differences in TOMCAT model performance, *Atmos. Chem. Phys.* 4, 1895–1912.
- Warwick, N.J., S. Bekki, K.S. Law, E.G. Nisbet, J.A. Pyle, 2002: The impact of meteorology on the interannual growth rate of atmospheric methane, *Geophys. Res. Lett.* 29, 1947, doi:10.1029/2002GL015282.

Multi-model Simulations of the Impact of International Shipping on Atmospheric Chemistry and Climate in 2000 and 2030

V. Eyring^{*}, A. Lauer

DLR - Institut für Physik der Atmosphäre, Oberpfaffenhofen, 82234 Wessling, Germany

D.S. Stevenson

University of Edinburgh, School of GeoSciences, Edinburgh, United Kingdom.

F.J. Dentener

European Commission, Joint Research Centre, Institute for Environment and Sustainability, Ispra, Italy.

T. Butler, M.G. Lawrence

Max Planck Institute for Chemistry, Mainz, Germany.

W.J. Collins, M. Sanderson

Met Office, Exeter, United Kingdom.

K. Ellingsen, M. Gauss, I.S.A. Isaksen

University of Oslo, Department of Geosciences, Oslo, Norway.

D.A. Hauglustaine, S. Szopa

Laboratoire des Sciences du Climat et de l'Environnement, Gif-sur-Yvette, France.

A. Richter

Institute of Environmental Research, University of Bremen, 28359 Bremen, Germany

J.M. Rodriguez, S.E. Strahan

Goddard Earth Science & Technology Center (GEST), Maryland, Washington, DC, USA.

K. Sudo, O. Wild

Frontier Research Center for Global Change, JAMSTEC, Yokohama, Japan.

T.P.C. van Noije

Royal Netherlands Meteorological Institute (KNMI), Atmospheric Composition Research, De Bilt, the Netherlands.

Keywords: international shipping, global modelling, tropospheric ozone, sulphate, radiative forcing

ABSTRACT: The global impact of shipping on atmospheric chemistry and radiative forcing, as well as the associated uncertainties, have been quantified using an ensemble of ten state-of-the-art atmospheric chemistry models and a pre-defined set of emission data. The analysis is performed for present-day conditions (year 2000) and for two future ship emission scenarios. In one scenario emissions stabilize at 2000 levels; in the other emissions increase with a constant annual growth rate of 2.2% up to 2030 (termed the 'Constant Growth Scenario'). The first key question addressed by this study is how NO_x and SO₂ emissions from international shipping might influence atmospheric chemistry in the next three decades if these emissions increase unabated. The models show future increases in NO₂ and ozone burden which scale almost linearly with increases in NO_x emission totals. For the same ship emission totals but higher emissions from other sources a slightly smaller response is found. The most pronounced changes in annual mean tropospheric NO₂ and sulphate columns are simulated over the Baltic and North Seas; other significant changes occur over the North Atlantic, the Gulf of Mexico and along the main shipping lane from Europe to Asia, across the Red and Arabian Seas. The second key issue was to examine the range of results given by the individual models compared to the ensemble mean. Uncertainties in the different model ap-

^{*} *Corresponding author:* Dr. Veronika Eyring, DLR-Institut für Physik der Atmosphäre, Oberpfaffenhofen, 82234 Wessling, Germany. Email: Veronika.Eyring@dlr.de

proaches in the simulated ozone contributions from ships are found to be significantly smaller than estimated uncertainties stemming from the ship emission inventory, mainly the ship emission totals, the neglect of ship plume dispersion, and the distribution of the emissions over the globe.

1 INTRODUCTION

Emissions from international shipping contribute significantly to the total budget of anthropogenic emissions from the transportation sector (Eyring et al., 2005) and have been recognized as a growing problem by both policymakers and scientists (Corbett, 2003). Here we use an ensemble of ten state-of-the-art global atmospheric chemistry models to assess the impact of NO_x emissions from international shipping on ozone for present-day conditions (year 2000). A subset of four models has been applied to investigate the changes in sulphate distributions due to SO₂ emissions from international shipping. This multi-model approach accounts for intermodel differences and therefore makes the results more robust compared to previous studies based on single models (e.g., Lawrence and Crutzen, 1999; Endresen et al., 2003). In addition, this study for the first time quantifies the potential impact of ship emissions in the future (year 2030) for two different future ship emission scenarios. The participating models have also been evaluated and used in accompanying studies (e.g. Stevenson et al., 2006; Dentener et al., 2006; Shindell et al., 2006, van Noije et al., 2006) as part of the European Union project ACCENT ('Atmospheric Composition Change: the European NeTwork of excellence'; <http://www.accent-network.org>). Full details of this study are given in Eyring et al. (2006) and only a brief summary is presented here.

2 MODELS AND MODEL SIMULATIONS

Ten global atmospheric chemistry models have participated in this study. Seven of these models are Chemistry-Transport Models (CTMs) driven by meteorological assimilation fields and three models are atmospheric General Circulation Models (GCMs). Two of the GCMs are driven with the dynamical fields calculated by the GCM in climatological mode, but the fully coupled mode (interaction between changes in radiatively active gases and radiation) has been switched off in the simulations of this study. The other GCM runs in nudged mode, where winds and temperature fields are assimilated towards meteorological analyses. Therefore, changes in the chemical fields do not influence the radiation and hence the meteorology in any of the model simulations used here; so for a given model, each scenario is driven by identical meteorology. The main characteristics of the ten models can be found in Table 1 of Eyring et al. (2006) and the models are described in detail in the cited literature.

Two of the five simulations that have been defined as part of the wider PHOTOCOMP-ACCENT-IPCC study have been used in this work: a year 2000 base case (S1) and a year 2030 emissions case (S4) following the IPCC (Intergovernmental Panel on Climate Change) SRES (Special Report on Emission Scenarios) A2 scenario (Nakicenovic et al., 2000). Full details on the emissions used in the S1 and S4 simulations are summarised in Stevenson et al. (2006). To retain consistency with all other emissions, ship emissions in the year 2000 (S1) are based on the EDGAR3.2 dataset (Olivier et al., 2001) at a spatial resolution of 1° latitude x 1° longitude. The global distribution of ship emissions in EDGAR3.2 is based on the world's main shipping routes and traffic intensities. EDGAR3.2 includes data for 1995, which have been scaled to 2000 values assuming a growth rate of 1.5%/yr, resulting in annual NO_x and SO₂ emissions of 3.10 Tg(N) and 3.88 Tg(S), respectively, similar to the emission totals published by Corbett et al. (1999). As noted in Stevenson et al. (2006) in the S4 simulation emissions from ships were included at year 2000 levels by mistake. All other anthropogenic sources (except biomass burning emissions, which remain fixed at year 2000 levels) vary according to A2 broadly representing a 'pessimistic' future situation. The simulation S4 is used in this study to assess the impact of ship emissions under different background levels. An additional model simulation for 2030 (S4s) has been designed to assess the impact of shipping if emission growth remains unabated. Ship emissions in S4s are based on a 'Constant Growth Scenario' in which emission factors are unchanged and emissions increase with an annual growth rate of 2.2% between 2000 and 2030. Vessel traffic distributions are assumed to stay

the same for all model simulations presented here. Full details on the model simulations and model analyses are given in Eyring et al. (2006).

3 RESULTS

For present-day conditions the most pronounced changes in annual mean tropospheric NO_2 and SO_4 columns are found over the Baltic and the North Sea, and also though smaller over the Atlantic, Gulf of Mexico, and along the main shipping lane from Europe to Asia. Maximum near-surface ozone changes due to NO_x ship emissions are simulated over the North Atlantic in July (~ 12 ppbv) in agreement with previously reported results (Lawrence and Crutzen, 1999; Endresen et al., 2003). However, in contrast to Endresen et al. (2003), a decrease in ozone in winter is found over large areas in Europe (~ 3 ppbv) due to titration (see Figure 1). Overall NO_x emissions most effectively produce ozone over the remote ocean, where background NO_x levels are small.

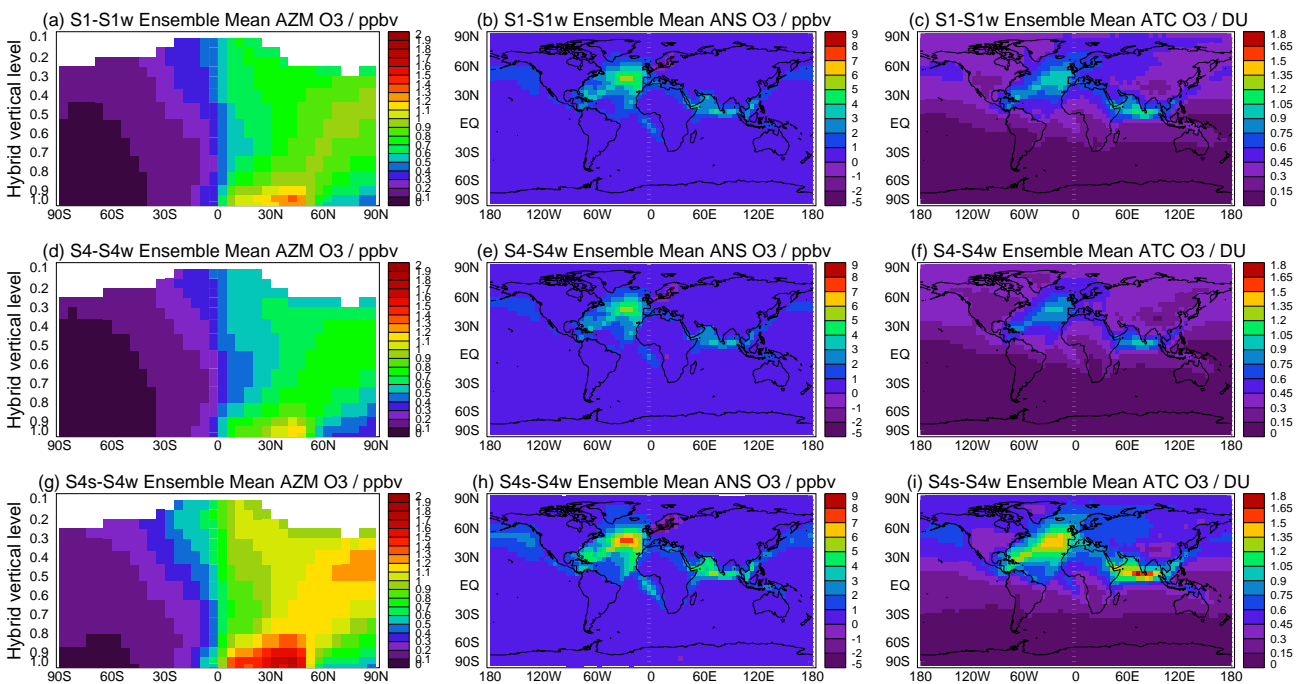


Figure 1: Modelled ensemble mean ozone change between (a-c) case S1 (year 2000) and S1w (year 2000 without ship emissions), (d-f) case S4 (year 2030) and S4w (year 2030 without ship emissions), and (g-i) case S4s (year 2030) and S4w. Figure 1a, 1d, and 1g are zonal mean changes (ppbv), Figures 1b, 1e, and 1h are near-surface ozone changes (ppbv) and Figure 1c, 1f, and 1i are tropospheric ozone column changes (DU). From Eyring et al. (2006).

The two 2030 scenarios both specify emissions following the IPCC SRES A2 scenario (Nakicenovic et al., 2000). The first future scenario assumes that ship emissions remain constant at 2000 levels and under this scenario a slightly smaller response in ozone and sulphate changes due to shipping is found compared to the present-day contribution from shipping. This indicates that higher background levels tend to slightly reduce the perturbation from ships. The second emission scenario addresses the question of how NO_x and SO_2 emissions from international shipping might influence atmospheric chemistry in the next three decades if these emissions grow unabated and one assumes a constant annual growth rate of 2.2% between 2000 and 2030 ('Constant Growth Scenario'). The models show future increases in NO_x and ozone burden which scale almost linearly with increases in NO_x emission totals under the same background conditions (see Figure 2).

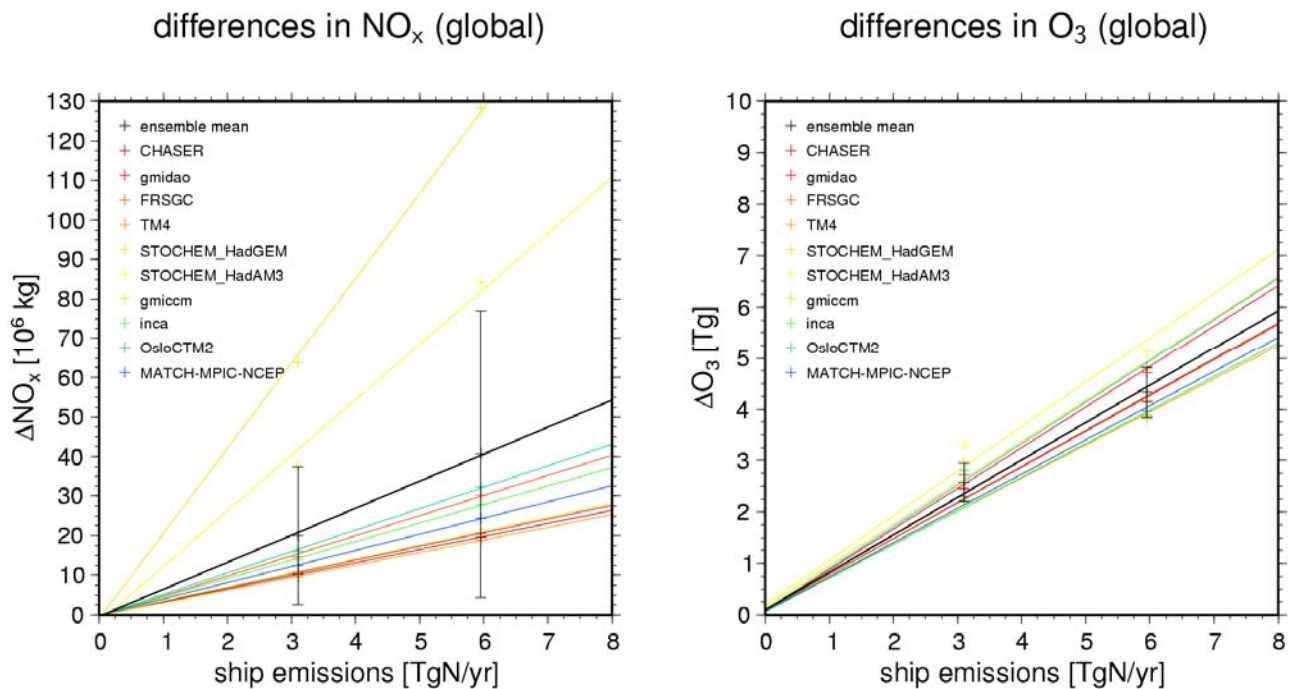


Figure 2. Global total change in annual mean tropospheric NO_x burden (left) and ozone burden (right) due to ship emissions (S4-S4w and S4s-S4w) in each individual model (coloured lines) and the ensemble mean (black line). Inter-model standard deviations are shown as bars. From Eyring et al. (2006).

Therefore, there is evidence that the ship NO_x effect is only weakly subject to saturation in its current magnitude range, and that saturation cannot be expected to help mitigate the effects of near-future increases. In other words a doubling of NO_x emissions from ships in the future might lead to a doubling in atmospheric ozone burdens due to ship emissions. In addition, increasing emissions from shipping would significantly counteract the benefits derived from reducing SO₂ emissions from all other anthropogenic sources under the A2 scenario over the continents for example in Europe. Under the ‘Constant Growth Scenario’ shipping globally contributes with 3% to increases in ozone burden until 2030 and with 4.5% to increases in sulphate. The results discussed above are calculated under the assumption that all other emissions follow the A2 scenario broadly representing a ‘pessimistic’ future situation. However, if future ground based emissions follow a more stringent scenario, the relative importance of ship emissions becomes larger.

Tropospheric ozone forcings due to ships of 9.8 mW/m² in 2000 and 13.6 mW/m² in 2030 are simulated by the ensemble mean, with standard deviations of 10-15%. Compared to aviation (~ 20 mW/m²; Sausen et al., 2005) tropospheric ozone forcings from shipping are of the same order in 2000, despite the much higher NO_x emissions from ships (Eyring et al., 2005). This can be understood because peak changes in ozone due to shipping occur close to the surface, whereas changes in ozone due to aviation peak in the upper troposphere. A rough estimate of RF from shipping CO₂ suggests 26 mW/m² in 2000 compared to 23 mW/m² from aviation CO₂. The direct aerosol effect resulting from SO₂ ship emissions is approximately -14 mW/m² in 2000 and decreases to a more negative value of -26 mW/m² in 2030 under the ‘Constant Growth Scenario’.

We have also investigated the range of results given by the individual models compared to other uncertainties. Uncertainties in the simulated ozone contributions from ships for the different model approaches revealed by the intermodel standard deviations are found to be significantly smaller than estimated uncertainties stemming from the ship emission inventory, mainly the ship emission totals, the neglect of ship plume dispersion, and the distribution of the emissions over the globe. This reflects that the simulated net change from ship emissions under otherwise relatively clean conditions in global models is rather similar and shows that the atmospheric models used here are suitable tools to study these effects.

4 SUMMARY

Maximum contributions from shipping to annual mean near-surface ozone quantified from an ensemble of ten state-of-the-art atmospheric chemistry models and a pre-defined set of emission data are found over the Atlantic (5-6 ppbv in 2000 reaching up to 8 ppbv in the 2030 Constant Growth Scenario). Large increases in tropospheric ozone column are found over the Atlantic and even stronger over the Indian Ocean (1 DU in 2000 and up to 1.8 DU in 2030). Tropospheric ozone forcings due to shipping are $9.8 \pm 2.0 \text{ mW/m}^2$ in 2000 and $13.6 \pm 2.3 \text{ mW/m}^2$ in 2030. Whilst increasing ozone, ship NO_x simultaneously enhances OH, reducing the CH_4 lifetime by 0.13 yr in 2000, and by up to 0.17 yr in 2030, introducing a negative radiative forcing. Over Europe, the increase in ship emissions under the 'Constant Growth Scenario' will enhance the positive trend in NO_2 over land up to 2030. In addition, efforts to lower European sulphate levels through reductions in SO_2 emissions from anthropogenic sources on land will be partly counteracted by the rise in ship emissions. Globally, shipping contributes with 3% to increases in ozone burden until 2030 and with 4.5% to increases in sulphate. The results discussed above are calculated under the assumption that all other emissions follow the IPCC SRES A2 scenario. However, if future ground based emissions follow a more stringent scenario, the relative importance of ship emissions becomes larger. The range of results given by the individual models compared to other uncertainties has also been investigated. Uncertainties in the simulated ozone contributions from ships for the different model approaches revealed by the intermodel standard deviations are found to be significantly smaller than estimated uncertainties stemming from the ship emission inventory, mainly the ship emission totals, the neglect of ship plume dispersion, and the distribution of the emissions over the globe. This reflects that the simulated net change from ship emissions under otherwise relatively clean conditions in global models is rather similar and shows that the atmospheric models used here are suitable tools to study these effects. Full details of this study can be found in Eyring et al. (2006).

ACKNOWLEDGEMENTS

Co-ordination of this study was supported by the European Union project ACCENT ('Atmospheric Composition Change: the European NeTwork of excellence'. <http://www.accent-network.org>). The study has also been supported by the Helmholtz-University Young Investigators Group SeaKLIM, which is funded by the German Helmholtz-Gemeinschaft and the Deutsches Zentrum für Luft- und Raumfahrt e.V. (DLR).

REFERENCES

- Corbett, J., 2003: New Directions: Designing ship emissions and impacts research to inform both science and policy, *Atmospheric Environment*, 37, 4719-4721.
- Corbett, J.J., P.S. Fischbeck, and S.N. Pandis, 1999: Global nitrogen and sulfur inventories for oceangoing ships, *J. Geophys. Res.*, 104(3), 3457-3470.
- Dentener, F., D.S. Stevenson, K. Ellingsen, T. van Noije, M. Schultz, et al., 2006: Nitrogen and sulphur deposition on regional and global scales: A multi-model evaluation, *Global Biogeochemical Cycles*, accepted.
- Endresen, Ø., E. Sørgård, J.K. Sundet, S.B. Dalsøren, I.S.A. Isaksen, T.F. Berglen, and G. Gravir, 2003: Emission from international sea transportation and environmental impact, *J. Geophys. Res.* 108, 4560, doi:10.1029/2002JD002898.
- Eyring, V., H.W. Köhler, J. van Aardenne, and A. Lauer, 2005: Emissions from international shipping: 1. The last 50 years, *J. Geophys. Res.*, 110, D17305.
- Eyring, V., D.S. Stevenson, A. Lauer, F.J. Dentener, T. Butler, W.J. Collins, K. Ellingsen, M. Gauss, D.A. Hauglustaine, I.S.A. Isaksen, M.G. Lawrence, A. Richter, J.M. Rodriguez, M. Sanderson, S.E. Strahan, K. Sudo, S. Szopa, T.P.C. van Noije, and O. Wild, 2006: Multi-model simulations of the impact of international shipping on atmospheric chemistry and climate in 2000 and 2030, *Atmos. Chem. Phys. Discuss.*, 6, 8553-8604.
- Lawrence, M.G., and P.J. Crutzen, 1999: Influence of NO_x emissions from ships on tropospheric photochemistry and climate, *Nature*, 402, 167-170.

- Nakicenovic, N., et al., 2000: IPCC Special Report on Emissions Scenarios, Cambridge University Press, Cambridge, UK, 570 pp.
- Olivier, J.G.J., and J.J.M. Berdowski, 2001: Global emissions sources and sinks, in *The climate system*, edited by J.J.M. Berdowski, R. Guicherit, and B.J. Heij, A.A. Balkema Publishers/Swets & Zeitlinger Publishers, Lisse, the Netherlands.
- Sausen, R., I.S.A. Isaksen, V. Grewe, D.A. Hauglustaine, D.S. Lee, G. Myhre, M.O. Köhler, G. Pitari, U. Schumann, F. Stordal, and C. Zerefos, 2005: Aviation radiative forcing in 2000: An update on IPCC (1999), *Meteorol. Z.*, 14, 555-561.
- Shindell, D.T., G. Faluvegi, D.S. Stevenson, L.K. Emmons, J.-F. Lamarque, G. Pétron, F.J. Dentener, K. Ellingsen, et al., 2006: Multi-model simulations of carbon monoxide: Comparison with observations and projected near-future changes, *J. Geophys. Res.*, in press.
- Stevenson, D.S., F.J. Dentener, M.G. Schultz, K. Ellingsen, T.P.C. van Noije, O. Wild, G. Zeng, et al., 2006: Multimodel ensemble simulations of present-day and near-future tropospheric ozone, *J. Geophys. Res.*, 111, D08301, doi:10.1029/2005JD006338.
- van Noije, T.P.C., H.J. Eskes, F.J. Dentener, D.S. Stevenson, K. Ellingsen, M.G. Schultz, O. Wild, et al., 2006: Multi-model ensemble simulations of tropospheric NO₂ compared with GOME retrievals for the year 2000, *Atmos. Chem. Phys.*, 6, 2943-2979.

Natural versus man-made trends in cirrus clouds

Kostas Eleftheratos^{*}, Christos S. Zerefos
Laboratory of Climatology & Atmospheric Environment, University of Athens, Greece

Prodromos Zanis
Research Centre for Atmospheric Physics & Climatology, Academy of Athens, Greece

George Tselioudis
Goddard Institute for Space Studies, NASA, USA

Keywords: Cirrus clouds, ENSO, NAO

ABSTRACT: The seasonal variability and the interannual variance explained by ENSO and NAO to cirrus cloud cover (CCC) are examined during the twenty-year period 1984–2004. Although the annual cycle is dominant in all latitudes and longitudes, peaking over the tropics and subtropics, its amplitude can be exceeded during strong El Nino/La Nina events. Over the eastern tropical Pacific Ocean the interannual variance of CCC which can be explained by ENSO is about 6.8% and it is ~2.3 times larger than the amplitude of the annual cycle. Natural long-term trends in the tropics are generally small (about –0.3% cloud cover per decade) and possible manmade trends in those regions are also small. The contributions of NAO and QBO to the variance of CCC in the tropics are also small. In the northern mid-latitudes, on the other hand, the effect of NAO is more significant and can be very important regionally. Over northern Europe and the eastern part of the North Atlantic Flight Corridor (NAFC) there is a small positive correlation between CCC and NAO index during the wintertime of about 0.3. In this region, the interannual variance of CCC explained by NAO is 2.6% and the amplitude of the annual cycle is 3.1%. Long-term trends over this region are about +1.6% cloud cover per decade and compare well with the observed manmade trends over congested air traffic regions in Europe and the North Atlantic as have been evidenced from earlier findings.

1 INTRODUCTION

Large-scale natural fluctuations such as the El Nino/Southern Oscillation (ENSO) and North Atlantic Oscillation (NAO) are known to alter the distribution and natural variability of various atmospheric parameters (i.e. temperature, precipitation) including cloudiness. Their impact, however, on the natural variability of cirrus clouds is less well quantified and much less it is known about the relative roles of long-term manmade (aviation) trends and natural variability.

Previous studies examining the effects of El Nino on upper tropospheric cirrus have based their results on observations by satellites from space (Sandor et al., 2000; Massie et al., 2000; Cess et al. 2001). Massie et al. (2000) analysed geographical distributions of aerosol extinction data in the troposphere and stratosphere for 1993–1998 from the Halogen Occultation Experiment (HALOE) and showed that during El Nino conditions of 1997 upper tropospheric cirrus increased over the mid-Pacific and decreased over Indonesia. More recently, Wang et al. (2003) examined the characteristics of cloud distributions with emphasis on cloud longwave radiative forcing during the peak of the 1997/1998 El Nino in relation to climatological conditions, based on SAGE II measurements. Their results indicated above-normal high-altitude opaque cloud occurrence over the eastern tropical Pacific and an opposite situation over the Pacific warm pool, generally consistent with the pattern of the tropical sea surface temperature and precipitation anomalies.

In the present study we calculate the percent of the interannual variance of CCC, caused by ENSO, NAO and long-term trends. The results are also compared with observed long-term trends

^{*} *Corresponding author:* Kostas Eleftheratos, Laboratory of Climatology & Atmospheric Environment, Faculty of Geology & Geoenvironment, University of Athens, 15784, Athens, Greece. Email: kelef@geol.uoa.gr

in CCC over congested air traffic regions in Europe and the North Atlantic (Zerefos *et al.*, 2003; Stordal *et al.*, 2005; Stubenrauch and Schumann, 2005) to evaluate the significance of the anthropogenic (aviation) effect with respect to the natural variability.

2 DATA SOURCES AND METHODOLOGY

The cloud dataset analyzed in this study was produced by the International Satellite Cloud Climatology Project (ISCCP) (Rossow and Schiffer, 1999) and covers the period 1984–2004. Cirrus clouds are defined as those with optical thickness less than 3.6 and cloud top pressure less than 440 mb. In order to avoid artificial satellite cloud retrievals after the Mt. Pinatubo eruption in 1991 (Luo *et al.*, 2002) cirrus cloud data taken in 1991 and 1992 were not used in our analysis.

The effect of ENSO on cirrus clouds has been examined by linear regression analysis between monthly mean CCC and Southern Oscillation Index (SOI) in the examined 21–years period. The occurrence of decadal–scale changes in cloud frequency in the tropics (Wang *et al.*, 2002) could affect our correlation analysis if they were not taken into account. In order to avoid possible effects from decadal changes in cloud occurrence in the tropics, we first removed from cirrus coverage variability related to the seasonal cycle and long–term trends for the period 1984–2004 based on the following regression model:

$$CCC(i, j) = S(i, j) + T(i, j) + residuals \quad (1)$$

Where i denotes the month and j is the year of CCC and its components, i.e., the seasonal (S) and the long–term trend (T). CCC data were deseasonalized by subtracting the long–term monthly mean (1984–2004) pertaining to the same calendar month. The residuals from Equation (1) were used as input for the correlation analysis between the anomalies of CCC and SOI. The correlation between CCC and NAO index has been computed for the winter–months (December, January and February) over Europe and the North Atlantic.

3 RESULTS AND DISCUSSION

After removing from the time series of cirrus coverage the variability related to the seasonal cycle and long–term trends, ENSO signals become dominant over the eastern and western tropical Pacific Ocean, determining a significant part of the cirrus cloud interannual natural variability. Figure 1 shows the correlation coefficients between the deseasonalized and detrended time series of CCC and SOI from 60°N to 60°S. Negative correlation suggests large amounts of thin cirrus clouds during warm (El Nino) episodes and positive correlation their absence. More analytically, Figure 2 shows the time series of the anomalies of CCC from 1984 to 2004 versus SOI over (a) the eastern tropical Pacific region (10°S–10°N, 80°W–180°W) and (b) the western tropical Pacific region (10°S–10°N, 80°E–150°E). From Figure 2 it appears that CCC is strongly anti–correlated with SOI over eastern Pacific ($R = -0.7$) and positively correlated ($R = +0.6$) over its western part, which practically confirms the correlation map of Figure 1. The two correlation coefficients are statistically significant at the 99% confidence level and suggest that southern oscillation and its associated events (warm and cold) play key roles in the distribution and appearance of thin cirrus clouds over these locations, explaining about one third to half of their large–scale natural variability.

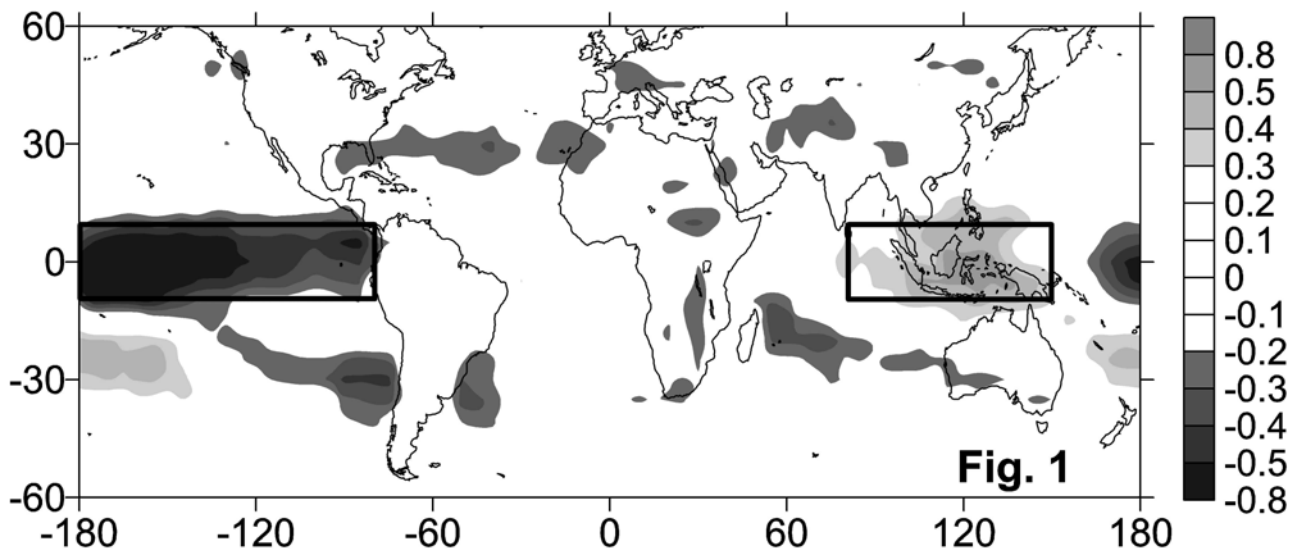


Figure 1. Correlation coefficients between CCC anomalies and SOI from January 1984 to December 2004 in the region (60°N–60°S). Only correlation coefficients above/below ± 0.3 are shown.

The percent of the interannual variance of CCC explained by ENSO over the two locations was investigated by reconstructing the time series of CCC from SOI, based on the following linear regression model:

$$a \times SOI(i, j) + b = \text{reconstructed CCC}(i, j) \quad (2)$$

Where a is the slope and b is the intercept of the correlation analysis between the deseasonalized and detrended time series of CCC and SOI. The reconstructed time series of CCC at the two locations is shown in Figure 2 by the lines with grey colour. Although the annual cycle is dominant in all latitudes and longitudes, peaking over the tropics and subtropics, its amplitude can be exceeded under circumstances of strong El Niño/La Niña events. More specifically, over the eastern tropical Pacific Ocean the annual mean CCC is 12.5% and the amplitude of the annual cycle is 3%. This means that CCC can range between 15.5% and 9.5%. However, this amplitude can be exceeded during strong ENSO episodes. As can be seen from Figure 2, during El Niño 1986/87, La Niña 1988/89 and El Niño 1997/98 the interannual variance of CCC explained by ENSO is 6.8% and it is about 2.3 times larger than the amplitude of the annual cycle. Accordingly, over the western part of the tropical Pacific the interannual variance of CCC explained by ENSO is 5.9%, which is about 2.4 times larger than the amplitude of the annual cycle.

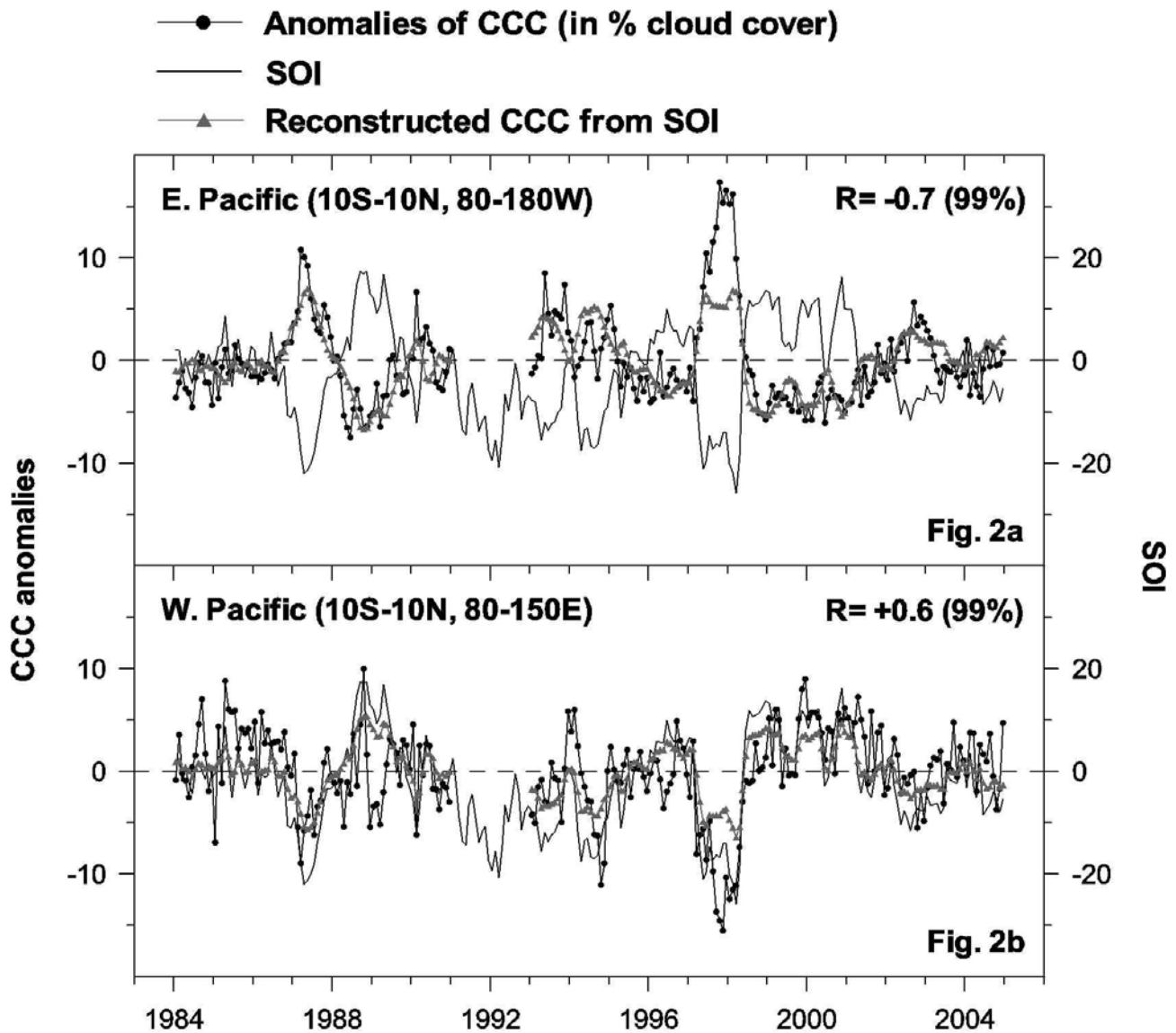


Figure 2. (a) Time series of CCC anomalies from 1984 to 2004 and of SOI over the eastern tropical Pacific (10°S – 10°N , 80°W – 180°W). (b) Same as (a) but for the western tropical Pacific (10°S – 10°N , 80°E – 150°E). The lines with grey colour indicate the interannual variance of CCC explained by ENSO (in %).

The other natural oscillation that has been examined as to its effect on CCC is the North Atlantic Oscillation (NAO). As it is known, NAO has two phases; a positive and a negative phase. To study its effect, Figure 3 shows the correlation coefficients between the deseasonalized and detrended time series of CCC and NAO index during the wintertime (December, January and February) in the region bounded by latitudes 15°N – 65°N and by longitudes 120°W – 80°E . The positive correlations between CCC and NAO index are shown by light grey colours whereas the negative correlations by dark grey colours. The dotted line in Figure 3 bounds the regions where the correlation coefficients are statistically significant at the 95% confidence level (Student's *t*-test).

As can be seen from Figure 3, the correlation coefficients of CCC with NAO index consist of negative correlations over regions extending from the eastern part of the North Atlantic to the Mediterranean (up to -0.5 at some locations) and positive correlations over northern Europe and the eastern part of NAFC, explaining part of the cirrus cloud long-term natural variability. Over these regions, the correlation coefficients are statistically significant at the 95% confidence level and compare well with those observed between VV300 and NAO (not shown here). The negative correlations over the eastern part of North Atlantic and the Mediterranean (25°N – 40°N , 30°W – 20°E) could suggest that when the NAO index is positive, CCC is lower than normal in the area, possibly due to enhanced sinking of air masses in the area caused by a stronger than usual high pressure system at Azores while less frequent west-east advection of moisture and more cold and dry air pene-

trations from north to southeast Europe is taking place. As we move to the north, the correlation coefficients over northern Europe and the eastern part of NAFC (50°N–65°N, 20°W–10°E) are less statistically significant and cover a smaller area when compared to those between VV300 and NAO (not shown here). Possibly, this could be explained by the fact that during the wintertime there are limited satellite cloud observations by ISCCP over 57°, and in that case our correlation results over 57° are likely to be underestimated. However, it should be considered that other factors i.e. existence of complicated weather conditions and high natural cloud variability during the wintertime in the area may also mask this issue.

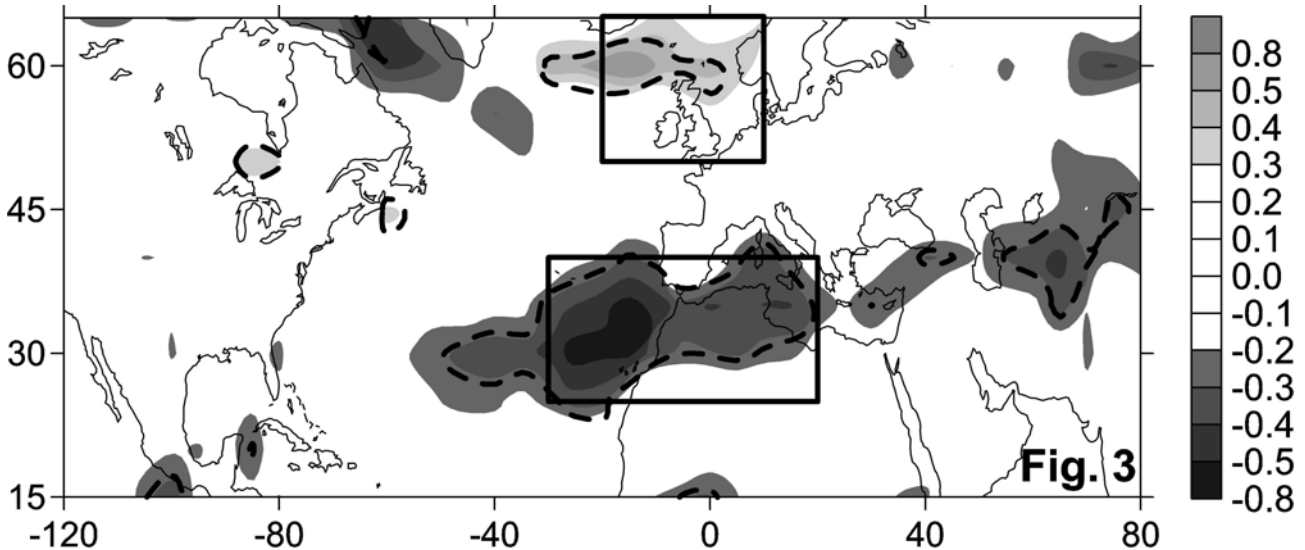


Figure 3. Correlation coefficients between CCC anomalies from 1984 to 2004 and NAO index during the wintertime (December, January and February) in the region (15°N–65°N, 120°W–80°E).

Figure 4 shows the time series of the anomalies of CCC from 1984 to 2004 versus NAO index during the wintertime over (a) the eastern part of the North Atlantic and the Mediterranean (25°N–40°N, 30°W–20°E) and (b) northern Europe and the eastern part of NAFC (50°N–65°N, 20°W–10°E). From Figure 4 it appears that CCC is anti-correlated with NAO index over the eastern part of the North Atlantic and the Mediterranean ($R = -0.5$, significant at the 95% confidence level) and positively correlated over northern Europe and the eastern part of NAFC ($R = +0.3$, significant at the 90% confidence level), confirming the correlation results of Figure 3.

As in the case of ENSO, we also calculated the percent of the interannual variance of CCC explained by NAO over the two regions by reconstructing the time series of CCC from NAO index based on Equation (2). The reconstructed time series of CCC at the two locations is shown in Figure 4 by the lines with grey colour. More specifically, over the eastern part of the North Atlantic and the Mediterranean (25°N–40°N, 30°W–20°E) the amplitude of the annual cycle of CCC is 3.6% and the interannual variance of CCC explained by NAO is up to 2.4%. Accordingly, over northern Europe and the eastern part of NAFC (50°N–65°N, 20°W–10°E) the interannual variance of CCC explained by NAO is up to 2.6% and it is also smaller than the amplitude of the annual cycle (3.1% cloud cover). Therefore, in northern mid-latitudes the percent of the interannual variance of CCC explained by NAO does not exceed the amplitude of the annual cycle.

Furthermore, to evaluate the significance of the anthropogenic (aviation) effect with respect to the natural variability we have compared our results with manmade long-term trends over Europe and the NAFC as evidenced from earlier studies (Zerefos *et al.*, 2003; Stordal *et al.*, 2005; Stubenrauch and Schumann, 2005). According to Sausen *et al.* (1998), at altitude levels around 300 hPa regions that are susceptible to the formation of contrails are located more in the extra-tropics than over the tropics. Over Europe and the NAFC, flight frequencies and flight consumption are high (shown, for example, in Fig. 1 of Zerefos *et al.*, 2003) and situations favourable for contrail formation have been estimated to occur about 7% over Europe and 5% over the NAFC (Stubenrauch and Schumann, 2005). Therefore, over Europe and the NAFC it is possible that cirrus amounts may also include persistent contrails and therefore the cirrus trends can be explained not only by natural long-term variability, but also by variability in manmade cirrus contrails. According to our find-

ings, long-term CCC trends in the region (50°N – 65°N , 20°W – 10°E) are about +1.6% per decade. These positive trends are statistically significant at the 95% confidence level and compare well with the observed positive manmade trends in cirrus clouds over congested air traffic regions in Europe and the North Atlantic (Zerefos et al 2003; Stordal et al., 2005; Stubenrauch and Schumann, 2005).

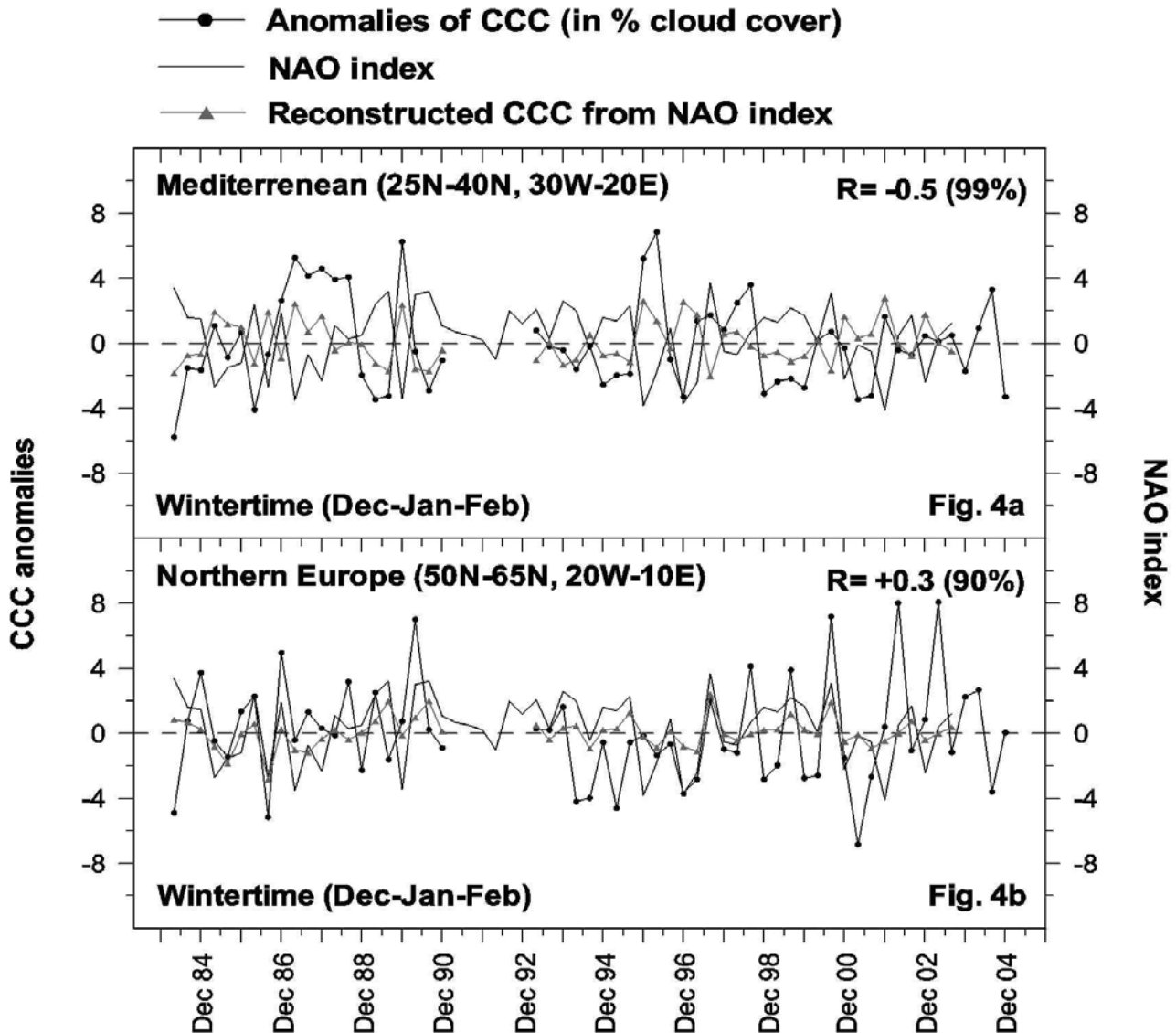


Figure 4. (a) Time series of CCC anomalies and NAO index from 1984 to 2004 during the wintertime (December, January and February) over the eastern part of the North Atlantic and the Mediterranean (25°N – 40°N , 30°W – 20°E). (b) Same as (a) but for northern Europe and the eastern part of NAFC (50°N – 65°N , 20°W – 10°E). The lines with grey colour indicate the interannual variance of CCC explained by NAO (in %).

4 CONCLUSIONS

This study analysed globally cirrus cloud data from ISCCP D2 1984–2004 dataset and calculated the percent of the interannual variance of CCC explained by ENSO, NAO and QBO. The major findings and conclusions can be summarized as follows:

The variability of cirrus clouds is different over different geographical regions and originates from different causes. Although the annual cycle is dominant in all latitudes and longitudes, peaking over the tropics and subtropics, its amplitude is exceeded during strong El Niño/La Niña events. Over the eastern tropical Pacific Ocean (10°N – 10°S , 80°W – 180°W) the annual mean CCC is 12.5% and the amplitude of the annual cycle is 3%. However during ENSO, the interannual variance of CCC explained by ENSO is 6.8% and it is about 2.3 times larger than the amplitude of the annual cycle at these regions. The effects of NAO and QBO on natural cirrus cloudiness in the tropics were

found to be small. Natural long-term trends in CCC in the tropics and subtropics are generally small (between -0.3% and -0.7% per decade) excluding the south extra tropics where no trends have been observed. Possible manmade trends in the tropics are small.

In the northern mid-latitudes, on the other hand, the effect of NAO is more significant and can be very important regionally. More specifically, over the region bounded by latitudes 25°N – 40°N and by longitudes 30°W – 20°E (eastern part of the North Atlantic and the Mediterranean) cirrus clouds are negatively correlated with NAO index during the wintertime by about -0.5 . Over the region between 50°N – 65°N and 20°W – 10°E (northern Europe and the eastern part of NAFC) the correlation is positive ($+0.3$). Over northern Europe and the eastern part of NAFC the percent of the interannual variance of CCC which is explained by NAO is $\sim 2.6\%$ and it is smaller than the amplitude of the annual cycle (3.1% cloud cover). QBO and ENSO were not found to be significantly correlated with variations in cirrus clouds in the northern mid-latitudes. The general trends in large-scale CCC over the northern mid-latitudes are according to ISCCP negative (-0.4% per decade).

In the region (50°N – 65°N , 20°W – 10°E) (northern Europe and the eastern part of NAFC) cirrus clouds may also include persistent contrails and therefore cirrus trends in those regions can be explained not only by natural long-term variability, but also by variability in manmade cirrus contrails. Over these regions, long-term trends in CCC are about $+1.6\%$ per decade and are statistically significant at the 95% confidence level. These trends compare well with the observed positive manmade trends in CCC over congested air traffic regions in Europe and the North Atlantic (Zerefos *et al* 2003; Stordal *et al.*, 2005; Stubenrauch and Schumann, 2005).

5 ACKNOWLEDGMENTS

This study was conducted within the FP6 Integrated Project “Quantifying the Climate Impact of Global and European Transport Systems” (QUANTIFY, Contract No 003893–GOCE) and contributes to the ECATS Network of Excellence, both funded by the European Commission.

REFERENCES

- Cess, R.D., M. Zhang, P.–H. Wang, and B.A. Wielicki, 2001: Cloud structure anomalies over the tropical Pacific during the 1997/98 El Nino. *Geophys. Res. Lett.* 28, 4547–4550.
- Luo, Z., W.B. Rossow, T. Inoue, and C.J. Stubenrauch, 2002: Did the Eruption of the Mt. Pinatubo Volcano Affect Cirrus Properties?. *J. Climate* 17, 2806–2820.
- Massie, S., P. Lowe, X. Tie, M. Hervig, G. Thomas, and J. Russell III, 2000: Effect of the 1997 El Nino on the distribution of upper tropospheric cirrus. *J. Geophys. Res.* 105(D18), 22725–22741.
- Rossow, W.B., and R.A. Schiffer, 1999: Advances in understanding clouds from ISCCP. *Bull. Amer. Meteor. Soc.* 80, 2261–2287.
- Sandor, B.J., E.J. Jensen, E.M. Stone, W.G. Read, J.W. Waters, and J.L. Mergenthaler, 2000: Upper tropospheric humidity and thin cirrus. *Geophys. Res. Lett.* 27(17), 2645–2648.
- Sausen, R., K. Gierens, M. Ponater, and U. Schumann, 1998: A diagnostic study of the global distribution of contrails, part I: present day climate. *Theor. Appl. Climatol.* 61, 127–141.
- Stordal, F., G. Myhre, E.J.G. Stordal, W.B. Rossow, D.S. Lee, D.W. Arlander, and T. Svendby, 2005: Is there a trend in cirrus clouds cover due to aircraft traffic?. *Atmos. Chem. Phys.* 5, 2155–2162.
- Stubenrauch, C.J., and U. Schumann, 2005: Impact of air traffic on cirrus coverage. *Geophys. Res. Lett.* 32, L14813, doi: 10.1029/2005GL022707.
- Wang, P. H., P. Minnis, B.A. Wielicki, T. Wong, and L.B. Vann, 2002: Satellite observations of long-term changes in tropical cloud and outgoing longwave radiation from 1985 to 1998. *Geophys. Res. Lett.* 29, 1397, 10.1029/2001GL014264.
- Wang, P.–H., P. Minnis, B.A. Wielicki, T. Wong, R.D. Cess, M. Zhang, L.B. Vann, and G.S. Kent, 2003: Characteristics of the 1997/1998 El Nino cloud distributions from SAGE II observations. *J. Geophys. Res.* 108(D1), 4009, doi:10.1029/2002JD002501.
- Zerefos, C.S., K. Eleftheratos, D.S. Balis, P. Zanis, G. Tselioudis, and C. Meleti, 2003: Evidence of impact of aviation on cirrus cloud formation. *Atmos. Chem. Phys.* 3, 1633–1644.

Application of LES and binned microphysics for sensitivity study on contrail evolution

W.W. Huebsch*, D.C. Lewellen
West Virginia University, Morgantown, WV, US

Keywords: contrails, LES, binned ice microphysics, sensitivity study

ABSTRACT: A preliminary sensitivity analysis on contrail evolution out to 1000 seconds has been performed using 3-D high-resolution large-eddy simulations to solve the wake and plume development, coupled with a binned ice microphysics model. The aircraft wake dynamics in the first few minutes can have profound effects on the properties of the resulting persistent contrails. This occurs both through its governing of the initial plume dispersion and through the loss of a significant fraction of the ice crystals due to adiabatic heating in the falling wake plume, even at large ambient supersaturation levels. Effects of both atmospheric and aircraft parameters are investigated including relative humidity with respect to ice, ambient stratification, wind shear, and the effective ice crystal emission index. It is shown that the use of binned microphysics can have a significant impact on the prediction for the contrail evolution. The use of the binned microphysics also allowed the simulations to capture a late-time crystal loss due to buoyant oscillations of the plume.

1 INTRODUCTION

Aircraft contrails have gained renewed interest in recent years due to the possible climate impact. It has become increasingly clear that for some conditions aircraft contrails can persist and grow into significant cloud cover that might otherwise be confused with natural cirrus (Minnis, 1998}. It is not uncommon for portions of the upper troposphere to be highly supersaturated with respect to ice and yet be cirrus free until the passage of an aircraft seeds its formation. The projected large increases in air traffic in the coming decades and potential impact of increased cloud cover on global climate change has led to a growing realization of the importance of understanding the formation, properties, and effects of persistent contrails (Penner et al., 1999).

Contrail formation and evolution is not simply a matter of fuel consumption and atmospheric conditions. It is a complex process involving many properties of the ambient atmosphere, the aircraft, and dynamics ranging on length scales from nanometers for the ice microphysics to kilometers for late time atmospheric dispersion. The specific goal of the current research is to investigate the impact of various atmospheric and aircraft parameters on key metrics of contrail evolution from ages of a few seconds out to 1000 s. Large-eddy simulations (LES) with a binned microphysics are employed, extending an earlier LES study with bulk microphysics (Lewellen and Lewellen, 2001).

2 MODEL AND SIMULATION OVERVIEW

Accurately capturing the wake fluid dynamics and its effects on passive species dispersion are important components in correctly modeling contrail evolution. If there were no ice crystal loss, then the local ice crystal number density evolution would be determined (for given distribution at some early time) solely by fluid dynamic advection, until sedimentation became important. For most of this evolution the local ice mass never strays far from equilibrium conditions so it is governed by fluid dynamic mixing as well. Generally there will be some ice crystal loss due to adiabatic heating when parcels descend significantly (Lewellen and Lewellen, 2001; Susmann and Gierens, 1999) - again a direct consequence of the fluid motions.

* *Corresponding author:* Wade W. Huebsch, MAE Dept., West Virginia University, PO Box 6106, Morgantown, WV, US, 26506-6106. Email: Wade.Huebsch@mail.wvu.edu

To reasonably model the dispersion of the engine exhausts and the basic features of the wake vortex evolution (i.e., how long the vortices persist, how far they drop, and how rapidly the wake volume increases) 3-D high resolution large eddy simulations are used. The model and run procedures are ones employed extensively in previous wake and contrail studies (Lewellen and Lewellen, 2001, 1996). The LES is a finite difference implementation of the incompressible Navier-Stokes equations with the Boussinesq approximation on stretched and staggered grids and second-order accurate in time and space. A piecewise parabolic model (PPM) algorithm is used for the advection of scalars. For the simulations presented in this paper the grids used were on the order of 2.5 million grid points with the finest resolution of 0.4 m and domain sizes up to 1.6 km. Grid independence studies with both finer and coarser resolution showed similar results.

The contrail code has both a bulk and binned option for handling the ice microphysics required for contrail development. The bulk ice microphysics parameterization is a relatively simple model (Lewellen and Lewellen, 2001) and therefore less costly (computationally) than the binned microphysics. In the binned version, the ice microphysics were improved by incorporating components of the NASA Ames Community Aerosol and Radiation Model for Atmospheres, or CARMA (e.g. Jensen et al., 1998). Diffusional growth/sublimation, sedimentation, buoyancy due to latent heat release, and perturbation pressure effects are included in both models.

The contrail simulation is initialized from a 2-D Boeing wake roll-up calculation generated with a Spalart-Allmaras (Spalart and Allmaras, 1992) turbulence model and taken at one second downstream of the B-767 aircraft. The fluid velocities and a passive exhaust tracer are then interpolated onto the contrail grid. The passive tracer is used to distribute the perturbation temperature, as well as the ice crystal and engine water distributions, based on the fuel flow rate, the assumed propulsion efficiency (30%), and appropriate emission indices. Separate LES simulations are used to generate ambient turbulence fields that are added to the contrail field.

Parameter variations are explored starting from the following base case: a wake from a B-767, flying at Mach = 0.8, initialized at one second; assuming fuel flow rate and effective ice crystal number emission index of $F = 5.6$ kg/km and $EI_i = 10^{15}$ (number/kg of fuel); for ambient conditions at flight altitude of no mean wind shear, stable stratification given by a potential temperature gradient of 2.5 K/km, pressure $P = 250$ hPa and temperature $T = 220$ K, and relative humidity with respect to ice $RH_i = 110\%$; simulated with the binned microphysics with a mass ratio between successive ice bins of 3.0, a smallest crystal radius of 50nm, and initial crystal radius of 0.2 μm .

3 RESULTS

In the following we consider in turn how different variables affect contrail metrics such as total ice crystal number and total ice mass per length of flight path. When comparing results from parameter variations, it should be noted that different turbulent realizations produce variations on the order of $\sim 10\%$ (e.g. in ice crystal number density, $N(t)$), which should be used in judging the significance of the differences.

3.1 Bulk vs. Binned Microphysics and RH_i

Figure 1 shows the total ice crystal number ($N(t)$ per meter of flight path) at two different ambient supersaturation levels with either the bulk or binned microphysics and illustrates why the added computational cost of the latter is required for many purposes. These results show a dramatic difference in the fraction of crystals lost during the descent of the vortices for the bulk and binned models. Since these crystals are never recovered, this leads to significant differences in contrail properties (e.g., optical depth or mean crystal size) that will persist in time. For the total ice mass and its vertical distribution, the results show only modest differences between the bulk and binned microphysics; these measures are largely governed by the evolution of the plume volume. There is a good physical reason for the greater crystal loss with the (physically more accurate) binned microphysics. As the vortex system falls there is a competition between the temperature rise due to adiabatic compression evaporating the ice crystals, and the mixing with the moist ambient air favoring growth. In the binned microphysics the smaller crystals within a parcel will sublimate away before the mean size crystal for that parcel would; indeed the mixing rates into that parcel for that period might be sufficient that the mean size crystal survives.

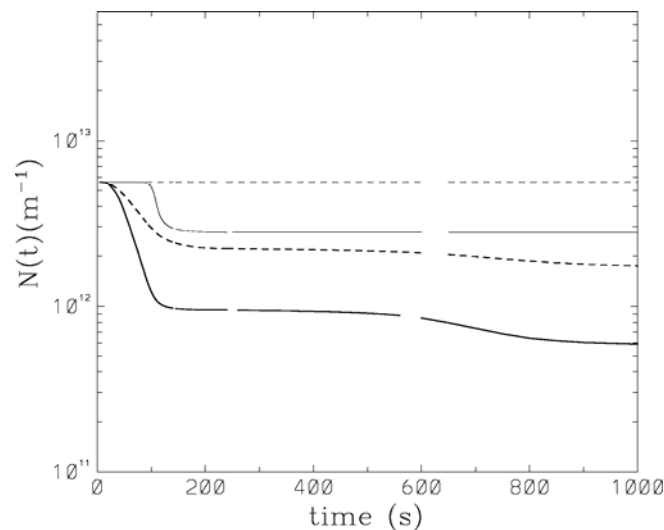


Figure 1. Changes in total ice crystal number as a function of time for B-767 at baseline conditions. Thin lines indicate bulk microphysics, thick lines binned microphysics. $RH_i = 110\%$ (solid lines) and $RH_i = 130\%$ (short dash).

The effects of RH_i were previously shown in Lewellen and Lewellen (2001) for the bulk model. With the binned microphysics, there is crystal loss due to adiabatic heating even for the higher RH_i value of 130%; the bulk model shows no crystal loss at this relative humidity level. As expected, the higher RH_i value produces less overall crystal loss and more total ice mass than the 110% case, but note that the crystal loss for the 130% binned case is greater than the 110% bulk case.

Figure 2 shows the cross-stream integrated drift plots of ice crystal number density for RH_i of 110% and 130%. The drift plot format was described by Lewellen, et al. (1998) and is inspired by scanning lidar measurements of wakes. The wake is sampled as if it were being advected at a steady rate by a mean wind aligned with the contrail. The horizontal axis in each case then varies over time as well as downstream distance, providing both temporal evolution and spatial structure. The 110% case loses a large portion of the bottom of the plume as compared to the 130% case where a larger portion survives the descent of the vortices.

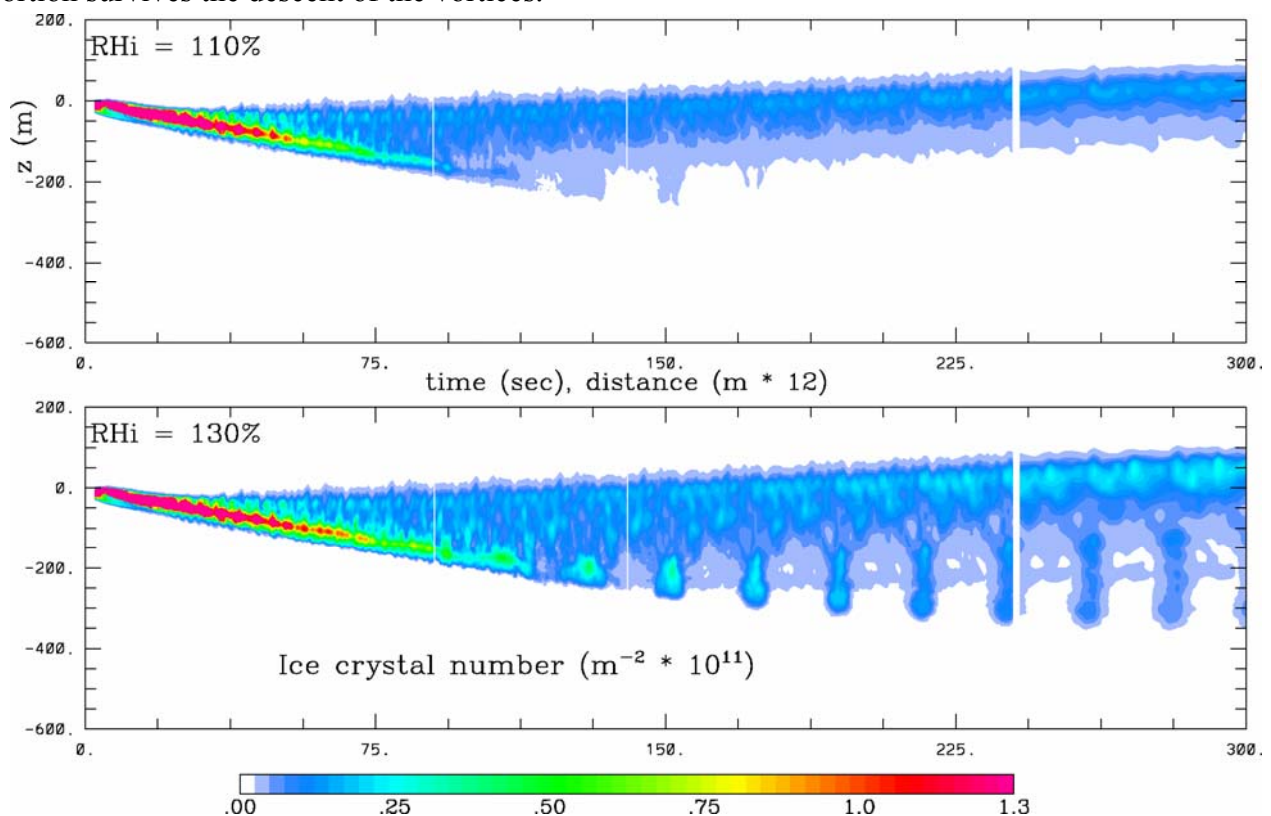


Figure 2. Drift plot of downstream space/time versus height of cross-stream integrated ice crystal number for B-767 contrail (binned microphysics) with $RH_i = 110\%$ (top) and 130% (bottom).

Figure 1 also has another point of interest with respect to the binned results. For both RH_i cases there is some late-time crystal loss which occurs well after the vortex system has died out. There is a buoyant “sloshing” of the wake plume that dominates the dispersion from the time of vortex demise (~ 200 s in the present case) out to ~ 2 Brunt-Väisälä periods. The bottom of the plume, which by 200 s has acquired significant positive buoyancy, buoyantly rises, overshoots its equilibrium level and then falls again. This second downward cycle (from ~ 500 -800 s) is apparently the origin of the secondary crystal loss seen, again due to adiabatic heating of the descending parts of the plume. The Brunt-Väisälä oscillations can clearly be seen in Figure 3, showing results out to 1000 s. This second round of crystal loss requires a competition between different size crystals and therefore was not found in the earlier bulk microphysics study.

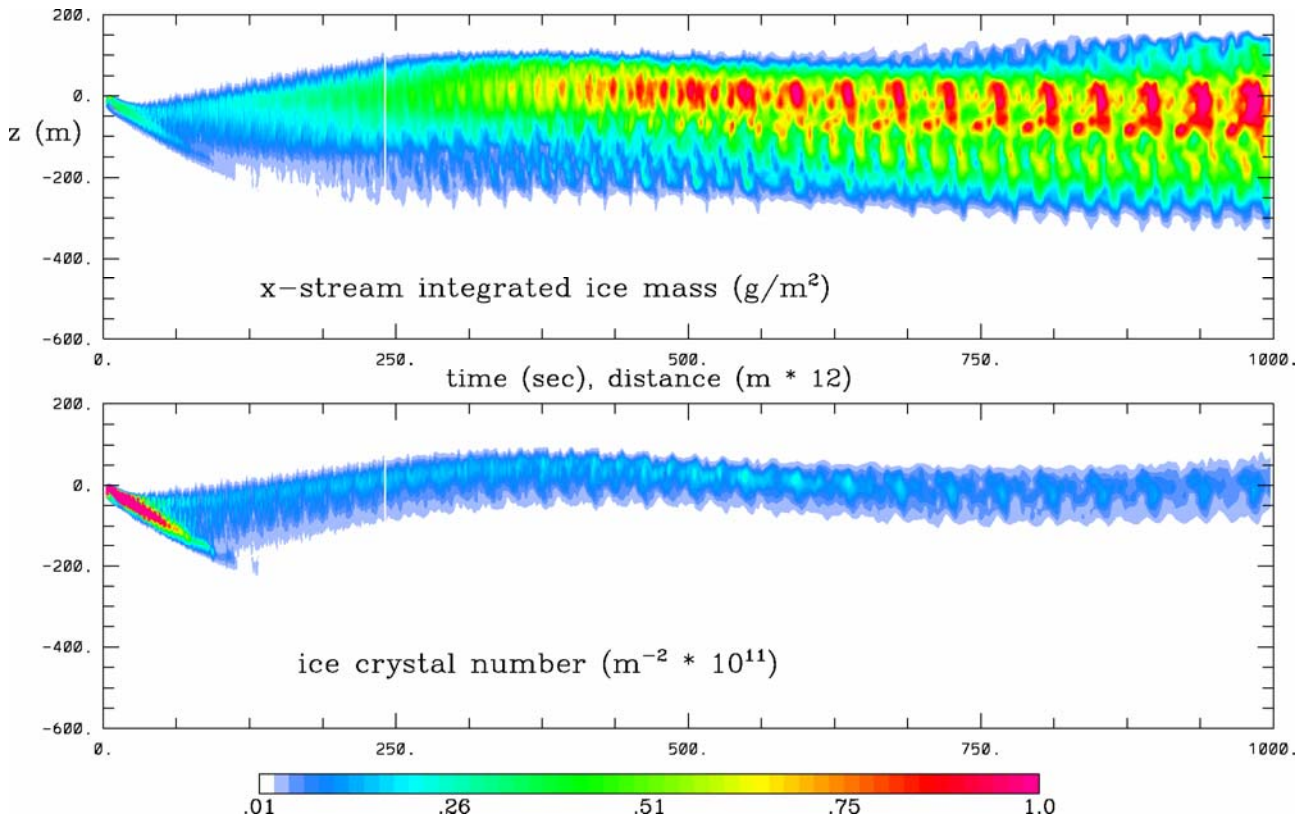


Figure 3. As in figure 2, but for B-767 at $RH_i = 110\%$ showing cross-stream integrated ice mass (top) and ice crystal number (bottom) out to 1000 s.

3.2 Ice Binning and Initialization Choices

Extensive studies were performed to ensure both proper initialization of the ice and proper selection of the binning parameters. Simulations showed that the contrail development was insensitive to the initial bin placement (within reasonable limits). The sensitivity to the uncertainty in the spatial distribution was tested and the results showed only modest changes to the contrail properties given sizable changes in distributions. Tests indicate that in cases similar to the present results, a bin mass ratio of 3.0 is likely the upper limit for adequate bin resolution. Simulations were also performed with a mass ratio of 2.5 which showed good agreement. The selection of the number of bins was based on the requirement that ice crystals do not pile up in the largest bin when atmospheric conditions dictate that continued growth is possible. The required number of ice bins ranged from 20 to 22, for RH_i of 110% and 130%, respectively, given a mass ratio of 3.0 and minimum radius of 50 nm; this corresponds to maximum crystal radii of 53 and 109 μm . At $t = 1000$ s, the use of these settings showed the largest two bins would either have no ice crystals or only be populated at a negligible level.

3.3 Ambient Stratification

For the baseline cases, the ambient potential temperature stratification was set to 2.5 K/km . Contrail simulations were also run with the stratification set to 1.0 and 10.0 K/km . In past work (Lewellen and Lewellen, 2001) it was found that increasing the stratification leads to an increase in detraining

ment, a decrease in the vertical plume size (stratification fights against the drop of the vortices), and a dampening of the late-time buoyant sloshing. Figure 4 shows $N(t)$ at the three different lapse rates with RH_i equal to 110%. The largest level of stratification has the greatest number of remaining ice crystals due to the decrease in total descent (~ 150 m compared to ~ 340 m), and hence less evaporation due to adiabatic heating. The figure also shows that the late-time crystal loss occurs earlier for the highest stratification level due to the reduced Brunt-Väisälä time scale.

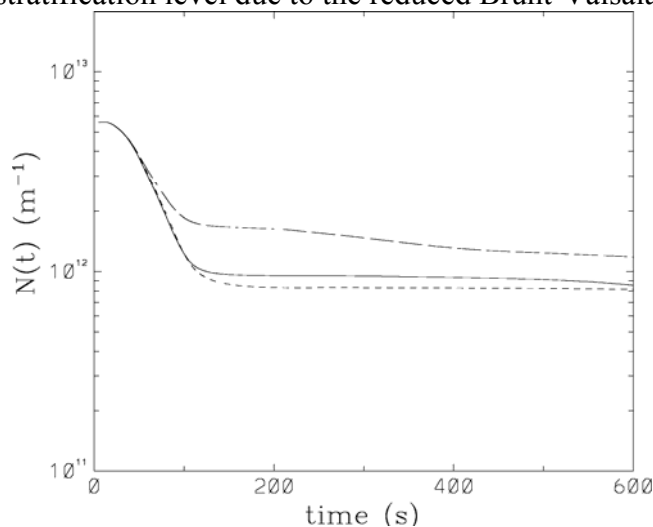


Figure 4. Effects of ambient stratification on contrail evolution for B-767 at $RH_i = 110\%$ with potential temperature gradients of 1.0 (short dash), 2.5 (solid line), and 10.0 K/km (long dash).

3.4 Cross-Stream Wind Shear

The cross-stream shear simulations apply a linear vertical wind shear (du/dz) that is perpendicular to the wake axis. Weak shear levels have little effect on the vortex dynamics. The primary difference comes in the appearance of the contrail since the cross-stream shear will horizontally smear the ice plume. Higher levels of cross-stream shear can significantly alter the baseline vortex dynamics. For the counter rotating vortex pair, one of the vortex cores will decay quicker since its vorticity has the opposite sign to that of the cross-stream shear vorticity, while the other vortex core will have its decay delayed. Even at high levels of cross-stream shear, the Crow instability can be the dominant decay mode for the vortex system, as long as the shear time scales are larger than the vortex dynamics time scales, which is the case for the shear levels considered here. Only modest differences are found in $N(t)$ between the shear and no shear cases. The temporal evolution of the total ice mass shows a more dramatic difference (figure 5). The cross-stream shear case has a $\sim 30\%$ higher ice mass at 200 s (approximate end of vortex lifetime) than the non-shear case. These differences continue to grow at later times as the cross-stream shear leads to increased mixing with ambient supersaturated air.

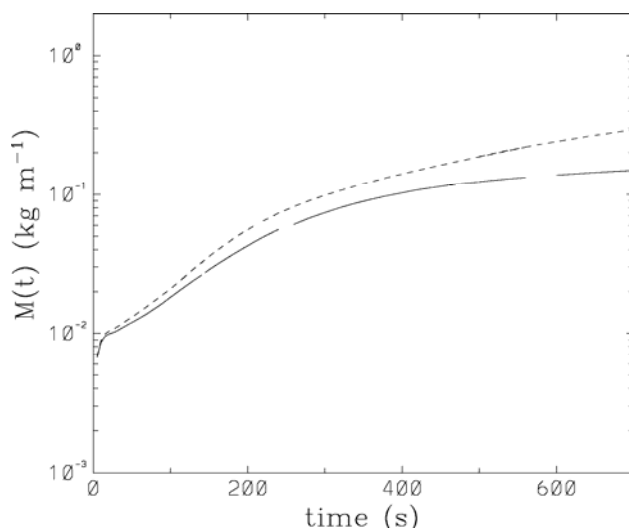


Figure 5. Effects of wind shear on total ice mass as a function of time for B-767 at $RH_i = 110\%$ with no shear (solid line) and cross-stream wind shear of 0.01/s (short dash).

3.5 Aircraft Parameters

A key aircraft parameter was also varied to investigate the effects on contrail evolution: assumed ice crystal emission index (EI_i). Simulations were conducted with EI_i an order of magnitude larger or smaller than the baseline value. Decreasing EI_i increases the average crystal size, causing a higher fraction of the crystals to survive. Thus an order of magnitude decrease in EI_i leads to a much less than order of magnitude decrease in $N(t)$ at late times. An increase in EI_i has the opposite effect; a larger fraction of ice crystals are lost to evaporation. Both trends are due to a competition for available moisture. Decreasing the number of initial crystals decreases the competition for moisture and hence a larger percentage of the crystals can grow large enough to survive the adiabatic heating phase. Increasing the number of initial crystals causes a greater competition for the moisture, which results in the ice crystals being more susceptible to evaporation. More work is needed to evaluate the sensitivity of these results to varying ambient conditions.

4 CONCLUSIONS

High-resolution LES has been coupled with binned ice microphysics to explore the sensitivity of contrail evolution to atmospheric and aircraft properties. There were significant differences seen with the binned microphysics as compared to the bulk model, primarily an overall difference in crystal loss, which will have a lasting impact on the late-time contrail properties such as radiative forcing. The simulations also demonstrated a previously undocumented late-time crystal loss that is only captured with a binned microphysics. The temperature stratification and wind shear results follow the trends shown in some past studies, but have now been obtained with LES using binned microphysics. Variation of the ice crystal emission index demonstrated the competing effects among crystal number, crystal size and the potential loss to evaporation. A more extensive sensitivity study varying aircraft type, EI_i , ambient pressure, temperature, humidity and wind shear and following the contrail development out to later times is ongoing and will be presented in future work.

ACKNOWLEDGMENTS

The authors would like to thank Steve Baughcum, Mikhail Danilin, Jeffrey Crouch and other colleagues at Boeing for their support and help in this work. The authors also thank Eric Jensen for initially providing us with the CARMA microphysics package.

REFERENCES

- Jensen, E.J., A.S. Ackerman, D.E. Stevens, O.B. Toon, and P. Minnis, 1998: Spreading and growth of contrails in a sheared environment. *J. Geophys. Res.* 103, 31557-31567.
- Lewellen, D.C. and W.S. Lewellen, 1996: Large-eddy simulations of the vortex-pair breakup in aircraft wakes. *AIAA J.* 34, 2337-2345.
- Lewellen, D.C., W.S. Lewellen, L.R. Poole, R.J. DeCoursey, G.M. Hansen, and C.A. Hostetler, 1998: Large-eddy simulations and lidar measurements of vortex-pair breakup in aircraft wakes. *AIAA J.* 36, 1439-1445.
- Lewellen, D.C. and W.S. Lewellen, 2001: The effects of aircraft wake dynamics on contrail development. *J. Atmos. Sci.* 58, 390-406.
- Minnis, P., D. Young, L. Ngyuen, D. Garber, W. Smith, and R. Palikonda, 1998: Transformation of contrails into cirrus during SUCCESS. *Geophys. Res. Lett.*, 25, 1157-1160.
- Penner, J.E., D.H. Lister, D.J. Griggs, D.J. Dokken, and M. McFarland, 1999: *Aviation and the Global Atmosphere*, Cambridge Univ. Press, New York.
- Spalart, P.R. and S.R. Allmaras, 1992: A one-equation turbulence model for aerodynamic flows. AIAA Paper 92-0439, 30th Aerospace Sciences Meeting and Exhibit.
- Sussmann, R. and K.M. Gierens, 1999: Lidar and numerical studies on the different evolution of vortex pair and secondary wake in young contrails. *J. Geophys. Res.* 104, 2131-2142.

Global distribution of ship tracks from one year of AATSR-data

M. Schreier*, H. Bovensmann

Institute of Environmental Research, University of Bremen, 28359 Bremen, Germany

H. Mannstein, V. Eyring

DLR - Institut für Physik der Atmosphäre, Oberpfaffenhofen, 82234 Wessling, Germany

Keywords: ship tracks, radiative forcing

ABSTRACT: The perturbation of a cloud layer by ship-generated aerosol changes the cloud reflectivity and is identified by elongated structures in satellite images, known as ship tracks. As ship tracks indicate a pollution of the clean marine environment and also affect the radiation budget below and above the cloud, it is important to investigate their radiative and climate impact. In this study we use satellite data to examine the effects of ship tracks on a particular scene as well as on the global scale. The cloud optical and microphysical properties are derived using a semi-analytical retrieval technique combined with a look-up-table approach. Within the ship tracks a significant change in the droplet number concentration, the effective radius and the optical thickness are found compared to the unaffected cloud. The resulting cloud properties are used to calculate the radiation budget below and above the cloud. Local impacts are shown for a selected scene from MODIS on Terra. The mean reflectance at top of atmosphere (TOA) is increased by 40.8 Wm^{-2} . For a particular scene chosen close to the West Coast of North America on 10th February 2003, ship emissions increase the backscattered solar radiation at TOA by 2.0 Wm^{-2} , corresponding to a negative radiative forcing (RF). A global distribution of ship tracks derived from one year of AATSR data shows high spatial and temporal variability with highest occurrence of ship tracks westward of North America and the southwest coast of Africa, but small RF on the global scale.

1 INTRODUCTION

Emissions from ships significantly contribute to the total budget of anthropogenic emissions. The principal exhaust gas emissions from ships include CO_2 , NO_x , SO_x , CO, hydrocarbons, and particulate matter (Eyring et al., 2005). Compared to other transport modes, the sulphur content of the fuel burned in marine diesel engines and the total amount of SO_x emissions is high. The average sulphur fuel content of today's world-merchant shipping fleet is 2.4% resulting into a large amount of SO_2 and particulate matter emission totals (EPA, 2000).

The SO_2 and particle emissions from ships change the physical properties of low clouds. This is the so-called indirect aerosol-effect, which has been observed in satellite data in many studies (e.g., Conover, 1966; Twomey et al., 1968; Radke et al., 1989). The natural number of cloud condensation nuclei is limited and reflected in larger droplets and a smaller droplet number concentration in low-level stratiform clouds over the ocean compared to continental clouds. In case of injection of additional aerosols, the changes of the aerosol concentration and amount result in a change in the droplet number concentration within the cloud (Facchini et al., 1999), depending on the solubility and size of the injected aerosol particles. Particles and their precursors from ship emissions are able to act as cloud condensation nuclei (CCN) in the water vapour saturated environment of the maritime cloud or can change the surface tension due to the solubility. Especially the high sulphur content of the fuel may be an important factor for the modification of clouds, because the resulting SO_x is able to act as CCN. Amount and size of these particles depends on the fuel and also the kind of combustion, but can possibly result in a higher droplet concentration (Twomey et al., 1968;

* Corresponding author: Mathias Schreier, Institute of Environmental Research, University of Bremen, 28359 Bremen. Email: schreier@iup.physik.uni-bremen.de

Twomey, 1974) and consequently in a change of reflectivity of the maritime cloud. The increased reflectivity is even higher in the near infrared, because here, the ratio of absorption to scattering is strongly depending on the droplet size (Coakley *et al.*, 1987; Kokhanovsky *et al.*, 2004). In this study the modification of clouds and the influence of the ship exhaust on the radiation budget of a given scene are examined. Full details can be found in Schreier *et al.* (2006) and only a brief summary is presented here. Satellite data are also used to retrieve cloud properties and their modifications due to ship emissions on the global scale.

2 METHODS

2.1 Cloud properties retrieval

A new algorithm has been developed that combines the semi-analytical cloud retrieval algorithm SACURA (Kokhanovsky *et al.*, 2003) and look-up-tables (LUTs) for thin clouds calculated with the libRadtran radiative transfer package (Mayer and Kylling, 2005). An advantage of the new algorithm is that it can be applied to different satellite instruments with channels in the near infrared (e.g. Terra-MODIS, AATSR).

The optical and microphysical parameters of the cloud were derived from the 0.9 μm and 1.6 μm channels for MODIS and AATSR. 1.6 μm was selected because the smaller absorption of liquid water enables more accurate results for the SACURA-retrieval. The two cloud retrieval algorithms - SACURA and LUTs - are different, but both derive the cloud optical thickness and also the effective radius r_{eff} , defined by the ratio of the third to second moment of the particle size distribution and therefore indicating a change of the ratio of volume to surface in the particle size distribution.

The columnar droplet number concentration for both retrievals is calculated via effective radius and cloud optical thickness by assuming a gamma droplet size distribution with a coefficient of variance of 0.37. Calculations of droplets per volume (N) were performed using a hypothetical vertical homogeneous cloud of a thickness 500 m, which is a reasonable value for low marine stratiform clouds.

2.2 Estimating impact on the radiation field

The derived optical parameters were used to estimate changes in solar radiation for the areas below and above the cloud as well as the thermal outgoing radiation by radiative transfer calculations. Optical thickness and the effective radius have been applied to create look-up-tables for the solar flux via the radiative transfer code libRadtran (Mayer and Kylling, 2005), by using the built in k-distribution by Kato *et al.* (1999) to calculate integrated solar irradiance with the solver disort2 (Stamnes *et al.*, 1988) for the wavelength range of 0.24 μm to 4.6 μm . The down-welling irradiance at the surface and the up-welling flux at TOA were calculated for the mid-latitude winter atmosphere. The different distributions of cloud optical properties were considered by using these look-up-tables to calculate the solar flux for every pixel and taking into account the local solar zenith angle. The cloud top height was chosen to be 1000 m and the cloud-bottom height was 500 m. The optical properties of the clouds were calculated according to Mie theory. The mean values for all low-cloud-pixels, ship-track-pixels and no-track-pixels were determined, to estimate the impact of ship tracks on both, the solar radiation at the surface and the backscattered radiation at TOA.

3 ANALYSIS OF SHIP A TRACK SCENE

A particular and adequate satellite scene from Terra-MODIS (King *et al.*, 1995) was selected to show local impacts. The scene from 10th February 2003, close to the West Coast of North America (153°W to 120°W and 40° N to 60° N), exhibits a number of anomalous cloud lines in the stratiform clouds over the ocean.

3.1 Cloud properties

The cloud retrieval algorithm (section 2) was used to calculate optical and microphysical parameters of low clouds (Fig. 1). A significant decrease of the average effective radius from 12 μm to 6

μm is visible across the ship-track-pixels (Fig. 1a). The optical thickness of unpolluted clouds is about 20 to 30 and is increasing in the track up to 45 and higher (Fig. 1b). Also the change in the droplet number concentration from around 100 cm^{-3} up to 800 cm^{-3} is substantial (Fig. 1c). Table 1 summarizes the mean values of the various parameters for all low-cloud-pixels, ship-track-pixels and no-ship-track-pixels. The decrease in the effective radius from 13.2 to $10.1\text{ }\mu\text{m}$ for the area is evident and also an increase in cloud optical thickness from 20.7 up to 34.6 is observed. There is also an obvious increase of droplet number concentration from 79 to 210 cm^{-3} .

Table 1. Mean values of cloud parameters for all low-cloud-pixels, ship-track-pixels and no-ship-track-pixels..

	Low-cloud-pixels	No-ship-track-pixels	Ship-track-pixels
Effective radius (μm)	13.0	13.2	10.1
Optical thickness	21.4	20.7	34.6
Droplet number (cm^{-3})	85	79	210

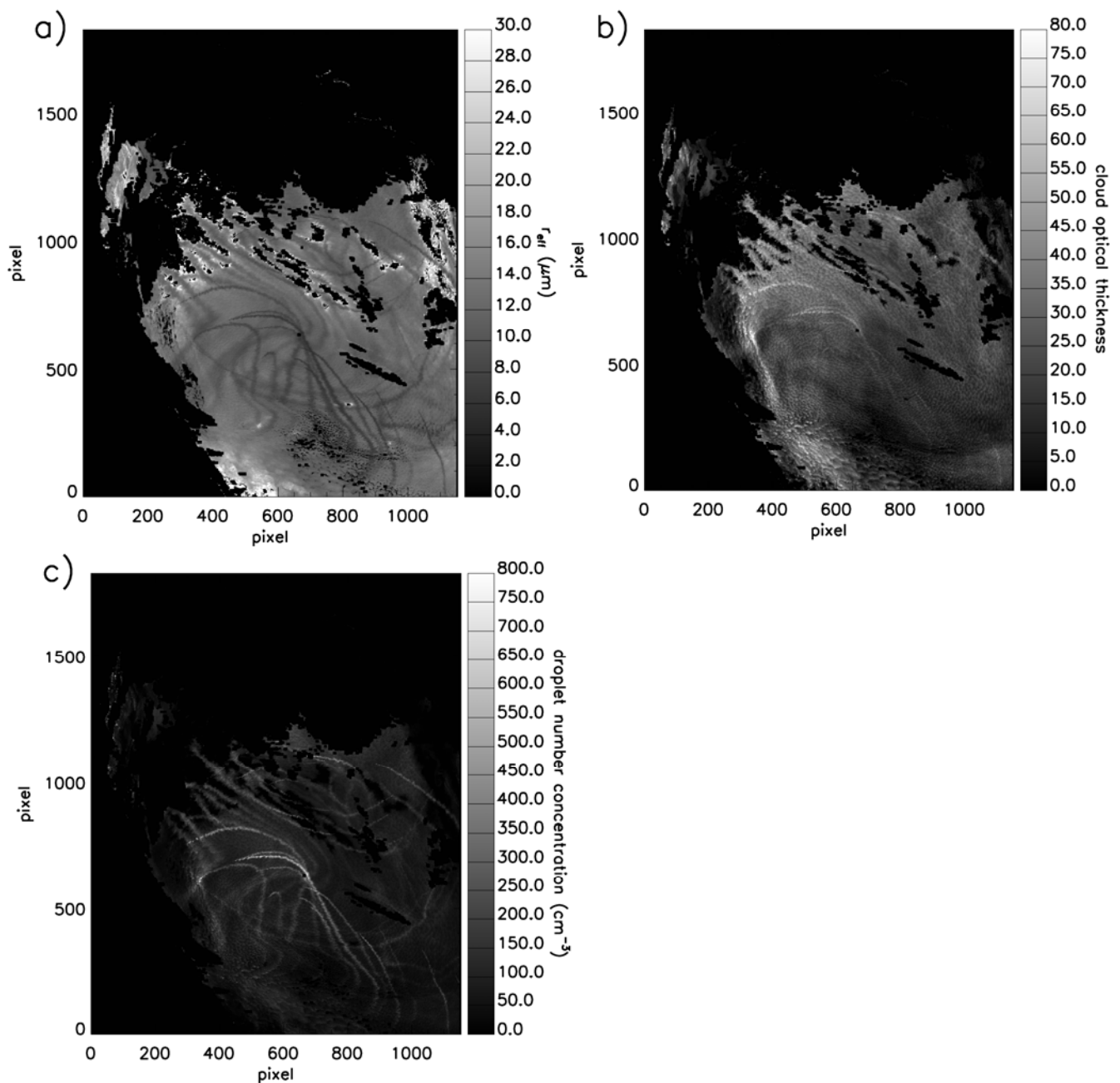


Figure 1: Effective radius (a), cloud optical thickness (b) and concentration of particles (c) (cm^{-3}) derived from the MODIS channels 2 and 6 for the analysed scene. From Schreier et al. (2006).

3.2 Radiative Effects

To separate the impact of changes in cloud parameters from ship tracks on the radiation field without the uncertainties represented by the solar zenith angle variations, radiative transfer calculations were performed assuming a mean solar zenith angle of 63° for all pixels. The calculated values now only depend on the cloud optical properties, as the influence of a varying solar zenith angle has been eliminated.

Assuming a constant solar zenith angle, at TOA, ship-track-pixels reflect 40.8Wm^{-2} more than the no-ship-track-pixels. The amount of ship-track-pixels in the scene is 6.7%. The net radiative effect of the change in cloud properties due to ships for the particular scene is estimated by calculating the difference of the absolute radiation values between all low-cloud-pixels ($E_{\text{low-cloud}}$) and the no-ship-track-pixels ($E_{\text{no-ship-track}}$). According to these values, the solar radiation at the surface is reduced on average by 2.1Wm^{-2} by the ship emissions and additional 2.0Wm^{-2} are reflected back at TOA.

4 GLOBAL DISTRIBUTION OF SHIP TRACKS

The global distribution of ship tracks is derived from data of the AATSR (Advanced Along Track Scanning Radiometer) instrument aboard the European ENVISAT satellite for the year 2004.

To select scenes dominated by low clouds over ocean, we applied the following criteria: (1) excluding clouds over land via the terrain height, (2) distinguish between ocean and clouds by the reflectance of a channel in the short wavelength and (3) estimation of cloud top height with the help of the $11\mu\text{m}$ channel. The remaining scenes include 'very low clouds', which were further examined and the scenes that included ship tracks were used to estimate the global coverage of ship tracks with a resolution similar to the International Cloud and Climate Project was calculated.

The results show highest occurrence of ship-tracks over the Northern Pacific and the Northern Atlantic (up to 0.2%). A comparable high amount of ship-tracks is also found at the Western Coast of Africa and in the Northern Atlantic. In addition to large regional variations, large seasonal variations have been found, with most ship-tracks occurring in springtime and in summer, and only few in wintertime and autumn.

Calculation of the increased backscattering compared to the surrounding for fixed solar zenith angle show most values are around 40Wm^{-2} . This indicates an increased cooling of the atmosphere on regional scale. On global scale, the estimations for radiative forcings show values smaller than -1mWm^{-2} , which is small compared to other radiative forcings.

5 CONCLUSIONS

On the basis of a particular satellite scene it has been shown that ship emissions modify existing clouds on a regional scale by decreasing the effective radius, while they increase droplet concentration and optical thickness (Schreier *et al.*, 2006). The results agree with the theory and experiment (Öström *et al.*, 2000; Hobbs *et al.*, 2000): Low clouds of the maritime boundary layer have less cloud condensation nuclei than clouds over land; in consequence, this results in larger droplet radii for similar water content and dispersion of droplet size distributions. Injection of aerosols and their pre-cursors by ships results in more CCNs causing the mean droplet radius to decrease and the droplet number concentration to increase. The derived parameters were used to calculate changes in the radiative energy budget below and above the cloud. The mean values show an increase of 40.8Wm^{-2} at TOA. If the whole low-cloud area with 6.7% ship-track-pixels is taken into account, an increase of 2.0Wm^{-2} in backscattered solar radiation was found, when assuming a constant solar zenith angle of 63° for the scene. Full details of this study can be found in Schreier *et al.* (2006).

The global distribution of ship tracks shows high occurrence over the Northern Pacific and the West Coast of Africa. A first estimate of the global impact of ship tracks result in only small radiative forcings compared to other ship-induced RFs. However, due to large seasonal and spatial variations ship tracks can impact the climate locally.

REFERENCES

- Coakley Jr., J.A., P.A. Durkee, K. Nielsen, J.P. Taylor, S. Platnick, B.A. Albrecht, D. Babb, F.L. Chang, W.R. Tahnk, C.S. Bretherton, P.V. Hobbs, 2000: The Appearance and Disappearance of Ship Tracks an Large Spatial Scales, *J. Atmos. Sci.*, 57, 2765-2778.
- Conover, J.H., 1966: Anomalous Cloud Lines, *J. Atmos. Sci.*, 23, 778-785.
- EPA, 2000: United States Environmental Protection Agency Air and Radiation, Analysis of Commercial Marine Vessels Emissions and Fuel, *EPA420-R-00-002*.
- Eyring, V., H.W. Köhler, J. van Aardenne, and A. Lauer, 2005: Emissions from international shipping: 1. The last 50 years, *J. Geophys. Res.*, 110, D17305.
- Facchini, M.C., M. Mircea, S. Fuzzi, R.J. Charlson, 1999: Cloud albedo enhancement by surface-active organic solutes in growing droplets, *Nature*, 401, 257-259.
- Hobbs, P.V., T.J. Garrett, R.J. Ferek, S.R. Strader, D.A. Hegg, G.M. Frick, W.A. Hoppel, R.F. Gasparovic, L.M. Russell, D.W. Johnson, C. O'Dowd, P.A. Durkee, K.E. Nielsen, G. Innis, 2000: Emissions from Ships with their respect to clouds, *J. Atmos. Sci.*, 57, 2570-2590
- Kato, S., T.P. Ackermann, J.H. Mather, E.E. Clothiaux, 1999: The k-distribution method and correlated-k approximation for a shortwave radiative transfer model, *J. Quant. Spectrosc. Radiat. Trans.*, 62, 109-121.
- Kokhanovsky, A.A., V.V. Rozanov, E.P. Zege, H. Bovensmann, J.P. Burrows, 2003: A semi-analytical cloud retrieval algorithm using backscattered radiation in 0.4-2.4 micrometers spectral range, *J. Geophys. Res.*, 108(D1), 4008.
- Kokhanovsky, A., 2004: Optical properties of terrestrial clouds, *Earth Science Reviews*, 64, 189-241.
- Mayer, B., A. Kylling, 2005: Technical note: The libRadtran software package for radiative transfer calculations, description and examples of use, *Atmos. Chem. Phys.*, 5, 1855-1877.
- Öström, E., K.J. Noone, R.A. Pockalny, 2000: Cloud Droplet Residual Particle Microphysics in Marine Stratocumulus Clouds Observed during the Monterey Area Ship Track Experiment, *J. Atmos. Sci.*, 57, 2671-2683.
- Radke, L.F., J.A. Coakley Jr., M.D. King, 1989: Direct and Remote Sensing Observations of the Effects of Ships on Clouds, *Science*, 346, 1146-1149.
- Schreier, M., A. A. Kokhanovsky, V. Eyring, L. Bugliaro, H. Mannstein, B. Mayer, H. Bovensmann, and J. P. Burrows, 2006: Impact of ship emissions on the microphysical, optical and radiative properties of marine stratus: a case study, *Atmos. Chem. Phys.*, accepted.
- Stamnes, K., S.C. Tsay, W. Wiscombe, K. Jayaweera, 1988: Numerically stable algorithm for discrete-ordinate-method radiative transfer in multiple scattering and emitting layered media, *Appl. Opt.*, 27, 2502-2509.
- Twomey, S., H.B. Howell, T.A. Wojciechowski, 1968: Comments on Anomalous cloud lines, *J. Atmos. Sci.*, 25, 333-334.
- Twomey, S., 1974: Pollution and the planetary albedo, *Atmosph. Environ.*, 8, 1251-1256.

Assessment of a Global Contrail Modelling Method

K. Klima*, I. Waitz

MIT, Cambridge, Massachusetts, USA

Keywords: contrail, contrails, aviation, contrail modelling, SAGE, RHi, satellite images, aircraft tracks, radar based trajectory, cloud formations, linear features, CONUS, RUC

ABSTRACT: Estimates of radiative forcing contributions from aircraft have raised concerns about the impacts of contrails and aviation-induced cirrus on climate. Increasing demand for aviation will further increase the incidence of contrails. This paper describes the assessment of a method for estimating the formation of contrails. The method couples radar-based flight trajectory information with hourly meteorological data. Estimates of persistent contrails were compared to results obtained from NASA satellite images. For the one week time period we considered, the contrail model coupled with measured aircraft flights tracks did not accurately estimate the occurrence of persistent contrails. This was due both to a limited ability to identify contrails in the satellite images (as a basis for validating the methods) and to uncertainties in the meteorological data and the contrail modeling methods.

1 INTRODUCTION

Estimates of radiative forcing contributions from aircraft have raised concerns about the impacts of contrails and aviation-induced cirrus on climate (IPCC 1999). Within four to six hours after initial formation, contrails, if they persist, may evolve into aviation-induced cirrus. In a study of one region in Europe, contrails were estimated to produce a local annual mean radiative forcing of 0.23 W/m^2 (Stuber et al., 2006). The global and annual average forcing was recently estimated to be 0.01 W/m^2 (Sausen et al., 2005).

There are currently only limited capabilities for evaluating the extent and effects of global contrail coverage. Examples of other work in this area include Williams et al. (2005) who analyzed fuel burn and carbon dioxide penalties as a function of contrail reduction, and Minnis et al. (2004), who described a method to calculate whether a contrail will form and persist along certain routes. Both of these studies used the Appleman criteria (1953) to determine whether or not a contrail will form and persist, and the method presented by Schumann (2000) to relate the thermodynamic conditions in the aircraft plume to the overall propulsive efficiency. Duda et al. (2005) improved upon Minnis's method by using flight data to compute air traffic density. A recent paper by Mannstein, Spichtinger, & Gierens (2005) studied high resolution vertical radiosonde meteorological data, and calculated the potential reduction of contrails by a small change in flight altitude (0 to 1000ft).

This paper presents the assessment of a method for estimating contrail formation and persistence. The method couples radar-based flight trajectories with assimilated meteorological data. The method is assessed through a direct comparison of contrail estimates to satellite imagery.

2 NUMERICAL MODEL

2.1 Aviation System Model

To estimate contrail formation, an aircraft model is needed to estimate aircraft overall propulsive efficiency and the emissions index of water. Note that contrail formation does not change greatly as a function of fuel burn (being more significantly influenced by local atmospheric conditions). How-

* Corresponding author: Kelly Klima, MIT, 54-1719, 77 Massachusetts Ave, Cambridge, MA, USA. Email: klima@mit.edu

ever, an accurate aviation system model is needed to examine the extent of contrail coverage. This study used the fuel burn and emissions module of the FAA's System for Assessing Aviation's Global Emissions (Kim et al. 2006a, Kim et al. 2006b).

SAGE accepts flight tracks from Enhanced Traffic Management System (ETMS) radar data and therefore contains detailed temporal and spatial information for most of the flights over the continental United States. These flights are processed through the SAGE model, which consists of individual modules (e.g. aerodynamics, engine thrust, etc.) that interact to create a fuel burn estimate. SAGE can therefore calculate the overall propulsive efficiency of each aircraft along the flight trajectory. For the purposes of this research, we examined 54,000 United States continental flights. Sensitivity to aircraft performance modelling was addressed and is discussed in Klima, (2005).

2.2 Meteorological Data

The Rapid Update Cycle (RUC) is an atmospheric prediction system comprised primarily of a numerical forecast model and an analysis system to initialize that model ([<http://ruc.noaa.gov>]). The RUC has been developed to serve users needing short-range weather forecasts. RUC runs operationally at the National Centers for Environmental Prediction (NCEP). Archived RUC data were obtained from a United States program called the Atmospheric Radiation Measurement Program (ARM, [<http://www.arm.gov/>]) for dates November 12-18, 2001 (to match available satellite imagery/contrail mask data) and October 2000 (to match available fuel burn data). This study used 40km resolution data so that its output could be compared to that of NASA Langley (Duda 2003, Minnis 2004). See Klima (2005) for implementation details.

Satellite data were provided by NASA Langley for the hours of 17-24 Universal Time Conversion (UTC) for the week of November 12-18, 2001. One set of data were satellite infrared radiances (IR) from the Sun-synchronous NOAA-16 Advanced Very High Resolution Radiometer (AVHRR) 1-km imager, 10.8 & 12 μm bands (Figure 1, right). Another set of data were contrail masks (Figure 1, left). The satellite data sets for deriving the contrail coverage consist of the NOAA-16 data and multispectral 1-km data from the MODerate Resolution Imaging Spectroradiometer (MODIS) on the Terra satellite (Duda, 2003). NASA Langley researchers applied Mannstein's algorithm (1999) to identify contrails in the satellite imagery. Filtering methods were provided by NASA Langley, and consist of removing points a) outside the satellite image range, and b) near the edges of the image where curvature is high (scan angle magnitude is more than 50°).

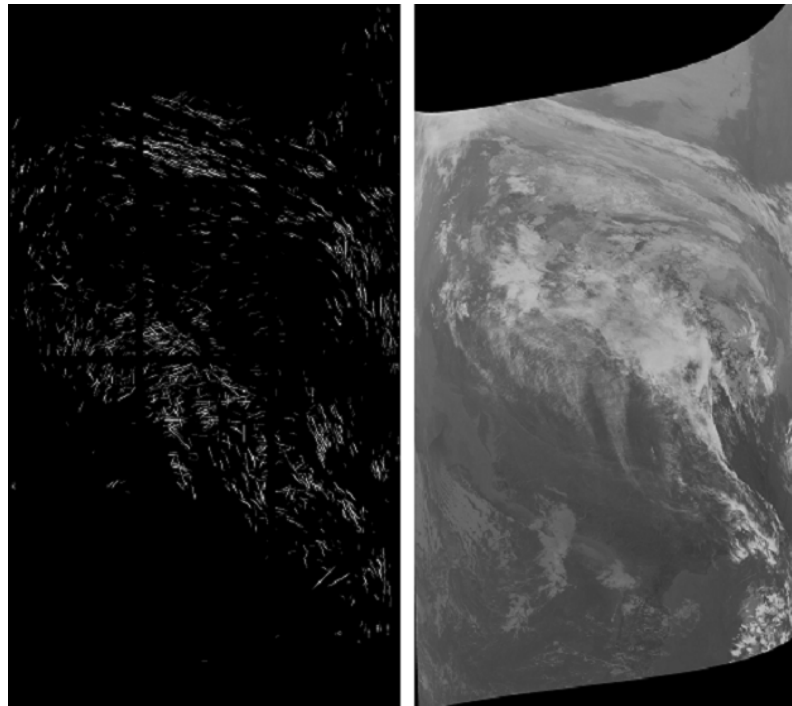


Figure 1 - NOAA-16 satellite image (left) and matching contrail mask (right, white pixel indicates contrail formation), November 18, 2001 1888 UTC. Note that the satellite image is reversed from east to west. This occurs due to the direction the satellite passes overhead.

2.3 Contrail Model

The aircraft type-specific emissions index of water and the type-specific engine efficiency are reported by SAGE along each chord of the radar trajectory. Then, the temporally and spatially matching relative humidity for ice (RH_i) is obtained from the meteorological data sets. The method used to estimate the formation of contrails is based on the methods of Appleman (1953) and Schumann (2000).

We implemented this model using an empirical saturation curve (Sonntag, 1994) and the derived mass-averaged moist air specific heat (Klima, 2005). Given gridded meteorological conditions, aircraft fuel burn, aircraft engine overall efficiency, and fuel characteristics, this model can be used to calculate whether a contrail will form or persist at each location in along the flight path. It reports contrail formation as percentage of distance traveled, and differentiates between contrails forming in clouds and in clear skies (if RH_i > 75%, the area is assumed to be a cloud). A first-order advection model is applied to the contrails to account for their change in location over time.

Due to the complexity of contrails (see for example, Atlas et al., 2006), several characteristics were not addressed. First, we did not estimate the time evolution of the shapes/sizes of contrails. Second, we did not address sub-grid scale variability in meteorological data. Third, optical depth and radiative forcing were not addressed in this study. Fourth, overlapping contrails were ignored due to the small average width of contrails (satellite images indicate less than 10km) and the small regions of ice-supersaturation. Fifth, we assumed winds are invariant from time of contrail formation. Sixth, the evolution of contrails into aviation-induced cirrus cloudiness was beyond the scope of this study. Finally, the environmental effect of contrails was not addressed.

3 RESULTS

Since contrail identification is integral to comparison of actual and model-predicted contrails, a brief description of the contrail identification method is necessary. Young contrails have a smaller crystal size than natural clouds, and hence have a higher IR transmissivity (brightness) in the 10.8 μ m image as compared to the 12 μ m image. Hence a brightness-differencing scheme can be used to identify all image pixels which may be contrails: the 10.8 μ m minus 12 μ m brightness temperature difference. However, using only a temperature differencing technique could identify singular pixels, edges of clouds, or ground features. A second property of contrails is their linear structure, especially at a young age. Hence a linear filter is used. Extended information on processing techniques is described by Mannstein et al. (1999).

There is only limited confidence in the ability of these techniques to identify contrails. Wind shear, turbulence and ice particle sizes will affect how the contrail grows and disperses. Young contrails (less than about 50 minutes) and weak contrails are too small to be sensed by the satellites, and therefore are typically not identified. Older contrails (greater than 2.5 hours) have begun to lose their linear features, and so would also not be identified with confidence (Duda, 2003).

NASA Langley estimate the false alarm rate for identification of contrails using these methods is 40% (Minnis, 2004). For example, for the satellite images we examined, many of the features identified as contrails were oriented north-south. Over the continental United States, most of the air traffic is east-west. Since an aircraft is necessary for contrail formation, these were probably false alarms. In particular, striated cirrus cloud formations were often misidentified as contrails.

3.1 Comparison of Contrail Mask to RH_i fields

Theoretically, clouds and/or contrails should sublime at RH_i < 100%. Visual comparison of the contrail masks to satellite data showed that the linear features with high brightness differences were usually either contrails or clouds; they were rarely associated with ground features. Consequently, an accurate RH_i data set would be expected to have RH_i > 100% in most areas identified as contrails (whether these areas corresponded to contrails or striated cirrus cloud formations). Contrail mask data from the satellite images and modeled contrail estimates were transferred into specific latitude and longitude points. Next these figures were overlaid on RH_i images. Figure 2a shows the contrail mask data on November 12, 2001 at 1996 hours, universal time. Note that this figure is filtered to contain only the region of data present in the satellite image (filter denoted by crosses).

Visual examination of Figure 2a shows that contrail pixels appear in areas of $RHi < 100\%$. Similar results were obtained for the other days examined. We then calculated the fraction of contrail mask pixels that would appear in the CONUS region (at 10973m, 36000ft altitude) given a variable RHi threshold. Based on this calculation, we determined that roughly 60-90% of the contrail pixels were misidentified. This result reflects the inability of the meteorological model to predict supersaturation. This exercise demonstrates that the RHi fields, although perhaps representative of the large scale features, did not accurately capture the atmospheric conditions on the days we examined.

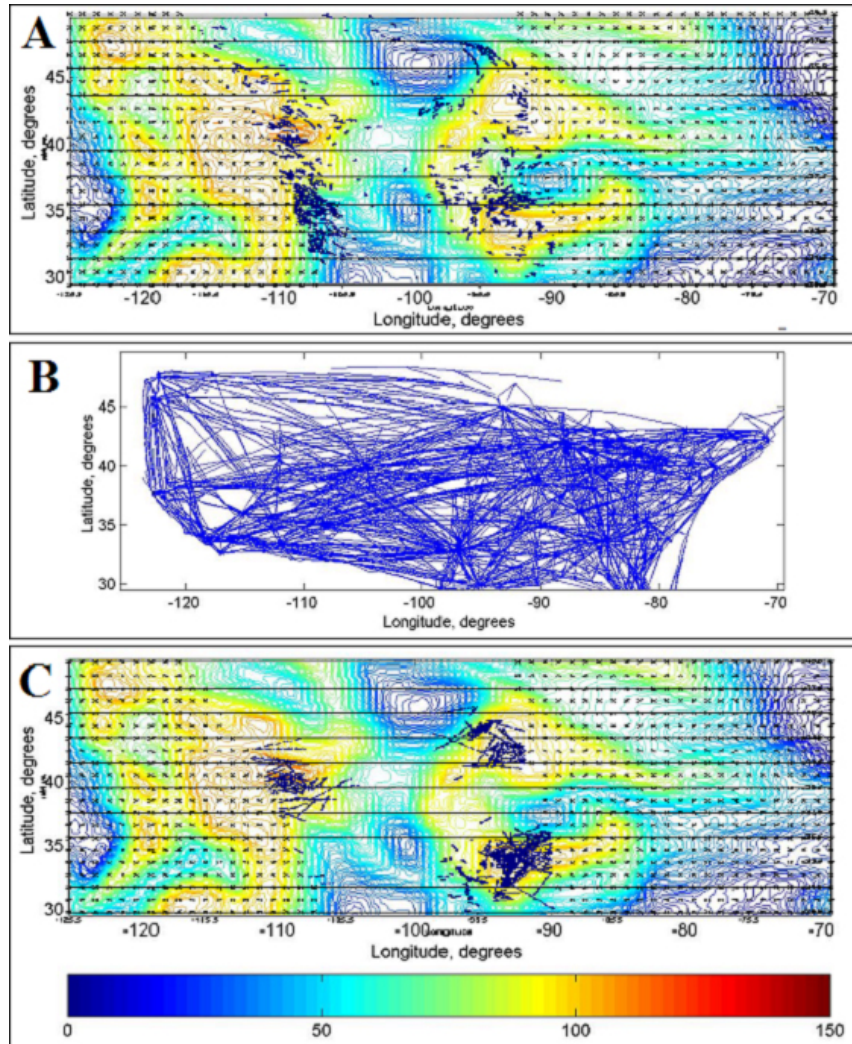


Figure 2 – 11/12/2001 hr 1996, RHi hour 19 field A) Filtered contrail mask. Contrails (47N 100W) caused by incorrect RHi field (temporally changing). Contrails (32N 110W) caused by threading B) Flights examined C) Filtered contrail estimation.

3.2 Comparison of contrail model and satellite image mask results

Comparisons were made for 53,844 U.S. continental flights performed during the week of November 11/12-18, 2001. Figure 2b shows the set of continental flights that temporally match the contrail mask image. Areas of contrail formation are generally consistent between the satellite images and the model estimates (see Figure 2a and Figure 2c). Where the images are not consistent, the estimated contrails match well with areas of high RHi in the meteorological data. The discrepancies can be attributed to the following reasons:

- Inability to represent RHi gradients with altitude – In the figure we overlay the contrail estimates (from throughout the atmosphere) on meteorological data from one altitude level.
- Incorrect RHi fields – The RHi fields in the meteorological data are imperfect reconstructions of the true RHi fields.
- Misidentification of striated clouds and ground features as contrails. There are also regions where the clouds are so thick that contrails are not identified.

- Incorrect contrail advection – A shearing of contrails will appear due to a combination of aircraft traveling the same route and wind advection; a better contrail advection model may more correctly locate these contrails. Wind shear, turbulence, contrail precipitation, and stratification will all be important in determining how a contrail evolves.
- Insufficient flight data – Recall that this study examined commercial, continental U.S. flights only. Neglecting international flights leads to an underestimate of persistent contrails near the edges of the United States. This discrepancy does not apply to our example figures, but was noted in other results shown in Klima (2005).

3.3 *Contrail Persistence Threshold*

One important parameter in the contrail model is the percent of RH_i at which contrails persist. For homogeneous nucleation of cirrus clouds, this threshold percent is thought to be 140-160% (Minnis 2004). However, contrails are formed primarily through heterogeneous nucleation. In the literature, the threshold is variously placed at somewhere between 95-105% (Duda 2003). The nominal value used in our study was 100%.

The effect of changing the contrail persistence threshold over the globe was examined. Assuming the RH_i data were flawed and the contrail persistence threshold varied from 90-110% RH_i (instead of the assumed 100% RH_i), one can calculate the change in ground coverage over which contrails could form. Based on this analysis, if the contrail persistence threshold was allowed to vary from 90-110%, contrail coverage area could vary between 13%-166% of the currently estimated coverage area. If the persistence threshold was allowed to vary as literature suggests from 95-105% RH_i (instead of 100% RH_i), continental coverage area could vary between 51%-135% of the currently estimated coverage area.

3.4 *Contrail Length*

The typical length of the estimated contrails was larger than 100km, (several degrees in length), while the typical length of the observed contrails was about 50km. This length is much larger than the meteorological grid scale resolution, so it is not a reflection of subscale RH_i gradients.

This occurs because the SAGE model uses preprocessed ETMS data; in order to shorten the dataset for storage purposes, “chords” are constructed on which the aircraft travels the same direction and magnitude for a long period of time. The discrepancy between the long predicted contrails and the short contrails observed in the satellite images implies that the chord lengths used within SAGE need to be shortened - at least to the extent to where they are consistent with length-scales observed in the RH_i data.

4 DISCUSSION

In this paper, we compared estimates of persistent contrails developed using radar-based flight trajectories and assimilated meteorological data to contrails identified from satellite data. This comparison highlighted the following issues.

First, it was not possible to match particular contrails observed in the satellite images to specific flight trajectories. This occurred largely because the contrail mask algorithm identified both contrails and striated cirrus cloud formations, suggesting limitations in the satellite sensing and extraction methods (Mannstein 1999). We estimate that perhaps 40-50% of the contrail pixels were misidentified.

Second, RUC RH_i fields did not accurately portray the true RH_i fields for the days examined in 2001. We found that 60-90% of the pixels identified as linear features (demonstrated to be contrails or clouds) were located in areas where the RH_i estimated by the RUC meteorological model was theoretically too low to support clouds or contrails. The RUC models do not have the resolution or the microphysics to represent the small scale vertical motions thought to be important for predicting cirrus and thus RH_i correctly. Hence at this point in time, it is unknown to what degree a contrail model coupled with measured aircraft flight tracks can be used to accurately estimate contrail formation as given by satellite images/contrail masks. Both the identification of contrails from satellite images and the estimation of upper atmospheric humidity are lacking.

Third, the typical length of the estimated contrails was larger than 100km, (several degrees in length), while the typical length of the observed contrails was about 50km. This length is much larger than the meteorological grid scale resolution, so is not a reflection of subscale RH_i gradients. Rather, this occurs because the SAGE aviation model shortens the ETMS dataset for storage purposes. The discrepancy between the long predicted contrails and the short actual contrails implies that the chord lengths used within SAGE need to be shortened until they are consistent with length-scales observed in the RH_i data.

These results are not necessarily general. We assessed only one week's worth of flights over the continental United States.

ACKNOWLEDGEMENT

This work was supported by the U.S. Federal Aviation Administration Office of Environment and Energy. Maryalice Locke and Mohan Gupta managed the project. We thank them for their guidance and contributions. We also thank Lourdes Maurice, Curtis Holsclaw and Carl Burlison of the FAA for their guidance and support. The work was the result of a long-standing collaboration with the Volpe National Transportation Systems Center and we thank Gregg Fleming, Brian Kim, Sathya Balasubramanian, Andrew Malwitz and Matt Maki for their contributions with the aviation system model, SAGE. We also thank Patrick Minnis, David Duda and Rabi Palikonda of NASA Langley Research Center for providing the satellite images and for their help interpreting them.

REFERENCES

- Appleman, H., 1953: The Formation of Exhaust Condensation Trails by Jet Aircraft. *Bulletin American Meteorological Society* 34, 14-20.
- Atlas, D., Z. Wang, D. Duda, 2006: Contrails to Cirrus – Morphology, Microphysics, and Radiative Properties. *Journal of Applied Meteorology and Climatology* 45, 5-19.
- Duda, D.P., P. Minnis, P.K. Costulis, R. Palikonda, 2003: *CONUS Contrail Frequency Estimated from RUC and Flight Track Data*. European Conference on Aviation, Atmosphere, and Climate.
- Kim, B., G. Fleming, S. Balasubramanian, A. Malwitz, J. Lee, J. Ruggiero, 2006a: *SAGE: Version 1.5 Technical Manual*. FAA-EE-2005-01 (http://www.faa.gov/about/office_org/headquarters_offices/aep/models/sage/)
- Kim, B., G. Fleming, S. Balasubramanian, A. Malwitz, J. Lee, J. Ruggiero, 2006b: *SAGE: Version 1.5 Technical Manual*. FAA-EE-2005-04 (http://www.faa.gov/about/office_org/headquarters_offices/aep/models/sage/).
- Intergovernmental Panel on Climate Change. Aviation and the Global Atmosphere. Cambridge University Press: USA, 1999.
- Klima, Kelly. Assessment of a Global Contrail Modeling Method and Operations Strategies for Contrail Mitigation. MIT: Boston, MA, 2005.
- Mannstein, H., R. Meyer, P. Wendling, 1999: Operational detection of contrails from NOAA-AVHRR-data. *International Journal of Remote Sensing* 20, 1641-1660.
- Mannstein, H., P. Spichtinger, K. Gierens, 2005: A Note on Avoiding Contrail Cirrus. *Transportation Research Part D* 10, 421-426.
- Minnis, P., J.K. Ayers, R. Palikonda, E. Phan, 2004: Contrails, Cirrus Trends, and Climate. *Journal of Climate* 17, 1671-1685.
- Sausen, R. I. Isaksen, V. Grewe, D. Hauglustaine, D. Lee, G. Myhre, M. Köhler, G. Pitari, U. Schumann, F. Stordal, C. Zerefos, 2005: Aviation radiative forcing in 2000: An update on IPCC (1999). *Meteorologische Zeitschrift* 14-4, 555-561(7).
- Schumann, U., 2000: Influence of Propulsion Efficiency on Contrail Formation. *Aersp. Sci. Technol* 4, 391-401.
- Sonntag, 1994: Advancements in the Field of Hygrometry. *Meteorol Zeit* 3, 51-66.
- Stuber, N., P. Forster, G. Rädcl, K. Shine, 2006: The importance of the diurnal and annual cycle of air traffic for contrail radiative forcing. *Nature* 441, 864-867.
- Williams, V., R. Noland, R. Toumi, 2005. "Variability of contrail formation conditions and the implications for polices to reduce the climate impacts of aviation". *Transportation Research Part D* 12, 269-280.

Probabilistic Forecast of Contrails within Cirrus Coverage

D. P. Duda*

National Institute of Aerospace, Hampton, VA, USA

R. Palikonda

Analytical Services and Materials, Inc., Hampton, VA, USA

P. Minnis

NASA Langley Research Center, Hampton, VA, USA

Keywords: contrails, cirrus, forecasting

ABSTRACT: Meteorological variables derived from high-resolution numerical weather analysis models (Rapid Update Cycle (RUC) and Advanced Regional Prediction System (ARPS)) are compared with cirrus and contrail cloud occurrence deduced from multi-spectral radiances measured by the Advanced Very High Resolution Radiometer (AVHRR) onboard the NOAA-16 polar-orbiting satellite between April 2004 and June 2005. The occurrence or non-occurrence of contrail and cirrus formation within the sample area is related to several upper tropospheric variables through logistic regression techniques. Probabilistic models are developed to predict the occurrence of persistent linear contrails forming both with and without surrounding cirrus clouds. The forecast models provide insight into which atmospheric conditions are most susceptible to the formation of possible climate-altering contrails.

1 INTRODUCTION

Contrails and cirrus tend to form in similar (but not identical) atmospheric conditions, and thus it is difficult to determine how much persistent contrail coverage affects cirrus coverage. It is clear, however, that contrails that form imbedded in thick cirrus clouds will have little or no radiative impact on the atmosphere, while persistent contrails that form in otherwise clear skies will have a greater direct effect on climate. Although the atmospheric conditions necessary for cirrus and contrail formation are well known, the diagnosis or prediction of such clouds is still complicated by uncertainties in measuring the atmospheric state in the upper troposphere. Several high-resolution numerical weather analyses (NWA), including the Rapid Update Cycle (RUC; Benjamin et al., 2005a, 2005b) and the Advanced Regional Prediction System (ARPS; Xue et al., 2003), operate over the domain of the continental United States of America (USA). The main purpose of these models, however, is to predict the formation of storms and precipitation, and the meteorological accuracy necessary to predict persistent contrail formation directly from these models is not currently available. Duda et al. (2004) demonstrated that the RUC has a dry bias in the upper tropospheric humidity, and a strict diagnosis of persistent contrail formation from the Schmidt-Appleman criteria (Schumann, 1996) is problematic. In addition, numerical weather models are periodically modified and upgraded, leading to abrupt changes in the modelled relative humidity fields. Nevertheless, there appears to be a relationship between the vertical structure of the relative humidity fields represented in the numerical models and the lifetime, spreading rate, and optical depths of observed contrails. The results from Duda et al. (2004) show that the thickest, widest-spreading and longest-lasting contrails tend to occur in the model regions with the most upper tropospheric moisture. Hence, NWAs appear to have some useful meteorological information that could be used to forecast contrails and cirrus.

To deal with the limitations of the numerical weather analyses, probabilistic models that use statistics from the NWA to diagnose and forecast the occurrence of contrails and cirrus can be devel-

* *Corresponding author:* David Duda, National Institute of Aerospace, NASA Langley Research Center, MS 420, Hampton, VA 23681, USA. Email: dduda@nianet.org

oped for each version of a numerical weather model. Weather forecasters have used statistically post-processed numerical model output to make probabilistic forecasts for many years. One of the earliest models reported in the literature was developed by Lund (1955), and model output statistics (MOS; see Glahn and Lowry, 1972) were one of the first widely used probabilistic forecasts developed from numerical weather forecasts. Some probabilistic forecasts of contrail formation have also been published. Travis et al. (1997) used a combination of rawinsonde temperature and GOES (Geostationary Operational Environmental Satellite) 6.7 μm water vapour absorption data to develop a prognostic logistical model of the occurrence of widespread persistent contrail coverage. Jackson et al. (2001) created a statistical contrail prediction model using surface observations and rawinsonde measurements of temperature, humidity and winds over the New England states.

Because probabilistic forecasts use numerical model statistics to develop forecasts, they do not require the same level of meteorological accuracy necessary for classical cirrus and contrail formation theories, and new probabilistic forecast models can be developed as new versions of numerical models are implemented. Also, reliable probabilistic forecasts inherently have extra value to users compared to categorical (simple yes or no occurrence) forecasts because users can take advantage of cost/loss analyses better with probabilistic forecasts (Keith, 2003).

This paper presents a group of probabilistic models that predict the occurrence (or non-occurrence) of persistent linear contrails forming both with and without surrounding cirrus coverage, in an attempt to distinguish the atmospheric conditions that produce both contrails and cirrus from those that only produce contrails. The next section briefly describes the numerical weather models and the contrail observations used to develop the probabilistic models.

2 DATA

2.1 Meteorological data

Atmospheric profiles of temperature, humidity, horizontal wind speed and direction, and vertical velocity were derived from the 20-km resolution, hourly RUC analyses and 1-day, 2-day and 3-day forecasts from the ARPS in 25-hPa intervals from 400 hPa to 150 hPa. The ARPS data were obtained from the 27-km resolution, 1-hourly contiguous US domain analyses. Several other variables including the vertical shear of the horizontal wind and the temperature lapse rate were also calculated from the model data. These additional variables are expected to influence the spreading rate of persistent contrails (Jensen et al., 1998). Atmospheric humidity is expressed in the form of relative humidity with respect to ice (RHI). Due to computer storage limitations, the RUC and ARPS data were available at 1×1 degree resolution.

To match the meteorological data with observations of contrails, data from the RUC and ARPS analyses closest in time with the contrail observations are linearly interpolated to the location of each contrail observation. An observation was not used if the time difference between the contrail observation and the analyses was greater than 2 hours (nearly all pairs matched to within 1 hour).

2.2 Surface data

Observations of contrail and cirrus occurrence and coverage across the contiguous USA were collected from primary and secondary schools across the country by the Global Learning and Observations to Benefit the Environment (GLOBE) program (see www.globe.gov for more information about the GLOBE program.). In May 2003, GLOBE initiated the contrail observation protocol to gather and classify contrail observations. A primary goal of the GLOBE program is to use detailed written protocols to enable students to provide scientifically valuable measurements of environmental parameters (Brooks and Mims, 2001). Over 14,600 observations were reported over the region between May 2004 and June 2005. They include contrail coverage, contrail number, cloud coverage, cloud type and a classification of contrails into three categories; short-lived, non-spreading persistent contrails, and spreading persistent contrails. A subset of 10 stations (see Figure 1) with at least 50 contrail observations under mostly clear skies (cloud coverage less than 25 percent) was chosen for building some of the probabilistic models.

2.3 Satellite data

To supplement the meteorological data from the NWAs, radiance data from the 6.7- μm water vapour absorption channel on *GOES-12* were also used as atmospheric predictors of contrail formation. The 6.7- μm channel is sensitive to the top three millimetres of water vapour profile in the atmospheric column, and most of the detected emission is from the layer between 500 to 200 hPa (Travis et al., 1997; COMET, 2002), with peak sensitivity near 400 hPa. Both the raw water vapour image counts and the calibrated 6.7- μm brightness temperature were collected.

In addition to the GOES data, multi-spectral measurements taken by the NOAA-16 Advanced Very High Resolution Radiometer (AVHRR) provided observations of contrail occurrence. Five hundred twenty-five afternoon overpasses were collected for a 4 by 6 degree area centred over the states of Ohio, western Pennsylvania and West Virginia (from 38°N to 42°N, and 84°W to 78°W). For each 1 by 1 degree grid box within the sample area, persistent contrails and cirrus were detected from the satellite radiances. The contrails were detected using the automated procedure of Mannstein et al. (1999), while the cirrus were identified from a visual inspection of the 10.8 μm brightness temperature data, and the 10.8 μm minus 12.0 μm brightness temperature difference measurements. To reduce the number of contrail false detections due to cloud street formations, the satellite viewing angle for each overpass was required to be less than 50 degrees. Although each 1 by 1 degree grid box provides one observation of contrails and cirrus, due to gaps in the availability of the datasets and the viewing angle restrictions, only about 6000 observations were possible from the satellite overpasses.

3 MODEL DEVELOPMENT

3.1 Data pre-processing

Nearly 15 months (April 2004 – 27 June 2005) of meteorological data from the RUC and ARPS were collected each day to a local computer. (After 12 UTC on 28 June 2005, the 13-km resolution version of the RUC model began operation, with significant differences in upper tropospheric humidity.) The data are subject to interruptions including computer and power failures, full disks, operator errors and other problems. Thus, approximately 77% of the hourly ARPS data was collected and 99.7% of the RUC data was collected during the time period. Two large gaps (between 20 August – 28 September 2004, and between 21 January – 21 February 2005) accounted for nearly 85% of the ARPS data loss.

The collected data were separated into a dependent (from which the statistical model was created) and an independent (on which the model was tested) dataset. Two-thirds of the observations were randomly selected to build the dependent dataset, while the independent dataset comprises the remaining one-third of the observations.

Before deriving the statistical forecast equations, the NWA data are checked for missing data. None of the missing data were replaced by surrogate values (such as persistence, interpolation or nearest-neighbour techniques) because this study focuses on the general meteorological conditions necessary for persistent contrail formation across the United States, rather than forecasting contrail formation for any particular time or location.

3.2 Statistical technique

Logistic regression (Hosmer and Lemeshow, 1989) was used to create a probabilistic estimate of persistent contrail formation. Logistic regression techniques are commonly used where the predictand, such as in this case, is a dichotomous (yes/no) variable. Two advantages of logistic regression compared with multiple linear regression are that the forecast values cannot fall outside of the 0 – 1 probability range, and that each predictor can be fit in a nonlinearly way to the predictand. The logistic model assumes the following fit in Equation 1:

$$P \approx \frac{1}{1 + \exp[-(\beta_0 + \beta_1 x_1 + \dots + \beta_p x_p)]} \quad (1)$$

P is the predictand (probability of persistent contrail formation) and β_i (for $i = 1, \dots, p$) are the set of coefficients used to fit the predictors (x_i) to the model.

The predictors $x_1, x_2, x_3, \dots, x_n$ are atmospheric variables derived from NWA and satellite measurements. A set of up to 80 possible predictors were tested. All predictors used in this study were based on meteorological quantities in the upper troposphere that are suspected to be related to the formation of spreading, persistent contrails including humidity, temperature, vertical velocity, wind shear, wind direction and atmospheric stability. GOES water vapour channel data were also used as predictors for some regressions.

The maximum likelihood method was used to estimate the unknown coefficients β_i and fit the logistic regression model to the data. The chi-square statistic (χ^2) was used to assess the goodness of fit of each logistic model to the NWA data. A total from 55 to 80 potential predictors from the RUC and ARPS models respectively were used to develop the statistical contrail model. To reduce the number of predictors to an optimal number, a forward stepwise regression technique was used. In each step of the technique, a new predictor is added to the logistic model and the chi-square statistic is compared with the previous model. The new predictor that produces the largest improvement in model fit (that is, the largest increase in χ^2) is added to the model. To avoid over-fitting of the dependent dataset, the stepwise regression technique is allowed to add predictors to the model until the test for statistical significance reaches a significance level (i.e. p -value) of 0.05. The stepwise technique usually resulted in 6 to 11 predictors for each model. Separate regressions were computed for 4 dependent variable scenarios. The scenarios include:

- Both contrails and cirrus form
- Only cirrus clouds form
- Only linear contrails form
- No cirrus or contrails form

As mentioned above, several meteorological variables were considered as predictors in the development of the statistical forecast model. In addition, several combinations of meteorological variables (such as temperature \times humidity) were also considered to account for interactions between variables.

3.3 Skill scores

As a simple method to assess the skill of the contrail/cirrus forecasts, the probabilistic forecasts were converted into categorical (i.e. yes/no, occurrence/non-occurrence) forecasts by simply forecasting the occurrence of the dependent variable when the probability was greater than or equal to 0.5, and forecasting non-occurrence when the probability was less than 0.5. A variety of statistical measures have been developed to evaluate the accuracy of categorical forecasts. Several of these have been used to measure the success of previous contrail formation forecasts (Jackson et al., 2001; Walters et al., 2000). The contrail formation forecasts are separated into four categories based on the forecast and its outcome: a is the number of cases where persistent contrail formation is forecasted and persistent contrails are observed (hits); b is the number of cases where contrails are predicted, but no contrails are observed (false alarms); c is the number of cases where contrails are not forecasted, but contrails are observed (misses); and d is the number of cases where contrails are not forecasted and no contrails are observed (correct rejections). Two of the measures are:

- Hit rate. The hit rate is calculated as $(a + d)/(a + b + c + d)$ and represents the percentage of forecasts in which the method correctly predicted the observed event.
- Heidke Skill Score (HSS). The HSS is calculated as $HSS = 2(ad - bc) / [(a + c)(c + d) - (a + b)(b + d)]$ (Wilks, 1995). This measure of forecasting skill compares the hit rate of the forecast method with the hit rate achieved with a random forecast. Perfect forecasts have an HSS of one, forecasts equal in skill to the random forecast have an HSS of zero, while a negative HSS indicates that the forecasts are less skillful than random forecasts.

4 RESULTS AND CONCLUSIONS

The most important predictors chosen in the logistic models (both those developed from the surface observations (not shown) and those developed from the satellite observations) tended to be related to temperature and humidity. Other variables including vertical velocity, wind direction and speed,

wind shear, and the altitude of maximum RHI were also common predictors. Table 1 shows the hit rates and Heidke skill scores from the models developed using the NOAA-16 cirrus and contrail observations. In all four scenarios for both the RUC and ARPS the hit rates are about 0.75 or greater. The best skill scores occur when both cirrus and contrails appear together, or no high cloudiness is observed.

The lack of skill indicated for the contrail-only models is mainly the result of having relatively few examples of grid boxes with only contrails visible (less than 15 percent of the total), and the nature of the atmospheric conditions in regions where contrails form in the absence of cirrus. The contrail-only grid boxes tend to occur at the edges of areas of high humidity and cooler tropospheric temperatures, and the exact locations of these regions are not always represented well in the numerical models. Also, the contrail detection results have not been checked for the possibility of false positive results due to cloud streets and other linear cloud features unrelated to contrails. Increasing the number of contrail-only cases and refining the contrail and cirrus detection results would allow for more accurate models and improved skill scores for the contrail-only scenario.

Table 1. Hit rates and skill scores from satellite observations over Ohio, Pennsylvania and West Virginia.

Scenario	Hit Rate	Skill Score
RUC (both CT/Ci)	0.74	0.32
ARPS (both CT/Ci)	0.76	0.37
RUC (cirrus only)	0.83	0.20
ARPS (cirrus only)	0.82	0.15
RUC (contrails only)	0.86	0.00
ARPS (contrails only)	0.86	0.02
RUC (no CT/Ci)	0.75	0.46
ARPS (no CT/Ci)	0.76	0.50

The most common predictors in the scenarios with the best overall skill scores (both CT/Ci and no CT/Ci) are variables related to temperature and humidity. For the “both CT/Ci” scenario, the most common predictors are temperature, RHI, temperature \times RHI, and vertical velocity, while for the “no CT/Ci” scenario the most common predictors are temperature², RHI², temperature \times RHI, the altitude of maximum RHI, and wind direction. The differences in common predictors chosen for each scenario suggest that some meteorological quantities are especially useful in determining regions of upper tropospheric cloudiness. Cirrus and contrails are likely to form in regions of positive vertical velocities, while the absence of high clouds is often indicated by the overall synoptic conditions that control wind direction and humidity within the upper troposphere. These results show that current numerical weather analyses describe the atmospheric state in the upper troposphere with sufficient accuracy to locate potential regions of contrail and cirrus formation within a region as small as 1 degree by 1 degree.

An example of multi-variable logistic regression was presented to address some of the limitations of using operational numerical weather prediction models in the diagnosis and prediction of contrail and cirrus cloud formation. More work is necessary to refine the accuracy of the contrail and cirrus observations. More specifically, more quality control work is needed with the contrail detection algorithm to eliminate false positives, and the use of the objective GOES-based gridded cloud products can improve estimates of cirrus occurrence. Techniques like logistic regression may be helpful in discovering robust relationships between the atmospheric variables represented in numerical models and the formation of cirrus and contrails in the atmosphere.

ACKNOWLEDGEMENTS

This material is based upon work supported by the NASA Earth Science Enterprise Radiation Sciences Division, NASA contracts NAG1-02044, NCCI-02043, and NIA-2579, and by the National Science Foundation under Grant No. 0222623.

REFERENCES

- Benjamin, S. G., G. A. Grell, J. M. Brown, T. G. Smirnova, and R. Bleck, 2004a: Mesoscale weather prediction with the RUC hybrid isentropic-terrain-following coordinate model. *Mon. Wea. Rev.*, *132*, 473–494.
- Benjamin, S. G., D. Dévényi, S. S. Weygandt, K. J. Brundage, J. M. Brown, G. A. Grell, D. Kim, B. E. Schwartz, T. G. Smirnova, T. L. Smith, and G. S. Manikin, 2004b: An hourly assimilation-forecast cycle: The RUC. *Mon. Wea. Rev.*, *132*, 495–518.
- Brooks, D. R., and F. M. Mims III, 2001: Development of an inexpensive handheld LED-based Sun photometer for the GLOBE program. *J. Geophys. Res.*, *106(D5)*, 4733–4740.
- COMET, 2002: Satellite meteorology: GOES channel selection. <http://meted.ucar.edu/satmet/goeschan/print/print.htm>
- Duda, D. P., P. Minnis, L. Nguyen, R. Palikonda, 2004: A case study of the development of contrail clusters over the Great Lakes. *J. Atmos. Sci.*, *61*, 1132–1146.
- Glahn, H. R., D. A. Lowry, 1972: The use of model output statistics (MOS) in objective weather forecasting. *J. Appl. Meteorol.*, *11*, 1203–1211.
- Hosmer, D. W., and S. Lemeshow, 1989: *Applied Logistic Regression*. John Wiley & Sons, New York, 307 pp.
- Jackson, A., B. Newton, D. Hahn, A. Bussey, 2001: Statistical contrail forecasting. *J. Appl. Meteorol.*, *40*, 269–279.
- Jensen, E. J., A. S. Ackerman, D. E. Stevens, O. B. Toon, and P. Minnis, 1998: Spreading and growth of contrails in a sheared environment. *J. Geophys. Res.*, *103*, 31,557–31,567.
- Keith, R., 2003: Optimization of value of aerodrome forecasts. *Weather and Forecasting*, *18*, 808–824.
- Lund, I. A., 1955: Estimating the probability of a future event from dichotomously classified predictors. *Bull. Amer. Meteorol. Soc.*, *36*, 325–328.
- Mannstein, H., R. Meyer, P. Wendling, 1999: Operational detection of contrails from NOAA-AVHRR data. *Int. J. Remote Sensing*, *20*, 1641–1660.
- Schumann, U., 1996: On conditions for contrail formation from aircraft exhausts. *Meteorologische Zeitschrift*, *5*, 4–23.
- Travis, D. J., A. M. Carleton, S. A. Changnon, 1997: An empirical model to predict widespread occurrences of contrails. *J. Appl. Meteorol.*, *36*, 1211–1220.
- Walters, M. K., J. D. Shull, J. P. Asbury III, 2000: A comparison of exhaust condensation trail forecast algorithms at low relative humidity. *J. Appl. Meteorol.*, *39*, 80–91.
- Wilks, D. S., 1995: *Statistical Methods in the Atmospheric Sciences*. Academic Press, 467 pp.
- Xue, M., D. -H. Wang, J. -D. Gao, K. Brewster, and K. K. Droegemeier, 2003: The Advanced Regional Prediction System (ARPS), storm-scale numerical weather prediction and data assimilation. *Meteor. Atmos. Physics*, *82*, 139–170.

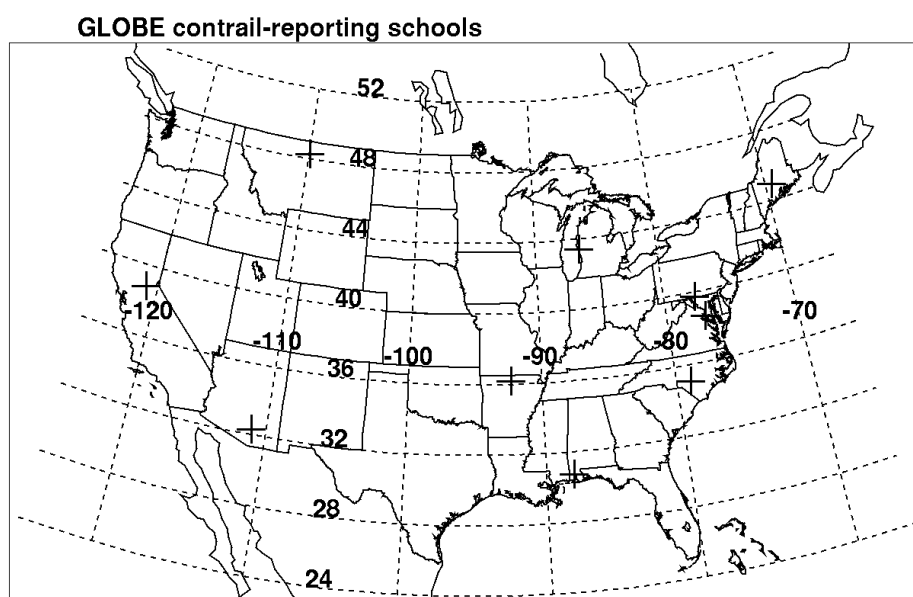


Figure 1: Location of contrail-reporting schools in the United States of America used in the development of logistic regression models.

Climate sensitivity of radiative impacts from transport systems

M. Ponater*, V. Grewe, R. Sausen, U. Schumann
DLR-Institut für Physik der Atmosphäre, Oberpfaffenhofen, Germany

S. Pechtl
Institut für Umweltphysik der Universität Heidelberg, Germany

E. J. Highwood, N. Stuber
Department of Meteorology, University of Reading, UK

Keywords: Efficacy, Climate Sensitivity, Aviation Climate Impact

ABSTRACT: Comparing individual components of a total climate impact is traditionally done in terms of radiative forcing. However, the climate impact of transport systems includes contributions that are likely to imply climate sensitivity parameters distinctly different from the “reference value” for a homogeneous CO₂ perturbation. We propose to introduce efficacy factors for each component into the assessment. The way of proceeding is illustrated using aviation as an example, and prospects for evaluating the other transport system in the EU project QUANTIFY are given.

1 INTRODUCTION

The traditional way to compare the global climate impact of individual emission sectors, as well as specific contributions forming the total effect of some emission sector, is the radiative forcing (RF, Shine et al., 1990). RF is easily calculated by means of radiative transfer models and provides meaningful results even for very small perturbations that are unable to force statistically significant response signals in three-dimensional climate models. RF is also less model-dependent than other metrics of climate change (like the response of surface temperature, precipitation, storminess etc.), because the complex (in part poorly understood) feedbacks within the climate system (cp., Bony et al., 2006) do not enter the radiative transfer calculations. Such practical advantages make RF (and its derivatives like, e.g., the global warming potential, GWP) a seemingly ideal metric for assessment purposes. Consequently, RF and GWP have formed the basis of established emission trading systems.

As research on the climate impact of distinctly non-homogeneous forcing agents (like aerosols, ozone, or clouds induced by aircraft or ships) has received mounting interest, doubts have increased concerning the adequacy of RF for intercomparing relative impacts (e.g., Hansen et al., 1997, 2005; Cook and Highwood, 2003; Joshi et al., 2003; Stuber et al., 2005; Ponater et al., 2005). Here, we will discuss the concept of the EU project QUANTIFY to assess the climate impact contributions from transport systems in the light of current caveats in using RF as a respective metric.

2 CLIMATE SENSITIVITY

The idea to use RF as a metric for the climate change to be expected from some forcing origins from a recurrent empirical finding in climate modelling. Such experience has suggested a linear relation,

$$\Delta T_{surf} = \lambda \cdot RF, \quad (1)$$

* *Corresponding author:* Michael Ponater, DLR-Institut für Physik der Atmosphäre, Oberpfaffenhofen, D-82230 Wessling, Germany. Email: michael.ponater@dlr.de

between the global mean surface temperature response, ΔT_{surf} , and global mean radiative forcing, RF . The relating climate sensitivity parameter, λ , can be, with reasonable reliability, assumed to be independent of the nature of the forcing agent, i.e., its magnitude, longwave to shortwave spectral distribution, spatial structure, or seasonal variation. While λ is known to vary between different climate models, mainly due to a considerable model dependency of cloud feedbacks (Cess et al., 1989, 1996), many simulations implying changes of CO_2 concentration, other well-mixed greenhouse gases, or of the solar constant have confirmed the basic assumption within one and the same model configuration. Consequently, once the value of λ has been determined for the CO_2 case, it is then considered as a model constant applicable to all other agents. However, evidence is growing (see papers mentioned in the introduction) that this approach may fail on several occasions.

Table 1: Equilibrium climate sensitivity parameters (λ) as determined from ECHAM4 simulations. Global changes of CH_4 , solar constant, CO_2 , and ozone in the middle troposphere (MT), upper troposphere (UT), and lower stratosphere (LS) have been used as horizontally homogeneous forcing perturbations. The latter four agents have also been applied as a forcing restricted to the northern hemisphere extratropics (last two columns). See Stuber et al. (2005), for more details.

Agent	RF (Wm^{-2})	λ (K/Wm^{-2})	RF (Wm^{-2})	λ (K/Wm^{-2})
	Global perturbation		NH extratropics perturbation	
CO_2	1.0	0.81	1.0	1.12
Solar	1.0	0.82		
CH_4	1.0	0.88		
$\text{O}_3(\text{MT})$	1.0	0.92	1.0	1.10
$\text{O}_3(\text{UT})$	1.0	0.58	1.0	0.87
$\text{O}_3(\text{LS})$	1.0	1.46	1.0	1.83

Table 1 gives an overview over equilibrium climate change simulations that have been conducted with the ECHAM4/T30.L19 climate model coupled to a mixed layer ocean module. The climate sensitivity parameter has been determined for a number of radiative perturbations, all normalised to a global mean of $RF=1 \text{ W/m}^2$. While the conventional perturbations behave more or less in line with the assumption of constant climate sensitivity, there is a clear tendency to higher sensitivity for perturbation impacting on the northern hemisphere extratropics (Joshi et al., 2003). Compared to the reference value for CO_2 , ozone has a distinctly higher sensitivity if the change occurs in the lower stratosphere, whereas the sensitivity is smaller for changes in the upper troposphere (Stuber et al., 2005). It is evident that non-homogeneous forcings may trigger specific feedbacks that are either less distinguished or less variable in the case of homogeneous forcings.

If the experience from non-homogeneous ozone perturbations already poses a challenge for the concept of constant climate sensitivity, simulations for non-homogeneous aerosol perturbations produce most embarrassing results: Table 2 recalls climate sensitivity experiments conducted by Cook and Highwood (2003) with the UREAD climate model of intermediate complexity. Forcing agents were scattering and absorbing aerosols in the lower troposphere (LT), the varied parameter was the aerosol single scattering albedo, ω .

Table 2: Climate sensitivity results from the UREAD climate model. Global horizontally homogeneous aerosol distribution, with fixed optical depth and asymmetry factor but varying single scattering albedo (ω) have been used as the forcing agent (see Cook and Highwood, 2003, for details).

Agent	ΔT_{surf} (K)	RF (Wm^{-2})	λ (K/Wm^{-2})
CO_2	1.9	3.81	0.50
Aero (LT), $\omega=1$	-1.70	-4.72	0.36
Aero (LT), $\omega=0.95$	-0.60	-3.02	0.20
Aero (LT), $\omega=0.9$	0.60	-1.40	-0.43
Aero (LT), $\omega=0.85$	1.80	0.14	12.86
Aero (LT), $\omega=0.8$	2.90	1.61	1.80

Scattering aerosols ($\omega=1$) cause negative RF and a surface cooling, yielding a climate sensitivity parameter smaller but still in the vicinity of the reference value for CO_2 . As the absorbing character of the aerosol increases the λ values get more anomalous, culminating at negative λ for a critical single scattering albedo around $\omega=0.9$, for which negative RF even causes a rise of global surface

temperature. As pointed out by Cook and Highwood (2003) the reason for the irregular sensitivity in this case is the feedback on lower troposphere cloud cover (the “semi-direct aerosol effect”), which markedly decreases as a result of absorption heating. Due to some observational evidence indicating distinguished impacts of lower tropospheric aerosols on the hydrological cycle (e.g., Ramanathan *et al.*, 2005), the semi-direct effect is not likely to be a mere model feature.

Summarising, climate model simulations with idealised non-homogeneous forcing agents suggest deviations from the reference climate sensitivity that are too strong to be ignored if, for example, ozone, aerosol, and CO₂ contributions to a total effect are to be compared. A way to account this for is the inclusion of efficacy factors (Hansen *et al.*, 2005) in equation (1), writing instead

$$\Delta T_{surf}^{(i)} = r_i \cdot \lambda_{CO_2} \cdot RF^{(i)} \quad (2)$$

where $r_i = \lambda_i / \lambda_{CO_2}$ would introduce the knowledge on an anomalous climate sensitivity λ_i for the component contributing the forcing $RF^{(i)}$. Quantifying individual components in terms of $\Delta T_{surf}^{(i)}$ rather than $RF^{(i)}$ may be expected to provide a fairer, more reliable, assessment. Introducing efficacy factors in this way is encouraged by the finding that the model dependence of those factors seems to be smaller than the model dependence of the climate sensitivity parameter itself (Hansen *et al.*, 1997; Joshi *et al.*, 2003). Another favourable point to mention is the possibility to include efficacies into the calculation of GWPs (Fuglestedt *et al.*, 2003; Berntsen *et al.*, 2005) or into other linear extensions of the radiative forcing concept (e.g., Ponater *et al.*, 2006).

3 EFFICACY OF AIRCRAFT CLIMATE IMPACT COMPONENTS – A TEST CASE

Compared to other transport sectors knowledge on the climate impact from aircraft is relatively far advanced. RF values for the various contributions were first quantified for an IPCC special report (Penner *et al.* 1999) and improved by subsequent research work. However, aviation effects beyond CO₂ and CH₄ just exhibit the properties that make anomalous climate sensitivity likely to occur: They are non-homogeneous in time and space (both horizontally and vertically). We have performed a series of equilibrium climate change simulations with the ECHAM4/T30.L39(DLR) climate model, in order to determine climate sensitivity parameters separately for each impact component (Ponater *et al.*, 2005; 2006). It is important to note that the calculation of a statistically significant surface temperature response (ΔT_{surf}) requires, in most cases, a scaling of the forcing perturbation, as the unscaled RFs generally range well below 0.1 Wm⁻² for present day conditions (Penner *et al.*, 1999; Sausen *et al.*, 2005). The results for the individual climate sensitivity and efficacy values are shown in Table 3:

Table 3: Results (global annual averages) from aircraft climate sensitivity simulations. CO₂ and CH₄ perturbations were normalised to 1 Wm⁻². Two aircraft O₃ perturbations of the Grewe *et al.* (2002, their Fig. 3) type (i.e., for year 2015) were used in two separate simulations. The perturbations for contrails and for H₂O were artificially scaled by factors between 50 and 80, relative to actual present day conditions. See Ponater *et al.* (2005, 2006) for more details.

	CO ₂	CH ₄	O ₃ (1)	O ₃ (2)	H ₂ O	contrails
RF (Wm ⁻²)	1.00	1.00	0.059	0.062	0.06	0.19
ΔT_{surf} (K)	0.74	0.86	0.060	0.071	0.05	0.08
λ (K/ Wm ⁻²)	0.74	0.86	1.02	1.15	0.83	0.43
r	1	1.18	1.37	1.55	1.14	0.59

As expected some r values differ significantly from unity. Aircraft ozone changes have a by 40 % higher efficacy, while the climate sensitivity of contrails is considerably lower than the reference value. Figure 1 shows the corresponding zonal mean RFs, and zonal mean cross sections of the atmospheric temperature response. Note the specific characteristics of aircraft ozone, water vapour, and contrail perturbations with respect to the latitudinal profile and the combination of longwave and shortwave radiative components. Moreover, contrail RF is extremely variable on short time scales, and ozone RF includes strong seasonal variability. While we emphasise that equations (1) and (2) may be applied only for global and annual means, the three-dimensional climate simulations basic to the averaged values of Table 3 offer ample opportunity to investigate local forcings and feedbacks and to discuss their relevance for the global response in each case (e.g., Stuber *et al.*,

2005; Ponater et al., 2005). Still, the current level of process understanding needs to be advanced and available knowledge on, e.g., model dependency issues is very sparse. In particular, important aspects of the interaction between aerosols, clouds and radiation are little explored. Even the sign of the indirect impact of aircraft emitted soot on climate is currently unknown (Hendricks et al., 2005).

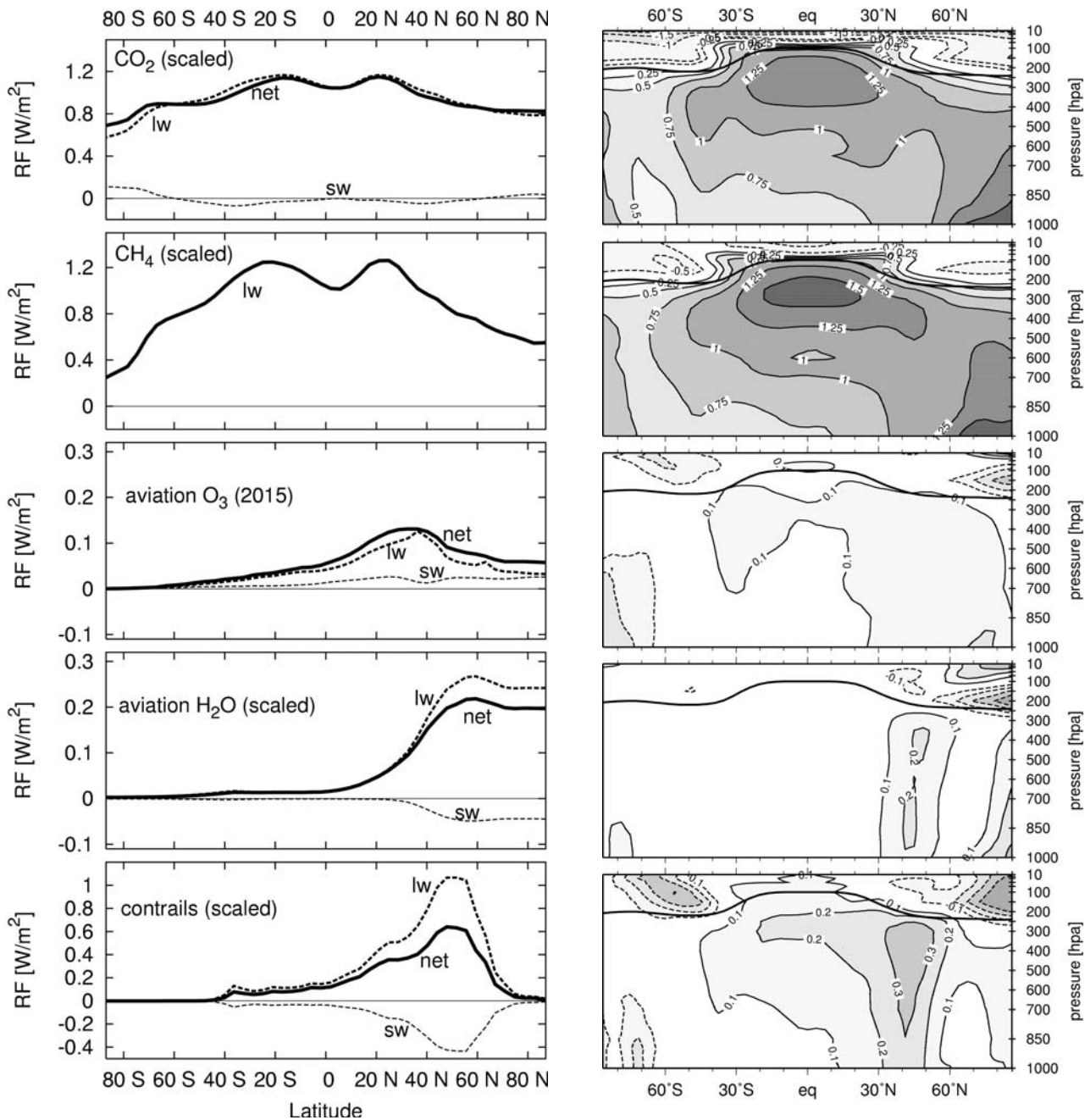


Figure 1: Zonal mean radiative forcing profile (Wm^{-2} , left) and zonal mean temperature reponse (in K, right) caused by various aircraft impact components as simulated with the ECHAM4 GCM. Note that the actual aircraft induced perturbations had to be scaled (see Table 3, and main text). Annual averages of forcing and response are shown. The essential part of the temperature response is statistically significant.

4 EFFICACY OF TRANSPORT CLIMATE COMPONENTS

The generalisation of the efficacy concept outlined in Section 2 to all transport related emissions, as it is intended in the QUANTIFY project, will add further complexity. First, aerosol induced forcings and feedbacks form a main part of the total effect for surface sources (this is particularly true for ships), and it is largely unknown how the aerosol-cloud interaction effects discussed in the context of Table 2 will manifest globally, if the perturbations are restricted to certain geographical re-

gions. This subject will be one of the central issues in QUANTIFY. Second, for both aerosols and ozone the individual spatial structure of the perturbation is likely to create an individual efficacy value. Figure 2 illustrates how different, e.g., the ozone change patterns of the different sectors of transport can be expected to be, and in view of the results shown in Table 1 this is almost certain to modify the climate sensitivity. However, if the approach we follow is to make sense, the climate sensitivity must remain well-defined, in reasonable limits, for each contributing perturbation.

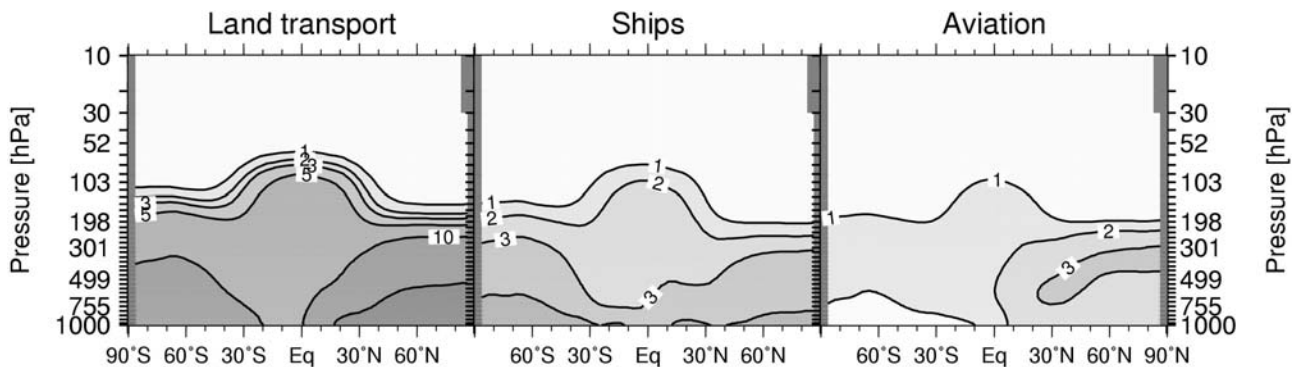


Figure 2: Annual mean ozone change induced by NO_x emissions from road transport, ship transport, and aviation, for typical 1990ies conditions. Values indicate fraction of the total ozone concentration (in %). Results are extracted from the interactive chemistry-climate model simulation discussed by Dameris et al. (2005) Contributions from individual NO_x sources were separated according to the Grewe (2004) method. Contour lines are 1, 2, 3, 5, 10, 20 %.

This requires, above all, a high degree of linearity for each contribution, i.e., the efficacy values in equation (2) must not depend significantly on the magnitude of RF. Otherwise any scaling, as has been done for the aviation perturbations discussed in Section 3, is prohibited and our concept would be bound to fail. Therefore, extra linearity checks are intended in QUANTIFY. Third, if distinctive efficacy values can indeed be determined for each contribution it will be necessary to identify the degree of additivity, if the components are recombined to yield an efficacy for the total effect (either for each single transport sector, or for the gross effect of total transport). Respective nonlinearities have been reported, e.g. for the overall interaction of greenhouse gas and aerosol forcing (Feichter et al., 2004). If such evidence consolidates, a sufficient understanding must be developed in order to arrive at a reasonable synthesis of the separate forcing, efficacy, and response results, and in order to eventually convert our knowledge of climate interaction processes to assessment numbers that are reliable enough to be translated into damage functions or other measures of socio-economic impact (see contribution by Shine, this volume).

REFERENCES

- Berntsen, T.K. et al., 2005: Response of climate to regional emissions of ozone precursors: sensitivities and warming potentials. *Tellus* 57B, 283-304.
- Bony, S., R. Colman, V.M. Kattsov, et al., 2006: How Well Do We Understand and Evaluate Climate Change Feedback Processes? *J. Clim.* 19, 3445-3481.
- Cess, R.D., G.L. Potter, et al., 1989: Interpretation of Cloud-Climate Feedback as Produced by 14 Atmospheric General Circulation Models, *Science* 245, 513-516.
- Cess, R.D., M.-H. Zhang, W.J. Ingram, G.L. Potter, et al., 1996: Cloud feedback in atmospheric general circulation models: An update. *J. Geophys. Res.* 101, 12791-12794.
- Cook, J. and E.J. Highwood, 2003: Climate response to tropospheric absorbing aerosols in an intermediate general-circulation model. *Q. J. R. Meteorol. Soc.* 130, 175-191.
- Dameris, M., et al., 2005: Long-term changes and variability in a transient simulation with a chemistry-climate model employing realistic forcing. *Atmos. Chem. Phys.* 5, 2121-2145.
- Feichter, J., E. Roeckner, U. Lohmann, and B. Liepert, 2004: Nonlinear Aspects of the Climate Response to Greenhouse Gas and Aerosol Forcing. *J. Clim.* 17, 2384-2398.
- Fuglestad, J.S., T.K., Berntsen, O. Godal, R. Sausen, K.P. Shine, and T. Skodvin, 2003: Metrics of climate change: Assessing radiative forcing and emission indices. *Clim. Change* 58, 267-331.

- Grewe, V., M. Dameris, C. Fichter, and R. Sausen, 2002: Impact of aircraft NO_x emissions. Part 1: Interactively coupled climate-chemistry simulations and sensitivities to climate feedback, lightning, and model resolution. *Meteorol. Z.* 11, 177-186.
- Grewe, V., 2004: Technical Note: A diagnostic for ozone contributions of various NO_x emissions in multi-decadal chemistry-climate model simulations. *Atmos. Chem. Phys.* 4, 729-736.
- Hansen, J., M. Sato, and R. Ruedy, 1997: Radiative forcing and climate response. *J. Geophys. Res.* 102, 6831-6864.
- Hansen, J., M. Sato, R. Ruedy, L. Nazarenko, A. Lacis, G.A. Schmidt, G. Russell, et al., 2005: Efficacy of climate forcings. *J. Geophys. Res.* 110, D18104, doi:10.1029/2005GL022740.
- Hendricks, J., B. Kärcher, U. Lohmann, and M. Ponater, 2005: Do aircraft black carbon emissions affect cirrus clouds on the global scale? *Geophys. Res. Lett.* 32, L12814, doi:10.1029/2005GL022740.
- Joshi, M.M., K.P. Shine, M. Ponater, N. Stuber, R. Sausen, and L. Li, 2003: A comparison of climate response to different radiative forcings in three general circulation models: towards an improved metric of climate change. *Clim. Dyn.* 20, 843-854, doi:10.1007/s00382-003-0305-9.
- Penner, J.E., D.H. Lister, D.J. Griggs, D.J. Dokken, M. McFarland (eds.), 1999: Intergovernmental Panel on Climate Change (IPCC) special report *Aviation and the Global Atmosphere*. Cambridge University Press, New York, 365pp.
- Ponater, M., S. Marquart, R. Sausen, and U. Schumann, 2005: On contrail climate sensitivity. *Geophys. Res. Lett.* 32, L10706, doi:10.1029/2005GL022580.
- Ponater, M., S. Pechtl, R. Sausen, U. Schumann, and G. Hüttig, 2006: Potential of the cryoplane technology to reduce aircraft climate impact: A state-of-the-art assessment. *Atmos. Environ.* 40, 6928-6944, doi:10.1016/j.atmosenv.2006.06.036.
- Ramanathan, V., C. Chung, D. Kim, T. Bettge, L. Buja, J.T. Kiehl, W.M. Washington, Q. Fu, and D.R. Sikka, 2005: Atmospheric brown clouds: Impacts on South Asian climate and hydrological cycle. *Proc. Nat. Acad. Sci.* 102, 5326-5333, doi:10.1073/pnas.0500656102.
- Sausen, R., I. Isaksen, V. Grewe, D. Hauglustaine, D.S. Lee, G. Myhre, M.O. Köhler, G. Pitari, U. Schumann, F. Stordal, and C. Zerefos, 2005: Aviation radiative forcing in 2000: An update on IPCC (1999). *Meteorol. Z.* 14, 555-561, doi:10.1127/0941-2948/2005/0049.
- Shine, K.P., R.G. Derwent, D.J. Wuebbles, and J.-J. Morcrette, 1990: Radiative Forcing of Climate. In: Houghton, J.T. et al. (eds.), *Climate Change: The IPCC Scientific Assessment*. Cambridge University Press, New York, 41-68.
- Stuber, N., M. Ponater, and R. Sausen, 2005: Why radiative forcing might fail as a predictor of climate change. *Clim. Dyn.* 24, 497-510, doi:10.1007/s00382-004-0497-7.

Results from pulse scenario experiments with the CNRM-CM3 global coupled model

D. Olivié*, H. Teyssède, D. Salas-Mélie, J.-F. Royer, F. Karcher
Centre National de Recherches Météorologiques (CNRM), Toulouse, France

D. Cariolle
Centre Européen de Recherches et de Formation Avancée en Calcul Scientifique (CERFACS), Toulouse, France

Keywords: simple climate model, coupled climate model, climate change, CO₂, solar constant, response time

ABSTRACT: In order to validate Simple Climate Models (SCMs), the response of the Atmosphere Ocean General Circulation Model (AOGCM) CNRM-CM3 to specific forcing scenarios is studied. Upon pre-industrial background conditions, a sudden perturbation in the solar constant or the CO₂ concentration was applied, followed by an exponential decay of the perturbation. Identical experiments performed with SCMs allow than a validation of the SCMs parameters.

The CNRM-CM3 model is a global coupled climate model which consists of an atmosphere general circulation model, an ocean general circulation model, and a sea ice model. In addition to the validation of SCMs, these experiments can also be used to better understand the characteristics of AOGCMs. The atmosphere and ocean show clearly distinct response times to the forcings. Where the response time for the atmosphere is between 5 and 10 year, the response time for the ocean varies between 60 and 120 year. Furthermore, the influence of the initial conditions is not very large and the response time of the ocean is not very robust with respect to the length of the perturbation.

Comparison with results from earlier simulations with the CNRM-CM3 model where the CO₂ concentration was increased in a gradual way show that, although the forcing scenarios used in these new simulations are strongly transient, they can give valuable information about the characteristics of the model.

1 INTRODUCTION

AOGCMs are the most accurate models to study the effect of different emission scenarios on the Earths climate. However, these models are too computationally expensive to be used for large sets of emission scenarios. Simple Climate Models (SCMs) which are computationally less expensive (and therefore also less accurate) can be used to study the impact of a large set of emission scenarios. Such models therefore allow to study the impact of separate transport sectors and to make sensitivity studies.

In a first step, the SCMs should be validated. Performing a limited set of dedicated experiments as well with the SCMs as with the AOGCMs could allow an interesting comparison between the behaviour of the SCMs and the AOGCMs. Two types of experiments which have a quite different impact on the atmosphere are chosen: changing the solar constant and changing the CO₂ concentration. Changing the solar constant affects the short-wave radiation and is felt mostly at the Earths surface; changing the CO₂ concentration affects the thermal infrared radiation and is initially felt mostly in the middle of the troposphere. The AOGCM experiments are performed with the Unified Model (UM) by the University of Reading, and with the CNRM-CM3 model by the CNRM. In a second step, the SCMs can be used to run a large set of climate simulations.

* *Corresponding author:* Dirk Olivié, Centre National de Recherches Météorologiques, 57 Avenue G. Coriolis, 31057 Toulouse, France. Email: dirk.olivie@cnrm.meteo.fr

The aim of this paper is to discuss the results from the climate scenario experiments obtained with the CNRM-CM3 model. Although these experiments are aimed to contribute to the validation of SCMs, the results of these experiments have also an intrinsic value. How differs the response to the solar forcing from the response to the CO₂ forcing? What is the response time of the model to these perturbations? What is the influence of the initial conditions on the response? Is the response time different for the ocean and the atmosphere?

This paper restricts itself mainly to the analysis of the time series of globally averaged annual mean values. In Section 2, we describe the experiments and the CNRM-CM3 model. In Section 3 we describe the results of the simulations, and in Section 4 we discuss the characteristics of the model response.

2 MODELS AND EXPERIMENTS

The CNRM-CM3 model is a global coupled climate model (Salas-Mélia et al., 2006). The system includes ARPEGE-Climat 3, which is the atmospheric part of the system (developed at CNRM), the OPA 8.1 ocean model (IPSL/LOCEAN, Paris, France), the GELATO-2 dynamic and thermodynamic sea ice model (CNRM) and the TRIP river routing scheme (University of Tokyo, Japan). These models are coupled together with OASIS2.2 (Terray et al., 1998). This software ensures that space interpolations between the different model grids and time synchronisation of the models are correct.

ARPEGE-Climat version 3 is fully described in Déqué et al. (1999) and Gibelin and Déqué (2003). The representation of most variables is spectral (T63 triangular truncation), while the physics are calculated on a 128 x 64 grid (about 2.8° resolution in longitude and latitude). This grid is reduced near the poles. The model contains 45 layers and the topmost layer is located at 0.05 hPa in order to correctly represent the atmospheric circulation in the stratosphere.

The OPA8.1 ocean model was developed by IPSL/LOCEAN (Paris, France) and is described in detail by Madec et al. (1998). It is used in its global configuration (182 x 152 points in the horizontal, without any North Pole singularity), i.e. about 2° resolution in longitude, while in latitude, its resolution varies from 0.5° at the equator to roughly 2° in polar regions. On the vertical, a z-coordinate is used (31 levels with 10 levels in the upper 100 m) is used.

The GELATO model was developed at CNRM and its second version is described in detail by Salas-Mélia (2002). The time step is 24 hours. GELATO-2 is a multi-category ice model (thickness dependant), and in CNRM-CM3, four categories were considered: 0-0.3m, 0.3-0.8m, 0.8-3m, and 3m or more.

The land surface scheme ISBA (Interactions Soil Biosphere Atmosphere) is used. The total runoff is converted into river discharge and transported to the ocean using the TRIP (Total Runoff Integrated Pathways) river routing system developed by T.Oki (Oki and Sud, 1998; Chapelon et al., 2002). The time step used in TRIP in the framework of CNRM-CM3 is 3 hours.

ARPEGE-Climat contains a parameterisation of the homogeneous and heterogeneous chemistry of ozone (Cariolle and Déqué, 1986; Cariolle et al., 1990).

A set of experiments (see Table 1) is performed with perturbations to CO₂ and the solar constant. They are represented by the letters C and S respectively. The perturbations consist in a sudden increase in CO₂ or the solar constant at time t_0 followed by an exponential decrease with a relaxation time τ_f of 2 or 20 year. The time evolution of $x(t)$ (which denotes either the CO₂ concentration or either the solar constant) can then be described by

$$\begin{aligned} x(t) &= x_b \quad \text{if } t < t_0 \\ x(t) &= x_b + x_a \exp\left(-\frac{t-t_0}{\tau_f}\right) \quad \text{if } t > t_0 \end{aligned} \quad (1)$$

where x_b = background value; and x_a = amplitude of the perturbation. The amplitude of the perturbations are chosen to give a comparable radiative forcing of around 10 Wm⁻² at t_0 . Therefore the solar constant was increased by 4.2 % (S20, S2 and S2b), and the pre-industrial CO₂ concentration of 286.2 ppmv was multiplied by a factor 6.5 (C20 and C2). In the experiment C2x where $\tau_f = \infty$

(which corresponds with a step forcing), the CO₂ concentration is only multiplied by two. The concentration of other green house gases (N₂O, CH₄, CFC's, ...) are kept constant at their pre-industrial value. The initial conditions are taken from a reference simulation R performed with the same model under pre-industrial conditions. All simulations use the same initial conditions, except S2b. The CNRM-CM3 model is run for 100 year in C20 and S20, for 90 year in C2x, and for 50 year in C2, S2, and S2b.

We will show mainly the anomaly due to the perturbation, i.e. the difference between the simulations in Table 1 and the reference simulation R.

Table 1 Overview of the different simulations.

Relaxation time (τ_f)	C (CO ₂)	S (Solar)
20 year	C20	S20
2 year	C2	S2, S2b
∞	C2x	

3 RESULTS

3.1 The atmosphere

Time series of the anomaly in the surface (2m) air temperature are shown in Figure 1. For C20 and S20 (Fig. 1, left panel) the response shows a strong increase in the first 5 year, a maximum between 5 and 15 year after t_0 , and later a smooth decay. This smooth decay at the end is very similar to the shape of the forcing. The increase in the surface temperature is stronger in C20 than in S20. The responses of C2, S2 and S2b (Fig. 1, right panel) show a similar behaviour, although the maximum anomaly is much smaller, and the maximum is reached after 2 or 3 year. The initial increase is very short, and only a few data points during this increase are available. In accordance to C20 and S20, the anomaly in C2 is bigger than in S2 and S2b. The different initial conditions for S2 and S2b do not lead to a large difference: the maximum anomaly is very similar.

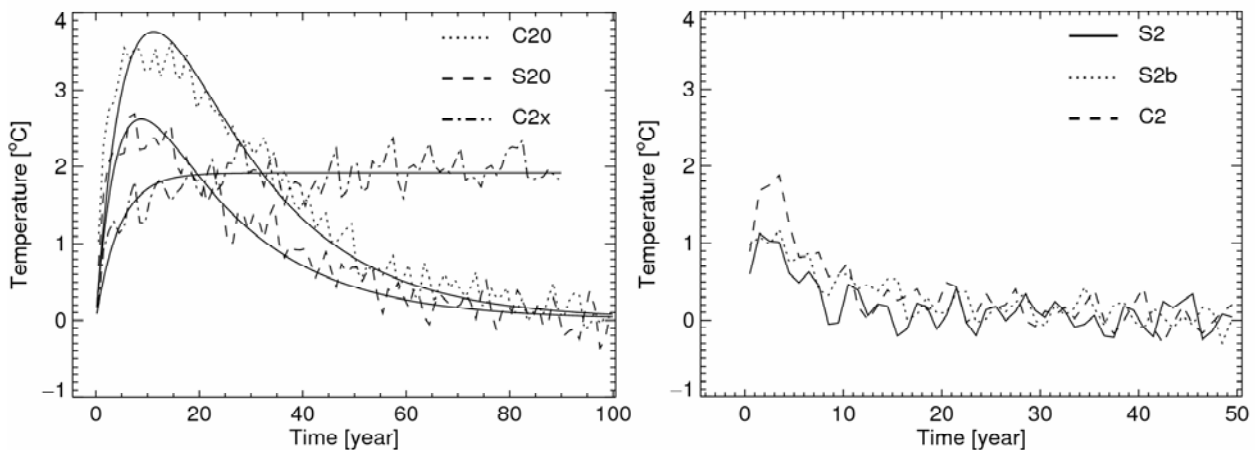


Figure 1: Anomaly of the surface (2m) air temperature. The left (right) panel gives the response when the relaxation time of the perturbation is 20 (2) year. Notice the different horizontal scale in the two panels.

Many other variables in the atmosphere (not shown) show a very similar behaviour as the surface (2m) air temperature. However, due to the disequilibrium at time t_0 , there is also a fast response in C20 and C2: the liquid precipitation, the latent heat flux, and the top net long-wave radiation, show an immediate response which is opposite to the later response. Further, one finds a decrease in the cloud amount and an increase in the precipitation amount.

3.2 The ocean

Figure 2 shows the anomaly in the ocean temperature in C20 and S20. The maximum anomaly is reached after 40 to 50 year in C20, and after 35 year in S20. In a second phase, the ocean temperature anomaly decays in a regular way.

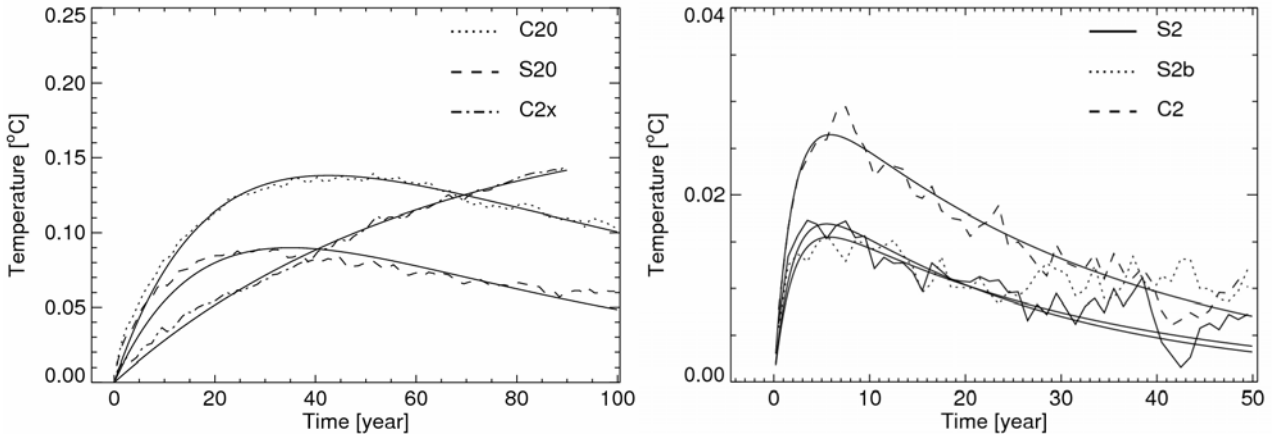


Figure 2: Anomaly of the ocean temperature for C20, S20 and C2x (left), and C2, S2, and S2b (right). Notice the different temperature scales.

Figure 3 shows the evolution of the vertical profile of the heat content anomaly in the ocean for C20. One clearly sees a maximum in the response at the depth of around 700 m after 50 to 60 year. At the surface there is a limited heating, during the first 20 year of the simulation. It takes a long time before the ocean actually starts heating. The heat is kept in a region below the mixed layer. In the last phase, one can also notice the start of the disappearance of the anomaly.

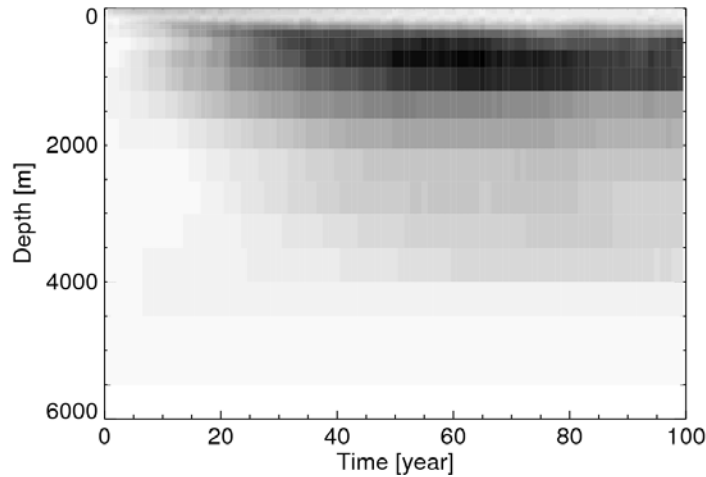


Figure 3: Profile of the ocean heat content anomaly in C20.

4 DISCUSSION

4.1 Response time of the atmosphere and the ocean

To study and interpret the time series, we use a simple model that describes rather well the response. The relation between the forcing $x(t)$ and the response $y(t)$ of this simple mode is

$$\frac{dy}{dt} + \frac{y}{\tau_s} = f x \quad (2)$$

where f = sensitivity; and τ_s = response time. If the forcing is given by Equation 1, then the solution of Equation 2 is described by

$$y(t) = 0 \quad \text{if } t < t_0$$

$$y(t) = \frac{f x_a}{\frac{1}{\tau_s} - \frac{1}{\tau_f}} \left(\exp\left(-\frac{t-t_0}{\tau_f}\right) - \exp\left(-\frac{t-t_0}{\tau_s}\right) \right) \quad \text{if } t > t_0 \quad (3)$$

This simple model allows us to derive the response time τ_s of the system. By fitting the curve suggested in Equation 3 through the observed time series, we find that the response time of the atmosphere derived from C20 and S20 lies for many variables between 5 and 10 year. The results from the curve-fitting are also indicated in Figures 1 and 2.

Table 2 gives the response time of the mean ocean temperature, derived in the different experiments. From the C20 and S20 experiments, a relaxation time of respectively 117 and 70 year has been derived. C2, S2 and S2b all give a relaxation time around 30 year. Apparently there is a strong difference depending on the relaxation time of the forcing. The results from C2, S2 and S2b should be taken with care, because the values in the time series of the anomalies fluctuate very strongly. Therefore we have for C2, S2 and S2b only used the first 25 year of the time series to do the curve fitting.

Table 2: Response time of the ocean temperature.

Experiment	Relaxation time (year)
C20	117
S20	70
C2	32
C2x	61
S2	25
S2b	30

In general, the response time of the ocean should be taken with care. In the reference simulation R, the ocean temperature shows a linear decrease of -0.08 °C / century. This trend has to be compared with the observed decreases in the model simulations and might complicate the interpretation of the ocean relaxation time.

4.2 Influence of the initial conditions

Concerning the influence of the initial conditions, Table 3 gives for a selection of atmospheric variables the maximum anomaly for the S2 and S2b simulations. These two simulations have the same forcings but different initial conditions. The values for most variables differ not more than 10 to 20 %, and their difference is often significantly smaller than the inter-annual variability (Table 3, last column). Only the anomaly in the high cloud amount seems to be quite different in the two simulations.

Table 3: Maximum anomaly for different variables in S2 and S2b. The last column shows the inter-annual variability in the reference experiment R.

		S2	S2b	R (inter-annual variability)
Surface (2m) air temperature	°C	1.12	1.17	0.17
Liquid precipitation	mm day ⁻¹	0.089	0.114	0.018
Solid precipitation	mm day ⁻¹	-0.0091	-0.011	0.0030
Total cloud amount	%	-0.85	-0.84	0.27
Low cloud amount	%	-0.86	-0.92	0.34
Medium cloud amount	%	-1.04	-1.06	0.21
High cloud amount	%	-0.45	-0.92	0.21
Surface latent heat flux	W m ⁻²	0.85	0.97	0.44
Surface sensible heat flux	W m ⁻²	-0.18	-0.17	0.14
Sea surface temperature	°C	0.88	0.84	0.13

For the ocean temperature (Fig. 2, right panel), one can see that the initial conditions have a very small effect on the maximum anomaly.

4.3 Comparison with other experiments

With the CNRM-CM3 model many other experiments have been performed. Two interesting experiments are simulations where the CO₂ concentration is increased gradually by 1 % per year till a doubling (Cg2) or a quadrupling (Cg4) is reached, after which the concentration is kept constant (Figure 4, left panel). The surface (2m) air temperature from the pulse experiment C20 and from

these experiments is compared. If one assumes that the response of the model to some forcing is linear, the response to an arbitrary forcing $x(t)$ can be found by convoluting this arbitrary forcing with the response of the pulse experiment

$$y(t) = \frac{H}{x_a} \otimes \left(\frac{x}{\tau_f} + x' \right) = \int_0^t \frac{H(t-t')}{x_a} \left(\frac{x(t')}{\tau_f} + x'(t') \right) dt' \quad (4)$$

where $H(t)$ = the response to the pulse perturbation. In the right panel of Figure 4, the response of the different experiments C20, R, Cg2 and Cg4 is indicated, together with the result of the convolution. For Cg2 the correspondence between the convolution and the real simulation is rather good, although the trend on the long term is lacking. For Cg4, the convolution gives much higher values than the real simulation, due to the fact that the perturbation experiment is seen as a perturbation in the CO₂ concentration, and not in the logarithm of the CO₂ concentration. Assuming a linear relation between the temperature change and the logarithm of the CO₂ concentration, one finds results which for the Cg4 simulation agree much better.

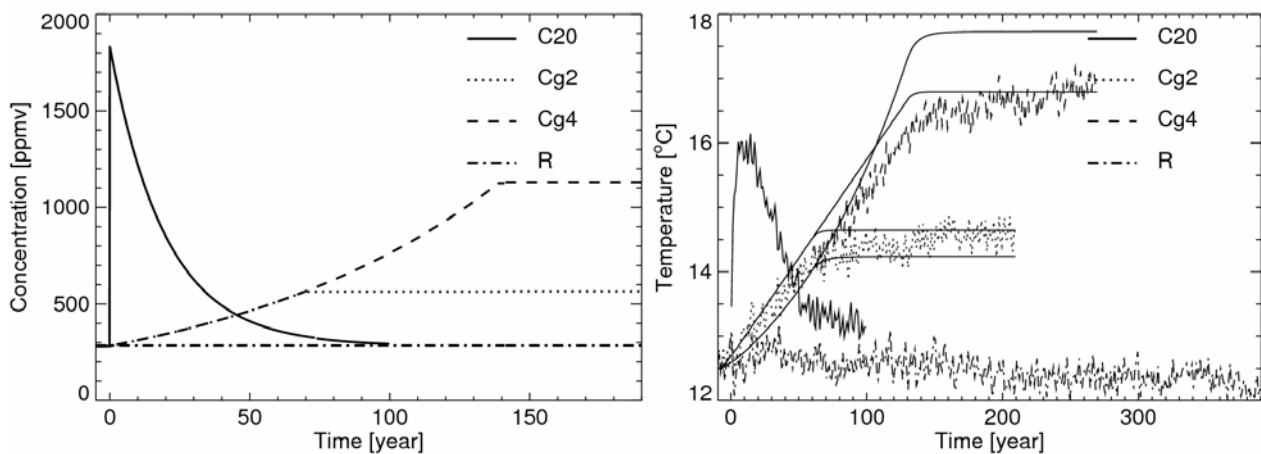


Figure 4: Left: different scenarios for the CO₂ concentration. Right: surface (2m) air temperature response in C20, C2g, and Cg4. The straight lines are the results of the convolution

REFERENCES

- Cariolle, D. and M. Déqué, 1986. Southern hemisphere medium-scale waves and total ozone disturbances in a spectral general circulation model. *J. Geophys. Res* 91, 10825-10846.
- Cariolle, D., A. Lasserre-Bigory, J.-F. Royer and J.-F. Geleyn, 1990. A general circulation model simulation of the springtime Antarctic ozone decrease and its impact on mid-latitudes. *J. Geophys. Res. Atmos.* 95, 1883-1898.
- Chapelon, N., H. Douville, P. Kosuth and T. Oki, 2002. Off-line simulations of the Amazon water balance: a sensitivity study with implications for GSWP. *Climate Dynamics* 19, 141-154.
- Déqué, M., A. Braun, J.-P. Piedelievre, P. Marquet, P. Dandin, J.-F. Guérémy, J.-F. Geleyn, E. Bazile, J.-M. Piriou, K. Yessad, P. Courtier and P. Rochas, 1999. *ARPEGE version 3, documentation algorithmique et mode d'emploi*, Météo-France, CNRM/GMEGEC, Toulouse 31057, France.
- Gibelin, A.-L. and M. Déqué, 2003. Anthropogenic climate change over the Mediterranean region simulated by a global variable resolution model. *Climate Dynamics* 20, 327-339.
- Madec, G., P. Delecluse, M. Imbard and C. Lévy, 1998. *OPA version 8.1 Ocean General Circulation Model Reference Manual*. Notes du Pôle de Modélisation No. 11, Institut Pierre-Simon Laplace, Université Paris VI, Laboratoire d'Océanographie Dynamique et de Climatologie, Paris 75252, France, 91 pp.
- Oki, T. and Y. C. Sud, 1998. Design of total runoff integrating pathways (TRIP) A global river channel network. *Earth Interactions*, vol. 2, paper 1.
- Salas-Méla, D., 2002. A global coupled sea-ice ocean model. *Ocean Modelling* 4, 137-172.
- Salas-Méla, D., F. Chauvin, M. Déqué, H. Douville, J. F. Guérémy, P. Marquet, S. Planton, J.-F. Royer and S. Tyteca, 2006. Description and validation of the CNRM-CM3 global coupled model. Submitted to *Climate Dynamics*.
- Terray, L., S. Valcke and A. Piacentini, 1998. *OASIS 2.2 User's Guide and Reference Manual*. TR/CMGC/98-05, CERFACS, Toulouse, France.

Quantifying the effects of aviation on radiative forcing and temperature with a climate response model

L. Lim^{*}, D.S. Lee,

Dalton Research Institute, Department of Environmental & Geographical Sciences, Manchester Metropolitan University, UK

R. Sausen, M. Ponater

Space and Atmospheric Research Group, Imperial College London, UK

Keywords: Climate response, aviation, efficacy

ABSTRACT: Simplified climate models can be used to calculate and to compare temperature response contributions from small forcings without the need for considerable computer resources. A linear climate response model using Green's functions has been formulated to calculate radiative forcing (RF) and the global mean temperature response from aviation. The model, LinClim, can calculate aviation RF for CO₂, O₃, CH₄, water vapour, contrails, sulphate and black carbon aerosols. From these RFs, temperature responses may be calculated for individual effects in order to determine their relative importance by applying preliminary values for efficacies. The LinClim model is tuned to reproduce the dominant mode of its parent coupled atmosphere-ocean GCM, ECHAM4/OPYC3. LinClim is able to reproduce the IPCC (1999) 2050 aviation-related forcings. The model is shown through some example application analyses to be a useful tool for exploring the effects of aviation on RF and temperature response.

1 INTRODUCTION

Aircraft emissions may influence climate from a number of emissions and effects. These effects have been reviewed and assessed in the Intergovernmental Panel on Climate Change (IPCC) Special Report '*Aviation and the Global Atmosphere*' (IPCC, 1999). More recently, Sausen et al., (2005) gave an update to the IPCC results on the aviation's impact on climate by means of the metric 'radiative forcing of climate'. This metric has been adopted by the IPCC (IPCC, 1990) and the scientific community to assess different anthropogenic effects on climate. The RF concept has proven useful as there is an approximately linear relationship between the global mean radiative forcing (*RF*) and the associated equilibrium global mean surface temperature change (ΔT_s), i.e.:

$$\Delta T_s \approx \lambda RF \quad , \quad (1)$$

where λ is the climate sensitivity parameter (unit K/Wm⁻²). For many years λ has been considered being a model constant, independent of the type of forcing. More recently, in a number of studies, it has been shown that λ is to some extent also dependent on the type of perturbation, in particular for non-homogeneously distributed climate change agents, e.g., aircraft-induced O₃ perturbations (Hansen et al., 1997; Forster and Shine, 1997; Ponater et al., 1999; Joshi et al., 2003). This is sometimes denoted the 'efficacy' (Hansen et al., 2005) and is defined as:

$$r_i = \lambda_i / \lambda_{CO_2} \quad , \quad (2)$$

where λ_i and λ_{CO_2} are the climate sensitivity parameters associated with perturbations of the climate change agent *i* and of CO₂, respectively. Considering also the efficacy, eq. (1) modifies to

$$\Delta T_s \approx r_i \lambda_{CO_2} RF \quad . \quad (3)$$

^{*} *Corresponding author:* Ling Lim, Dalton Research Institute-CATE, Manchester Metropolitan University, Faculty of Science and Engineering, John Dalton East Building, Chester St, Manchester M1 5GD, UK. Email: l.lim@mmu.ac.uk

The ideal way to explore climate scenarios would be to perform simulations with general circulation models (GCMs). However, GCMs are very complex and computationally demanding: a scenario may need to be run (depending on the climate perturbation) for decades of simulation time taking processing time in the order of weeks to months on a high performance computer (in particular if chemistry is included). The necessity for long simulation periods arises from climate inertia effects and the requirement to separate signal from noise. For aircraft perturbations that are relatively small, this is a particularly difficult problem. In order to overcome the high computational costs associated with determining environmental responses with GCMs, simplified climate response models may be used. Such models are generally tuned or parameterized to reproduce the main characteristic responses of GCMs (such as the temporal evolution of the global mean near surface temperature) and have been used extensively by the IPCC to explore the impacts of a large range of climate scenarios (IPCC, 2001).

Sausen and Schumann (2000) (hereafter referred to as S&S 2000) demonstrated that some of the global mean environmental responses to particular engine technology development scenarios could be conveniently explored with a simple linear climate response model that was computationally efficient. This model went beyond RFs to compute temperature responses over various timescales. Using temperature response rather than RF allows an examination of the effects of r_i by looking at the time-development of changes in ΔT_s , and an assessment of the relative merits of abatement technologies in terms of climate protection.

In this paper, a simplified climate response model, LinClim, which builds upon the approach of S&S (2000) is presented. The scope of the model has been expanded to include the full suite of aviation-specific effects identified by the IPCC (1999). These include RFs and temperature response formulations for CO₂, formation of O₃ and CH₄ destruction due to NO_x, water vapour, contrails, sulphate, soot and indirect clouds.

2 MODEL DESCRIPTION

The modelling approach adopted was to calculate the emissions and subsequent concentrations of a climate gas, calculate its RF, and then to calculate the ΔT_s due to the RF using a simplified climate response function. LinClim includes formulations which are consistent with either the IPCC (1999) or TRADEOFF (Sausen *et al.*, 2005) data (denoted ‘99’ and ‘TO’, respectively). For methodologies that involves reference year scaling, the values may be obtained from various sources.

2.1 Carbon dioxide (CO₂)

In order to calculate the full CO₂ contribution to RF and temperature response, historical fuel and extrapolation out to 2100 were calculated using S&S (2000) methodology. Emissions of CO₂ are then calculated using carbon mass fraction of 0.86 for aviation fuel (S&S 2000). The response of CO₂ concentrations to an emissions rate is modelled using Hasselmann *et al.*, (1997), which approximates to the results of the carbon cycle model of Maier-Reimer and Hasselmann (1987).

The RF of a CO₂ increase is dependent upon the reference concentration because of spectral saturation, such that in calculating the impacts of CO₂ from aviation, it is necessary to know the ‘background’ RF. Historical CO₂ concentration data from 1800 until 1995, and thereafter until 2100 from IPCC scenario IS92a (all natural and anthropogenic sources including aircraft emissions) were used as background (S&S 2000). The contribution of aviation CO₂ concentrations are calculated explicitly, the concentration being assumed to be the difference between background and aviation concentrations. The RF of CO₂ may then be calculated using the simplified expression adopted by IPCC (1997) or IPCC (2001).

2.2 NO_x-induced ozone (O₃) and methane (CH₄)

The aviation O₃ and CH₄ RF methodology assumes that there is a linear relationship between aviation NO_x emissions and O₃ (and indirect CH₄) RF changes (IPCC, 1999), i.e.:

$$RF_{O_3, CH_4}(t) = RF_{O_3, CH_4}(ref\ year) \times \frac{E_a(t)}{E_a(ref\ year)} \times \frac{EI_{NO_x}(t)}{EI_{NO_x}(ref\ year)}, \quad (4)$$

where E_a is the aircraft fuel burnt per year, and EI_{NO_x} is the emissions index of nitrogen oxides per mass of fuel burnt.

2.3 Water vapour (H_2O)

Similar to the calculation of aviation induced O_3 and CH_4 , a simplified linear approach is taken for water vapour where the RF scales linearly with fuel use, i.e.:

$$RF_{H_2O}(t) = RF_{H_2O}(ref\ year) \times \frac{E_a(t)}{E_a(ref\ year)}, \quad (5)$$

2.4 Line-shaped contrails

Contrails RF is assumed to scale with fuel burn and an additional factor, F , to account for the evolution of fleet and flight routes over time (IPCC, 1999) and F was then derived by scaling this RF value to the published values in IPCC (1999) for the years 2015 and 2050. Post 2050, F is assumed to be constant. The F values are summarized in Table 1.

Table 1: Correction factor, F to account for fleet evolution and flight routes

Year	Technology 1	Technology 2
1992	1.00	1.00
2015	1.48	1.48
2050	1.70	1.64

2.5 Sulphate (SO_4) and soot (BC) particles

Aviation SO_4 particle emissions were derived from the sulphur content of fuel, as in eq. (6), where $E_{SO_4}(t)$ is the aviation emissions at time t (Tg S), $EI_{Sulphur}$ is the emissions index 0.0004 kg S per kg fuel, β is the effective conversion factor from fuel-sulphur to optically active sulphate, following IPCC (1999), we adopt $\beta = 50\%$.

$$E_{SO_4}(t) = \beta \times EI_{Sulphur} \times E_a(t) \quad (6)$$

Aviation soot (black carbon, BC) is calculated using eq. (7), where $E_{BC}(t)$ is the aviation emissions at time t (Tg BC) and EI_{BC} is the emissions index 0.00004 kg black carbon per kg fuel (IPCC, 1999).

$$E_{BC}(t) = EI_{BC} \times E_a(t) \quad (7)$$

RF for particles is scaled to the respective particle emissions and externally calculated RF.

$$RF_{SO_4,BC}(t) = RF_{SO_4,BC}(ref\ year) \times \frac{E_{SO_4,BC}(t)}{E_{SO_4,BC}(ref\ year)} \quad (8)$$

2.6 Aviation-induced cirrus

Similar to the water vapour RF calculation, it is assumed that RF of aviation-induced cirrus scales with fuel usage. However, due to the large uncertainties in aviation-induced cirrus calculation (c.f., Sausen et al., 2005; or Mannstein and Schumann, 2007), we refrain from including the contribution from this effect in the final results.

2.7 Temperature response

The temperature response approach was devised by Hasselmann et al., (1993) and has been widely used thereafter (e.g., Hasselmann et al., 1997; S&S 2000). The formulation presented by S&S (2000) has been rearranged to include the perturbation's efficacy:

$$\Delta T_i(t) = r_i \lambda_{CO_2} \int_0^t \hat{G}_T(t-t') RF_i(t') dt', \quad (9)$$

$$\hat{G}_T(t) = \frac{1}{\tau} e^{-t/\tau}, \quad (10)$$

where ΔT_i is the temperature response (K) due to perturbation i . r_i is the associated efficacy, λ_{CO_2} is the CO_2 climate sensitivity parameter (K/Wm^{-2}) of the parent GCM, RF_i is the associated radiative forcing (Wm^{-2}). The revised Green's function is $\hat{G}_T(t)$, τ is the lifetime (e-folding time) of a temperature perturbation (years). The current version of LinClim is tuned to reproduce the transient behaviour of the full-scale atmosphere ocean model ECHAM4/OPYC3 (Roeckner et al., 1999). The value of λ_{CO_2} is $0.64 K/Wm^{-2}$ and τ is 37.4 years. The values for r_i are summarized in Table 2.

Table 2: Efficacies, r_i

Perturbation	Reference	r_i (range)
CO_2, SO_4, BC		1
Aviation O_3	Ponater et al., 2006	1.37 (1 – 2)
CH_4	Ponater et al., 2006	1.18 (1 – 1.2)
H_2O	Ponater et al., 2006	1.14
Contrails	Ponater et al., 2006	0.59

3 APPLICATION

The aviation RF results from LinClim using the '99' parameters (scaled to IPCC (1999) reference values parameters summarized in Table 3), denoted as LC-99, are presented in Table 4. The IPCC (1999) results are basically reproduced. The deviations in RF_{CO_2} result from a slightly different CO_2 concentration. There were noticeable differences in the 1992 RF_{O_3} and $RF_{Contrails}$. This is due to the difference in the 1992 fuel burnt in LinClim (165.1 Tg from S&S, 2000) and the IPCC (1999) (160.3 Tg). Small differences were yielded also for RF_{O_3} and RF_{CH_4} in future years. This is because the IPCC (1999) RF_{O_3} and RF_{CH_4} results were obtained from CTM runs, whereas the results from LC-99 were simply scaled to the NO_x emissions.

Table 3: Reference year (1992 and 2000) parameters used in the example applications

Parameter	Unit	Reference values in 1992 (used in LC-99)	Reference values in 2000 (used in LC-TO)
E_a	Tg/Yr	160.3 [*]	169.0 [†]
E_{SO_4}	Tg S	0.032 [*]	0.0338 [‡]
E_{BC}	Tg BC	0.006 [*]	0.0068 [‡]
$EI NO_x$	g NO_2 /kg fuel	12.0 [*]	12.7 [†]
RF_{O_3}	W/m^2	0.023 [*]	0.0219 [‡]
RF_{CH_4}	W/m^2	-0.014 [*]	-0.0104 [‡]
RF_{H_2O}	W/m^2	0.0015 [*]	0.0020 [‡]
$RF_{Contrails}$	W/m^2	0.020 [*]	0.0100 [‡]
RF_{SO_4}	W/m^2	-0.003 [*]	-0.0035 [‡]
RF_{BC}	W/m^2	0.003 [*]	0.0025 [‡]

^{*}IPCC (1999), [†]Gauss et al. (2006), [‡]Sausen et al. (2005).

A second set of parameters from the TRADEOFF study (Sausen et al., 2005) were used to form an updated version of LinClim, denoted as LC-TO (Table 3). These updated results (see Table 4) show that the contribution of aviation RF is lower than in the previous assessments, both for 1992 and for future scenarios.

Figure 1 shows the total aviation RF (without aviation-induced cirrus) and the associated temperature changes (with and without considering the efficacies) for scenario Fa1 calculated using LinClim with the TRADEOFF parameters (LC-TO). It is interesting to note the role of efficacies in the temperature prediction. Using an efficacy of 1 for all perturbations, the temperature response is approximately the same as the prediction including individual efficacy values for specific perturbation (as listed in Table 2). By chance, the larger contributions from O_3 and H_2O are offset by the smaller contribution from contrails and the more negative contribution from CH_4 . However, by changing the efficacy of O_3 to the lower ($r_{O_3} = 1$) and upper ($r_{O_3} = 2$) bounds, the temperature response is 20% lower ($r_{O_3} = 1$) or 33% higher ($r_{O_3} = 2$) than the case where $r_{O_3} = 1.37$ (as in Table 2) at 2100. This shows that the role of efficacies may become increasingly important in determining

the tradeoffs between different engine technology options, in particular with respect to NO_x which causes component impacts of high efficacy.

Table 4: RF comparison of LinClim with the IPCC (1999) parameters (LC-99) and with the TRADEOFF parameters (LC-TO). (Cont. = Contrails)

Scenario	Data source	CO ₂ (ppmv)	Radiative forcing (W/m ²)					Cont.	SO ₄	BC	Total
			CO ₂	O ₃	CH ₄	H ₂ O					
NASA-1992	IPCC	1.0	0.018	0.023	-0.014	0.002	0.020	-0.003	0.003	0.049	
	LC-99	1.3	0.022	0.024	-0.014	0.002	0.021	-0.003	0.003	0.054	
	LC-TO	1.3	0.019	0.020	-0.012	0.002	0.010	-0.003	0.002	0.038	
NASA-2015	IPCC	2.5	0.038	0.040	-0.027	0.003	0.060	-0.006	0.006	0.114	
	LC-99	2.8	0.044	0.052	-0.032	0.003	0.060	-0.006	0.006	0.128	
	LC-TO	2.8	0.038	0.044	-0.025	0.004	0.028	-0.007	0.005	0.087	
FESGa (tech1) 2050	IPCC	6.0	0.074	0.060	-0.045	0.004	0.100	-0.009	0.009	0.193	
	LC-99	6.3	0.080	0.086	-0.052	0.004	0.100	-0.009	0.009	0.218	
	LC-TO	6.3	0.068	0.073	-0.044	0.006	0.047	-0.010	0.007	0.147	
FESGa (tech2) 2050	IPCC	6.1	0.075	0.047	-0.035	0.005	0.100	-0.009	0.009	0.192	
	LC-99	6.4	0.081	0.066	-0.040	0.005	0.100	-0.009	0.009	0.212	
	LC-TO	6.4	0.069	0.057	-0.027	0.006	0.047	-0.010	0.007	0.149	

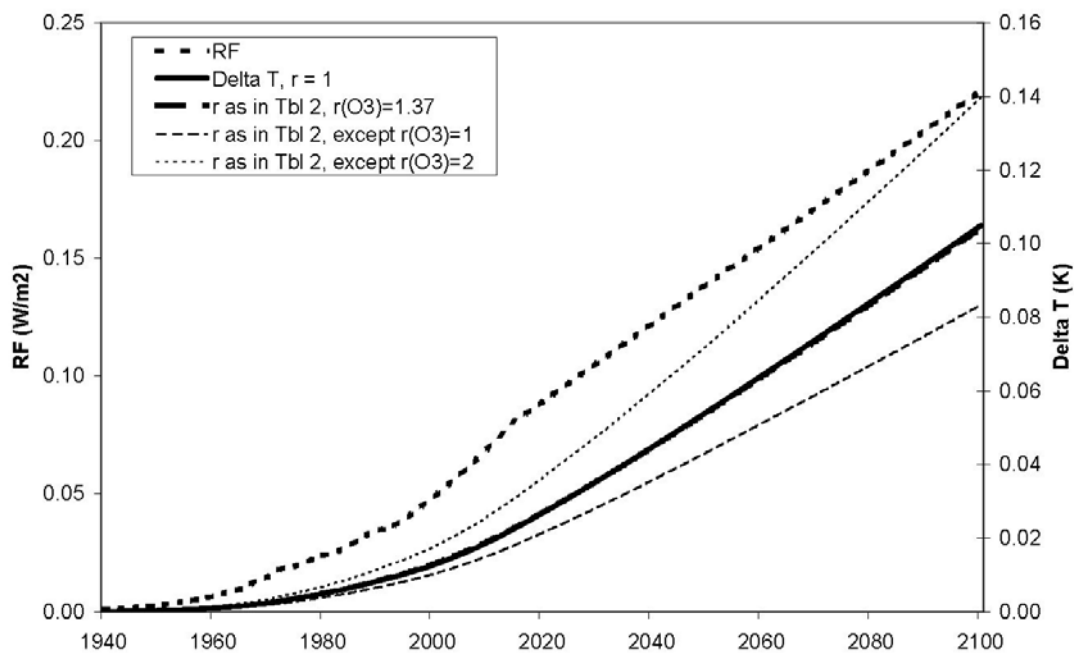


Figure 1: Aviation RF and associated temperature changes (with and without considering the efficacies) for scenario Fa1

4 CONCLUSIONS AND FURTHER WORK

The RF and temperature response results of the simple climate response model, LinClim, are presented. LinClim is able to predict the temperature response from the full suite of aviation perturbations. The present day and future scenario RF results compared well with the published IPCC (1999) values. LinClim's RF results are not intended to replace other RF estimates, but are rather used to describe the contribution of individual impact components to the total aviation effect for transient emission scenarios. In future work the model will be applied more extensively to various technology and growth scenarios to understand the role of aviation and by how technology im-

provements may be best targeted. Moreover, the model will also be useful in exploring more appropriate climate metrics than RF for policy applications.

5 ACKNOWLEDGEMENTS

This study was funded by the EU IP QUANTIFY and EU NoE ECATS. Further support was given from the UK Department of Trade and Industry (DTI) and the UK Department for Transport (DfT).

REFERENCES

- Forster, P.M.D. and K.P. Shine, 1997: Radiative forcing and temperature trends from stratospheric ozone changes. *J. Geophys. Res.* *102*, 10841–10855.
- Gauss, M., I.S.A. Isaksen, D.S. Lee and O.A. Søvde, 2006: Impact of aircraft NO_x emissions on the atmosphere – tradeoffs to reduce the impact. *Atmos. Chem. Phys.* *6*, 1529–1548.
- Hansen, J.E., M. Sato and R. Ruedy, 1997: Radiative forcing and climate response. *J. Geophys. Res.* *102*, 6831–6684.
- Hansen, J., M. Sato, R. Ruedy, L. Nazarenko, A. Lacis, G.A. Schmidt, G. Russell and 38 other co-authors, 2005: Efficacy of climate forcings. *J. Geophys. Res.* *110*, D18104, doi:10.1029/2005JD005776.
- Hasselmann, K., R. Sausen, E. Maier-Reimer and R. Voss, 1993: On the cold start problem in transient simulations with coupled atmosphere-ocean models. *Clim. Dyn.* *9*, 53–61.
- Hasselmann, K., S. Hasselmann, R. Giering, V. Ocana and H. von Storch, 1997: Sensitivity study of optimal CO₂ emission paths using a Simplified Structural Integrated Assessment Model (SIAM). *Clim. Change* *37*, 345–386.
- IPCC, 1990: *Climate Change: The IPCC Scientific Assessment*. Contribution of Working Group I to the First Assessment Report of the Intergovernmental Panel on Climate Change. J.T. Houghton, G.J. Jenkins and J.J. Ephraums (eds). Intergovernmental Panel on Climate Change, Cambridge University Press, UK.
- IPCC, 1997: *An introduction to simple climate models used in the IPCC Second Assessment Report*. IPCC Technical Paper II. J.T. Houghton, L. Gylvan Meira Filho, D.J. Griggs and K. Maskell (eds), Intergovernmental Panel on Climate Change, Switzerland.
- IPCC, 1999: *Aviation and the Global Atmosphere*. A Special Report of IPCC Working Groups I and III in collaboration with the Scientific Assessment panel to the Montreal Protocol on Substances that Deplete the Ozone Layer. J.E. Penner, D.H. Lister, D.J. Griggs, D.J. Dokken and M. McFarland (eds). Intergovernmental Panel on Climate Change, Cambridge University Press, UK.
- IPCC, 2001: *Climate Change 2001: The Scientific Basis*. Contribution of Working Group I to the Third Assessment Report of the Intergovernmental Panel on Climate Change. J.T. Houghton, Y. Ding, D.J. Griggs, M. Noguer, P.J. van der Linden, X. Dai, K. Maskell and C.A. Johnson (eds). Intergovernmental Panel on Climate Change, Cambridge University Press, UK.
- Joshi, M., K. Shine, M. Ponater, N. Stuber, R. Sausen and L. Li, 2003: A comparison of climate response to different radiative forcings in three general circulation models: towards an improved metric of climate change. *Clim. Dyn.* *20*, 843–854.
- Maier-Reimer, E. and K. Hasselmann, 1987: Transport and storage of CO₂ in the ocean – An inorganic ocean-circulation carbon cycle model. *Clim. Dyn.* *2*, 63–90.
- Mannstein, H. and U. Schumann, 2007: Corrigendum to "Mannstein, H., U. Schumann, 2005: Aircraft induced contrails over Europe. *Meteorol. Zeit.* *14*, no. 4, p. 549–554.", *Meteorol. Zeit.*, in press.
- Ponater, M., R. Sausen, B. Feneberg and E. Roeckner, 1999: Climate effect of ozone changes caused by present and future air traffic. *Clim. Dyn.* *15*, 631–642.
- Ponater, M., S. Pechtl, R. Sausen, U. Schumann and G. Hüttig, 2006: Potential of the cryoplane technology to reduce aircraft climate impact: A state-of-the-art assessment. *Atmos. Environ.* *40*, 6928–6944.
- Roeckner, E., L. Bengtsson, J. Feichter, J. Lelieveld and H. Rodhe, 1999: Transient climate change simulations with a coupled atmosphere-ocean GCM including the tropospheric sulfur cycle. *J. Climate* *12*, 3004–3032.
- Sausen, R. and U. Schumann, 2000: Estimates of the climate response to aircraft CO₂ and NO_x emissions scenarios. *Clim. Change* *44*, 27–58.
- Sausen, R., I. Isaksen, V. Grewe, D. Hauglustaine, D.S. Lee, G. Myhre, M.O. Köhler, G. Pitari, U. Schumann, F. Stordal and C. Zerefos, 2005: Aviation radiative forcing in 2000: an update on IPCC (1999). *Meteorol. Zeit.* *114*, 555–561.

Radiative forcing and temperature response from shipping

D. S. Lee*, L. Lim

Dalton Research Institute, Manchester Metropolitan University, John Dalton Building, Chester Street, Manchester M1 5GD, United Kingdom

V. Eyring, R. Sausen

DLR-Institut für Physik der Atmosphäre Oberpfaffenhofen, Germany

Ø. Endresen, H.-L. Behrens

Det Norske Veritas, Veritasveien1, N-1322 Høvik, Norway

Keywords: Radiative forcing, simple climate model, shipping emissions, temperature response

ABSTRACT: A simplified global climate response model was used to calculate radiative forcings and temperature responses from the emissions of shipping. Radiative forcings were calculated for 2000, which were: 0.043 W m^{-2} (CO_2); 0.021 W m^{-2} (O_3); -0.011 W m^{-2} (CH_4). If these forcings are combined with literature values for SO_4 , black carbon and the indirect aerosol effect, a total forcing of -0.08 W m^{-2} was calculated. Comparing the 2000 CO_2 shipping radiative forcing and temperature responses with those for aviation showed them to be approximately $1.8\times$ and $2.7\times$ greater.

1 INTRODUCTION

Ocean-going shipping provides an important means of international transportation of goods, along with other purposes such as fishing, leisure transport etc. Shipping has been operational on an international scale since approximately the industrial revolution, initially as sail ships, then steam ships powered by coal. Since *circa* 1910, diesel engines were introduced. By 1961, there were still over 10,000 steam engine powered ships and $\sim 3,500$ steam turbine powered ships in operation.

The combustion of coal and diesel results in a variety of emissions including carbon dioxide (CO_2), oxides of nitrogen (NO_x), carbon monoxide (CO), methane (CH_4), other non-methane volatile organic compounds (VOCs) and particles. In addition to sulphate particles (SO_4) resulting from SO_2 emissions, ships also release black carbon (BC) and particulate organic matter (POM).

These emissions contribute to perturbation of the global carbon, sulphur and nitrogen budgets. They result in both direct warming effects from CO_2 and CH_4 , potential indirect warming effects from the emission of ozone (O_3) precursors (NO_x , CH_4 , CO and VOCs) and indirect cooling effects from shipping emissions of NO_x , which increases OH resulting in a reduction in CH_4 lifetime (Endresen et al., 2003; Eyring et al., 2007). The increases in SO_4 and BC concentrations also have direct but opposing effects resulting from enhanced scattering and reflection of solar radiation/downwelling of long-wave radiation and an indirect effect from the formation of 'ship tracks' (e.g. Schreier et al., 2006) and large-scale low marine clouds (Capaldo et al., 1999).

In this work, the global mean radiative forcing (RF) and temperature response from shipping emissions was calculated for most of the forcing agents. A climate response model was adapted to deal with shipping radiative effects in a parameterized way from a similar model developed for evaluating global mean aviation effects (Lim et al., 2007), which in turn was developed from the simpler model of Sausen and Schumann (2000). Such climate response modelling was originally developed by Hasselmann et al. (1993), which has been adapted for a variety of applications.

Since much research has been dedicated to understanding the response of the climate system to aircraft emissions, some simple comparisons are made between the two transportation sectors and projected emissions scenarios in the future.

* *Corresponding author:* D. S. Lee, Dalton Research Institute-CATE, Manchester Metropolitan University, Faculty of Science and Engineering, John Dalton East Building, Chester St, Manchester M1 5GD, UK. Email: D.S.Lee@mmu.ac.uk

2 METHODOLOGY

In this section, the emissions estimations are summarized and details of the climate response model provided that are particular to the quantification of shipping RF and temperature responses.

2.1 Emissions

Present day shipping emissions are taken from Eyring et al. (2005a; hereafter EY2005a) for CO₂, NO_x, VOCs, CH₄ and CO. Historical emissions from shipping were taken from two different sources for comparison. EY2005a calculated emissions from 1950 to 2001. However, engine-driven shipping has a much longer history that dates back to *circa* 1870. For earlier shipping emissions, shipping emissions data are taken from Endresen et al. (2007). Two estimations of shipping CO₂ radiative forcing can be made to 2000; one using the data of Endresen et al. (2007; hereafter EN2007) and another using these data from 1870 to 1950 combined with EY2005a from 1950 to 2000.

For future emissions, Eyring et al. (2005b) provided estimations according to four demand scenarios (DS1-DS4) and four technology scenarios (TS1-TS4) to 2050. However, in order to better represent the climate response, transient runs to 2100 are needed. Therefore, the central demand/technology scenario (DS1-TS4) of Eyring et al. (2005b) has been extrapolated out to 2100.

For the comparison with aviation, a full historical and projected scenario of emissions from 1940 through to 2050, extrapolated out until 2100 has been taken from Sausen and Schumann (2000).

2.2 Climate response model

The LinClim climate response model (Lim et al., 2007) has been adapted to calculate RFs and temperature responses from shipping emissions. The contribution of shipping emissions of CO₂ to concentrations was calculated according to the method of Hasselmann et al. (1997) and these were subtracted from historical 'background' CO₂ concentrations up until 1995, thereafter using concentrations from the IS92a scenario to 2100. The CO₂ RF was then calculated from the CO₂ concentrations according to the method of IPCC (2001). The temperature response was calculated via a convolution integral method (Hasselmann et al., 1993) using an updated fit to the parent GCM, ECHAM4/OPYC3 (Lim et al., 2007).

For CH₄, a global mean mass balance equation was used, which accounts for changes in CH₄ lifetime from tropospheric, stratospheric and soil sinks (Wigley et al., 2002). The tropospheric lifetime, τ_{OH} , was determined from Equation [1] (IPCC, 2001).

$$\delta \ln(\tau_{OH})_t = -0.32\delta \ln(C)_{t-1} + 0.0042\delta(e - NO_x)_t - 0.000105\delta(e - CO)_t - 0.000315\delta(e - VOC)_t \quad [1]$$

where $(\tau_{OH})_t$ is the tropospheric sink at time t (yr), $(e - NO_x)_t$ are the anthropogenic NO_x emissions at time t (Tg(N)/yr), $(e - CO)_t$ are the anthropogenic CO emissions at time t (Tg/yr), and $(e - VOC)_t$ are the anthropogenic VOC emissions at time t (Tg/yr)

It was assumed that all changes in lifetime, concentration and emissions are relative to the year 2001. It was also assumed that the natural emissions of CH₄, NO_x, CO and VOC remain constant. The mass balance equation predicts background CH₄ and the same equation was used to calculate the shipping component, using the difference between background and shipping emissions of NO_x, CO, CH₄ and VOCs in Equation [1].

The RF arising from the CH₄ perturbation was calculated from the method presented by IPCC (2001) which accounts for N₂O overlap.

$$RF_{CH_4} = \alpha(\sqrt{C_{(t)}} - \sqrt{C_0}) - (f(C_t, N_0) - f(C_0, N_0)) \quad [2]$$

where α is 0.036, C_t is the CH₄ concentration at time t (ppbv), C_0 is the pre-industrial CH₄ concentration (700 ppbv), N_0 is the pre-industrial N₂O concentration (280 ppbv) and $f(C, N)$ is the correction for overlap with N₂O:

$$f(C, N) = 0.47 \ln(1 + 2.01 \times 10^{-5} (C \cdot N)^{0.75} + 5.31 \times 10^{-15} C(C \cdot N)^{1.52}) \quad [3]$$

The CH₄ RF from shipping emissions was calculated from Equation [4]

$$RF_{CH_4}(shipping) = RF_{CH_4}(C_{Background}) - RF_{CH_4}(C_{Background - shipping}) \quad [4]$$

A simple relationship between a change in O₃ column (Dobson Units – DU) and O₃ RF was presented by IPCC (2001). The pre-industrial global mean O₃ column was taken as 25 DU and historical O₃ forcings were also taken from IPCC (2001) to 2000, for which the RF was estimated to be 0.38 W m⁻². The mean forcing per DU is 0.042 W m⁻²/DU. For future changes in column O₃ the relationship presented by IPCC (2001) between O₃ DU and NO_x, CH₄, CO and VOC emissions was used:

$$\delta(O_3)_t = +5.0\delta\ln(CH_4)_{t-1} + 0.125\delta(e-NO_x)_t + 0.0011\delta(e-CO)_t + 0.0033\delta(e-VOC)_t \quad [5]$$

where $(O_3)_t$ is the tropospheric O₃ at time t (DU), CH₄ (ppbv), $(e-NO_x)_t$ are the anthropogenic NO_x emissions at time t (Tg(N)/yr); $(e-CO)_t$ are the anthropogenic CO emissions at time t (Tg/yr), and $(e-VOC)_t$ are the anthropogenic VOC emissions at time t (Tg/yr).

It was also assumed that the natural emissions of CH₄, NO_x, CO and VOC remain constant. Therefore, the emissions scenario describes all changes in emissions.

It was assumed that equation [5] predicts background tropospheric O₃ (in DU) relative to the year 2001 and the same equation was used to calculate the shipping component, using shipping emissions of NO_x, CO, CH₄ and VOCs. Therefore, the O₃ concentrations arising from shipping are assumed to be the difference between the background and shipping O₃ concentrations as in Equation [5]. The RF from the O₃ perturbation was calculated using Equation [6].

$$(RF_{O_3})_t = 0.042 \times \delta(O_3)_t + (RF_{O_3})_{2000} \quad [6]$$

3 RESULTS

Two time-evolved CO₂ RF responses from shipping have been calculated from the emission datasets (i.e. EN2007, and EN2007+EY2005a) to 2000. The emissions are shown in Figure 1a and the subsequent CO₂ RF in Figure 1b. The time-evolution of emissions is evidently quite different over the period 1940 to 2000, with the estimates of EY2005a being based on interpolation of individual years (1950, 1960, 1970, 1980, 1995 and 2001), such that the reductions and subsequent increases between 1980 and 1990 as shown by EN2007 are not featured. By contrast, the emissions estimates of EN2007 between 1940 and 1975 are greater than those of EY2005a. These two features in the data have a cancelling effect in the CO₂ RF (Figure 2) by 2000 such that they reach approximately the same value of ~ 0.0425 W m⁻².

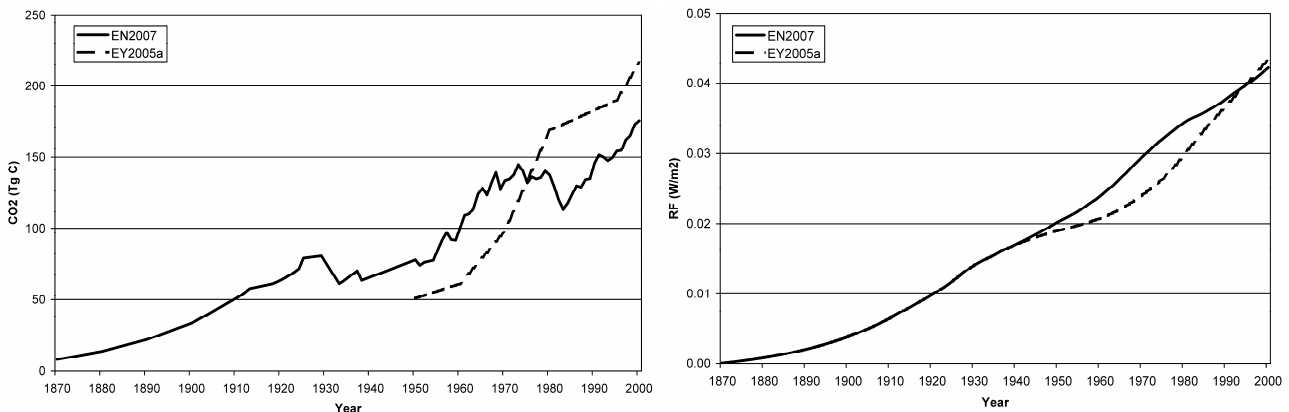


Figure 1. Panel a. Emissions of CO₂ from shipping between 1870 and 2000 according to EY2005a and EN2007, including back-extrapolation from 1925 to 1870. Panel b. Radiative forcing of CO₂ from shipping according to estimates of EY2005a and EN2007, including back-extrapolation from 1925 to 1870.

4 DISCUSSION

4.1 An estimation of the total radiative forcing impact from shipping in 2000

The model can be used to estimate RFs from shipping for CO₂, O₃ and CH₄, and SO₄. Currently, it does not have BC and the indirect aerosol effect implemented. If shipping RFs for 2000 calculated here are combined with independent estimates of these RFs not calculated in the model, an overall RF chart for 2000 can be given in a similar fashion (Figure 2) to those presented for aviation (IPCC, 1999; Sausen et al., 2005).

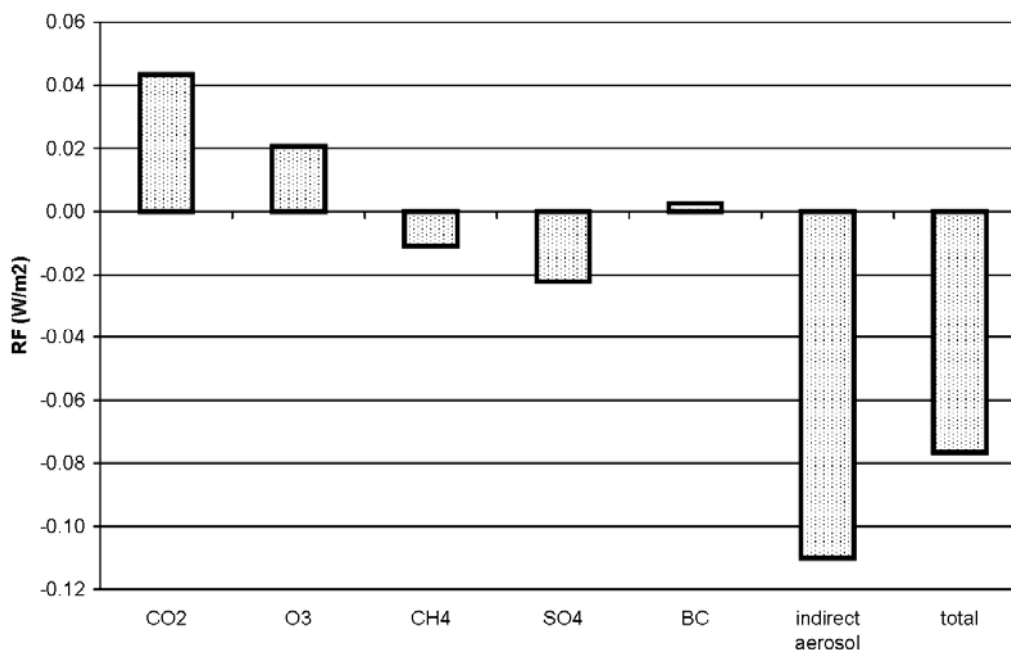


Figure 2. Radiative forcing from shipping effects in 2000: CO₂, O₃, CH₄ responses as calculated with the linear response model; BC and the indirect effect from Berntsen (2004) and Capaldo et al. (1999).

The O₃ RF was calculated to be 0.021 W m⁻². This is approximately twice the value of 0.0098 ± 0.002 W m⁻² calculated by Eyring et al. (2007) using a suite of chemical transport models (CTMs). However, the emissions used by Eyring et al. (2007) were approximately one half those (in 2000) used in this study (3.10 TgN instead of 6.51 Tg N yr⁻¹), such that the response scales linearly.

Since the negative RFs from the direct effect of SO₄ and the indirect effect dominate, the total RF is negative, implying an overall cooling on a global mean basis. However, it is questionable as to whether such a global mean additivity is meaningful where strong positive and negative forcings are involved, some of which are spatially heterogeneous – this is basically a question over the usefulness of the RF metric which is a subject of debate for issues such as this. An overall negative RF from shipping that comprises both positive and negative forcings could mistakenly be interpreted as either being benign, or even *in extremis* counteracting other positive RFs. The fallacy of this interpretation is that if the sulphur in the fuel were removed, then the negative SO₄ RF would disappear in a matter of weeks, and a similar response is possible for the overall indirect aerosol effect due to shipping. In such a case where S was reduced, and the RF from this effect reduced, one would still be left with a long-term positive RF and warming from historical CO₂ emissions.

4.2 A comparison of shipping and aviation CO₂ radiative forcing and temperature response

It is of interest to compare aviation with shipping effects on climate since the international emissions from both of these sectors are not covered by the Kyoto Protocol because of the complication of allocating emissions. Here, only the CO₂ RF and temperature responses for shipping and aviation are compared. A more comprehensive comparison of RF effects is not yet possible because of limited emissions data availability.

In the comparison made here, the responses from the ‘beginning’ of shipping and aviation, i.e. 1870 and 1940 were calculated for a range of scenarios through to 2050, and thereafter to 2100 for

a single scenario. In 2000, the CO₂ RF from shipping was approximately 1.8 times that of aviation's CO₂ RF. However, the assumed growth of aviation and shipping CO₂ emissions means that the difference between the RFs diminishes and starts to converge by 2100.

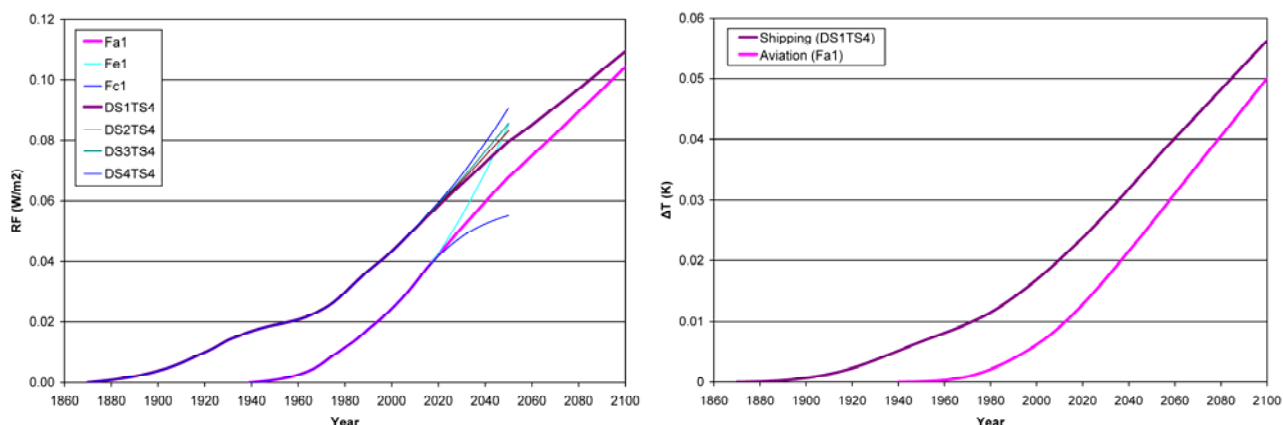


Figure 3. Panel a. Time evolution of CO₂ radiative forcing from shipping and aviation from 1870 and 1940, respectively, to 2050 under assumptions of central emission scenarios, thereafter linearly extrapolated to 2100. Panel b. Time evolution of CO₂ temperature response from shipping and aviation from 1870 and 1940, respectively, to 2050 under assumptions of central emission scenarios, thereafter linearly extrapolated to 2100.

If Figure 3b is examined for the temperature response effect on climate from these sectoral CO₂ emissions, the shipping temperature effects is a factor of ~ 2.7 times that of aviation in 2000 and ~ 1.1 times that of aviation in 2100.

4.3 Future work and limitations of the modelling approach

The purpose of the model is to calculate *time-evolved* RFs for the calculation of temperature response(s). For some forcing agents such as CO₂, O₃ and CH₄, the RFs can be calculated explicitly, albeit in a parameterized manner. For other agents such as the direct effect from SO₄ and BC or the indirect aerosol effect, individual yearly values may be used with some parameter (such as fuel) to scale these RFs over time in order to calculate temperature responses. As independent estimates of some of these forcing effects become available, they will be implemented in the model. Whilst the RF response to shorter-lived climate forcing agents such as O₃, SO₄ etc. is relatively fast, it should be remembered that the *temperature* response to these forcings is longer because of the thermal inertia of the climate system arising from the slow exchange times of heat between the ocean and the atmosphere. In the future, a complete history of emissions of NO_x, CO, VOCs and CH₄ are needed to calculate the temperature response from shipping-induced changes in O₃ and CH₄ RFs.

The nature of the model has limitations that should be born in mind when interpreting the output: it is a *global mean* model, such that it is a robust method to calculate temperature response for homogeneous forcings (assuming that it is appropriately tuned to some GCM). For other forcings such as O₃, BC, SO₄ or the indirect aerosol effect, the spatial forcing is highly heterogeneous and it is not necessarily the case that a global mean response is entirely appropriate for interpreting the overall temperature response to, e.g., shipping emissions in an additive manner. However, to a first order, such global mean models can produce useful initial data for a first-order interpretation of the impacts of a transport sector such as shipping.

5 CONCLUSIONS

- This study addresses time-evolved RFs and temperature responses from some of the effects of shipping, particularly CO₂, O₃ and CH₄.
- A robust estimate of shipping CO₂ RF has been made for 2000 with the usage of a full history of shipping's emissions of 0.043 W m⁻². A shipping O₃ RF of 0.021 W m⁻² in 2000 has been calculated using a simple method, which is in agreement with independent calculations using complex

3D chemical transport models, allowing for a linear scaling of emissions. Shipping NO_x emissions result in a negative CH₄ RF of -0.01 W m⁻² in 2000, as calculated with a simplified methodology.

- Combining these RFs with others not calculated with the model result in an overall global mean RF due to shipping in 2000 of approximately -0.08 W m⁻².
- Shipping CO₂ RF was approximately 1.8 times that of aviation in 2000 and the resultant temperature response of (CO₂ only) for shipping was found to be 2.7 times that of aviation in 2000.

6 ACKNOWLEDGEMENTS

This work is a contribution to the EU Sixth Framework Project 'Quantify', contract no.003893 (GOCE). DSL and LL (MMU) were additionally funded by UK Dft & DTi; RS and VE (DLR) were funded by the Quantify project and the Helmholtz-University Young Investigators Group SeaKLIM. ØE and HLB (DNV) were funded by the Quantify project.

7 REFERENCES

- Berntsen T. 2004: impacts of aviation and other transport modes on the atmosphere: a European perspective. Presentation at NERC Town Meeting, 'Aviation Impacts on the Atmosphere', 11-12th November, Birkbeck College, NCAS workshop, UK.
- Capaldo K., Corbett J. J., Kasibhatla P., Fischbeck P and Pandis S. N. 1999: Effects of ship emissions on sulphur cycling and radiative climate forcing over the ocean. *Nature* 400, 743 – 746.
- Endresen, Ø., E. Sørgård, J. K. Sundet, S. B. Dalsøren, I. S. A. Isaksen, T. F. Berglen, and G. Gravir., 2003: Emission from international sea transportation and environmental impact. *J. Geophys. Res.* 108, 4560, doi:10.1029/2002JD002898.
- Endresen Ø., P. O. Brett, H. L. Behrens, E. Sogård and I. S. A. Isaksen, 2006: A historical reconstruction of ships energy consumption and emissions. *J. Geophys. Res.* (submitted).
- Eyring, V., H.W. Köhler, J. van Aardenne, and A. Lauer 2005a: Emissions from international shipping: 1. The last 50 years. *J. Geophys. Res.* 110, D17305, doi:10.1029/2004JD005619.
- Eyring, V., H. W. Köhler, A. Lauer, and B. Lempert 2005b: Emissions from international shipping: 2. Impact of future technologies on scenarios until 2050. *J. Geophys. Res.*, 110, D17306, doi:10.1029/2004JD005620.
- Eyring, V., D. S. Stevenson, A. Lauer, F. J. Dentener, T. Butler, W. J. Collins, K. Ellingsen, M. Gauss, D. A. Hauglustaine, I. S. A. Isaksen, M. G. Lawrence, A. Richter, J. M. Rodriguez, M. Sanderson, S. E. Strahan, K. Sudo, S. Szopa, T. P. C. van Noije and O. Wild 2007: Multi-model simulations of the impact of international shipping on atmospheric chemistry and climate in 2000 and 2030. *Atmos. Chem. Phys.*, accepted.
- Hasselmann K., R. Sausen, E. Maier-Reimer, and R. Voss, 1993: On the cold start problem in transient simulations with coupled atmosphere-ocean models. *Clim. Dynamics* 9, 53–61.
- IPCC 1999: Aviation and the global atmosphere, J.E. Penner, D.H. Lister, D.J. Griggs, D.J. Dokken, M. McFarland (Eds), Cambridge University Press, Cambridge, UK.
- IPCC 2001: Climate change 2001: The Scientific Basis. Contribution of Working Group 1 to the Third Assessment Report, J.T. Houghton (Eds), Cambridge University Press, Cambridge, UK.
- Lim L. L., D. S. Lee, R. Sausen, and M. Ponater 2007: Quantifying the effects of aviation on radiative forcing and temperature with a climate response model. *Clim. Change* (submitted).
- Sausen R. and U. Schumann, 2000: Estimates of the climate response to aircraft CO₂ and NO_x emissions scenarios. *Clim. Change* 44, 27-58.
- Sausen R., I. Isaksen, V. Grewe, D. Hauglustaine, D. S. Lee, G. Myhre, M. O. Köhler, G. Pitari, U. Schumann, F. Stordal, and C. Zerefos, 2005: Aviation radiative forcing in 2000: and update on IPCC (1999). *Met. Zeitschrift* 114, 555–561.
- Schreier, M., A. A. Kokhanovsky, V. Eyring, L. Bugliaro, H. Mannstein, B. Mayer, H. Bovensmann, and J. P. Burrows, 2006: Impact of ship emissions on the microphysical, optical and radiative properties of marine stratus: a case study. *Atmos. Chem. Phys.* 6, 4925–4942.

Contrails, contrail cirrus, and ship tracks

K. Gierens*

DLR-Institut für Physik der Atmosphäre Oberpfaffenhofen, Germany

Keywords: Aerosol effects on clouds and climate

ABSTRACT: The following text is an enlarged version of the conference tutorial lecture on contrails, contrail cirrus, and ship tracks. I start with a general introduction into aerosol effects on clouds. Contrail formation and persistence, aviation's share to cirrus trends and ship tracks are treated then.

1 INTRODUCTION

The overarching theme above the notions “contrails”, “contrail cirrus”, and “ship tracks” is the effects of anthropogenic aerosol on clouds and on climate via the cloud's influence on the flow of radiation energy in the atmosphere. Aerosol effects are categorised in the following way:

- Direct effect: Aerosol particles scatter and absorb solar and terrestrial radiation, that is, they interfere directly with the radiative energy flow through the atmosphere (e.g. Haywood and Boucher, 2000).
- Semidirect effect: Soot particles are very effective absorbers of radiation. When they absorb radiation the ambient air is locally heated. When this happens close to or within clouds, the local heating leads to buoyancy forces, hence overturning motions are induced, altering cloud evolution and potentially lifetimes (e.g. Hansen et al., 1997; Ackerman et al., 2000).
- Indirect effects: The most important role of aerosol particles in the atmosphere is their role as condensation and ice nuclei, that is, their role in cloud formation. The addition of aerosol particles to the natural aerosol background changes the formation conditions of clouds, which leads to changes in cloud occurrence frequencies, cloud properties (microphysical, structural, and optical), and cloud lifetimes (e.g. Lohmann and Feichter, 2005).

Water clouds always form right at water saturation because there are always enough aerosol particles present, so that the vapour can immediately condense and form droplets. The addition of anthropogenic aerosol, for water clouds therefore leads to more numerous but smaller droplets (Twomey effect, Twomey, 1974, 1977). Since radiation scattering gets stronger with decreasing droplet size (when the water mass stays constant) the Twomey effect makes clouds more reflective of solar radiation. Ship tracks are a good example of this effect. Since the droplets get smaller when additional aerosol is present, their tendency to fall relative to the air will be reduced. This weakens the cloud's tendency to form drizzle.

Ice clouds are more complicated than water clouds, because they do not form right at ice saturation. Instead, the natural way of cirrus formation is freezing of supercooled aqueous solution droplets, which needs supersaturations of 45% and more, depending on temperature. Ice nuclei (from anthropogenic sources) that commence to form ice at lower supersaturations may inhibit the build-up of the large supersaturations necessary for freezing of the solution droplets. This generally leads to less and larger ice crystals with a corresponding higher tendency to precipitate. Aerosol particles from aviation could act in this way, but this is yet a hypothesis.

Contrails can form in the blue sky when the ambient air is not supersaturated enough to allow natural formation of cirrus. In the wake of an aircraft, the humidity can reach transiently very high supersaturation, sufficient to let the exhaust particles act as condensation nuclei. Once formed, the contrail ice crystals (at least a fraction of them) can survive as soon as the ambient air is supersaturated. In such a case the contrail can grow laterally into a so-called contrail cirrus, i.e. a naturally

* *Corresponding author:* Klaus Gierens, DLR-Institut für Physik der Atmosphäre, Oberpfaffenhofen, D-82205 Wessling, Germany. Email: Klaus.Gierens@dlr.de

looking cirrus cloud that would not exist without the prior formation of a contrail. This kind of cirrus formation occurs quite frequently.

2 CONTRAILS AND CONTRAIL CIRRUS

2.1 Contrail formation

Contrail formation is like breathing in cold air: Mixing of hot and moist exhaust gases with sufficiently cold ambient air can lead to transient water supersaturation. Exhaust particles and ambient aerosol particles entrained by the vigorous swirling vortex act as condensation nuclei, the supersaturated vapour condenses and quickly freezes in the cooling mixture. Contrail formation takes about 1/3 s.

Whether or not a contrail forms can be decided by the Schmidt-Appleman criterion (Schumann, 1996), a thermodynamic criterion that says that the mixture of the exhaust gases with ambient air must achieve supersaturation with respect to water. In-flight tests of the Schmidt-Appleman criterion have shown its validity (Busen and Schumann, 1995; Jensen et al., 1998; Kärcher et al., 1998). The fact that water saturation must be reached and that ice saturation is not sufficient for contrail formation is due to the poor ice nucleating efficiency of the exhaust particles.

An interesting consequence of the Schmidt-Appleman theory is that modern aircraft can produce contrails in warmer air than old aircraft, that is at lower altitudes (Schumann, 2000; Schumann et al. 2000). The reason behind that is that the exhaust gases of modern, more efficient, engines are cooler than those of old engines (a larger fraction of the fuel energy is used for propulsion), so that water saturation can be achieved in warmer ambient conditions.

Another way of contrail formation is by the aerodynamic cooling of the air flowing over the wing (see Gierens et al., this volume). This process is independent of the Schmidt-Appleman criterion.

2.2 Contrail-to-Cirrus transition

The Schmidt-Appleman criterion says only whether or not a contrail can form. It says nothing about the persistence of a contrail. Whether a contrail is persistent or not depends on the ambient relative humidity with respect to ice. One should note that water supersaturation is required only for a fraction of a second during the mixing process to trigger droplet condensation; in principle, a contrail can be formed even in totally dry air, yet a very short one. A contrail can survive until the wake vortices burst (after about 2 min) when the humidity is closer to but below ice saturation. Such a condition can easily be recognized by a ground observer by watching how the contrail evolves into closed rings that quickly vanish. An example is given in Figure 1.



Figure 1. Short non-persistent contrail that forms vortex rings and evaporates then (source: DLR).

Contrail persistence beyond the lifetime of the vortices requires ice supersaturation. Ice supersaturation is a relatively frequent phenomenon in the upper troposphere; it even occurs sometimes in the stratosphere, just above the tropopause. From MOZAIC data we can derive that commercial air traffic routes are about 15% of their way in ice supersaturated air masses (Gierens et al., 1999). Ice supersaturated regions have a mean horizontal extension of 150 km, but specimens with extensions of several thousand kilometres have been found (Gierens and Spichtinger, 2000). Their mean vertical extension is about half a kilometre, at least over Lindenberg in eastern Germany where the measurements took place (Spichtinger et al., 2003). Lifetimes exceeding a day have been found in case studies (Spichtinger et al., 2005), and a few days lifetime of contrail clusters have been found in satellite imagery as well (Bakan et al., 1994).

Contrail-to-cirrus transition starts with the break-up of the vortices. The number of ice crystals that survive the vortex phase is an important initial condition for contrail-to-cirrus transition, as well as the vertical extent and distribution of the ice in the contrail. Both depend strongly on aircraft parameters and ambient conditions, in particular, the degree of supersaturation and temperature. For instance, the fraction of ice crystals surviving the vortex phase is nearly zero just at saturation, and increases to nearly all at about 10-20% supersaturation. Unterstrasser et al. (this volume) give more details on this. The large variability of initial conditions for contrail-to-cirrus transition probably implies a large variation in the properties of the resulting contrail cirrus. The prime mechanism of the transition is spreading of the contrail due to vertical variation of horizontal wind speed, the wind shear. Spreading rates increase with increasing wind shear and with increasing initial vertical extension of the contrail (Dürbeck and Gerz, 1996; Gerz et al., 1998). Horizontal spreading rates ranging from 18 to 140 m/min have been measured with a scanning lidar (Freudenthaler et al., 1995; Freudenthaler, 2000). In a case study, Duda et al. (2004) estimated contrail spreading rates of 2.7 km/h from satellite imagery and weather forecast wind fields.

The later evolution of contrail cirrus depends on the spreading rates and the ambient humidity field. Spreading alone implies dispersion of the ice crystals over a large area, decreasing the optical thickness of the contrail. However, the crystals grow in the supersaturated air, and fresh moisture is mixed into the contrail during the spreading process. The ice mass per crystal increases, and so does the optical thickness. At the same time, the growing crystals may grow enough to eventually fall out of the ice supersaturated region and to evaporate, again decreasing the optical thickness of the contrail cirrus. Usually, persistent contrails don't appear as single objects, and the spreading of several contrails finally leads to a contrail deck (Gierens, 1998) in which the evolution of one contrail cannot be considered separately from the others. Contrail decks also often evolve close to natural cirrus clouds. There is not much known about the evolution of contrail decks nor about the evolution of contrails close to or within cirrus clouds.

2.3 *Aviation's share of cirrus trends*

A long-standing question in relation to air traffic has been whether aviation increases the average cloudiness and whether it affects other weather parameters like daily sunshine duration and temperature range. Here I concentrate on studies that relate aviation with trends of cirrus cloudiness.

Boucher (1999) took ground and ship based cloud observations of the period 1982-1991, grouped into early (1982-1986) and late (1987-1991). He then correlated the late minus early differences of cirrus frequency of occurrence, ΔC , in $3^\circ \times 3^\circ$ grid boxes with the aviation fuel consumption, F , in the same area. He found that essentially ΔC increases with F . Highest ΔC occurred in main air flight corridors, NE USA (+13.3%/decade), and North Atlantic Flight Corridor (+7.1%/decade). Boucher stated that effects of volcanoes, long term changes in relative humidity, or climate variations related to the North Atlantic Oscillation (NAO) could not solely explain the trend in C , nor its regional distribution.

Minnis et al. (2001) performed a similar study, adding satellite data. They found consistency in trends of cirrus and contrails over USA, but not so over Europe, which could point to other important influences on cloudiness, that are stronger in Europe than in USA.

Zerefos et al. (2003) took other potential influence factors into account in their study, namely El Niño Southern Oscillation (ENSO), NAO, and the Quasi Biennial Oscillation (QBO). They deseasonalised the cirrus time series and removed the ENSO, NAO, and QBO signals. Possible effects of changing tropopause temperatures and convective activity were removed by linear regression. Only the residuals were correlated with air traffic. These were found to increase, sometimes statistically

significantly, in regions with heavy air traffic, although an overall decrease of cirrus frequency was found. Consistent with Minnis et al., the most significant correlations were found over North America (winter season) and over the NAFC (summer season), while the correlations over Europe were insignificant (at a 95% level).

Stubenrauch and Schumann (2005) studied satellite data (1987-1995) for trends of effective high cloud amount. They introduced a new element in these studies by grouping their data into three classes, according to the retrieved upper tropospheric humidity over ice, UTHi (an average of relative humidity over a thick layer in the upper troposphere, say from 200 to 500 hPa): (1) UTHi high enough for cirrus formation; (2) UTHi not sufficient for cirrus formation, but sufficient for contrail formation; (3) clear sky. It turned out that this additional classification of the data led to a very clear positive trend (+3.7%/decade over Europe, +5.5% over NAFC) in effective high cloud amount, while the overall trend (all classes) was weak.

Stordal et al. (2005) found from an analysis of satellite data (1984-2000) that the time series of cirrus coverage $C(t)$ and air traffic density $D(t)$ (flown distance per km^2 and hour) are generally positively correlated. The correlation is inferred from a linear ansatz: $dC/dt = b dD/dt$. Estimated correlations are not strong (partly because other influences have been left in the $C(t)$ time series). They conclude that over Europe aviation produces an extra cirrus coverage of 3 to 5%.

Mannstein and Schumann (2005) also correlated $C(t)$ with $D(t)$, however for 2 months of cirrus data from METEOSAT and actual air traffic data from EUROCONTROL. For relating cirrus cover and traffic density they used an ansatz that takes overlapping of contrails and saturation effects (e.g. finite size of ice-supersaturated regions) into account: $C(t) = C_i(t) + C_{\text{pot}}[1 - \exp(-D/D^*)]$, where $C_i(t)$ is cover of natural cirrus, C_{pot} is the potential coverage of persistent contrails (Sausen et al., 1998), and the term in square brackets is the fraction of C_{pot} that is actually covered by contrails. It was shown that the relation between additional cirrus coverage and air traffic density indeed followed roughly the exponential model. The main result of this study was that over Europe aviation is responsible for an additional cirrus coverage of 3% (consistent with the result of Stordal et al.). This implies that the mean coverage of contrail cirrus over Europe exceeds the corresponding mean coverage of linear contrails by almost one order of magnitude.

Krebs (2006) extended the study of Mannstein and Schumann, by analysing cirrus coverage and air traffic of 11 months in 2004, for Europe, North Africa, and the North Atlantic. Over this extended region he still found a significant correlation between cirrus coverage and air traffic density. But the air traffic induced cirrus cover was smaller than in the Mannstein and Schumann study, namely $0.6 \pm 0.2\%$. The inclusion of regions with essentially no air traffic of course leads to smaller mean additional cirrus coverage. Krebs also investigated the effect of the additional cirrus on the radiation budget of the earth. He found a warming of 1.1 W/m^2 for the region of interest, a value that is more than eight times larger than the value estimated by Boucher (1999). It is currently not clear how much of the correlation in this work between air traffic and cirrus cloudiness is actually due to a causal relationship. Hence the determination of the radiative forcing of contrail cirrus is fraught with very large uncertainties; studies to resolve the differences and to constrain the error margins are certainly needed.

All these studies suggest that air traffic actually induces additional cirrus clouds which seems plausible. However it is extremely difficult to demonstrate and prove such a correlation because the variation of cirrus cloudiness due to natural influences is much larger than the possible aviation effect. Hence, to look for the latter is like looking for a signal hidden in strong noise.

3 SHIP TRACKS

Ship tracks are a good example of the Twomey effect. The clean marine boundary layer (MBL) contains mainly sea salt and sulphate aerosol with a number density of about 500 cm^{-3} . When these act as condensation nuclei, a water cloud forms with a low number density of relatively large droplets. Ship stacks release a lot of soot (and other) particles into the MBL. A part of them also act as cloud condensation nuclei: more but smaller droplets form. The water content of the clouds is hardly affected. Now, the same water amount has a larger optical effect when it is distributed into more but smaller droplets (like a big block of ice can be translucent while crushed ice is opaque).

Thus, the cloud areas that are contaminated by ship emissions have a signature of higher reflectivity than their surroundings on satellite images, which is used to detect them.

The largest measurement campaign to date devoted to the study of ship tracks was conducted in June 1994 off the coast of California, the so-called Monterey Area Ship Track (MAST) Experiment (Durkee et al., 2000a). It produced the largest dataset so far of direct measurements of the effects of ship emissions on the microphysical and radiative properties of marine stratocumulus clouds as an analogue for the indirect effects of anthropogenic pollution on cloud albedo. An analysis of 131 ship-ship track correlation pairs by Durkee et al. (2000b) gave the following ship track characteristics (mean values \pm standard deviation): length 296 ± 233 km, width 9 ± 5 km, age 7.3 ± 6 h (but many tracks get older than 12 h), the head of the ship track is 16 ± 8 km behind or 25 ± 15 min. after the ship. Significant variability of the values around their respective averages may be noted. Ship tracks form in a MBL that is between 300 and 750 m deep, and never deeper than 800 m during MAST. Low level clouds must be close to the surface (less than one km), otherwise ship tracks do not form (Coakley et al., 2000). The relative humidity is usually high, temperature differences between air and sea are low, and winds are moderate with wind speeds of 7.7 ± 3.1 m/s. However, statistical distributions of MBL and cloud properties overlap a lot for ship track and non-ship track regions. The statistical significance of the differences in the mean have not been given for the MAST experiment.

Not all ships produce tracks. Ships powered by Diesel units that emit high concentrations of accumulation mode aerosol can produce ship tracks. Ships that produce few particles (e.g. nuclear ships) or particles too small for activation as cloud drops (even if in high concentration) do not produce ship tracks. The most likely, if not the only, cause of the formation of ship tracks is the direct emission of cloud condensation nuclei from the stack of a Diesel powered ship. Still then it needs a cloud layer susceptible to aerosol perturbation, and the atmospheric stability must be such to enable aerosol to be mixed throughout the MBL. Furthermore, not all exhausted particles are active as additional cloud condensation nuclei. The type of fuel burned seems to be more important than the type of ship engine in determining whether a ship will produce a track or not. Ships, burning Marine Fuel Oil (a low-grade oil) or navy distillate fuel (high-grade) produce between 4×10^{15} to 2×10^{16} particles per kg fuel burned. About 12% of the particles from Marine Fuel Oil burning serve as cloud condensation nuclei, whereas burning of higher-grade fuels produces particles that are less efficient as cloud condensation nuclei. Ship exhaust particles are composed primarily from organics, possibly combined with H_2SO_4 generated by gas-to-particle conversion from SO_2 . 10% (by mass) are water soluble materials. There is no evidence that salt particles from ship wakes cause ship tracks. Water and heat fluxes do not produce detectable perturbations that have an effect on MBL clouds (Hobbs et al., 2000).

As the droplets in a ship track are smaller than usual in a MBL cloud, their coagulation rate to form larger droplets that eventually precipitate in the form of drizzle is diminished. In other words, ship tracks suppress drizzle formation which affects cloud life time and the budget of latent heat. As drizzle formation causes the transition from closed to open cellular convection (Rosenfeld et al., 2006), this transition does not occur in ship tracks. Analysis of satellite data (Schreier et al., 2006) with comparison between non-ship-track pixels and ship-track pixels shows a large increase in the droplet number concentration from 100 cm^{-3} to 800 cm^{-3} . Since the condensed water mass is probably unaffected by the ship track (the satellite data shows that the liquid water path is hardly affected), the droplet's effective radius experiences a significant decrease of from 12 to 6 μm , a clear indication of the Twomey effect. Accordingly, the optical thickness of unpolluted clouds is 20-30, whereas in the ship track it increases up to 45.

Comparing the ocean regions where ship tracks occur with the regions where ship traffic occurs shows that ship tracks is a very selective phenomenon. The special combination of meteorological conditions necessary for formation of ship tracks is rarely given. Thus the direct radiative impact of ship tracks on the Earth's energy budget is probably small. However, ship emissions can have more diffuse effects on low-level clouds that might be of higher climatic relevance, although much harder to detect. Devasthale et al. (2006) analysed time series of satellite data of the region around the English Channel (an ocean strait with very heavy ship traffic) and detected trends of cloud albedo and top temperature, that were ascribed to increasing ship emissions.

4 CONCLUSIONS

Clouds are of utmost importance in the climate system because of their interaction with the hydrological cycle and the radiant energy flow. The transportation sector may cause changes in cloud coverage and frequency and changes in cloud properties. These influences are exerted via semi-direct and indirect aerosol effects. Research currently is focused on ship and aviation emissions and does not include the impact of road traffic emissions on clouds. This is because of the following two reasons: (1) There are evident cloud effects from both shipping (ship tracks) and aviation (contrails) whereas there are no evident cloud effects from road traffic. (2) The road traffic source is rather diffuse (many cars almost everywhere in Europe) whereas aviation is more regulated and shipping by large vessels is more confined to distinct routes. Their movements are recorded which makes source attribution better identified than it would be the case for road traffic. Nevertheless, future research must take the cloud effects of surface transport and of industrial emissions into account, in order to enable fair comparisons of the effects. The knowledge gained from current research on contrails, contrail cirrus, and ship tracks will certainly help for the future topics.

REFERENCES

- Ackerman, A. S., O. B. Toon, D. E. Stevens, A. J. Heymsfield, V. Ramanathan, and E. J. Welton, 2000: Reduction of tropical cloudiness by soot. *Science*, 288, 1042–1047.
- Bakan, S., M. Betancor, V. Gayler, and H. Graßl, 1994: Contrail frequency over Europe from NOAA-satellite images. *Ann. Geophys.*, 12, 962–968.
- Boucher, O., 1999: Air traffic may increase cirrus cloudiness. *Nature*, 397, 30–31.
- Busen, R., and U. Schumann, 1995: Visible contrail formation from fuels with different sulfur contents. *Geophys. Res. Lett.*, 22, 1357–1360.
- Coakley Jr., J.A., and 10 co-authors, 2000: The appearance and disappearance of ship tracks on large spatial scales. *J. Atmos. Sci.*, 57, 2765–2778.
- Devasthale, A., O. Krüger, and H. Graßl, 2006: Impact of ship emissions on cloud properties over coastal areas. *Geophys. Res. Lett.*, 33, L02811, doi:10.1029/2005GL024470.
- Duda, D.P., P. Minnis, L. Nguyen, and R. Palikonda, 2004: A case study of the development of contrail clusters over the Great Lakes. *J. Atmos. Sci.*, 61, 1132–1146.
- Dürbeck, T., and T. Gerz, 1996: Dispersion of aircraft exhausts in the free troposphere. *J. Geophys. Res.*, 101, 26007–26015.
- Durkee, P.A., K.J. Noone, and R.T. Bluth, 2000a: The Monterey Area Ship Track experiment. *J. Atmos. Sci.*, 57, 2523–2541.
- Durkee, P., A., R.E. Chartier, A. Brown, E.J. Trehubenko, S.D. Rogerson, C. Skupniewicz, K.E. Nielsen, S. Platnick, and M.D. King, 2000b: Composite ship track characteristics. *J. Atmos. Sci.*, 57, 2542–2553.
- Freudenthaler, V., F. Homburg, and H. Jäger, 1995: Contrail observations by ground-based scanning lidar: Cross-sectional growth. *Geophys. Res. Lett.*, 22, 3501–3504.
- Freudenthaler, V., 2000: Lidarmessungen der räumlichen Ausbreitung sowie mikrophysikalischer und optischer Parameter von Flugzeugkondensstreifen. Dissertation, Schriftenreihe des Fraunhofer Instituts Atmosphärische Umweltforschung, Garmisch-Partenkirchen, Band 63-2000, 135 pp. (in German).
- Gerz, T., T. Dürbeck, and P. Konopka, 1998: Transport and effective diffusion of aircraft emissions. *J. Geophys. Res.*, 103, 25905–25913.
- Gierens, K.M., 1998: How the sky gets covered with contrails. *Meteorol. Z.*, N.F. 7, 181–187.
- Gierens, K., U. Schumann, M. Helten, H.G.J. Smit, and A. Marenco, 1999: A distribution law for relative humidity in the upper troposphere and lower stratosphere derived from three years of MOZAIC measurements. *Ann. Geophys.*, 17, 1218–1226.
- Gierens, K., and P. Spichtinger, 2000: On the size distribution of ice-supersaturated regions in the upper troposphere and lowermost stratosphere. *Ann. Geophys.*, 18, 499–504.
- Gierens, K., B. Kärcher, H. Mannstein, and B. Mayer, 2006: Aerodynamically induced contrail formation, this volume.
- Hansen, J., M. Sato, and R. Ruedy, 1997: Radiative forcing and climate response. *J. Geophys. Res.*, 102, 6831–6864.
- Haywood, J. M., and O. Boucher, 2000: Estimates of the direct and indirect radiative forcing due to tropospheric aerosols: A review. *Rev. Geophys.*, 38, 513–543.
- Hobbs, P.V., and 13 co-authors, Emissions from ships with respect to their effects on clouds. *J. Atmos. Sci.*, 57, 2570–2590.

- Jensen, E.J., O.B. Toon, S. Kinne, G.W. Sachse, B.E. Anderson, K.R. Chan, C. Twohy, B. Gandrud, A. Heymsfield, and R.C. Mialke-Lye, 1998: Environmental conditions required for contrail formation and persistence. *J. Geophys. Res.*, *103*, 3929–3936.
- Kärcher, B., R. Busen, A. Petzold, F.P. Schröder, U. Schumann, and E.J. Jensen, 1998: Physicochemistry of aircraft-generated liquid aerosols, soot, and ice particles. 2. Comparison with observations and sensitivity studies. *J. Geophys. Res.*, *103*, 17129–17148.
- Krebs, W., 2006: Analyse des Einflusses des Flugverkehrs auf die natürliche Zirusbewölkung über Europa, Nordafrika und dem Nordatlantik. Dissertation, Ludwig-Maximilians Universität München, 211 pp. (in German).
- Lohmann, U., and J. Feichter, 2005: Global indirect aerosol effects: a review. *Atmos. Chem. Phys.*, *5*, 715–737.
- Mannstein, H., and U. Schumann, 2005: Aircraft induced contrail cirrus over Europe. *Meteorol. Z.*, *14*, 549–554.
- Minnis, P., J.K. Ayers, R. Palikonda, D.R. Doelling, U. Schumann, and K. Gierens, 2001: Changes in cirrus cloudiness and their relationship to contrails. Proceedings American Meteorological Society, Boston, USA, No. 11.9, 239–242.
- Rosenfeld, D., Y.J. Kaufman, and I. Koren, 2006: Switching cloud cover and dynamical regimes from open to closed Benard cells in response to the suppression of precipitation by aerosols. *Atmos. Chem. Phys.*, *6*, 2503–2511.
- Sausen, R., K. Gierens, M. Ponater, and U. Schumann, 1998: A diagnostic study of the global distribution of contrails, Part I. Present day climate. *Theor. Appl. Climatol.*, *61*, 127–141.
- Schreier, M., A.A. Kokhanovsky, V. Eyring, L. Bugliaro, H. Mannstein, B. Mayer, H. Bovensmann, and J.P. Burrows, 2006: Impact of ship emissions on the microphysical, optical and radiative properties of marine stratus: a case study. *Atmos. Chem. Phys.*, *6*, 4925–4942.
- Schumann, U., 1996: On conditions for contrail formation from aircraft exhausts. *Meteorol. Z., N.F.* *5*, 4–23.
- Schumann, U., 2000: Influence of propulsion efficiency on contrail formation. *Aerospace Sci. Technol.*, *4*, 391–401.
- Schumann, U., R. Busen, and M. Plohr, 2000: Experimental test of the influence of propulsion efficiency on contrail formation. *J. Aircraft*, *37*, 1083–1087.
- Spichtinger, P., K. Gierens, U. Leiterer, and H. Dier, 2003: Ice supersaturated regions over Lindenberg, Germany. *Meteorol. Z.*, *12*, 143–156.
- Spichtinger, P., K. Gierens, H. Wernli, 2005: A case study on the formation and evolution of ice supersaturation in the vicinity of a warm conveyor belt's outflow region. *Atmos. Chem. Phys.*, *5*, 973–987.
- Stordal, F., G. Myhre, E.J.G. Stordal, W.B. Rossow, D.S. Lee, D.W. Arlander, and T. Svendby, 2005: Is there a trend in cirrus cloud cover due to aircraft traffic? *Atmos. Chem. Phys.*, *5*, 2155–2162.
- Stubenrauch, C.J., and U. Schumann, 2005: Impact of air traffic on cirrus coverage. *Geophys. Res. Lett.*, *32*, L14813, doi:10.1029/2005GL022707.
- Twomey, S., 1974: Pollution and the planetary albedo. *Atmos. Environ.*, *8*, 1251–1256.
- Twomey, S., 1977: The influence of pollution on the shortwave albedo of clouds. *J. Atmos. Sci.*, *34*, 1149–1152.
- Unterstrasser, S., K. Gierens, and P. Spichtinger, 2006: Initial conditions for contrail-to-cirrus transition. This volume.
- Zerefos, C.S., K. Eleftheratos, D.S. Balis, P. Zanis, G. Tselioudis, and C. Meleti, 2003: Evidence of impact of aviation on cirrus cloud formation. *Atmos. Chem. Phys.*, *3*, 1633–1644.

Novel engine concept to suppress contrail and cirrus cloud formation

F. Noppel*, R. Singh
Cranfield University, Bedfordshire, UK

M. Taylor
Rolls-Royce, Derby, UK

Keywords: sustainable aviation, novel engine concept, contrail avoidance

ABSTRACT: Greenhouse gas emissions, contrails and artificially induced cirrus clouds are the principal pollutants from air traffic which contribute to the anthropogenic global warming. Recent climate assessments have stressed the importance of contrails and aviation induced cirrus clouds. They might contribute more than all other aircraft emissions combined. Revolutionary technologies will contribute to accommodate the increasing demand in air transport at a sustainable level. In this paper, a novel propulsion concept is presented with the intention to provide greener propulsion for future aircraft. It is based on gas turbine technology, derived from the intercooled and recuperated engine concept. Exhaust water condensation is facilitated inside the engine to avoid the formation of contrails in the plume. Particles and aerosols are being scavenged from the exhaust gases during condensation. The condensed water is redirected into the combustor to mitigate NO_x emissions via water injection technique. The new concept allows higher thermal efficiencies than conventional designs to cut back greenhouse gas emissions. It is concluded that significant advances in heat exchanger technology are required to make this concept feasible.

1 INTRODUCTION

There is evidence that anthropogenic greenhouse gas emissions have an impact on the Earth's radiation budget and cause a long term increase in the Earth's mean surface temperature. Air traffic pollutants are placed in the upper atmosphere where their impact is different. Water vapour and aerosol emissions are responsible for the formation of persistent contrails and cirrus clouds, both causing a net heating of the Earth's atmosphere. The steady state response in the Earth's mean surface temperature due to a certain pollutant can be related linearly to its radiative forcing (RF). There is the potential that the RF from persistent contrails, contrail cirrus, secondary cirrus and cirrus cloud modification exceeds the RF of all other emissions from air traffic combined (Sausen et al., 2005).

Early jet engines suffered from poor component efficiencies, restricted turbine inlet temperatures and low achievable pressure ratios. This had a deteriorating effect on the fuel economy of early models. The advent of advanced combustor technology, high component efficiencies, new materials, blade cooling techniques, higher pressure ratios thanks to multi spool arrangements, and large bypass ratios caused significant advances in engine performance. There is still potential for further improvements in fuel economy considering conventional engine architecture. However, these improvements take place on a system level and are becoming increasingly difficult to achieve. The theoretical limit for thermal efficiency is 60%, whereby a stoichiometric turbine entry temperature (TET) and an overall pressure ratio (OPR) in excess of 80 are considered (Green, 2005). The theoretical limit for propulsive efficiency is 92.5% which represents an open rotor configuration. This approach stays in conflict with NO_x emission standards and will cause an increase in contrail cover due to the increase in overall efficiency. However, revolutionary changes in engine design can lead to further significant advances in engine fuel economy and environmental compatibility.

* *Corresponding author:* Frank Noppel, Cranfield University, Bedfordshire, MK43 0AL, UK. Email: f.g.noppel@cranfield.ac.uk

2 RATIONALE

The following requirements are set for a novel engine concept: significantly increased thermal efficiency, a reduction in water vapour, soot and aerosol emissions to avoid the formation of contrails and cirrus clouds, and low NO_x emissions. The engine weight should not offset engine performance improvements. Although theoretical approaches which utilise fuel cells and similar mechanisms may be feasible (Alexander et al., 2002), they require significant deviation from current gas turbine practice. Hence, it would be more desirable to provide a practical solution with respect to existing gas turbine technology which operates with any available hydrocarbon based fuel.

The novel concept presented herein is based on the intercooled and recuperated engine cycle in a two spool arrangement as shown in figure 1(b). A substantial improvement in thermodynamic work potential can be realized by combining intercooling and exhaust regeneration. The intercooler is a heat exchanger placed between the low pressure compressor (LPC) and high pressure compressor (HPC). The flow on the cold side of the intercooler is usually bypass air. Intercooling reduces the work required for the compression of the air in the HPC. The hot gases leaving the low pressure turbine (LPT) are used to heat the pre-combustor air in the recuperator, so more heat is used to generate useful work.

Contrails form in the exhaust plume of an aircraft if saturation with respect to water occurs during the mixing process of the exhaust gases with ambient air. Considering current engine architecture, they form more likely with increasing overall engine efficiency (Schumann, 2000). Hence, fuel burn and contrail formation are in conflict with each other. The formation of contrails would not occur for low exhaust water content at relatively high temperature. Water could be removed from the exhaust if the temperature after the LPT is sufficiently reduced to provoke water condensation within the engine. This can be accomplished with an intercooled and recuperated cycle in a novel arrangement. Therefore, the flow exiting the recuperator is further cooled by applying an additional heat exchanger: the condensation stage. For a sufficiently low temperature, this will cause condensation of the exhaust water within the engine. Condensation occurs also on particles and aerosols contained in the exhaust. This effect can be utilized to provoke particle and aerosol scavenging inside the engine. The water from the condensation stage can be stored on the aircraft or released into the atmosphere in liquid or ice phase for precipitation. A fractional part of the condensed water is redirected into the combustor to suppress the formation of NO_x through water injection. The dry and cold air leaving the condensation stage is used to chill the compressor air in the intercooler. This causes an increase of the flow temperature of the core exhaust. Because contrails are less likely to form with increasing exhaust temperature, it has the effect of further reducing the potential for contrail formation.

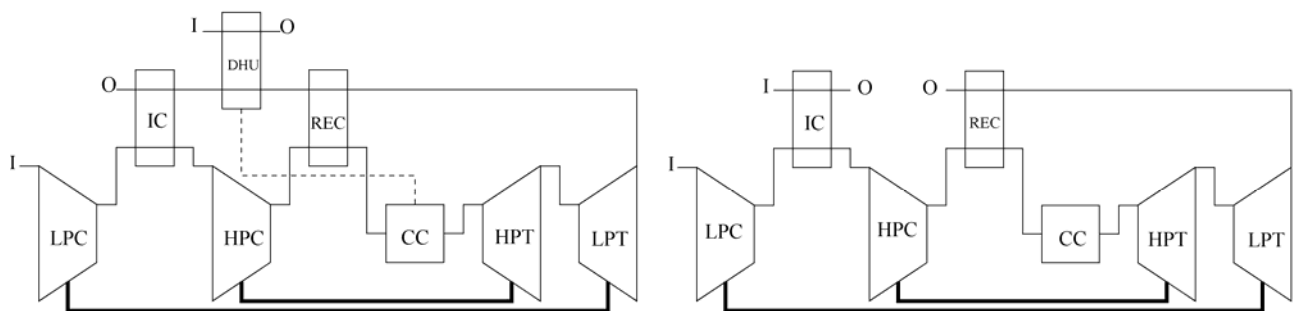


Figure 1: novel concept (a) vs. intercooled recuperated engine cycle (b)

Figure 1(a) shows the flow schematic of the novel engine concept. Compared to the ordinary intercooled and recuperated cycle, the major differences are that the conventional intercooled recuperated cycle works with bypass air on the cool side of the intercooler whereas in the novel concept bypass air is used in the condensation stage and the intercooler operates with core air on both sides.

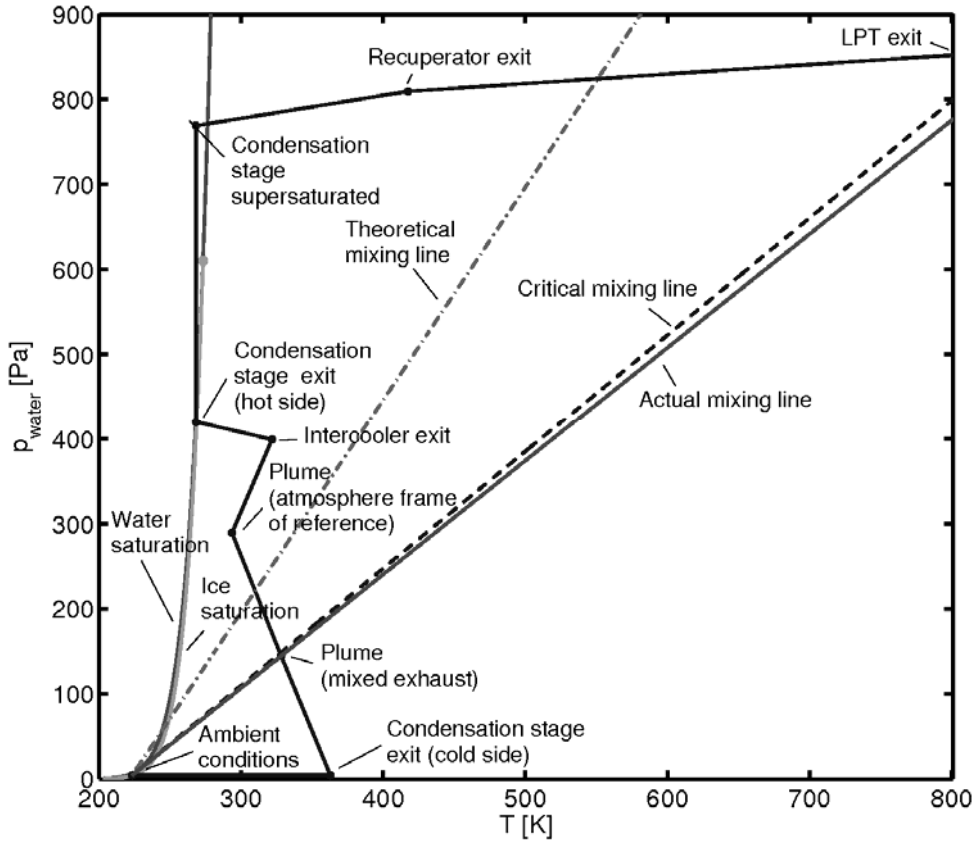


Figure 2: engine stations on a phase diagram of water

Figure 2 shows the water partial pressure on a phase diagram of water for different stations within the engine and in the plume. The water partial pressure in the flow exiting the hot side of the condensation stage is determined by the water saturation pressure at the flow temperature. In this study, the water saturation pressure is calculated from Flatau et al., 1992. Whereas static flow temperatures and pressures are considered for the stations within the engine, stagnation properties relative to the atmosphere frame of reference are considered in the plume. Mixing is assumed to take place adiabatically and isobarically. The two exhausts, the core exhaust and the exhaust from the cold side of the condensation stage, are assumed to mix prior to the mixing with ambient air. The actual mixing line represents the mixing of the mixed exhausts with ambient air. Furthermore, figure 2 shows also the critical mixing line, which is a tangent to the water saturation pressure line originating from the ambient state of the atmosphere. Together with the actual mixing line, it is used for contrail prediction. If the actual mixing line is below the critical mixing line, contrail formation is not facilitated. This is because contrails only form if the actual mixing line surpasses the region for which water is present in the liquid phase in a phase diagram (Jensen, 1998). Additionally, the theoretical mixing line is shown. It represents the mixing line of the mixed exhaust with ambient air if no dehumidification took place. Originating from the ambient state of the atmosphere, its slope is calculated from (Schumann, 2000)

$$G_{theo.} = \frac{c_p EI_{H_2O} p_a}{(1 - \eta_0) q_{net} \omega} \quad (1)$$

where c_p is the specific heat capacity of air, EI_{H_2O} is the water emission index for a certain fuel, p_a is the ambient static pressure, η_0 is the overall engine efficiency, q_{net} is the fuel net calorific value and ω is the molar mass ratio of water to air. The actual mixing line and the theoretical mixing line are identical if water condensation is not facilitated within the engine.

3 CYCLE STUDY

A cycle study has been carried out for performance prediction and to comprehend the system behaviour. To this end, a performance model, a standard atmosphere model and a contrail prediction model were linked together. The performance model considers a thermodynamic cycle as shown in figure 1(a) delivering shaft power to drive a fan or a propeller. The propulsive efficiency is not taken into account in the calculations. The cycle is solved so that the exhaust exiting the cold side of the intercooler matches ambient velocity and does not produce a propulsive force. The cooling air exiting the cold side of the dehumidifier produces a propulsive force due to its increase in momentum. Even though it is small, it is taken into account when calculating the overall thermal efficiency. The design variables are engine overall pressure ratio, turbine inlet temperature and the ratio LPC pressure ratio to HPC pressure ratio (R). Isentropic compressor efficiencies are assumed to be 0.88, turbine efficiencies are assumed to be 0.92, nozzle and inlet efficiencies are assumed to be 0.99. The combustor total pressure loss is assumed to be 4%, heat exchanger total pressure losses are assumed to be 5% for each side. These component efficiencies and pressure losses represent advanced technology levels. The water content of the flow exiting the condensation stage is determined by its static temperature and pressure. Therefore, the flow Mach number through the heat exchanger was assumed to be 0.1 for all calculations. All calculations are carried out assuming constant fluid properties. Ambient conditions are determined by the cruise altitude using the ISA standard atmosphere model and specifying ambient relative humidity with respect to ice.

A commercially available optimisation algorithm was used for cycle optimisation. The ratio of the actual mixing line slope to the critical mixing line slope ($G/G_{crit.}$) acts as an indicator of whether contrail formation is facilitated or not. Values above 1 imply contrail formation whereas values below 1 imply no contrail formation. The ratio of the actual mixing line slope to the theoretical mixing line slope ($G/G_{theo.}$) is used to predict whether condensation takes place inside the engine. The ratio can only have values of 1 or below. Values below 1 imply that water is removed from the exhaust; a value of 1 implies the opposite. Furthermore, the temperature differences between the inlet and outlet for each side of the heat exchangers are calculated. The cumulative of the maximum temperature differences (ΔT_{HE}) is used as an indicator of the overall size of all heat exchanging devices.

With a fixed value of TET and OPR, the cycles were optimised for maximum thermal efficiency ($\eta_{thermal}$) varying R . The considered values for TET are 1700K to 2000K and for OPR are 19 to 49. Flight conditions are 10000m altitude at Mach 0.8 with an ISA temperature deviation of 0K. Three levels of ambient ice supersaturation are taken into account: 100%, 130% and 150%. The effectiveness of all heat exchangers is assumed to be 90%.

Although condensation of water within the engine is facilitated for all cycles considered, the water content is not low enough to avoid the formation of contrails¹. Both exhaust water content and thermal efficiency are dependent on R . Therefore, the objective function was modified to give $G/G_{crit.}$ for $G/G_{crit.} > 1$ and $-\eta_{thermal}$ for $G/G_{crit.} \leq 1$. This resulted in the optimisation algorithm minimising $G/G_{crit.}$ to obtain a cycle facilitating contrail avoidance and optimising for maximum thermal efficiency. Cycles optimised for contrail avoidance are not operating at maximum achievable thermal efficiency anymore and the value for ΔT_{HE} increases. Figure 4 shows the change in $\eta_{thermal}$ and ΔT_{HE} for $RH_i=100\%$ and $RH_i=150\%$ compared to cycles optimised for maximum thermal efficiency only. For the spaces left out, the performance calculation did not converge and no solution exists. The thermal efficiency for the cycles optimised for maximum thermal efficiency only is in the range between 0.56 and 0.65. Efficiency penalties are more severe if higher ice supersaturation is considered during optimisation and for larger OPR's. The same is true for ΔT_{HE} .

Considering a cycle with TET=2000K, OPR=31 and ISS = 150%, the thermal efficiency of the cycle optimised for contrail avoidance is about 0.64. Assuming a propulsive efficiency of 93%, the overall engine efficiency becomes 0.6. This is still well above the maximum theoretical achievable efficiency of engines with conventional architecture.

¹ It would be facilitated for sufficiently low OPR's and TET's

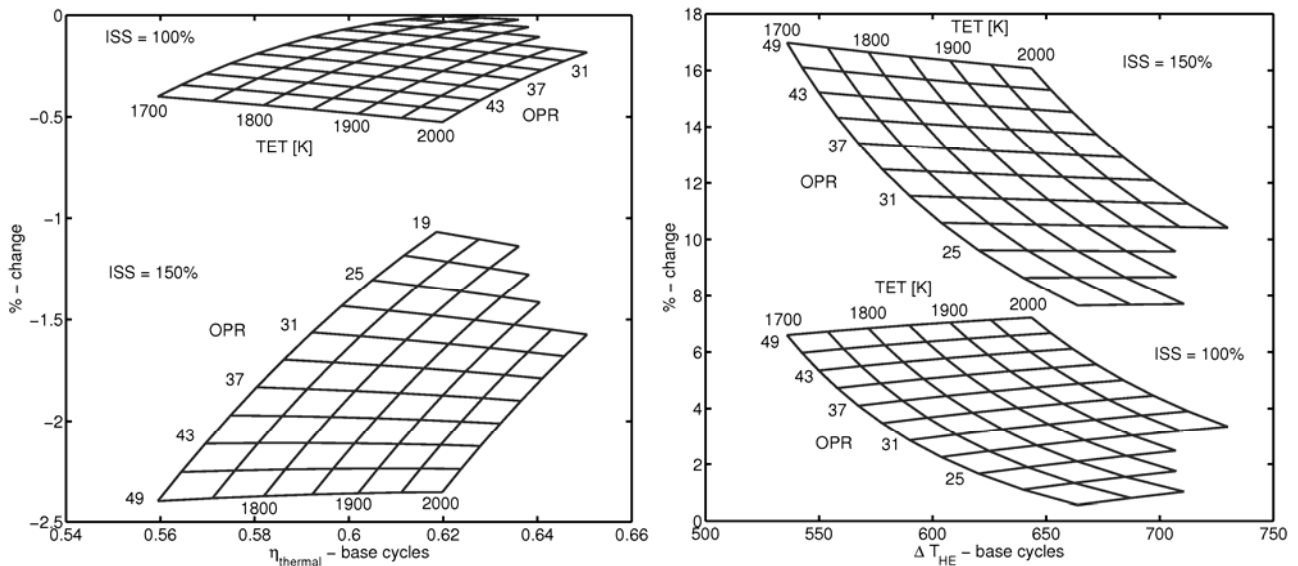


Figure 4: changes in η_{thermal} and ΔT_{HE} compared to cycles optimised for η_{thermal} only

Further results are shown in figure 5 on a specific fuel consumption (SFC) - specific work (W_s) chart and ΔT_{HE} - G/G_{theo} chart. An ambient ice supersaturation of 150% is considered. It is desirable to choose a cycle with low specific fuel consumption and high specific work output to reduce the size of the turbomachinery. This can be achieved with high TET's and low OPR's. However, high values of TET and low values of OPR imply relatively large values of ΔT_{HE} which is not desired. Water condensation occurs inside the engine for all considered cycles because the ratio $G/G_{\text{theo}} \leq 1$ in all cases.

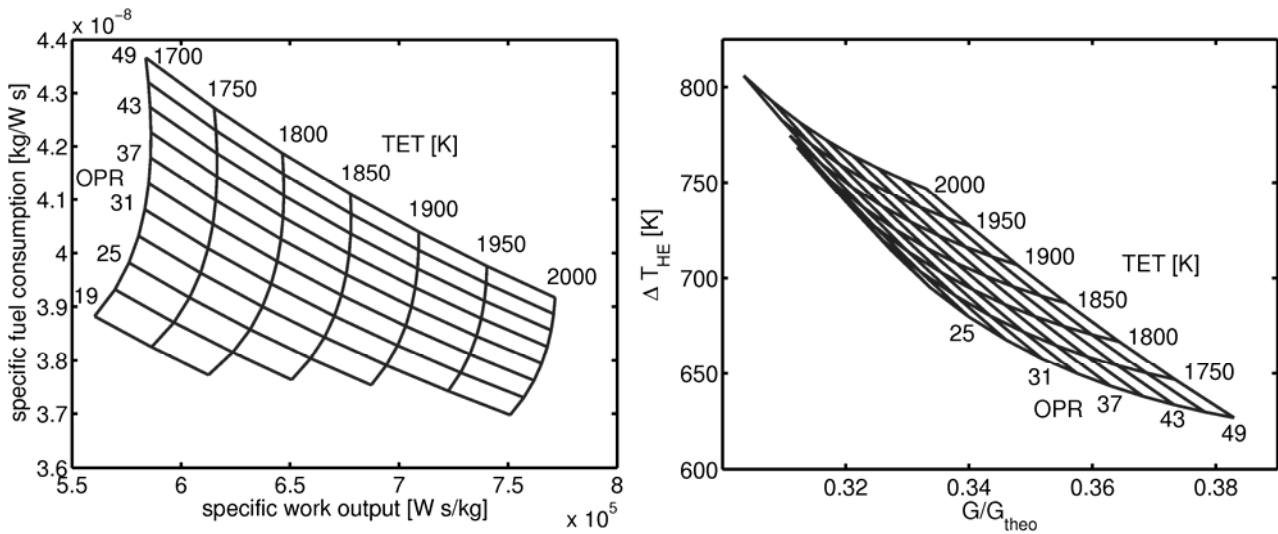


Figure 5: cycle study results of the new engine concept optimised for maximum η_{thermal} and contrail avoidance considering 150% ambient ice supersaturation

4 NO_x REDUCTION

A reduction in primary zone temperature can be achieved through water injection into the combustion chamber. A water flow rate 2 times the fuel flow rate can reduce NO_x emissions by up to 80% (Lefebvre, 1983). The feasibility of water injection has been demonstrated by Daggett, 2004. Liquid water from the condensation stage would provide water for injection into the combustion chamber. The water content in the flow between the combustor and condensation stage will increase until part of the water is drawn off from the condensation stage. Drawn off water can either be stored on board the aircraft or released into the atmosphere for precipitation. The novel engine concept allows any desired water flow rate into the combustor.

5 FURTHER CONSIDERATIONS

Heat exchanger size is predominantly dependent on heat exchanger effectiveness and the desired temperature change. The cycles respond with an increase in ΔT_{HE} to a decrease in heat exchanger effectiveness'. A relatively high effectiveness in the condensation stage is crucial in order to achieve a low temperature within the engine that facilitates water condensation. This temperature is within the ambient temperature range, so the temperature difference between the flows that exit the condensation stage at the core side and enter at the bypass side is relatively small. Hence, it can be concluded that advanced heat exchanger technology in terms of heat transfer, weight, and pressure loss is essential for the feasibility of this concept. Superconducting heat transfer material is being investigated and similar materials could be available in the future (Qu, 2000).

Because the required temperature in the condensation stage is determined by the temperature at which water condensation occurs, a reduction in water saturation pressure would cause a reduction in the required temperature difference. A reduction in water saturation pressure could be achieved applying curved surfaces within the heat exchanger (Kelvin effect). Fluid properties could be changed applying exhaust seeding in order to activate condensation surfaces and reduce the partial pressure at which condensation occurs.

6 SUMMARY AND FINAL REMARKS

A novel propulsion concept is proposed which exhibits significantly reduced emissions, in particular CO_2 , NO_x and water vapour, soot and aerosols to avoid the formation of contrails and aviation induced cirrus clouds. It is intended to encourage the aeronautical community to further discuss this concept or develop other concepts with similar purposes.

This novel concept can operate at higher thermal efficiency than current designs and the formation of contrails is avoided. This is achieved by combining the advantages of heat exchangers in terms of performance improvement and to enforce water condensation inside the engine. A reduction in NO_x emissions is achieved through water injection. Any water to fuel ratios are theoretically achievable and water injection could take place during the entire journey.

We conclude that the feasibility of the cycle depends on the available future heat exchanger technology. The results of this study are based on a cycle study where mechanical issues are not addressed. It is intended to further investigate this propulsion concept using a comprehensive aircraft and engine model.

7 ACKNOWLEDGEMENTS

This study is part of a Ph.D. project sponsored by the Cranfield Rolls-Royce University Technology Centre in Gas Turbine Performance Engineering.

REFERENCES

- Alexander, D. Y.-M. Lee, M. Guynn, and D. Bushnell, 2002: *Emissionless aircraft study*, AIAA-2002-4056
- Daggett, D., L. Fucke, R. C. Hendricks, and D. J. Eames, 2004: *Water injection on commercial aircraft to reduce airport NO_x* , AIAA-2004-4198
- Flatau, P. J., L. Walko, and W. R. Cotton, 1992: Polynomial fits to saturation pressure, *Journal of Applied Meteorology*, 31, 1507–1513
- Green, J. E., 2005: Mitigating the environmental impact of aviation: Opportunities and priorities, *The Aeronautical Journal*, 109, 361-416
- Jensen, E. J., O. B. Toon, S. K. Kinne, G. W. Sachse, B. E. Anderson, K. R. Chan, C. H. Twohy, B. Gandrud, A. Heymsfield, and C. Miake-Lye, 1998: Environmental conditions required for contrail formation and persistence, *Journal of geophysical research*, 103, 3929-3936
- Lefebvre, A. H., 1983: *Gas turbine combustion*, Hemisphere Publishing, USA, 0-07-037029-X, pp 485
- Qu, Y., 2000: *Superconducting heat transfer medium*, U.S.P. 6,132,823

- Sausen, R., I. Isaksen, V. Grewe, D. Hauglustaine, D. Lee, M. Gunnar, M. O. Kohler, G. Pitari, U. Schumann, F. Stordal, and C. Zerefos, 2005: Aviation radiative forcing in 2000: An update on IPCC (1999), *Meteorologische Zeitschrift*, 14, 555–561
- Schumann, U., 2000: Influence of propulsion efficiency on contrail formation, *Aerosp. Sci. Technol.*, 4, 391–401

On how to consider the Earth's Atmosphere in Aircraft Design

R. Egelhofer*

Technische Universität München – Lehrstuhl für Luftfahrttechnik, Garching, Germany

C. Marizy

Airbus France, Toulouse, France

C. Bickerstaff

Airbus UK, Filton, Bristol, UK

Keywords: Aircraft design, two-stage operations, atmospheric impact

ABSTRACT: The increasing knowledge in atmospheric sciences and modelling has started to enable the environmental assessment of aircraft emissions. Aeronautical engineering must therefore begin to consider the atmosphere in future aircraft design. Aviation being a complex business with many different stakeholders, both configurational and operational design solutions for minimum atmospheric impact have to be evaluated for real flight operations. This paper presents a methodology providing a systemic structure for such evaluations. Two-stage operations illustrate this methodology as an example that incorporates both configurational and operational aspects. The methodology highlights the fact that, in a global operational context, there remains a large gap between theoretical benefits and actual performance.

1 INTRODUCTION

Civil aviation is confronted with increasing public attention concerning its impact on the environment. Whereas noise has been the principal cause of anxiety since the early years of commercial air transport, air quality around airports and climate change have only been considered more recently. The aviation business is very complex, since many different stakeholders – authorities, air traffic control (ATC), airlines, airports, aircraft and engine manufacturers – have to satisfy their respective needs and contribute to a safe and economic means of transport for leisure and business passengers.

When it comes to reducing the aviation's environmental impact, each of the contributors is asked to evaluate his part of the story and to undertake any reasonable effort of mitigation. Aircraft and engine manufacturers have achieved large increases in fuel efficiency over the last decades, which, apart from the economic interest, have reduced the environmental impact. Today, it appears that other stakeholders still have large potentials to further mitigate the impact of aviation on the environment. According to Lufthansa German Airlines, ATC improvements could allow for a reduction of 8 % to 18 % of fuel consumption over Europe and, military airspaces still cause substantial deviations leading to a higher fuel burn (Lufthansa, 2006). Yet, reducing the impact on climate change still remains a task of the aircraft designer.

The contribution of aviation to climate change was estimated at around 3.5 % of the global anthropogenic radiative forcing for the year 1992 in the IPCC Special Report (Penner et al., 1999). This impact is determined by the quantity, type and location of engine exhaust gas emissions. These parameters are mainly, though not exclusively, determined through the design of an aircraft and its engine. Whereas non-optimal flight routing, holding patterns and other extra-fuel-consuming events are difficult to account for in aircraft design, as they are difficult to predict, the scheduled flight network is well defined and can therefore be interlinked with the design process for new aircraft (i.e., along with other parameters such as need for specific ranges and/or capacities). This linkage is particularly important when it comes to evaluating the atmospheric impact of an aircraft concept.

* *Corresponding author:* Regina Egelhofer, Technische Universität München, Lehrstuhl für Luftfahrttechnik, Boltzmannstr. 15, D-85747 Garching, Germany. Email: egelhofer@tum.de

The methodology presented here provides a systemic superstructure for the evaluation of the atmospheric impact of an aircraft concept, embedded in global operations, and thus prepares for its optimisation for minimum contribution to climate change. Two-stage operations are assessed in this regard, as concrete example for atmosphere-compatible design approaches. This example will also highlight operational implications of such approaches for “environmental” aviation.

2 RELEVANCY OF THE ENVIRONMENT IN AVIATION

The protection of the environment has influenced the development of the aviation system for a long time. In the public arena, aviation is well appreciated by business and tourists on the one side, strongly analysed and criticised on the other side. Aircraft have become far more fuel-efficient through advances in lightweight structures, the reduction of aerodynamic drag and more efficient jet engines. Emission indices of nitrogen oxides (NO_x) have been and are still being further reduced with innovative combustor concepts and heat exchangers etc. (Egelhofer, in press). As fuel contributes to a significant extent to aircraft operating cost and as fuel prices continue to increase, the reduction of fuel consumption remains a major concern for future aircraft. The impact of an individual aircraft on climate change should thus continue to be reduced in future.

However, it is not the aircraft itself, but its operation that has an environmental impact, so that the aviation system as a whole needs to be considered when evaluating the atmospheric impact of an aircraft concept. Many different stakeholders have an impact on the “production” of each flight.

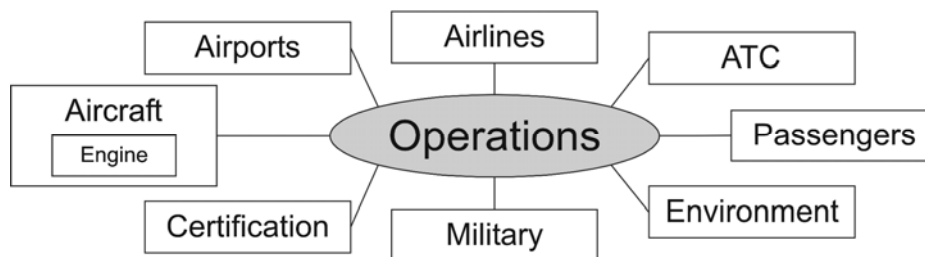


Figure 1. Relevant stakeholders of aviation

The consideration of the atmosphere in aircraft design turns out as a complex task as not only does it involve the aircraft and engine manufacturers, but also airlines (business models, fleet planning), airports (capacity, traffic management, environmental restrictions), Air Traffic Management (ATM) and ATC (quality of flight routing, congestion), certification and even the military (restricted airspaces). Passengers are involved both by their personal requirements for a flight (e.g., desire for convenience and speed and environmental consciousness) and by their behaviour during the flight (e.g., an aircraft has to fly faster to catch up following delays caused by passengers arriving late, and thus consumes more fuel).

Each of the issues referred above is interlinked directly or indirectly with aircraft design. The design engineer then has the difficult task of trying to handle many different and often contradictory requirements, one of which is a minimum contribution to climate change.

3 DESIGN PROCESS FOR MINIMUM ATMOSPHERIC IMPACT

In current aircraft optimisation loops, noise starts being integrated as important requirement, even at preliminary design level. As referred above, emissions are largely minimised in aircraft design through the minimisation of fuel consumption, which also impacts on direct operational cost. An effective evaluation of aviation's emissions' impact on the atmosphere is undertaken only after attempting to consider the complete problem and does not apply to a single aircraft type, but rather to the global fleet.

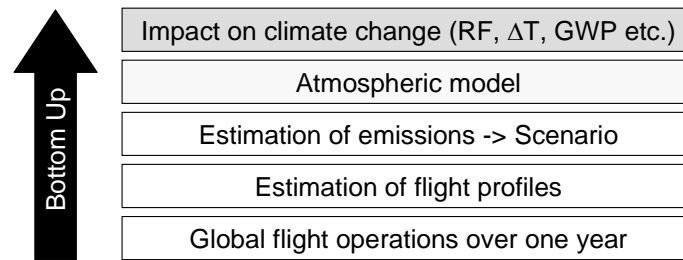


Figure 2. Current evaluation of the atmospheric impact of aviation: bottom up, no feedback.

Our approach embeds a new aircraft concept in a global fleet on a real route network. With a market forecast and aircraft performance data, global emission scenarios are created. This process enables the assessment of the various operational adaptations such as new flight altitudes or speeds, which will result from the new aircraft concept. For the subsequent evaluation of the impact on the atmosphere, some atmospheric metrics and modelling will be included in the process as soon as these are available. A sufficient reliability of the metrics is a prerequisite for their confident integration into the design process. Varying aircraft parameters of the investigated aircraft concept enables a comparative study between the resulting emission scenarios and their respective atmospheric impacts.

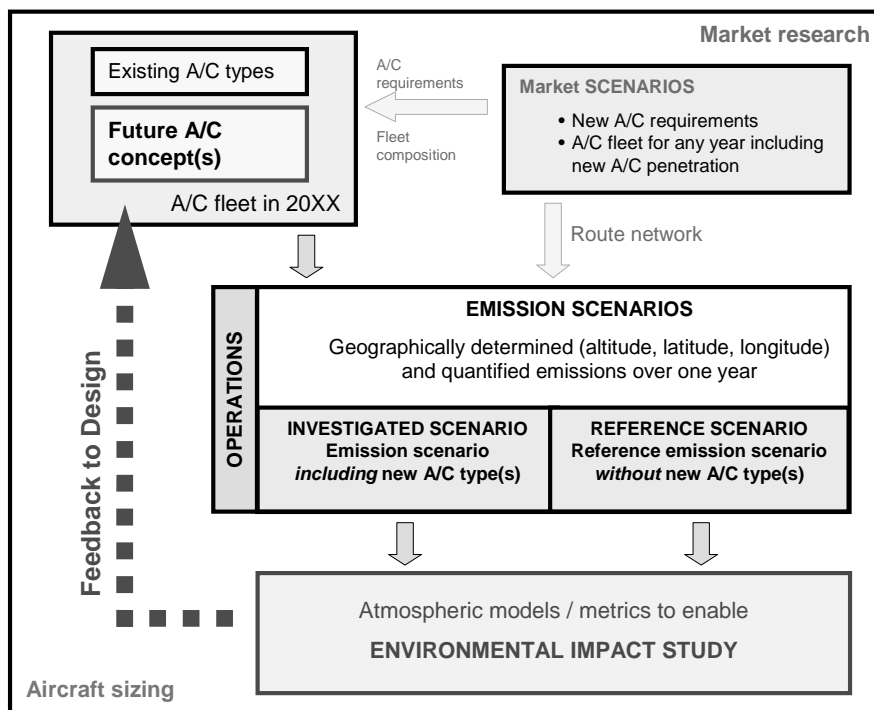


Figure 3. Design approach for minimum atmospheric impact, with feedback

For the application of the methodology for new aircraft, data for the future global fleet have to be estimated, which necessitates sound support from market research. The comprehensive character of the approach makes a proper organisation and setting up of parameters and methods essential. The precision levels of all modules have to be synchronised and the consistency of the data has to be guaranteed. Not only does a real integration of the atmospheric impact in aircraft design enable its evaluation or minimisation, but it also enables tradeoffs with noise and local air quality, that tend to foster other design solutions. The approach aims at contributing to a reasonable compromise of design parameters for economically viable, environmentally friendly and thus sustainable aircraft.

4 TWO-STAGE OPERATIONS (TSO) AS EXAMPLE OF USE OF THE METHODOLOGY

Two-stage operations (TSO) reflect both operational and configurational advances in design and were thus chosen as illustrative example of the methodology. For the time being, fuel burn (proportional to CO₂ and H₂O emissions) was chosen as metric for the atmospheric impact of aviation.

In steady flight, the thrust of an aircraft is equivalent to its drag, most of which is caused by the aerodynamic lift of the aircraft. Consequently, an increased aircraft weight demands more thrust and leads to higher fuel consumption. On longrange flights, aircraft use a lot of fuel just to transport fuel. On the other hand, the takeoff procedure is very fuel-consuming. For each aircraft, a distance for minimum fuel consumption per flown kilometre can be determined. In the example given in Figure 4, the optimum stage length is 4300 km.

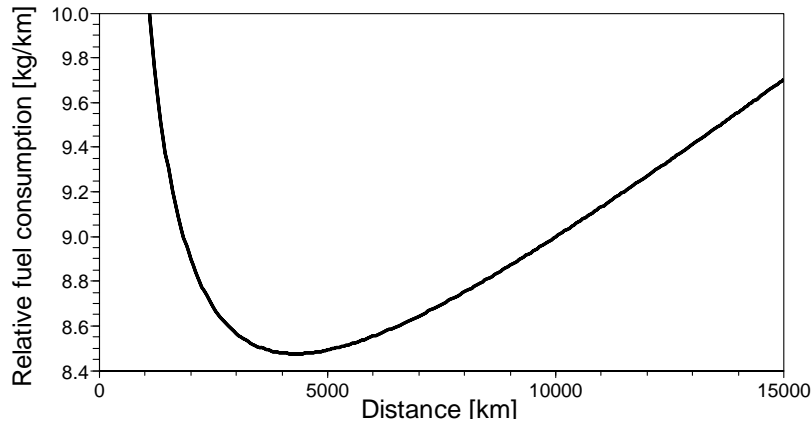


Figure 4. Relative fuel consumption in kg/km for an example longrange aircraft

An approach to reducing the fuel consumption for longrange flights is to separate the flown distance into two or more stages (“two-stage operation” or “multi-stage operation”), of which each length should be as close as possible to this minimum.

4.1 Theoretical fuel reduction potential with TSO

If the distance to be flown is only slightly longer than the optimum distance, a TSO may not save fuel. The curve plotted in Figure 4 can be approached by a function of the type

$$y = ax + b + \frac{c}{x} \quad (1)$$

where x is the distance to be flown and y is the relative fuel consumption per flown kilometre. The parameters a , b and c are chosen such that the curve is best estimated, e.g. for stage lengths between 300 km and 12,000 km. The potential relative fuel saving of a TSO is

$$z = y_{total} - \frac{y_1 \cdot x_1 + y_2 \cdot x_2}{x_{total}} \quad (2)$$

where x_1 and x_2 are the lengths of the two stages, y_1 and y_2 are the respective relative fuel consumptions of the two stages and x_{total} is the total distance with a total relative fuel consumption of y_{total} , if flown in one flight. Considering that $x_{total} = x_1 + x_2$ and equation (1), we get

$$z = 2ax_1 - \frac{c + 2ax_1^2}{x_{total}} \quad (3)$$

Dividing (3) by (1) gives the potential fuel economy e in percent:

$$e = \frac{-2ax_1^2 + 2ax_1x_{total} - c}{ax_{total}^2 + bx_{total} + c} \quad (4)$$

Plotting function $e(x_{total}, x_1)$ shows for which total distances and which partial distances considerable fuel savings can be obtained, if operating as TSO:

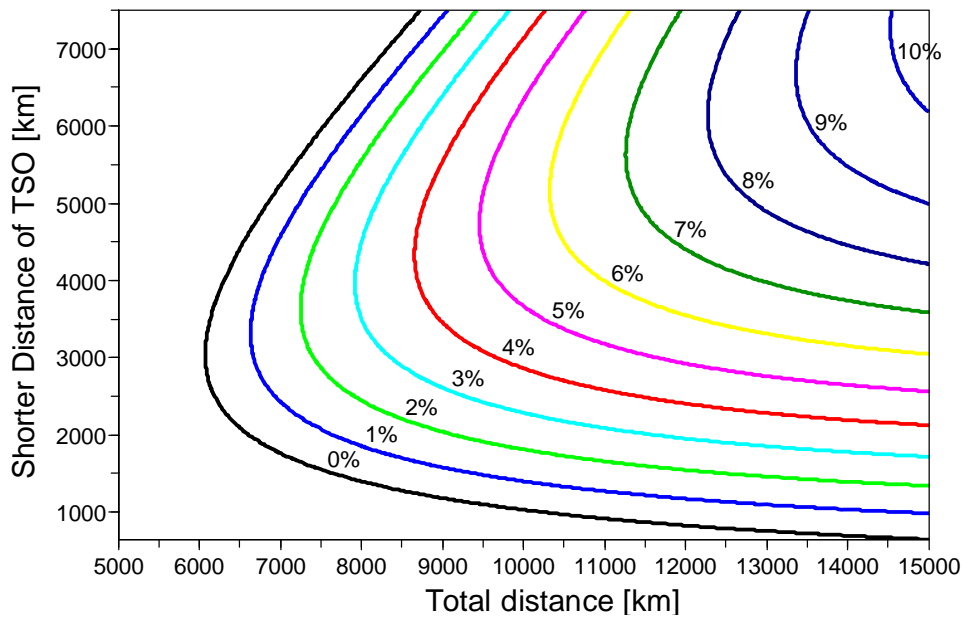


Figure 5. Theoretical fuel economy for an example longrange aircraft with TSO in percent (isolines), depending on the total distance (abscissa) and the shorter of the two stages with TSO (ordinate).

4.2 Market share of TSO-capable routes

Considering a fuel saving of 2 % “interesting”, routes of more than 7200 km would be worth a TSO with the considered example aircraft. In the global air traffic (OAG data from 2005), such flights represent only 2.7 % of all annual flights by aircraft greater than one hundred seats, but 27 % of available seat-kilometres (see Table 1).

Table 1. Theoretical maximum fuel economy operating in two stages with an existing longrange aircraft and respective fractions of flights and available seat kilometres of the global traffic of aircraft with more than one hundred seats.

Theoretical fuel economy	Distance greater than [km]	Fraction Flights	Fraction ASK
0%	6100	4.2%	37%
1%	6600	3.4%	32%
2%	7200	2.7%	27%
4%	8700	1.5%	17%
6%	10,300	0.43%	5.5%
8%	12,300	0.05%	0.5%

This means that, despite the high fraction of “TSO-capable” routes in the global traffic of aircraft with more than one hundred seats, operating the aircraft considered here on all flights above 6100 km at the respective optimum stage length, would theoretically save only around one percent of the global fuel consumption.

4.3 Theoretical reduction potential with redesigned aircraft

A higher potential for savings could be attained, if aircraft were designed for shorter ranges. The smaller fuel quantities needed would allow a lower structural weight of the aircraft. A lighter structure again leads to reduced fuel consumption (see 4.1), which feeds back into a reduced structural weight. According to Green et al. (2005), an aircraft designed for 7400 km operating in stages on current real routes would save 10 % in fuel burn compared to an aircraft designed for 14,800 km. Compared to 4.1, this estimation allows for real routes. The theoretical potential of redesigning aircraft would be higher:

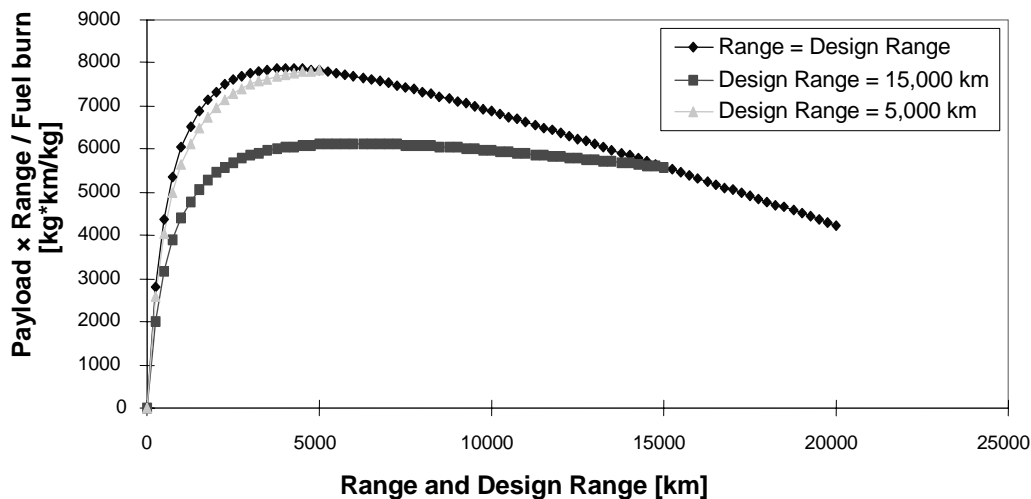


Figure 6. Variation of payload fuel efficiency with range and design range: swept wing kerosene-fuelled aircraft (from Green et al. (2005), arranged by Hans Schnieder (2006))

As shown in Figure 6, the payload fuel efficiency of an aircraft designed for 5000 km on a 5000 km leg would exceed the one of an aircraft designed for 15,000 km by almost 30 %. Of course, this number cannot be generalised in real operations, as aircraft cannot be designed specifically for each needed range, neither for each seat capacity (which is optimised, too, in Figure 6).

4.4 Impact of TSO on the atmosphere

In addition to the smaller quantity of emissions, TSO would lead to emissions at lower altitudes compared to single stages. Concerning nitrogen oxides, this might reduce the radiative forcing of such operations. In terms of condensations trails, the answer remains uncertain, as their radiative forcing does not only depend on the altitude, but also on latitude, season and daytime of a flight. Also, their radiative forcing has not yet been evaluated conclusively.

At low altitudes, especially beneath the atmospheric mixing height (~ 3000 ft), high thrust levels at takeoff bring about high NO_x emissions. Requirements from local authorities might limit the traffic or induce design tradeoffs that lead to a higher fuel consumption in cruise flight, but lower NO_x emission indices at takeoff. This would adulterate the initial benefit of TSO in terms of atmospheric impact. A profound assessment of the benefit of TSO for climate change would presume the integration of a reliable atmospheric model or metric in the loop.

4.5 Operational involvements and economic interest of TSO

The potential fuel savings presented in chapters 4.1 to 4.3 are theoretical. Several aspects would counteract the benefit of TSO:

- Availability of appropriate airports: Even if an airport was available near the mid-range of a certain route, it is not sure it would be able to handle additional traffic, and that it has the necessary infrastructure (runway strength, fuel supply, navigation aids etc.).
- Maintenance cost due to the higher number of flight cycles
- Additional landing and takeoff cycles affecting local air quality (see 4.4) and noise concerns, especially important at busy airports
- Organisational effort for airlines: crew management, airline subsidies at mid-way airports
- Less flexibility for airlines to choose routes, if aircraft are designed to lower ranges
- Value of time for the passenger: A full landing and takeoff cycle with refuelling takes one to two hours, which might not be acceptable for many passengers, those with children, the old and those paying high ticket prices (business passengers).

The overall economic interest of TSO, justifying the effort of severe modifications of the aviation system, is impacted by all of the aspects mentioned above. TSO are interesting and applicable on specific routes only, but cannot be considered a generally fuel-reducing measure today. An expansion of such operations would presume substantial adaptations in the aviation infrastructure, especially at airports. The overall benefit of TSO depends essentially on the fuel price.

5 SUMMARY AND CONCLUSION

A methodology to consider the atmospheric impact in aircraft design was presented. Two-stage operations illustrated the interest in a systemic view of aviation in this regard. The approach highlighted the discrepancy between purely theoretical considerations and real flight operations.

For the evaluation of the benefit of a new approach in aircraft design and operations in terms of climate change, it is necessary to have a good overview of both the different stakeholders of aviation and the impact of aircraft engine emissions on the atmosphere. The methodology presented here is an approach to allowing for the equitable consideration of aircraft design, market requirements, operational issues and the atmospheric impact. The interaction between aircraft design and atmospheric impact can then be treated not only “bottom up”, but as a fully integrated analysis and optimisation loop.

Increasing the complexity of the studied system and the required competences – from aircraft engineering to atmospheric sciences – takes its toll on the precision of results. In order to get realistic and meaningful conclusions, not only are comprehensive methods needed, but also scientific exchange between the respective specialists' communities. Then the correctness of conclusions – within a given precision – can be reasonably assured. The approach presented here proposes a methodological platform for such an integration of both aircraft engineering and atmospheric sciences.

REFERENCES

- Lufthansa, 2006: *Balance – Das Wichtigste zum Thema Nachhaltigkeit*. Company report, Frankfurt, Germany, 82 pp.
- Penner, J., D.H. Lister, D.J. Griggs, D.J. Dokken and M. McFarland (eds.): *Aviation and the Global Atmosphere*. A Special Report of IPCC Working Groups I and III. Published for the Intergovernmental Panel of Climate Change. Cambridge University Press, Cambridge, United Kingdom, 373 pp.
- Egelhofer, R., in press: *Reduzierung des durch Luftverkehr verursachten Atmosphärenschadens durch ganzheitliche Betrachtung im Flugzeugvorentwurf*. Conference Proceedings of the German Aerospace Congress 2005, Vol. III, DGLR-2005-016. Deutsche Gesellschaft für Luft- und Raumfahrt, Friedrichshafen, Germany, 10 pp.
- Green, J., 2005: *Air Travel – Greener by Design. Mitigating the Environmental Impact of Aviation: Opportunities and Priorities*. Report of the Greener by Design Science and Technology Sub-Group. Royal Aeronautical Society, London, United Kingdom, 64 pp.
- Schnieder, H., 2006: Personal communication.

Operational impacts of trajectory adjustments to avoid ice supersaturated regions

V. Williams^{*}, R. B. Noland
Centre for Transport Studies, Imperial College London, UK

R. Toumi
Space and Atmospheric Research Group, Imperial College London, UK

Keywords: Aviation, contrail formation, climate, mitigation

ABSTRACT: Contrails and the cirrus clouds they form may have a climate impact as large as that of the CO₂ emitted by aircraft. One opportunity for reducing the climate impact of aviation could be offered by in-flight adjustments to the flight profile to avoid regions of ice super-saturated air, to prevent the formation of contrails.

We explore the potential operational impacts of such a policy, including the consequences for air traffic management and the impact on emissions. The fast-time air traffic simulator RAMSPlus is used to assess the feasibility of such an approach in areas with high air traffic density. The simulations use a 1-day traffic sample for the UK to test the possible disruption associated with an imposed contrail avoidance zone with a diameter of 150 nautical miles and thickness of 1800 ft situated in the South East region. Three altitudes for the base of the contrail avoidance zone are considered. This extended abstract considers the impact of zone avoidance on three sample flights.

1 INTRODUCTION

Contrails, and particularly the cirrus clouds which they can spread to form, are believed to be a significant factor in aviation's contribution to global climate change.

The scope for technological measures to reduce contrail formation is limited. Options to manipulate the radiative properties of the cirrus cloud formed may be possible (for example by increasing the number of condensation nuclei in the exhaust, to result in more, smaller particles in the contrail), but at present the radiative consequences of such a measure are not well understood and the impact on climate may well be increased. A more feasible alternative is to divert aircraft to avoid regions in which persistent contrails form. For many years, this has been a strategy to preserve the secrecy of military aircraft movements, but it may also have benefits for climate.

Fixed monthly altitude restrictions have been identified from the atmospheric conditions in Western European airspace and air traffic simulations used to assess the potential impacts on both fuel burn and on airspace (Williams et al., 2002). A follow-on study took into account shorter term variability, using an efficiency based criteria to simulate application of altitude restrictions selected every six hours based on atmospheric conditions in order to minimize the fuel burn penalties (Williams and Noland, 2005). Both these studies were based on coarse (2.5°x2.5°) resolution global atmospheric data and considered the application of maximum cruise altitudes across a large area (the European 5 States region). Recent analysis of radiosonde data to identify ice-supersaturated regions has suggested the mean vertical extent of these layers is 560m (Spichtinger et al., 2003). It has been suggested that the thinness of these layers would provide scope for in flight adjustments to cruise altitudes to avoid contrail formation in conjunction with a free-flight policy (Mannstein et al., 2005). By incorporating real time information on local atmospheric conditions, this approach would provide much more targeted adjustments in cruise altitude. This would reduce the fuel burn penalty as only unnecessary altitude adjustments would be made, and the altitude change would be mini-

^{*} *Corresponding author:* Victoria Williams, Centre for Transport Studies, Department of Civil and Environmental Engineering, Imperial College London, Exhibition Road, London, SW7 2AZ, UK. Email: v.williams@imperial.ac.uk

mised. However, from an airspace management perspective, the policy becomes more complex than the monthly shifting region-wide maximum cruise altitude proposed in (Williams *et al.*, 2002) or even the variable policy in (Williams and Noland, 2005). These would both allow a limited number of cruise altitude restriction scenarios to be applied and airspace configuration to be appropriately designed for each. However, new air traffic control technologies expected in the future could decrease the difficulties associated with real time avoidance of contrail formation conditions (Williams *et al.*, 2006).

While flight adjustments to filed flight plans are not uncommon, for example to avoid convective weather systems, a scheme of this nature for contrail avoidance would place an additional planning and monitoring burden on both pilots and controllers. Some incentive-based scheme may also be required for contrail avoidance to be effective. Airlines have always had an incentive to minimise fuel consumption in order to keep costs low and to increase payload and range. Increases in fuel costs have enhanced this pressure. Any policy to avoid contrail formation is likely to require diversion from the fuel-optimising preferred route. The costs to airlines would be further increased if diversions were large enough to significantly impact on journey time. If the onus were placed on the pilot to inform the controller of contrail formation conditions, then some incentive based scheme such that the cost of contrail formation exceeded the fuel and time penalty would be required. In the future, aircraft-based detection and reporting of contrail formation conditions could be automated by linking humidity and temperature sensors to datalink systems, thereby transmitting atmospheric data along with aircraft position and intent information to the air traffic controller and to other aircraft in the vicinity.

Increasing cruise altitudes to fly above the contrail formation layer may also offer some benefit but there are caveats. One is that some existing aircraft would not be capable of achieving these altitudes; for those that are, additional fuel is required in the climb phase to achieve higher altitude. Clearly, there would also be some contrail and cirrus cloud formation from aircraft flying through ice-supersaturated layers during their climb to higher altitudes. Of greater significance for very high altitude flights is the long lifetime of water vapour in the lower stratosphere. Although, in this region, condensation will not occur, there will be a radiative impact from the accumulation of water in its vapour form.

2 METHOD

This study uses the RAMS fast-time simulation model to identify some of the characteristics associated with the avoidance of contrail formation regions. We assume that contrail formation regions are sufficiently stable to be designated as restricted airspace regions, with the designated region allowed to persist. This simulation approach addresses both the changes in fuel burn and NO_x emissions from the altered flight trajectories and the airspace complexity issues associated with diverting traffic into or out of highly congested routes to avoid contrail formation regions. It does not address the additional pilot or controller workload associated with monitoring the changes in atmospheric conditions and identifying the extent of the contrail formation region to be designated for avoidance.

The contrail formation region is defined within the model as restricted use airspace, exactly analogous to the definition of military airspace. The region is centred over the heavily trafficked south east region of the UK and is shown in Figure 1, which also shows the flight routes for the control traffic sample. Three altitude scenarios were considered. The thickness of the avoidance region was set at 1800 ft and the base level is at 24000 ft, 29100 ft and 37200 ft for the LOW, MID and HIGH simulations respectively. These altitudes are consistent with radiosonde observations (Spichtinger *et al.*, 2003). The horizontal extent of the avoidance region was 150 nautical miles, consistent with aircraft observations of path length through ice supersaturated air (Gierens and Spichtinger, 2000). As the simulator requires airspace to be defined as a set corners joined by straight boundaries, the circular avoidance zone is approximated as a 16-sided polygon. Three avoidance scenarios are considered for each altitude zone.

3 TRAJECTORY CHANGES FOR SAMPLE FLIGHTS

For this initial presentation of results, 3 flights were selected for analysis. This allows the trajectory adjustments imposed by the simulator to be explored. Figure 2 shows the trajectory adjustments tested for each flight. Changes in emissions are summarised in Table 1.

3.1 *Flight 1: Tenerife – Nottingham East Midlands*

In the control simulation, this Airbus A320 aircraft crosses the contrail avoidance area at FL250, so travels through the low avoidance zone. The aircraft enters UK airspace to the South of the avoidance zone, flying North East before completing a positioning manoeuvre to approach the runway at Nottingham East Midlands from the North West (Fig 2, top). For the AROUND scenario, the diversion in the simulation model is imposed so as to return the aircraft to its original planned route at the earliest opportunity (i.e. to the first navaid on the original route falling outside of the avoidance zone), rather than to optimise the trajectory. As such, the scenario gives an upper limit on the time and emission increases incurred by flying around the region. These penalties could be reduced with better routing optimisation. Similarly, in the UNDER scenario the aircraft returns to its initial cruise altitude on leaving the avoidance zone, shortly before beginning descent. Further simulations are required to determine whether the journey time and emissions penalties would be reduced by maintaining the lower cruise altitude on exit from the avoidance zone.

At these low altitudes for this aircraft type, diverting the aircraft over the avoidance zone increases the cruise speed and so reduces the journey time. It also reduces the fuel burn rate.

3.2 *Flight 2: Athens – Manchester*

This Boeing 737 flight crosses the avoidance zone from South East to North West in the control simulation. At a cruise altitude of 30,000 ft. In the UNDER scenario, the aircraft returns to its initial altitude before immediately beginning its descent to the airport. This requires an additional fuel burn in the climb phase without the benefit of greater efficiency at cruise, so emissions will be higher than if the aircraft were allowed to continue at the lowered avoidance altitude before descending. The AROUND scenario for this flight route provides a more realistic diversion than that offered for Flight 1, with the avoidance trajectory closer to the minimum distance required to avoid the zone, leading to reduced penalties for journey time and emissions. For Flight 2, diverting over the contrail zone reduces the cruise speed, increasing journey time and emissions.

3.3 *Flight 3: Chicago – Frankfurt*

Flight 3 is an over flight, crossing the UK in the cruise phase of flight, en route from Chicago to Frankfurt. The aircraft is an Airbus A330. Journey time penalties for diverting either above or below the avoidance zone are negligible, although emissions increase in both cases. Diverting around the contrail zone yields a journey time penalty of almost 10 minutes, although as with Flight 1, this represents an upper limit; better routing optimisation could reduce this substantially.

Table 1 Summary of changes in journey time and emissions of CO₂ and NO_x. Percent emissions changes are shown as a fraction of the total flight.

Flight	Diversion	Journey time	CO ₂	NO _x
1 LOW Tenerife – Nottingham East Midlands	Under	+35 s	+0.2 %	+0.5 %
	Over	-19 s	-0.1 %	+0.1 %
	Around	+296 s	+2.0 %	+1.7 %
2 MID Athens - Manchester	Under	+0 s	+0.1 %	+0.3 %
	Over	+24 s	+0.05 %	+0.2 %
	Around	+112 s	+1.1 %	+0.9 %
3 HIGH Chicago – Frankfurt	Under	+0 s	+0.5 %	+1.0 %
	Over	+0 s	+0.4 %	+0.6 %
	Around	+576 s	+2.8 %	+3.3 %

4 DISCUSSION

4.1 *Technological developments*

The technological requirements for monitoring and mapping the contrail formation regions, and particularly for forecasting their future positions, are considerable, but systems could be based on currently available technology. Best results for contrail reduction would be achieved using accurate global satellite observations with high horizontal and vertical resolution of relative humidity and temperature, but for humidity particularly, this data is not currently available. Radiosonde data can provide very detailed local profiles, but the spatial extent of a contrail formation cell could not be accurately determined in this way. One approach would combine data from a range of sources, including satellites, ground based observations and on-board instrumentation. Real time satellite photography could also be potentially used as an identifier of contrail formation regions, when coupled with traffic data and aircraft observations to identify the altitudes at which formation was occurring. These approaches, or a combination of them, would not provide complete contrail avoidance, but would allow subsequent aircraft on the same route to avoid contrail formation, thereby reducing the total climate impact.

4.2 *Innovative airspace and ATM concepts*

This approach to assessing operational impacts of an adaptive contrail formation policy does not include innovative concepts in airspace design that are currently being researched. One such innovative approach is the introduction of dedicated 'highways' for air traffic, which would contain several lanes of air traffic travelling along parallel defined routes defined to be clear from other traffic, with aircraft given responsibility for maintaining separation. These highways would be designed to reduce en-route delay on highly trafficked routes by having fixed access and departure points and procedures and strict constraints on the aircraft permitted to use the routes. These highways would be dynamically designed to optimise performance based on fuel efficiency and/or journey time, but there is additional scope to reduce the environmental impact on these routes by including an assessment of contrail formation conditions in the selection of the highway route.

Other innovative research areas currently being explored, such as improved weather visualisation systems for controllers, could also be adapted to facilitate contrail avoidance (Williams *et al.*, 2006).

5 CONCLUSIONS

These assessments of the impacts of avoiding a contrail formation zone apply only to the three flights described. Even for the same size avoidance zone, a different position relative to the original flight trajectory would lead to different impacts of avoidance.

For each of the three sample flights described here, diversion around the contrail avoidance zone leads to greater time and emissions increases than diversion above or below the zone. This preliminary analysis of the response of sample flights to the diversions imposed by the simulation model has informed the design process for future work to address the system wide implications of such a policy. Diverting around the avoidance zone imposes unrealistic flight trajectories and overestimates the impacts of diversion; it is a worst-case scenario. Manual specification of preferred avoidance routes could address this, but would be impractical for analysis of large traffic samples.

One issue yet to be confirmed is the use of appropriate indicators of the impacts of diversion when considering impacts on a system wide basis. Here, we have used percent changes in emissions relative to the full flight trajectory (assuming great circle routes outside UK airspace). Any measure of the impact will be indicative of the simulated situation only; avoidance trajectories and their impacts will be sensitive to the location of the avoidance zone, and to the traffic sample.

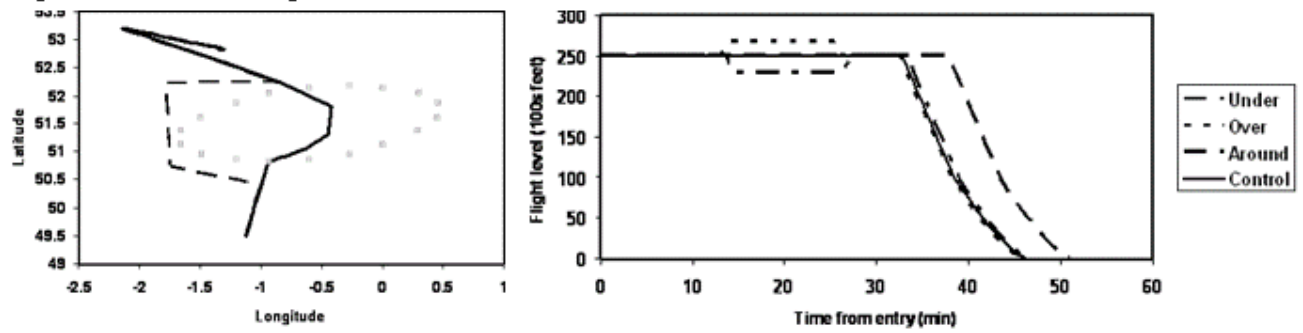
REFERENCES

- Gierens, K. and P. Spichtinger, 2000, On the size distribution of ice-supersaturated regions in the upper troposphere and lowermost stratosphere, *Annales Geophysicae-Atmospheres Hydrospheres and Space Sciences* 18 (4), 499-504.
- Mannstein, H., P. Spichtinger and K. Gierens, 2005, A note on how to avoid contrail cirrus, *Transportation Research Part D: Transport and Environment* 10 421-426.
- Spichtinger, P., K. Gierens, U. Leiterer and H. Dier, 2003, Ice supersaturation in the tropopause region over Lindenberg, Germany, *Meteorologische Zeitschrift* 12 (3), 143-156.
- Williams, V., R. B. Noland and R. Toumi, 2002, Reducing the climate change impacts of aviation by restricting cruise altitudes, *Transportation Research Part D: Transport and Environment* 7 (6), 451-464.
- Williams, V. and R. B. Noland, 2005, Variability of contrail formation conditions and the implications for policies to reduce the climate impacts of aviation, *Transportation Research Part D: Transport and Environment* 10 (4), 269-280.
- Williams, V., A. Majumdar, R. B. Noland, W. Ochieng and R. Toumi, 2006, ITS in the Sky - Scope for Reducing Environmental Impacts of Aviation with Innovative Air Traffic Management Technologies, *Intelligent Transport Systems World Congress*, London.

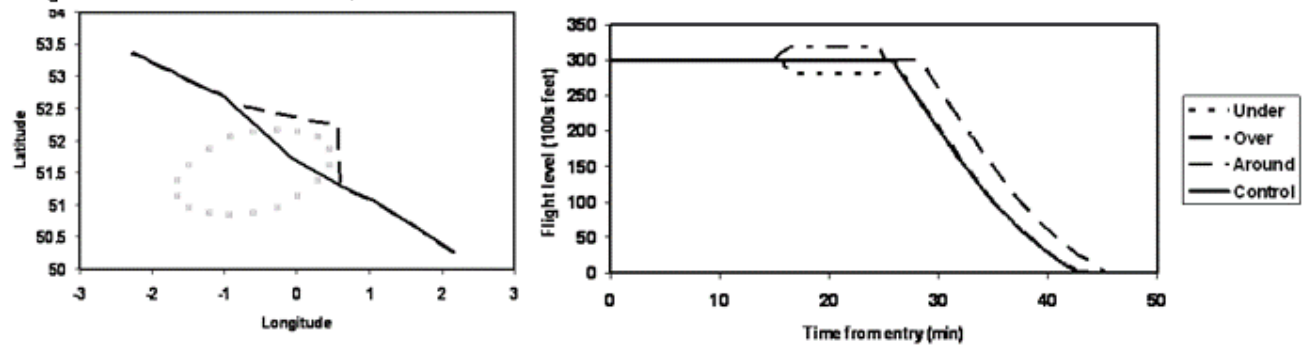


Figure 1 The location of the contrail avoidance region imposed and flight routes in the control traffic sample.

Flight 1: Tenerife – Nottingham East Midlands; LOW contrail avoidance zone



Flight 2: Athens – Manchester; MID contrail avoidance zone



Flight 3 Chicago – Frankfurt; HIGH contrail avoidance zone

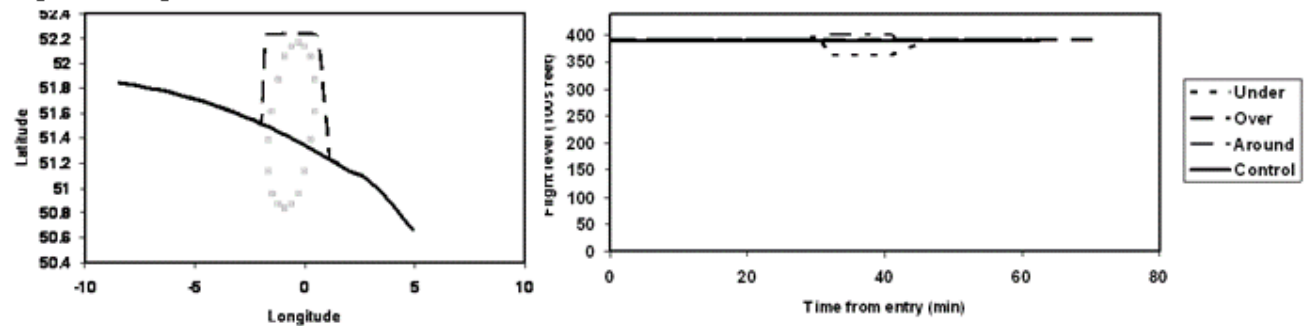


Figure 2 Flight routes (left) and profiles (right) for the three sample flights showing the diversion under, over and around the contrail avoidance zone.

The effect of temporal resolution of PAH emission data on transport and deposition patterns simulated with the Community Multiscale Air Quality modelling system (CMAQ)

I. Bewersdorff*, A. Aulinger, V. Matthias, M. Quante
GKSS Research Centre Geesthacht, Germany

Keywords: polycyclic aromatic hydrocarbon, PAH, air quality modelling, deposition, time-variant emissions

ABSTRACT: The effect of temporal variation of polycyclic aromatic hydrocarbon (PAH) emission data on transport and deposition patterns were simulated with the Community Multiscale Air Quality modelling system (CMAQ) for Europe, 54 km grid, for the year 2000. The carcinogenic benzo(a)pyrene (B(a)P) was used as a representative for the group of PAHs. The official emission data are only provided as one-year bulk emissions but the major emission sources of B(a)P vary within seasonal, diurnal and weekly cycles, respectively. The seasonal variability showed the greatest effects. However, on a regional scale diurnal cycles possessed significant effects as well. Comparison with measured weekly average concentration indicated the same trend for simulation and observation.

6 INTRODUCTION

Polycyclic aromatic hydrocarbons (PAHs) are semivolatile, lipophilic persistent organic pollutants (POPs), which originate primarily from incomplete combustion of organic material. Surveys have revealed that a variety of PAHs possess a high carcinogenic potential to animals and humans (ATSDR, 1995) and are bio-accumulated in the food chain. They can be transported over long distances in the atmosphere resulting in a widespread distribution across the earth, including regions where they have never been used. Due to their toxic and ecotoxic characteristics they pose a threat to humans and the environment, and therefore the international community has called for actions to reduce and eliminate the release of POPs, such as the Protocol to the UN-ECE Convention on Long-range Transboundary Air Pollution (CLRTAP) on POPs. Benzo(a)pyrene (B(a)P) is one of the best investigated PAHs both because of its severe toxicity and its relatively good availability to measurements. In our modelling study it was for this reason used as a marker for carcinogenic PAHs. The release of PAHs into the environment is highly dependent on human activities whereas their distribution over e.g. Europe is driven by their physical-chemical characteristics and meteorological conditions. Thus, to investigate the pathways of PAHs and to assess the threat they may pose to particular ecosystems it is indispensable to apply proper emission scenarios and meteorological data together with a sophisticated chemical transport model.

Significant emission sources of PAHs are residential combustion and road traffic both of which show considerable temporal variations. Residential combustion is mostly dependent on the season whereas traffic varies primarily within diurnal and weekly cycles. Since the meteorological conditions which drive the atmospheric transport model change with time the input emissions of the modelled compounds should present an appropriate temporal variation as well. It will make a significant difference in transport and deposition of pollutants whether high wind speeds, certain wind directions or precipitation events meet with emission peaks or time-invariant emissions. Emission data for B(a)P was provided to us by TNO (Denier van der Gon et al., 2005), but only as annual bulk emissions. In our study we present a first approach of implementing time-resolved B(a)P emissions. We then compared the model output of our B(a)P version of CMAQ when applying time-

* *Corresponding author:* Ines Bewersdorff, GKSS Research Centre Geesthacht, D-21502 Geesthacht, Germany.
Email: ines.bewersdorff@gkss.de

variant emissions, emissions with only seasonal and weekly variability or with seasonal, weekly and diurnal variability. For validation purposes, the model results were also compared to B(a)P measurements in ambient air.

To evaluate the mean air concentrations the focus was put on the lowest model layer that is 35 m thick. Additionally, accumulated wet deposition patterns were investigated. Model runs were conducted for the months January, April, July and October that were selected as representatives for the whole year.

7 MODEL DESCRIPTION AND –SET UP

For the simulation of transport and chemical transformations the Models-3 Community Multiscale Air Quality (CMAQ) Modeling System was used (Byun and Ching, 1999; Byun and Schere, 2006). The CMAQ system consists of three primary components which are devoted to meteorology, emissions, and chemical transport, respectively. The chemistry transport module is mainly designed for classical air pollutants like SO₂, NO_x, O₃, and particulate matter (PM).

At GKSS the CMAQ systems was extended to cope with the transport of B(a)P in the gas phase and three particulate modes (Aulinger *et al.*, 2006). Thereby, special emphasis was laid on considering the mass transfer of B(a)P between the gaseous and the particulate phase. Because the majority of our target substances is transported in the particulate phase the extended aerosol module of CMAQ (Binkowski and Roselle, 2003) is of primary importance for realistic simulations.

The meteorological fields were derived from MM5, the Fifth-Generation Pennsylvania State University/National Center for Atmospheric Research (NCAR) Mesoscale Model (Grell *et al.*, 1995). Since wet deposition is the dominant sink for our applications, a more complex ice physics (Reisner 2 scheme) was employed and the Kain-Fritsch 2 convection scheme was used. The meteorological output fields were then processed using version 3 of Meteorology–Chemistry Interface Program (MCIP) for generating the input for the chemistry transport module.

MM5 as well as the CMAQ models were set up on a 54 x 54 km² grid for Europe, covering the entire North Sea and Baltic Sea in the North-West as well as the Mediterranean Sea and Black Sea in the South East. Thirty unevenly distributed vertical layers were used for all models employing a higher resolution in the atmospheric boundary layer. The meteorological model was run in a hind-cast mode with six-hourly ERA-40 data (Uppala *et al.*, 2005) as controlling input.

The chemistry model simulations used the CB-IV gas-phase chemistry mechanism and the efficient Euler Backward Interactive (EBI) solver. Fixed profiles of the relevant species were provided as boundary conditions. The model runs considered a spin-up of two days.

8 EMISSIONS

B(a)P emission data are available on the 50 x 50 km² polar stereographic EMEP grid as annual bulk emissions (Denier van der Gon *et al.*, 2005) for eight emission sectors: Public power and heat, residential combustion, industrial combustion and processes, solvent and product use, road transport, non-road transport, waste incineration, agriculture. The major source, residential combustion, has a strong variability with the season and a lesser weekly and diurnal variability. The second important emission sector, industrial combustion and processes, is seasonally invariable and varies only within weekly and di-

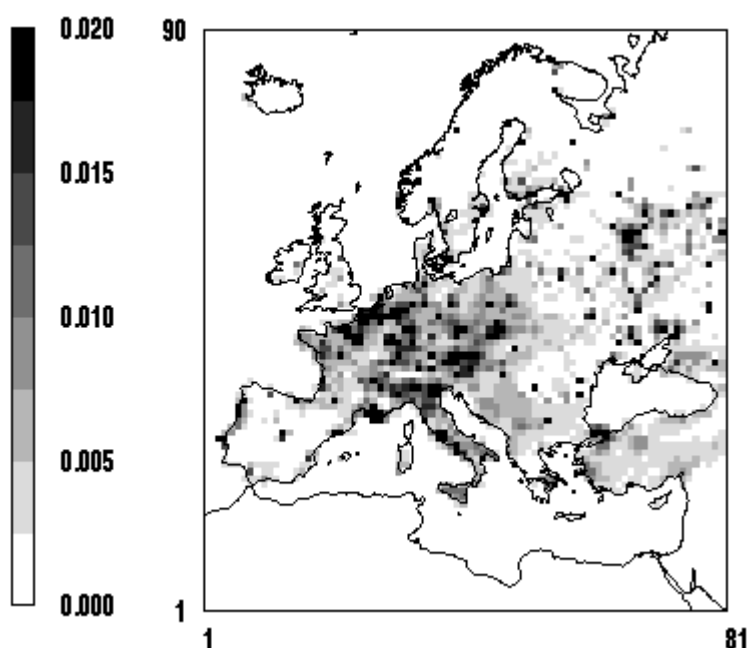


Figure 2. Average B(a)P emissions in g/s for 2000

urnal cycles. The latter is also true for emissions from road transport while the remaining sectors are negligible for B(a)P and are kept constant for simplicity. CMAQ requires emissions with a one hour time step. Three different temporally resolved emission data (cases A, B and C) sets were used as input data for CMAQ (Tab. 1).

Table 4. Overview of the three different temporally resolved emission data sets

Case	Temporal variations considered		
	Annual cycle	Weekly cycle	Daily cycle
A (constant)	-	-	-
B (seasonal)	+	+	-
C (daily)	+	+	+

At first, constant emissions for each hour of the year were generated to feed into the Eulerian air quality model (case A). In a second approach we employed seasonal variations of the emissions including annual and weekly cycles. In addition to the seasonal variation the third dataset with daily resolved emissions included also a diurnal cycle. Table 2 provides information on the different temporally resolved emission cycles that were applied to the annual bulk emissions.

Table 5. Temporally emission resolution

Emission resolution	Description
Constant emissions	Constant emissions each hour of the year
Annual cycle	Influenced by residential heating, deduced from B(a)P measurements in Kosetice, Czech Republic, which reflects the seasonal cycle (Holoubek et al., 1992)
Weekly cycle	Ascribed to working days, influenced by residential heating, traffic and industry
Daily cycle	Dependent on working hours, scaling factor deduced from NO emission variations for emissions originating from road traffic and CO emission variations for residential combustion

9 RESULTS AND DISCUSSION

9.1 Regional distributions depending on different emission cycles

In the entire model domain, the time-variant emissions lead to much higher B(a)P concentrations and depositions in January than in the other tested months due to the implemented annual cycle of B(a)P emissions which is dominated by residential heating. In January B(a)P concentrations up to 2.5 ng/m³ were modelled whereas in July in large parts of Europe the concentrations simulated with daily resolved emissions (case C) did not exceed 0.06 ng/m³. The B(a)P concentration level reached in winter could already cause noticeable human health effects (Hellmeier and Huhmann, 2001). Thus, figures of the B(a)P concentration and deposition distribution over Europe are only displayed for January (Figs. 2, 4, 6, 8).

9.1.1 Comparison of case A with case B

Although the total amount of annual emissions was kept constant, the mean annual concentrations were different – depending on the region – when running the model with constant (case A) or seasonally/weekly resolved emissions (case B). Figure 3 shows that especially in the region north of the Black Sea, in parts of the European part of Russia and in the area from Slovenia over Austria and Slovakia to Poland estimated B(a)P concentrations were significantly higher when considering the seasonal cycle. Even larger differences could of course be observed in the monthly mean concentrations. In January the differences between cases A and B were more pronounced than in the other investigated months (Fig. 7).

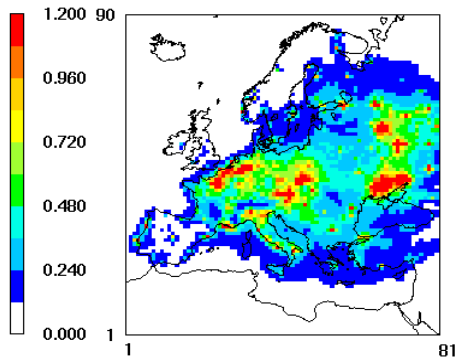


Figure 2: Average annual ground level concentrations in ng/m^3 (case A)

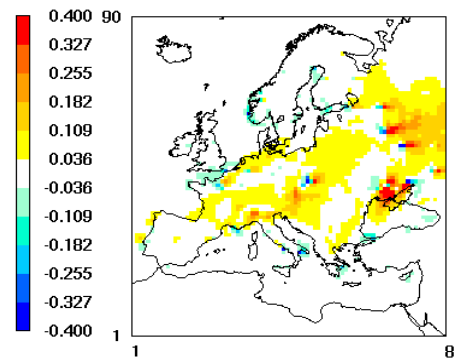


Figure 3: Differential plots of annual mean concentrations in ng/m^3 ; case B - case A

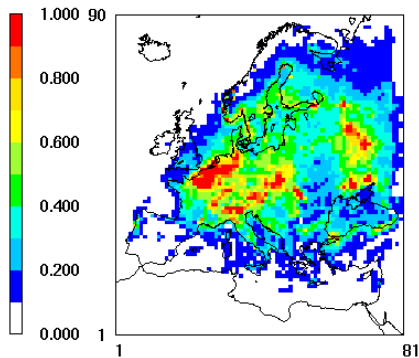


Figure 4: Annual depositions in $\text{g}/\text{hectare}$ (case A)

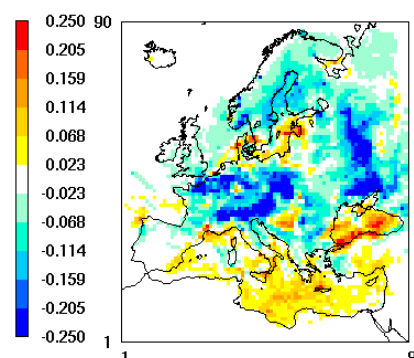


Figure 5: Differential plots of annual depositions in $\text{g}/\text{hectare}$; case B - case A

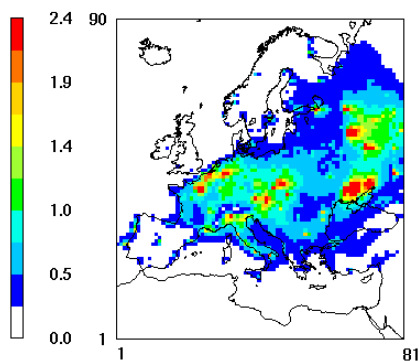


Figure 6: Average ground level concentrations in January in ng/m^3 (case A)

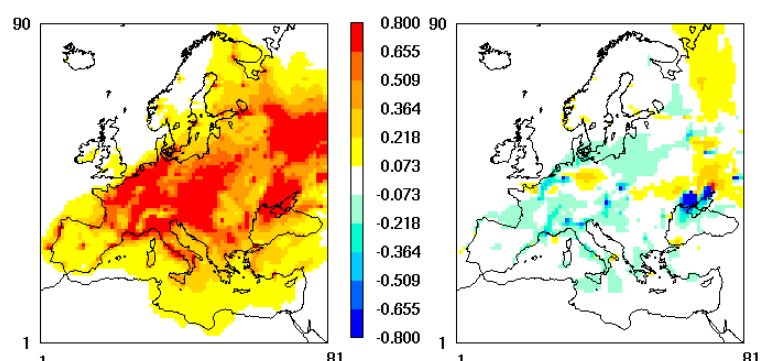


Figure 7: Differential plots of ground level concentrations in January in ng/m^3 ; left: case B - case A; right: case C - case B

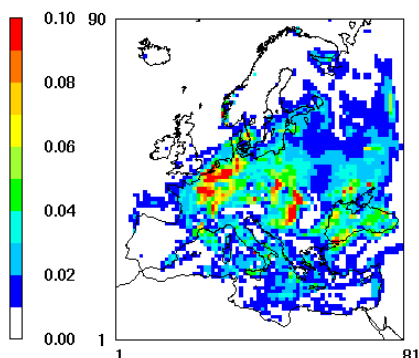


Figure 8: Depositions in January in $\text{g}/\text{hectare}$ (case A)

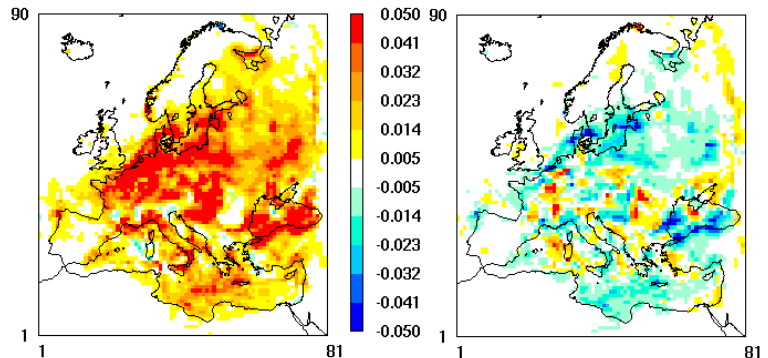


Figure 9: Differential plots of depositions in January in $\text{g}/\text{hectare}$; left: case B - case A; right: case C - case B

The concentrations showed an increase by at least 70 %, but reached up to 130 % over the North Sea and in the north of the Black Sea. In contrast, in April and July the B(a)P concentrations were decreased, in April by around 40 % and in July by around 90 %. October showed no general trend. In some regions the differences were -10 % and in other regions +10 %. The differences in monthly depositions reflected in general the differences in concentrations (Figs. 5, 9). The application of time-variant emissions lead to increased B(a)P deposition in January, from 0.02-0.04 g/ha to 0.03-0.1 g/ha over a wide area of Europe, but especially in Central Europe and over the Black Sea. In July the depositions with constant emissions ranged from 0.03-0.07 g/ha. With seasonally resolved emissions they decreased by over 90 %. Furthermore, April showed a Europe-wide decrease of deposition with annual and weekly cycles as well, but with a more moderate slope. In April the depositions dropped off between 30 % and 50 %. The Differences in October amounted to -30 % up to +30 %.

9.1.2 Comparison of case B with case C

The differences of model results between simulations with the seasonal and daily cycle turned out lesser and at smaller regional scales (Fig. 7). In January again the differences were most pronounced. In the greater Moscow area the concentrations for case C were up to 50 % elevated compared to the results from emissions with seasonal variations (case B). Other spots of increased B(a)P concentrations for case C could be observed in the centre of Europe (Germany and Poland) where the concentrations rose by approximately 25 %. In July, where the concentration of B(a)P hardly exceeded 0.03 ng/m³, the differences between cases B and C were still visible but significantly smaller – at most 10 % – than in January. Concerning the annual mean concentrations between case B and C reveals that mainly in the area north of the Black Sea a decrease of the B(a)P concentration is noticed.

The differences of the depositions between the seasonal and diurnal cycle draw a comparable picture as described for the concentration deviations (Fig. 9). Between the two different time-variant emission cycles (case B and C) January are responsible for the main deviation to the annual B(a)P depositions which accounts for 50 % in some parts of Europe, e. g. parts of Poland, Romania and Bulgaria. During the other months in most areas of Europe the difference is not larger than +/-10 %.

9.2 Comparison with ground measurements

B(a)P ground level measurements from two sites belonging to the air quality assessment program of UBA (German Federal Environmental Agency) were used to evaluate the simulated concentrations in the lowest model layer. At Bornhoeved, a rural site in the north of Germany, the measurement data were provided as weekly average concentrations and at Radebeul, an urban site in the east of Germany, as daily average concentrations. Thus, weekly and daily averages were calculated from the model output that has a time resolution of one hour. Predominantly, all three approaches with differently time-variant emission files described the same trend as the measurements. For both tested sites the concentration levels calculated with cases B and C diverged only at the most 10 % from each other, whereas the differences between cases A and B were up to 75 % in January and 94 % in July. For Bornhoeved the simulations constantly overestimated the B(a)P concentrations. The largest deviation was found in January where the simulated monthly mean with case C was 400 % above the measured mean and 200 % with case A. In July, in contrast, the deviation was only 6 % with case C while 1500 % with case A. At Radebeul the simulated monthly mean concentration was 8 % (case C) higher or 40 % lower (case A) and in July 265 % higher with case A and 77 % lower with case C than the measured one. In general, the case C simulations fitted best to the observations.

Taking into account that it cannot be assured that the measurement sites are representative for the entire grid cell in which they lie and that the shape of the concentration curves is well reproduced by the simulations the performance of the model can be regarded as acceptable. Differences in absolute values between measurements and simulations may rather be owed to uncertainties in absolute emissions.

10 CONCLUSION

As expected, the results confirmed that seasonally resolved emission data has a Europe-wide effect on the simulated B(a)P concentrations and depositions. A diurnal cycle induces significant effects on a regional scale solely. The greatest influences of time-variant emissions were observed in January, in April and July the effects were less pronounced and the least in October. A comparison with ground level measurements showed that the simulations reflect the observed trends in concentration. However, the deviations depend strongly on the site, industrialised or rural area, and the month considered.

The seasonal variability of emissions as it was employed in this study reflects the seasonality only at one particulate site in the Czech Republic which is probably not representative for the whole model domain. In order to reflect a locally specific seasonality, we will proceed by creating emissions that are directly correlated with the temperature in each grid cell.

None the less it is evident that emissions that vary with the season are an indispensable prerequisite for realistic model results. We regard it even as recommendable to include a daily cycle as well to achieve a better spacial resolution of concentration and deposition patterns. A more representative evaluation of the model results could only be achieved with data of long-term studies which should include several seasonal cycles.

11 ACKNOWLEDGEMENTS

TNO Netherlands is gratefully acknowledged for providing emission data of B(a)P. Furthermore, we thank IER Stuttgart for providing emission data of main pollutants and the German Federal Environment Agency is acknowledged for the use of measurement data.

REFERENCES

- ATSDR (Agency for Toxic Substances and Disease Registry), 1995: *Toxicological Profile for Polycyclic Aromatic Hydrocarbons (PAHs)*. Public Health Service, US Department of Health and Human Services, Atlanta, GA, USA.
- Aulinger, A., V. Matthias, and M. Quante, 2006: Introducing a partitioning mechanism for PAHs into the Community Multiscale Air Quality modelling system and its application to simulating the transport of benzo(a)pyrene over Europe. *submitted to J. Appl. Meteorol.*
- Binkowski, F.S. and S.J. Roselle, 2003: Models-3 Community multiscale air quality (CMAQ) model aerosol component, 1 Model description. *J. Geophys. Res.* 108(D6), 4183, doi:10.1029/2001JD001409.
- Byun, D. and J.K.S. Ching, 1999: *Science Algorithms of the EPA Models-3 Community Multiscale Air Quality Modelling System*. EPA report, EPA/600/R-99/030, Office of Research and Development, Washington DC 20406.
- Byun, D., and K.L. Schere, 2006: Review of the Governing Equations, Computational Algorithms, and Other Components of the Models-3 Community Multiscale Air Quality (CMAQ) Modeling System. *Appl. Mech. Rev.* 59, 51-77.
- Denier van der Gon, H.A.C., M. van het Bolscher, A.J.H. Visschedijk, and P.Y.J. Zandveld, 2005: *Study of the effectiveness of UNECE Persistent Organic Pollutants Protocol and cost of possible additional measures. Phase I: Estimation of emission reduction resulting from the implementation of the POP Protocol*. TNO-report. B&O-A R 2005/194. Appeldoorn, Netherlands.
- Grell, G.A., J. Dudhia, and D.R. Stauffer, 1995: *A Description of the Fifth-Generation Penn State/NCAR Mesoscale Model MM5*. NCAR Technical Note, NCAR/TN-398+STR, Boulder, CO, 138 pp.
- Hellmeier, W. and H. Huhmann, 2001: Gesundheitsindikator 5.8, Polycyclische, aromatische Kohlenwasserstoffe (PAK) in der Außenluft. Landesinstitut für den öffentlichen Gesundheitsdienst, http://www.loegd.nrw.de/1pdf_dokumente/4_umweltmedizin_umwelthygiene/kommentierung_indikatoren_umwelt/ind_5-8_ueberarbeitet_01_2001.pdf, 15.09.2006.
- Holoubek, I. and 11 authors, 1992: Project TOCOEN - The Fate of Selected Organic Compounds in the Environment. Part XI. The PAHs, PCBs, PCDDs/Fs in Ambient Air at Area of Background GEMS Station. Seasonal Variations. *Toxicol. Environ. Chem.*, 36, 115-123.
- Uppala S.M. and 44 authors, 2005: The ERA-40 reanalysis. *Quart. J. Roy. Meteor. Soc.* 131, 2961-3012.

Physical Characterization of PM Emissions from In-Service Commercial Gas Turbine Engines – Projects APEX and JETS APEX2

D.E. Hagen*, P. Lobo, P.D. Whitefield

University of Missouri – Rolla Center of Excellence for Aerospace Particulate Emissions Reduction Research, Rolla, MO, USA

Keywords: APEX, JETS APEX2, PM emissions, CFM56

ABSTRACT: On-wing PM measurements were made on GE CFM56 class engines at the exhaust nozzle exit (~1m) and at downstream locations (30m and 50m) in the near field plume. At the engine exit plane, size distributions were generally lognormal. EIn – number-based emission index was a minimum at mid-level thrusts compared to the idle and high thrust settings. For measurements made at downstream locations in the near-field plume, the onset of gas-to-particle conversion was apparent for low to medium thrusts. Non-lognormal size distributions were often observed where the mean sizes (~12-15nm) were found to be smaller than the 1m case. EIn also decreased with increasing thrust, and was an order of magnitude higher than that for the engine exit cases at low thrusts. Elm – mass-based emission index was found to increase with thrust, ranging from 0.001-0.37 g/kg fuel burnt.

1 INTRODUCTION

The University of Missouri – Rolla (UMR) Center of Excellence was involved in two recent ground-based aircraft emissions measurement campaigns – Project APEX (NASA Dryden Flight Research Center, April 2004) and JETS APEX2 (Oakland International Airport, August 2005). The goal of these studies was to advance the understanding of particle emissions and their evolution in the atmosphere from in-service commercial gas turbine engines. Extractive particulate matter (PM) emission measurements were made on GE CFM56 class engines at the exhaust nozzle exit (~1m) and at downstream locations (30m and 50m) in the near field plume. The roles of fuel composition and engine power setting were also explored. These engines were mounted on three airframes: DC8-50, B737-300, and B737-700. These measurement campaigns involved a multi-agency team: NASA (DFRC, GRC, LaRC), EPA, FAA, DoD (AEDC, NAVAIR, NFESC, WPAFB), Aviation Industry (GE, Boeing, PW), and Research Community (ARI, MIT, PM, UCF, UCR, UMR).

At Project APEX, three different fuels were used – a baseline JP-8 fuel (Base Fuel - 383 ppm sulfur and 17.6% aromatics), Base Fuel doped with tertiary butyl disulfide (High Sulfur Fuel - 1595 ppm sulfur and 17.3% aromatics), and Jet A fuel which had a considerably higher aromatic content than the two other fuels used (High Aromatic Fuel - 530 ppm sulfur and 21.6% aromatics). Fuel sulfur and aromatic concentrations reported are in parts per million mass and % by volume, respectively. The fuel for JETS APEX2 was JET A having a total aromatics in the range 19.6-22.8% by volume and a sulphur content ranging from 125-419 ppm. At both these tests, the test matrix consisted of a modified LTO cycle with power settings of 4%, 5.5%, 7%, 15%, 30%, 40%, 60%, 65%, 70%, 85% and 100%. The times on each power condition were nominally 4 minutes, except for the 100% case which was limited to 1.5 minutes. At Project APEX, the test aircraft was parked on a pad. In contrast at JETS APEX 2, the aircraft was parked at a Ground Runup Enclosure which eliminated problems associated with changing wind directions.

* *Corresponding author:* Donald E. Hagen, UMR Center of Excellence for Aerospace Particulate Emissions Reduction Research, G-7 Norwood Hall, University of Missouri – Rolla, Rolla, MO 65409, USA. Email: hagen@umr.edu

2 SAMPLING TRAIN AND INSTRUMENTATION

Custom-designed probes and extensive support equipment were used to sample jet exhaust in the on-wing position. Particle-laden exhaust was extracted directly from the engine exhaust flow through probes and supplied to the measurement devices. The primary probe for collecting samples and data was positioned within 1 meter of the exhaust nozzle exit plane, as this position is representative of the engine signature and the certification data in the International Civil Aviation Organization (ICAO) database (ICAO, 2006). The PM probes are designed to provide both probe tip and upstream (0.09 meters from tip) dilution flows, thereby reducing and/or eliminating probe effects. The rake quadrant and probes are water cooled to protect them from thermal degradation during testing. The dilution flows are drawn from particle-free, dry air sources located in the mobile laboratories and conducted to the probes through 0.006-meter (inside diameter) flexible gas lines. The sample for PM measurements are conducted to the mobile laboratories through a 3/4" SS sample line for which line losses have been calibrated.

Dry nitrogen for dilution was introduced into the flow at the probe tips on the 1m rakes. The dilution was used to suppress particle-particle interactions and gas-to-particle conversion. The amount of dilution gas was controlled by observing the CO₂ concentration in the sample line and keeping it at a desired level. Typical dilution ratios were in the range 10-40. No diluent was provided at the downstream locations since sufficient dilution with ambient air was found to have occurred naturally in the plume.

UMR has developed a state-of-the-art mobile diagnostic facility and a sophisticated sampling methodology for nanometre scale PM optimized for jet engine exhaust characterization (Schmid et al., 2004; Lobo et al. 2006). The instrumentation consists of 2 state-of-the-art fast particulate spectrometers (Cambustion DMS500) to gather real-time size distribution information and total concentration of engine exhaust PM; a differential mobility analyzer (DMA) (TSI model 3071), a more traditional tool for particle size measurement, sacrificing speed for greater sensitivity when compared to the DMS500; Condensation Particle Counters (CPCs) (TSI models 3022 and 3025) to measure total number concentration; a fast response carbon dioxide (CO₂) detector (Sable Systems model CA-2A) to monitor sample dilution and establish emission factors; and a weather station to monitor the ambient conditions of temperature, relative humidity, pressure, and wind speed and direction. Two fast particulate spectrometers were used to get both volatile and non-volatile particulate information. To achieve this differentiation, one of the spectrometers was preceded by a thermal denuder operating at 300°C to remove volatile material.

3 RESULTS

Detailed data from Project APEX can be found at public website: <http://particles.grc.nasa.gov> and in the recently released NASA final report (Wey et al., 2006). Similar data for Project JETS APEX2 is anticipated to be released to the public in December 2006. In this paper the data for the CFM56 class of engines from both projects will be used to explore PM emissions dependencies on selected operational parameters.

Figure 1 shows the emission indices (EIn – number-based emission index, and EIm – mass-based emission index) as functions of power, fuel type, and distance downstream of the engine exit. There is a difference in EIn between the 1m and 30 m probe locations. At the 30m probe location, EIn is highest at the lowest power, and is an order of magnitude higher than that for the 1 case. It then decreases with power until ~85% is reached, where it becomes constant. The greatest differences between the 1m and 30m data are observed at low powers where the residence time in the plume affords more opportunity for gas-to-particle conversion to occur resulting in larger EIn values. For all three fuels, at both probe locations, EIm tends to increase with power, with a low power minimum near 20%, and a high power maximum above 85%. At high fuel flow rates, the EIm values for the 1 and 30m cases converge suggesting that the mass at these higher fuel flow rates is dominated by the non-volatile component of the aerosol.

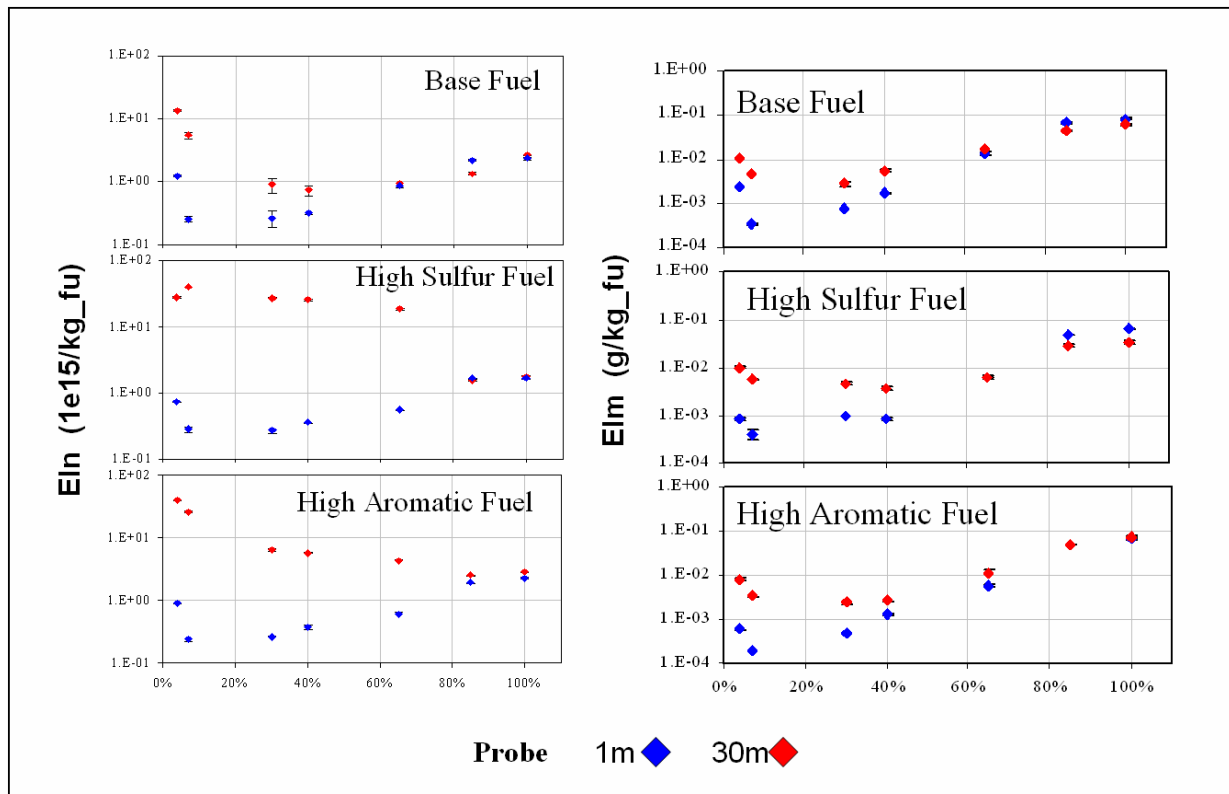


Figure 3. Emission indices as functions of power, fuel type and distance downstream of the engine exit

Figure 2 shows the engine to engine variability in emission indices (EIn and Elm) close to the engine exit plane (~1m) plotted versus power. All engines demonstrate the power dependence discussed above. However, engine to engine variance exceeded that associated with power change for a given engine. In the case of EIn, the new technology engines on the -700 series aircraft produce fewer particles per kilogram of fuel burned. This difference is large and statistically significant. Averaged across all powers, this difference represents a (79 ± 12) % reduction in number-based emissions normalized to fuel flow. EIn for the Project APEX engine falls between those of the -300 and -700 series and the differences between all engines are statistically significant at higher powers. Mass-based emission index exhibited a trend to increase with power. The trend is stronger for the older engine technology (-300 series). There is a large and statistically significant difference at high power representing a 72% reduction in mass-based emissions normalized for fuel flow at 85% power. This is also the case for the CFM56-2C1 engine studied in Project APEX.

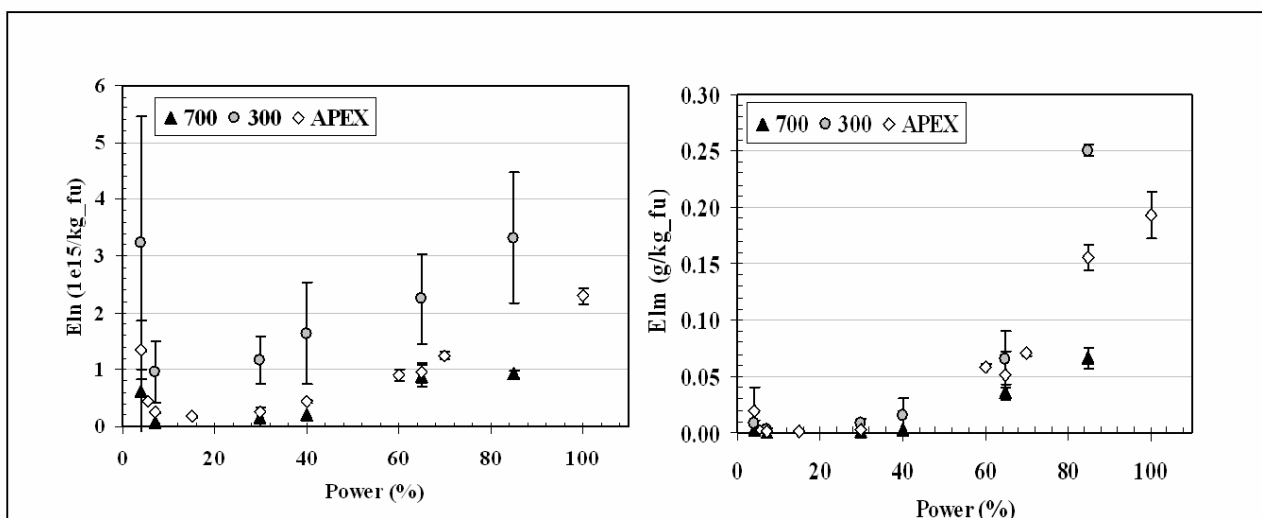


Figure 4. Engine to engine variability in emission indices

Figure 3 compares the emission indices (EIn and EIm) for the total aerosol and non-volatile component at the 50m sampling location. Plume processing in the expanding exhaust plume results in the production of a large number of small particles (volatile material) observed in the total aerosol but not present in the non-volatile component. The production of these small particles results in an order of magnitude increase in EIn. These particles also contribute to the mass dependent parameter values, but to a lesser extent.

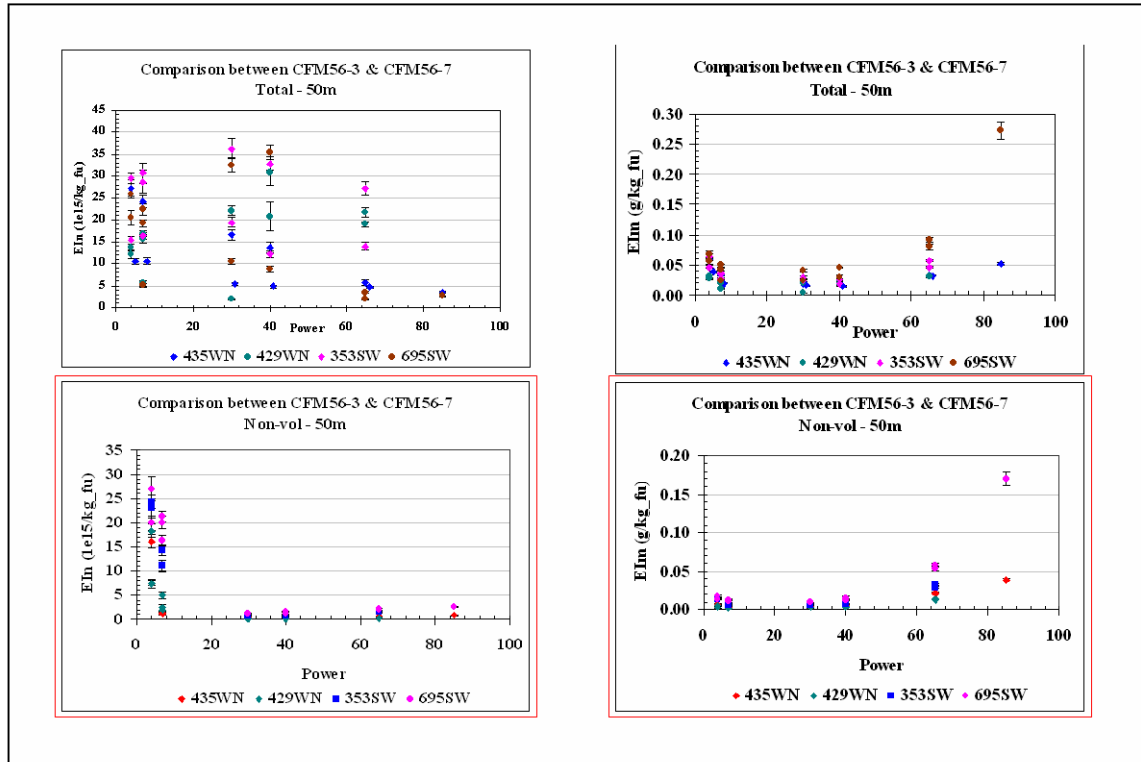


Figure 5. Comparison of emission indices for the total aerosol and non-volatile component at the 50m sampling location

Table 1 summarizes the range of PM parameter values measured for the CFM56 class of engines in these sampling campaigns, and compares them to published values for individual engine measurements using estimated size distributions.

Table 6. Range of PM parameter values measured for the CFM56 class of engines

Parameter	Min	±%	Max	±%	Average	±%	Slope
EIn (10 ¹⁵ /kg _{fuel})							
Non-vol 1m	0.67	64	4.1	61	1.7	56	-
Non-vol plume	0.54	68	17.9	32	6.0	49	-
Total 1m	0.68	87	10.2	130	4.5	129	±
Total plume	7.95	85	28.0	38	16.1	28	-
IPCC (Penner et al. 1999)	0.30		50.0				
EIm (g/kg _{fuel})							
Non-vol 1m	0.002	69	0.060	55	0.016	49	+
Non-vol plume	0.004	74	0.045	75	0.014	62	+
Total 1m	0.002	84	0.084	55	0.023	61	+
Total plume	0.012	65	0.078	52	0.031	47	±
IPCC (Penner et al. 1999)	0.010		0.200				

4 CONCLUSIONS

The following conclusions for the CFM56 PM Emission Indices can be drawn from the APEX and JETS APEX2 data sets when averaged for all powers and engines studied.

- Number-based emission indices exhibit a minimum at low to mid power, range from 0.5 to $28 \times 10^{15}/\text{kg}_{\text{fuel}}$, and increase by as much as an order of magnitude with plume processing.
- Mass-based emission indices tend to increase with power and range from 0.002 to 0.08 $\text{g}/\text{kg}_{\text{fuel}}$, bound the fleet average estimated for the mid 1990s fleet (Döpelheuer, 1997), and are at the low end of emission index range reported for individual engines using estimated size distributions (Penner et al., 1999).
- Engine to engine variability is difficult to estimate when the engine sample size is small. The value of accurately estimating these parameters warrants further study. The experimental approach developed through the APEX series of studies provides the blueprint for future studies.

ACKNOWLEDGEMENTS

The authors would like to acknowledge the sponsorship of California Air Resources Board, National Aeronautics and Space Administration, Federal Aviation Administration and the UMR Center of Excellence for Aerospace Particulate Emission Reduction Research throughout the work described in this paper.

REFERENCES

- Döpelheuer, A. (1997). "Berechnung der Produkte unvollständiger Verbrennung aus Luftfahrttriebwerken. IB-325-09-97, Deutsche Zentrum für Luft- und Raumfahrt, Cologne, Germany, 38 pp.
- ICAO, International Civil Aviation Organization *Aircraft Engine Emissions DataBank*. (2006)
- Lobo, P., Hagen, D.E., and Whitefield, P.D. (2006). Physical characterization of aerosol emissions from a Commercial Gas Turbine Engine – Project APEX. submitted to the Journal of Propulsion and Power.
- Penner, J. E., Lister, D. H., Griggs, D. J., Dokken, D. J., and McFarland, M. (eds.), *Aviation and the Global Atmosphere*, IPCC Report, Cambridge University Press, Cambridge, UK, 1999, p. 373
- Schmid, O., Hagen, D., Whitefield, P., Trueblood, M., Rutter, A., and Lilenfeld, H. (2004). "Methodology for particle characterization in the exhaust flow of gas turbine engines", *Aerosol Sci. & Technol.* 38:1108-1122.
- Wey, C.C., Anderson, B.E., Hudgins, C., Wey, C., Li-Jones, X., Winstead, E., Thornhill, L.K., Lobo, P., Hagen, D., Whitefield, P., Yelvington, P. E., Herndon, S.C., Onasch, T.B., Miake-Lye, R.C., Wormhoudt, J., Knighton, W.B., Howard, R., Bryant, D., Corporan, E., Moses, C., Holve, D., and Dodds, W. (2006) "Aircraft Particle Emissions eXperiment (APEX)" NASA TM-2006-214382

Aircraft Emissions Characterization

S.C. Herndon, T.B. Onasch, J.T. Jayne, E.C. Wood, P.E. Yelvington*, J. Wormhoudt, M.J. Northway, P. Mortimer, D.R. Worsnop, M.S. Zahniser, D.D. Nelson, J.H. Shorter, J.B. McManus and R.C. Miake-Lye

Aerodyne Research, Inc., MA 01821 USA

W. Berk Knighton

Department of Chemistry, Montana State University, USA

L.C. Marr

Virginia Tech, Blacksburg, VA USA

B.E. Anderson, C.-L. Wey

NASA, Langley and Glenn Research Centers (respectively) USA

P.D. Whitefield

University of Missouri, Rolla,

Keywords: Aircraft engine, NO_x, CO, formaldehyde, particles, gaseous, hydrocarbon, emissions

ABSTRACT: Recent engine exhaust measurements have been performed to better characterize the gaseous and particle emissions from aircraft engines as a function of engine power and distance downstream in the exhaust plume. Speciation of NO_x and hydrocarbon emissions, and their dependence on engine power, have been quantified for engines that are used extensively in the commercial fleet. In addition to these gaseous species, non-volatile and volatile contributions to aerosol emissions have also been quantified, identifying sulfate and organic contributions to the volatile condensed mass at downstream plume locations. Sulfate mass emission indices (g/kg fuel), due to sulfur contained in the fuel, do not have a strong dependence on engine power, while organic mass emission indices are highest at low powers. Non-volatile particle mass emission indices increase strongly from low to high powers.

1 INTRODUCTION

The quantification of the emissions from an aircraft gas turbine engine is complicated by the high temperature and high velocity of the exhaust as it leaves the engine. In addition, many species of interest are present in low concentrations and detailed information is sought about the small particles emitted. Several recent studies (Whitefield et al., 2002; Anderson et al., 2005; Herndon et al., 2004, 2005, 2006, C.C. Wey et al., 2006, ARB, 2006) have been directed at tackling these challenging measurement problems in order to have better understanding of the emissions from aircraft engines and how they evolve immediately downstream of the engine so that better assessments of the environmental impacts can be performed.

A poster was prepared for the TAC meeting, which presented a wide range of measurement results from aircraft emissions measurements, spanning the range from

- At the exit of a combustor - as used in an aircraft engine but measured in a test rig that simulates the engine conditions,
- In the plume of an aircraft engine – with the engine mounted in a test facility or on a stationary aircraft, and sampled at the engine exit or various downstream locations (see Figure 1)
- From advected downwind plume – beside active runways, using fast time response instruments on a non-interference basis at commercial airports.

* *Corresponding author:* Paul Yelvington, Aerodyne Research Inc., 45 Manning Road, Billerica, Massachusetts, USA. Email: paul@aerodyne.com. This material does not necessarily represent the views or recommendations of the U.S. DOT and its agencies.

The data presented included both gaseous emissions data and measurements of particle emission parameters, focusing on data obtained in those studies by Aerodyne Research, Inc. Gas phase emissions measurements of NO, NO₂, HONO, CO, and a variety of hydrocarbons were obtained using chemiluminescence, Tunable Infrared Laser Differential Absorption Spectroscopy (TILDAS), and Proton Transfer Reaction Mass Spectroscopy (PTR-MS). Particle measurements that were presented focused on those measured using Multi-Angle Absorption Photometry (MAAP), and Aerosol Mass Spectroscopy (AMS).



Figure 1. The APEX experiment measured emissions from a CFM56-2C1 engine mounted on the NASA DC-8 airplane. Measurements were performed using specially prepared sample probes and mounding rakes at 1, 10, and 30 m nominal distances downstream of the engine.

The breadth of data presented in the TAC poster is too extensive to include in this brief conference proceedings, but much of that data is available in the referenced papers and reports. An example of the particulate emissions data from APEX is presented in Figure 2, in which particle composition data is presented as a function of engine operating power. The mass associated with the emitted black carbon (soot) is the most notable feature (in black), which increased dramatically at high engine powers. The volatile contributions from sulfate (sulfuric acid) and organics vary much less with power, although the both increase when fuel sulfur content is increased (right panel). Notably, at low powers when the black carbon contribution decreases, the volatile components of the emitted particles become more significant. These volatile contributions are compared in the figure with masses inferred from particle size distributions measured with an SMPS, but note that the SMPS measures particles to a smaller size than the AMS (sulfate and organic). Thus the volatile volume from the SMPS (lines with symbols) is greater than the sum of sulfate and organic from the AMS, due to many small volatile particles less than the AMS ~ 30 nm cutoff.

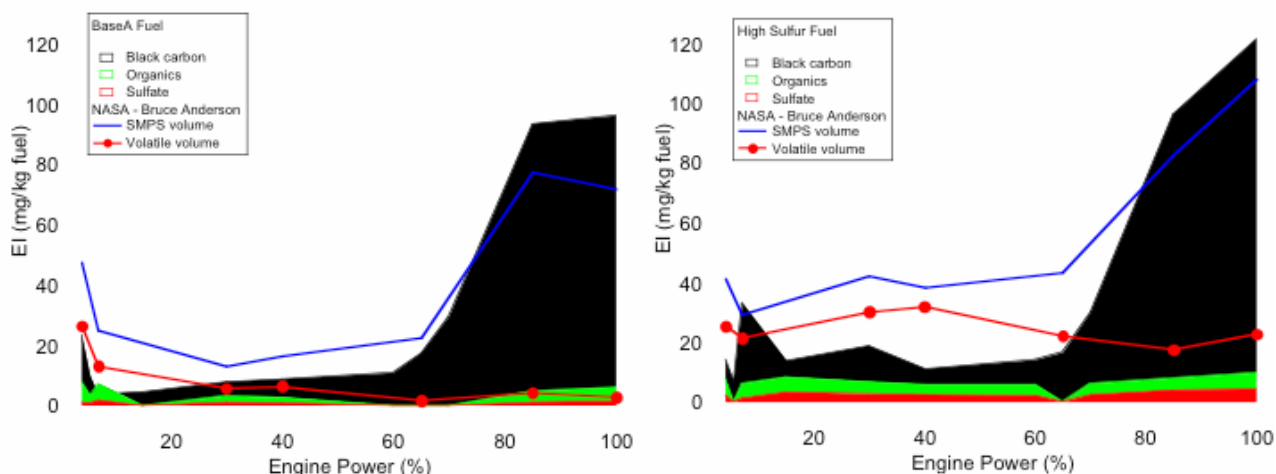


Figure 2. The composition of emitted particles is plotted versus engine power for the APEX engine measurements. The shaded-in contributions represent black carbon (upper most, black contribution), organic (middle), and sulfate (bottom).

A variety of hydrocarbons measured using a combination of TILDAS and PTR-MS are presented in Figure 3. Also in that figure, for comparison, are measurements of the total unburned hydrocarbons measured using a flame ionization detector (FID). The general agreement between the sum of the individual species and the FID is reasonably good on a ppm carbon/ppm CO₂ basis. The individual hydrocarbon measurements provide the additional insight as to which important hydrocarbons are present, from an environmental hazard perspective, and also how the hydrocarbon composition in the gas phase varies with engine power. At least for the lower engine powers, where hydrocarbon emissions are most pronounced, the most numerous individual hydrocarbons all decrease in proportion to each other and to the most prevalent hydrocarbon emissions measured: formaldehyde (by concentration) and ethylene (by mass).

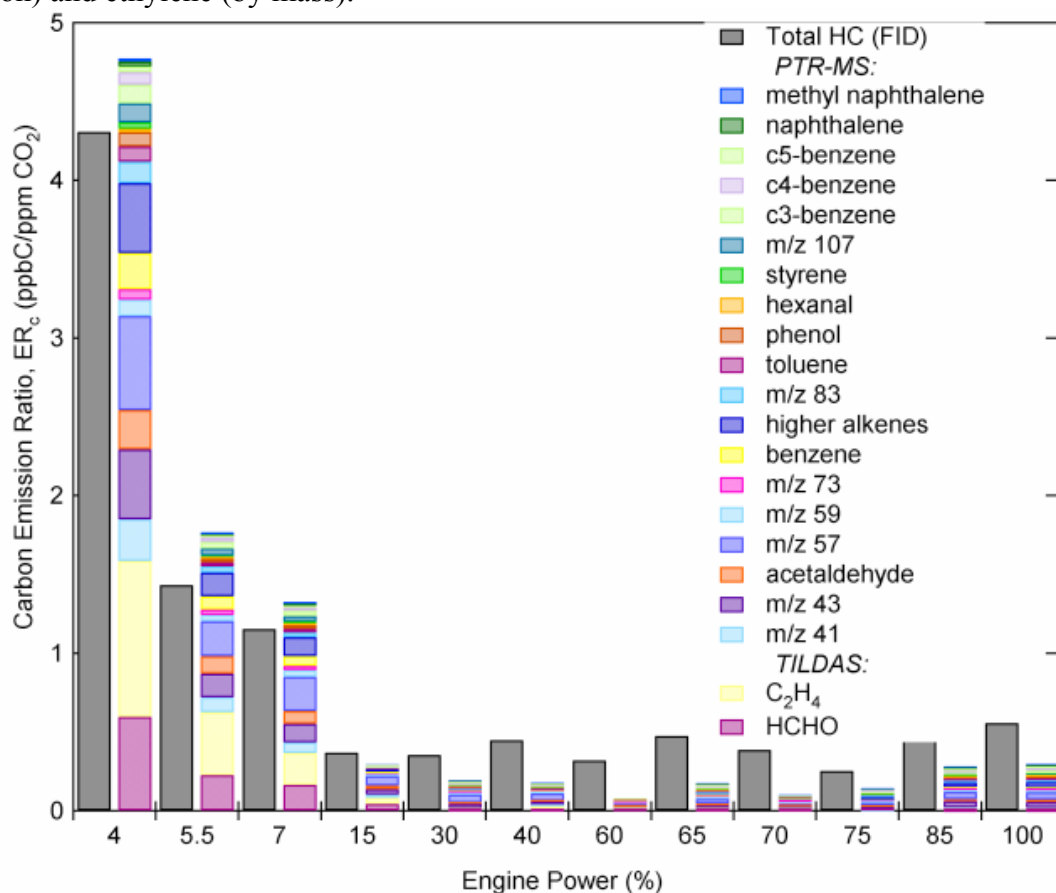


Figure 3. Hydrocarbon emissions as plotted versus engine operating power. Measurements of individual species are summed based on their carbon content (ppm C atoms) and compared to FID measurements of the total UHCs, also on a ppmC basis.

2 CONCLUDING REMARKS

Significant data has been accumulated from recent studies in characterizing aircraft emissions of particles and gases. While only a few examples of such data are presented here, the capability of measuring a wide variety of gaseous and particle parameters over a range of engine operating conditions will allow the emissions performance of aircraft engines to be quantified in great detail. This, in turn, will provide inputs to better understanding of how these emissions may impact the environment, and will permit a better evaluation of whether and to what degree any of these emissions may have important consequences for human health for populations in the proximity of airport operations.

ACKNOWLEDGMENTS

Sponsorship of NASA, CARB, FAA and the UMR Center of Excellence for Aerospace Particulate Emission Reduction Research is gratefully acknowledged. Support and interaction with the various mission team members, including airports, airlines and other research teams contributed greatly to the overall missions' successes.

REFERENCES

- Anderson, B.E., H.-S. Branham, C.H. Hudgins, J.V. Plant, J.O. Ballenthin, T.M. Miller A.A. Viggiano, D.R. Blake, H. Boudries, M. Canagaratna, R.C. Miake-Lye, T.B. Onasch, J. Wormhoudt, D.R. Worsnop, K.E. Brunke, S. Culler, P. Penko, T. Sanders, H.-S. Han, P. Lee, and D.Y.H. Pui, L.K. Thornhill, and E. Winstead, 2005: Experiment to Characterize Aircraft Volatile Aerosol and Trace-Species Emissions (EXCAVATE), NASA TM-2005-213783, NASA Langley Research Center, Hampton VA, USA, 175 pp.
- ARB, 2006 The Development of Exhaust Speciation Profiles for Commercial Jet Engines, Final report in press.
- Herndon, S.C., J.H. Shorter, M.S. Zahniser, D.D. Nelson, J.T. Jayne, R.C. Brown, R.C. Miake-Lye, I.A. Waitz, P. Silva, T. Lanni, K.L. Demerjian, and C.E. Kolb, 2004: NO and NO₂ emission ratios measured from in-use commercial aircraft during taxi and takeoff, *Environ. Sci. Technol.* 38, 6078-6084.
- Herndon, S.C., T.B. Onasch, B.P. Frank, L.C. Marr, J.T. Jayne, M.R. Canagaratna, J. Grygas, T. Lanni, B.E. Anderson, D.R. Worsnop, and R.C. Miake-Lye, 2005: Particulate emissions from in-use commercial aircraft, *Aerosol. Sci. Technol.* 39, 799-809.
- Herndon, S.C., T. Rogers, E.J. Dunlea, J.T. Jayne, R.C. Miake-Lye, and B. Knighton, 2006: Hydrocarbon emissions from in-use commercial aircraft during airport operation, *Environ. Sci. Technol.* 40, 4406-4413.
- Wey, C.C., B.E. Anderson, C. Hudgins, C. Wey, X. Li-Jones, E. Winstead, L.K. Thornhill, P. Lobo, D. Hagen, P. Whitefield, P. E. Yelvington, S.C. Herndon, T.B. Onasch, R.C. Miake-Lye, J. Wormhoudt, W.B. Knighton, R. Howard, D. Bryant, E. Corporan, C. Moses, D. Holve, and W. Dodds, 2006: Aircraft Particle Emissions eXperiment (APEX), NASA TM-2006-214382 and ARL-TR-3903, NASA Glenn Research Center, Cleveland OH, USA, 514 pp.
- Whitefield, P.D., D. Hagen, J. Wormhoudt, R.C. Miake-Lye, C. Wilson, K. Brundish, I.A. Waitz, S. Lu-kachko, and C.K. Yam, 2002: NASA/QinetiQ Collaborative Program – Final Report, NASA TM-2002-211900 and ARL-CR-0508, NASA, Washington, DC, USA, 193 pp.

New Aviation Scenarios for 2050

B. Owen*, D. S. Lee, L. Lim

Dalton Research Institute, Department of Environmental and Geographical Sciences, Manchester Metropolitan University, United Kingdom

Keywords: aviation, emission scenarios, simple climate model

ABSTRACT: New emission scenarios for aviation are provided to 2050. The emission scenarios have been developed using the SRES growth assumptions and provide an update to the emission scenarios in the IPCC Special Report *Aviation and the Global Atmosphere*. The emission scenarios are input to a simple climate model to provide radiative forcing and temperature response estimates.

1 INTRODUCTION

This study has used a global model of aircraft movements and emissions (FAST) to calculate new future emissions for the time period 2000 to 2050. The SRES GDP projections are used in this study (IPCC, 2000) and the results represent an update on aviation emissions scenarios of CO₂ to 2050 made in a consistent manner with those from the IPCC's Special Report *Aviation and the Global Atmosphere*, (IPCC, 1999) which uses the older IPCC IS92 GDP projections. The FAST model (Lee *et al.*, 2005) has been used as the principal tool in this study. FAST has been used to calculate a global total of fuel, CO₂ and NO_x emissions for aviation emissions for the baseline and future scenarios to 2050. The results are global spatially resolved, 3 D global emissions inventories (1° by 1° grid with 610 m vertical resolution). The aviation emissions for the SRES A1 and B1 marker scenarios have been used as input to a linear climate response model LinClim (Lim *et al.*, 2006) to produce the associated radiative forcing and temperature response values.

2 THE FAST MODEL

The FAST model works by combining a global aircraft movements database with data on fuel flow provided by a separate commercial model PIANO, which is an aircraft performance model (Simos, 2004). These data with knowledge on aircraft and engine types, allow calculation of emissions via a recognized and validated algorithm that corrects ICAO LTO Certification Data for altitude. Baseline calculations have used the year 2000 and these calculations have been undertaken using the OAG global aircraft movement database. Future fleet predictions are made using the FAST model. The model requires the characteristics of hypothetical future generic aircraft to be defined. The FAST methodology imposes the restriction that any hypothetical aircraft must be based on a configuration that can be generated using the PIANO aircraft performance program. Whilst this approach ensures that the resulting aircraft characteristics remain within the realm of reality, for a future scenario one might wish to project these characteristics beyond the limits set by PIANO. For this reason, a scaling factor can be applied to fuel consumption. This factor is applied uniformly (*i.e.* to all phases of the flight cycle).

Future aircraft movements have been calculated using the ICAO (CAEP) forecasts (Wickrama *et al.*, 2003) in conjunction with the IPCC SRES GDP growth assumptions. The ICAO traffic forecasts to 2020 of revenue passenger kilometers (RPK) and seat kilometres offered (SKO) have been used directly. The ICAO SKO forecasts are provided regionally and according to the seat-banding of the aircraft. The forecast totals are summarized in Table 1.

* *Corresponding author:* Bethan Owen, Dalton Research Institute, Department of Environmental and Geographical Sciences, Manchester Metropolitan University, Manchester M1 5GD, United Kingdom. Email: b.owen@mmu.ac.uk

Table 1. ICAO Long Term Global Forecasts (FESG/CAEP6, 2003)

	2005	2010	2015	2020
Seat kilometers offered (SKO) in billions	4685	5998	7542	9365
Revenue passenger kilometers (RPK) in billions	3304	4312	5508	7050

In order to provide future fleet predictions, the carrying capacity of freight also needs to be considered. The ICAO forecast in Table 1 does not include freight and relates to passenger traffic only. The OAG movements data used for the base case do include freight movements but they are not identified explicitly. A simple methodology was devised to include freight. A comparison of time series of RPK from 1970 to 1995 used by the IPCC (1999) was compared with the ICAO RPK (passenger movements only) for the same period. A linear relationship was apparent between the two data sets and a factor of 1.16 was derived that was taken to represent the freighter movements (in terms of RPK) in the IPCC data. This factor when applied to the ICAO 2000 data also brought the ICAO RPK up to the OAG 2000 RPK value (used as the base case in this study). The factor was applied to all scenarios and years which is clearly a simplistic approach bearing in mind that the passenger and freight growth can be very different.

For dates after 2020, an alternative approach is used, similar to the IPCC (1999) methodology, whereby a global relationship between RPK and GDP is used according to a non-linear regression model and predicting SKO from SRES A1 and B2 GDP data. A logistics growth curve was derived using published ICAO traffic statistics and UN GDP statistics from 1970 to 2000.

The model was used to extrapolate future global RPK values from 2020 to 2050 using the SRES GDP global growth scenarios A1 and B2. The SRES scenarios A1 and B2 were chosen as the main ones for calculation of emissions as IPCC is currently using these as “baselines” against which mitigation possibilities are being considered by its Working Group 3. Selection of other SRES scenarios would give different results. A wider range is explored in terms of RPK projections (including A2 and B1) but the step from RPK to emissions involves much computation and hence the two main scenarios focused upon A1 and B2 in terms of their GDP projections.

Table 2. Annual average percentage growth factors for global GDP growth forecasts (IPCC, 2000)

Scenario	2020–2030	2030–2040	2040–2050
SRES A1B-AIM	4.66	3.52	3.71
SRES A2	2.36	3.52	1.21
SRES B1	3.35	3.26	3.02
SRES B2	2.67	2.62	2.50
IS92a	2.3	2.3	2.3
IS92c	1.2	1.2	1.2
IS92e	3.0	3.0	3.0

The SRES GDP data are provided at 10 yearly intervals as shown in Table 2 and these data were applied for the 2020-2050 period to provide global projections of RPK (Table 3). The SRES A1B scenario produces the highest GDP growth over this period, higher than the IS92e (high growth scenario) leading to higher predictions of RPK. The A2 and B2 scenarios produce similar RPK projections to the IS92Fa (medium growth) scenario in 2050. None of the selected SRES scenarios resulted in projections as low as the IS92Fc (low growth) scenario.

Table 3. RPK projections for SRES and IS92 a, c and e GDP growth forecasts (in billions)

Year	A1B	A2	B1	B2	IS92a	IS92e	IS92c
2020	7042	7042	7042	7042	6553	8302	5071
2050	24407	16896	21632	18100	13934	21978	7817

Table 4. Traffic efficiency (as SKO/kg of fuel) improvement in percent per year

Time Period	Improvement (percent per year)
2000-2010	1.3
2010-2020	1.0
2020-2050	0.5

Future trends in traffic efficiency improvements from the IPCC report (IPCC, 1999) are shown in Table 4. These “efficiencies” include improvements arising from the introduction of new aircraft into the fleet and changes to operating conditions and passenger management i.e. not simply a change in engines but the overall operational efficiency of the engine/airframe/passenger management. The FAST model requires a fuel factor input that can be changes to account for future improvements in the fuel efficiency of the aircraft. This is different to the overall traffic efficiency described above, as this relates only to the technological improvements and not changes in fleet or passenger management. For the purposes of this study it was necessary to prescribe a fuel factor based on technological improvements independent of the operation of the fleet. The factors shown in Table 5 below together with the forecast changes in aircraft size etc from the CAEP forecasts produce the improvements in traffic efficiency commensurate with those improvements given in Table 4.

Table 5. Fuel factor assumptions applied to future periods

Period	Fuel factor
2005	1
2020	0.84
2030	0.80
2040	0.76
2050	0.72

3 EMISSION SCENARIO RESULTS

The results of the FAST emission scenarios are shown in Figure 1. The FAST-A1 2050 results lie just above the IPCC (1998) Fe1 (high) scenario, whilst FAST-B2 is greater than the mid-range Fa1 scenario. For 2040 and 2050 the updated SRES A1B traffic projections and hence emissions are larger than those derived from the IS92 GDP assumptions. The SRES GDP growth rates are similar to the IS92 values however, application of the ten year average growth rates generally exceed the equivalent but longer term IS92 growth rates producing higher traffic and ultimately higher emission estimates. The FAST-A1 emission estimates are in the order of five times greater than the 2000 emissions and the FAST-B2 estimates are approximately 3 times greater than the 2000 emissions. The CONSAVE (2005) scenarios ‘ULS’ (Unlimited Skies) is consistent with SRES A1 and has slightly higher values than the FAST-A1 estimates.

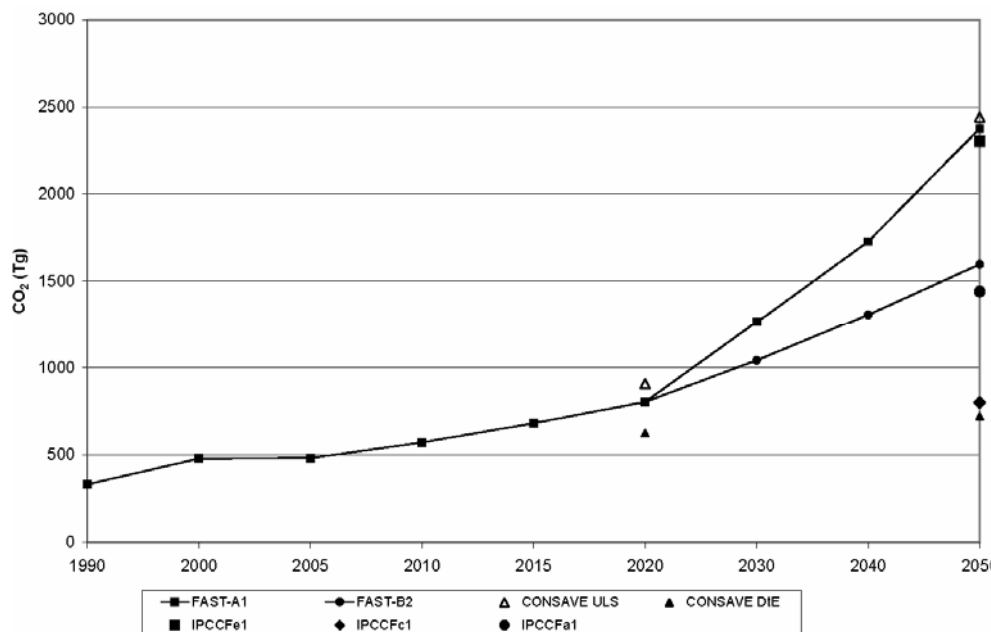


Figure 1. Comparison of global aviation CO₂ emissions (Tg yr⁻¹), 1990 to 2050 using FAST and showing other estimates for 2020 and 2050.

4 THE LINCLIM MODEL

The resultant emission scenarios were scaled by appropriate scaling factors to account for systematic underestimation of fuel due to great circle routing, military aviation and non-scheduled traffic, as in the IPCC (1999) work. The emissions have then been applied to the LinClim model which is a linear climate response model formulated to calculate radiative forcing (RF) and temperature response (Lim et al., 2006). Aviation emissions post-2050 are assumed to grow at a rate of 1% per annum to 2100 (Sausen and Schumann, 2000). Background CO₂ concentrations corresponding to each SRES scenario have been used for CO₂ RF and temperature response calculations and the RF for other perturbations were scaled to reference year 2000 values published by Sausen et al., 2005. The temperature response uses climate sensitivity parameter of 0.64 K/Wm⁻² and the efficacies published by Ponater et al., 2006: i.e. CO₂, SO₄, and BC 1; O₃ 1.37; CH₄ 1.18; H₂O 1.14 and contrails 0.59.

5 RESULTS

The estimated RF values associated with the emission scenarios are shown in Figure 2 together with the RF values associated with the IPCC (1999) Fa1, Fc1 and Fe1 emission scenarios (Sausen and Schumann, 2000). The temperature response values associated with the emission scenarios are shown in Figure 3.

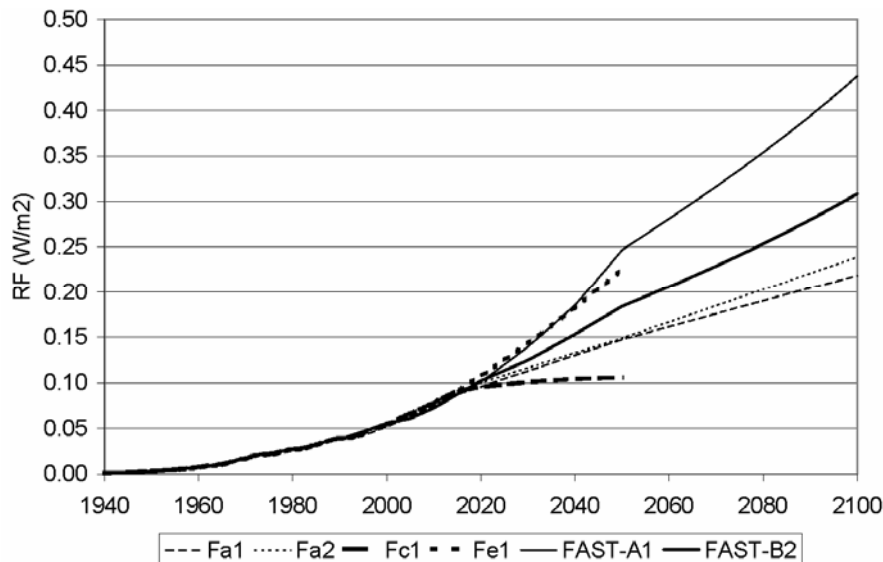


Figure 2. RF values for emission scenarios produced using LinClim.

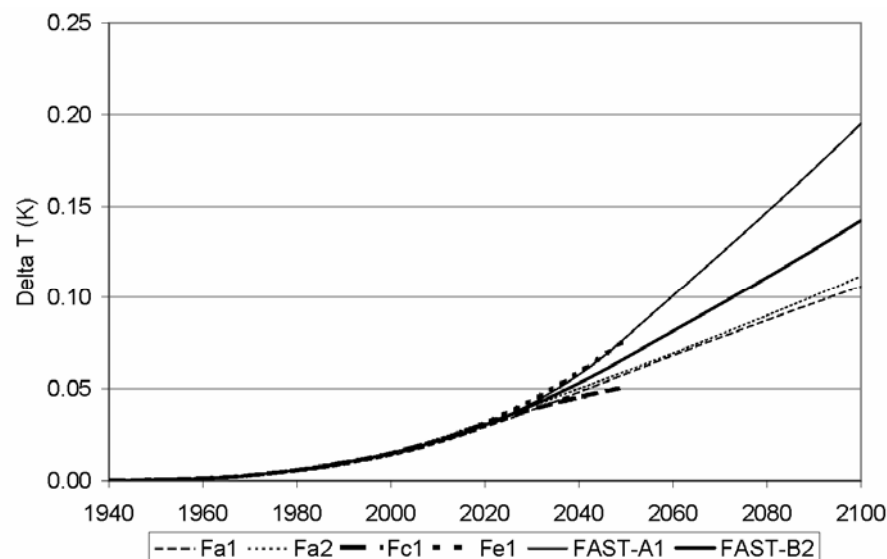


Figure 3. Temperature response values for emission scenarios produced using LinClim.

6 CONCLUSIONS AND FUTURE WORK

The 2050 FAST-A1 and FAST-B2 scenarios provided here show an initial update of the FESG work incorporating the SRES GDP growth assumptions. The CO₂ RF values associated with the A1 SRES marker and IPCC Fe1 emission scenarios in 2050 are 0.247 Wm⁻² and 0.225 Wm⁻² respectively. The corresponding temperature response in 2050 is calculated as 0.0795 K for the FAST-A1 emission scenario and 0.0772 K for the IPCC Fe1 scenario. In 2100, the temperature response values associated with the FAST-A1 and FAST-B2 aviation scenarios are calculated to be 0.1953 K and 0.1425 K respectively.

The next step in this work will be to review the technology assumptions with regard to fuel use and NO_x emission indices in the light of the most recent research and the industry technology targets. Further development of the traffic growth at a regional level consistent with the SRES A1 and B2 storylines is also underway.

REFERENCES

- CONSAVE (2005) Final Technical Report Berghof R., A. Schmitt C. Eyers, K. Haag, J. Middel, M. Hepting, A. Grübler, R. Hancox G4MA-CT-2002-04013 July 2005
- IPCC (1999) Aircraft emissions: current inventories and future scenarios. Chapter 9 of *Aviation and the Global Atmosphere* J.E. Penner, D.H. Lister, D.J. Griggs, D.J. Dokken and M. McFarland (Eds) Special Report of the Intergovernmental Panel on Climate Change, Cambridge University Press, Cambridge.
- IPCC (2000) Emission Scenarios: A Special Report of Working Group3 of the Intergovernmental Panel on Climate Change, Cambridge University Press, Cambridge.
- Lee, D.S., B. Owen, C. Fichter, L. Lim and D. Dimitriu (2005): Allocation of International aviation emissions from scheduled air traffic – present day and historical (report 2 of 3). Manchester Metropolitan University, Centre for Air Transport and the Environment, CATE-2005-3[c]-2, Manchester, UK.
- Lim, L.L., D.S. Lee, R. Sausen and M. Ponater, 2007: Quantifying the effects of aviation on radiative forcing and temperature with a climate response model. This volume.
- Ponater, M., S. Pechtl, R. Sausen, U. Schumann and G. Hüttig, 2006: Potential of the cryoplane technology to reduce aircraft climate impact: A state-of-the-art assessment. *Atmos. Environ* 40, 6928–6944.
- Sausen, R. and U. Schumann, 2000: Estimates of the climate response to aircraft CO₂ and NO_x emissions scenarios. *Clim. Change* 44, 27–58.
- Sausen, R., I. Isaksen, V. Grewe, D. Hauglustaine, D.S. Lee, G. Myhre, M.O. Köhler, G. Pitari, U. Schumann, F. Stordal and C. Zerefos, 2005: Aviation radiative forcing in 2000: and update on IPCC (1999). *Meteorol. Zeit.* 114, 555–561.
- Simos D., 2004: PIANO: PIANO users guide version 4.0, Lissys Limited, UK (www.piano.aero).

SPIDER model process studies of aircraft plume dilution using simplified chemistry

N. Dotzek*, R. Sausen

DLR-Institut für Physik der Atmosphäre Oberpfaffenhofen, Germany

Keywords: Aircraft emissions, plume dilution, simplified chemistry, effective emission indices.

ABSTRACT: The box model SPIDER was developed to test and compare various approaches to include the effect of aircraft plume processes (effective emissions indices) in large scale chemistry transport models and climate-chemistry models. Its simplified NO_x-O₃ chemistry parameterises only the most relevant non-linear processes. SPIDER reproduces the main features of more sophisticated plume models. Multi-plume interactions illustrate the capability of the SPIDER model.

1 MOTIVATION

Emissions from aircraft impact on global climate (cf. Brasseur et al., 1998; IPCC, 1999; Sausen et al., 2005). They are usually implemented in General Circulation Models (CGM) or Chemistry Transport Models (CTM) by an instantaneous dispersion of the emitted matter over the large-scale grid boxes. Following Petry et al. (1998), this is called the instantaneous dispersion (ID) approach. The ID approach neglects non-linear chemical conversion processes in the evolving single plume. To resolve these by a plume model is called the single plume, or SP approach. However, detailed SP chemical modelling is computationally too demanding, both for more complex principle studies of plume-plume interaction in a grid box, and for operational implementation in large-scale models.

For improvement of the ID approach in GCMs, Effective Emission Indices (EEIs) can be used (e.g., Möllhoff, 1996; Petry et al., 1998). These, and several other approaches to the problem, e.g., by Meijer et al. (1997), Karol et al. (1997, 2000), Kraabøl et al. (2000) and Kraabøl and Stordal (2000) all applied detailed chemistry schemes, while a simplified model to test and compare the various EEI concepts, and to perform studies of multi-plume interactions remains desirable.

The present paper reports on the development of such a box model with simplified chemistry, the SPIDER (SP-ID Emission Relations) model. The following sections focus on setup of the model, validation and first application to a plume-plume interaction. Further model development and applications will be described in a forthcoming paper.

Motivated by the work by Petry et al. (1998) who applied a detailed chemistry scheme, we aim at computing plume dilution, and comparing of ID and SP results using a computationally efficient box model with greatly simplified chemistry. The resulting SPIDER model avoids explicit solution of the chemical rate equations. Chemistry enters the equations only in parameterized form by "dynamic forcing" terms, and the only species considered are NO_x and O₃.

The objectives are to apply the validated SPIDER model to more complex cases, e.g. multiple plumes or the interaction between neighbouring GCM grid cell NO_x or O₃ fields, and to eventually evaluate different EEI approaches.

1.1 SPIDER model setup

The main process to be covered by the model is the non-linear production of ozone by aircraft NO_x emissions at cruise altitude. Hence, the first simplification in the SPIDER system of equations is to include only these two species: NO_x and O₃.

The physical processes which are to be explicitly included in and resolved by the model within a typical GCM grid box volume are a) the emission of NO_x inside the GCM box, S_{NO_x} , b) non-linear production of ozone, P_{O_3} , and c) the decay of the NO_x and O₃ fields by conversion to reservoir spe-

* *Corresponding author:* Nikolai Dotzek, DLR-Institut für Physik der Atmosphäre, Oberpfaffenhofen, D-82234 Weßling, Germany. Email: nikolai.dotzek@dlr.de

cies. For treatment of the SP approach, additionally the background (outer domain, superscript o) and plume fields (inner domain, superscript i) have to be integrated separately, and the entrainment of background matter by turbulent mixing at the growing-plume boundary enters as another individual term in the budget equations.

1.1.1 ID budget equations

In Eqs. (1-4), the following units hold $[NO_x] = \text{mol}$, $[O_3] = \text{mol}$, $[no_x] = \text{nmol mol}^{-1}$, following the well-known convention to denote extensive quantities by upper-case, and intensive quantities by lower-case letters:

$$d_t NO_x = S_{NO_x} \delta(t-t') - \frac{1}{\tau_{NO_x}} NO_x \quad , \quad (1)$$

$$d_t O_3 = P_{O_3}(no_x) - \frac{1}{\tau_{O_3}} O_3 \quad . \quad (2)$$

The reference background state without aircraft emissions follows for $S \equiv 0$, and d_t denotes the temporal derivative d/dt .

The decay, or conversion of NO_x and O_3 to reservoir species, is modeled as an exponential decay with fixed half-time periods τ ($\tau_{NO_x} = 10$ days, $\tau_{O_3} = 30$ days, cf. Köhler and Sausen, 1994). Future versions of SPIDER will include a typical diurnal variation of these time scales, but this is a second-order effect, and neglecting the diurnal cycle here has little consequence on the results.

1.1.2 SP budget equations

In Eqs. (3) and (4), each species must be treated with one budget equation for the plume (superscript i) and the background (superscript o). As the box model reference volume is one GCM grid box, the computation of entrainment, with a linear plume growth rate, in Eqs. (3-4) is terminated as soon as the plume volume V^i is equal to the reference volume V_{GCM} .

$$d_t NO_x^i = S_{NO_x} \delta(t-t') + NO_x^o / V^o d_t V^i - \frac{1}{\tau_{NO_x}} NO_x^i \quad , \quad (3a)$$

$$d_t NO_x^o = - NO_x^o / V^o d_t V^i - \frac{1}{\tau_{NO_x}} NO_x^o \quad , \quad (3b)$$

$$d_t O_3^i = P_{O_3}(no_x^i) + O_3^o / V^o d_t V^i - \frac{1}{\tau_{O_3}} O_3^i \quad , \quad (4a)$$

$$d_t O_3^o = P_{O_3}(no_x^o) - O_3^o / V^o d_t V^i - \frac{1}{\tau_{O_3}} O_3^o \quad . \quad (4b)$$

Eq. (3a) allows including the case in which a fresh aircraft plume is emitted along the axis of an aged plume emitted by another aircraft earlier on. This case was already investigated by Kraabøl and Stordal (2000), and will also be treated here in Sec. 3.2

1.2 Parameterisation of $P_{O_3}(no_x)$ terms

The non-linear production of ozone as a function of the ambient NO_x concentrations remains to be specified for the SPIDER model equations (2) and (4). As treated in detail by, e.g., Johnson and Rohrer (1995), Brasseur et al. (1996), Groß et al. (1998), and Meilinger et al. (2001), the production of ozone does not only depend on NO_x concentrations, but is a highly variable function of other species like O_3 itself, H_2O , CO , hydrocarbons, state variables p , and T , and the actinic flux J . A perfect parameterisation in this multidimensional phase space is impossible, and likely has prevented earlier studies using simplified chemistry studies of aircraft plume dilution.

However, in the present context, the objective is to develop a model which allows for principle studies of plume dilution, plume interaction, and methods to derive EEIs. Hence, a parameterisation of ozone production as a function of nitrogen oxides for some typical atmospheric conditions at cruise altitude following the data presented in the literature is possible. Aside from the NO_x concen-

tration, also the solar elevation angle must be taken into account, in order to capture the diurnal cycle of photochemical ozone production.

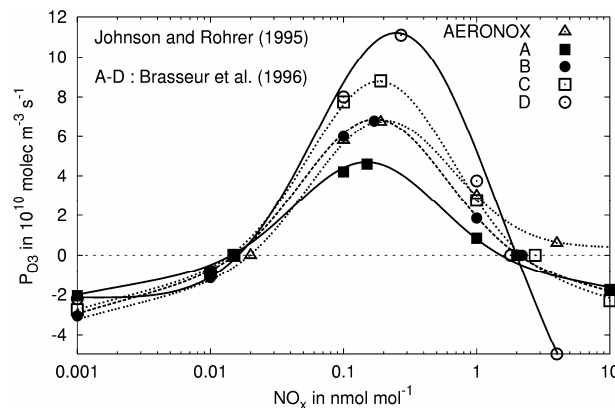


Figure 1. Net ozone production rate P_{O_3} as a function of ambient NO_x concentration. The symbols are data from Johnson and Rohrer (1995) from the AERONOX project, and from Brasseur et al. (1996). The curves are fits to these data and form the selectable SPIDER P_{O_3} parameterisations.

Figure 1 shows five different parameterisations of which D was selected in the SPIDER model. Curve D from the Brasseur et al. (1996) data includes effects of the diurnal cycle, the other curves are very similar in shape, and their variation comes mainly from different ambient chemical conditions.

Note the non-linearity, or rather non-monotonicity, of all P_{O_3} curves. Low and very high NO_x concentrations are characterized by ozone depletion, while the peak ozone production is found in the range of 0.15 to 0.27 $nmol\ mol^{-1}$. The fact that the shape of the curves is quite uniform in the upper troposphere gives us some confidence that the SPIDER parameterisation of P_{O_3} holds in a general sense and is adequate for principle process studies.

2 RESULTS

Here, we present the SPIDER model validation and its first application of multiple plume effects.

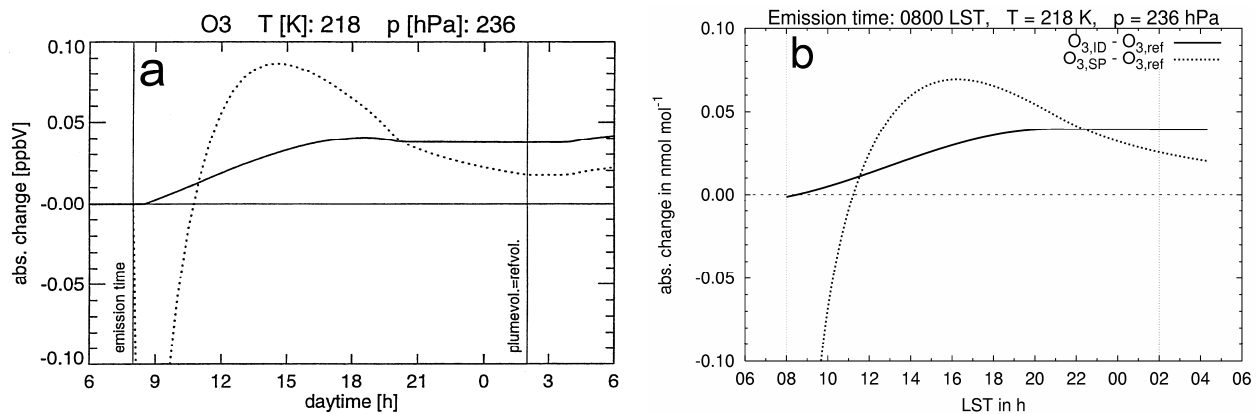


Figure 2. Absolute aircraft-induced change of O_3 concentration compared to the background state for ID (solid) and SP simulations (dotted). (a) is from Möllhoff (1996), (b) shows the corresponding SPIDER run.

2.1 SPIDER model validation and sensitivity

We used the original model cases from the work by Möllhoff (1996) to validate the SPIDER model. There, without wind shear or cross-plume wind components, the exhaust of a typical B747 airplane was emitted as a line-source at 0800 LST (local solar time) in a $V_{GCM} = 50 \times 50 \times 1\ km^3$ reference volume. Ambient conditions were mid-latitude summer, $T = 218\ K$ and $p = 236\ hPa$ (about 10 km above sea level, ASL). The initial values of NO_x and O_3 in the plume were chosen to be representative of the early dispersion regime (about 100 s after emission). Linear plume growth was specified such that after 18 h of plume dilution, the plume volume was equal to the reference volume V_{GCM} .

Figure 2b shows that the qualitative behaviour of the Möllhoff (1996) simulation in Figure 2a is captured well by the SPIDER model. The quantitative agreement is adequate; the main difference is that in the SP simulation, the peak change in O_3 is at a lower level and slightly later for the SPIDER run. For the ID run, the small peak before converging to the night time stable state is not resolved by SPIDER; instead, it merely converges towards the night time conditions.

The first few minutes after plume emission are characterised by ozone titration within the plume due to the very high NO_x concentrations (cf. Fig. 1, curve D). As the SPIDER model equations are formulated for the plume dispersion regime (the far-field solution), they cannot resolve the initial titration, which is a near-field plume process. Following Veenstra and Beck (1994), the initial ozone level in the plume must be lowered slightly compared to the background state to provide the proper initialisation values for the early dispersion regime¹.

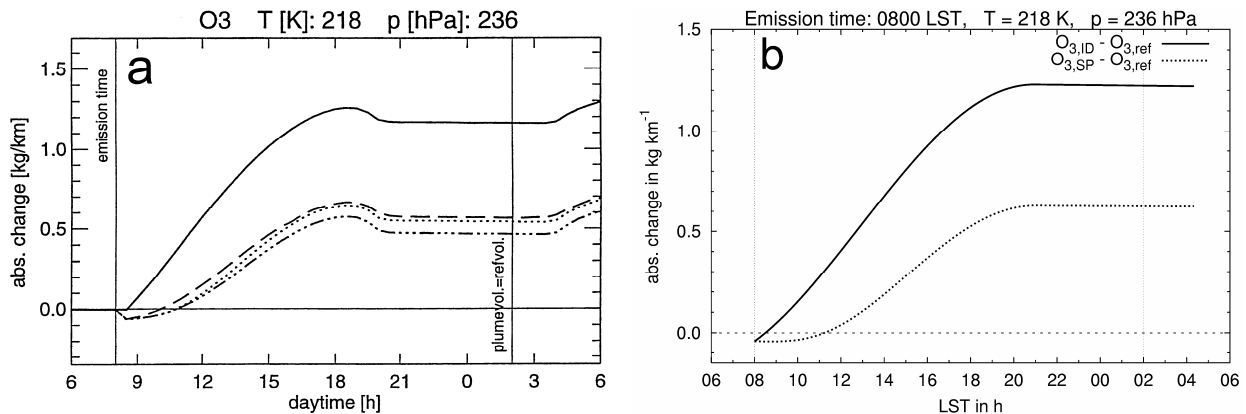


Figure 3. As Figure 2, but for the absolute change in O_3 mass per kilometre plume along the flight path. The dashed and dash-dotted lines in (a) from Möllhoff (1996) are not interpreted here.

Figure 3 shows the comparison between Möllhoff (1996) and the SPIDER results in terms of ozone mass difference per kilometre plume. Again, the small peak just before reaching the night time levels with zero photochemistry is not reproduced by SPIDER. Otherwise, the qualitative and quantitative agreement is good. Note that SPIDER correctly shows the extended period of negative change in ozone between 0800 and 1100 LST, and that the night time levels are well-captured.

2.2 Aircraft following on track of initial one

The first SPIDER model application case is a second, identical, aircraft exactly following the track of the first one after 4.5 h, injecting (and instantaneously distributing) a fresh plume into the aged, diluted one. For regions like the North Atlantic flight corridor, we consider this scenario to be quite realistic. Then, ID and SP simulations are continued and compared to the reference run. A similar case was investigated by Kraabøl and Stordal (2000), but for emission of the young plume 1 h after the first one (and additional runs for 2 h and 3 h release time lag).

Figure 4 shows the effects for the absolute change in ozone concentration (a) and mass per kilometre plume (b). The results should be compared to the reference case in Figs. 2b and 3b. The immediate effect of the young plume is visible in both panels by the initial drop in ozone due to titration. After recovery, the rate of ozone production is significantly enhanced, and higher night time levels of ozone result. For the ozone changes in Figure 4, the enhancement is about 50% for both the ID and SP runs, and for both the concentration and mass changes.

The response to the increase in aircraft NO_x is not linear here (in contrast to GCM simulations, cf. Grewe et al., 1999), as SPIDER experiences the full non-linearity of the P_{O_3} term due to the initially high NO_x concentrations. I.e., the ozone production is not doubled by injection of the second plume after 4.5 h. Yet what can be said is that the gap between the results of the ID and SP approaches widens by roughly 50% due to the interaction of the two plumes. Thus, conclusions derived from single plume comparisons between SP and ID results, like that of Petry et al. (1998) stat-

¹ For completeness, we note that SPIDER is capable of reproducing initial ozone titration when the ozone concentration in the plume is initialised to the reference value. However, this titration is much weaker than that of Fig. 2

ing that for diurnal or seasonal averages, the difference between SP and ID plume dilution is not significant, may not remain justified in regions with frequent interaction of plumes.

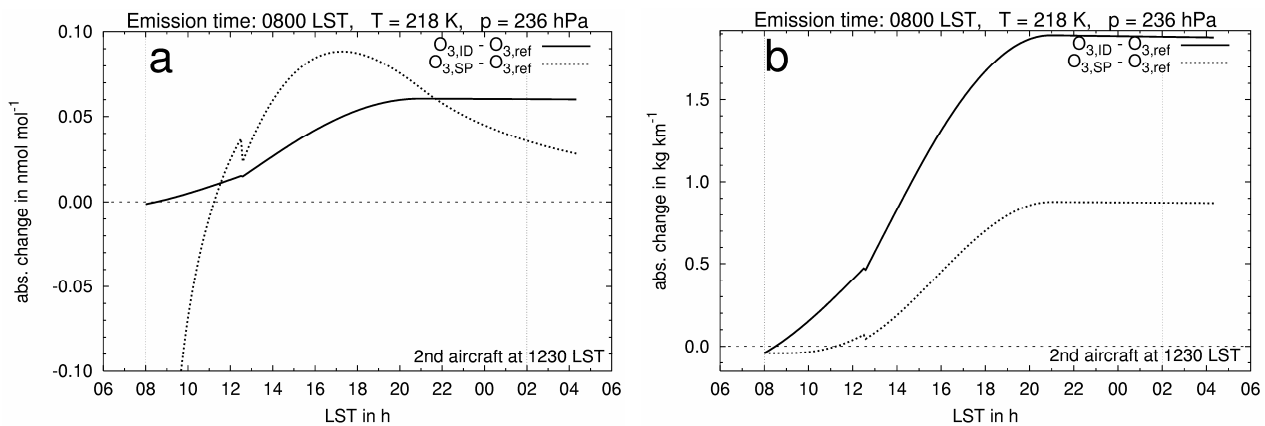


Figure 4. As Figs. 2b (a) and 3b (b), but with a second, identical aircraft plume emitted along the original flight path 4.5 h after emission of the first plume. Emission time 0800 LST is marked by the dotted line.

3 DISCUSSION

The SPIDER model could be validated in the framework of its simplifying assumptions. The basic plume dilution processes are well represented, in part even quantitatively. Some details are missing in the model which would require the complete set of chemical reactions – or an improved description of either the plume growth (being linear only on average, cf. Schumann et al., 1998) or the actinic flux in the P_{O_3} term. These latter points are current work in SPIDER development.

In our simulation of interaction of two coaxial plumes, a net increase in produced ozone was found, and the gap between SP and ID approaches widened. Kraabøl and Stordal (2000) did a similar study, but for emission of the young plume 1 h after the old one. They employed a full chemistry model, slightly different release time (0700 LST), and other initial values of plume and background NO_x and O_3 concentrations. In contrast to our findings, they reported a net decrease in ozone compared to the single-plume run, and less conversion of the emitted NO_x . Qualitatively similar results were reported for secondary plume release after time lags of 2 h and 3 h, respectively.

There may be several reasons for these differences to our SPIDER results. Kraabøl and Stordal (2000) emitted their second model plume in ambient conditions characterised by very high NO_x concentrations ($6.8 \text{ nmol mol}^{-1}$). Without further debate on the realism of these high NO_x values for 1 to 3 h old plumes, their young plume experienced conditions of strong ozone titration (cf. Fig. 1). In the SPIDER model run 4.5 h after emission of the first plume, the aged plume NO_x concentration is well below 2 nmol mol^{-1} , i.e., definitely in a region of the P_{O_3} term of Figure 1 with at least weak ozone production. Besides, Kraabøl and Stordal (2000) compared their plume concentrations with background conditions which changed with time on injection of the second plume. In the present SPIDER case, the background was not altered after introduction of the young plume, in order to be able to compare the results to the single-plume reference run.

4 CONCLUSIONS

Our study using the SPIDER box model showed:

- The model is well-suited for principle studies, and could be validated qualitatively and in part quantitatively using results by Möllhoff (1996) and Petry et al. (1998);
- The model reproduces the high sensitivity to plume and background NO_x and O_3 concentrations;
- Multi-plume interactions can alter the gap between of ID and SP plume dilution approaches.

Aside from more complex multi-plume and GCM grid box interactions, future work will encompass refinement of the computation of plume growth, actinic flux, and NO_x or O_3 decay times.

ACKNOWLEDGMENTS

We are grateful to Johannes Hendricks for further information on the Möllhoff (1996) simulations and for commenting on a draft of this paper. This work was partly funded by the European Commission in the FP6 integrated project QUANTIFY under contract no. 003893 (GOCE).

REFERENCES

- Brasseur, G. P., J.-F. Müller, and C. Granier, 1996: Atmospheric impact of NO_x emissions by subsonic aircraft: A three-dimensional model study. *J. Geophys. Res.*, 101 D, 1423-1428.
- Brasseur, G. P., R. A. Cox, D. Hauglustaine, I. Isaksen, J. Lelieveld, D. H. Lister, R. Sausen, U. Schumann, A. Wahner, and P. Wiesen, 1998: European scientific assessment of the atmospheric effects of aircraft emissions. *Atmos. Environ.*, 32(13), 2329-2418.
- Grewe, V., M. Dameris, R. Hein, I. Köhler, and R. Sausen, 1999: Impact of future subsonic aircraft NO_x emissions on the atmospheric composition. *Geophys. Res. Lett.* 26, 47-50.
- Groß, J.-U., C. Brühl, and T. Peter, 1998: Impact of aircraft emissions on tropospheric and stratospheric ozone. Part I: Chemistry and 2-D model results. *Atmos. Environ.*, 32(18), 3173-3184.
- IPCC, 1999: Aviation and the global atmosphere. – A special report of IPCC working groups I and III. (Perner, J. E., D. H. Lister, D. J. Griggs, D. J. Dokken, and M. McFarland (eds.)). Intergovernmental Panel on Climate Change. – Cambridge University Press, Cambridge, UK and New York, NY, USA, 365 pp.
- Johnson, C., and F. Rohrer, 1995: NO_x and O₃ chemistry in the upper troposphere and lower stratosphere. In: Schumann (1995), 325-335.
- Karol, I. L., Y. E. Ozolin, and E. V. Rozanov, 1997: Box and Gaussian plume models of the exhaust composition evolution of subsonic transport aircraft in- and out of the flight corridor. *Ann. Geophys.* 15, 88-96.
- Karol, I. L., Y. E. Ozolin, A. A. Kiselev, and E. V. Rozanov, 2000: Plume transformation index (PTI) of the subsonic aircraft exhausts and their dependence on the external conditions. *Geophys. Res. Lett.* 27(3), 373-376.
- Kraabøl, A. G., and F. Stordal, 2000: Modelling chemistry in aircraft plumes 2: The chemical conversion of NO_x to reservoir species under different conditions. *Atmos. Environ.* 34, 3951-3962.
- Kraabøl, A. G., P. Konopka, F. Stordal, and H. Schlager, 2000: Modelling chemistry in aircraft plumes 1: Comparison with observations and evaluation of a layered approach. *Atmos. Environ.* 34, 3939-3950.
- Köhler, I., and R. Sausen, 1994: On the global transport of nitrogen oxides from emissions of aircraft. In: Schumann and Wurzel (1994), 193-198.
- Meijer, E. W., P. F. J. van Velthoven, W. M. F. Wauben, J. P. Beck, and G. J. M. Velders, 1997: The effects of the conversion of nitrogen oxides in aircraft exhaust plumes in global models. *Geophys. Res. Lett.* 24(23), 3013-3016.
- Meilinger, S. K., B. Kärcher, R. von Kuhlmann, and T. Peter, 2001: On the impact of heterogeneous chemistry on ozone in the tropopause region. *Geophys. Res. Lett.* 28(3), 515-518.
- Möllhoff, M., 1996: Modellierung der chemischen Umwandlung reaktiver Flugzeugabgase im Tropopausenbereich unter Berücksichtigung ihrer Dispersion. Diploma thesis, Institut für Geophysik und Meteorologie, Universität zu Köln, 110 pp.
- Petry, H., J. Hendricks, M. Möllhoff, E. Lippert, A. Meier, A. Ebel, and R. Sausen, 1998: Chemical conversion of subsonic aircraft emissions in the dispersing plume: Calculation of effective emission indices. *J. Geophys. Res.* 103 (D5), 5759-5772.
- Sausen, R., Isaksen, I., Grewe, V., Hauglustaine, D., Lee, D.S., Myhre, G., Köhler, M.O., Pitari, G., Schumann, U., Stordal, F., Zerefos, C., 2005: Aviation radiative forcing in 2000. An update on IPCC (1999). *Meteorol. Z.* 14, 555-561.
- Schumann, U. (Ed.), 1995: The impact of NO_x emissions from aircraft upon the atmosphere at flight altitudes 8 - 15 km (AERONOX). Final report to the Commission of the European Communities, 471 pp.
- Schumann, U., and D. Wurzel (Eds.), 1994: Impact of emissions from aircraft and spacecraft upon the atmosphere. DLR Mitteilung 94-06, DLR, Köln, 496 pp.
- Schumann, U., H. Schlager, F. Arnold, R. Baumann, P. Haschberger, and O. Klemm, 1998: Dilution of aircraft exhaust plumes at cruise altitudes. *Atmos. Environ.* 32, 3097-3103.
- Veenstra, D., and J. Beck, 1994: An aircraft exhaust plume model. In: Schumann and Wurzel (1994), 286-291.

Aerodynamically induced formation of contrails

K. Gierens*, B. Kärcher, H. Mannstein, B. Mayer
DLR Oberpfaffenhofen, Institut für Physik der Atmosphäre, Germany

Keywords: Aerodynamics, Microphysics, Optics, Contrails

ABSTRACT: We study the formation and growth of ice particles induced by the cooling of the air while flowing over the wings of cruising aircraft.

1 INTRODUCTION

Photographs taken in flight show that condensation sometimes starts right above the wings of cruising aircraft. This demonstrates the existence of contrails different from the well studied jet exhaust contrails. Below we present a first investigation of the conditions that lead to the appearance of aerodynamic contrails, along with a characterisation of their basic microphysical and optical properties. Studies of aerodynamic contrails require interdisciplinary research on compressible gas flow over airfoils, ice and aerosol microphysics, and optics of ice crystals, such as outlined here.

2 AERODYNAMICS

As a first step into this new research area, we make simplifying yet sufficiently accurate assumptions that allow us to compute the flow field by straightforward numerical means, circumventing the use of a sophisticated CFD code. As a motivation, we start with a simple back-of-the-envelope calculation.

2.1 Back-of-the-envelope calculation

The average pressure difference above minus below the wings is the force that carries the aircraft. Let the aircraft weight be W , its wing area A , then the pressure difference is $\Delta p = -W/A$. For wide body aircraft (e.g. A340, B747) this amounts to a surprisingly large value of typically -50 hPa. Now assume that this pressure difference arises adiabatically in the flow. The corresponding temperature difference is given by $\Delta T / T = [(\kappa-1)/\kappa] (\Delta p / p)$ with $\kappa = c_p/c_v = 1.4$ being the ratio of the specific heats of air. For typical conditions at cruise altitudes (e.g. $T = 220$ K, $p = 220$ hPa) we get $\Delta T = -14$ K, i.e. a sudden cooling above the wing that suffices to turn even relatively dry air of, say, $RH_i = 20\%$, into a transient supersaturated state that may allow condensation. This rough calculation suggests that aerodynamically induced condensation should occur at times. The question arises why, on the contrary, it apparently is a rare event. In order to answer this and other questions, we have to perform a more detailed flow calculation.

2.2 Linearised 2-dimensional flow calculation for compressible flow

We assume that the flow is adiabatic and circulation free, furthermore that the flow is strictly two-dimensional and stationary. First we define the shape of the airfoil, i.e. the cross section of the wing. We have chosen a simple analytical shape, the Joukowski wing. This already quite realistic wing shape results from a conformal mapping of a unit circle, which is appropriate for our goal (although the Joukowski wing is not used in practice). In particular, it has one sharp (trailing) and one round (leading) edge. If we had an incompressible flow, we could compute the velocity potential and stream functions for the Joukowski wing simply from the corresponding quantities in a flow around a circular cylinder. The analytical form of the latter is known, and applying the same con-

* Corresponding author: Klaus Gierens, DLR-Institut für Physik der Atmosphäre, Oberpfaffenhofen, D-82234 Wessling, Germany. Email: Klaus.Gierens@dlr.de

formal mapping to these fields as to the wing shape (i.e. the Joukowski transformation) yields the desired result. However, flow incompressibility requires flow speeds with small Mach numbers, while modern airliners typically cruise at $Ma = 0.8$. Therefore, we must not assume that the flow is incompressible, and we need another way of computation.

The details of our method will be given elsewhere, here we only present the essential assumptions that lead to the solution. Under the stipulated assumptions, the continuity and Euler equations combine to an equation for the flow potential Φ . We assume that the parallel background flow, (u_∞, v_∞) , is perturbed only little by the wing and that the background flow has a small angle of attack relative to the wing. With these assumptions, we may linearise the potential equation. Then perturbations caused by the thickness of the wing and by its camber can be treated separately and are additive, leading to the following ansatz for the potential:

$$\Phi = u_\infty x + v_\infty y + \varphi + \psi, \quad (1)$$

where φ and ψ are the perturbation potentials for wing thickness and camber, respectively. Neglecting perturbation quantities of quadratic and higher order in the equation for the potential then gives:

$$\beta^2 \varphi_{xx} + \varphi_{yy} = 0 \quad \text{and} \quad \beta^2 \psi_{xx} + \psi_{yy} = 0 \quad \text{with} \quad \beta^2 = 1 - Ma^2 \quad (2)$$

The simple (non-conformal) coordinate transformation $x = \xi$, $\beta y = \eta$, yields the classical Laplace equation for the potentials, for instance $\varphi_{\xi\xi} + \varphi_{\eta\eta} = 0$, which can be solved by various means. We employ the method of singularities, where the perturbation potentials are constructed by suitable superpositions of potentials for singular sources, sinks, and vortices.

From the flow field, we computed a set of trajectories, both below and above the wing, using a 4th-order Runge-Kutta scheme (Press et al., 1989). The perturbation of the (dominating) x-component of the flow speed on the trajectories, $u - u_\infty$, is inserted into a generalised Bernoulli equation to yield the temperatures along the trajectories, viz.

$$T = T_\infty - [(\kappa - 1)/\kappa R_a] (u^2 - u_\infty^2)/2 \quad (3)$$

where R_a is the specific gas constant of dry air ($287 \text{ J kg}^{-1} \text{ K}^{-1}$). The corresponding pressure is obtained from the Poisson equation, viz.

$$p = p_\infty (T/T_\infty)^{\kappa/(\kappa-1)}. \quad (4)$$

Figures 1 and 2a/b show the flow field (streamlines) and the temperature and pressure histories on the trajectories for a case with $p_\infty = 350 \text{ hPa}$ and $T_\infty = 235 \text{ K}$. The wing depth is 11.7 m , wing thickness 1.7 m , and the effective angle of attack is 1° .

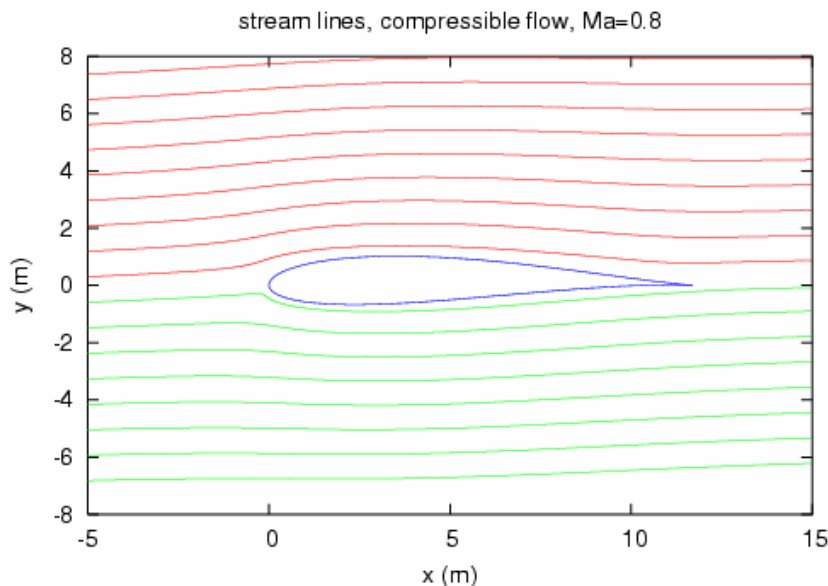


Figure 1. Two-dimensional potential flow field (compressible flow) around a Joukowski airfoil, calculated with the method of singularities. Effective angle of attack: 1° . Mach number: 0.8 . The dimensions of the airfoil are typical of a wide-body aircraft close to the fuselage.

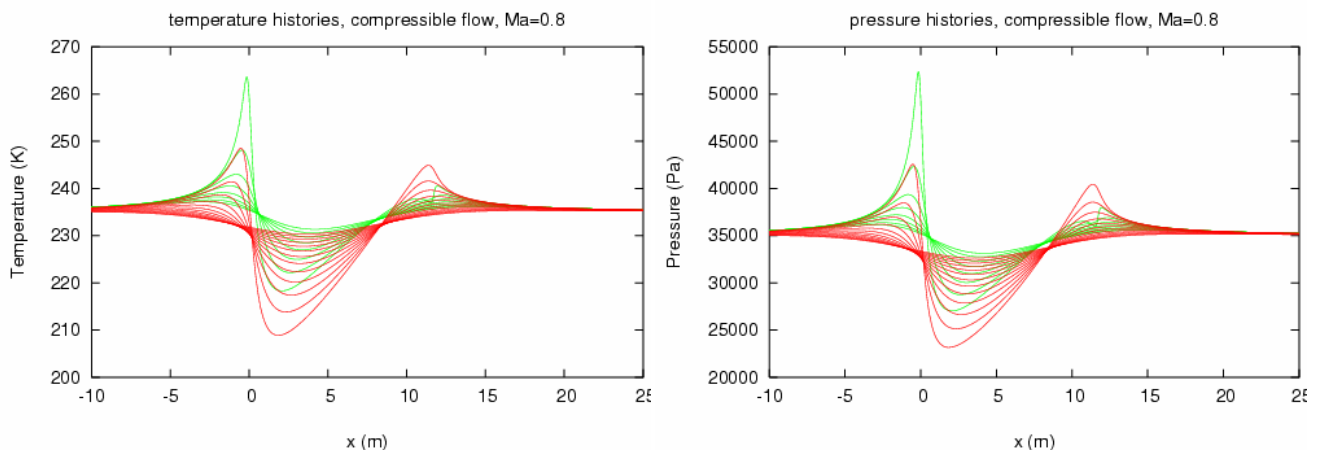


Figure 2. Temperature (left) and pressure (right panel) histories along the streamlines shown in Figure 1.

3 MICROPHYSICS

We employ a comprehensive gas-aerosol-ice trajectory model (Kärcher, 2003) to track the following non-equilibrium processes along one of the T- and p-trajectories close to the wing as shown above. (i) Water condensation on liquid aerosol droplets composed of aqueous H_2SO_4 . (ii) Homogeneous freezing of ice from these supercooled aerosol particles. (iii) Depositional growth of the spherical ice particles.

Water uptake on particles is coupled with the gas phase in a strictly mass-conserving manner, so that the evolution of the supersaturation is accurately simulated. A relatively broad lognormal aerosol size distribution has been used for aerosols (mean mass radius 80 nm, geometric standard deviation 1.6, total number concentration 500 cm^{-3}) to cover both Aitken and accumulation mode sizes. Growth of aerosol particles is treated in a Lagrangian manner. This allows us to accurately simulate the water mass fraction in each particle size category to which freezing nucleation rates are extremely sensitive. Growth of ice particles is treated with a moving centre size structure that is virtually free of numerical diffusion. We prescribe an ambient ice supersaturation of $\text{RH}_i = 140\%$ just below the homogeneous freezing threshold and an H_2O deposition coefficient of unity to maximize ice particle growth. We use a time step of $1 \mu\text{s}$ for these simulations.

Figure 3 shows results of the microphysical calculations. The legend denotes times and corresponding distances behind the leading wing edge. The ice crystal size distributions (solid curves) are generated from homogeneous freezing of liquid aerosol droplets (dashed). Nucleation is finished as the air parcel moves across the wing (after $\sim 16 \text{ m}$). In the subsequent growth phase in the highly supersaturated air, mean ice particle radii increase to $\sim 2.8 \mu\text{m}$ after $\sim 680 \text{ m}$.

Note that the ice particle spectrum becomes essentially monodisperse shortly after nucleation. Laminar flow and monodispersity are the key prerequisites for the colourful appearance of aerodynamic contrails, as studied in Section 4. Jet exhaust contrails, on the contrary, appear white because plume turbulence quickly mixes contrail ice particles with slightly different sizes and thus broadens their size spectrum.

Interestingly, the smallest droplets freeze first, followed by freezing of larger droplets, until practically all available aerosol particles are depleted. At first glance, this seems to contradict the common notion that larger particles freeze first owing to their larger volume. However, this assumes that aerosol particles are in equilibrium with ambient H_2O , regardless of size. During the formation of aerodynamic contrails, RH_i changes dramatically on the time scale of $\sim 10 \mu\text{s}$. This is of the same order as the composition change time scale dictated by diffusion of H_2O molecules in air. For the small aerosol particles, the latter time scale is proportional to particle surface area. This implies that they adjust faster to increasing RH_i and become water-rich much faster than larger particles, and hence freeze earlier despite a smaller volume. The fact that the time scale for a change in radius is somewhat longer than the time scale for freezing explains why the ice particles start to grow significantly only after nucleation is shut off. It is possible that more and slightly smaller ice

particles would form if we prescribed a larger concentration of aerosol particles. These and other aspects will be addressed in more detail in future work by means of sensitivity studies.

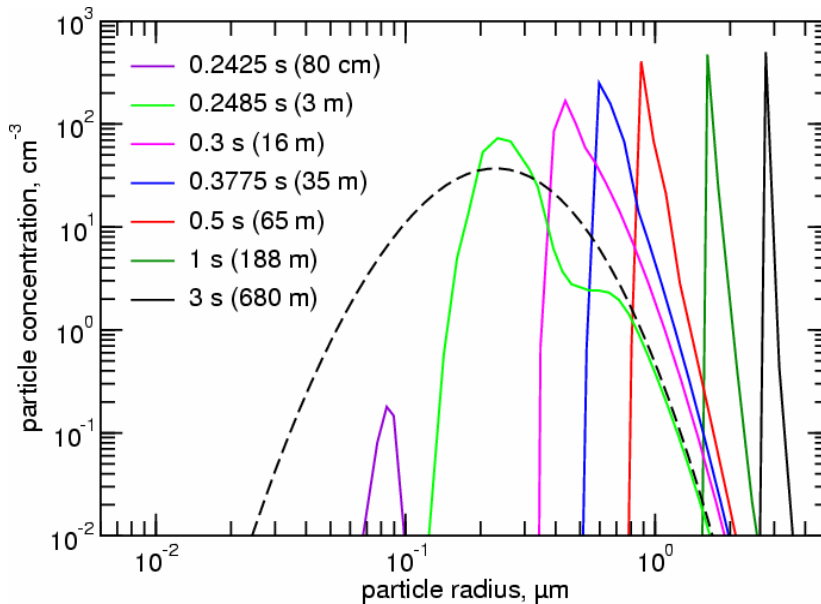


Figure 3. Ice crystal size distributions for various distances (times) behind the leading edge of the wing along the trajectory closest to and above the wing.

4 RADIATION

To determine the colour of the contrail, the scattering coefficient was calculated from the size distributions in Figure 3 using the theory by Mie [1908] for spherical ice particles. The well-known Mie code by Wiscombe [1979] as provided by the libRadtran radiative transfer package [Mayer and Kylling, 2005] was used for this purpose.

Figure 4a shows the extinction efficiency at 550 nm (solid line) as function of the particle radius. The typical features of a monodisperse particle distribution are clearly visible: the Rayleigh limit for particles much smaller than the wavelength, where the extinction efficiency increases rapidly with particle size; and the geometrical optics limit for particles much larger than the wavelength, where the extinction efficiency approaches 2 (that is, the extinction cross section is twice the geometrical cross section). In the size range where the particle radius is comparable to the wavelength, the extinction efficiency shows characteristic oscillations and reaches its maximum where the radius equals the wavelength of the radiation. In the visible spectral range, absorption is negligible and the scattering efficiency equals the extinction efficiency.

From these considerations we may immediately conclude that the scattering coefficient of a monodisperse particle distribution strongly depends on wavelength; if illuminated with white light, selective scattering of colours will cause the scattered radiation to be coloured: e.g., crystals with 400 nm radius will scatter blue most efficiently and the scattered radiation will appear blue; crystals with 700 nm will appear red as the maximum of the scattering cross section occurs at 700 nm. For a polydisperse size distribution, these effects are reduced, and if the size distribution is too wide, they will vanish completely. Hence the appearance of colours indicates a narrow size distribution.

To calculate the actual colour of the contrail, a full radiative transfer calculation is required in principle, to calculate spectral radiance. However, since the optical thickness is small we used a very simple single-scattering approximation: the scattered radiance is assumed to be proportional to the incident (extra-terrestrial) irradiance times the scattering coefficient. This calculated spectral irradiance is converted to colours using “specrend” by John Walker, available at <http://www.fourmilab.ch/documents/specrend/>. Spectral radiance is converted to X, Y, and Z using the respective CIE colour matching functions, which are then converted to device-dependent colour-coordinates R, G, and B with the respective EBU matrix.

Figure 4a shows the calculated colours as a function of ice particle radius for a monodisperse size distribution. As outlined above, colours are most pronounced in the size range where the change of the extinction efficiency with wavelength is strongest. Figure 4b, finally, shows the colours to be expected for the size distributions from Figure 3. Size distributions were provided every 0.001 seconds from 0.24 seconds to 6 seconds. Extinction efficiencies were calculated with Mie theory and integrated over the size distribution to get the spectral extinction coefficient, multiplied with the spectral extraterrestrial irradiance, and converted to colours. Figure 4b shows the effective ice particle radius. The colours nicely match the colours in the photograph, indicating that growth with time as well as the width of the size distribution were realistic.

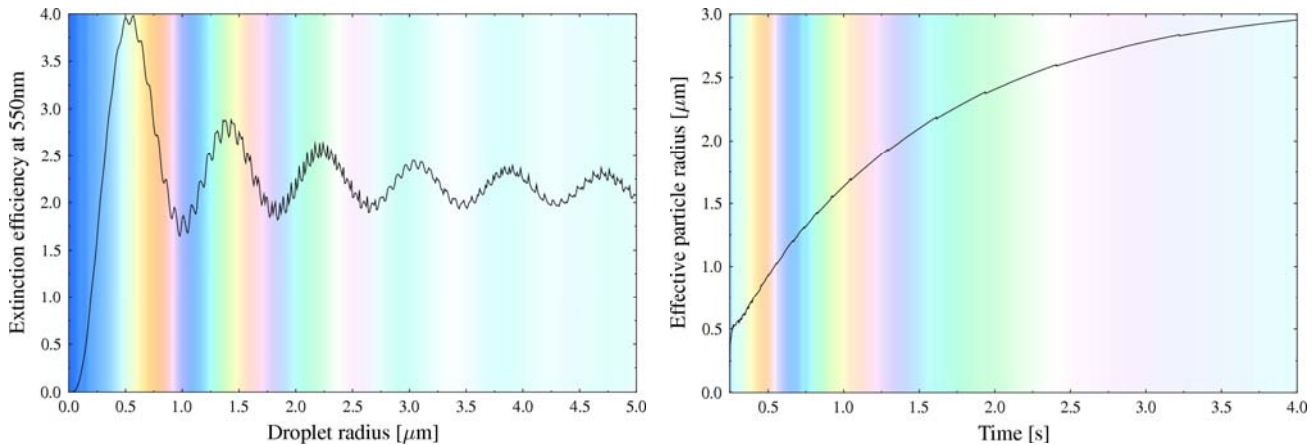


Figure 4. (a) Extinction efficiency for a monodisperse ice particle distribution and colour of the scattered radiation in single-scattering approximation; (b) effective radius and colour for the size distributions from Figure 3 as a function of time.

5 EXAMPLE

On 12 June 2005 from 14:59 to 15:06 Beijing time ($\sim 07:00$ UTC), pilot and photographer Jeff Well took a series of photos of an exceptionally colourful iridescent contrail produced by an A340-313X aircraft in 9600 m altitude, just 1200 m above his position on the same route over eastern China. Both aircraft were heading to North-West (329°) from $32^\circ 14.8' \text{ N}$, $119^\circ 46.7' \text{ E}$ to $32^\circ 56.8' \text{ N}$, $119^\circ 10.1' \text{ E}$. From NCEP reanalysis data we estimate a temperature of -40°C , the aircraft altitude is very close to the 300 hPa pressure level.

The series of photos displayed in Figure 5 shows the development of contrails that cannot be explained by the Schmidt-Appleman criterion. Jet contrails produced from the mixing of exhaust gases with the ambient air would show up as 4 separate lines behind the engines and start later. The onset of the aerodynamic contrails occurs directly above the wings and is stronger close to the body of the aircraft. Thin vortex lines originate from the wing tips and get mixed into the wake vortices.

6 CONCLUSIONS AND OUTLOOK

Photographs demonstrate that aerodynamic contrails occur preferentially above the inner parts of the wings, where the uplift is largest. Hence, aerodynamic contrails may become more relevant for a potential future fleet of blended wing-body aircraft with significantly larger wing depths.

Future work will study the properties of the numerous small ice crystals produced in the adiabatic air flow over wings of airliners, the impact of ambient conditions and background aerosol properties on early aerodynamic contrail formation and evolution, and how common this process occurs relative to jet exhaust contrails that form according to the Schmidt-Appleman theory.

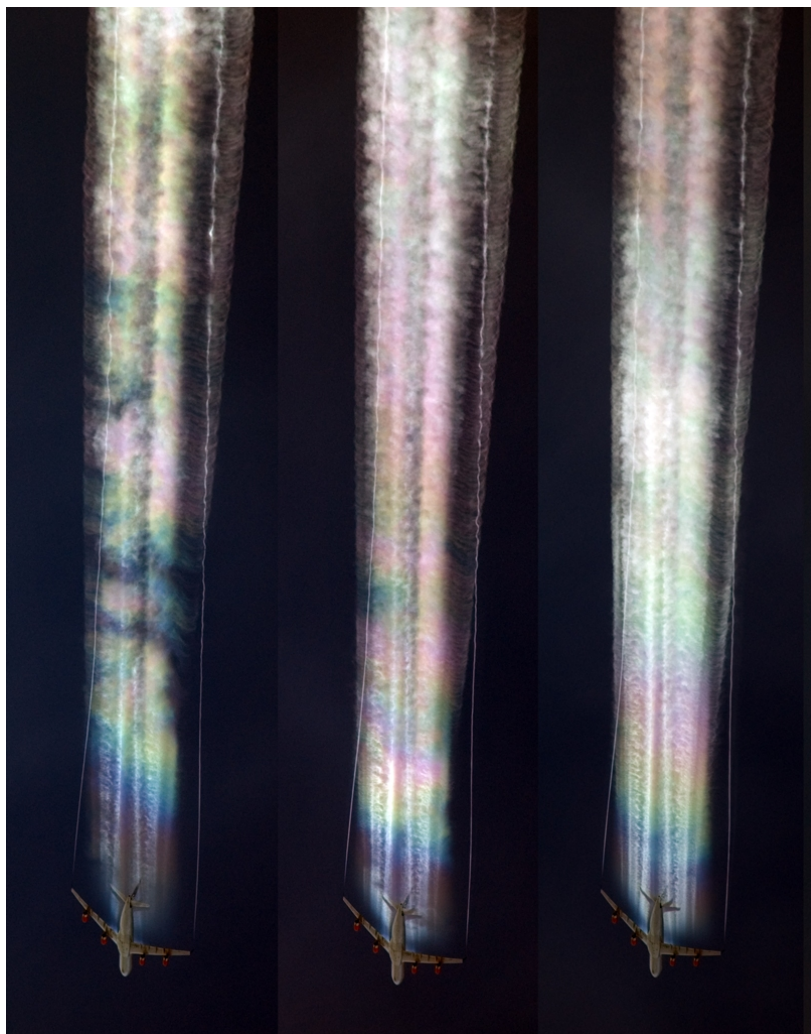


Figure 5. Series of photographs of an aerodynamically induced contrail. Note the iridescent colours. The formation and colourful appearance of such contrails are explained by the combination of aerodynamical, microphysical, and radiative processes outlined in this paper.

ACKNOWLEDGEMENT

The photographs shown here are all taken by pilot Jeff Well. We thank Jeff Well for allowing us to use his photographs of aerodynamic contrails. Many other photographs of aerodynamic contrails can be found on www.airliners.net. This work is supported by the DLR/HGF project Particles and Cirrus Clouds (PAZI-2).

REFERENCES

- Kärcher, B., 2003: Simulating gas-aerosol-cirrus interactions: Process-oriented microphysical model and applications. *Atmos. Chem. Phys.*, 3, 1645–1664.
- Mayer, B., and A. Kylling, 2005: Technical Note: The libRadtran software package for radiative transfer calculations: Description and examples of use. *Atmos. Chem. Phys.*, 5, 1855–1877.
- Mie, G., 1908: Beitrage zur Optik trueber Medien, speziell kolloidaler Metalloesungen. *Annalen der Physik*, Vierte Folge, 25(3):377–445.
- Press, W.H., B.P. Flannery, S.A. Teukolsky, and W.T. Vetterling, 1989: *Numerical Recipes*. Cambridge University Press, Cambridge, UK, ISBN 0 521 38330, 702 pp.
- Wiscombe, W.J., 1996: Mie Scattering Calculations: Advances in Technique and Fast, Vector-Speed Computer Codes. Technical Report TN-140+STR, NCAR, 1979, edited and revised 1996.

Contrails in a global climate model – effect of reducing systematic errors

A. Guldberg*

Danish Meteorological Institute, Copenhagen, Denmark

Keywords: Contrails, radiative forcing, systematic errors

ABSTRACT: The contrail parameterization of Ponater et al. (2002) has been implemented in the global climate model IFSHAM. The global mean net radiative forcing due to contrails is in this model positive, but small, and in areas over Europe and the United States the net forcing is negative. In order to investigate this result a series of experiments has been performed modifying contrail optical properties. Results from these experiments are shown. The climate model exhibits certain systematic errors and the impact of these systematic errors is analysed. The model is run in nudged mode, where the model is relaxed towards observed data thereby reducing the systematic errors of the model substantially. Comparing runs with the model in standard mode and in nudged mode gives the possibility for analysing the impact of model systematic errors on contrail properties and contrail radiative forcing. Results from these experiments are shown as well.

1 INTRODUCTION

The radiative forcing due to line shaped contrails was given a best estimate of 20 mW/m^2 in the IPCC special report “Aviation and the Global Atmosphere” (IPCC, 1999) for 1992 air traffic conditions. There is some uncertainty on this estimate and some of the results published later indicate smaller values for the contrail radiative forcing.

Marquart et al. (2003) has implemented the contrail parameterization scheme of Ponater et al. (2002) in the global climate model ECHAM4 and simulations with this model give an estimate of the radiative forcing due to line shaped contrails of 3.5 mW/m^2 – an order of magnitude smaller than the IPCC estimate. The same contrail parameterization as used in Marquart et al. (2003) has been implemented in the global climate model IFSHAM (Guldberg and Nielsen, 2004). Using this model setup simulations similar to the Marquart et al. (2003) simulations result in an estimate of radiative forcing due linear contrails of 0.26 mW/m^2 – an order of magnitude smaller than the Marquart et al. (2003) estimate. The geographical distribution of the radiative forcing shows areas – over Europe and the United States – where the net radiative forcing is negative. This is not seen in the results of Marquart et al. (2003) – here the net forcing is positive everywhere.

In order to be able to explain the reason for this very small and in some areas negative radiative forcing in the simulations of the IFSHAM model two sets of experiments were performed. In one set contrail optical properties were modified in order to study the impact of these properties. In another set of experiments the impact of model systematic errors were investigated. The IFSHAM model has as all global models systematic errors and in the experiments performed here these systematic errors were substantially reduced using the nudging technique, where the model is forced to follow observed data. Comparing with simulations in standard climate mode the importance of the systematic errors for the estimation of contrail radiative forcing was studied.

2 MODEL AND EXPERIMENTS

The IFSHAM model is developed at DMI (Yang, 2004) as a combination of the dynamical core from ARPEGE, version 3 (Déqué et al. 1994) and the physical parameterization package from

* *Corresponding author:* Annette Guldberg, Danish Meteorological Institute, Lyngbyvej 100, 2100 Copenhagen, Denmark. Email: ag@dmi.dk

ECHAM5 (Roeckner et al. 2003). The IFSHAM model uses semi-Lagrangian advection and a two-level semi-implicit time stepping scheme. The cloud scheme is the PCI scheme (Lohmann and Roeckner, 1996), where cloud water and cloud ice are treated as separate prognostic variables. The radiation scheme consists of the Morcrette short wave scheme (Morcrette, 1991) and the RRTM scheme (Mlawer et al., 1997) for the long wave part. Contrails are described by the parameterization scheme of Ponater et al., 2002. The resolution of the model used in these experiments is T63 with 31 vertical layers.

2.1 Optical properties

In order to investigate the impact of contrail optical properties on contrail radiative forcing a set of one year long experiments were performed in which the optical properties effective radius and optical depth were modified. The effect of changing the effective radius on the radiative forcing was minor in these experiments – for results see Guldberg and Nielsen (2004).

The optical depth of contrails is parameterized in IFSHAM and is a function of ice water path and ice water content. A set of sensitivity experiments were performed in which the optical depth was fixed at a constant value. Figure 1a shows the resulting annual mean contrail net radiative forcing at the top of the atmosphere (TOA) from a one year long experiment with a variable optical depth determined by the parameterization scheme whereas figure 1b shows the net radiative forcing also from a one year long experiment, but with the optical depth set to a constant value of 0.1. The global mean of the contrail coverage is relatively low in these experiments: 0.07 %.

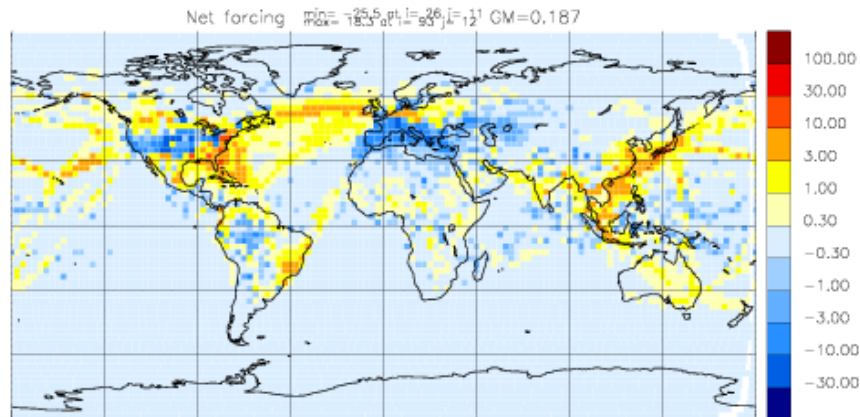


Figure 1a Annual mean of net radiative forcing at TOA from an experiment with variable optical depth (Unit: mW/m^2)

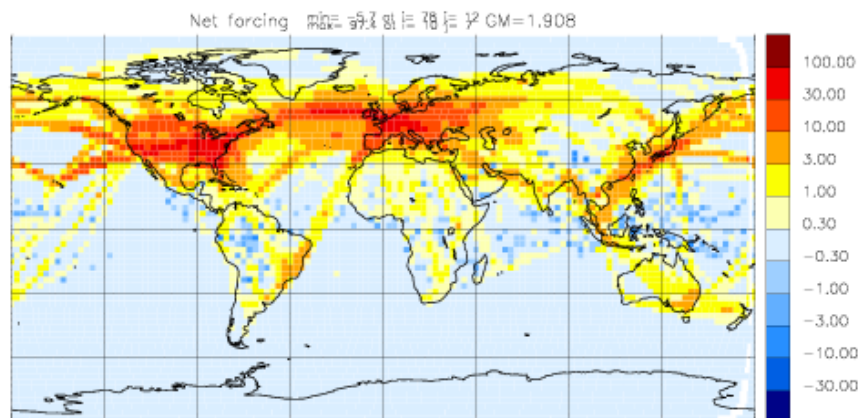


Figure 1b Annual mean of net radiative forcing at TOA from an experiment with constant optical depth of 0.1 (Unit: mW/m^2)

Fixing the optical depth at a constant value of 0.1 leads to a substantial increase in the short wave forcing but an even larger increase in the long wave forcing and therefore the resulting net forcing is also substantially increased. The global mean of the net forcing is 0.2 mW/m^2 in the experiment with variable optical depth and 1.9 mW/m^2 in the experiment with an optical depth of 0.1. This means a factor of ten larger net forcing in the experiment with constant optical depth. It is also seen

when comparing figure 1a and 1b that the areas over Europe and the United States with negative net forcing in the experiment with variable optical depth have a positive net forcing in the experiment with constant optical depth. From these experiments it is seen that optical depth has a large impact on the estimation of contrail radiative forcing.

2.2 Systematic errors

As all climate models the IFSHAM model suffers from certain long term systematic errors when compared to observations and these errors may influence the estimation of contrail properties. In order to analyse the effect of model systematic errors simulations were performed with the model in so called nudged mode. Using the nudging technique (Jeuken et al., 1996) the model is forced towards a reference data set, and when the reference data set represents observed data the systematic errors of the model are minimized, because in each time step the model is following closely the observed values of the prognostic variables. Nudging is a simple 4-dimensional assimilation of the reference data, where the prognostic model variables are relaxed towards the reference data. In the experiments described here the ECMWF Re-Analysis data (ERA-15) (Gibson et al., 1997) are used as the reference data set towards which the model is relaxed.

Two sets of simulations have been performed with the IFSHAM model in order to study the impact of systematic errors. In the first set – the standard simulations – the model is forced with observed sea surface temperatures for ten winter seasons and ten summer seasons in the period covered by the ERA-15 data set (1973-1993). In the second set – the nudged simulations – the model is run in nudged mode and the model is relaxed towards observed data for the same ten winter and summer seasons and also observed sea surface temperatures are used. In the following only averages of the ten summer seasons are shown. Results for the winter season can be found in Guldberg and Nielsen, 2004.

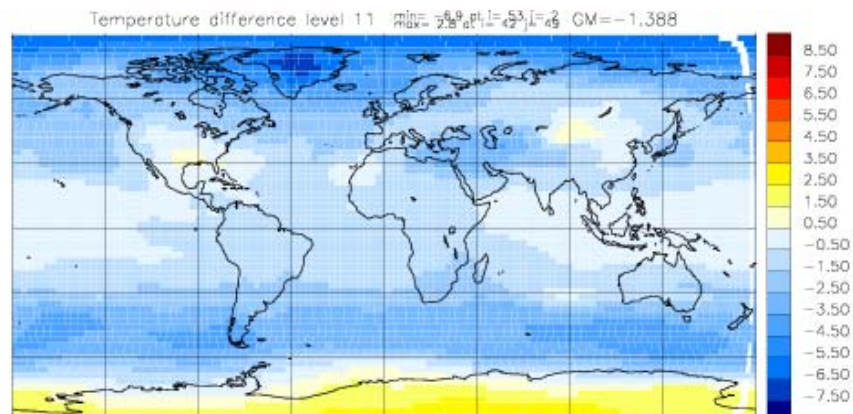


Figure 2a Ten year mean difference of temperature between standard and nudged simulations at ~240 hPa (Unit: K)

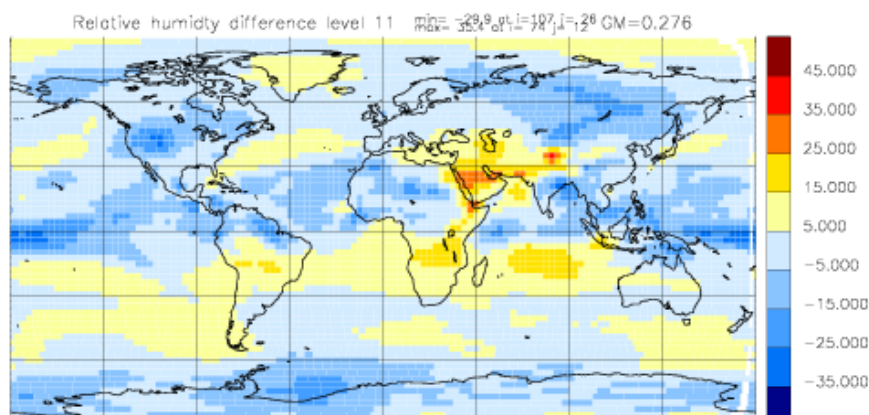


Figure 2b Ten year mean difference of relative humidity with respect to ice between standard and nudged simulations at ~240 hPa (Unit: %)

Figure 2a shows the average difference of temperature between the standard and the nudged simulations at approximately 240 hPa. This difference represents well the temperature systematic error of

the model as the nudged simulation follows closely the ERA-15 data. It is seen that in summer the model is too cold almost everywhere, except over Antarctica where the model is too warm. The largest cold biases are seen at northern high latitudes.

Figure 2b is similar to figure 2a but shows relative humidity with respect to ice. In summer the relative humidity with respect to ice is too low in most of the Northern hemisphere. It should be noted that humidity is not nudged in these experiments, so the humidity in the nudged simulations are determined by the model based on close to observed values of the other prognostic variables.

The annual global mean of the contrail coverage in these simulations is 0.13 % and the model systematic errors have little impact on the contrail coverage. But the differences actually seen between the two model simulations follow to a large degree the pattern of the differences of the relative humidity, indicating that relative humidity is likely the determining factor for these differences. Also differences in ice water path between the standard and the nudged simulations are rather small, but there is a tendency of too large values in the tropics and too small values in the extratropics in the standard simulations. As the effective radius and the optical depth are determined from the ice water path, the same tendency is seen for the effective radius and the optical depth. More detailed information on these differences can be found in Guldberg and Nielsen (2004).

The main question is how the model biases affect the radiative forcing of contrails in the IFSHAM model. Figure 3a and 3b show the changes in the short wave and long wave forcing. As the sign of the short wave forcing is negative positive values in the difference plot in figure 3a mean that the magnitude is too low in the standard simulation. For the summer season the magnitude of the short wave forcing is too low over the northern part of the United States, the North Atlantic flight corridor and northern Europe. In the southern part of the United States and southern Europe the magnitude of the forcing is too large in the standard simulation. The global mean of the short wave forcing is increased by 0.4 mW/m^2 when the model is nudged. The long wave forcing is too weak, respectively too strong in the areas where the short wave forcing is too weak, respectively too strong. The global mean of the long wave forcing is increased by 0.6 mW/m^2 , when the model is nudged.

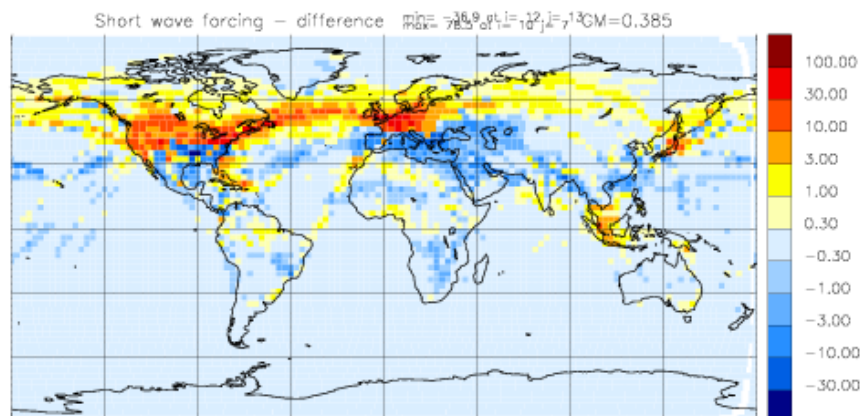


Figure 3a Ten year mean difference of short wave radiative forcing at TOA between standard and nudged simulations (Unit: mW/m^2)

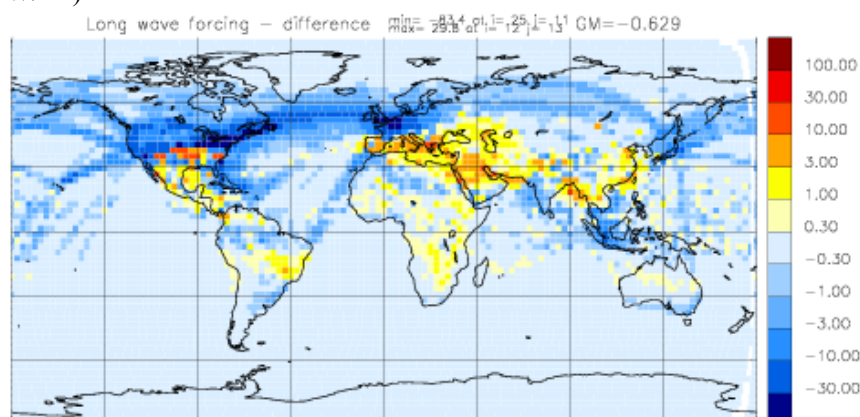


Figure 3b Ten year mean difference of long wave radiative forcing at TOA between standard and nudged simulations (Unit: mW/m^2)

Figure 4a and 4b show the contrail net radiative forcing at TOA in the standard simulation and the nudged simulation of the summer season. The global mean of the net forcing is increased by 0.2 mW/m^2 from 0.8 mW/m^2 to 1.0 mW/m^2 . Although the magnitude of the net forcing is changed the pattern of the forcing is to a large degree unchanged.

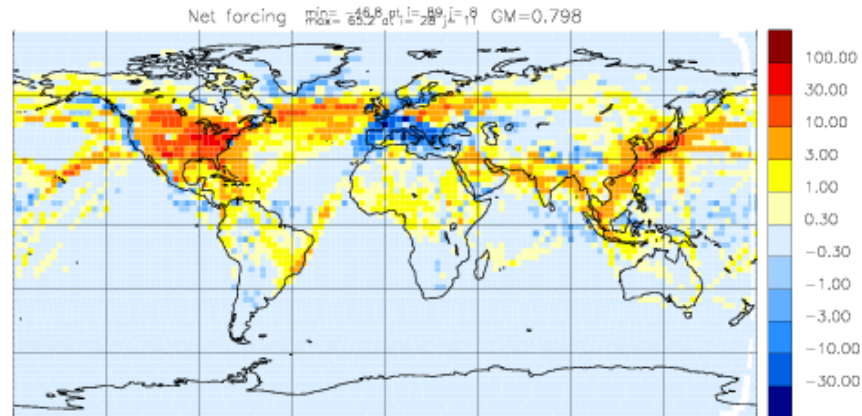


Figure 4a Ten year mean of net radiative forcing at TOA for standard simulation (Unit: mW/m^2)

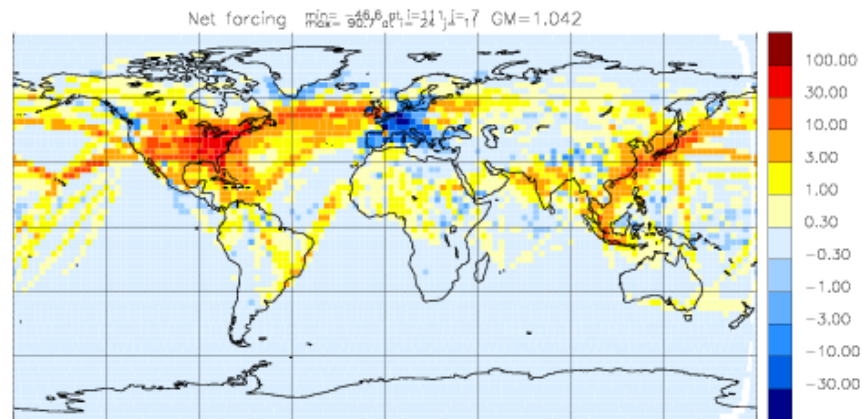


Figure 4b Ten year mean of net radiative forcing at TOA for nudged simulation (Unit: mW/m^2)

3 CONCLUSIONS

The contrail parameterization of Ponater et al. (2002) has been implemented in the IFSHAM model. The net radiative forcing due to contrails is in this model an order of magnitude smaller than obtained by Marquart et al. 2003. Furthermore the net forcing shows areas with negative values.

In order to investigate the reasons for these results experiments with modifications of the optical properties of the contrails have been performed. It turns out that setting the optical depth to a constant value of 0.1 results in a net radiative forcing in better agreement with other results. Furthermore the areas over Europe and the United States with negative net forcing do in the experiment with constant optical depth have positive net radiative forcing. But the question is how realistic it is to set a constant value for the optical depth.

The impact of systematic errors of the model have been studied using the nudging technique. The systematic errors are causing a 10-20 % too low estimate of the short and long wave forcing. The net forcing is 75 % too low in winter and 20 % too low in summer in the standard mode compared to the nudged version of the model. But the geographical distribution of the net forcing is unchanged and areas with negative net forcing still exist.

In order to understand better the model estimation of contrail radiative forcing a detailed investigation of the radiation parameterization for both short and long wave radiation is needed. Also an analysis of the many different parameterizations of optical properties available could be of importance for understanding the effect of contrails on the radiation balance.

REFERENCES

- Déqué, M. C. Drevet, A. Braun and D. Cariolle, 1994: The ARPEGE/IFS atmosphere model: a contribution to the French community climate modelling. *Climate Dynamics*, 10:249-266.
- Gibson, J. K., P. Källberg, S. Uppala, A. Hernandez, A. Nomura and E. Serrano, 1997: *ERA-15 Description*, Volume 1 of ECMWF Re-analysis Project Report Series, ECMWF, Reading, UK.
- Guldberg, A. and J. K. Nielsen, 2004: *Contrails and their climate impact*, Scientific Report 04-06, DMI, Denmark, www.dmi.dk/dmi.sr04-06
- IPCC, 1999: *Aviation and the global atmosphere*, Cambridge University Press, Cambridge, UK.
- Jeuken, A. B. M., P. C. Siegmund, L. C. Heijboer, J. Feichter and L. Bengtsson, 1996: On the potential of assimilating meteorological analyses in a global climate model for the purpose of model validation, *J. Geophys. Res.*, 101:16939-16950.
- Lohmann, U. and E. Roeckner, 1996: Design and performance of a new cloud microphysics scheme developed for ECHAM general circulation model. *Climate Dynamics*, 12:557-572.
- Marquart, S., M. Ponater, F. Mager and R. Sausen, 2003: Future Development of Contrail Cover, Optical Depth and Radiative Forcing: Impacts of Increasing Air Traffic and Climate Change. *Journal of Climate Change*, 16:2890-2904.
- Mlawer, E. J., S. J. Taubman, P. D. Brown, M. J. Iancu and S. A. Clough, 1997: Radiative transfer for inhomogeneous atmospheres: RRTM, a validated correlated-k model for the longwave. *Journal of Geophysical Research*, 102:16663-16682.
- Morcrette, J.-J., 1991: Radiation and cloud radiative properties in the European Centre for Medium Range Weather Forecasts forecasting system, *J. Geophys. Res.*, 96:9121-9132.
- Ponater, M., S. Marquart and R. Sausen, 2002: Contrails in a comprehensive global climate model: Parameterization and radiative forcing results. *Journal of Geophysical Research (Atmosphere)*, 107(D13):ACL 2 1-15.
- Roeckner, E., G. Bäuml, L. Bonaventura, M., R. Brokopf, M. Esch, M. Giorgetta, S. Hagemann, I. Kirchner, L. Kornblüeh, E. Manzini, A. Rhodin, U. Schlese, U. Schulzweida and A. Tompkins, 2003: *The atmospheric general circulation model ECHAM5. Part I: Model Description*, Max-Planck-Inst. Meteorol. Rep., 349, Germany.
- Yang, S., 2004: The DKCM Atmospheric Model. The Atmospheric Component of the Danish Climate Model, Danish Climate Centre Report 04-05, DMI, Denmark

Comparison of cirrus cloud coverage calculated from reanalysis meteorological data with satellite data

L. Lim^{*}, D.S. Lee

Dalton Research Institute, Department of Environmental & Geographical Sciences, Manchester Metropolitan University, UK

R. Ismail, R.G. Grainger

Sub-Department of Atmospheric, Oceanic and Planetary Physics, University of Oxford, UK

K. Gierens, M. Ponater

Institut für Physik der Atmosphäre, Deutsches Zentrum für Luft und Raumfahrt (DLR), Oberpfaffenhofen, Germany

Keywords: Cirrus cloud, satellite, reanalysis meteorology

ABSTRACT: An offline cirrus cloud coverage calculation was conducted using a parameterisation similar to that adopted in ECHAM (Chen et al., 1997), as part of a preliminary analysis from ongoing work on estimating the uncertainties from contrail radiative forcing. The resulting cirrus cloud coverage, calculated from ECMWF ERA-40 reanalysis specific humidity and temperature data, was compared with ISCCP cirrus cloud data. Monthly mean results showed that computed coverage statistics between 45° South and 45° North were comparable with those from satellite observations. Similar spatial coverage structures, i.e. the high and low coverage values, were captured by both the parameterised calculation and the ISCCP dataset. A sensitivity analysis on the critical value of relative humidity over ice (U_{ci}) necessary for clouds to form highlights the importance of selecting an appropriate value of U_{ci} , optimized for the meteorological dataset used.

1 INTRODUCTION

The IPCC ‘Aviation and the Global Atmosphere’ report (1999) identified contrails and cirrus clouds as being, potentially, the largest effects from aviation on radiative forcing. This work forms part of a wider investigation to identify the sources of uncertainties in estimating radiative forcing from contrails. Cirrus coverage is required to determine which fraction of a grid cell is available for potential contrail formation. Therefore, it is important to compare calculated cirrus cloud coverage with observations.

2 METHODOLOGY

2.1 Cirrus cloud parameterisation

A method to calculate contrail coverage has previously been published by Sausen et al., 1998. The first stage of this work uses this method to produce an offline model that calculates the cirrus cloud coverage from different sources of meteorological data. In order to produce a suitable coverage map, it is necessary to have access to sufficiently resolved meteorological data in time and space. The European Centre for Medium-Range Weather Forecasts (ECMWF) Re-Analysis (ERA-40) datasets fulfil these criteria. From these datasets, fractional cirrus cloud coverage is calculated from specific humidity and temperature data using a parameterisation similar to that adopted for the general circulation model, ECHAM (Chen et al., 1997).

^{*} *Corresponding author:* Ling Lim, Dalton Research Institute-CATE, Manchester Metropolitan University, Faculty of Science and Engineering, John Dalton East Building, Chester St, Manchester M1 5GD, UK. Email: l.lim@mmu.ac.uk

Fractional cirrus cloud coverage (cirrus cloud by levels), b_{ci} , is calculated from Equation (1), where U_i is the relative humidity over ice and U_{ci} the critical value of relative humidity over ice. Total cirrus cloud coverage (over different levels) was then calculated from b_{ci} using random and maximum overlap assumptions (Sausen et al., 1998).

$$b_{ci} = 1 - \sqrt{\frac{1 - \max(U_i, U_{ci})}{1 - U_{ci}}} \quad (1)$$

The parameter U_{ci} determines whether cirrus cloud will form in a particular grid box, i.e. U_{ci} has to be exceeded for cirrus cloud to form (Sundqvist, 1978). Generally, U_{ci} is optimized for a given General Circulation Model (GCM) in order to yield a cloud distribution that leads to an optimal closure of the global annual radiation balance at the top of the atmosphere. If a modification is made to the resolution of a GCM or the cloud-radiative interaction, then the radiation balance at the top of the atmosphere may be disturbed. It is therefore necessary to restore the radiative balance either by modifying parameters affecting the cloud optical properties or by modifying the U_{ci} value. Various U_{ci} values have been used for previous ECHAM runs, e.g. ECHAM3 ($U_{ci} = 0.85$), ECHAM4 ($U_{ci} = 0.6$), ECHAM4.L39 ($U_{ci} = 0.7$).

In this preliminary work, total cirrus cloud calculated using $U_{ci} = 0.6$ (as adopted by Sausen et al., 1998) is compared with satellite data. U_{ci} values ranging from 0.5 to 0.85 are then applied to the parameterisation to determine the sensitivity of U_{ci} in predicting cirrus cloud coverage using ERA-40 data.

2.2 Satellite data

The International Satellite Cloud Climatology Project (ISCCP) was established in 1982 to produce global, reduced resolution datasets of basic properties of the atmosphere from which cloud parameters could be derived (Rossow et al., 1996). Five geostationary and two polar orbiting satellites have been used to infer the global distribution of cloud properties and their diurnal, seasonal and inter-annual variations. ISCCP analysis correlates radiances measured by satellites with temperature, humidity, ice and snow from TOVS (TIROS Operational Vertical Sounder) in order to determine information about clouds and the surface. Satellites (apart from TOVS) which cover January 1999 are NOAA-12, NOAA-14, GOES-8, METEOSAT-5 and GMS-5.

2.3 Comparison study

In this work we select a way of evaluating cirrus coverage that is directed towards identifying the sources of uncertainties in the intended contrail coverage analysis. Factors taken into consideration include the availability of satellite data, temporal resolution and high air traffic movement regions (Europe, North America, North Atlantic corridor and the Far East). Table 1 provides a summary of the data used to produce cirrus cloud coverages for this initial comparison work.

Table 1: Data used in the comparison study ($U_{ci} = 0.6$)

	Meteorology	Satellite
Dataset	ECMWF ERA-40	ISCCP climatological summary product (D2)
Parameters	Specific humidity and temperature	Daytime cloud (cirrus) amount (%)
Year	January 1999	January 1999
Horizontal resolution	2.5° x 2.5° globally	Equal area grid, latitudinally 2.5°
Vertical range	500 to 50 hPa	440 to 50 hPa
Temporal resolution	Monthly mean calculated from 00, 06, 12, 18 UTC	Monthly mean calculated from 00, 03, 06, 09, 12, 15, 18 and 21 UTC

3 RESULTS AND DISCUSSION

3.1 Comparison between cloud parameterisation and observations

The resulting cirrus cloud coverage for the case where $U_{ci} = 0.6$ (Figure 1) is compared with observed global cloud data from the ISCCP dataset (Figure 2) for one calendar month (January 1999).

In this study, only data for latitudes between 45° South and 45° North were used to evaluate cirrus cloud coverage from the cirrus parameterisation and ISCCP.

This initial attempt indicates that a longer time period, such as one year or more, is necessary because there are not enough data from ISCCP at important contrail-affected regions such as North America and Northern Europe (mainly due to January being a winter month). A comparison of the calculated cirrus cloud coverages with the ISCCP dataset shows that ISCCP has a higher maximum coverage (99%) and mean value (30%) than the calculated maximum coverage (92%) and mean value (24%) from the ERA-40 dataset.

Relative maxima of cirrus coverage were calculated over Polynesia in the Pacific Ocean, Amazon basin, central Africa and along the Inter Tropical Convergence Zone (ITCZ). These are similar to the ISCCP data, even though the ISCCP cirrus coverage in these areas was higher than that calculated from ERA-40 data. Relative minima were calculated over the East Pacific Rise, Central America, North Africa and India. Similar structures were observed in ISCCP data but again with higher values. Spatial patterns from both sources were comparable but computed coverages lacked the finer details that were observed in ISCCP data.

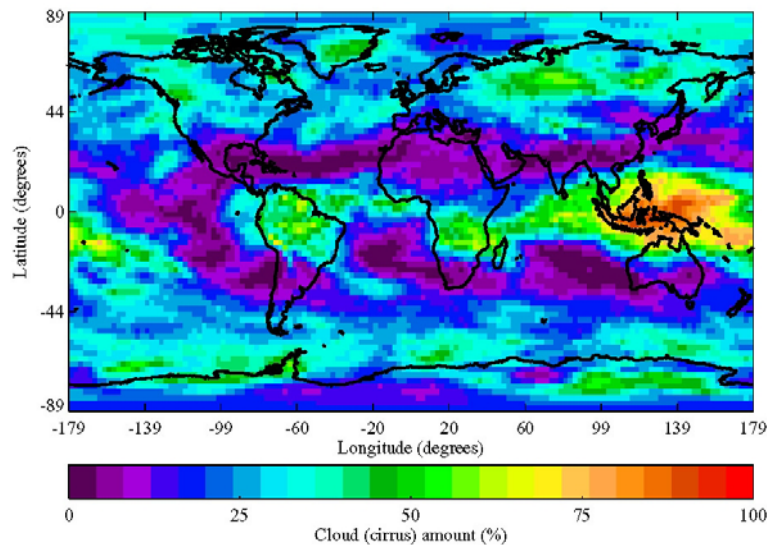


Figure 1. Cirrus cloud coverage calculated from ERA-40 data using ECHAM parameterisation for reference case ($U_{ci} = 0.6$)

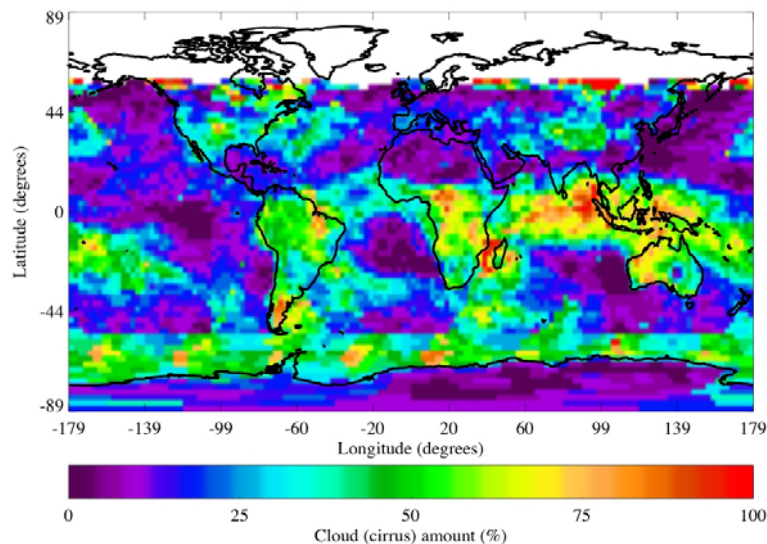


Figure 2. Cirrus cloud coverage from ISCCP

3.2 Sensitivity of U_{ci}

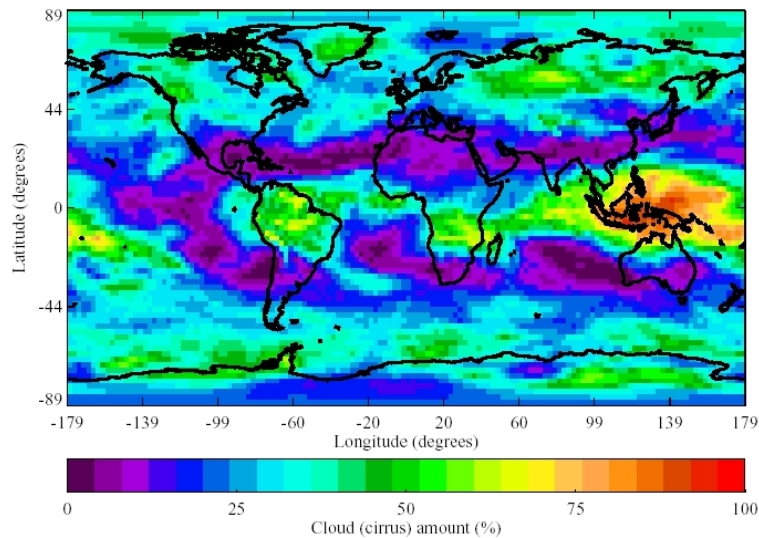
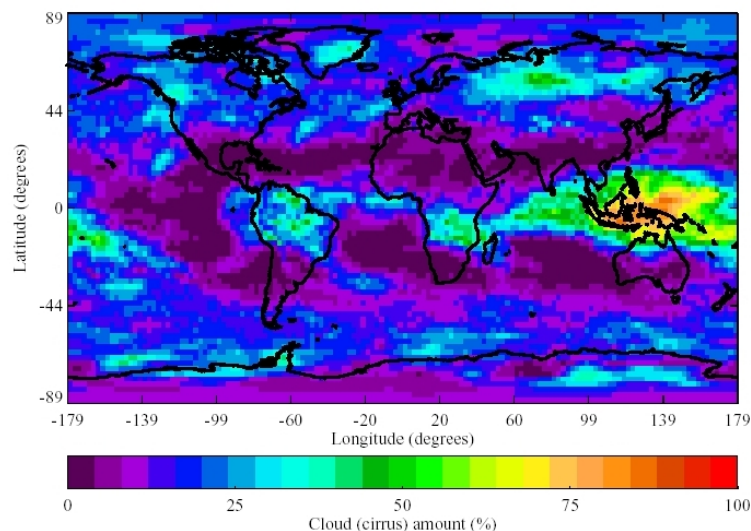
Results of the sensitivity analysis on U_{ci} in predicting cirrus cloud coverage using ERA-40 data are presented in Table 2. As expected, there is a variation of global mean coverage values for different U_{ci} values. The lowest U_{ci} value tested (0.5) produced the highest maximum coverage (92.9%) and the highest global mean coverage (30.3%). There was a gradual decrease of maximum and global

mean coverage with increasing U_{ci} . For $U_{ci} = 0.5$ and $U_{ci} = 0.85$, there was a difference of 6% for the maximum coverage and 14% for the global mean coverage. In this preliminary study, even though the global mean coverage decreases approximately linearly with increasing U_{ci} , this is not reflected on a cell-by-cell basis.

Table 2: Comparison of global coverage statistics

Statistic	Parameterisation (%)								
	U_{ci}	0.5	0.55	0.6	0.65	0.7	0.75	0.8	0.85
Maximum		92.9	92.5	92.1	91.5	90.8	89.9	88.8	87.2
Mean		30.3	28.5	26.6	24.7	22.8	20.9	18.9	16.8

Spatial plots for $U_{ci} = 0.5$ and $U_{ci} = 0.85$ are presented in Figures 3 and 4, respectively. These show that they have the same basic patterns but the structural details are different. For instance, low cirrus cloud coverage ($< 12\%$) was observed in both figures over the Pacific Ocean, west of Mexico. However, the low coverages from the $U_{ci} = 0.85$ test case extend further northwards onto the west coast of the United States when compared with the coverage produced using $U_{ci} = 0.5$.

Figure 3. Cirrus cloud coverage calculated from ERA-40 data using ECHAM parameterisation for test case $U_{ci} = 0.5$ Figure 4. Cirrus cloud coverage calculated from ERA-40 data using ECHAM parameterisation for test case $U_{ci} = 0.85$

The results of this sensitivity analysis demonstrate the importance of selecting an appropriate U_{ci} value for the meteorological dataset used. This value may influence the spatial distribution of cirrus coverage calculations and, therefore, the global mean coverage. A possible approach is to optimize the U_{ci} value to the high cloud field inherent in the ERA-40 dataset. Theoretically, the U_{ci} values

can be below 0.5 (the lower limit tested) and higher than 0.85 (the upper limit tested) (Walcek, 1994). Therefore, it is possible to further adjust U_{ci} for ERA-40 data to produce an optimized cloud distribution for regions with high aircraft movements.

4 CONCLUSIONS AND FURTHER WORK

Cirrus cloud coverage is an important parameter in estimating the uncertainties for contrail coverage as it is required to determine which fraction of a grid cell is available for potential contrail formation. There was good agreement between the cirrus cloud coverage calculated using the ECHAM cirrus cloud parameterisation and the dataset obtained from ISCCP. Spatial patterns from both sources were comparable with each other. However, computed coverages lacked the finer details that were observed in ISCCP data.

January 1999 ISCCP data did not have enough data capture (due to January being a winter month) for important contrail coverage regions such as high air traffic regions in North America and Northern Europe. Hence, a longer time period is necessary to yield an evaluation that serves the purpose of this study. There are also other data sources for cirrus climatology that can be used for such a comparison, such as SAGE and HIRS data (well established) and the University of Oxford's MIPAS and GRAPE datasets (under development). However, ISCCP is still the most widely used and commonly accepted dataset.

A sensitivity analysis on U_{ci} showed the importance of this parameter in determining cirrus coverages resulting from the parameterisation. The first step in the next stage of work is to optimize U_{ci} for the ERA-40 dataset to match its global high cloud dataset. Then, U_{ci} can be optimized for latitudes with high air traffic and then tested in other regions. Other planned further work includes comparison of calculated coverage using this new U_{ci} value; comparisons of different temporal statistics (diurnal, seasonal and inter-annual variations) and detailed comparisons over specific regions.

5 ACKNOWLEDGEMENTS

The authors wish to acknowledge the following data sources: ECMWF for supplying the ERA-40 reanalysis data; ISCCP data were obtained from the NASA Langley Research Center Atmospheric Science Data Center. LL Lim, DS Lee and R Ismail acknowledge funding by the UK Department of Transport.

REFERENCES

- Chen, C.T., and E. Roeckner, 1997: Cloud simulations with the Max-Planck-Institute for Meteorologie general circulation model ECHAM4 and comparison with observations. *J. Geophys. Res.* 102, 9335-9350.
- Penner, J.E., Lister, D.H., Griggs, D.J., Dokken, D.J., and McFarland, M. (eds.), 1999: *Aviation and the Global Atmosphere*. Intergovernmental Panel on Climate Change (IPCC), Cambridge University Press, UK. 373 pp.
- Ovarlez, J., P. van Velthoven, G. Sachse, S. Vav, H. Schlager, and H. Ovarlez, 2000: Comparison of water vapor measurements from POLINAT2 with ECMWF analyses in high-humidity conditions. *J. Geophys. Res.* 105, 3737-3744.
- Rossow, W.R., A.W. Walker, D.E. Beuschel, and M.D. Roiter, 1996: *International Satellite Cloud Climatology Project (ISCCP) documentation of new cloud datasets*. Science Systems and Applications Inc. at NASA Goddard Institute for Space Studies.
- Sausen, R., K. Gierens, M. Ponater, and U. Schumann, 1998: A diagnostic study of the global distribution of contrails Part 1: Present day climate. *Theor. Appl. Climatol.* 61, 127-141.
- Sundqvist, H., 1978: A parameterization scheme for non-convective condensation including prediction of cloud water content. *Q. J. R. Meteorol. Soc.* 104, 677-690.
- Walcek, C.J., 1994: Cloud cover and its relationship to relative humidity during a springtime midlatitude cyclone. *Monthly Weather Review* 122, 1021-1035

Simulation of Contrails in the vortex regime – Examination of the microphysical properties

S. Unterstrasser*, K. Gierens

DLR-Institut für Physik der Atmosphäre Oberpfaffenhofen, Germany

P. Spichtinger

ETH Zürich-Institut für Atmosphäre und Klima, 8092 Zürich, Switzerland

Keywords: Contrails, Numerical modelling

ABSTRACT: In the vortex regime the contrail development is governed by the wake dynamics. The major fraction of the ice crystals is trapped inside the downward travelling vortex pair. For ambient supersaturations below a certain threshold, none of the trapped crystals survive the vortex phase. Only crystals detrained during the descent form the contrail. The ambient relative humidity has a strong impact on the vertical extent of the contrail and on the number of surviving ice crystals, especially in the vortex. Contrail development during the vortex regime was modelled with ambient supersaturations ranging from 0% to 20%. The computationally cheap 2D-code permits a large number of simulations. A realistic vortex decay was ensured using parameterisations of 3D-simulations. The obtained results give detailed information on initial states for contrail-to-cirrus simulations.

1 INTRODUCTION

Contrails form when the Schmidt-Appleman criterion is fulfilled (Schumann, 1996). Contrails are persistent when the surrounding air is supersaturated with respect to ice. During the vortex phase the majority of the ice crystals is trapped in the counter-rotating vortex pair and is transported downwards. Inside the descending vortices, adiabatic compression/heating reduces the relative humidity and leading eventually to the sublimation of ice mass (Sussmann and Gierens, 1999; Lewellen and Lewellen, 2001). The final vertical displacement depends on the initial strength of the vortex (aircraft parameter) and on its decay (controlled by meteorological parameters like turbulence, stratification). We identify the parameters which predominantly control the number and the distribution of ice crystals surviving the vortex phase. The main parameter discussed here is relative humidity. Further important parameters are flight level (i.e. temperature), initial circulation, turbulence, stratification, aircraft parameters (their effect is not discussed here).

2 MODEL DESCRIPTION AND SETUP

The large-eddy simulations have been carried out with the non-hydrostatic anelastic 3D model EULAG (Smolarkiewicz and Margolin, 1997) which was supplemented with an ice microphysics code (Spichtinger, in prep). The parameterised microphysical processes are deposition growth/condensation and sedimentation. The simulations run on a 2D domain. The horizontal direction x is along wingspan and z is the vertical coordinate. The domain has an horizontal/vertical extent of $x_D=256\text{m}$ and $z_D=500\text{m}$ with 1m-resolution in each direction. The time step is $dt=0.02\text{s}$. The simulations start at the beginning of the vortex phase and end with vortex break-up after 135s. The aircraft properties typical of a large aircraft are implemented (initial circulation $\Gamma_0 = 650 \text{ m}^2/\text{s}$, wing span $b_{\text{span}}=60\text{m}$). The ice crystals are uniformly distributed in circles ($r=20\text{m}$) around the vortex

* *Corresponding author:* Simon Unterstrasser, DLR-Institut für Physik der Atmosphäre, Oberpfaffenhofen, D-82205 Wessling, Germany. Email: simon.unterstrasser@dlr.de

centres. The total emitted water ($1.46 \cdot 10^{-2}$ kg per m flight path) is contained in the ice crystals ($3.4 \cdot 10^{12}$ per m flight path). Furthermore, the nucleation of the ice crystals is assumed to be completed during the jet phase and no further nucleation is considered during the vortex phase. The temperature at cruise altitude is 222K. The pressure is $p_0=250$ hPa at the lower boundary. The atmosphere is stably stratified (Brunt-Väisälä frequency $N=10^{-2}$ s $^{-1}$) with an initially constant relative humidity with respect to ice. The supersaturation s_i ranges from 0% to 20%. The eddy dissipation rate is $3.5 \cdot 10^{-5}$ m 2 s $^{-3}$

3 VORTEX DYNAMICS

The decay of the vortex pair depends on meteorological parameters (stratification and eddy dissipation rate) as well as on aircraft parameters (initial circulation Γ_0 and initial vortex separation b_0). The vortex decay can be divided into two regimes. During the diffusion phase the vortex weakens independently of the latter parameters. After a certain onset time T_2 the rapid decay phase sets in. Generally, time T_2 is smaller and the rapid decay is faster for higher turbulence and for stronger stratification. The temporal evolution of Γ in dependence of the parameters mentioned above is given in Holzäpfel, 2003 (see Fig. 1, solid line).

In 2D-simulations the vortex decay is generally too slow as the Crow instability (the most efficient destructive process) is not resolved (see Fig. 1, dashed line). The diffusion coefficient in the simulations is artificially increased around the vortex cores and adapted each second in order to assure a realistic decay. The simulated circulation (see Fig. 1, dotted line) is in good agreement with the values given in Holzäpfel, 2003.

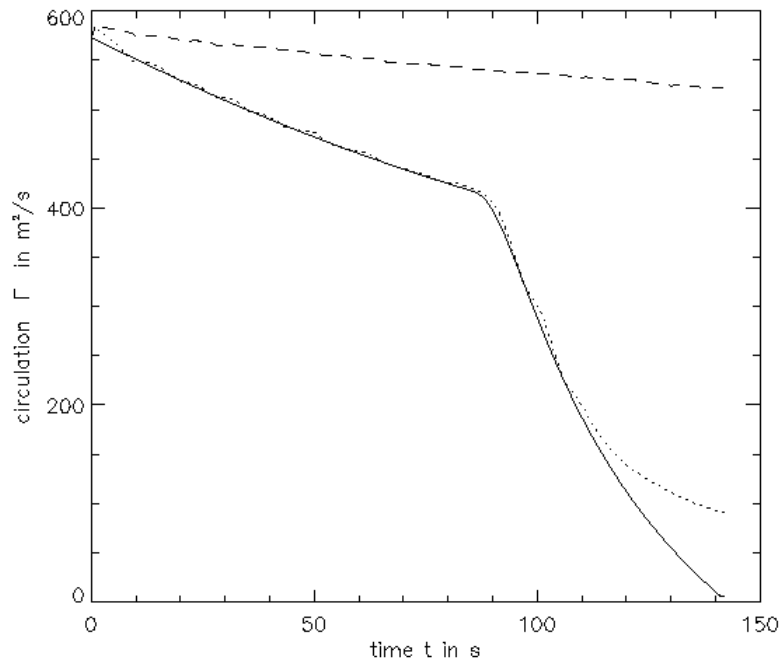


Figure 1: Temporal evolution of the circulation Γ

4 RESULTS

The total ice mass per flight path $tIWC$ [kg/m] is computed with the following integral.

$$tIWC = \iint IWC(x, z) dx dz$$

In order to determine the ice mass contained in the primary wake $pIWC$, the integral is restricted to 40m-circles around the vortex centres. The area of the secondary wake is one 50m-circle centred at the flight altitude in the middle of the domain (i.e the position that was crossed by the body of the aircraft). The according integral quantity is called $sIWC$. Analogously, the number of ice crystals in the different areas (tN, pN, sN) is determined. In some figures, the latter quantities are normalised by

the initial ice mass or crystal number, resp. These quantities tell us which fraction of ice mass and crystals is still present after a certain time. In general, the contrail loses a major part of its crystals in the primary wake. At the beginning of the simulation, the areas of the primary and the secondary wake overlap. At later times, there is a vertical gap, as the vortex pair travelled downwards. The amount of ice in the so-called curtain (i.e. the vertical stripe between the vertically displaced vortex and flight altitude) can be determined by $tIWC$ - $pIWC$ - $sIWC$.

The temporal evolution of the normalised quantities is shown in Figure 2. The temperature at cruise altitude is $T_{CA}=222K$ and the relative humidity RH_i is 105%.

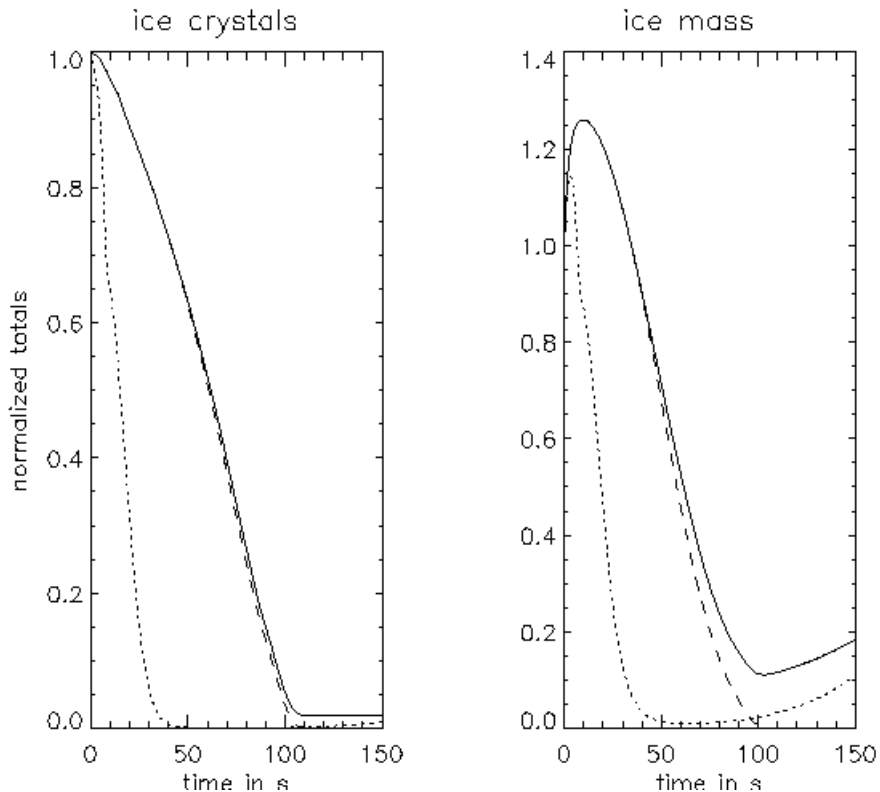


Figure 2: left panel: temporal evolution of the number of ice crystals in the total area tN (solid line), in the primary wake pN (dashed line) and in the secondary wake sN (dotted line). Right panel: Analogously for ice mass. The ambient supersaturation was 5%.

Initially, $tIWC$ increases due to deposition growth of the ice crystals until the excess moisture from ambient supersaturation is consumed. During the downward transport the local RH_i in the vortices decreases due to adiabatic heating and the number of ice crystals declines in the primary wake. Later the minor number of crystals in the secondary wake becomes significant, as these crystals steadily grow. Figure 3 shows the vertical profiles of ice mass and crystals at vortex break-up time $t=135s$. The profiles are shown for various relative humidities (100%, dotted; 105% dashed; 110% dash-dotted; 120% dash-dot-dotted). Again, the temperature is 222K.

The initial ice crystal distribution was centred around $z=400m$ (solid line). After 135s the vortex pair travelled below $z=200m$. A substantial fraction of the trapped ice crystals survives only for high supersaturation ($s_i \geq 10\%$). This threshold s_i -value depends on vortex break-up time, descent speed and temperature. It can be concluded that the mean ice crystal mass in the primary wake is smaller than in the secondary wake at the end of the vortex phase. The earlier the crystals are detrained and mix with ambient air, the larger they are. The moister it is, the larger is the vertical extent of the contrail and the more ice crystals survive the vortex phase.

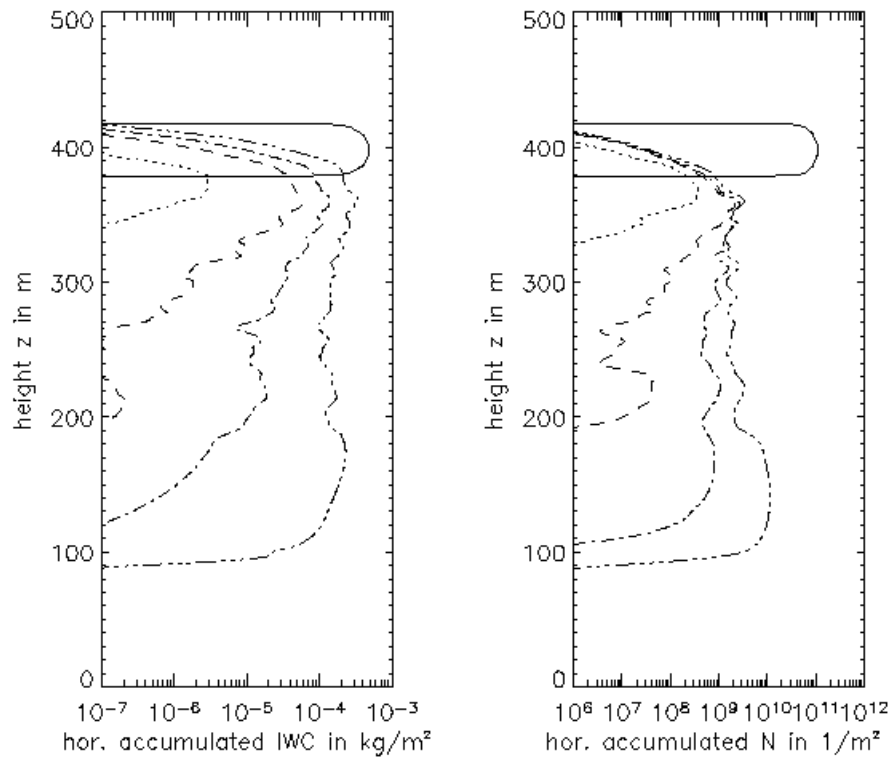


Figure 3: vertical profiles of ice mass (left) and crystals (right) for various supersaturations s_i (0%, dotted; 5% dashed; 10% dash-dotted; 20% dash-dot-dotted).

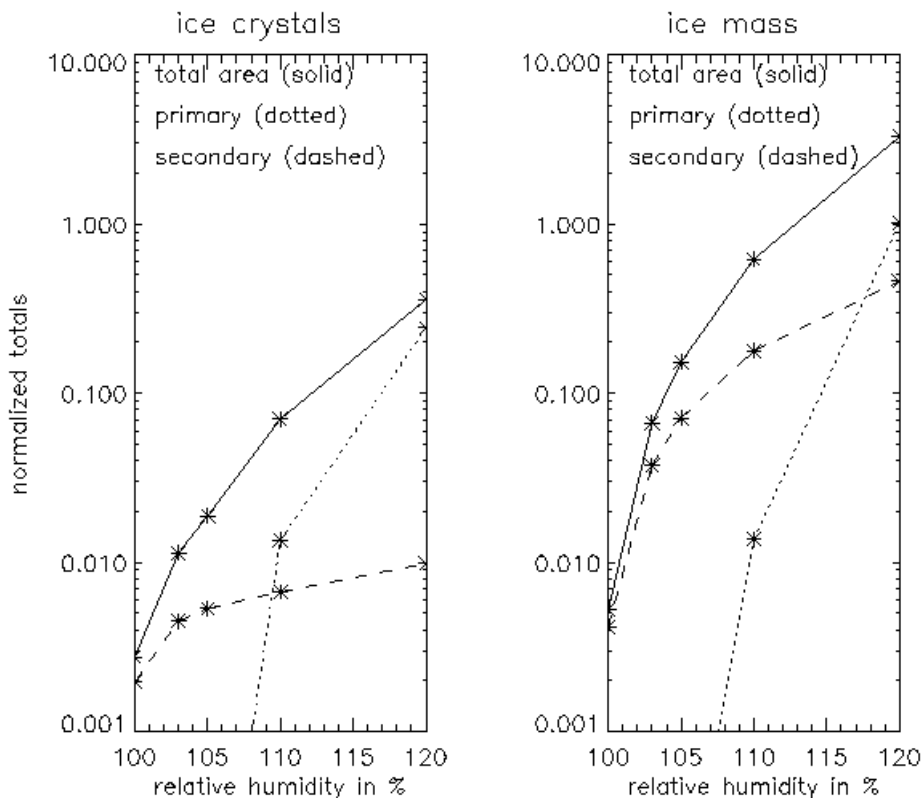


Figure 4 left panel: Normalised totals of surviving ice crystals tN, pN and sN as a function of RH_i . Analogously, the surviving ice mass on the right hand side.

Figure 4 shows the normalised totals of ice mass/crystals at the time of vortex break-up as a function of RH_i . In all cases, the normalised number of surviving crystals is below unity. Not surprisingly, a moister environment is favourable for less ice crystal loss. The normalised tN ranges from 40% at $s_i = 20\%$ to less than 1% at $s_i = 0\%$. The number of ice crystals in the secondary wake sN is

weakly dependent of humidity and nearly all crystals which were not trapped inside the initial vortex pair survive, as long as the ambient relative humidity $RH_i \geq 100$. Generally, the fraction of crystals in the secondary wake increases relative to the primary wake with decreasing supersaturation. The right panel of Figure 4 shows the normalized value of surviving ice mass. It is apparent, that the ice mass in the secondary wake increases with relative humidity, as more excess moisture condenses on the crystals. At high supersaturation a major part of the ice mass is inside the secondary wake, although less than 1% of the crystals are detrained in the beginning.

At vortex breakup time, the total ice mass and number of crystals present as a function of RH_i can be fitted with a power law $a \cdot (RH_i - b)^\alpha$. The exponent α is roughly 3 for the present simulations, but it may depend on other meteorological variables.

5 CONCLUSION/ACKNOWLEDGEMENTS

Relative humidity was identified as one key parameter for the microphysical properties of a contrail at the end of the vortex phase. The number of surviving ice crystals grows with supersaturation. In cases with $RH_i \leq 110\%$, the total IWC after 135s was below the initial level. The vertical profile of the ice crystal distribution strongly depends on RH_i and the concentration and the mass of the crystals is different for the primary and secondary wake. Many more parameters (as given in the introduction) can be studied with the existing code. Especially, the variation of temperature has also an major impact on the contrail properties. The presented results will be used as initial states for simulations of the dispersion phase. This will help to understand and simulate the contrail-to-cirrus transformation.

We want to thank Andreas Dörnbrack for help with EuLag and for many fruitful discussions. We further acknowledge stimulating discussions with Bernd Kärcher, Thomas Gerz and Frank Holzäpfel. The simulations were carried out on the high computing facilities at the ECMWF (special project “Ice supersaturation and cirrus clouds”).

REFERENCES

- Lewellen, D.C., W.S. Lewellen, 2001: The effects of Aircraft wake Dynamics on Contrail Development, *J Atmos. Sci.*, 58, 390-406
- Schumann, U., 1996: On conditions for contrail formation from aircraft exhausts, *Meteor. Z.*, 5, 4-23
- Smolarkiewicz, P.K., G.Margolin, 1997: On Forward-in-time Differencing for Fluids: An Eulerian/Semi-Lagrangian Non-hydrostatic Model for Stratified Flows, *Atmos. Ocean Special*, 33, 127-152
- Sussmann, R., K. Gierens, 1999: Lidar and numerical studies on the different evolution of vortex pair and secondary wake in young contrails, *J. Geophys. Res.*, 104, 2131-2142

Homogeneous freezing of ice particles, including effects of aerosol size distribution in the University of L'Aquila CCM

G. Pitari*, D. Iachetti and V. Montanaro
Department of Physics, University of L'Aquila, Italy

Keywords: homogeneous freezing, aerosol size effects.

ABSTRACT: The numerical code developed by Kärcher and Lohmann [*JGR 2002*], for the parametrization of cirrus cloud formation via homogeneous freezing of supercooled aerosols is introduced on-line in the climate-chemistry coupled model of the University of L'Aquila (ULAQ-CCM). In this paper we briefly describe the parameterization adopted and the model results for the basic quantities (updraft velocities, particle size distributions, top of the atmosphere radiative fluxes). A future application will be to calculate the radiative forcing due to ice particle perturbations produced by aircraft induced changes of the aerosol size distribution.

1 INTRODUCTION.

A low resolution climate-chemistry coupled model, including a microphysics code for aerosols formation and growth, is used to study ice particle formation in cirrus clouds, including the effects of the aerosol size distribution. The parameterization used is that for homogeneous freezing of supercooled aerosols of Kärcher and Lohmann [*JGR 2002a*], extended to include the effects of aerosol size on the freezing process in adiabatically rising air particles [*Kärcher and Lohmann, JGR 2002b*]. Homogeneous freezing is considered as the most important ice formation mechanism under upper tropospheric conditions. The adiabatic cooling due to the vertical ascent rate is the key parameter determining the population of ice particles (number density and radius). For this reason, in order to have a realistic representation of small-scale freezing, the vertical velocities field used in the ice-formation code is the sum of the large scale vertical velocity (almost negligible) and a small-scale term, calculated as a function of the turbulent kinetic energy. Changes of the aerosol size distribution can modify the homogeneous freezing process when the timescale of the freezing event is fast (low temperatures and high vertical velocities).

We present here the results of the ULAQ-CCM about the feedback of the aerosol size distribution on the mechanism of formation and growth of ice particles in the UT/LS region, obtained with the two parameterizations (with/without impact of the aerosol size distribution). We also show preliminary results on the top of atmosphere radiative fluxes due to ice cloud particles in the UT/LS.

2 DESCRIPTION OF THE MODEL.

The ULAQ model is a low-resolution three-dimensional (3D) climate-chemistry coupled model (CCM). The chemical-transport module uses a $10^\circ \times 22.5^\circ$ grid in latitude-longitude (19 latitudes and 16 longitudes) and 26 log pressure levels, from the ground to about 0.04 hPa, with an approximate spacing of 2.84 km. Dynamical fields (streamfunction, velocity potential and temperature) are taken from the output of a spectral general circulation climate model GCM [*Pitari et al., JAS 2002*], which is in turn coupled to the CTM via the radiatively active species (O_3 , H_2O , WMGHGs and aerosols). The vertical velocity is calculated from the horizontal divergence. A flux-form Eulerian fully explicit advection scheme is used, with 1 h time step, used for both dynamics and chemistry. Relative humidity, warm cloud distribution and net precipitation rates are taken from climatological data. A vertical diffusion coefficient K_{zz} is used to simulate those transport processes not explicitly included in the model. The scheme adopted for tropospheric deep convection takes inspiration from

* *Corresponding author:* Giovanni Pitari, Università degli Studi de L'Aquila, Dipartimento di Fisica, via Vetoio, 67010 Coppito, L'Aquila, Italy. Email: gianni.pitari@aquila.infn.it

that described in Muller and Brasseur [JGR 1995]: the rate at which a chemical compound is transported at a given altitude in the free troposphere is calculated as a function of a convective uplift rate and the species mixing ratio in the boundary layer.

The main removal processes of aerosol particles parameterized in the model are wet deposition, dry deposition and sedimentation. ULAQ model includes the major components of tropospheric aerosols (sulphates, carbonaceous, soil dust, sea salt). Aerosol particles are divided in size bins and each one is separately transported. Surface fluxes of SO₂, DMS, black carbon, organic carbon and mechanically generated particles are those provided for Experiment B of the AEROCOM international assessment campaign [Textor et al., ACP 2006].

The parameterization of homogeneous freezing by Kärcher and Lohmann [JGR 2002a and 2002b], (K & L hereafter) was derived from first principles, based on the supersaturation and ice crystal growth equations. In contrast to previous parameterizations, this scheme considers the basic physical processes that eventually determine the number of ice crystals N_i forming during an adiabatic ascent, including the dependences of N_i on temperature and updraft speed. In particular, it was found that this dependence is quite insensitive to details of the aerosol size distribution in many cases, but increases rapidly with updraft velocity and decreases with temperature. In the reference simulation HOM, the number of frozen ice crystals formed via homogeneous freezing, at temperatures below 235 K is obtained as:

$$N_i^{HOM} = \min \left[\frac{m_w}{\rho_i} \left(\frac{b_2}{2\pi b_1} \right)^{\frac{3}{2}} \frac{a_1 S_{cr}}{a_2 + a_3 S_{cr}} \cdot \frac{\omega}{\sqrt{\tau}}; N_a \right] \quad (1)$$

where m_w is the molecular weight of water, ρ_i is the ice crystal density (=925 kg m⁻³), S_{cr} is the critical supersaturation ratio, where freezing starts, ω is the updraft velocity, $\tau \propto l/\omega$ is the characteristic time scale of the nucleation event and $a_1, a_2 = l/N_{si}, a_3, b_1 \propto N_{si}(S_{cr}-1), b_2$ are temperature-dependent variables, N_{si} denotes the water vapor number density at ice saturation, depending on temperature. Note that the nucleation rate is limited by the number of hygroscopic aerosol particles N_a defined as:

$$N_a = N_{seasalt} + N_{BC}^{phil} + N_{OC}^{phil} + N_{dust} + N_{SO_4} \quad (2)$$

If the effects of the aerosol size are not taken into account, one can deduce the approximate scaling relationship :

$$N_i^{HOM} \propto \omega^{3/2} N_{si}^{-1/2} \quad (3)$$

The mesoscale updraft velocity ω is obtained as the sum of the large scale vertical velocity and a small scale term, calculated as a function of the turbulent kinetic energy TKE [Abdella and McFarlane, JGR 1997]:

$$\omega = \bar{\omega} + 0.7\sqrt{TKE} \quad (4)$$

In deriving (3), K & L argued that aerosol size effects on the homogeneous freezing process are unimportant whenever the initial growth time scale of ice particles is shorter than the time scale of the nucleation event (fast growth regime). Here the number of ice crystals is independent of the initial aerosol size.

Aerosol size effects (simulation HOM-Size) are important in the slow growth regime, characterized by high vertical velocities and cold temperatures; the freezing growth term becomes considerably more complicated. Assuming a monodisperse aerosol particle size distribution:

$$N_i^{HOM-Size} \propto a_1 S_{cr} \cdot \omega \cdot \frac{N_{si}}{R_{i,m}(r_0)} \quad (5)$$

where $R_{i,m}(r_0)$ is the monodisperse freezing/growth integral explained by K & L, that depends on the initial particle radius r_0 . The parameterization scheme considers a multimodal aerosol size structure, with four modes, each one characterized by a lognormal distribution curve. Consequently, the parameterization is called by the ULAQ model with the mean radius, number density and geometric width for each mode.

Short wave (SW) top of the atmosphere radiative fluxes are calculated as the top-of-atmosphere solar flux changes due to ice crystals, using a multi-layer δ -Eddington approximation. To evaluate long wave (IR) fluxes, we use pre-calculated tropopause IR fluxes, scaled with appropriate σT^4 for absorption/emission, as described in Lacis and Hansen [JRL 1992]).

3 RESULTS AND DISCUSSION.

The simulations were conducted over a period of 5 years after an initial spin-up of 5 years using climatological sea surface temperature (Hadley Center data). As the reference simulation HOM does not take into account the effects of aerosol size, the simulation HOM-Size includes aerosol size effects.

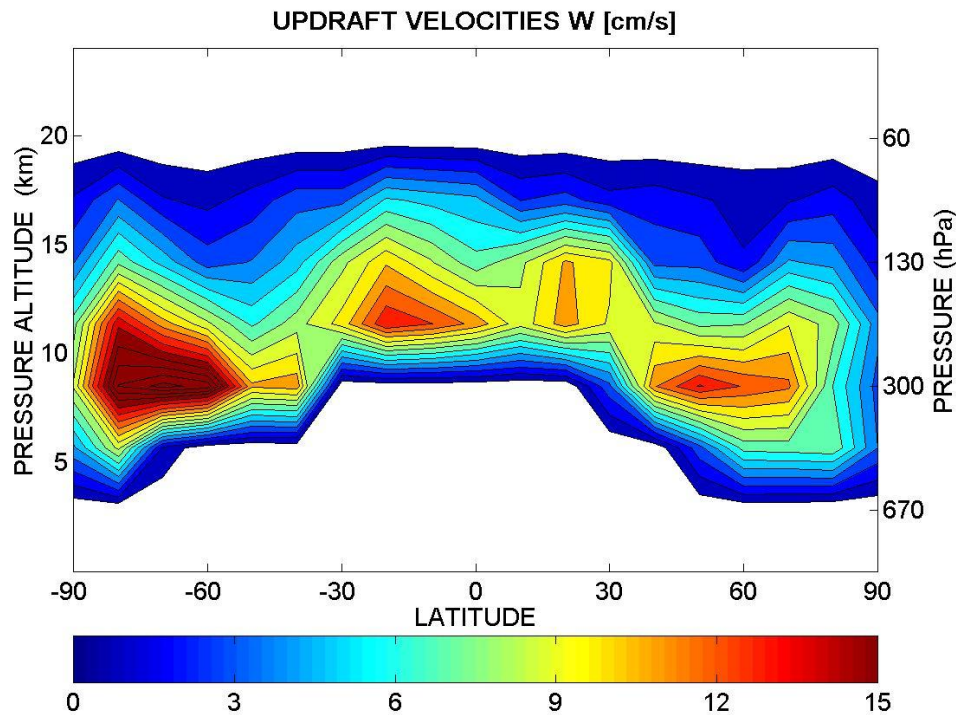


Figure 1: zonally and annually averaged background updraft velocities [cm/s].

Figure 1 shows the mesoscale updraft velocities calculated in the model as a function of the turbulent kinetic energy: typical values in the upper troposphere are in the 10–15 cm/s range. As shown by K & L [JGR 2002a], the vertical velocities play a critical role for the adiabatic cooling and the formation of ice crystals. The expected number density and size of the particles are $0.1\div 1\text{ cm}^{-3}$ and $3\div 20\text{ }\mu\text{m}$, respectively. This is confirmed by the calculated ice crystal number and mass density size distributions shown in Figure 2.

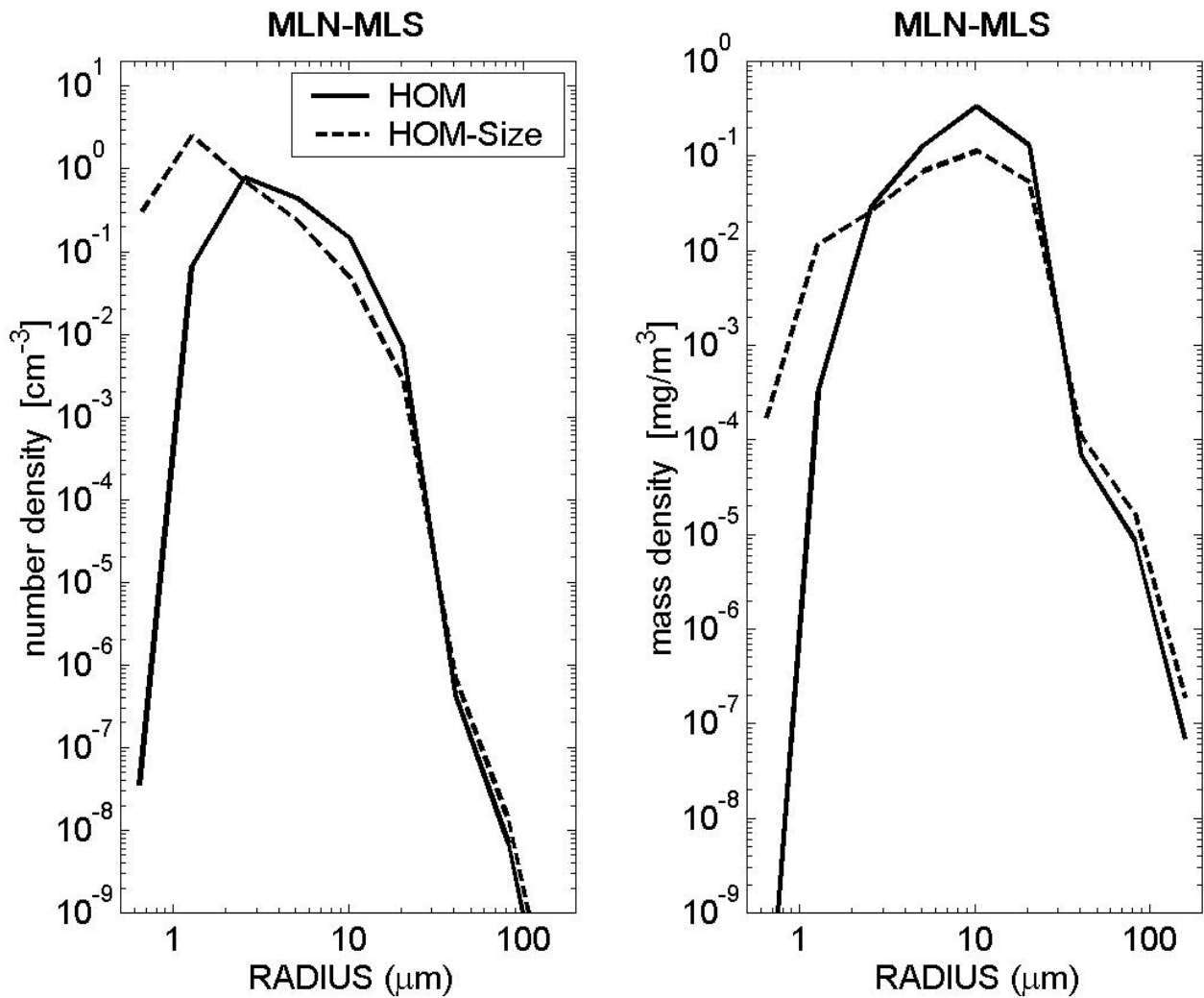


Figure 2: ice crystals number density [cm^{-3}] and mass density [mg m^{-3}] size distributions at mid latitudes (average of Northern Hemisphere (MLN) and Southern Hemisphere (MLS) values). Solid and dashed lines are for HOM and HOM-Size simulations, respectively.

Here we see that the effects of the aerosol size distribution is to increase the number density of particles smaller than $3 \mu\text{m}$. For this reason the difference HOM-Size – HOM gives an increase of the total number concentration of ice crystals ($1 \div 5 \text{ cm}^{-3}$), as shown in Figure 3.

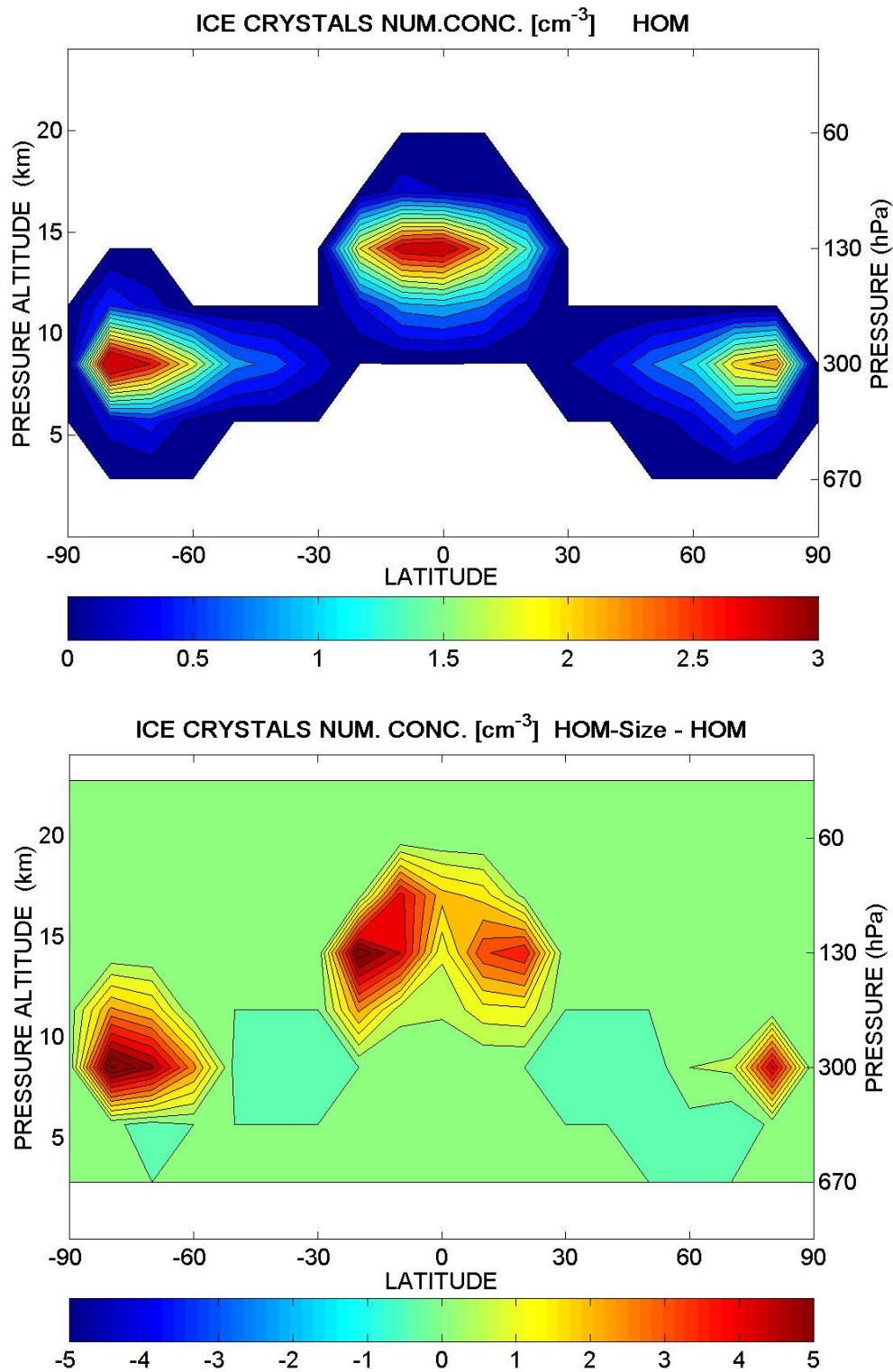


Figure 3: zonally and annually averaged ice crystals number densities for simulation HOM (top panel) and the difference between simulations HOM-Size and HOM (bottom panel), [cm⁻³].

The key role of the vertical ascent rate for the adiabatic cooling and water vapour freezing is clear when comparing Figure 1 and 3a.

A preliminary calculation of radiative flux changes due to ice particles is presented in Figure 4. Additional refinements are needed here for the infrared fluxes (since we use pre-calculated fluxes of IR absorption/emission) which are appropriate for H₂O-H₂SO₄ mixtures.

These radiative calculation will soon be used to estimate the radiative forcing produced by ice particle size distribution changes due to aircraft induced aerosol size distribution perturbations.

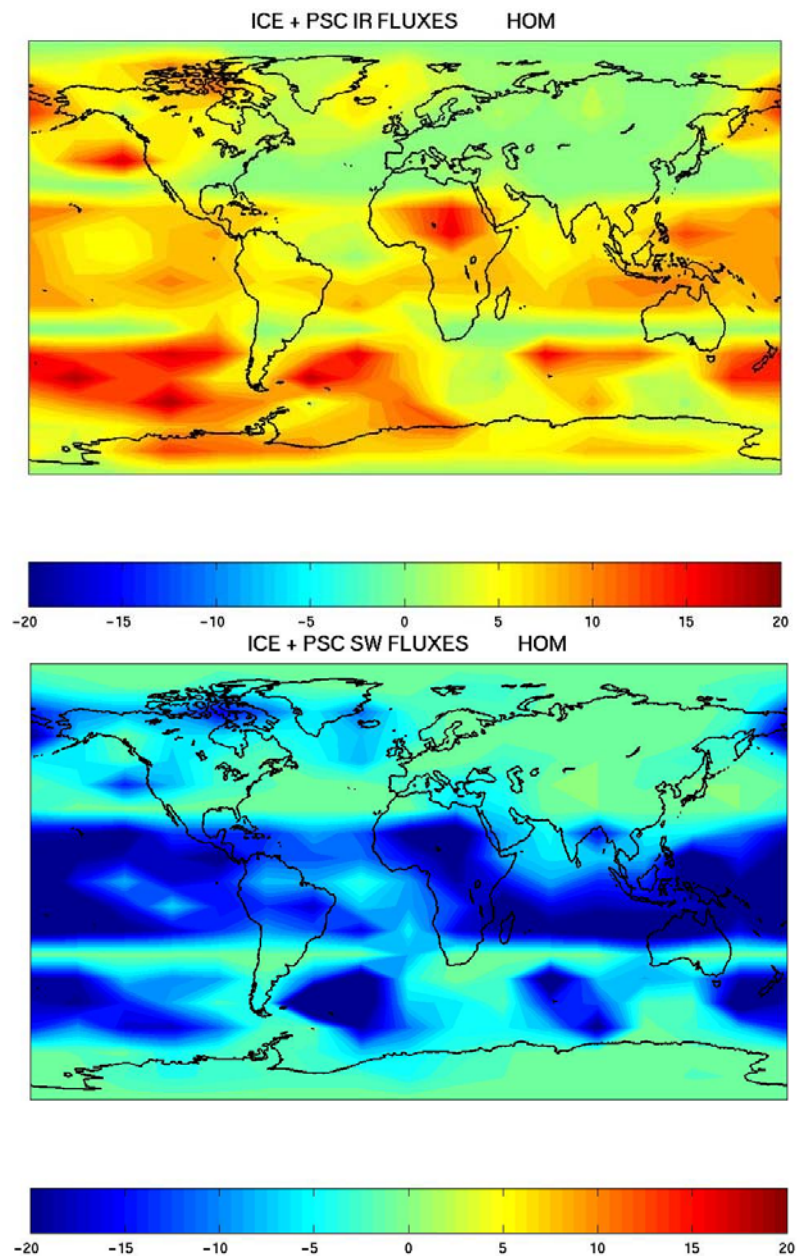


Figure 4. Geographical distribution of annually averaged top of the atmosphere IR fluxes (top panel) and solar fluxes (bottom panel), due to ice particles in the UT/LS [mW/m^2]. Results are for the simulation HOM.

REFERENCES

- Abdella K., and N. McFarlane, 1997: A new Second order turbulence closure scheme for the planetary boundary layer, *J. Geophys. Res.*, *54*, 1850 – 1867.
- Kärcher, B., and Lohmann, U., 2002a: A parameterization of cirrus cloud formation: homogeneous freezing of supercooled aerosols, *J. Geophys. Res.*, *107*, 4010, 10.1029/2001JD000470.
- Kärcher, B., and Lohmann, U., 2002b: A parameterization of cirrus cloud formation: homogeneous freezing including effects of aerosol size, *J. Geophys. Res.*, *107*, 4698, 10.1029/2001JD001429.
- Lacis, A., J. Hansen, and M. Sato, 1992: Climate forcing by stratospheric aerosols. *Geophys. Res. Lett.*, *19*, 1607-1610.
- Muller, J.-F. and G. Brasseur, 1995: A Three Dimensional Transport Model of the Global Troposphere, *J. Geophys. Res.*, *100*, 16445 – 16490.
- Pitari, G., E. Mancini, V. Rizi, and D. T. Shindell, 2002: Impact of future climate and emissions changes on stratospheric aerosols and ozone, *J. Atmos. Sci.*, *59*, 414-440.
- Textor, C., M. Schultz et al., 2006: Analysis and quantification of the diversities of aerosol life cycles within AeroCom, *Atmos. Chem. Phys.*, *6*, 1777-1813.

Calculating contrail radiative forcing with the Edwards-Slingo radiative transfer code

R. Rodriguez De León*, D. S. Lee

Dalton Research Institute, Department of Environmental and Geographical Sciences, Manchester Metropolitan University, UK

Keywords: radiative transfer, optical properties, ice crystals, particle size distribution, hexagonal cylinders

ABSTRACT: The Edwards-Slingo radiative transfer code has been used to examine the radiative forcing that might arise from contrails. A set of conditions as used by Meerkötter et al. (1999) provided a convenient benchmark for the results. The assumption of a hexagonal cylinder habit was tested with the Edwards-Slingo code and compared to Meerkötter et al.'s (1999) spheroidal approximation to hexagonal cylinders. Overall, a more realistic assumption of hexagonal crystals resulted in a smaller net forcing than if spherical particles or spheroidal approximations are assumed.

4 INTRODUCTION

Persistent line-shaped contrails induced by air traffic have been estimated to cover at least 0.5% of central Europe's skies at noon (Mannstein et al., 1999). Under favourable temperature and humidity conditions, these clouds can expand in their vertical and horizontal extent to become contrail-cirrus, potentially increasing their influence on the planet's radiative balance (IPCC, 1999; Stordal et al., 2005). Meerkötter et al. (1999) (hereafter M99) found that in all the relevant study areas contrails enhance the "greenhouse effect" because they reduce outward longwave fluxes more than they increase reflected shortwave fluxes. The balance between these opposite effects depends upon the characterization of macro- and micro-physical properties of contrails, which represents a significant challenge for both measurements and theoretical modelling.

The microphysical properties of young contrails are likely to depend in a non-trivial way on the dynamics and thermodynamics of the atmosphere-engine system. Line-shaped contrails, like young cirrus, are mostly composed of small particles, which do not deviate largely from a spherical geometry; but as a persistent contrail ages, its particles may acquire more complex non-spherical habits.

In this study the Edwards-Slingo (E-S) radiative transfer code (Edwards and Slingo, 1996) was used for the first time to study contrails by incorporating into it a new radiative parameterization based on the optical properties of hexagonal cylinders. The instantaneous or static radiative forcing of a 200 metres contrail layer is presented and compared with M99's results.

5 METHODOLOGY

As a guiding principle, we use the model conditions described by Meerkötter et al. (1999) since they used three different radiative transfer codes and provided a useful 'benchmark' which includes seven cases for the cloud's microphysics (particle size), macrophysics (cloud ice water content, cloud thickness and cloud height) and the environment's physics (seasonal temperature profile and surface albedo). Following M99, the simulations were run to calculate the daily mean (24 h) net

* *Corresponding author:* Rubén Rodríguez De León, Department of Environmental and Geographical Sciences, Faculty of Science and Engineering, John Dalton Building, Chester Street, Manchester, M1 5GD. Email: r.deleon@mmu.ac.uk

forcing caused by a 200 metres thick contrail layer. We used hexagonal cylinders as a representative habit, for which the optical properties were taken from Yang et al. (2000) in the shortwave (SW) and from Baran et al. (2002) in the longwave (LW) regions of the spectrum.

In the following section our results for hexagonal cylinders are compared with M99's results for equivalent spheroids and equivalent spheres using his suggested contrail size distribution, corresponding to a generalized size (Fu, 1996) of 29.2 micrometres.

Table 1. Daily mean (24 h) radiative flux changes at the top of the atmosphere (TOA, 50 km) in $W m^{-2}$ for hexagonal cylinders (first entry) integrated over Strauss et al's (1997) contrail size distribution. For comparative purposes the calculations from Meerkötter et al. (1999) for spheroids and spherical particles are also presented (second and third entries).

Region	Albedo	IW C	Cloud Top (km)	Shape	Effective size (microns)	SW Wm^{-2}	LW Wm^{-2}	NET Wm^{-2}
a) Midlatitude summer continent 45°N	0.2	21	11	Hex-cyl	29.2	-18.7	38.4	19.7
				Spheroids	29.2	-22.0	51.5	29.5
				Spheres	29.2	-13.4	51.6	38.2
b) Midlatitude winter continent 45°N	0.2	7.2	11	Hex-cyl	29.2	-5.5	9.6	4.0
				Spheroids	29.2	-4.6	18.3	13.7
				Spheres	29.2	-4.2	18.4	14.2
c) Midlatitude winter continent with snow, 45°N	0.7	7.2	11	Hex-cyl	29.2	-2.6	9.6	7.0
				Spheroids	29.2	-2.0	18.3	16.3
				Spheres	29.2	-2.3	18.4	16.1
d) North Atlantic summer ocean 55°N	0.05	21	11	Hex-cyl	29.2	-21.1	38.4	17.2
				Spheroids	29.2	-32.7	50.9	18.2
				Spheres	29.2	-21.5	53.3	31.8
e) Tropical ocean (Equator, June)	0.05	23	11	Hex-cyl	29.2	-27.6	51.8	24.2
				Spheroids	29.2	-25.9	57.4	31.5
				Spheres	29.2	-16.0	63.0	47.0
f) Subarctic summer ocean 62°N	0.05	28.2	9	Hex-cyl	29.2	-45.8	38.6	-7.2
				Spheroids	29.2	-45.3	49.1	3.7
				Spheres	29.2	-30.8	55.7	24.9
f) Subarctic winter ocean ice 62°N	0.7	7.2	9	Hex-cyl	29.2	-0.7	8.9	8.2
				Spheroids	29.2	-0.7	13.2	12.5
				Spheres	29.2	-0.6	14.6	14.0

6 RESULTS

The calculated shortwave (SW), longwave (LW) and net (SW+LW) radiative forcings arising from a 200 metres thick contrail layer represented by hexagonal cylinders are presented in Table 1 (top entry of each row) together with M99's results for spheroids and spheres (second and third entries, respectively). All cases were calculated using the contrail particle size distribution suggested by M99 (e.g. Strauss et al., 1997) corresponding to a generalized size (Fu, 1996) of 29.2 microns. The differences are only linked to the particle shape adopted and show that the LW forcing is proportional to the particle's sphericity. Given this proportionality and the fact that any other shape will represent an intermediate case between a sphere and a column, it is understood that any other habit used as a representative shape to model contrails will produce net forcings between the values

given by our hexagonal cylinder and M99's spherical calculations. The spherical case was chosen by M99 as their best estimate, but given that the purpose of our study is to find representative forcings for persistent contrails, it seems sensible to consider values closer to the hexagonal case than to the spherical one.

The contrail RF is influenced by the latitude in various ways, in the SW through the daytime length, in the LW through the humidity profile and the temperature difference between the surface, and in both cases through the altitude at which the necessary conditions for contrail formation are met. Taking into account all these factors it is not unexpected to obtain differences in the net RF between cases d) and f), both with summer-ocean conditions but with different latitude profiles, cloud heights and ice water contents. These differences are important because for the hexagonal calculations they produce a negative net forcing in the subarctic region, which was not predicted when applying the other habits. Using an IWC value equal to 21 mg m^{-3} in case f) produces 30.4 (LW), -36.2 (SW) and -5.8 (NET) Wm^{-2} forcings, showing that the height of the contrail and atmospheric profile in which we place it have a larger influence on the sign of the net forcing than the IWC.

7 CONCLUSIONS

The E-S radiative transfer code has been shown to be suitable for undertaking calculations of contrail radiative forcing. The results are sensitive to the assumptions about the representative shape and size distribution of contrail particles, which may depend on the contrail's age. Hexagonal cylinders present smaller LW forcings, which translate in smaller net forcings, and may become negative at high latitudes with small albedos

On balance, it would seem more realistic to use the hexagonal parameterization facilitated by the E-S model in both SW and LW domains; the results obtained here would indicate a smaller net forcing than if spherical particles are assumed.

Future work will focus on integrating these results into a global model of the impact of contrails on the planet's radiative balance.

REFERENCES

- Baran, A. J., S. Havemann, and D. Mackowsky, 2002: A database of hexagonal column optical properties for wavelengths ranging between 0.2 to 30 microns produced for ANNEX, Contract no 4b/3/02, DEFRA, UK.
- Edwards, J. M., and A. Slingo, 1996: Studies with a flexible new radiation code. I: Choosing a configuration for a large-scale model. *Quarterly Journal of the Royal Meteorological Society*, 122, 689–719(31)
- Fu, Q., 1996: An accurate parameterization of the solar radiative properties of cirrus clouds for climate models. *Journal of Climate*, 9, 2058–2082.
- Fu, Q. and K. N. Liou, 1993: Parameterization of the radiative properties of cirrus clouds. *Journal of Atmospheric Science*, 50, 2008–2025.
- IPCC, 1999: Aviation and the Global Atmosphere. J. E. Penner, D. H. Lister, D. J. Griggs, D. J. Dokken and M. McFarland (Eds). Special Report of the Intergovernmental Panel on Climate Change, Cambridge University Press, Cambridge.
- Mannstein, H., R. Meyer, and P. Wendling, 1999: Operational detection of contrails from NOAA-AVHRR-data, *International Journal of Remote Sensing*, 20(8), 1641–1660.
- Meerkötter, R., U. Schumann, D.R. Doelling, P. Minnis, T. Nakajima, Y. Tsushima, 1999: Radiative forcing by Contrails. *Annales Geophysicae*, 17, 1080–1094.
- Stordal F., G. Myhre, E. J. G. Stordal, W. B. Rossow, D. S. Lee, D. W. Arlander and T. Svenby T., 2005: Is there a trend in cirrus cloud cover due to aircraft traffic? *Atmospheric Chemistry and Physics* 5, 2155–2162.
- Strauss, B., R. Meerkötter, B. Wissinger, P. Wendling, and M. Hess, 1997: On the regional climatic impact of contrails: microphysical and radiative properties of contrails and natural cirrus clouds. *Ann. Geophysicae*, 13, 1457–1467.
- Yang, P., K. Liou, D. Wyser and D. Mitchell, 2000: Parameterization of the scattering and absorption properties of individual ice crystals. *Journal of Geophysical Research*, 105(D4), 4699–4718.

Pedestrian exposure to vehicle emissions: the role of traffic signal timings

Muhammad M. Ishaque, R.B. Noland*
Imperial College London, UK

Keywords: pedestrian, micro-simulation, air quality, VISSIM, CMEM, CAL3QHC

ABSTRACT: This paper analyses pedestrian exposure to vehicle emissions and the role played by signal timings. A simple junction is coded in a micro-simulation model and time series data on vehicle performance, i.e., speed and acceleration is generated for various signal time settings. This data is then used to calculate vehicle emissions with a modal emissions model. The effects of these emissions on the pedestrian paths and crossings adjacent to the traffic junction are then estimated using an air dispersion model. The suitability of various traffic signal plans in terms of pedestrian exposure to harmful vehicular emissions is discussed.

1 INTRODUCTION

The present work is an endeavour to measure Carbon Monoxide (CO) exposure of waiting pedestrians at pedestrian crossings on a traffic intersection and the effect of different signal timings. The objective is to relate signal timings to pedestrian exposure in addition to pedestrian delay and is a continuation of research work by the authors analysing various MOE (measures of effectiveness) trade offs between vehicular and pedestrian traffic from changing traffic management policies. Previous work has shown that the signal timings designed to facilitate vehicle flow, minimising vehicle delay and providing only minimum time for pedestrians might not be the optimal solution when relative values of time are taken into account and pedestrian volumes are high (Ishaque and Noland, 2005a; 2005b). That work, however, did not consider vehicle emissions, to which pedestrians are exposed, as a measure of effectiveness and this paper attempts to fill that gap in the previous research.

This work relies heavily on various simulation models for experimenting with signal timings under controlled conditions and for estimation of emissions and dispersion of pollutants. The simulation models used are all well known models that have been repeatedly used, validated and documented. VISSIM is used for traffic simulations for generating vehicle performance data, CMEM is used for generating vehicle emissions and CAL3QHC for CO dispersion.

2 METHODOLOGY

Vehicle flow data was collected in 15 min. increments for the morning peak hour in October, 2005 at a busy traffic intersection (Baker Street and Marylebone Road) in London. The layout of the intersection is shown in Figure 1. Simulations were carried out for a comprehensive range of wind speed and headings. Data was also collected on traffic composition by mode, signal timings, intersection geometry, queue discharge rate and crossing pedestrian flows. The intersection was coded in VISSIM micro-simulation software as an isolated traffic intersection. The signal timings were changed in increments of 10 sec. The signal changes consisted of changing the times available to traffic on the Marylebone Road (except for right turning traffic in the eastbound direction). Timings for Baker Street were constant for all signal cycles. The traffic flow was also kept constant.

* *Corresponding author:* Robert B. Noland, Centre for Transport Studies, Department of Civil and Environmental Engineering, Imperial College London, UK. Email: r.noland@ic.ac.uk

The coded model was calibrated to result in the same mean queue discharge rate as was observed in the field. An initial simulation run was carried out with a signal cycle length of 96 sec. as was observed during high flow rates on site. Based on changes in vehicle velocity and acceleration, the journey distance was divided into five zones.

Pedestrian crossings were stretched to 4 m beyond the curb to include pedestrian waiting time in the road crossing travel time. Pedestrians were coded with default VISSIM pedestrian parameters as no-interaction type; where pedestrian movements are not influenced by the presence of other pedestrians. The pedestrian speed range was coded as 50 to 100 percentile speed for adult pedestrians on road crossings as given by Sjøstedt (1967) to give a minimum speed of 1.4 m/s which corresponded to the pedestrian behaviour observed in the morning peak hour. Pedestrian compliance to traffic signals was also coded in line with field observations and the simulated pedestrian phase was extended to 1 sec. before and half the clearance interval after the actual pedestrian green phase on all pedestrian crossings.

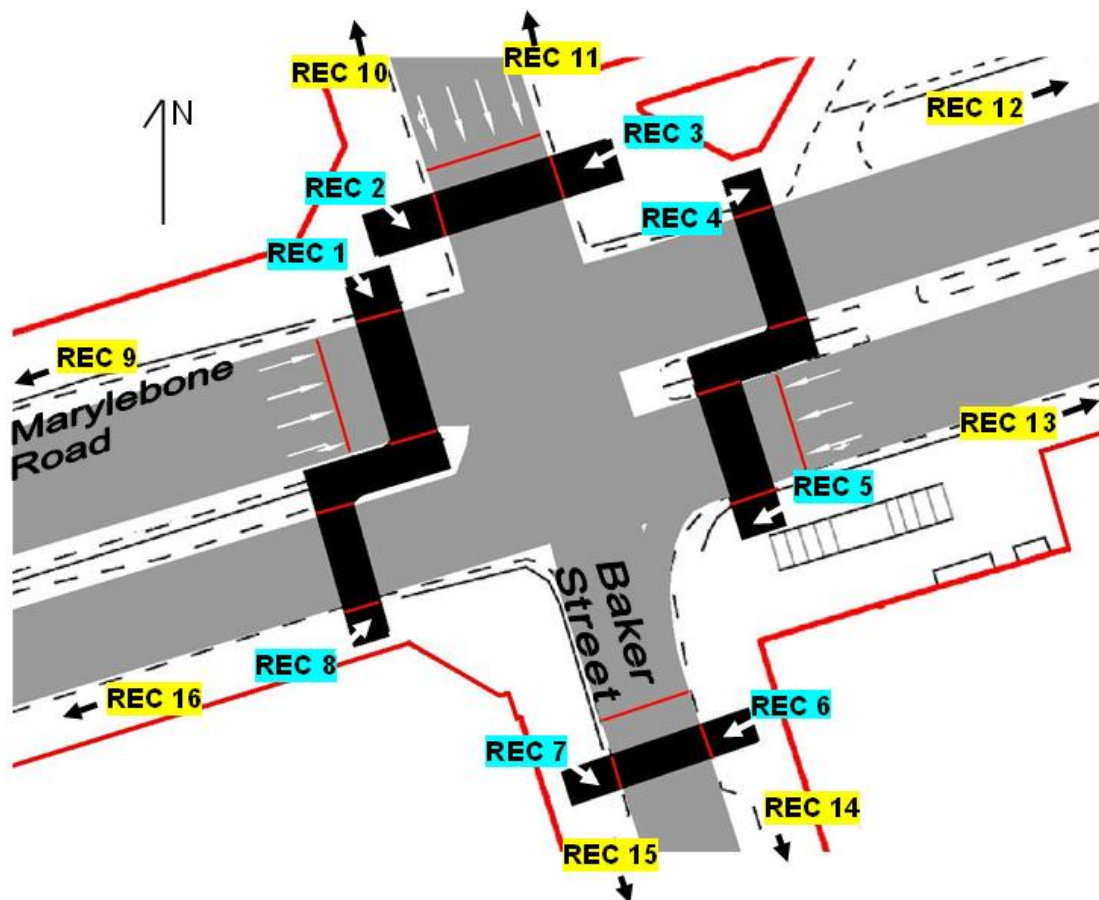


Figure 1. Layout of the Marylebone Road and the Baker Street intersection with the location of stop lines and pedestrian crossings. Receptor locations, as defined in CAL3QHC, are marked with arrows for receptors REC 1 to REC 8. For receptors REC 9 to REC 16 the arrows indicate the direction in which the labelled receptor is located, 60 m further away from their neighbour near-junction receptor.

3 ANALYSIS

All simulations were carried out for a duration of one hour at the maximum possible simulation resolution of 10 simulation-seconds per second. That means 10 data points were generated for every second of simulation run. The high simulation resolution eliminated unexpected acceleration/deceleration surges that may result with low resolution simulations. Vehicle performance data was generated for vehicle speed, acceleration and distance travelled. For pedestrians, data was generated on pedestrian travel times to cross the road. The pedestrian path consisted of actual pedestrian crossings across the vehicle carriageway, the staggered median refuges (on the Marylebone Road) and a 4 m stretch on the curb on either end of the crossing. Pedestrian travel paths were divided into two halves and travel time was recorded separately for each half. Exposure to CO at a

particular crossing x travelling from point a to point b was then expressed by the CO Exposure Index CEI which was calculated as follows

$$CEI_{x(a-b)} = \tau_{1x}\zeta_a + \tau_{2x}\zeta_b$$

where τ_{1x} = the travel time on the first half of the crossing x (sec); ζ_a = the CO concentration measured at the nearest receptor to a (ppm: parts per million); τ_{2x} = the travel time on the second half of the crossing x (sec); and ζ_b = the CO concentration measured at the nearest receptor to b (ppm). The CMEM output was used to generate emissions for CO for each of the 15 datasets. CAL3QHC requires two separate emission values for each link defined in it (15 links in our case). The first value is based on emissions from all the vehicles for their whole journey (per unit distance) while the second value is based on emissions only for the idling state of the vehicles (per unit time). Emissions for idling vehicles were obtained when the vehicle speeds were zero. These emission values obtained from the CMEM were then used as input to the CAL3CQH pollutant dispersion model along with data on signal timings, network coordinates, receptor locations, meteorological data and traffic data. Traffic and signal timings data was obtained from the VISSIM simulations while for the meteorological data wind speeds from 1 m/s to 20 m/s and headings from 1 to 360 degrees (1 degree increments) were employed.

Background concentrations in CAL3QHC were assumed to be zero. Sixteen receptors were coded as shown in Figure 1. These are receptors 1 to 8 (REC 1 to REC 8 in Figure 1) at 3 m from the curb at each end of the pedestrian crossing, and receptors 9 to 16 (REC 9 to REC 16) at a distance of 60 m (away from the intersection) and from the receptors at the pedestrian crossing ends. No receptor was placed on the pedestrian crossings across the carriageway or on the pedestrian refuge in the staggered pedestrian crossings. This was because CAL3QHC defines a mixing zone for pollutants (CO in this case) that extends to 3 m on either side of the vehicle carriageway.

4 RESULTS

Carbon monoxide concentrations were estimated at the receptors for a one hour simulation period. The worst case scenarios in terms of wind speed and headings are discussed. Wind speed of 1 m/s invariably resulted in the maximum observed concentrations while different receptors experienced maximum concentrations at different wind headings. For each receptor the highest concentration out of all 360 results for the wind headings is used. Results show that CO concentration drops rapidly with increasing wind speed until about 4 m/s after which the change is more gradual.

Analyzing results for changes in wind headings along the Marylebone Road it is observed that higher concentrations take place when wind is blowing somewhat parallel to the road along which the receptor is located, although the peaks do not occur at exact parallel headings. Low concentrations result when winds are blowing perpendicular to the road direction. However for receptors along Baker Street, these results hold only for receptors REC 11 and REC 14 which are located away from the intersection. Receptors near the pedestrian crossings on the intersection show a more complex variation as a large proportion of emissions actually come from traffic on the Marylebone Road.

The change in CO concentration at various receptors with changes in signal cycle length is illustrated by the bar charts in Figure 2 for a soak time of zero (i.e., optimal emissions control performance). The results from each receptor can be broadly separated into three categories.

- CO concentrations decrease with increasing signal cycle length along Marylebone Road. Representative results from this group are shown for receptors REC 1 and REC 5 which are located near pedestrian crossings in front of stop lines for approaching traffic from either direction of the Marylebone Road. Other receptors located along the Marylebone Road display similar trends, though the magnitude of CO concentrations is smaller on the discharge roads in comparison to the approach roads. These results reflect the increased green time available to traffic on the Marylebone Road with increasing signal cycle resulting in less idling and subsequent accelerating vehicles. However there is a draw back and that is pedestrians have to wait longer on the curbside. Hence, even if the emissions decrease per unit time pedestrian exposures increase especially as pedestrians cross north to south (see Figure 3).

- CO concentrations decrease with increasing signal cycle length on Baker Street approaches. Results representative of this group are shown for receptors REC 2 and REC 3 both of which are located near the pedestrian crossings in front of stop lines for the approaching Baker Street traffic. As the signal cycle increases the green time available to traffic on the Baker Street remains constant which results in an increase in idling vehicles waiting for longer times on the stop line. The receptors would have recorded increasing CO concentrations with an increase in signal cycle lengths if only emissions from Baker Street were considered in isolation. These receptors are, however, also exposed to emissions from the nearby eastbound Marylebone Road which not only offsets any expected increase but, shows a decrease in emissions with increasing signal cycle durations. Receptors on the discharge arm of Baker Street also show similar results but in their case the results are due to comparatively lower traffic flow and large available green times for the vehicular traffic.
- An increase in CO concentrations with increases in signal cycle length. Two receptors show this trend; REC 10 and REC 11. These receptors are located away from the intersection on the approach arm of the Baker Street and are somewhat immune to the emissions generated by traffic at the Marylebone Road hence they are able to pick up the increased emissions resulting from increasing traffic queues forming on Baker Street as the green time available for cross traffic falls, in parallel with reduced pedestrian green time.

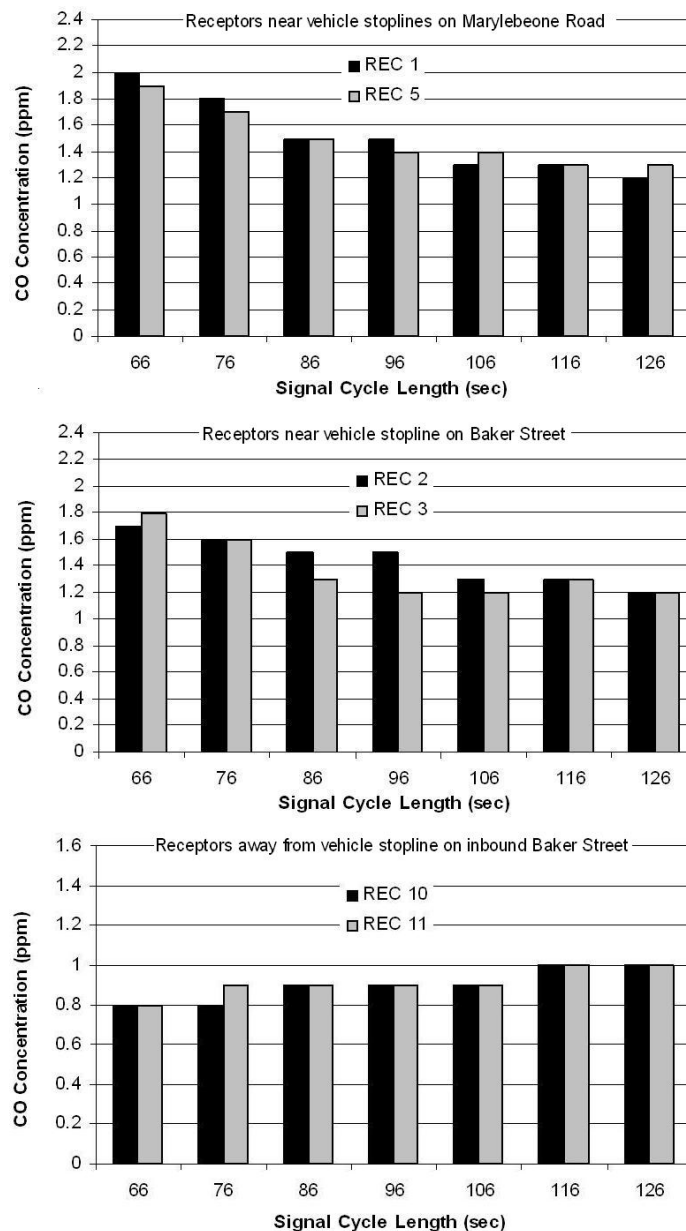


Figure 2. Change in CO concentrations with change in signal cycle length for 1 m/s of wind speed and worst case scenario for wind direction.

In terms of magnitudes the receptors nearer the intersection record higher concentrations than those further away. This difference is, however, small when the more distant receptors are located on the approach arm of the road on which traffic is queuing.

Pedestrian exposure is shown graphically in Figure 3 based on the CO Exposure Index defined above. Pedestrians crossing the Marylebone Road north to south face the largest levels of exposure to CO in magnitude and face the largest increase with increasing signal cycle lengths. This is because they have the shortest pedestrian green phase of all the pedestrian crossings in the intersection and must cross the path of the heaviest traffic flow. While waiting on the curbside pedestrians on these crossings are also exposed to the idling traffic on the inbound Baker Street further increasing their exposure levels. For pedestrians crossing the Marylebone Road from south to north the exposure is less mainly because they have to stay on the staggered pedestrian refuge for a shorter duration compared to those crossing from north to south. This is due to the sequence of changes in signal phases which provide better coordination for pedestrians crossing from south to north.

Pedestrians crossing the Baker Street inbound arm benefit from increased signal cycle lengths as the length of the pedestrian phase also increases correspondingly. For the pedestrians crossing on the outbound arm of Baker Street the pedestrian phase remains constant and hence the available time for pedestrians to cross the road decreases in real terms as the signal cycle increases.

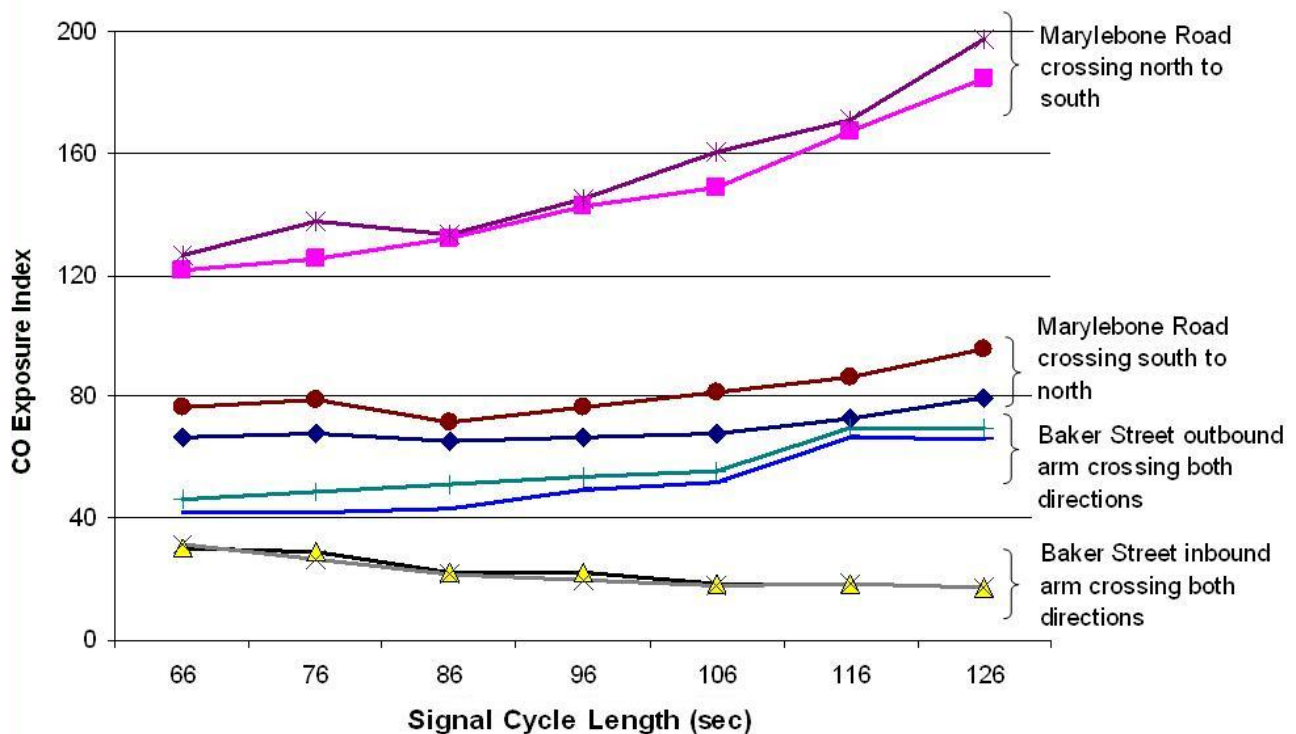


Figure 3. Pedestrian CO exposure for the four pedestrian crossings (both directions). CO Exposure Index is the multiplicative factor of mean pedestrian crossing time (including waiting time at the curb) and the CO concentrations recorded at the nearest receptors.

5 CONCLUSIONS

This work has illustrated how changes in signal cycle timings result in changes in pollutant exposure of pedestrians at pedestrian crossings. There is clearly a trade-off between pedestrian exposure and the reduction in emissions as a result of smooth traffic flow, achieved usually by employing longer signal cycle lengths. Long signal cycles, resulting in less total vehicle emissions, cause increased pedestrian delay and longer exposure to slightly reduced emission levels. Measuring this trade-off would require devising values of time for pedestrians in terms of exposure to harmful pollutants such as CO in addition to delays in terms of lost time. No such work is currently available and this is clearly an area open for further research.

This work has also highlighted a number of intersection traffic control measures that allow smooth traffic flows and reduce vehicle delays but increase pedestrian exposure to vehicle emissions. The

first is the use of long signal cycle times which has already been discussed. The second is the use of a parallel pedestrian phase where pedestrians cross the road only when the vehicular traffic on the parallel road is also moving. This technique further allows for dividing a single road crossing into two multiple arms and pedestrians have to wait twice to cross a single road; once at the curb and again at the refuge while also increasing their geometric delay through staggering of the median refuge and hence further increasing their exposure. As shown in the results the pedestrians who cross the staggered crossing with some measure of coordination between the two legs are less exposed to pollutants than those who have to spend greater time on the refuge.

REFERENCES

- Ishaque, M.M. and R.B. Noland, 2005a: A multimodal micro-simulation of vehicle and pedestrian signal timings. *Journal of the Transportation Research Board: Transportation Research Record*. 1919, 107–114.
- Ishaque, M.M. and R.B. Noland, 2005b: Trade-offs between vehicular and pedestrian traffic using micro-simulation methods. Paper presented at the *16th International Symposium on Transport and Traffic Theory (ISTTT)*, College Park, Maryland.
- Sjostedt, L., 1967: Behaviour of pedestrians at pedestrian crossings. National Swedish Road Research Institute. Quoted by R.B. Sleight, 1972 in *The Pedestrian*. Ed. T.W. Forbes' *Human factors in traffic safety research*.

ACKNOWLEDGEMENT

We acknowledge support from the Rees Jeffreys Road Foundation for which we are grateful.

Potential methods to include the full climate impact of aviation emissions into the European Emissions Trading Scheme and their scientific integrity

D. S. Lee*

Dalton Research Institute, Manchester Metropolitan University, John Dalton Building, Chester Street, Manchester M1 5GD, United Kingdom

R. C. N. Wit

Natuur en Milieu (N&M) Donkerstraat 17 Utrecht, Postbus 1578, 3500 BN, the Netherlands Utrecht NL

Keywords: Aviation emissions, emissions trading scheme, metrics.

ABSTRACT: The European Commission has expressed a preference that for future inclusion of aviation into the European Emissions Trading Scheme, non-CO₂ effects should be accounted for. Three scenarios are outlined here: utilizing some ‘multiplier’ on CO₂ emissions; accounting for non-CO₂ effects on a flight-by-flight using an approach that would be compatible with GWPs; and utilizing alternative policy instruments for the non-CO₂ effects. All approaches had serious difficulties in terms of their scientific integrity. A multiplier approach using radiative forcing, or its direct derivatives was shown not to be robust. There are difficulties with formulating GWPs for ozone and contrails. Other policy instruments such as a NO_x landing charge and cruise NO_x charges were considered: NO_x landing charges may not be a good proxy for cruise NO_x, whereas NO_x en-route charges were technically robust, relatively straightforward but have difficulties with their political acceptability.

6 INTRODUCTION

Aviation contributes to climate change through its carbon dioxide (CO₂) and other emissions/effects (IPCC, 1999). In 2002, international civil aviation accounted for 2.8% of the total national CO₂ emissions across the 25 Member States of the European Union and increased by 60% over the last decade. This increase is a result of demand for air transport which has outpaced improvements in fuel efficiency arising from engine/aircraft technology and in the air traffic control system. Thus, without any policy intervention, the growth of global CO₂ emissions from aviation is expected to double in the coming decades.

In addition to emissions of CO₂, aviation contributes to climate change through emissions of nitrogen oxides (NO_x), which are particularly effective in forming the greenhouse gas ozone (O₃) when emitted at subsonic aircraft cruise altitudes. Aircraft also trigger the formation of contrails in certain conditions and may enhance the formation of cirrus clouds, both of which add to the overall global warming effect. In 1999 the Intergovernmental Panel on Climate Change (IPCC) estimated that the total radiative forcing (RF) from aviation was 2.7 times that of its CO₂ RF alone in 1992 (this ratio was termed the Radiative Forcing Index, or RFI), excluding potential cirrus cloud enhancement. More recent data on aviation’s radiative impact for 2000 (Sausen et al., 2005) imply an RFI of 1.9, once again excluding cirrus cloud enhancement. This means the environmental effectiveness of any mitigation policy will depend on the extent to which these non-CO₂ effects are also taken into account and the time-frame over which ‘effects’ are considered and quantified.

The European Commission has stated a preference for the inclusion of all aviation’s climate impacts into the European Emissions Trading Scheme (E-ETS). In this work, three potential scenarios by which this might be achieved were examined where the scientific/technical integrity was a pre-

* *Corresponding author:* D. S. Lee, Dalton Research Institute-CATE, Manchester Metropolitan University, Faculty of Science and Engineering, John Dalton East Building, Chester St, Manchester M1 5GD, UK. Email: D.S.Lee@mmu.ac.uk

requisite. They are: firstly, by utilizing a ‘multiplier’; secondly, by considering an individual ‘effects-based’ approach; and lastly a CO₂ approach with so-called ‘flanking instruments’ (i.e. additional policies or measures) to cover non-CO₂ effects (Wit et al., 2005). This work and its other economic and policy impacts are documented in greater detail elsewhere (Wit et al., 2005).

7 THE ‘MULTIPLIER’ APPROACH

In this approach, CO₂ is traded but some multiplier is used to capture the non-CO₂ effects. The IPCC (1999) introduced the radiative forcing index (RFI) as a means of comparing the total radiative effects from aviation to its CO₂ RF over some emissions scenario. Usage of the RFI as a multiplier for *emissions* is unsuitable as it does not take into account future effects of CO₂ in the way that the Global Warming Potential (GWP) does since RF is essentially a *backward looking* metric (since it includes CO₂'s history). Moreover, the value of the RFI is not a constant and is entirely dependent upon the emissions scenario adopted – the close agreement found between ‘present day’ value of 2.7 and 2.6 for 2050 for scenario Fa1 by the IPCC (1999) was entirely fortuitous. This was demonstrated by Wit *et al.* (2005). If a hypothetical scenario is conceived whereby emissions remain constant after 2000, it can be seen that RFI damps and CO₂ forcing increases over time (see Fig. 1).

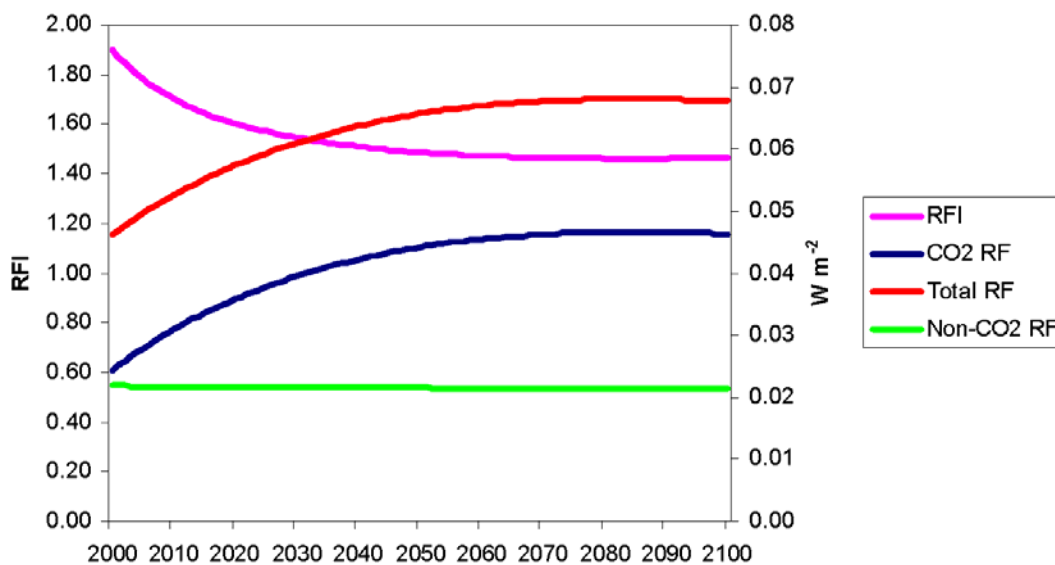


Figure 1. Modelled RFI and RF for aviation using constant 2000 emissions, model tuned to Sausen et al. (2005) forcings.

The Global Temperature Potential (GTP) (Shine et al., 2005) has been shown to be close to GWP in that it allows a comparison of a global mean temperature response from some forcing to that from CO₂ over some arbitrary time horizon. If an RFI is reformulated using GTPs for constant emissions (Global Temperature Index – GTI), a linear relationship between CO₂ *emissions* and CO₂ and non-CO₂ temperature effects is apparent (note that this calculation assumes efficacies of non-CO₂ forcings of unity). Such an approach is attractive in that it more closely relates the total effect to the *emissions* of CO₂ but in progressing further down the cause-effect chain, it introduces more complexities and therefore uncertainties. Over a 100 year time-integration for *constant* emissions, non-CO₂ effects comprise approximately 30% of the total temperature effect and CO₂ represents 70%: this attribution is clearly different if an actual emission scenario is considered. Currently, the underlying GTP has only been used for constant emissions *c.f.* a pulse, as in the GWP. A pulse response is perhaps more useful in terms of determining a response to a marginal emissions change. More work is needed to test whether the GTP and derivative GTI can be used to determine an emissions multiplier for aviation CO₂ to capture non-CO₂ effects but the initial results are promising.

Thus, it is concluded that RFI cannot be used with scientific integrity as a multiplier but a GTI may be useful but requires more work.

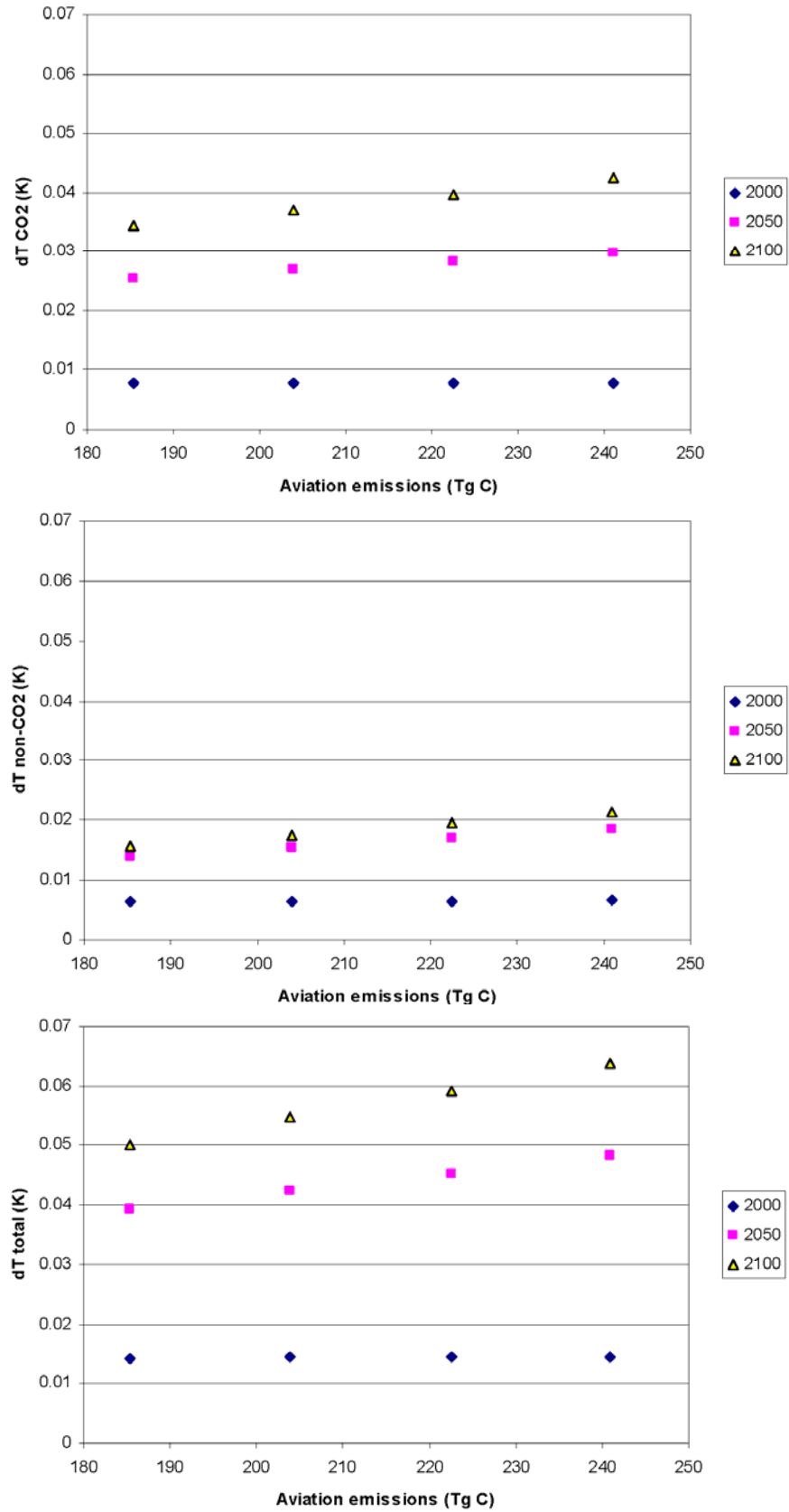


Figure 2. Modelled temperature response for CO₂ (a), non-CO₂ (b) and total (c) aviation effects for constant CO₂ emissions at 2000, 2050 and 2100 for different emission rates.

8 'EFFECTS-BASED' APPROACH

The aim of this approach was to examine whether individual non-CO₂ effects of aviation could be addressed using *different metrics* that might be compatible with the GWP under an emissions trading scheme. This approach requires a consideration of effects on an individual flight basis.

A flight-based approach for non-CO₂ effects requires sophisticated modelling to account for O₃/CH₄ changes from NO_x emissions, and contrails/cirrus. Such models are still in the research domain and it is not possible to recommend one over another. Moreover, the aircraft impact depends upon the background conditions and these conditions – and the ultimate effect – are time and space dependent. If it were possible to agree a model and it was accepted that globally, aggregated emissions produce a certain global production rate of O₃, then under such assumptions it might be reasonable to disaggregate an O₃ (mass) production rate per unit mass NO_x. However, to take such disaggregation to the next level, i.e. RF, and disaggregate to individual flights, involves more assumptions that are difficult to justify at such a level of detail.

For contrails, similar difficulties arise: there are uncertainties in the calculation of both contrail coverage and the RF. Again, to attribute an effect down to an individual flight level cannot currently be done robustly since environmental conditions dictate whether a contrail is formed or not and the RF effect depends *inter alia* on time of day.

For calculating both O₃ and contrail effects on a flight-by-flight basis, this would only be possible on a statistical basis or by accepting an approach of scaling a global estimation of the effects to a flight km basis assuming a linear relationship.

It is, in principle, possible to formulate a GWP for O₃ but this is a contentious issue, vigorously debated in the literature; for contrails, it is not possible to derive a GWP since a contrail cannot be easily related to a mass emission. Therefore, this approach cannot be recommended.

9 FLANKING INSTRUMENTS

In this approach, CO₂ is covered by the E-ETS and 'flanking instruments' would be used to tackle non-CO₂ effects – i.e. by using more than one policy instrument. A critical question with a CO₂-only scheme is whether any *negative* tradeoffs will occur as a result. Historically, the overall emissions index of the fleet for NO_x (EINO_x – g NO_x/kg fuel) has increased as a result of higher combustor temperatures and pressures that have resulted from increases in the fuel efficiency of gas turbine engines. But, under this approach, the question is whether the EINO_x increase would proceed at a *faster* rate if aviation were incorporated into the E-ETS because of an increased impetus to reduced CO₂? Engine manufacturers claim that this would not be the case but this remains uncertain with increasing fuel prices. In addition, modern engines have a higher propensity to cause contrails over a greater depth of the atmosphere than was the case with older technology (Schumann et al., 2000). This is expected to increase in the future, based upon assumptions over the increase in propulsive efficiency (η). It has been suggested that values of η for 2050 will result in 20% greater contrail coverage over today's global estimation of η (Gierens et al., 1999). Thus, it is concluded that negative tradeoffs are more likely than not to occur under the scenario of aviation being incorporated into a CO₂-only emissions trading scheme, without flanking instruments. However, for contrails and contrail-cirrus, the magnitude of the RF effect is still rather uncertain.

The current ICAO landing/take-off cycle (LTO) NO_x Certification regime provides one potential flanking instrument. The EINO_x over the LTO cycle has been claimed by industry and an ICAO Working Group to correlate with cruise EINO_x although no formal statistical correlation has been presented. The disadvantage to this approach is that Certification limits engine NO_x (amongst other things), according to overall pressure ratio of the engine. Since the EINO_x has increased as a result of moving to higher overall pressure ratios, this approach would leave open the possibility of NO_x actually *increasing* if the EINO_x increased at a rate greater than fuel consumption decreased.

Alternatively, an airport NO_x landing charge might be employed. If a landing charge were introduced, this could be done independently of ICAO and if implemented on a mass NO_x/landing charge (using ICAO NO_x Certification data), this would bring pressure to utilize lower-NO_x technologies that would have a co-benefit for local air quality. This approach, whilst crude, and only

tackling NO_x, is critically dependent upon the claim of a ‘correlation’ between LTO EINO_x and cruise EINO_x.

Perhaps the most effective flanking instrument that has the fewest uncertainties would be to formulate a cruise NO_x charge. Emissions of NO_x can be calculated within an uncertainty of ±10% from fuel consumption (which is known accurately and could be reported by the airline on a flight-by-flight basis) and the industry could calculate this with much more accuracy from engine performance models. Unfortunately, the concept of emissions *charges* has proved to be very contentious, particularly within the ICAO forum and the potential political acceptability is low.

10 CONCLUSIONS

Formulating a scientifically robust metric for dealing with non-CO₂ effects of aviation on climate that can be incorporated into an emission trading regime represents a challenge.

Multiplying CO₂ emissions by an RFI is inherently unsuitable although a temperature-based metric under development over an integration time-period (similar to a GWP) appears promising.

No suitable metrics have been found for non-CO₂ effects that can be applied on a flight-by-flight basis that are readily compatible with a GWP.

11 REFERENCES

- Gierens K., Sausen R. and Schumann U., 1999: A diagnostic study of the global distribution of contrails part II: future air traffic scenarios. *Theoretical and Applied Climatology* **63**, 1–9.
- IPCC 1999: Special report on aviation and the global atmosphere, J.E. Penner, D.H. Lister, D.J. Griggs, D.J. Dokken, M. McFarland (Eds), Cambridge University Press, Cambridge, UK.
- IPCC 2001: Climate change 2001: The scientific basis. Contribution of Working Group 1 to the Third Assessment Report, J.T. Houghton (Eds), Cambridge University Press, Cambridge, UK.
- Lim L. L., D. S. Lee, R. Sausen, and M. Ponater 2007: Quantifying the effects of aviation on radiative forcing and temperature with a climate response model. Manuscript to be submitted.
- Sausen R. and U. Schumann, 2000: Estimates of the climate response to aircraft CO₂ and NO_x emissions scenarios. *Climatic Change* **44**, 27–58.
- Sausen R., I. Isaksen, V. Grewe, D. Hauglustaine, D. S. Lee, G. Myhre, M. O. Köhler, G. Pitari, U. Schumann, F. Stordal, and C. Zerefos, 2005: Aviation radiative forcing in 2000: and update on IPCC (1999). *Meteorologische Zeitschrift* **114**, 555–561.
- Schumann, U., R. Busen, and M. Plohr, 2000: Experimental test of the influence of propulsion efficiency on contrail formation, *Journal of Aircraft*, **37**, 1083–1087.
- Sausen R., Isaksen I., Grewe V., Hauglustaine D., Lee D. S., Myhre G., Köhler M. O., Pitari G., Schumann U., Stordal F. and Zerefos C. (2005) Aviation radiative forcing in 2000: and update on IPCC (1999). *Meteorologische Zeitschrift* **114**, 555 – 561.
- Shine K. P., Fuglestedt J. S., Hailemariam K., Stuber N. (2005) Alternatives to the global warming potential for comparing climate impacts of emissions of greenhouse gases. *Climatic Change* doi:10.1007/s10584-005-1146-9.
- Wit R. C. N., Boon B. H., van Velzen A., Cames M., Deuber O. and Lee D. S. 2005: Giving wings to emission trading. Inclusion of aviation under the European emission trading system (ETS): design and impacts. CE-Delft, No. ENC.C.2/ETU/2004/0074r, the Netherlands.

List of Participants:

Alexander MP Rt Hon Douglas

Secretary of State for Transport
no email

Anderson Kevin

Tyndall Centre for Climate Change Research
University of Manchester
PO Box 88
Manchester, M601QD, UK
Tel. +44 1613063715
harriet.pearson@manchester.ac.uk;
kevin.anderson@manchester.ac.uk

Andrews David

University of Oxford
no email

Aulinger Armin

GKSS Research Centre
Max-Planck-Str. 1
21502 Geesthacht, Germany
Tel. +49-4152-872335
aulinger@gkss.de

Balkanski Yves

CNRS/LSCE
yves.balkanski@cea.fr

Bass Catherine

DEFRA
katherine.bass@DEFRA.GSI.GOV.UK

Bauer Hans-Joerg

University of Karlsruhe
hans-joerg.bauer@its.uni.karlsruhe.de

Baughcum Steven

The Boeing Company,
P. O. Box 3707, MC 02-XL
Seattle, WA 98124, USA
Tel. +1 425 294 5314
Steven.L.Baughcum@boeing.com

Baumgardner Darrel

Centro de Ciencias de la Atmosferas
Universidad Nacional Autonoma de Mexico
Ciudad Universitaria
Circuito Exterio
Mexico City, Mexico 04150
Tel. +52 555 622 4248
darrel@servidor.unam.mx

Bewersdorff Ines

GKSS Research Center Geesthacht
Institute for Coastal Research
Department of Environmental Chemistry
Max-Planck-Str. 1
21502 Geesthacht
Germany
Tel. +49-4152-87-2334
ines.bewersdorff@gkss.de

Borken Jens

DLR - Transportation Research
Rutherfordstr. 2
12489 Berlin
Germany
Tel. +49-30-67055-238
Jens.Borken@dlr.de

Borsoi Andrea

60 Forest Court
Snaresbrook
London E11 1PL, UK
Tel. +44 7726748410
andrea.borsoi@hotmail.co.uk

Bows Alice

Tyndall Centre for Climate Change Research
H2, Pariser Building
University of Manchester
PO Box 88
Manchester, M60 1QD, UK
Tel. +44 161 306 3737
alice.bows@manchester.ac.uk

Brook Peter

QinetiQ
Fuels and Lubricants Centre
Building 442
Cody technology Park
Farnborough, Hants GU14 0LX, UK
Tel. +44 1252 397072
psbrook@qinetiq.com

Brüning Claus

European Commission, DG Research,
Directorate Environment
Unit 'Environment-Climate Systems'
Marsfeldstraat 21
CDMA 3/119
1049 Brussels, Belgium
Tel. +32 2 29 54484
claus.bruning@ec.europa.e

Burnett Keith

University of Oxford
[no email](#)

Campmany Elies

University of Oxford
[no email](#)

Caro Dimitri

CEA/CNRS - LSCE, UMR 1572
CEN de Saclay
L'Orme des Merisiers, Bât 712
91191 GIF SUR YVETTE Cedex
France
Tel. +33 (0) 1 69 08 40 01
Dimitri.Caro@cea.fr

Collins Bill

Met Office
Exeter, EX1 3PB, UK
Tel. +44 1392 884634
bill.collins@metoffice.gov.uk

Danilin Michael

The Boeing Company
MS 02-XL
P.O. Box 3707
Seattle, WA 98124, USA
Tel. +1-425-266-8603
danilin@h2o.ca.boeing.com

Davison Brian

Dr Brian Davison
Faculty of Science and Technology
Department of Environmental Sciences
Lancaster University
Lancaster, LA1 4YQ, UK
Tel. +44 (0)1524 593932
b.davison@lancaster.ac.uk

Demirdjian Benjamin

CRMC-N / UPR CNRS 7251
Campus de Luminy - case 913
13288 MARSEILLE cedex 09,
France
Tel. +33 6 60 36 28 18
demirdjian@crmcn.univ-mrs.fr

Dessens Olivier

CAS - Dept. of Chemistry
University of Cambridge
Lensfield Road
CB2 1EW CAMBRIDGE, UK
Tel. +44 1223 763815
olivier.dessens@atm.ch.cam.ac.uk

Devasthale Abhay

University of Hamburg and,
Max-Planck-Institute for Meteorology
Bundesstrasse 53
20146, Hamburg, Germany.
Tel. +49 40 41173541
abhay@dkrz.de

Dickson Neil

Centre for Atmospheric Science
Department of Chemistry
University of Cambridge
Lensfield Road
Cambridge. CB2 1EW, UK
Tel. +44 1223 336345
ncd27@cam.ac.uk

Dotzek Nikolai

DLR-IPA
Oberpfaffenhofen
82234 Wessling, Germany
Tel. +49 8153 28 1844
nikolai.dotzek@dlr.de

Duda David

National Institute of Aerospace
100 Exploration Way
Hampton, VA 23666-6147
United States of America
Tel. +1 757 864 9881
dduda@nianet.org

Egelhofer Regina

Technische Universität München
Lehrstuhl für Luftfahrttechnik
Boltzmannstr. 15
D-85747 Garching, Germany
Tel. +49 89 289 15958
egelhofer@tum.de

Ekstrom Marie

Climatic Research Unit
School of Environmental Sciences
University of East Anglia
Norwich, Norfolk NR4 7TJ, UK
Tel. +44 1603-592721
m.ekstrom@uea.ac.uk

Eleftheratos Kostas

Laboratory of Climatology & Atmospheric
Environment, Faculty of Geology &
Geoenvironment, University of Athens, 15784
Athens, GREECE
Tel.+30 210 7274195
kelef@geol.uoa.gr

Elliff Ted

EUROCONTROL Experimental Centre
Centre de Bois des Bordes
BP15
91222 Bretigny sur Orge cedex
France
Tel. +33 1 69 88 73 36
ted.elliff@eurocontrol.int

Eyring Veronika

DLR-Institut für Physik der Atmosphäre
Oberpfaffenhofen
82234 Wessling,
Germany
Tel. +49 8153 28 2533
Veronika.Eyring@dlr.de

Faull Nickolas

University of Oxford
AOPP
Clarendon Laboratory
Parks Road, UK
Tel. +44 1865 272887
nfaull@atm.ox.ac.uk

Fichter Christine

DLR-Institut für Physik der Atmosphäre
Oberpfaffenhofen
82234 Wessling
Germany
Tel. +49 8153 28 3022
christine.fichter@dlr.de

Franke Klaus

Institute of Environmental Physics and Remote
Sensing
University of Bremen - FB1
P.O. Box: 330440
28334 Bremen, Germany
Tel. +49 421 218 8126
kfranke@iup.physik.uni-bremen.de

Fuglestedt Jan

CICERO,
Pb 1129 Blindern,
N-0318 Oslo, Norway
Tel. +47 22858764
j.s.fuglestedt@cicero.uio.no

Ganev Kostadin

Geophysical Institute
Acad.G.Bontchev, bl.3
1113 Sofia, Bulgaria
Tel. +359 2 979 3708
kganev@geophys.bas.bg

Garnier Francois

ONERA
29 AVE DE LA DIVISION LECLERC
92320 CHATILLON
FRANCE
Tel. +33 1 46 73 47 27
francois.garnier@onera.fr

Gauss Michael

Department of Geosciences
PO. 1022 Blindern
0315 Oslo
Norway
Tel. +47 22855775
michael.gauss@geo.uio.no

Gierens Klaus

Institut für Physik der Atmosphäre
DLR Oberpfaffenhofen
D-82234 Wessling
Germany
Tel. +49 8153 28 2541
klaus.gierens@dlr.de

Graham Angus

CATE, Manchester Metropolitan University
Dept. Environmental & Geographical Sci.
Chester St
Manchester, M1 5GD, UK
Tel. +44 161 247 6209
a.graham@mmu.ac.uk

Grainger Don

University of Oxford
Clarendon Laboratory
Parks Road
Oxford OX1 3PU, UK
Tel. +44 1865 272888
r.grainger@physics.ox.ac.uk

Grewe Volker

Institut für Physik der Atmosphäre
DLR-Oberpfaffenhofen
82234 Wessling
Germany
Tel. +49 8153-282536
volker.grewe@dlr.de

Grigoryev Maksim

Moscow Region
Garnaev str. 2, 140182 Zhukovsky,
Russia
Gromov Flight Research Institute
Tel. +7-(495)-556-52-18
Lab22@Progtech.ru

Guldberg Annette

Danish Meteorological Institute
 Lyngbyvej 100
 DK-2100 Copenhagen, Denmark
 Tel. +45 39 15 74 33
ag@dmi.dk

Gupta Mohan

AEE-300
 Office of Environment and Energy
 Federal Aviation Administration
 800 Independence Avenue, S.W.
 Washington, DC 20591, USA
 Tel. +1 (202) 267 3496
Mohan.L.Gupta@faa.gov

Hagen Donald

G-7 Norwood Hall
 University of Missouri-Rolla
 Rolla, MO 65409, USA
 Tel. +1 573-341-4351
hagen@umr.edu

Halenka Tomas

Charles University in Prague,
 Fac. of Mathematics and Physics
 Dept. of Meteorology and Environment Protection
 V Holesovickach 2, 180 00 Prague,
 Czech Republic
 Tel. +420 2 2191 2514
tomas.halenka@mff.cuni.cz

Heinen Falk

Federal Environment Agency
 Woerlitzer Platz 1
 06844 Dessau, Germany
 +49 34021032038
falk.heinen@uba.de

Highwood Eleanor

Department of Meteorology
 University of Reading
 PO Box 243
 Reading RG6 6BB, UK
 Tel. +44 118 378 6688
e.j.highwood@reading.ac.uk

Huebsch Wade

West Virginia University
 333 Engr. Sciences Bldg.
 PO Box 6106, MAE Dept.
 Morgantown, WV 26506-6106, USA
 Tel. +1 304 293 3111 2331
Wade.Huebsch@mail.wvu.edu

Hume Chris

Airbus-UK New Filton House
 Future Projects Office
 Building 071 (Module 1)
 Bristol BS99 7AR, UK
 Tel. +44 117 936 2484 /-3493
chris.hume@airbus.com

Hurley Jane

University of Oxford
[no email](#)

Huszar Peter

Charles University, Prague
 Fac. of Mathematics & Physics
 Department of Meteorology & Environmental
 Protection
 V Holesovickach 2
 180 00 Prague, Czech Republic
 Tel. +420 608951927
huszarpet@gmail.com

Iachetti Daniela

University of L'Aquila
 via Roma, 1
 64039 Penna S. Andrea
 TERAMO, Italy
 Tel. +39 086166676
daniela.iachetti@aquila.infn.it

Ihebioha Daniel

National Space Research and Climatic
 Development Agency
gov_conf@yahoo.com

Kelly Frank

Chief Scientist, DfT
F.P.Kelly@statslab.cam.ac.uk

Kershaw Andy

British Airways
 Waterside HBA3
 PO Box 365
 UB7 0GB, UK
 Tel. +44 (0)20 8738 7158
andy.kershaw@ba.com

Klima Kelly

MIT, Dept. of Aeronautics and Astronautics
kklima@mit.edu

Koehler Marcus

Centre for Atmospheric Science
University of Cambridge
Department of Chemistry
Lensfield Road
Cambridge, CB2 1EW, UK
Tel. +44 (0)1223 763815
marcus.koehler@atm.ch.cam.ac.uk

Kousta Jonilda

University of Athens
School of Physics
Atmospheric Modeling and Weather Forecasting
Group
University Campus, Bldg PHYS-V
15784 Athens, Greece
Tel. +30 210 727 6835
kousta@mg.uoa.gr

Kraai Aline

Westerduinweg 3, 1755 LE, Petten, NL
Tel. +31(0) 224-564308
Kraai@ecn.nl

Lee David

Manchester Metropolitan University
Department of Environmental & Geographical
Sciences
Chester Street
Manchester M1 5GD, UK
Tel. +44 161 247 3663
d.s.lee@mmu.ac.uk

Lim Ling

Centre for Air Transport and the Environment
Department of Environmental and Geographical
Sciences,
Manchester Metropolitan University,
John Dalton Building, Chester Street,
Manchester M1 5GD, UK
Tel. +44 161 2473653
l.lim@mmu.ac.uk

Lobo Prem

G-7 Norwood Hall, University of Missouri -
Rolla, Rolla, MO 65409, USA
Tel. +1-573-341-4338
plobo@umr.edu

Lockley Peter, AEF

pete@aef.org.uk

Lourdes Maurice, FAA

Lourdes.Maurice@faa.gov

Lundman Maria Therése

Swedish Civil Aviation Authority
SE-601 73 Norrköping, Sweden
Tel. +46 11 415 21 44
therese.lundman@luftfartsstyrelsen.se

Madden Paul

Combustion Systems Engineering (ML92)
Rolls-Royce plc
P.O. Box 31
Derby DE24 8BJ, UK
+44 1332 249184
paul.madden@rolls-royce.com

Mannstein Hermann

DLR Oberpfaffenhofen
Institut fuer Physik der Atmosphaere
82234 Wessling, Germany
Tel. +49 8153 28 2503
Hermann.Mannstein@mnet-mail.de

Marais Karen

MIT
Dept. of Aeronautics and Astronautics
77 Massachusetts Ave
Room 33-141
Cambridge MA 02139, USA
Tel. +1 6172533'9
karenm@mit.edu

Marizy Corinne

Airbus France
Emissions & Environmental Impact
Policy & Development - EED
316 route de Bayonne
31060 Toulouse cedex 9, France
Tel. +33 561184564
corinne.marizy@airbus.com

Massey Neil

Atmospheric, Oceanic and Planetary Physics,
University of Oxford, Clarendon Laboratory,
Oxford, Parks Road, OX1 3PU, UK
Tel. +44 1865272925
massey@atm.ox.ac.uk

Matheys Julien

Vrije Universiteit Brussel (V.U.B.)
Faculty of Engineering Sciences
Department of Electrotechnical Engineering and
Energy Technology (ETEC)
Building Z, Pleinlaan 2, B-1050 Brussels
Belgium
Tel. +32 026293804
jmatheys@vub.ac.be

Matthews Ben

Institut d'Astronomie et de Géophysique
2, chemin du Cyclotron
Université catholique de Louvain
Louvain la Neuve
1348 Belgique, Belgium
Tel. +32 10473365
matthews@climate.be

Meijer Ernst

KNMI
Wilhelminalaan 10
3732 GK De Bilt, The Netherlands
Tel. +31 302206411
meijere@knmi.nl

Miake-Lye Richard C.

Aerodyne Research, Inc.
45 Manning Road
Billerica, MA 01821, USA
Tel. +1 (978) 932-0251
rick@aerodyne.com

Minnis Patrick

MS 420
NASA Langley Research Center
Hampton, VA 23681, USA
Tel. +1 757 864 5671
p.minnis@nasa.gov

Moldanová Jana

IVL, Swedish Environmental Research Institute
Box 5302
SE-40014 Göteborg, Sweden
Tel. +46 31 7256213
janam@ivl.se

Mosedale Jonathan

DfT, Great Minster House
76 Marsham Street
London SW1P 4DR, UK
Tel. +44 2079448176
Jonathan.Mosedale@dfat.gsi.gov.uk

Neary Lori

York University, Canada
lori@yorku.ca

Nickolaus Chris

Cambustion Ltd,
J6 The Paddocks,
347 Cherry Hinton Road,
Cambridge CB1 8DH, United Kingdom
Tel. +44 1223 210250
cn@cambustion.co.uk

Niemeier Ulrike

Max Planck Inst. for Meteorology
Bundesstr 53
20149 Hamburg, Germany
Tel. +49 (0)40 41173130
niemeier@dkrz.de

Noland Robert

Centre for Transport Studies
Dept of Civil & Environmental Engineering
Imperial College London
London SW7 2AZ, UK
Tel. +44 207 594 6036
r.noland@imperial.ac.uk

Noppel Frank

Department of Propulsion, Power, and Aerospace
Engineering
School of Engineering, Bldg 183, Office 816
Cranfield University, Bedfordshire MK43 OAL,
United Kingdom of Great Britain
Tel. +44 7891 785460
f.g.noppel@cranfield.ac.uk

Olivié Dirk

Centre National de Recherches Météorologiques
42, avenue Gaspard Coriolis
31057 Toulouse, France
Tel. +33 5 61 07 99 68
dirk.olivie@cnrm.meteo.fr

Omobude David Desmond

National Space Research and Climatic
Development Agency, gov_conf@yahoo.com

Owen Bethan

CATE, Dept of Env and Geog
Manchester Metropolitan University
Chester Street, M1 5GD, UK
+44 161 2471591
b.owen@mmu.ac.uk

Palikonda Rabindra

NASA Langley Research Center
1 enterprise parkway, suite 300
Hampton, VA 23602, UK
Tel. +44 757 827 4664
r.palikonda@larc.nasa.gov

Paoli Roberto

CERFACS
42 Avenue Gaspard Coriolis,
31057 Toulouse, France
Tel. +33 5 61193133
paoli@cerfacs.fr

Paugam Ronan

Cerfacs, 42, avenue Gaspard Coriolis
31057 Toulouse Cedex 01, France
Tel. +33 (0)5 61 19 30 86
paugam@cerfacs.fr

Peeters Paul

NHTV
p/a Rodestein 12
6714 CG Ede, The Netherlands
Tel. +31-318-692390
peeters.p@nhtv.nl

Pejovic Tamara

Centre for Transport Studies
The Department of Civil and Environmental
Engineering
Imperial College London
South Kensington Campus
London SW7 2AZ, UK
Tel. +44 2075946055
tamara.pejovic@imperial.ac.uk

Penner Joyce

University of Michigan
2455 Hayward St.
Ann Arbor, MI 48109-2143, USA
Tel. +1-734-936-0519
penner@umich.edu

Petron Gabrielle

CIRES, NOAA/ESRL
Global Monitoring Division
325 Broadway R/GMD1
Boulder, CO 80305-3328, USA
Tel. +1 303 497 4890
gap@noaa.gov

Petzold Andreas

DLR-Oberpfaffenhofen
Institut für Physik der Atmosphäre
82234 Wessling, Germany
Tel. +49 8153 28 25 92
andreas.petzold@dlr.de

Pitkethly Eirik

dft
eirik.Pitkethly@dft.gsi.gov.uk

Ponater Michael

DLR- Oberpfaffenhofen
Institut für Physik der Atmosphäre,
D-82230 Wessling, Germany
Tel. +49 8153 282539
michael.ponater@dlr.de

Popovicheva Olga

Department of Microelectronics
Institute of Nuclear Physics
Moscow State University
119 992, Moscow, Russia
Tel. +7 495 946 09 54
polga@mics.msu.su

Radel Gaby

Department of Meteorology
University of Reading
Earley Gate, P.O. Box 243,
Reading RG6 6BB, UK
Tel. +44 118 378 6607
g.radel@reading.ac.uk

Rindlisbacher Theo

Federal Office of Civil Aviation
CH-3003 Bern, Switzerland
Tel. +41 31 325 93 76
theo.rindlisbacher@bazl.admin.ch

Rodriguez De Leon Ruben

Centre for Air Transport and the Environment
Loxford Tower
Lower Chatham Street
Manchester M15 6HA, UK
Tel. +44 (0)161 2473656
R.Deleon@mmu.ac.uk

Rogers Helen

Institute for Aviation and the Environment
Department of Chemistry
University of Cambridge
Lensfield Road, Cambridge, UK
Tel. +44 1223 763825
helen.rogers@atm.ch.cam.ac.uk

RUIZ Eliane

ONERA
Physics, Sensing and Instrumentation Department
Atmospheric Environment Unit
BP 72,
29, avenue de la Division Leclerc
F-92322 CHATILLON cedex, France
Tel. +33 146 734 311
Eliane.Ruiz@onera.fr

Ryman Jenny

Luftfartsstyrelsen (Swedish Civil Aviation
Authority)
Vikboplan 7
601 73 Norrköping, SWEDEN
Tel. +46 11 4152123
jenny.ryman@luftfartsstyrelsen.se

Sausen Robert

DLR- Oberpfaffenhofen
Institut für Physik der Atmosphäre
D-82234 Wessling, Germany
Tel. +49 8153 282500
robert.sausen@dlr.de

Sayer Andrew

University of Oxford
Atmospheric, Oceanic and Planetary Physics
Clarendon Laboratory
Parks Road, Oxford OX1 3PU, UK
Tel. +44 7734859851
sayer@atm.ox.ac.uk

Schlager Hans

DLR Oberpfaffenhofen
Institut fuer Physik der Atmosphaere
82234 Wessling, Germany
Tel. +49 8153 282510
hans.schlager@dlr.de

Schmid Otmar

GSF -Research Center for Environment and Health
Ingolstaedter Landstrasse 1
D-85764 Neuherberg, Germany
Tel. +49 89 3187 2557
otmar.schmid@gsf.de

Schreier Mathias

Institute of Environmental Physics and Remote Sensing
University of Bremen - FB1
P.O. Box: 330440
28334 Bremen, Germany
Tel. +49 421 2188126
schreier@iup.physik.uni-bremen.de

Schrooten Liesbeth

Vito NV
Boeretang 200
2400 Mol
Belgium
tinnie.meulemans@vito.be

Schumann Ulrich

Deutsches Zentrum
für Luft- und Raumfahrt e.V.
Institut für Physik der Atmosphäre
Oberpfaffenhofen
D-82234 Weßling
Tel. +49 8153 28 2520
ulrich.schumann@dlr.de

Shine Keith

Department of Meteorology
University of Reading
Earley Gate, Reading RG6 6BB, UK
Tel. +44 118 378 8405
k.p.shine@reading.ac.uk

Shustov Andrey

1, Zhukovsky Str.
Zhukovsky, Moscow Region,
140180, Russia
TsAGI
Tel. +7 495 5564478
shustov@tsagi.ru, shustov_a@bk.ru

Skeie Ragnhild Bieltvedt

CICERO
P.O. Box. 1129 Blindern, N-0318 Oslo,
NORWAY
Tel. +47 22 85 87 66
r.b.skeie@geo.uio.no

Streibel Martin

European Ozone Research Coordinating Unit
University of Cambridge Department of Chemistry
Lensfield Road, Cambridge CB2 1EW, UK
Tel. +44 1223 3 11 772
martin.streibel@ozone-sec.ch.cam.ac.uk

Stuber Nicola

Department of Meteorology
The University of Reading
Earley Gate, PO Box 243
Reading, Berks. RG1 6BB, UK
Tel. +44 (0) 118 378 6017
N.Stuber@reading.ac.uk

Syed Saadat

Pratt & Whitney
155 High Ridge Drive
Tolland CT 06084, USA
Tel. +1 860 871 7626
syed@pweh.com

Syrakov Dimiter

Department of Atmosphere and Hydrosphere
Composition
National Institute of Meteorology and Hydrology
66, Tzarigradsko chaussee Blvd.
Sofia 1784, BULGARIA
Tel: 8072-754, 8072-736
Tel. +359 2 975-39-86
dimiter.syrakov@meteo.bg

Ismail Raveem

Flat B
26 Norham Gardens
Oxford
OX2 6QD
UK
Tel. +44 7950 188 249
r.Ismail1@physics.ox.ac.uk

Tejero Cantero Álvaro

DLR Institute for Atmospheric Physics
Oberpfaffenhofen,
D-82234 Wessling,
Germany
+49-8153-28-1108
alvaro.tejero@dlr.de

Thomas Gareth

Atmospheric, Oceanic and Planetary Physics
Clarendon Laboratory
University of Oxford
Oxford OX1 3PU
Tel. +44 1865272892
gthomas@atm.ox.ac.uk

Thompson Terence

Neometsys
7, rue du Theatre
91300 Massy
France
Tel. +33 1-703-362-8299
terry.thompson@neometsys.fr

Unterstrasser Simon

Institut fuer Physik der Atmosphaere
DLR Oberpfaffenhofen
Muenchner Str. 20
D-82234 Wessling
Germany
Tel. +49 8153 28 2553
Simon.Unterstrasser@dlr.de

Valette Pierre

European Commission
no email

van Velthoven Peter

Royal Netherlands Meteorological Institute
KNMI
P.O. box 201
NL 3730 AE De Bilt
The Netherlands
Tel. +31-30-2206419
velthove@knmi.nl

Vancassel Xavier

ONERA
29 avenue de la Division Leclerc
92322 Chatillon cedex
France
Tel. +33 146 734 767
xavier.vancassel@onera.fr

Vazquez-Navarro Margarita

DLR Oberpfaffenhofen
Institut fuer Physik der Atmosphaere
82234 Wessling
Germany
Tel. +49 8153 28 3514
Margarita.Vazquez@dlr.de

Vieira Joao

T&E
joao.vieira@transportenvironment.org

waibel Andreas

lufthansa
andreas.waibel@dlh.de

Waitz Ian

MIT
Dept. of Aeronautics and Astronautics
77 Massachusetts Ave
Room 33-408
Cambridge MA 02139, USA
Tel. +1 617 253 0218
iaw@mit.edu

Wallington Timothy

Ford Research and Advanced Engineering,
Phys. & Environ. Sci. Dept.,
Mail Drop RIC-3083
2101 Village Road, Dearborn,
MI 48121-2053, USA
Tel. +1 313-390-5574
Fax: +1 313 323-1129
twalling@ford.com

Weimer Silke

PSI
CH-5232 Villigen
Switzerland
Tel. +41 56 310 4098
silke.weimer@psi.ch

Wey Chowen

NASA Glenn Research Center
chowen.c.vey@grc.nasa.gov

White Matthew

Department for Transport
Great Minster House
76 Marsham Street
London SW1P 4DR, UK
Tel. +44 207 944 5038
matthew.white@dft.gsi.gov.uk

Whitefield Philip

UMRCOE
G-11 Norwood Hall
University of Missouri - Rolla
1870 Miner Circle
Rolla, MO 65409, USA
Tel. +1 573 341 4340
pwhite@umr.edu

Williams Victoria

Centre for Transport Studies,
Department of Civil and Environmental
Engineering,
Imperial College London,
Exhibition Road,
London, SW7 2AZ, UK
Tel. +44 2075945924
v.williams@imperial.ac.uk

Yelvington Paul

Aerodyne Research, Inc.
45 Manning Road
Billerica, MA 01821, USA
Tel. +1 978-932-0265
paul@aerodyne.com

Index of Authors

- Anderson B.E. 252
 Anderson K. 48
 Arnold F. 83
 Aulinger A. 241
 Avallone L. 34
 Bauer H.-J. 116
 Baumann R. 83
 Baumgardner D. 34
 Behrens H.-L. 208
 Berk Knighton W. 89, 252
 Bewersdorff I. 241
 Bickerstaff C. 228
 Boardman C. 133
 Borcken J. 61
 Bovensmann H. 173
 Bows A. 48
 Butler T. 154
 Cariolle D. 107, 196
 Collins W.J. 154
 Cuenot D. 107
 Davison B. 133
 De Vlioger I. 67
 De Wilde H.P.J. 72
 Delhay D. 22
 Demirdjian B. 22
 Dentener F.J. 154
 Dessens O. 141, 147
 Dotzek N. 261
 Duda D.P. 184
 Duyzer J.H. 72
 Egelhofer R. 228
 Eleftheratos K. 160
 Ellingsen K. 154
 Endresen Ø. 208
 Eyring V. 154, 173, 208
 Ferry D. 22
 Fiebig M. 78
 Fischer H. 83
 Flores M. 34
 Franke K. 78
 Gauss M. 141, 154
 Gierens K. 214, 267, 279, 284
 Gouge J. 22
 Grainger R.G. 279
 Grewe V. 190
 Guldberg A. 273
 Gurk C. 78, 83
 Hagen D.E. 95, 247
 Hauglustaine D.A. 154
 Hensen A. 72
 Hermann R. 34
 Herndon S.C. 27, 89, 252
 Highwood E. J. 190
 Hollander J.C.Th. 72
 Huebsch W.W. 167
 Iachetti D. 289
 Int Panis L. 67
 Isaksen I.S.A. 154
 Ishaque M.M. 298
 Ismail R. 279
 Jayne J.T. 252
 Kalnajs L. 34
 Kärcher B. 267
 Karcher F. 196
 Klima K. 178
 Köhler M.O. 147
 Kok G.L. 34
 Kos G.P.A. 72
 Kraai A. 72
 Lauer A. 154
 Lauer P. 78
 Lawrence M.G. 154
 Lee D.S. 202, 208, 256, 279, 295, 304
 Lewellen D.C. 167
 Lichtenstern M. 78, 83
 Lim L. 202, 208, 256, 279
 Lobo P. 95, 247
 Mannstein H. 173, 267
 Marizy C. 141, 228
 Marr L.C. 252
 Matthias V. 241
 Mayer B. 267
 McManus J.B. 252
 Miake-Lye R.C. 27, 89, 252
 Middel J. 42
 Minnis P. 184
 Mohr C. 137
 Mohr M. 137
 Montanaro V. 289
 Mortimer P. 252
 Nelson D.D. 252
 Noland R.B. 55, 235, 298
 Noppel F. 221
 Northway M.J. 89, 252
 Olivie D. 196
 Onasch T.B. 27, 89, 252
 Owen B. 256
 Palikonda R. 184
 Paoli R. 107
 Paugam R. 107
 Pechtl S. 190
 Peeters P. M. 42
 Pejovic T. 55
 Penanhoat O. 22

- Persiantseva N.M. 101
Petzold A. 78, 83
Pitari G. 141, 289
Ponater M. 190, 202, 279
Popovicheva O.B. 101
Prévôt A.S.H. 137
Pyle J.A. 141, 147
Quante M. 241
Richter A. 154
Rodriguez De León R. 295
Rodriguez J.M. 154
Rogers H.L. 141, 147
Ross M. 34
Royer J.-F. 196
Ruiz E. 22
Salas-Mélia D. 196
Sanderson M. 154
Sausen R. 190, 202, 208, 261
Schlager H. 83
Schreier M. 173
Schrooten L. 67
Schumann U. 190
Shonija N.K. 101
Shorter J.H. 252
Singh R. 221
Speidel M. 83
Spicher U. 116
Spichtinger P. 284
Starik A.M. 101
Steller H. 61
Stevenson D.S. 154
Strahan S.E. 154
Stuber N. 190
Sudo K. 154
Sullivan J.L. 16
Suzanne J. 22
Szopa S. 154
Taylor M. 221
Teyssèdre H. 196
Thompson T. 34
Toohey D. 34
Torfs R. 67
Toumi R. 55, 235
Tselioudis G. 160
Unterstrasser S. 284
van Noije T.P.C. 154
Waitz I. 178
Wallington T.J. 16
Weimer S. 137
Weingartner E. 78
Weinzierl B. 78
Weststrate H. 72
Wey C.-L. 252
Whitefield P.D. 95, 247, 252
Whyatt D. 133
Wild O. 147, 154
Williams V. 55, 235
Wit R. C.N. 304
Wood E.C. 27, 89, 252
Wormhoudt J. 252
Worsnop D.R. 252
Yelvington P.E. 27, 89, 252
Zahniser M.S. 252
Zanis P. 160
Zerefos C.S. 160